Harald Drück · Radhakrishna G. Pillai
Manoj G. Tharian · Aysha Zeneeb Majeed
Editors

Green Buildings and Sustainable Engineering

Proceedings of GBSE 2018

Springer

Springer Transactions in Civil and Environmental Engineering

More information about this series at http://www.springer.com/series/13593

Harald Drück · Radhakrishna G. Pillai
Manoj G. Tharian · Aysha Zeneeb Majeed
Editors

Green Buildings and Sustainable Engineering

Proceedings of GBSE 2018

Springer

Editors
Harald Drück
Research and Testing Centre for Thermal
    Solar Systems (TZS), Institute of
    Thermodynamics and Thermal
    Engineering
University of Stuttgart
Stuttgart, Germany

Radhakrishna G. Pillai
Department of Civil Engineering
Indian Institute of Technology Madras
Chennai, Tamil Nadu, India

Manoj G. Tharian
Department of Mechanical Engineering
Rajagiri School of Engineering
    and Technology
Kochi, Kerala, India

Aysha Zeneeb Majeed
Department of Civil Engineering
Rajagiri School of Engineering
    and Technology
Kochi, Kerala, India

Preface

The first International Conference on Green Building and Sustainable Engineering (GBSE 2018) was held at Rajagiri School of Engineering and Technology (RSET), Kochi, India, on January 24 and 25, 2018. GBSE 2018 was jointly organized by RSET and Research and Testing Centre for Thermal Solar Systems (TZS), ITW, University of Stuttgart, Germany.

The conference was inaugurated by Dr. Syed Ibrahim, Honorary Consul of the Federal Republic of Germany, in Kerala. The conference chairs, Prof. Dr.-Ing. Harald Drück and Prof. Dr.-Ing. Varghese Panthalookaran, introduced the theme to the participants.

GBSE 2018 provided a common platform for students, academicians, researchers, green building advocates, industries, policy-makers, and architects across the globe to express their views and share their experiences in the field of sustainable engineering. The conference was a step toward achieving the dream of a clean and healthy, livable environment.

GBSE 2018 attracted many regional and international delegates, and a total of 86 abstracts were received. After an initial review, 64 papers were selected for the peer review process. The review panel included eminent academicians and experts in the field of green building and sustainable engineering from India and abroad including Germany, USA, Spain, Denmark, and China. Forty-four papers selected for the final presentation were presented in front of technical experts in eight sessions spread over two days. Program Committee selected 40 (acceptance rate 46.51%) articles that met standards set for publication, after careful discussions and considering opinions from a wide audience.

GBSE 2018 was enriched with an Indo-German dialogue on Smart and Sustainable Habitats. Mr. M. Selvarasu, Director, LEAD Consultancy and Engineering Services (India) Pvt. Ltd.; Mr. V. Suresh, Chairman, National Building Code of India; Dr.-Ing. Harald Drück, Head, TZS, University of Stuttgart, Germany; Mr. Sathish Kumar Pai, CIAL Ltd.; Dr. Jyotirmay Mathur, Department of Mechanical Engineering, MNIT Jaipur; Mr. Verghese Jacob, Chairman, STEAG Energy Services (India) Pvt. Ltd.; Prof. Dr. Michael Pfeffer, Pro-Vice Chancellor, Ravensburg-Weingarten University, Germany; Dr. Ananthakumar S., Senior Principal Scientist, NIIST; Mr. Ajay Gupta,

Head of Security Enterprises, Siemens India; Mr. Siddalingesh Kittur, Business Excellence Leader, Honeywell India; Dr. Sridhar H. V., Head, Design and Engineering, Bosch Energy and Building Solutions, India; and Ar. Mayank Barjatya, Managing Director, PrithweEarthing Center, India, presented technical sessions during the two-day program. About 50 delegates participated in the event. The Indo-German dialogue delivered high-quality, stimulating and enlightening contents.

In connection with GBSE 2018, an exhibition of smart and sustainable products was held on January 24 and 25, 2018, at Rajagiri School of Engineering and Technology, Kochi, India. Many industries gained the opportunity to exhibit their products. Companies including Latston Building Materials, Malabar Cements, Digitex, Surya Energy Solutions, IOCL, iCLEBO Intelligent Cleaning Robot, CADmarC Software Private Limited, Enagic Kangen Water, NeST Technologies, Excel Earthings, V-Guard, Solgen Energy, and Noel had set up stalls in the exhibition.

GBSE 2018 also included two pre-conference workshops. The first workshop was on "Solar and Electric Water Boats" by Mr. Arjun Bhaskar, Marketing Manager, Navalt Boat Ltd. The design, technical, and safety features of solar water boats were explained by Mr. Bhaskar. The second workshop was on "Sustainable Building Technology" by Mr. T. P. Madhusudhanan, Chief Consultant of Habitat Group. The session highlighted the use of bamboo as reinforcing material and various other alternative methods of construction.

We would like to thank all the Steering Committee members, Technical Committee members, and additional reviewers for their hard work in reviewing papers carefully and rigorously. In addition, we thank all the sponsors of GBSE 2018, especially STEAG Energy Services (India) Pvt. Ltd., NeST Technologies, CIAL Ltd., and the Kerala State Council for Science, Technology and Environment (KSCSTE).

We hope that you will find this proceedings to be a valuable resource in your professional, research, and educational activities.

Stuttgart, Germany	Harald Drück
Chennai, India	Radhakrishna G. Pillai
Kochi, India	Manoj G. Tharian
Kochi, India	Aysha Zeneeb Majeed

Organizing Committee

International Conference on Green Buildings and Sustainable Engineering
GBSE 2018
&
Indo-German Dialogue and Exposition on Smart and Sustainable Habitat for
Smart Cities
SASH 2018

The International Conference on Green Buildings and Sustainable Engineering (GBSE 2018) is organized by the departments of Mechanical Engineering and Civil Engineering, Rajagiri School of Engineering and Technology, Kochi, India, together with the Research and Testing Centre for Thermal Solar Systems (TZS), Institute of Thermodynamics and Thermal Engineering (ITW), University of Stuttgart, Germany, with the theme Transforming Our Built Environment Through Innovation and Integration Toward a Smart and Sustainable Future.

Patrons

Rev. Dr. Mathew Vattathara CMI
Rev. Fr. Jose Alex CMI

General Chairs

Dr. A. Unnikrishnan, RSET, India
Prof. C. V. R. Murty, Director, IITJ, India

Program Chairs

Dr.-Ing. Harald Drück, University of Stuttgart, Germany
Dr.-Ing. Fr. Varghese Panthalookaran, RSET

Steering Committee

Dr. Abraham Thomas, RSET, India
Dr. Antony V. Varghese, RSET, India

Dr. Benny Raphael, IITM, India
Prof. C. G. Nandakumar, CUSAT, India
Prof. Eldho T. I., IITB, India
Prof. Frank Spate, Amberg-Weiden University, Germany
Prof. Ganesh L. S., IITM, India.
Prof. Dr.-Ing. Gerhard Seelmann, Hochschule Aalen, Germany
Dr. Jaison Jacob, RSET, India
Fr. Dr. Jaison Paul Mulerickal CMI, RSET, India
Dr. John Jose, IITG, India
Dr. John M. George, RSET, India
Prof. Dr.-Ing. Jürgen Trost, Hochschule Aalen, Germany
Prof. Dr. sc. techn. Michael Pfeffer, Ravensburg-Weingarten University, Germany
Prof. K. A. Ouseph, RSET, India
Dr. Mohammad Arif Kamal, Aligarh Muslim University, India
Dr. Ramesh Rayudu, Victoria University of Wellington, New Zealand
Prof. Rupen Goswami, IITM, India
Dr. Thankachan T. Pullan, RSET, India
Dr. Unnikrishnan P. C., RSET, India
Dr. Varghese Paul, RSET, India

Technical Program Committee

Dr. Amba Shetty, NITK, India
Prof. Amritanshu Shriwastav, IITB, India
Dr. A. Veeraragavan, IITM, India
Prof. Bale Reddy, University of Ontario, Canada
Dr. Beena P. R., CET, TVM
Dr. Bharati Raj, MCE,TVM
Dr. Bino I. Koshy, RIT, India
Dr. Brijesh Paul, MACE, India
Dr. Daniel Mugnier, TECSOL, Perpignan, France
Mr. David Kaufman, National Solar Institute, Energy Solutions, USA
Dr. Deepa Raj, CET, TVM
Dr.-Ing. Elke Malleier, Sustainability and Green Building Consultant, Singapore
Dr. Girija K., CET, TVM
Dr. Glory Joseph, CUSAT, India
Dr. Himadri Roy, CMERI, Durgapur, India
Dr. Honey John, CUSAT, India
Dr. Jayadas N. H., CUSAT, India
Prof. Jean-Christophe Hadorn, EPFL, Switzerland
Dr. Job Thomas, CUSAT, India
Prof. Dr.-Ing. Jörg Londong, Faculty of Civil Engineering, Bauhaus-Universität Weimar, Germany

Dr. Kavitha P. E., SNGC, India
Mr. Ken Guthrie, Director of Sustainable Energy Transformation Pty. Ltd., Australia
Dr. Kim Augustin, Hamburg Wasser, Hamburg, Germany
Dr. Lakshman Nandagiri, NITK, India
Mr. Lex Bosselaar, The Dutch IEA SHC Executive Committee member, Netherlands
Dr. L. Rekha, GEC Thrissur, India
Prof. Luisa F. Cabeza, University of Lleida, Spain
Dr. M. Satyakumar, MBCET, India
Dr. M. V. L. R. Anjaneyulu, NIT Calicut, India
Dr. Manju V. S., CET, India
Dr. Meril George, SCMS, India
Dr. Mini Soman, CET, TVM
Dr. Nisa Salim, Deakin University, Australia
Dr. Nishar Hameed, University of Swinburne, Australia.
Dr. Padmakumar R., CET, India
Mr. Qingtai Jiao, Jiangsu Sunrain Solar Energy Co., Ltd., China
Dr. Radhakrishna Panicker M. R., CUSAT, India
Dr. Rakesh J. Pillai, NITW, India
Dr. Ravi K., IITG, India
Dr. Ruby Abraham, MCE, India
Prof. Sandra Contreras, Universitat Rovira i Virgili, Spain
Dr. Santhosh Thampi, NIT Calicut, India
Dr. Smitha K. K., SNGCE, India
Dr. Sobha Cyrus, CUSAT, India
Dr. Suhas Ranjan Dey, IITH, India
Prof. Sumathi Suresh, IITB, India
Dr. Suresh A. Kartha, IITG, India
Mr. Thomas Giese, Hamburg Wasser, Hamburg, Germany
Prof. Dr. Ursula Eicker, University of Applied Sciences Stuttgart, Stuttgart
Prof. Yogendra Shastri, IITB, India

Track Chair

Dr. Ajith Kumar. A., RSET, India
Dr. Benny Mathews Abraham, CUSAT, India
Prof. Dr.-Ing. Harald Mandel, Duale Hochschule Baden-Württemberg, Germany
Dr.-Ing. Henner Kerskes, University of Stuttgart, Germany
Dr. Lakshman Nandagiri, NITK, India
Dr. Santhosh Thampi, NIT Calicut, India
Prof. Simon Furbo, Technical University of Denmark
Dr. Sreekumar V. M., RSET, India
Mr. Werner Weiss, Director, AEE—Institute for Sustainable Technologies, Austria
Prof. Zinian He, Beijing Solar Energy Research Institute, China

Event Chairs

Mr. Jibin Noble, RSET, India
Ms. Sindhu U., RSET, India

Publication Chairs

Dr. Aysha Zeneeb Majeed, RSET, India
Dr.-Ing. Harald Drück, University of Stuttgart, Germany
Dr. Manoj G. Tharian, RSET, India
Dr. Radhakrishna G. Pillai, IITM, India

Workshop Chairs

Mr. Arun T. Moonjely, RSET, India
Mr. Jithin P. Narayanan, RSET, India

Publicity Committee

Ms. Anitha Varghese, RSET, India
Mr. Bibin Hezakiel, RSET, India
Ms. Elsa Paul, RSET, India
Mr. Jayakumar J., RSET, India
Mr. Jeffin Johnson, RSET, India
Mr. Jibin Joseph, RSET, India
Mr. John Paul C. D., RSET, India
Ms. Kavitha M., RSET, India
Mr. Krishna Das, RSET, India
Mr. Mathew Baby, RSET, India
Mr. Tony Chacko, RSET, India
Mr. UdaySankar K., RSET, India
Mr. Vishnu Sankar, RSET, India

Finance Chair

Mr. Sidheek P. A., RSET, India
Ms.Tressa Kurian, RSET, India

Indo-German Dialogue—Program Committee

Mr. Abinson Paul N., RSET, India
Mr. Akash James, RSET, India
Ms. Anu Mathew, RSET, India
Mr. Arun Balan, RSET, India
Ms. Aswathy G., RSET, India
Ms. Deepthi I. Gopinath, RSET, India
Mr. Felix Xavier, RSET, India
Mr. Ginnes K. John, RSET, India
Mr. Harikrishnan C., RSET, India
Mr. Jaison M. T., RSET, India
Mr. James Mathew, RSET, India
Mr. Jebin Francis, RSET, India
Mr. Jiju K. Mathew, RSET, India
Mr. Jithin K. Francis, RSET, India
Mr. Jobin Jose, RSET, India
Mr. Jose Steevson Rodrigues, RSET, India
Ms. Joseena Joseph, RSET, India
Mr. Krishnakumar M. R., RSET, India
Mr. Krishnaraj P. P., RSET, India
Mr. Manu Joseph, RSET, India
Ms. Maria Michael, RSET, India
Mr. Mrudhul Mohan, RSET, India
Mr. Naveen N., RSET, India
Mr. Nithin P. Vijayan, RSET, India
Dr. Nivish George, RSET, India
Mr. Rathish T. R., RSET, India
Mr. Rejeesh T. Chacko, RSET, India
Mr. Sabeesh Robinson, RSET, India
Mr. Saji, RSET, India
Mr. Senjo Manuel, RSET, India
Dr. Shibu P. P., RSET, India
Mr. Vineeth Krishna P., RSET, India

Contents

Editors and Contributors

About the Editors

Dr.-Ing. Harald Drück is a mechanical engineer who has been working at the Institute of Thermodynamics and Thermal Engineering (ITW), University of Stuttgart, Germany, for more than 20 years. Since 1999, he has been the Head of the Research and Testing Centre for Thermal Solar Systems (TZS), ITW, University of Stuttgart, Germany. His main research interests lie in the field of solar thermal technology, focusing on advanced heating and cooling systems, thermal energy storage, and the development of performance testing methods as well as energy-efficient solar buildings. He has authored or co-authored around 300 publications in the fields of solar thermal energy and heat storage. He is the convenor of several German and European working groups related to the standardization and testing of solar thermal systems and components, such as the Solar Keymark Network, the Global Solar Certification Network, and the Solar Certification Fund. He acts as an advisor to several high-level international organizations, is chairman or member of the scientific board of several conferences and workshops, and teaches a highly successful postgraduate course on solar thermal energy at the University of Stuttgart, Germany. Furthermore, he was one of the initiators of the German and European solar thermal technology platforms and is currently a member of the steering committees of both platforms. In addition to his activities at the university, he is the director of SWT—Solar- und Wärmetechnik Stuttgart. SWT is a spin-off company of ITW and is a service provider in the field of solar thermal energy.

Dr. Radhakrishna G. Pillai is an associate professor at the Department of Civil Engineering, Indian Institute of Technology Madras. After completing his M.S. and Ph.D. in Civil Engineering at Texas A&M University, he worked as a postdoctoral researcher at Texas A&M Transportation Institute and Oregon State University's School of Civil and Construction Engineering, before joining IIT Madras. His research interests include the repair and rehabilitation of concrete structures, monitoring and prevention of corrosion, and development of methods to test for

corrosion. He has published numerous research papers in international journals and conferences, co-authored research reports, and served as an editor for a number of conference proceedings.

Dr. Manoj G. Tharian associate professor in the Department of Mechanical Engineering at Rajagiri School of Engineering and Technology (RSET), Kochi, India, completed his B.Tech. in Mechanical Engineering at the Government Engineering College, Thrissur, in 1995. He worked as a project associate at the Department of Ocean Engineering, IIT Madras, for a short period, before completing his postgraduate diploma in Marine Engineering at the Marine Engineering and Research Institute, Mumbai, in 1996. As a marine engineer he has worked with Chevron Shipping Company, San Francisco, and Anglo-Eastern Ship Management, Hong Kong, on merchant ships from 1996 to 2003. He completed his master's in Computer-Aided Structural Analysis and Design and Ph.D. at the Department of Ship Technology, Cochin University of Science and Technology. He has fourteen years of teaching experience and also has taken classes for postgraduate students at the university.

Dr. Aysha Zeneeb Majeed is currently an associate professor at RSET where she has been working since 2005. She has been in the field of teaching since 2003 and worked as a structural design consultant for two years prior to teaching. She obtained her B.Tech. in Civil Engineering from National Institute of Technology Calicut in 1999, with a proficiency award in academics, and obtained her M.Tech. in Construction Engineering and Management from CUSAT in 2009. She completed her Ph.D. in Structural Engineering at IIT Madras.

Contributors

R. Abhijith Department of Civil Engineering, Viswajyothi College of Engineering and Technology, Ernakulam, Kerala, India

Margaret Abraham Civil Engineering, Vimal Jyothi College of Engineering, Kannur, India

Nikil Thomas Abraham Department of Computer Science and Engineering, Amal Jyothi College of Engineering, Kanjirapally, Kottayam, Kerala, India

N. Aby Biju Mechanical Engineering, Rajagiri School of Engineering and Technology, Kochi, India

P. V. Afzal National Institute of Technology Calicut, Kozhikode, Kerala, India

Monika Agrawal Department of Renewable Energy, Rajasthan Technical University, Kota, India

Shaun Thomas Alex Rajagiri School of Engineering and Technology, Kochi, India

Ashwin Alias Department of Civil Engineering, Viswajyothi College of Engineering and Technology, Ernakulam, Kerala, India

Amaljith National Institute of Technology Calicut, Kozhikode, Kerala, India

Shivamanth Angadi Applied Mechanics Department, S V National Institute of Technology, Surat, Gujarat, India

P. Arun Mechanical Engineering Department, National Institute of Technology Calicut, Kozhikode, India

M. Asok Rajkumar Dean—R&D, Gnanamani College of Technology, Namakkal, Tamil Nadu, India

R. Aswathy Cochin University of Science and Technology, Cochin, Kerala, India

K. R. Athul Krishna Mechanical Engineering, Rajagiri School of Engineering and Technology, Kochi, India

Arun Balan Civil Engineering, Mangalam College of Engineering, Kottayam, India; Civil Engineering, Rajagiri School of Engineering and Technology, Kochi, India

P. Balasubramanian Department of Biotechnology & Medical Engineering, NIT Rourkela, Odisha, India

K. S. Beena Cochin University of Science and Technology, Cochin, Kerala, India

Melbin Benny National Institute of Technology Calicut, Kozhikode, Kerala, India

Kriti Bhalla Ramaiah Institute of Technology, Bangalore, India

A. B. Bhasi CUSAT, Cochin, India

Sam Biju National Institute of Technology Calicut, Kozhikode, Kerala, India

Agnimitra Biswas National Institute of Technology, Silchar, Assam, India

Sanjana Sangamitra Chandra VIT University, Chennai, India

R. K. Chethan Gowda Department of Civil Engineering, Ramaiah University of Applied Sciences, Bengaluru, Karnataka, India

Bharathi Kannamma Chezian VIT University, Chennai, India

K. Chithra Department of Architecture & Planning, NIT Calicut, Kozhikode, Kerala, India

Sounak Kumar Choudhury Department of Mechanical Engineering, Indian Institute of Technology Kanpur, Kanpur, India

Sobha Cyrus Civil Engineering, School of Engineering, CUSAT, Kochi, Kerala, India

Babitha Davis Rajagiri School of Engineering and Technology, Kochi, India

Mayank K. Desai Applied Mechanics Department, S V National Institute of Technology, Surat, Gujarat, India

L. Divakar Department of Civil Engineering, Ramaiah University of Applied Sciences, Bengaluru, Karnataka, India

Goudappa R. Dodagoudar Department of Civil Engineering, IIT Madras, Chennai, India

Anand Prakash Dwivedi Department of Mechanical Engineering, Indian Institute of Technology Kanpur, Kanpur, India

V. J. Fainusa Rajagiri School of Engineering and Technology, Civil Engineering, Ernakulam, India

Kevin Shelly Fernandez Rajagiri School of Engineering and Technology, Kochi, India

Rushikesh Fopase Department of Biotechnology & Medical Engineering, NIT Rourkela, Rourkela, India

Jeffin Francis Mechanical Engineering, Rajagiri School of Engineering and Technology, Kochi, India

Sajo Francis FACT RCF Building Products Ltd, FACT CD Campus, Kochi, India

Veeresh Fuskele Maulana Azad National Institute of Technology, Bhopal, MP, India

Iragavarapu Akhil Gargey Department of Biotechnology and Medical Engineering, NIT Rourkela, Rourkela, Odisha, India

Joel George Mechanical Engineering Department, National Institute of Technology Calicut, Kozhikode, India

Deepthi I Gopinath Civil Engineering, Mangalam College of Engineering, Kottayam, India; Civil Engineering, Rajagiri School of Engineering and Technology, Kochi, India

Rajat Gupta Department of Mechanical Engineering, National Institute of Technology Mizoram, Aizawl, India

Apurva Hiravennavar Civil Engineering Department, BMIET, Surat, India

Dash Indira Department of Life Science, NIT Rourkela, Rourkela, Odisha, India

Nidhi Jain Department of Applied Mechanics, Government College of Engineering, Amravati, Maharashtra, India

M Geo James Department of Computer Science and Engineering, Amal Jyothi College of Engineering, Kanjirapally, Kottayam, Kerala, India

R. Jayabalan Department of Life Science, NIT Rourkela, Rourkela, Odisha, India

P. N. Jithin Mechanical Engineering, Rajagiri School of Engineering and Technology, Kochi, India

Bijil John Mechanical Engineering, Rajagiri School of Engineering and Technology, Kochi, India

Bony John Cochin University of Science and Technology, Kochi, Kerala, India

Anupama Johnson Mechanical Engineering, Rajagiri School of Engineering and Technology, Kochi, India

Albin Joy National Institute of Technology Calicut, Kozhikode, Kerala, India

Anu Joy Rajagiri School of Engineering and Technology, Civil Engineering, Ernakulam, India

Paresh Kale Department of Electrical Engineering, NIT Rourkela, Rourkela, India

Uday Sankar Kandolath Rajagiri School of Engineering & Technology, Kochi, Kerala, India

Anjan Karmakar National Institute of Technology, Aizawl, Mizoram, India

M. Kavitha Civil Engineering, Rajagiri School of Engineering and Technology, Kakkanad, Kochi, Kerala, India

S. N. Khante Department of Applied Mechanics, Government College of Engineering, Amravati, Maharashtra, India

T. Krishnadath National Institute of Technology Calicut, Kozhikode, Kerala, India

P. P. Anil Kumar NIT, Calicut, India

Tarun Kumar CPDM, Indian Institute of Science, Bangalore, India

Basil Kuriachen National Institute of Technology, Aizawl, Mizoram, India

Tressa Kurian Rajagiri School of Engineering and Technology, Kochi, India

Nina Lazar Department of Architecture & Planning, NIT Calicut, Kozhikode, Kerala, India

Aysha Zeneeb Majeed Rajagiri School of Engineering and Technology, Kochi, India

Shweta Manchanda School of Planning and Architecture, New Delhi, India

Nissy Susan Mani Civil Engineering, Vimal Jyothi College of Engineering, Kannur, India; Civil Engineering, Mangalam College of Engineering, Kottayam, India

P. S. Manoharan Department of Electrical and Electronics Engineering, Thiagarajar College of Engineering, Madurai, Tamil Nadu, India

H. C. Maruthi Department of Civil Engineering, Ramaiah University of Applied Sciences, Bengaluru, Karnataka, India

Khushal Matai School of Planning and Architecture, New Delhi, India

Amala V. Mathew Rajagiri School of Engineering and Technology, Kochi, India

Anu Mathew Civil Engineering, Mangalam College of Engineering, Kottayam, India; Civil Engineering, Rajagiri School of Engineering and Technology, Kochi, India

Jeswant Mathew Mechanical Engineering, Rajagiri School of Engineering and Technology, Kochi, India

Maria Michael Rajagiri School of Engineering and Technology, Civil Engineering, Ernakulam, India

Laxman Mishra Department of Mechanical Engineering, National Institute of Technology Mizoram, Aizawl, India

Vishal Mishra Vijaya Vittala Institute of Technology, Bangalore, India

Monalisha Mohanta Department of Electrical Engineering, NIT Rourkela, Rourkela, India

C. Muraleedharan Mechanical Engineering Department, National Institute of Technology Calicut, Kozhikode, Kerala, India

S. Murugan Department of Mechanical Engineering, NIT Rourkela, Rourkela, Odisha, India

B. Nagesh Department of Civil Engineering, Ramaiah University of Applied Sciences, Bengaluru, Karnataka, India

Ashwath Nambiar Mechanical Engineering, Rajagiri School of Engineering and Technology, Kochi, India

Suman Nayak Department of Biotechnology & Medical Engineering, NIT Rourkela, Rourkela, India

M. K. Nirmal Mechanical Engineering, Rajagiri School of Engineering and Technology, Kochi, India

N. Nirmal National Institute of Technology Calicut, Kozhikode, Kerala, India

Jibin Noble Mechanical Engineering, Rajagiri School of Engineering and Technology, Kakkanad, Kochi, Kerala, India

Kar Parthsarathi Department of Mechanical Engineering, NIT Rourkela, Rourkela, Odisha, India

Akshaya Paul Rajagiri School of Engineering and Technology, Civil Engineering, Ernakulam, India

Jibin T. Philip National Institute of Technology, Aizawl, Mizoram, India

Krishna Kant Prasad Department of Metallurgical & Materials Engineering, National Institute of Technology Karnataka, Surathkal, PO Srinivasnagar, Mangalore, India

Abhishek Pulgur Department of Civil Engineering, Ramaiah University of Applied Sciences, Bengaluru, Karnataka, India

C. Irine Raju Rajagiri School of Engineering and Technology, Civil Engineering, Ernakulam, India

S. Rangabhashiyam Department of Biotechnology & Medical Engineering, NIT Rourkela, Odisha, India

Jananee Rangaswamy Ramaiah Institute of Technology, Bangalore, India

K. V. S. Rao Department of Renewable Energy, Rajasthan Technical University, Kota, India

Ashikha Raoof NIT, Calicut, India

S. Sofana Reka VIT University, Chennai, India

Vishnu Sankar Mechanical Engineering, Rajagiri School of Engineering and Technology, Kochi, Ernakulam, India

R. M. Sarviya Maulana Azad National Institute of Technology, Bhopal, MP, India

Bharat Kumar Saxena Department of Renewable Energy, Rajasthan Technical University, Kota, India

Yogita Sharma Department of Renewable Energy, Rajasthan Technical University, Kota, India

Abhijit Sinha Department of Mechanical Engineering, National Institute of Technology Mizoram, Aizawl, India

Nikhil Sivaramakrishnan Civil Engineering, Government Engineering College, Kannur, Kannur, Kerala, India

Chandresh H. Solanki Applied Mechanics Department, S V National Institute of Technology, Surat, Gujarat, India

R. Sreepriya Electrical and Electronics Engineering, Rajagiri School of Engineering and Technology, Kochi, India

Subin Suresh Department of Computer Science and Engineering, Amal Jyothi College of Engineering, Kanjirapally, Kottayam, Kerala, India

G. Swagathnath Department of Biotechnology and Medical Engineering, NIT Rourkela, Rourkela, Odisha, India

T. N. Syamala Department of Civil Engineering, Cochin University of Science and Technology, Cochin, Kerala, India

Ruby Maria Syriac CUSAT, Cochin, India

Nassif Nazeer Thaickavil Department of Civil Engineering, Cochin University of Science and Technology, Cochin, Kerala, India

Vineetha Thankachan Department of Civil Engineering, Viswajyothi College of Engineering and Technology, Ernakulam, Kerala, India

Job Thomas Department of Civil Engineering, School of Engineering, Cochin University of Science and Technology, Cochin, Kerala, India

Rony N Thomas Department of Mechanical Engineering, SJCET, Palai, Kerala, India

Anitha Varghese Department of Civil Engineering, Rajagiri School of Engineering and Technology, Cochin, Kerala, India

James Varghese Cochin University of Science and Technology, Kochi, Kerala, India

J. Vishnupriyan Department of Electrical and Electronics Engineering, Thiagarajar College of Engineering, Madurai, Tamil Nadu, India

Part I
Smart and Sustainable Energy Technologies

LST Mapping of SPV to Gauge Their Influence on Near-Surface Air Temperature of New Delhi City

Khushal Matai and Shweta Manchanda

1 Introduction

Solar energy is at the forefront of the technological developments in the field of renewable energy due to its abundance all over the world. Recent estimates of achievable solar power in the world range from 400 to 8,800 TW —current system performance; topographic limitations; and environmental, land use constraints [1]. It is also one of the few renewable energy sources that can be implemented on a large scale within cities themselves.

India is endowed with vast solar energy potential. Most parts of the country have about 300 sunny days and the average solar radiation incident over the land is in the range of 4–7 kWh per day [2]. With an objective of increasing energy security, reducing fossil fuel imports and a cleaner environment, the Ministry of New and Renewable Energy, has set an ambitious target of 100,000 MW installation, out of which 40,000 MW is solar rooftop PV installation, in India by 2022.

Driven by various national schemes and rising energy crisis, solar panels have now started becoming integral part of the urban fabric. Solar panels absorb solar energy to produce energy, either in the form of heat (in case of solar thermal panels) or in the form of electricity. Thus, they modify the energy balance of the urban surface in contact with the atmosphere, and so possibly influence the urban microclimate. They also change the radiation received by the roof and influence the overall heat fluxes (radiative and convective) to the atmosphere. The impact of these plants on the microclimate of the area, specifically the urban heat island effect, is being speculated, but has not been researched yet.

This chapter focuses on mapping the solar photovoltaic installations in the city of New Delhi, the capital of India, to gauge their influence on the near-surface temperature.

K. Matai (✉) · S. Manchanda
School of Planning and Architecture, New Delhi, India
e-mail: arkhushal@live.com

2   Urban Heat Island Effect and SPV

Rapid urbanization and industrialization have resulted in warmer cities. The urban heat island effect (UHIE) is defined as the rise in temperature within man-made areas [3]. Increased temperatures have a negative effect on the micro-climate and human health.

Effect of UHIE on the Surroundings Few studies considering the relation of SPV and heat island effect in deserts as well as urban areas have produced a mixed bag of results. Turney and Fthenakis investigated 32 impacts from the life-stages of solar farms [4], which have been categorized as either beneficial or neutral, except for the "local climate" effects for which they concluded that research and observation are needed (Table 1).

Another study arrives at the conclusion that the processes triggered by solar panels have consequences that modulate the global atmospheric circulation, resulting in changes in regional precipitation [1] (see Fig. 1). The warming in India and eastern Australia up to 1 °C is associated with a precipitation feedback on land. Precipitation is reduced in these two regions when the solar panels are installed. This reduces the evaporative cooling on land and leads to warming [1].

2.1   Selection of the Study Area

The National Capital Territory of Delhi is 97.5% urbanized [5], lying between latitude 28.6139°N and longitude 77.2090°E. The density varies from 4,000 to 36,000 persons/km^2 [6].

Table 1 Impacts to climate change from solar power, relative to traditional US power generation [4]

Impact category	Effect relative to traditional power	Beneficial or detrimental	Priority	Comments
Global climate				
CO_2 emissions	Reduces CO_2 emissions	Beneficial	High	Strong benefit
Other GHG emissions	Reduces GHG emissions	Beneficial	High	Strong benefit
Change in surface albedo	Lower albedo	Neutral	Low	Low magnitude of the effect
Local climate				
Change in surface albedo	Lower albedo	Unknown	Moderate	Needs research and observation
Other surface energy flows	Unknown	Unknown	Low	Needs research and observation
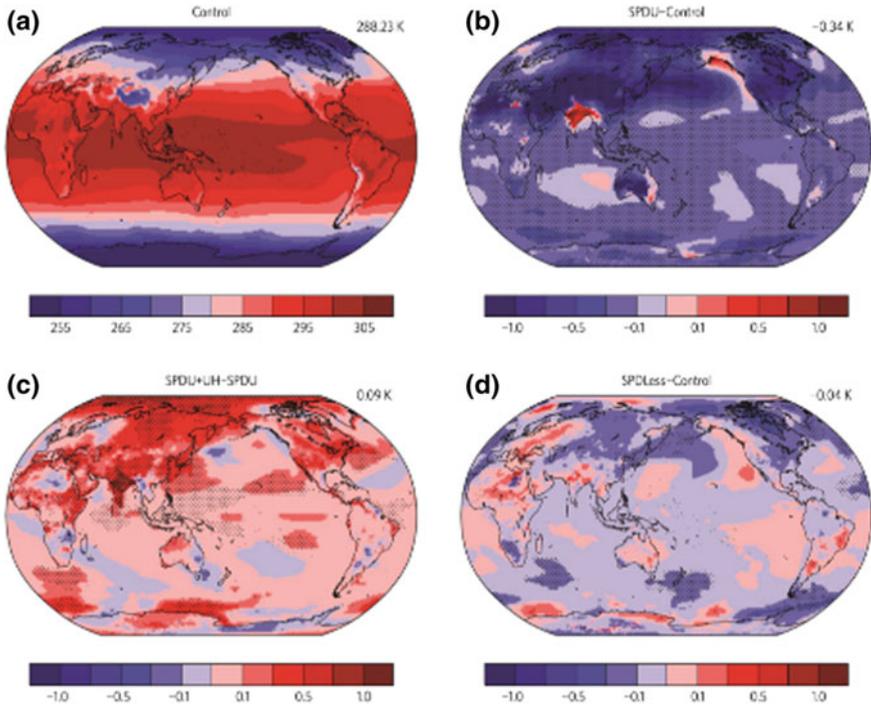
Fig. 1 Surface temperature anomalies [1]. **a** Surface temperature in the control experiment.
b Surface temperature anomaly relative to the control experiment in the SPDU experiment.
c Surface temperature anomaly relative to the SPDU experiment in +UH experiment. **d** Surface
temperature anomaly relative to the control experiment in the SPD less experiment. The numbers
at the upper right corner of each panel represent the global average

With the push to achieve the solar photovoltaic installation targets, Delhi, being
the national capital along with a high-energy demand, is in the center of such
proposals. The installations could compound the urban heat island effect or provide
some respite from the temperature increase. Whichever way the pendulum may
swing, it will create intense ripple effect. Therefore, the city was selected for the
research. The climate of Delhi is an overlap between monsoon-influenced humid
subtropical (Köppen climate classification Cwa) and semiarid (Köppen climate
classification BSh), with high variation between summer and winter temperatures
and precipitation (see Table 2).

2.2 Land Surface Temperature

Land surface temperature (LST) is defined as the temperature felt when the land
surface is touched with the hand or the skin temperature of the ground [8]. The

Table 2 Climate data of New Delhi [7]

	January	February	March	April	May	June	July	August	September	October	November	December
Avg. Temperature (°C)	14.2	16.9	22.7	28.6	33.5	34.3	31.1	29.8	29.2	25.8	20.1	15.6
Min. Temperature (°C)	7.3	10.1	15.1	20.9	26.4	28.6	27.1	26	24.5	18.6	11.7	7.9
Max. Temperature (°C)	21.2	23.8	30.3	36.3	40.6	40	35.2	33.6	34	33	28.6	23.4
Avg. Temperature (°F)	57.6	62.4	72.9	83.5	92.3	93.7	88.0	85.6	84.6	78.4	68.2	60.1
Min. Temperature (°F)	45.1	50.2	59.2	69.6	79.5	83.5	80.8	78.8	76.1	65.5	53.1	46.2
Max. Temperature (°F)	70.2	74.8	86.5	97.3	105.1	104.0	95.4	92.5	93.2	91.4	83.5	74.1
Precipitation / Rainfall (mm)	15	10	14	3	11	42	205	246	112	26	3	6

The precipitation varies 243 mm between the driest month and the wettest month. The average temperatures vary during the year by 20.1 °C.

surface urban heat islands, being the lowest layer of the urban atmosphere, influence the comfort of the inhabitants. LST is an important factor in many areas of studies, such as global climate change, hydrological and agricultural processes, and urban land use/land cover. It could be understood as a combination of green vegetation, water surfaces, impervious surface materials, and soil surface [9].

Database and Methodology Land surface temperature (LST) extraction of Delhi NCT is done with Landsat-8 datasets for a period of 4 years, starting from April 2013 to June 2017. The Landsat 8 satellite which was successfully launched on January 11, 2013, images the entire Earth, every 16 days with two push-broom instruments: The Operational Land Imager (OLI) and Thermal Infrared Sensor (TIRS).

Extracting Land Surface Temperature In this study, thermal infrared (TIR) band 10 of Landsat-8 highest quality Level-1 data is used for brightness temperature and surface temperature estimation, whereas band 4 (Red) and band 5 (Near Infrared) have been used for Normal Difference Vegetation Index (NDVI). Conversion process of different images for the required data is done in ArcGIS Desktop.

LST of 3 sites was extracted, having different land use and surroundings such as roads, a water body, and green area in Delhi NCT region. The 3 sites, i.e., Terminal 3 Indira Gandhi International Airport, Gas power station—IP Estate and NTPC Piyala Power Plant—Jajru are named L 01, L 02, and L 03, respectively.

1. **OLI and TIRS at Sensor Spectral Radiance**: Images are processed in units of absolute radiance using 32-bit floating-point calculations [10]. These values are then converted to 16-bit integer values in the finished Level 1 product. These values can then be converted to spectral radiance using the radiance scaling factors provided in the metadata file:

$$L_\lambda = M_L * Q_{cal} + A_L \qquad (1)$$

where

L_λ Spectral radiance (W/(m^2 * sr * μm))

M_L Radiance multiplicative scaling factor for the band (RADIANCE_MULT_BAND_n from the metadata)

A_L Radiance additive scaling factor for the band (RADIANCE_ADD_BAND_n from the metadata)

Q_{cal} L1 pixel value in DN

2. **OLI Top of Atmosphere Reflectance**: Similar to the conversion to radiance, the 16-bit integer values in the L1 product can also be converted to TOA reflectance (see Fig. 2). The following equation is used to convert Level 1 DN values to TOA reflectance:

$$\rho\lambda' = M\rho * Q_{cal} + A\rho \qquad (2)$$

where

$\rho\lambda'$ TOA Planetary Spectral Reflectance, without correction for solar angle (Unitless).

$M\rho$ Reflectance multiplicative scaling factor for the band (REFLECT ANCEW_MULT_BAND_n from the metadata).

$A\rho$ Reflectance additive scaling factor for the band (REFLECT ANCE_ADD_BAND_N from the metadata).

Q_{cal} L1 pixel value in DN.
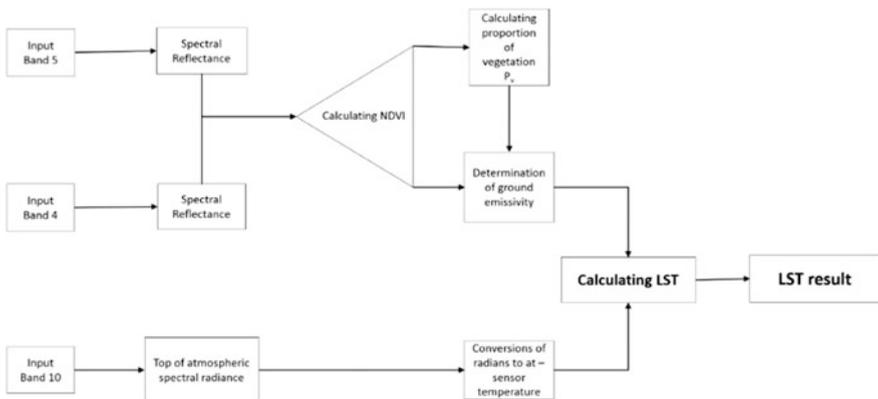
Fig. 2 Flow chart for LST retrieval

Once a solar elevation angle is chosen, the conversion to true TOA reflectance is as follows:

$$\rho\lambda = \frac{\rho\lambda'}{\sin\theta} \tag{3}$$

$\rho\lambda$ TOA Planetary Reflectance (Unitless)
θ Solar Elevation Angle (from the metadata, or calculated)

3. **TIRS Top of Atmosphere Brightness Temperature**: TIRS data can also be converted from spectral radiance (see Fig. 2) to brightness temperature, which is the effective temperature viewed by the satellite under an assumption of unity emissivity. The conversion formula is as follows:

$$T = \frac{K_2}{\ln\left(\frac{K_1}{L_\lambda} + 1\right)} \tag{4}$$

where

T TOA Brightness Temperature, in K
L_λ Spectral radiance (W/(m^2 * sr * μm))
K_1 Thermal conversion constant for the band (K1_CONSTANT_BAND_n from the metadata)
K_2 Thermal conversion constant for the band (K2_CONSTANT_BAND_n from the metadata)

4. **Normal Difference Vegetation Index (NDVI) calculation**: In order to calculate NDVI, near-infrared band (NIR) and red band are required. The NDVI calculation is important as it is the first step in calculating proportion of vegetation and land surface emissivity (see Fig. 2).

$$NDVI = \frac{\{NIR\ (band\ 5) - R(band\ 4)\}}{\{NIR(band\ 5) + R(band\ 4)\}} \tag{5}$$

5. **Land surface emissivity calculation**: When the NDVI value is between 0.2 and 0.5, the pixel is a mixture of bare soil and vegetation. In this case, the emissivity is calculated according to the proportion of bare soil to vegetation [11].

$$\varepsilon_\lambda = \varepsilon_{v\lambda}P_v + \varepsilon_{s\lambda}(1 - P_v) + c_\lambda \tag{6}$$

where

ε_v Vegetation emissivity
ε_s Soil emissivity
C Surface roughness
P_V Proportion of vegetation

with the vegetation proportion, P_v; calculated from [12] where $NDVI_{min}$ and $NDVI_{max}$ are the NDVI values for bare soil and full vegetation, respectively [13], suggested using $NDVI_{min} = 0.2$ and $NDVI_{max} = 0.5$ for global-scale remote-sensing applications.

$$P_v = \left[\frac{NDVI - NDVI_{min}}{NDVI_{max} - NDVI_{min}} \right]^2 \qquad (7)$$

6. **Land Surface Temperature (LST) calculation**: This calculation is done by single window algorithm (see Fig. 2).

$$T_s = \frac{BT}{\left\{ 1 + \left[\left(\frac{\lambda BT}{\rho} \right) \ln \varepsilon_\lambda \right] \right\}} \qquad (8)$$

where

T_s LST in Celsius
BT   At sensor brightness temperature (°C)
λ Wave length of emitted radiance
ε_λ Emissivity
ρ 1.438×10^{-2} m K.

3   Results and Discussion

Three study areas were selected in the city (see Fig. 3). Terminal 3, Indira Gandhi International Airport (L 01), is located in the suburbs of Palam, which lies in south-west of Delhi. The solar power plant commissioned in January 2014 had initial installed capacity of 2.14 MW, which grew to 7.84 MW by 2017. Majority of the site is surrounded by barren land. The runway is on the Northern side and on Southern side across the Urban Extension Road-II is a residential area.

The gas turbine power station (L 02) is located in IP estate area, which falls in central zone of New Delhi. The solar power plant was commissioned in October 2015. The river Yamuna flows along the Eastern side of the site, while the Western side is flanked by Mathura highway. L 03 was commissioned by NTPC at the village Jajru, Faridabad in January 2015. It is a 5 MW solar power plant. Majority of the site is surrounded by agriculture land and Delhi–Mathura railway track along
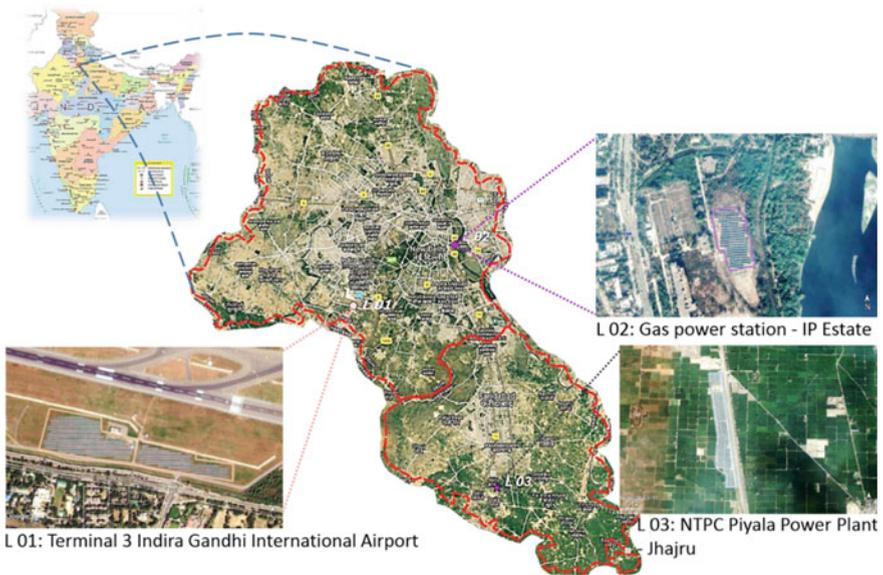
Fig. 3 Location of L 01, L 02, and L 03 on Delhi map

the Eastern side of the site. The results before SPV installation and after SPV installation are as following:

L 01 Pre SPV The LST images (see Figs. 4 and 5) show a ridge formation along the Urban Extension Road-II. Temperature is 2–3 °C lower toward South of Urban Extension Road-II than that of North all year except for two months (August and September), when there is marginal difference. However, the site which is located toward north of Urban Extension Road-II, inside Airport boundary, has no particular LST signature because at that time there was no photovoltaic installation on site. Therefore, LST difference between L 01 and surroundings is 3°–5°C, with the surroundings being at the lower side (see Figs. 6 and 7).

L 02 Pre SPV Since there is no SPV installation on site, the land surface images (see Figs. 4 and 5) show a uniform distribution of land surface temperature on site and near surroundings except the river and highway; where the temperature is 2 °C lower and 2 °C higher, respectively (see Figs. 6 and 7).

L 03 Pre SPV In the absence of SPV installation on site, there is no pattern to the LST distribution (see Figs. 4 and 5) on site and in the surroundings in the land surface images. Due to this, a varied temperature range on the site is visible (see Figs. 6 and 7).

L 01 Post SPV After the installation of solar Photovoltaic Plant in January 2014 (see Figs. 8 and 9), there is a noticeable difference in LST of L 01 and the Northern, Southern surroundings. The temperature at the site is 1–2 °C lower than northern surroundings and at the same time 2–3 °C higher than southern surroundings (see Figs. 10 and 11).
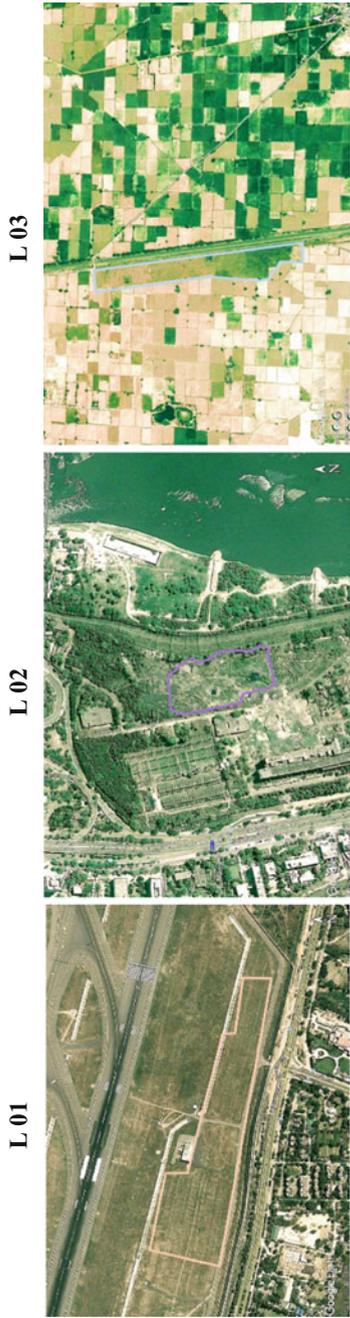
Fig. 4 L 01, L 02, and L 03, respectively (before SPV installation)
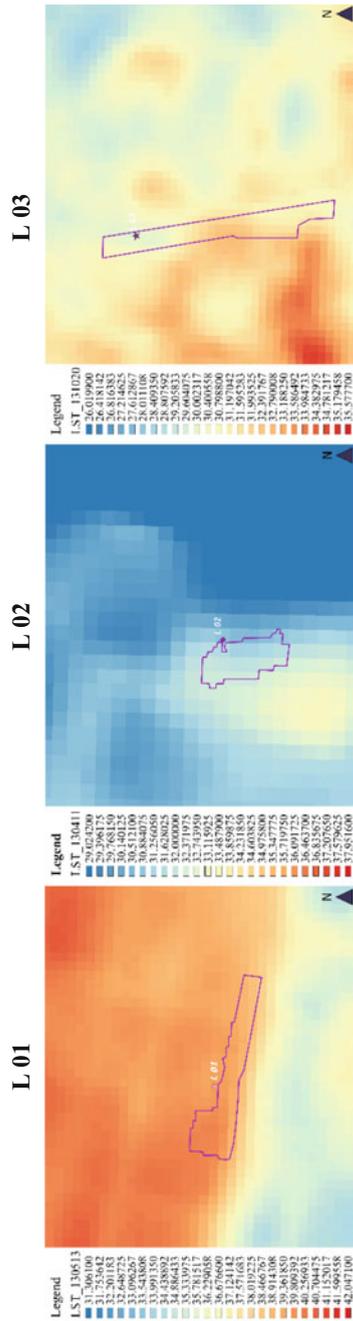
Fig. 5 LST map of L 01, L 02, and L 03, respectively (before SPV installation)
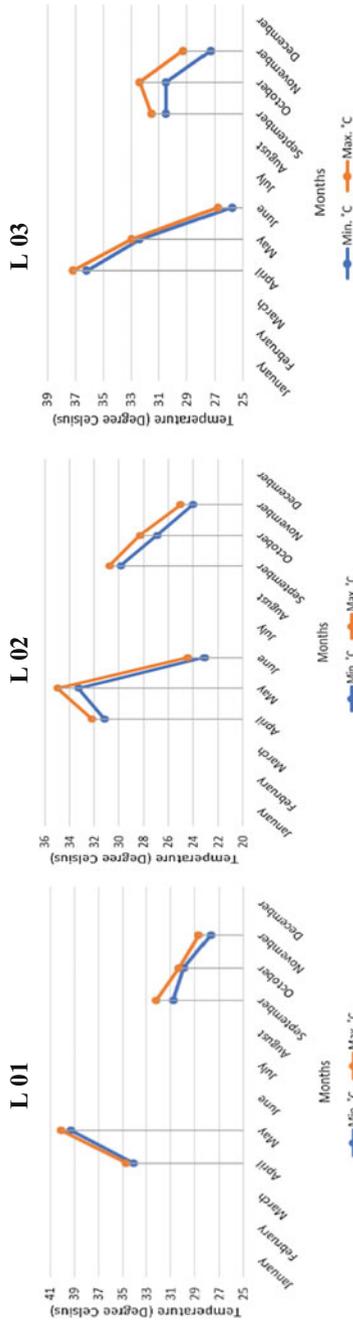
Fig. 6 Temperature variation within the sites L 01, L 02, and L 03, respectively (before SPV installation)
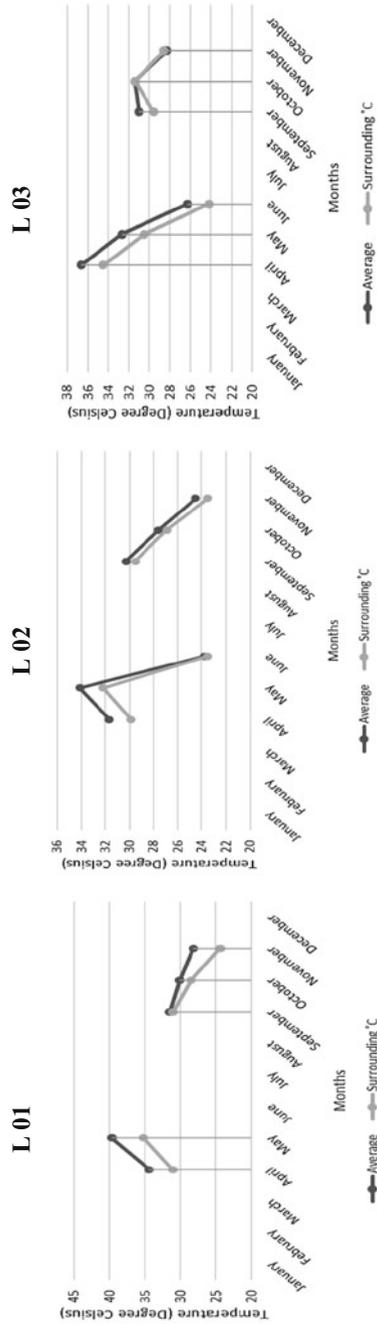
Fig. 7 Temperature variation between the sites L 01, L 02, and L 03, and their respective surroundings (before SPV installations)

Fig. 8 L 01, L 02, and L 03, respectively (after SPV installation)
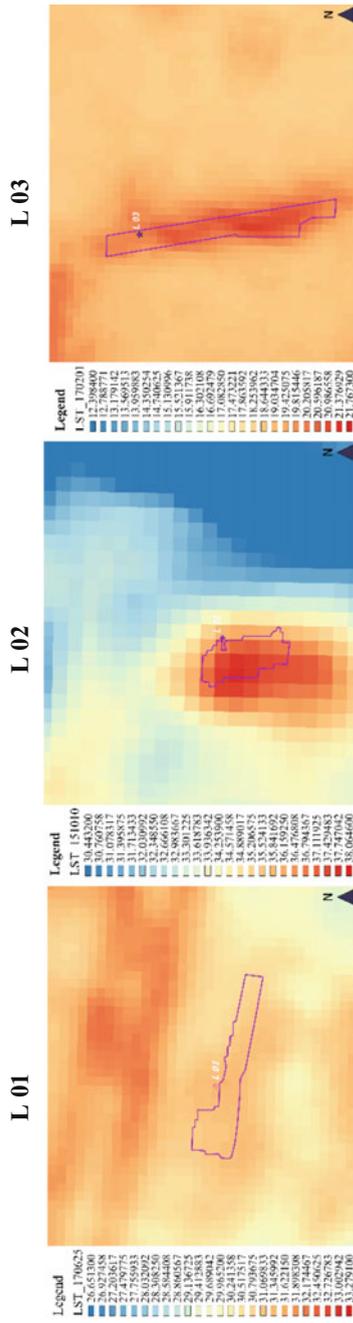
Fig. 9 LST map of L 01, L 02, and L 03, respectively (after SPV installation)
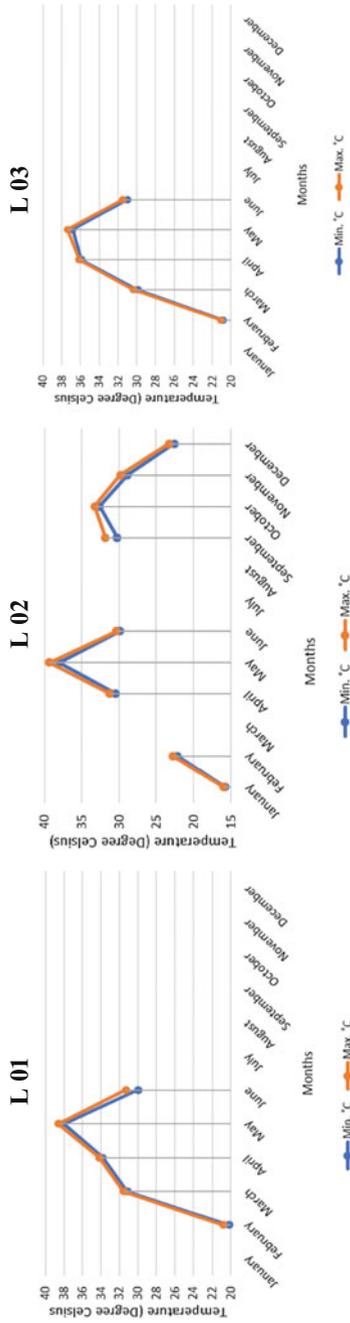
Fig. 10 Temperature variation within the sites L 01, L 02, and L 03, respectively (after SPV installation)
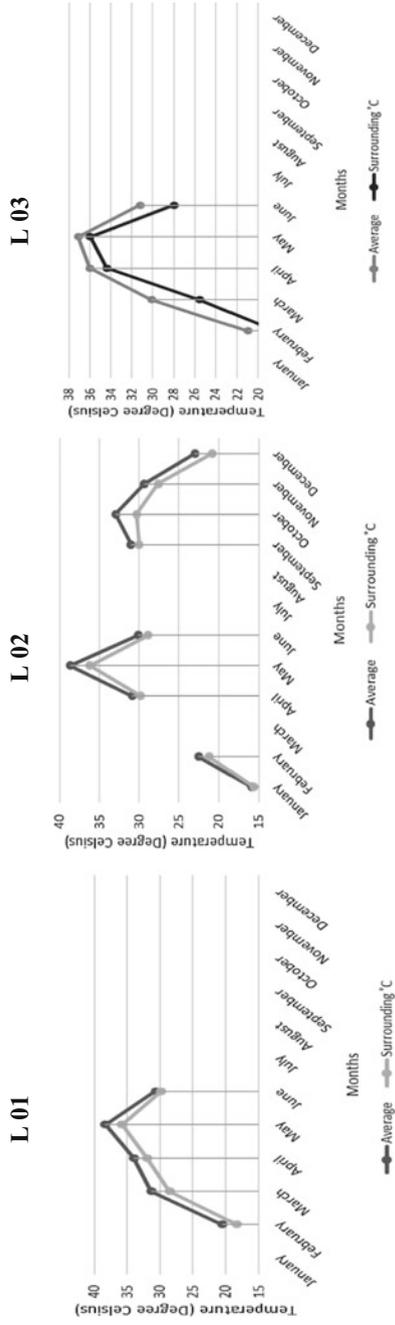
Fig. 11 Temperature variation between the sites L 01, L 02, and L 03 and their respective surroundings (after SPV installations)

L 02 Post SPV A steep rise of 2.5–3 °C is evident on site with respect to the surroundings, when the SPV was installed on site (see Fig. 11). After that the trend stabilizes and shows 1°–2 °C rise which jumps up to 3–4 °C in the month of March to May, which is clearly visible in the image of March 21, 2017, and May 8, 2017.

L 03 Post SPV After the SPV installation in 2015, the difference between LST of site and surroundings in winters (see Fig. 9) is significant compared to summers; that is, 1–2 °C rise is visible in the temperature of site with respect to the surroundings in the winters, whereas in summers, the difference is minimal till 2016 (see Fig. 11).

The following graphs plot the variation between the site LST and surroundings LST in all sites throughout the year. Clear LANDSAT imagery for July is unavailable due to monsoon.

In the absence of SPV installation, the average annual LST for the site has been uniformly dropping during summers and winters, from April 2013 to January 2014. However, after SPV installation, a gradual rise is observed during 2014–2015, which plummeted during the summers of 2015–2016. The dip in the temperature of 2013 and 2017 is primarily due to the absence of data availability.

L 01 site has runway on the northern side, which has more absorption level and increased surrounding air temperature due to burning of aviation fuel. This might be the reason of the anomaly, i.e., higher surroundings temperature than the site temperature (see Fig. 12).

The LST of the site and surroundings in winters was declining till October 2015 in the absence of SPV installations; however, a steady increase is visible till 2016 after the SPV was installed. The anomaly of decline in 2017 could be attributed to the incomplete data as the year is not yet complete. The LST of the site and surroundings in summers were increasing steadily till 2015, with the temperature of site staying 1°–2 °C more than the surroundings. A drop of 1.5 °C in the LST of surroundings is visible between 2015 and 2016, contrasted by a marginal decrease of 0.5 °C in the LST of site. A rise in the LST of the site could be seen irrespective of the unavailable data as the year is not yet complete (see Fig. 13).

The LST of the site and surroundings is consistently decreasing in winters; however, the rate of decline in LST of the site is constantly much lesser than that of its surroundings. In summers, the LST difference between the site and surroundings is 1–2 °C in 2013 and 2017, whereas it is only 0.5–0.7 °C from 2014 to 2016. In general, the LST trend of winters is declining, while it is increasing in summers (see Fig. 14).

3.1 Approach and Limitations

The selected approach has particular limitations such as the absence of LANDSAT 8 image of Monsoon season (July and August) due to cloud cover, which affects the overall results. MODIS data are available, but has low resolution which cannot be
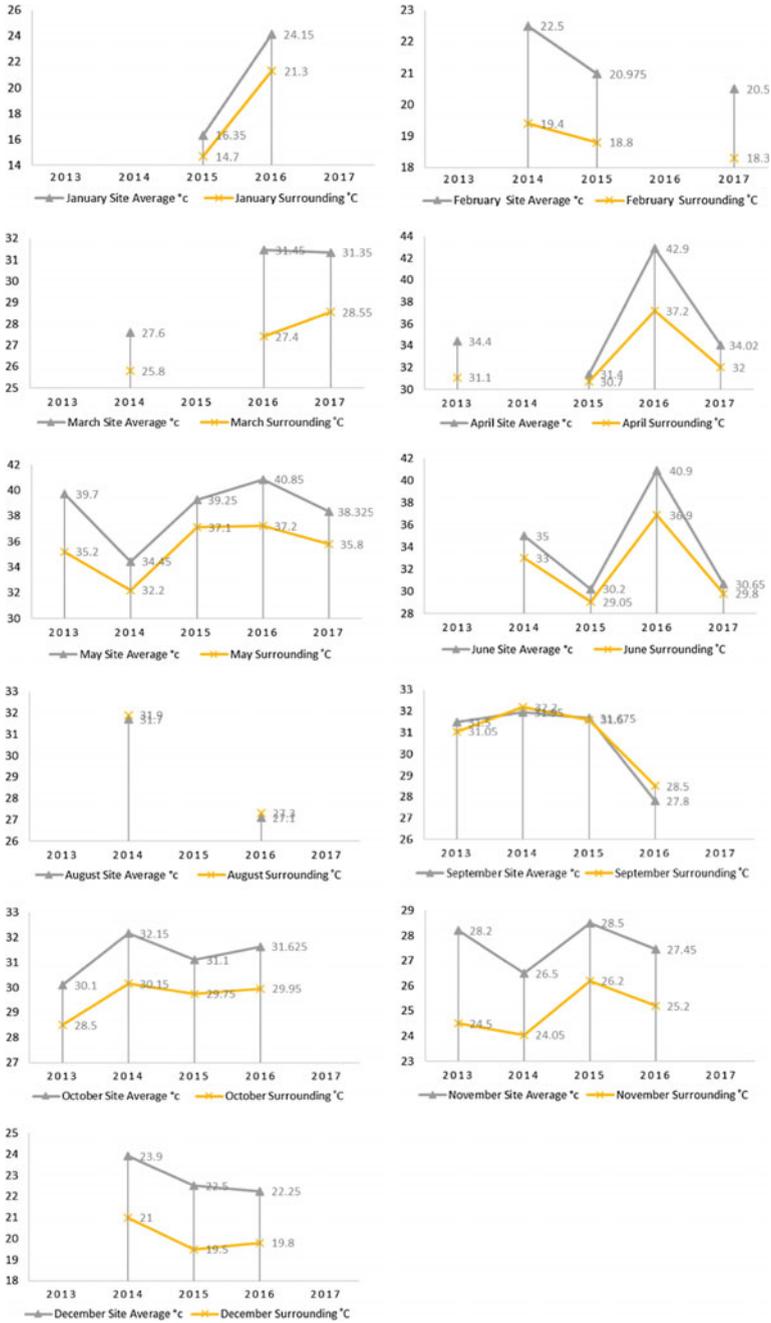
Fig. 12 L 01—monthly graphs: January to December (L to R)
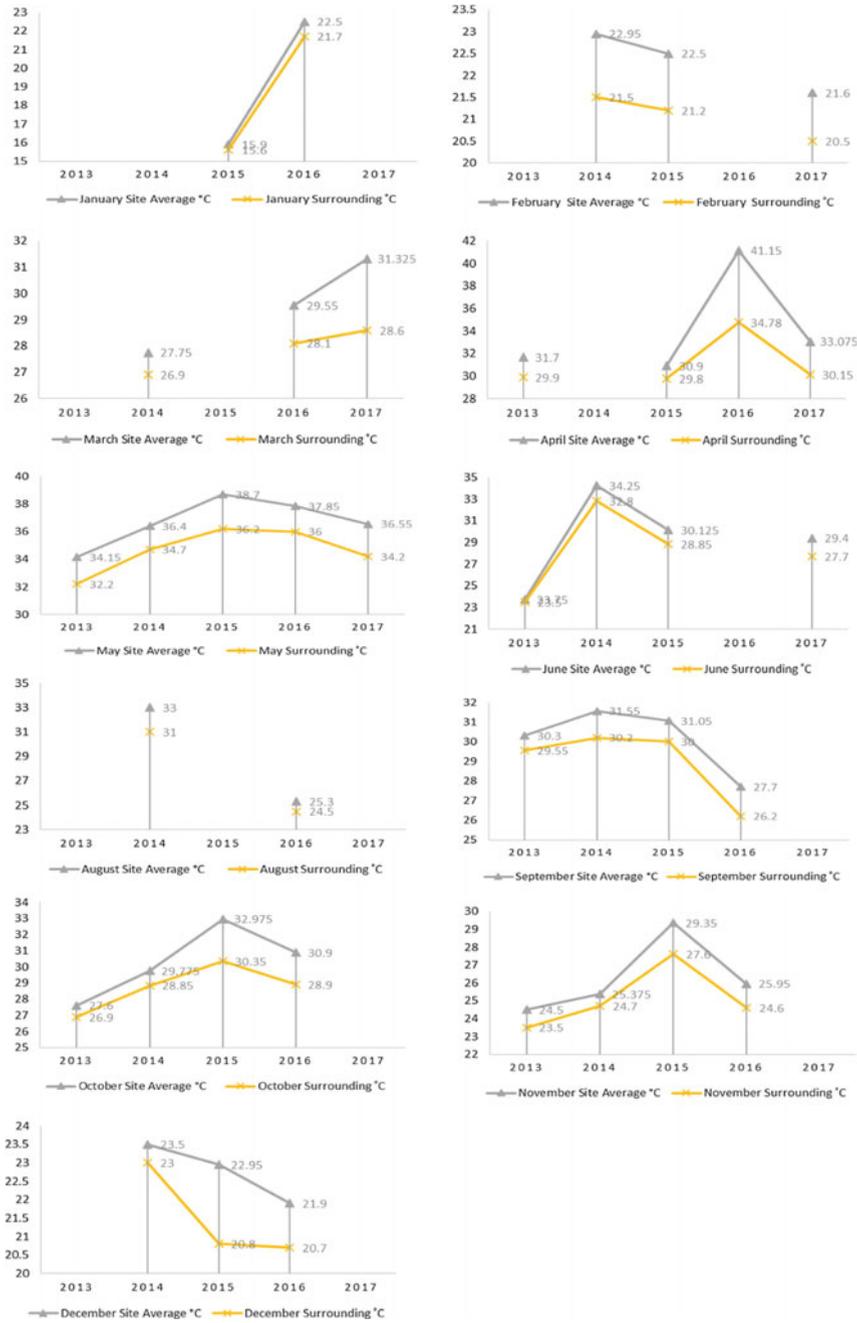
Fig. 13 L 02—monthly graphs: January to December (L to R)
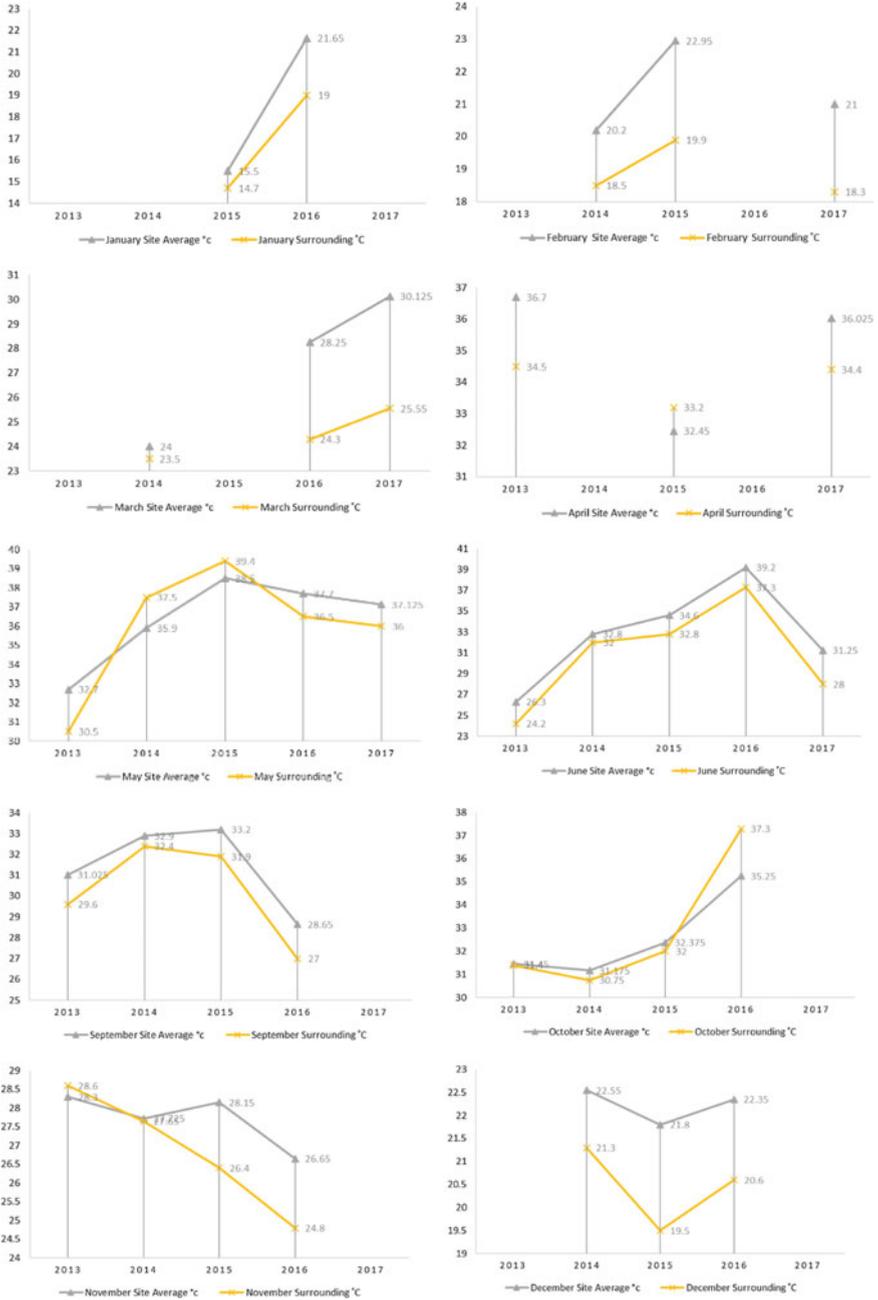
Fig. 14 L 03—monthly graphs: January to December (L to R)

used at a microscale. Additionally, complete data of winter season for year 2013 and 2017 are unavailable as the satellite started working in April 2013 and the mapping of the current year is partially complete as the year is not yet complete.

4   Conclusion

UHI is a localized phenomenon, but it is becoming a significant aspect of climate change mitigation and adaptation as global populations urbanize, especially in the developing countries that lie in the warm climatic belts. At the global level, all major stakeholders are drawing attention to the challenge of urbanization and to the environmental stress in cities, including UHI, impacting the urban poor the most. They also emphasize the need for further research on urban systems and climate change to enable integrated urban planning for mitigation.

The study demonstrates clearly that the temperature within the site was varying in all 3 sites by 0.2°–0.5 °C, after SPV installation, which shows the overall albedo level of the site increased in comparison with vegetated surface or bare soil, whereas the temperature within the site was varying in all 3 sites by 1°–1.5 °C before SPV installation.

The effect on UHI cannot be inferred at this stage, since only LST has been mapped; however, it cannot be excluded either as an influential factor. On field data collection is required to fill the gaps, verify simulation results, and develop an understanding of current and possible future changes in the magnitude of the UHI to ensure planning and developing of adaptation and mitigation strategies.

References

1. Hu, A., Levis, S., Meehl, G.A., Han, W., Washington, W.M., Oleson, K.W., van Ruijven, B. J., He, M., Strand, W.G.: Impact of solar panels on global climate. Nat. Clim. Change November (2015)
2. MNRE: National Solar Mission report. s.l.: MNRE (2017)
3. Oke, T.R.: The energetic basis of the urban heat island (1982)
4. Turney, D., Fthenakis, V.: Environmental Impacts from the installation and operation of large-scale solar power plants. 3261–3270 (2011)
5. KPMG: Urbanisation in the National Capital Region. s.l.: KPMG (2017)
6. The Indian Express. http://indianexpress.com/article/india/india-others/ncr-urbanisation-delhi-remains-the-epicentre/. Last accessed 30 Sept 2017
7. Climate - data. https://en.climate-data.org/location/30/. Last accessed 30 Sept 2017
8. Rajeshwari, A., Mani, N.: Estimation of land surface temperature of Dindigul district using landsat 8 data. **3**(5), 122–126 (2014)
9. Becker, F., Li, Z.L.: Towards a local split window method over land surfaces. **11**(3), 369–393 (1999)
10. Landsat 8 (L8): Data Users Handbook. U.S. Geological Survey (USGS) Landsat Project Science Office, NASA, South Dakota (2016)

11. Sobrino, J.A., Raissouni, N., Li, Z.-L.: A comparative study of land surface emissivity retrieval from NOAA data. **75**(2), 255–266 (2001)
12. Carlson, T.N., Ripley, D.A.: On the relation between NDVI, fractional vegetation cover, and leaf area index. **62**, 241–252 (1997)
13. Sobrino, J.A., Raissouni, N.: Toward remote sensing methods for land cover dynamic monitoring: application to Morocco. **21**, 353–366 (2000)

Recent Developments in Latent Heat Energy Storage Systems Using Phase Change Materials (PCMs)—A Review

Laxman Mishra, Abhijit Sinha and Rajat Gupta

1 Introduction

With increase in demand for energy, there is also an increased need for storing it. There has been a new outlook toward renewable sources of energy to meet the increasing demand. It is also important because these sources are environment friendly and available at free of cost. However, the intermittent nature of these sources makes it necessary to have proper storage mechanism. Several methods have been developed to store different forms of energy. Thermal energy is an attractive form of renewable energy [1]. Thermal energy may be stored in the form of sensible and latent heat and as thermochemical reactions. Major drawback to the development of solar thermal applications arises from the space and weight constraints that would be encountered during the storage of the collected energy [2]. The latent heat storage is advantageous over sensible heat storage due to their high energy storage density [3]. The thermochemical storage systems which are still in research phase have even superior energy storage density than the latent heat storage. Both sensible and latent heat storage systems are applicable in wide variety of thermal systems.

Latent heat storage system (LHS) is gaining much attention due to its ability to store and release heat isothermally. In a typical solid–liquid PCM, heat storage system heat is absorbed by the PCM during charging where it gains its latent heat of melting. During the discharging process, the stored heat is released back to the surrounding (or working fluid) that is at temperature below the freezing point of the PCM material. The energy released during its discharge can be used for applications such as building heating, heat pumps, drying applications in agriculture and industries, and several other applications.

L. Mishra (✉) · A. Sinha · R. Gupta
Department of Mechanical Engineering, National Institute of Technology Mizoram, Aizawl, India
e-mail: laxmanmishra17@gmail.com

This review provides an overview on the methods and developments in the latent heat storage systems using phase change materials for storing thermal energy from low temperature sources, viz., solar energy and waste heat.

2   Selection Criteria of PCM for Use in Latent Heat Storage Systems

PCMs may be classified into organic, inorganic, and eutectics. Organic PCMs can undergo repeated cycles of melting and freezing without causing any segregation in its phases which could cause degradation of its latent heat of fusion [4, 5]. They also have self-nucleating property which enables them to crystalize with almost no supercooling. Their non-corrosive nature offers the flexibility of choosing from different storage materials [6]. Common phase change materials are salt hydrates, metallics, paraffins and non-paraffin organic materials, and eutectics. The desirable properties of any PCM includes: (1) high latent heat of fusion, (2) high thermal conductivity, (3) moderate melting point, (4) stability at different temperatures, (5) high specific heat, C_p (6) ability to undergo repeated cycles of melting and solidification without significant change in its properties, and (7) non-toxicity and non-flammability [6, 7]. Latent heat of melting dictates on the amount of heat a given mass of PCM can store. Therefore, it is desirable to have a high latent heat of melting to provide high energy storage density. Large latent heat values of PCMs make them an attractive means for thermal energy storage [8]. The rate of storage and release of heat by a PCM is influenced by its thermal conductivity. A higher thermal conductivity gives faster rate of absorption and release of heat. Enhancement of heat transfer in PCM is essential to increase domain of its application in thermal systems [9]. A higher specific heat implies a higher heat storage density for sensible part of the heat stored. An ideal PCM should also possess thermal stability when it is subjected to several cycles of melting and solidification. This enables the PCM to be used for longer period of time without replacement.

However, these combinations of properties are not available in any single material. This has led to several research and modification in design of PCM-based LHS (Latent Heat Storage) systems. Choice of PCM also depends on its application: Temperature being the most important factor because different materials undergo phase change at different temperature. This necessitates to make a choice of the PCM material based on the temperature that a particular application requires.

3 Developments in Latent Heat Storage System for Storing Solar Energy

Storage of solar thermal energy and methods to utilize it in most efficient ways have been sought out in several studies. This section discusses some of the recent developments in the utilization of solar thermal energy for various purposes using PCM as the latent heat storage material.

Youssef et al. [10] designed an indirect expansion solar-assisted heat pump system using a PCM heat exchanger for domestic use. This energy was used in the heat pump cycle during the night. The schematic is shown in Fig. 1. The system worked on two different loops. First loop was made to bypass the PCM heat exchanger tank and used for heating the water in the water storage tank without the application of the heat pump. In the second loop, the solar heat from the solar collector was made to pass through the evaporator of the heat pump whose condenser was used for heating the water in the storage tank.

An automated control was used for efficient system operation that kept the temperature at the outlet of the water storage tank fixed at 55 °C. Incorporation of the PCM heat storage system increased the mean COP of the heat pump by 6.1% on sunny days and 14% on cloudy days. Qi et al. [11] proposed a new model for cooling car cabin (shown in Fig. 2a) where solar energy was converted into electricity in solar panels for powering air and water pumps. A PCM cabinet, as shown in Fig. 2b, was designed such that it could use ambient air for charging PCM during the daytime and cool water to discharge it during the night. The hot ambient air while passing through the PCM chamber would release its heat and charge the PCM, thus itself getting cooled. This cooled air was then passed into the car cabin to maintain a lower temperature. During night hours, the water from the water storage area was pumped into the PCM chamber which would discharge the PCM and prepare it for next day. This model had an advantage of wireless power transmission from the solar panels to the super-capacitor which avoided any
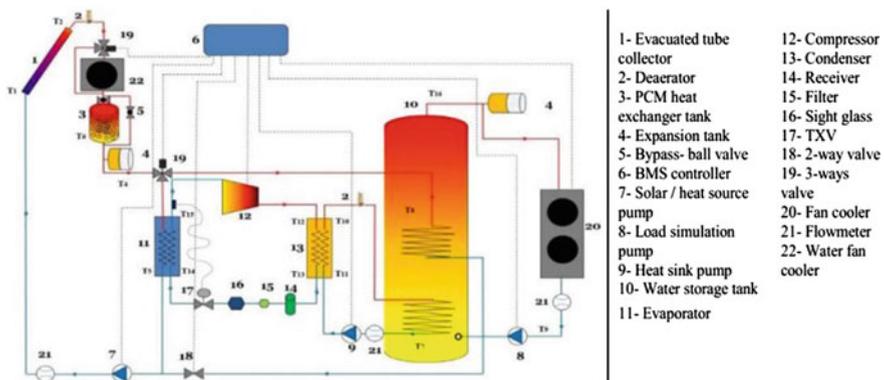
Fig. 1 Schematic diagram of the test rig [10]
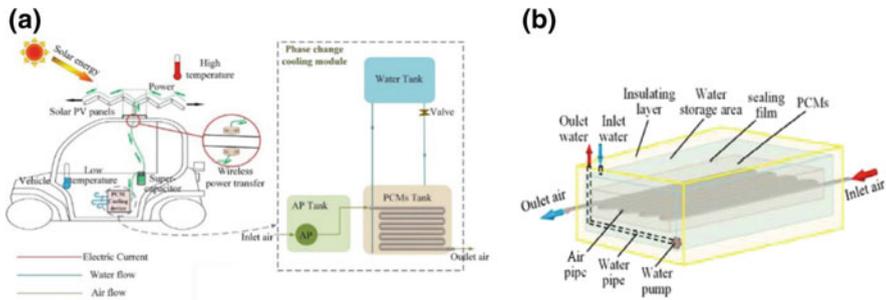
Fig. 2 **a** Schematic of the solar-powered cooling system for car cabin. **b** Schematic of internal PCM chambers [11]

modifications in the car body structures. A temperature drop of up to 30 °C was obtained between the inlet and the outlet air through this system.

Rabha and Muthukumar [12] used two double-pass solar air heaters to heat the PCM used in drying of red chilli using solar heat only (Fig. 3). The air from the solar air heaters was passed through a shell and tube heat exchanger where the PCM was contained in the shell. The hot air charged the PCM and was forced through a parallel flow drying chamber for drying chilli using a blower. The presence of PCM module allowed a constant temperature of air at drying chamber even when the sky was cloudy during intermediate hours.

Eswaramoorthy [13] studied the thermal performance of a V-trough solar air heater for drying applications using paraffin wax as the latent heat storage material. Experiments were conducted with and without the PCM module. It was seen that the thermal performance of the system was 10% higher with the incorporation of the thermal storage than without it. The schematic of the V-trough solar air heater is shown in Fig. 4. Okello et al. [14] experimentally investigated the use of PCM and rock particles for a comparative study on the thermal storage with rock only and rock with PCM. A vertical downward flow of hot air was made through the energy storage unit. It was observed that use of copper cylinders containing PCM increased the total heat content of the heat storage unit. Also, the high thermal conductivity of copper tubes led to a thermal equalization in the storage tank which caused a faster rise in temperature at the bottom of the tank.

Reyes et al. [15] constructed a hybrid solar dryer for mushroom dehydration (Fig. 5). The setup consisted of a wavy solar collector is made from zinc with fins to increase the surface area. The dryer operated in a closed-circuit mode with an electric heater in the main circuit and 70 and 80% of the air being recirculated while the difference was supplied through the solar collector and solar accumulator. The solar energy accumulator came into operation in the evening when it was able to raise the air to 20 °C above the ambient temperature for 2 h. For the daytime, the required heat was supplied by the solar collector and the electric heaters. This helped in constantly supplying a heated air at a higher temperature to the dryer.
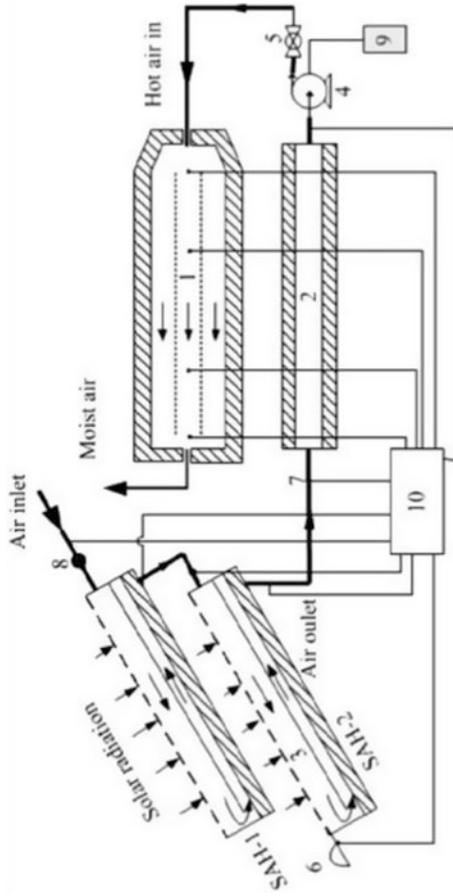
Fig. 3 Schematic diagram of the forced convective solar dryer; 1. Parallel flow tunnel dryer, 2. Shell and tube heat exchanger (energy storage), 3. Solar air heater, 4. Air blower, 5. Ball valve, 6. Pyranometer, 7. Thermocouples, 8. Flow meter, 9. Energy meter, 10. Data acquisition system [12]
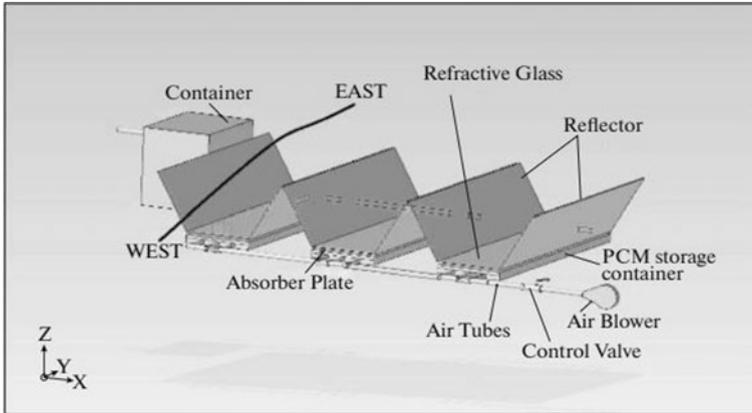
Fig. 4 Schematic diagram of the V-trough solar air heater [13]

Fig. 5 Hybrid-solar dryer, (A) solar panel, (B) solar energy accumulator, (C) electrical heater, (D) drying chamber, (E) centrifugal fan: T_i air temperature, V_i valves, ΔP pressure drop [15]
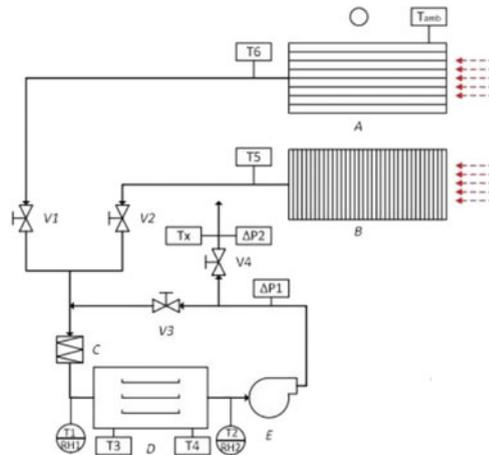
4 Advances in Latent Heat Storage Systems for Waste Heat Recovery

In this section, we present some of the recent advancements in recovering waste energy through the use PCMs. Exhausts of several energy conversion devices carry a significant amount of energy which goes into the ambient air. Recapture of this heat can save huge amount of fuels that would otherwise be utilized to produce the same heat. Pandiyarajan et al. [16] used a finned shell and tube heat exchanger to experimentally study the recovery of heat from diesel engine exhaust gases using cylindrical PCM capsules. This system used castor oil as heat transfer fluid between the exhaust gas and the storage tank which contained paraffin stored in 48 capsules.

This offered dual advantage of sensible and latent heat storage. Copper fins were installed on the exterior of the tubes in the shell and tube heat exchanger to increase the heat exchange area available on the gas side. Through this system it was possible to save 10–15% of the heat contained in the exhaust gases. High thermal conductivity of stainless steel used as storage tank for PCM enabled a uniform distribution of heat throughout the TES (Thermal Energy Storage) tank. The charging rate and efficiency were found to be higher at higher loads. Gopal et al. [17] conducted a similar study on a two-cylinder diesel engine and carried out energy and exergy analyses of the complete system. The schematic of the experimental work and the exhaust heat exchanger is shown in Fig. 6a, b, respectively. They incorporated water as a heat transfer fluid to carry heat from the exhaust gases to the TES unit using an exhaust heat exchanger. The heat exchanger consisted of a mild steel tube around which copper tubes that carry water were wound. Lathe scrap was placed in the empty spaces around the mild steel tube to promote heat transfer to the copper tubes. The charging of PCM occurred by the natural circulation of water due to temperature difference between the exhaust heat exchanger and TES unit. The use of PCM storage unit enabled 6.13% of energy savings from the fuel input and 0.14% of the chemical exergy of the fuel.

Shon et al. [18] studied on the methods for heat storage rate improvement and heat exchanger efficiency when the heat exchanger was filled with PCM for an automobile coolant waste heat recovery system. The time required and the heat transfer rate were theoretically evaluated in a PCM-filled tube heat exchanger. It was observed that the natural convective heat transfer on the PCM side decreased drastically with the formation of the liquid layer. Hence, the liquid layer should be thin for better heat transfer through natural convection. A high viscosity resulted in a lower heat transfer by natural convection in the liquid phase of the PCM.

Jia and Lee [19] conducted an experiment under laboratory conditions to recover heat from an air-conditioning system by use of PCM. The test facility consisted of two chambers to simulate the indoors and outdoors conditions (Fig. 7a). The indoor conditions were kept at 22 °C and 55% relative humidity while the outdoor
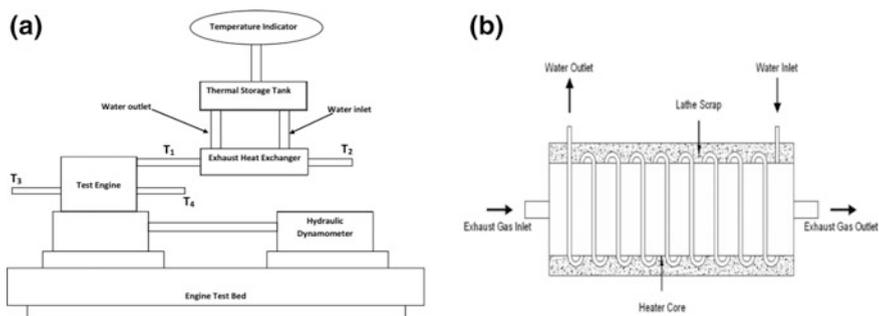
Fig. 6 **a** Schematic diagram of the experimental setup. **b** Schematic diagram of the exhaust heat exchanger [17]
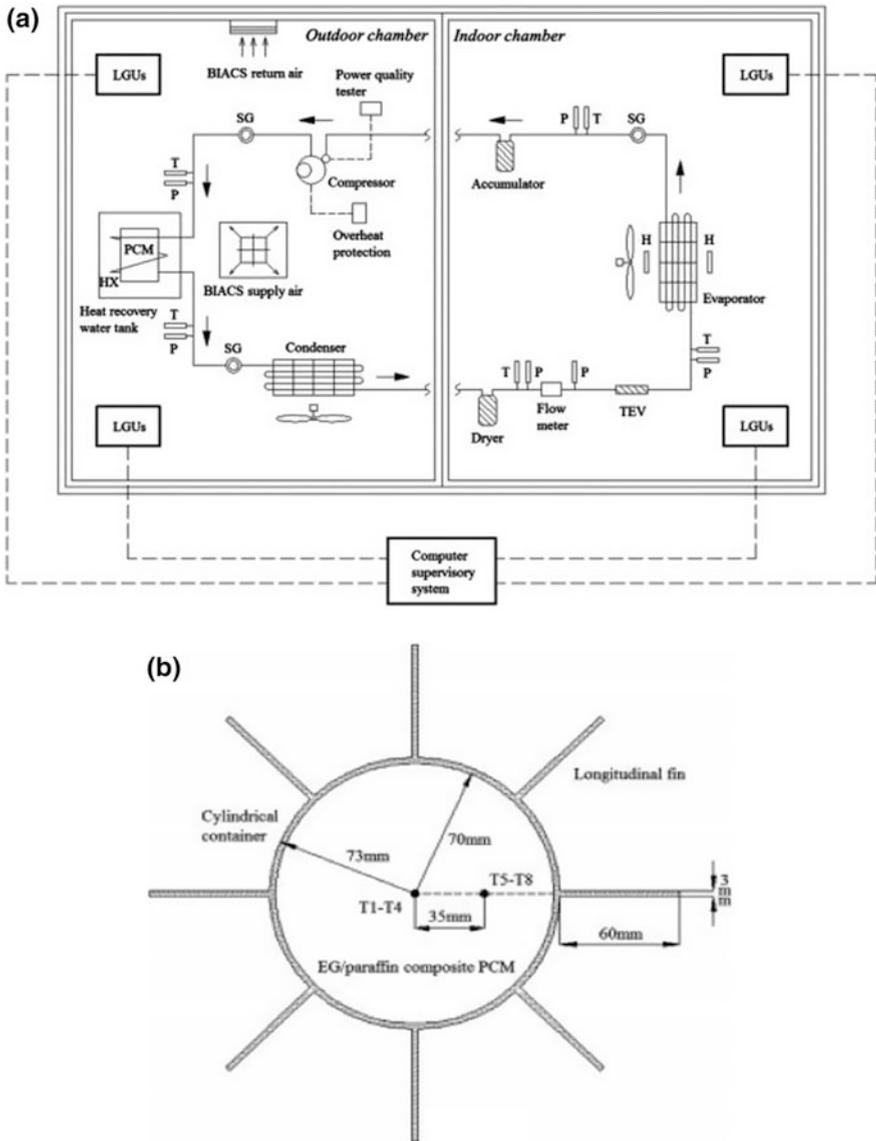
Fig. 7 **a** Schematic of the experimental setup [19]. **b** Cross-sectional view of the PCM container [19]

temperature was varied between 25 and 35 °C with 5 °C intervals. A cylindrical heat recovery water tank was placed between the compressor and the condenser of the air-conditioning unit. The heat exchanger consisted of helical coils of copper containing a cylindrical PCM container with longitudinal fins inside the helical
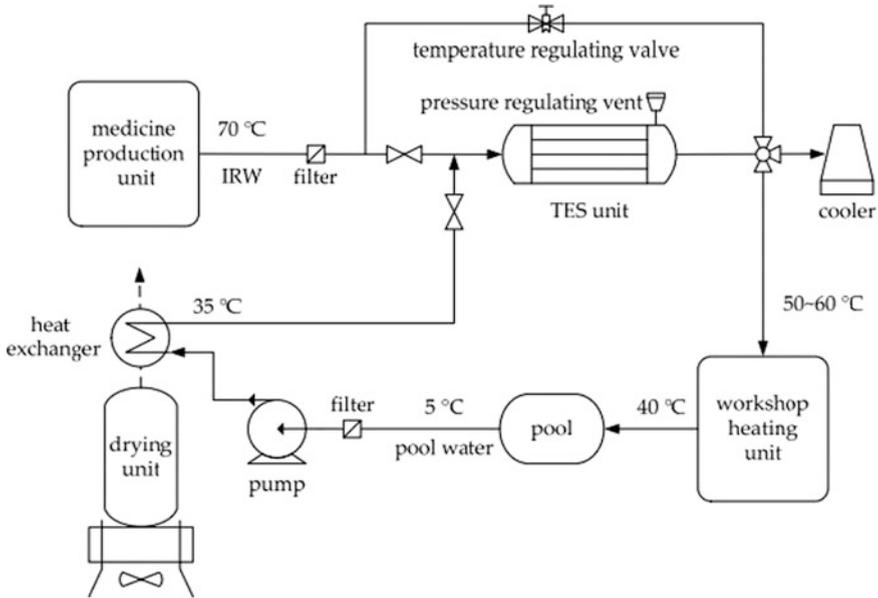
Fig. 8 System configuration of a workshop heating system [20]

coils. The cross section of the PCM cylinder is shown in Fig. 7b. The performance of the air-conditioning system was tested in with PCM and without PCM scenarios. An overall gain of 6.9–9.8% was observed for the with PCM scenario while the heat retention time of the water tank increased by 21.1%. Sun et al. [20] conducted an analysis of a TES unit for recovery of heat from industrial residual water. The schematic of the facility is shown in Fig. 8. A TES unit using PCM was designed for supplying the required heating load to the workshop for 3.6 h when the production unit was not operated.

The heating of the workshop during the non-operation hours of the medicine production unit was achieved by first preheating pool water from 5 to 35 °C using the heat obtained from the drying unit; then this water was passed through the TES where it absorbs heat from PCM. They estimated 10.25% savings through the application of waste heat recovery system that could be achieved by the medicine production plant.

5   New Innovations in Latent Heat Storage Systems for Increasing Storage Density and Capacity of PCM

In this section, the recent innovative approaches and ideas in the PCM-based latent heat storage systems are discussed. Focus is given to the ways to improve the heat storage capacity and heat storage rate.

Akeiber et al. [21] tested three local PCMs extracted from petroleum products in Iraq for building encapsulation to study the energy saving achievable when the rooms are maintained at 24 °C against ambient temperature of 40–44 °C. Three different combinations of oil and wax, (40% oil + 60% wax), (50% oil + 50% wax) and (60% oil + 40% wax), were initially tested to find the best combination. The third combination was selected for building encapsulation due to its higher heat storage capacity as compared to others. Two identical rooms were constructed of equal dimensions (3 m × 2.5 m × 2 m) with identical wall material. One of the rooms was encapsulated with the selected PCM contained in aluminum slabs on the roof and walls. Both rooms were maintained at 24 °C using an air-conditioning system and the difference in cooling load of the air-conditioners was observed for studying the effectiveness of the PCM in saving energy. They reported that the room with PCM (test room) consumed 4.356 kWh as compared to the room without PCM that consumed 7.92 kWh which is 45% more than the test room.

Yamada and Nagano [22] developed and demonstrated the use of heat storage panel for micro- and nano-satellites. The heat storage panel (HSP) consists of carbon-fiber-reinforced polymer (CFRP) in which the PCM was injected. The HSP was used for increasing the heat bearing capacity of the satellite communication equipments where periodic heat generation was encountered. The testing and validation of the HSP were conducted on-orbit testing, model analysis, and thermal vacuum testing. The tests confirmed the temperature stabilization ability of the HSP. Thermal tests showed the temperature uniformity was achieved by the system. The HSP was loaded in Hodoyoshi-4, a Japanese satellite, and was found to function successfully in space. Li and Wu [23] made a numerical study on $NaNO_3$ as PCM inside porous copper matrix. The effects of natural convection, heat conduction, pore density, and porosity were studied numerically. The thermal conductivity was observed to improve with porosity of the copper matrix. However, the natural convection of the liquid PCM was hampered with higher porosity due to the restrictions from the metal frames. The lower pore density on the other hand decreased the melting and solidification rate by reducing the contact area for the PCM with the matrix. In the solid phase, the heat transfer coefficient due to conduction was increased by 28.1 times with the incorporation of the metal matrix, while in the liquid phase it was increased by 3.1 times due to the combined effect of natural convection and conduction. Joybari et al. [24] carried a numerical analysis of simultaneous charging and discharging of PCM with different fin configurations in a triplex tube heat exchanger. They studied the effects of fin thickness, length and number on the melting process of PCM and suggested the most optimal values for different configurations. It was recommended that for simultaneous charging and

discharging there should be three internal fins and one external fin while in the absence of simultaneous charging and discharging four fins are required in both internal and external cylinders. The fin thickness did not have significant influence on the heat transfer. However, the fin length and number of fins were crucial for better thermal performance of the configurations.

Tasnim et al. [25] performed a scale analysis followed by numerical analysis on nano-PCM (cyclohexane + CuO nanoparticles) to study the effects of convection on its melting process. A rectangular enclosure having impermeable walls was considered for numerical study with left wall subjected to a heat source of temperature above the melting point of the PCM and other three walls taken as adiabatic. They reported that the presence of nano-PCM slowed down the process of melting of the PCM. Addition of nanoparticles at fixed *Ra* (Rayleigh Number) decreased the width of the melt front and reduced the stream function values. Similar study was conducted by Hossain et al. [26] where the top wall of the rectangular enclosure was subjected to a heat source having temperature above the melting point of the PCM (Cyclohexane). The porous medium consisted of aluminum and the nanoparticles used was CuO. They reported that the melting rate was higher at lower porosity of the medium. Higher porosity was associated with higher amount of energy required to melt the PCM. However, a higher volume fraction of the nanoparticles increased the rate of melting for any given porosity of the medium.

6 Conclusions

An overview of the recent developments in latent heat storage systems using PCM as storage medium was presented in this chapter. First, some important criteria for selection of PCM for a particular application have been discussed. Various applications of PCM-based TES including space heating, drying and dehydration, car cabin cooling were discussed along with the system designs and the benefits derived from them. In the second part, some of the recent methods adopted for recovery of waste heat have been discussed and system designs and analyses were presented. Some recent innovative methods incorporated in order to achieve better PCM properties, storage density, and heat storage capacity such as the use of nano-PCM and role of porous medium have also been presented. This chapter is intended to serve as a guideline for designing new thermal energy storage units and help in decision making while selecting the PCM. Future work may be done in the areas of improving the thermal properties of the PCM. Also, methods to improve the heat transfer coefficients in the liquid phase of the PCM have to be developed for achieving faster rate of heat absorption and release.

References

1. Pelaya, U., Luoa, L., Fan, Y., Stitou, D., Rood, M.: Thermal energy storage systems for concentrated solar power plants. Renew. Sustain. Energy Rev. **79**, 82–100 (2017)
2. Murray, R., Desgrosseilliers, L., Stewart, J., Osbourne, N., Marin, G., Safatli, A., Groulx, D., White, M.A.: Design of a latent heat energy storage system coupled with a domestic hot water solar thermal system. World renewable energy congress 2011, Sweden. Solar Thermal Applications (2011)
3. Farid, M.M., Khudhair, A.M., Razack, S.A.K., Al-Hallaj, S.: A review on phase change energy storage: materials and applications. Energy Convers. Manage. **45**, 1597–1615 (2004)
4. Zalba, B., Marın, J.M., Cabeza, L.F., Mehling, H.: Review on thermal energy storage with phase change: materials, heat transfer analysis and applications. Appl. Therm. Eng. **23**, 251–283 (2003)
5. Khudhair, A.M., Farid, M.M.: A review on energy conservation in building applications with thermal storage by latent heat using phase change materials. Energy Convers. Manage. **45**, 263–275 (2004)
6. Sharma, A., Tyagi, V.V., Chen, C.R., Buddhi, D.: Review on thermal energy storage with phase change materials and applications. Renew. Sustain. Energy Rev. **13**, 318–345 (2009)
7. Alva, G., Liu, L., Huang, X., Fang, G.: Thermal energy storage materials and systems for solar energy applications. Renew. Sustain. Energy Rev. **68**, 693–706 (2017)
8. Zhang, Y., Faghri, A.: Analysis of thermal energy storage system with conjugate turbulent forced convection. J. Thermophys. Heat Transf. **9**(4) (1995)
9. Youssef, W.M.K.A.: Experimental and computational study of indirect expansion solar assisted heat pump system with latent heat storage for domestic hot water production. PhD thesis, College of Engineering, Design, and Physical Sciences Brunel University London (2017)
10. Youssef, W., Ge, Y., Tassou, S.A: Indirect expansion solar assisted heat pump system for hot water production with latent heat storage and applicable control strategy. In: 1st International Conference on Sustainable Energy and Resource Use in Food Chains, ICSEF 2017, Berkshire, UK (2017)
11. Qi, L., Pan, H., Zhu, X., Zhang, X., Salman, W., Zhang, Z., Li, L., Zhu, M., Yuan, Y., Xiang, B.: A portable solar-powered air-cooling system based on phase-change materials for a vehicle cabin. Energy Convers. Manage. **150**, 148–158 (2017)
12. Rabha, D.K., Muthukumar, P.: Performance studies on a forced convection solar dryer integrated with a paraffin wax-based latent heat storage system. Sol. Energy **149**, 214–226 (2017)
13. Eswaramoorthy, M.: Thermal performance of V-trough solar air heater with the thermal storage for drying applications. Appl. Solar Energy **52**(4), 245–250 (2016)
14. Okello, D., Foong, C.W., Nydal, O.J., Banda, E.J.K.: An experimental investigation on the combined use of phase change material and rock particles for high temperature (350 °C) heat storage. Energy Convers. Manage. **79**, 1–8 (2014)
15. Reyes, A., Mahn, A., Vásquez, F.: Mushrooms dehydration in a hybrid-solar dryer, using a phase change material. Energy Convers. Manage. **83**, 241–248 (2014)
16. Pandiyarajan, V., Pandian, M.C., Malan, E., Velraj, R., Seeniraj, R.V.: Experimental investigation on heat recovery from diesel engine exhaust using finned shell and tube heat exchanger and thermal storage system. Appl. Energy **88**, 77–87 (2011)
17. Gopal, K.N., Subbarao, R., Pandiyarajan, V., Velraj, R.: Thermodynamic analysis of a diesel engine integrated with a PCM based energy storage system. Int. J. Thermodyn. **13**(1), 15–21 (2010)
18. Shon, J., Kim, H., Lee, K: Improved heat storage rate for an automobile coolant waste heat recovery system using phase-change material in a fin–tube heat exchanger. Appl. Energy **113**, 680–689 (2014)

19. Jia, J., Lee, W.L.: Experimental investigations on using phase change material for performance improvement of storage enhanced heat recovery room air-conditioner. Energy **93**, 1394–1403 (2015)
20. Sun, W., Zhao, Z., Wang, Y.: Thermal analysis of a thermal energy storage unit to enhance a workshop heating system driven by industrial residual water. Energies **10**, 219 (2017). https://doi.org/10.3390/en10020219
21. Akeiber, H.J., Hosseini, S.E., Hussen, H.M., Wahid, M.A., Mohammad, A.T.: Thermal performance and economic evaluation of a newly developed phase change material for effective building encapsulation. Energy Convers. Manage. **150**, 48–61 (2017)
22. Yamada, K., Nagano, H.: Development of a heat storage panel for micro/nano-satellites and demonstration in orbit. Appl. Therm. Eng. **91**, 894–900 (2015)
23. Li, Z., Wu, Z.G.: Numerical study on the thermal behavior of phase change materials (PCMs) embedded in porous metal matrix. Sol. Energy **99**, 172–184 (2014)
24. Joybari, M.M., Haghighata, F., Seddegh, S., Al-Abidi, A.A.: Heat transfer enhancement of phase change materials by fins under simultaneous charging and discharging. Energy Convers. Manage. **152**, 136–156 (2017)
25. Tasnim, S.H., Hossain, R., Mahmud, S., Dutta, A.: Convection effect on the melting process of nano-PCM inside porous enclosure. Int. J. Heat Mass Transf. **85**, 206–220 (2015)
26. Hossain, R., Mahmud, S., Dutta, A., Pop, I.: Energy storage system based on nanoparticle-enhanced phase change material inside porous medium. Int. J. Therm. Sci. **91**, 49–58 (2015)

Portable Bio-electric Plant

M Geo James, Subin Suresh and Nikil Thomas Abraham

1 Introduction

Biogas plays a major role in relation to two interconnected policy goals currently pursued by the European Union and its member States: increasing the share of renewable energy and achieving a transition toward a bio-economy. Recent trends have shown a tremendous increase in the number of biowastes which are generated in a bulk quantity on an everyday basis. The problem of safe disposal of these materials is one of the prime concerns of the hour. Recent studies on Urban Waste Management have shown that lifestyle and the allotted space compel an individual to dispose of the organic waste of his premises to an open world. The problem is raised at this point. When these biowastes are collected and taken away, they are mainly carried to a remote area of less inhabitation, where they are left off for degradation. This is the case if there is some common agency to collect the bio-wastes of individual households and to dispose of them. But in a general scenario, the household wastes including the vegetable peels, food wastes, other degradable wastes etc., are disposed off to the open air as they produce foul smell over time. The present stage of these degrading wastes, either on a common ground or the backyards of residential areas, will form the breeding grounds for those insects which are the root cause of most airborne diseases.

On the one side, the management of the much-produced biowastes is causing the problem; the other side is facing the shortage of energy resources. The fact is that

M. G. James (✉) · S. Suresh · N. T. Abraham
Department of Computer Science and Engineering, Amal Jyothi College
of Engineering, Kanjirapally, Kottayam, Kerala, India
e-mail: mgeojames@gmail.com

S. Suresh
e-mail: subinsuresh365@gmail.com

N. T. Abraham
e-mail: nikiltabraham@gmail.com

both these are the prime need of the hour. While the fossil fuels are predicted to come to an end by coming years, the world is now looking for an alternative source that compromises the energy requirements of these fuels in all fields. With the automobile industry switching to electric power and the implementation of solar panel and other ways to extract renewable energy sources, the world is now looking forward to the utilization of new technologies to support their lifestyle. So, a product that is capable of addressing both these aspects is of prime importance at this point in time. The simplest solution that can be adopted is the implementation of biogas plants which will have all the degradable wastes dumped into it. The energy value of the biogas is also considered in the calculation, where it shows its significance with respect to the conventional sources [1]. But it shows a problem, i.e., the large size of the normal biogas plant. The plant requires a considerable area for its construction, and the maintenance of the same is a matter of consideration. This has led to the reduced number of biogas plants as it demands a minimum of land requirement.

Portable Bio-electric Plant is a product that holds all the behaviors of a normal biogas plant but with the additional feature that it is of that size to be accommodated at a corner portion of the room. This feature provides the capability that the product can be shifted as per convenience. The unit with the conversion technique of converting biogas to electricity is of prime importance as both the problems that have been stated at the beginning are provided with a solution. The biowastes, including all the degradable wastes that are generated in a household, can be given as input to the portable plant, and this will be converted to biogas. The produced biogas can then be given as input to the converter, which is a generator basically, to convert it to electric current (Fig. 1). Thus, the problem of the disposal of the wastes can be minimized and simultaneously reduced consumption of the fossil fuels can be achieved with ease.

Following the Renewable Energy Directive (RED), the European Union aims at a 20% share of renewable energy in the total energy consumption in 2020 [2] (Present usage statistics is shown in Fig. 2 [3]). Electricity and heat production from biogas are important building blocks to achieve the European 20% goal.

The Portable Bio-electric Plant enhances the fulfillment of this task by incorporating the two main objectives:

- Management of biowastes—With this product implemented on sources of biowaste including household, food courts, live-stock centers etc., all degradable waste can be dumped to this portable plant and thus it is managed [4].

Fig. 1 Schematic representation of a typical biogas production process

Fossil fuels ~ 79 %

Oil reserves ~ 170 Gtoe
Consumption 4.0 Gtoe/a

Gas reserves ~ 180 Gtoe
Consumption 2.8 Gtoe/a

Coal reserves ~ 1500 Gtoe
Consumption 3.4 Gtoe/a

31 % oil

22 % gas

26 % coal

5 Nuclear power

6 Hydropower

10 Biomass

Doubling from ca. 13 today to ca. 25 Gtoe/a in ca. 50–100 a
1 toe (tonne oil equivalent) = 44 GJ; 1 kW(th) = 0.375 kW(el) hydropower conversion
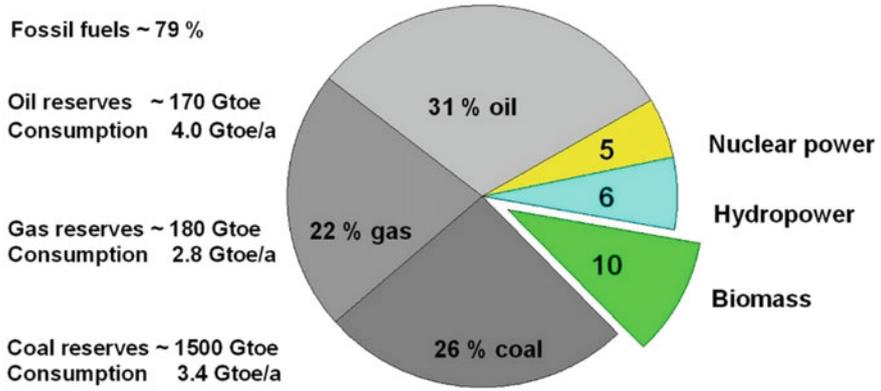
Fig. 2 Present usage chart of various fuels

- Reduced dependency on fossil fuel—The same biogas generated can be used for cooking, as an alternative source of electricity in automobiles etc., thus reducing the dependency on fossil fuel.

The prime advantage that the biofuel holds is that it is pollution-neutral; meaning that, during the combustion process of a biogas, the carbon dioxide emitted is the same that has been absorbed by those biomaterials from the atmosphere during their lifetime. So, burning simply means only the replacement of what has been absorbed. Nothing is produced in excess and thus is coined the term 'pollution-neutral.' Figure 1 schematically shows a biogas production chain with typical routes for energy production. Especially, heat production from biogas has a high potential to reduce CO_2 emissions [5].

2 Methods

To analyze the current practice of biogas production and the utilization of bio-resources, we analyzed the results and the statistical data from various sources to find out the methodology. We conducted semi-structured interviews with those who hold the bio-resources (farmers, food court owners, and households) and framed the product based on the points coined by them. We selected them because they had a good knowledge of the resource availability and the ways of handling those biowastes. Furthermore, they were able to reflect on the experiences they gained with the treatment and the discharge of those materials. The interviews were concerned with the views and ideas of the interviewees regarding the relationships of current biogas practices with renewable energy and the need domains. The interviewees were regarded as
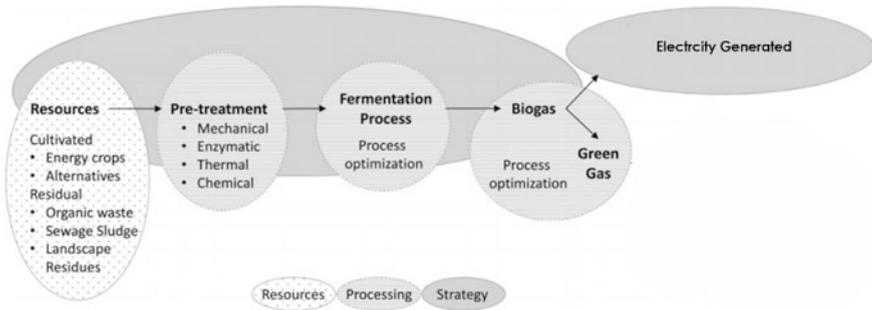
Fig. 3 Topics addressed in the product development

stakeholders involved in current practice in the biogas sector, not necessarily as policy experts but as knowledgeable people on the impact of current policies.

The interview questions were based on topics like resources, products, waste management, technology, results of their practices, their views on the potential of biogas production, and the relationship between biogas and the policy goals of renewable energy production and the bio-economy.

Figure 3 shows the various topics addressed in the product development and their relationship to a schematic biogas supply chain, incorporating various options of feedstock choices, processing steps, and distribution pathways. The fact that this product addressed so many different aspects of biogas is of particular value regarding the objective of this paper, since opportunities and constraints may be found along the whole biogas supply chain.

An analysis was also done on the utilization of the energy resources and the various areas where these resources are implemented. The best utilization of biogas as a fuel was studied, and the possibilities of incorporating it to achieve the goals mentioned above were taken into consideration.

3 Prototype Development

The product was prototyped with respect to all the conditions and observations briefed above. The Portable Bio-electric Plant is a mobile unit that can be kept according to consumer needs. The product occupies a space of 60 cm × 60 cm at the base and has a height of 90 cm (measurements are not precise). The dimensioning is made to suit the small area requirement that is demanded by most people. With a total weight less than 15 kg, the product becomes easier to transport. The line diagram of the product is shown in Fig. 4.

The main components of this system are:

(1) Inlet pipe.
(2) Digester tank.
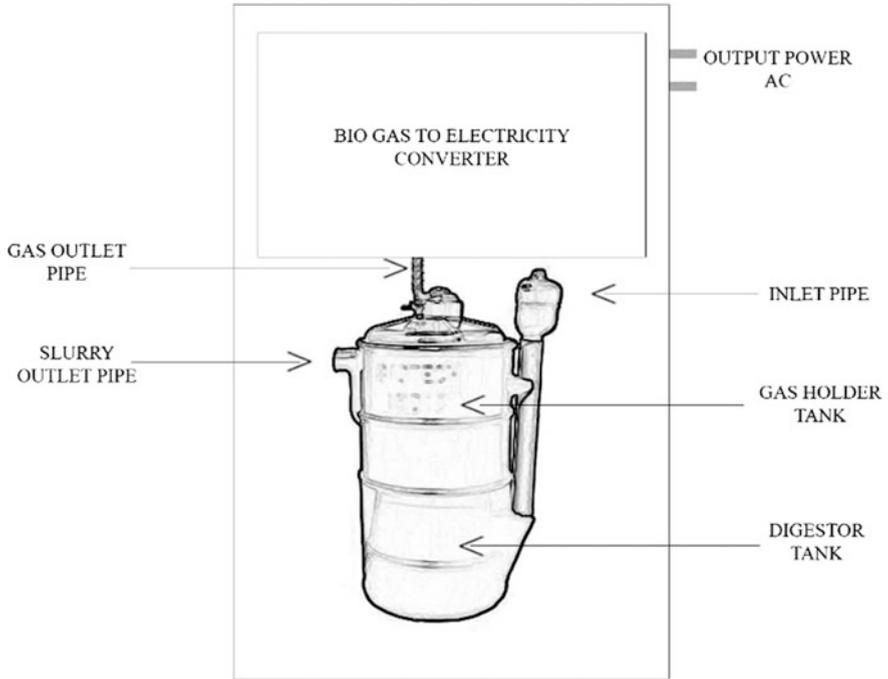
Fig. 4 Line diagram of the product

(3) Gas holder tank.
(4) Slurry outlet pipe.
(5) Gas outlet pipe.

The working of the model is as follows.

- The degradable waste materials are fed through the input valve to the biogas plant.
- It then undergoes anaerobic respiration, producing biogas.
- The slurry, which is a supreme quality fertilizer, is pumped out through the remove duct.
- The gas, when is of required pressure, is pumped from the plant to the converter unit just above the plant.
- The generated AC current is taken out through the output port on the top.

    - And the process repeats.

The additional technical enhancement is the information-providing service that can be incorporated into the product. This feature requires a smartphone which shows the consumer that a sufficient amount of biogas has been generated and he may start its conversion to electricity. When the gas amount is depleted, the same

application alerts the user to switch off the same. Any leakage of gas could be easily detected and an alert can be passed to the user. All these can be implemented using sensors and a programming board which is programmed to function well.

The physical aspects of the product are described with respect to its constituents, i.e., the biogas plant and the motor. The portable small-scale plant consists of a digester tank and a gas collector tank along with the inlet and the slurry output channel. The digester has 30 cm as base diameter, height of 50 cm, and a volume of 32 kgs. The gas collector has a base diameter of 26 cm, height of 25 cm, and volume of 13 L.

The motor used is a 76 cc four-stroke side valve engine with RPM 3600 and power output of 1.6 HP and 550 W.

Technical specifications of the product are as follows. The digester tank has a capacity of 32 kg and the gas holder tank, a capacity of 13 L. The product is having two sensors: a pressure sensor and a gas leakage detecting sensor. The pressure sensor is used to detect the pressure level and this triggers an alert system when the amount of pressure that is generated is above the level required for the production of electricity. The other sensor is the gas leakage detecting sensor used to detect the leakage of the gas from the gas tank. The prototype was made to function with an additional Arduino board to which both the above sensors were attached. The board was uploaded with a program to alert the user when the conditions of the sensors were met using a GSM module; the WiFi module may be incorporated to update the cloud database with the data, and the user can login with their corresponding login credentials to retrieve the data from the Arduino cloud. The components used and the overall lookup of the product are as shown in Fig. 5.
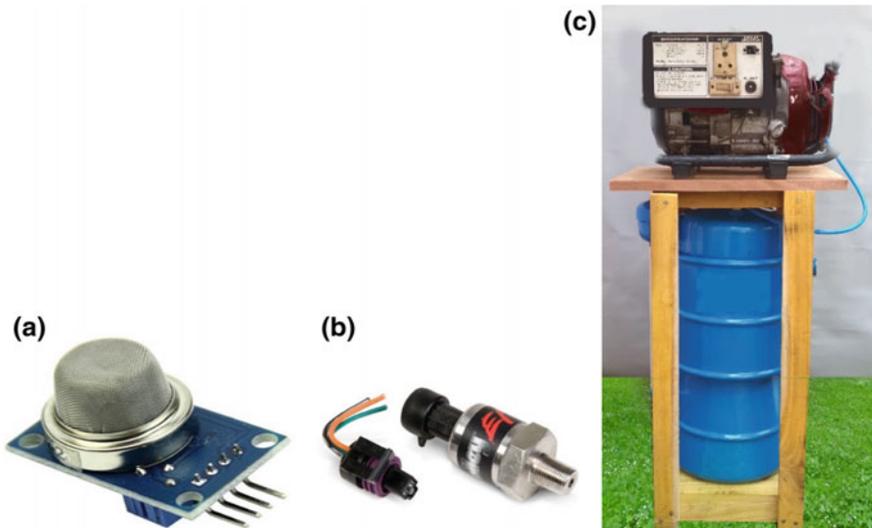
Fig. 5 **a** Gas leakage sensor, **b** pressure sensor, **c** Portable Bio-electric Plant

4 Comparison with Existing Model

The existing product in the market is a portable biogas plant, which may be utilized as the biogas plant for the proposed product. But the product as a whole, which generates electricity from the biogas and a product of simple design and which suits any environment, is entirely a new application that is not available as a single unit.

5 Results

Based on the results of the study conducted, the present conditions in which biogas plants work are shown in Fig. 6. The figure shows the various technical connections between biogas production and various policies associated with it.

The product was prototyped and was tested with the initial inputs. The digester tank was filled with cow dung to the maximum level to initiate the process and was kept for two days by the end of which carbon dioxide was produced. It was released and the mixture was stirred, and methane was produced in the later days. The engine was modified such that the fuel tank is removed and the carburetor is fed directly with biogas with the manual mixing of air to the fuel. The fuel has to be injected in a controlled manner to start the engine, and then the air and the supply have to be adjusted to control the speed of the engine. With an amount of 13 L of biogas produced in the gas chamber, the engine was able to work to produce energy of 2.94 kWh.
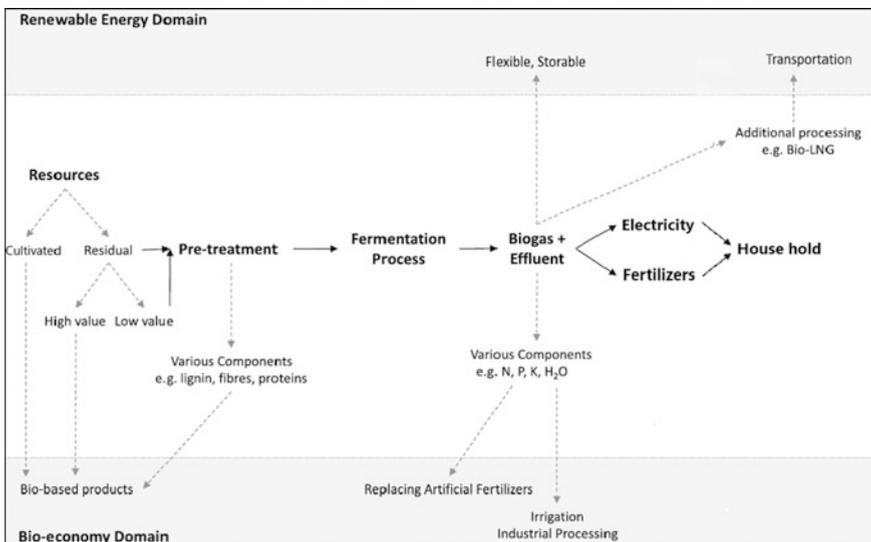
Fig. 6 Schematic diagram of potential technical connections between biogas renewable energy and bio-economy domains

As biogas is a renewable source of energy, it is given much importance as a major resource as an alternative to non-renewable sources. The biogas obtained from the plant can be used to generate heat, store and produce electrical energy, and can also be transported. In the present economy, biogas is produced from least valued biomass which is obtained as a by-product of some reactions. The need to find new methods to connect the economy with the biogas production by being able to procure the various components required for the functioning of the plant demands the attention of the hour.

The bio-economy is in tight competition for obtaining the resources needed to sustain the economy and get the required profit from selling them. Many of the existing technologies depend on biomass that is homogeneous and has a high quality. The owners of the plant may have to depend on sellers of biomass if they are in short of the source. The applications in the industry that require high-quality biomass for their operations need to pay a high price for obtaining them from the sellers. The sellers are also really careful, not to engage in a long-term contract with their clients as keeping a fixed price for their biomass will lead them to a loss. As the grade of biomass increases, the price to obtain also increases. These resources also compete with their counterparts (fossil fuels such as coal, petroleum etc.) with respect to their prices. The growth of biomass in value is expected but cannot be said accurately as people will be willing to pay more for it than the conventional energy sources.

The decrease in price that is given by the government for getting the renewable resources is needed in the present condition as the transition from non-renewable to renewable energy resources is slow. So, to cope up with the change, the government's help for this transition is essential. In the case of non-renewable energy sources, the price is not much high as in the case of renewable ones. As the non-renewable resources are still dominant in the energy industry, this will limit the potential of biomass. So, the machines have to be modified to be able to use the renewable resources in its operation. This limits the chance for biomass to achieve goals in the renewable energy domain and economy domain.

The focus should be on the combination of high-grade biomass with organic waste obtained from households as well as from farming. The residual biomass is also used as a source of biogas production. Its function may be lost when it is given into biogas production [4]. As the source required is coming from the household itself, there is no problem of availability of resources for using in the biogas plant.

As the plant is made for a household, there is no problem of getting the raw material to be used in the biogas plant. The product can also be used in places where there is a chance of obtaining food wastes such as restaurants and canteens. It is not limited to the household but also to small-scale industries. So, there is no need for any transportation of the produced gas from the plant. It can be stored and used in the house itself, thereby giving them an alternative to a conventional source of energy.

These are the results obtained from the interview held as part of the research. These are the major views we got from the interviewees. The answers to various questions were based on their daily living style and their background. It also

showcases the importance of shifting to renewable resources from non-renewable resources. Most of the interviewees are of the opinion that biogas is an upcoming energy source which has the huge potential to change the present energy conditions.

6 Conclusions

The purpose of this paper is to discuss a new solution to manage biowastes and generate electricity from them. Our study has revealed the immense potential of biogas and the supreme need of the hour to shift toward the green energy sources. In the renewable energy domain, upgrading to green gas has the potential to make biogas the envisioned system service provider. The present system of using small-scale biogas plants for cooking purposes will give way toward a multipurpose environment where cooking is only a small purpose that is achieved.

The use of biomass to produce biogas right now can furthermore provide an incentive for biomass owners to harvest and use or sell their biomass, thus increasing the availability of biomass and the fertilizer that is obtained as a by-product. Biogas can thus serve as a stepping stone in the transition toward a bio-economy: Biomass can be used for feasible applications now while also enabling the development of new technologies for improved efficiency in the future including the facility to dry up the slurry and to form powdered fertilizer.

The maximum utilization of the biowastes is objective, and by converting it to electric energy, we are capable of empowering the user by reducing the dependency on fossil fuel and a very useful mechanism by which he can get rid of the biowastes, which otherwise could have been a major issue to be dealt with. Portable Bio-electric Plant thus is a solution for the energy problems of the hour.

References

1. Müller-Langer, F., et al.: Benchmarking biofuels—a comparison of technical, economic and environmental indicators. Energy Sustain. Soc. **4**, 20 (2014)
2. Parliament, European: Directive 2009/28/EC of the european parliament and of the council of 23 April 2009. Off. J. Eur. Union **140**, 16–62 (2009). https://doi.org/10.3000/17252555.L_2009.140.eng
3. Dahmen, et al.: The bioliq®® bioslurry gasification process for the production of biosynfuels, organic chemicals, and energy. Energy Sustain. Soc. **2**, 3 (2012)
4. Sorathiya, L.M.: Eco-friendly and modern methods of livestock waste recycling for enhancing farm profitability. Int. J. Recycl. Org. Waste Agric. **3**, 50 (2014)
5. Bundesministerium BMU, Bundesministerium BMELV: Nationaler Biomasseaktionsplan für Deutschland—Beitrag der Biomasse für eine nachhaltige Energieversorgung. Bundesministerium für Umwelt, Naturschutz und Reaktorsicherheit (BMU) and Bundesministerium für Ernährung, Landwirtschaft und Verbraucherschutz (BMELV). Berlin (2010)

Structural Health Monitoring of Smart Composites: A Review

Ruby Maria Syriac and A. B. Bhasi

1 Introduction

Materials which have a unique ability to respond to stimuli are known as smart materials. Smart structures react to environmental conditions like stress, strain, temperature, pressure, an electric field and behave in an intelligent way to the associated functions of sensing, processing, and actuation [1]. Smart structures technology is a currently emerging field which can revolutionize the areas of structural design, manufacturing, and maintenance and is considered as the evolution from simple homogenous materials to multi-material (composite material). Nowadays, a homogenous material is replaced by composite materials, especially in the aeronautic domain. For example, Boeing's 7E7 Dreamliner project has 50% of its structures made of composites [2, 3].

Integrating smart materials with composite enables the composite structures to become "intelligent," that is, able to perform self-structural health monitoring and provide an actuating response without human intervention. In short, structural health monitoring is a way of making materials and structures smart. It involves the integration of sensors, smart materials, computational power, data transmission, and processing ability inside the structures. Boeing's 7E7 Dreamliner project is the first one to embed SHM systems for impact detection [3]. Smart composite structures also find its application in marine structures, civil structures like long bridges and tall buildings, pipeline systems, etc. This ensures structural integrity, safety, economic improvement, weight and time savings, and auto-control, through on-event and periodic inspection that detects damages. The future in developing and

R. M. Syriac (✉) · A. B. Bhasi
CUSAT, Cochin, India
e-mail: rubymaria00@gmail.com

A. B. Bhasi
e-mail: bhasiab@gmail.com

analyzing engineering structures will be increasingly shaped by our ability to monitor, inspect, and detect damage.

2   Structural Health Monitoring

Structural health monitoring (SHM) denotes a system with the ability to detect and interpret adverse "changes" in a structure to improve reliability and reduce life cycle costs [4]. A typical SHM system consists of a sensor, a data processing system, and a health evaluation system [5]. In general, SHM is the process of mechanizing various diagnostic and prognostics techniques together. SHM techniques are used in many fields of engineering like aerospace [2, 6–11], civil structures like building and bridges [5, 12–16], offshore structures [17] and ships [18], and many more (Fig. 1).

2.1   Installation

The sensors can be installed on the surface of composites, using additives or by using protective cladding only after the base structure has been manufactured. This minimizes the disruption to the conventional manufacturing cycle. However, this method necessitates the need of a skilled laborer, cabling and adds on the cost and weight of the entire structure. Moreover, installing sensor upon a thick composite may not be able to locate the damage precisely, and this will influence the reliability of the smart structure. So, as an alternative to installation, sensors can be embedded into the base structure at the time of manufacturing, and this eliminates the need for additives and protective support [18].

Fig. 1 Typical SHM system
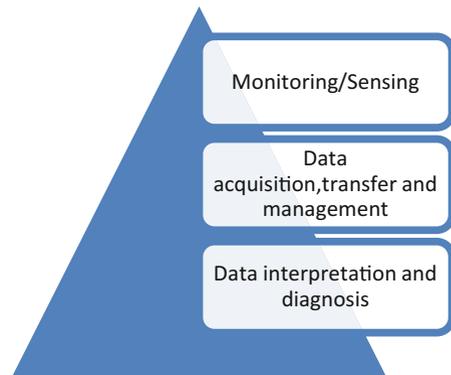
Care should be given at the time of installing or embedding the sensors, such that it should not alter the current system used in aircraft or other civil structures. Here comes the need of a self-powered and a wireless communicating system which does not alter the current system on which it is working [9].

2.2 SHM Classification

Smart materials can be classified as active or passive (Fig. 2).

2.2.1 Active Materials

Active smart materials are those which possess the ability to alter their geometric or material properties under the application of various external stimuli, thereby acquiring an inherent capacity to transduce energy. Piezoelectric materials, SMAs, ER fluids, and magnetostrictive materials are the active smart materials and are capable of acting as force transducers and actuators [2, 19].

- *Piezoelectric material.* The most promising and widely used actuators for SHM and structural repair are piezoelectric actuators and sensors. In the phenomenon of piezoelectricity, materials possessing piezoelectricity will generate an electrical charge when mechanical pressure is applied, and the material will experience a geometric modification on the application of electrical charge. Based on electrical–mechanical conversions, piezoelectric materials display simultaneous actuator/sensor behavior.

Piezoelectric ceramics (Lead Zirconate Titanate, PZT), piezoelectric polymers (Polyvinylidene Fluoride, PVDF), and Piezoelectric Ceramic/Polymer Composites are the frequently used natural materials which act as actuators and sensors for structural health monitoring and structural repair [20]. Among various types,

Piezoelectric material	• Stress	Electric field
	• Electric field	Mechanical strain
Optic fibre	• Temperature/Pressure	Change in Optical signal
	• Mechanical strain	Opto-electronic signals
Magnetostrictive material	• Magnetic field	Mechanical strain
Electro-rheological material	• Electric field	Change in Viscosity
Shape memory alloy	• Heat	Original memorized shape

Fig. 2 Common smart materials and associated stimulus–response [19]

piezoelectric ceramics/composites are the frequently used piezoelectric actuators for SHM due to its superior properties which include low impedance, high dielectric constants, and good electromechanical coupling [19]. The reciprocal energy transforming characteristics of piezoelectricity enables piezoelectric materials to function as sensors, actuators, or transducers [20–24].

Piezoelectric patches are in great demand as it is much lighter and creates less concentrated stress on the damaged structure. They are chemically inert and have high elastic modulus, stiffness and strain coefficient. The beneficial features also include their wide diversity of sizes, possibility to incorporate them in very remote and inaccessible locations, fast response, long-term stability, and high energy conversion efficiency. Also, piezoelectric sensors are much consistent, reliable, and self-powered. However, piezoelectric materials are brittle and have low tensile strength. Wang et al. [25] and Huang et al. [26] have explained certain piezoelectric-based, conservative methods of crack detection in beams and plates using time-of-flight analysis of Lamb wave propagation. Also, Quek et al. [27] have developed an experimental setup for monitoring and detecting damage in beams using piezoelectric sensors. Schematic representation of similar sensors is available in [28].

- *Magnetostrictive material.* Likewise, in piezoelectric materials, magnetostrictive materials respond only to magnetic fields rather than electric. They find applications in low-frequency, high-power transducers. Magnetostrictive materials are considered as the promising component for active vibration damping. When placed in a magnetic field, ferromagnetic materials are mechanically deformed and this effect is termed as the magnetostrictive effect. The reverse phenomenon, in which the magnetic induction of the material alters when the material is mechanically deformed, is called the inverse magnetostrictive effect [29]. Magnetostrictive materials are having moderately high elastic stiffness, elastic modulus, and strain coefficients. An example of the magnetostrictive material is TERFENOL-D which is rarest of rare earth material. So, these sensors are costly. SHM of fiber-reinforced composite structures with embedded magnetostrictive patches has been done using finite element method and artificial neural networks by Ghosh et al. [30]. He has also incorporated frequency domain analysis using spectrally formulated beam elements.
- *Electro-rheological fluid.* Electro-rheological (ER) fluid actuators are used for monitoring vibration of smart composite structures. ER fluids are suspensions which undergo reversible changes in rheological properties such as viscosity, elasticity, and plasticity when subjected to electric fields or magnetic fields, correspondingly. When the strength of the external field goes ahead of critical value, ER fluid can change its state from liquid to solid in a short time frame. Because of this unique property as convenient, rapid, reversible suspension, ER fluids are one among the critical type of actuators used in smart material systems and structures [12, 13, 31, 32]. These types of sensors are suitable to transfer shear stress.

These electro-rheological fluids (ERFs) exhibit a rapid, reversible, and tunable transition from a fluid state to a solid-like state upon the application of an external electric field [33]. Some of the advantages of ERFs are their high yield stress, low current density and fast response, high electrically controlled resistive forces, long life, and very small size. Their long life and ability to function in a wide temperature make them suitable for extreme environments [33]. The commercialization of ERFs is difficult due to complexity and nonlinearities of their behavior and difficulty in forming a closed-loop control to solve. Besides, the need for high voltage to control ERF-based devices and relatively high cost makes them unfeasible to use in typical situations [34]. The role of EFRs as active dampers for vibration suppression is explained by Furusho et al. [35].

- *Shape memory alloys.* Shape memory alloys (SMAs) or shape memory polymers are materials which change their shapes with the change in temperature. So, they are also termed as thermo-responsive materials. They can get deformed and go back to their original shape on heating by generating an actuating force. Examples of shape memory alloy include nitinol, a nickel–titanium alloy, which is mainly used in biomechanical applications. Its advantages include greater ductility, more recoverable motion, stable transformation temperatures, high biocompatibility, excellent corrosion resistance, and for shape recovery the ability to be electrically heated [36]. However, they are not suitable for structural health monitoring of composites due to their lower bandwidth operation and low efficiency. The role of SMA as actuators has been explained by Mavroidis [34].
- *PH-sensitive materials.* PH-sensitive materials can change their color with the change in acidity. Chromogenic systems change color in response to electrical, optical, or thermal variation. An example of such type is liquid crystal displays. Similarly, photochromic materials are those which can change their color in response to light. Polymer gels, like hydrogels, can swell or shrink due to small changes in temperature or pH [19].

2.2.2 Passive Materials

The non-active materials are called passive smart materials. Although smart, they lack the inherent capability to transduce energy. Passive materials can perform as sensors but not as actuators or transducers [2, 19]. Fiber optic material is a good example of a passive smart material.

- *Fiber optic sensors.* An important passive sensor that can be used in smart structures is fiber optic sensors (FOSs). As FOS offers inherent immunity to electromagnetic interference, they do not degrade structural integrity entrenched in the composite material [12, 37–39]. Among all smart sensors, FOS has been used solely to monitor numerous practical civil structures effectively. This shows that FOS is more promising toward SHM of civil engineering structures

than other smart sensors. Monitoring of the local strain and displacement of the civil structures can be used to detect the working conditions of components [5]. The large sensing scope, low transmission loss, and anti-electromagnetic interference make the usage of FOS suitable to the harsh natural environment. The SHM of composite aircraft structures has been reviewed by Di Sante [10]. His work considered both the multi-point and distributed sensing techniques.

3 SHM Strategies

3.1 Monitoring

Health monitoring of structures can be accomplished by embedding active smart materials within the structure so that they can act as actuators or transducers. Actuators generate, mostly, a strain in the material, which can be altered into a force. Health monitoring can be done using various techniques.

3.1.1 Strain-Based Systems

In strain-based systems, the change in the local distribution of strain in the presence of damages or cracks is used for determining the defect. In real-time, defects in the composites can be identified by using these types of sensors which include electrical resistance strain gauges, fiber optics, and piezoelectric transducers [17].

3.1.2 Vibration-Based Systems

This system uses the changes in vibration response in detecting the presence of damage in composite structures. Active and passive stress wave technique is the common approach adopted in SHM. The active technique includes acoustic emission monitoring, and passive technique includes acousto-ultrasonics. Both techniques use piezoelectric transducers for monitoring. These techniques use environmental loading for structural excitation which limits the requirement for an external exciter [40].

3.1.3 Sensor Rupture-Based Systems

Sensor breakage is also used as the basis for SHM as in Comparative Vacuum Monitoring system. Cracks in the structure can be identified as they reach the galleries of the patch, which is on the surface, cause a change in relative pressure.

Crack gauges, which depend on the electrical resistive strain gauge failure, are used to detect the length of the cracks [11, 41].

3.2 Damage Detection

Damage detection includes determining the location, nature, extent, and the cause of damage. Damage detection is a process of pattern recognition [42]. The information measured using sensors are used to correlate a damaged state using a diagnostic tool. To characterize damage, sophisticated data processing is required which depends on the type of sensor used. Sensor data is used to calculate damage using artificial intelligence algorithms or damage detection algorithms, based on statistical novelty detection [5, 21, 43, 44]. A damage detection method based on constrained vibration deflection shape was presented by Schulz et al. [45]. The proposed method could be extended to complex heterogeneous structures too. A piezoelectric-based diagnostic technique was developed by Jeong for diagnosing fatigue crack growth in metallic structures [46].

3.3 Self-healing

Reliable diagnosis of damage in composites structures provides a better opening to predict the rate of progression of damage and the extent of continuing safe life. Composite structures are designed on the basis that any damage, which is not apparent, will not grow under the design loads. Accurate information on loading and boundary conditions and intimate knowledge of the properties of the structure are required for correct prediction or structural health prognosis. Unlike structural diagnosis, structural health prognostics is highly specific to the target structure and necessitates the use of effective numerical models. It also requires related structural information beyond its immediate vicinity to make an appropriate prediction. So, the majority of the works in SHM of composite structures are concentrated on health monitoring and diagnosis rather than prognosis. However, without prognosis capabilities, the information from damage diagnosis in SHM has limited use.

4 SHM Benefits

The motivation for SHM of structures includes:

- *Safety*: The primary drive for SHM is safety. The importance of SHM is apparent after spectating some incidents due to unsatisfactory maintenance and ill-controlled manufacturing process, for example, in the aeronautic field, the

accident of Aloha Airlines [OTT 88], or the collapse of the Mianus River
Bridge, in the civil engineering field. Studies have shown that after the intro-
duction of SHM, the rate of aircraft accidents have globally decreased by less
than 10% [3, 15].

- *Reduction in weight*: As the sensors are permanently present in the structure, at
  the design stage, certain safety margins are relaxed in some critical areas. This
  results in weight reduction, giving higher aircraft performance, lower fuel
  consumption, and greater maximum range.
- *Economy*: The introduction of SHM system brings down the maintenance cost
  with the reduction in the frequency of inspection and maintenance. The eco-
  nomic benefits are particularly strong for end-users. In effect, SHM in structures
  promotes constant maintenance costs and reliability.
- *Time and effort*: Reduction in the frequency of inspection allows optimal use of
  the structure and a minimized downtime. Reports reveal that for military aircraft,
  in [BAR 97], featuring both metal and composite structure, an estimated 40% or
  more can be saved on inspection time using smart monitoring systems [3, 9].
- *Effective maintenance*: SHM in composite materials enables the replacement of
  scheduled and periodic maintenance (time-based) with performance-based
  maintenance (condition-based) or at least by reducing the present maintenance
  labor. The concept of condition-based maintenance is that a sensing system on
  the structure will monitor the system response and notify the operator that
  damage has been detected. Life-safety and economic benefits are associated with
  this maintenance philosophy. Effective maintenance drastically minimizes the
  human involvement, and consequently, reducing labor, human errors, and thus
  improving reliability. This drastic change in maintenance philosophy are exe-
  cuted in military air vehicles [DER 03] and in civil aircraft [BER 03, GOG 03]
  [2.36,60].

Apart from these benefits, optimized design of SHM incorporated structures
improves design efficiencies and greater accessibility to remote portions, which can
be counted as a long-term benefit [8].

5   Possibilities to Research

One advantage of SHM systems is that they deliver continuous data which can
eliminate one-off errors. However, robust design with strong sensor embedding and
connecting method is required to avoid systematic errors. A robust SHM system
design demands the durability of sensors and actuators under severe environmental
conditions and loads. Moreover, any SHM technology should not conflict with the
current systems, which encompass the need for self-powered and wireless com-
municated methods. Also, reported works on actual predicting models for high
strain and through-thickness stresses are limited.

6   Conclusion

SHM is recognized as the pivotal step to technological advancement in the design and operation of engineering structures. Its role is more relevant in composite materials of high-valued assets. In this paper, applicability of various smart composite actuators in SHM has been discussed. Due to their excellent mechanical and electric coupling properties, piezoelectric materials hold many potential applications in the fields of structural health monitoring and repair. Also, SHM of the smart composite is a growing area with much research potential.

References

1. Mackerle, J.: Smart materials and structures-a finite element approach-an addendum: a bibliography (1997–2002). Model. Simul. Mater. Sci. Eng. **11**, 707–744 (2003)
2. Khan, A.A., Zahid, N.: History, current status and challenges of SHM in aviation. J. Space Technol. **4**(1) (2014)
3. http://www.iste.co.uk/data/doc_xqjujdlhnfls.pdf
4. http://www.MetisDesign.com
5. Sun, M., Staszewski, W.J., Swamy, R.N.: Smart sensing technologies for structural health monitoring of civil engineering structures. Adv. Civil Eng. 13 (2010). Article ID 724962
6. Goranson, U.G: Jet transport structures performance monitoring. In: Proceedings of the Stanford Workshop on Structural Health Monitoring, pp. 3–17. Palo Alto, California (1997)
7. Hunt, S.R., Hebden, I.G.: Validation of the eurofighter typhoon structural health and usage monitoring system. In: European COST F3 Conference on System Identification and Structural Health Monitoring, pp. 743–753. Madrid, Spain (2000)
8. Stefani, A.M.: Review of air carriers use of aircraft repair stations. FAA Report Number AV-2003–047 (2003)
9. Galea S.C., Powlesland I.G., Moss S.D., Konak M., Van der Velden S., Stade B., Baker A.A.: Development of structural health monitoring systems for composite bonded repairs on aircraft structures. In: SPIE 8th Annual International Symposium on Smart Structures and Materials: Smart Structures and Integrated Systems Conference, Newport Beach, CA, USA, paper 4327–4333, 4–8 (2001)
10. Di Sante, R.: Fibre optic sensors for structural health monitoring of aircraft composite structures: recent advances and applications. Sensors **15**, 18666–18713 (2015)
11. Stehmeier, H., Speckman, H., Bolten, J.: Comparative vacuum monitoring of fatigue cracking in aircraft structures. In: Proceedings 2nd European Workshop on SHM, Munich Germany 7–9 July (2004)
12. Leng, J., Asundi, A., Liu, Y.: Vibration control of smart composite beams with embedded optical fiber sensor and ER fluid. Trans. ASME **121**, 508 (1999)
13. Leng, J.S., Liu, Y.J., Du, S.Y., Deng, Y., Wang, D.F.: Dynamic characteristics of beam specimen featuring electro-rheological fluids. Exp. Mech. **37**(1), 1–4 (1997)
14. Maeck, J., Abdel Wahab, M., Peeters, B., De Roeck, G., Visscher, J., De Wilde, W.P., Ndambi, J.M., Vantomme, J.: Damage identification in reinforced concrete structures by dynamic stiffness determination. Eng. Struct. (Elsevier Science Ltd.) **22**, 1339–1349 (2000)
15. Peeters, J.M.B., Maeck, J., De Roeck G.: Excitation sources and dynamic system identification in civil engineering. In: European COST F3 Conference on System Identification and Structural Health Monitoring, pp. 341–350. Madrid, Spain (2000)

16. Di Scalea, F.L., Karbhari, V.M., Seible, F.: The I-5/Gilman advanced technology bridge project, Smart structures and materials: smart systems for bridges, structures, and highways. In: Proceedings of SPIE, vol. 3, 988, pp. 10–17. Newport Beach, California (2000)
17. Bethel, K., Catha, S.C., Ekelund, A., Gallagher, J., Charbonneau, K.R., Kanninen, M.F., Mandich, I., Stonesifer, R., Stringfellow, W.D.: The development and validation of a high strength, self-monitoring, composite tight fit liner for offshore pipelines and risers. In: Fourth International Conference on Composite Materials for Offshore Operations, Houston, Texas, USA, 4–6 October (2005)
18. Herszberg, I., Li, H.C.H., Dharmawan, F., Mouritz, A.P.: Damage assessment and monitoring of composite ship joints. Compos. Struct. **67**, 205–216 (2004)
19. Gandhi, M.V., Thompson B.S.: Smart Materials and structures, vol. 4, pp. 496–50. Chapman & Hall, London (1992)
20. Duan, W.H., Wang, Q., Quek, S.T.: Applications of piezoelectric materials in structural health monitoring and repair: selected research examples. Materials **3**, 5169–5194 (2010)
21. Kamila, Susmita: Introduction, classification, and applications of smart materials: an overview. Am. J. Appl. Sci. **10**(8), 876–880 (2013)
22. Wu, F., Chang, F.K.: Diagnosis of debonding in steel reinforced concrete with embedded piezoelectric elements. In: Proceedings of the 3rd International Workshop on Structural Health Monitoring: The Demands and Challenges, pp. 670–679. CRC Press, New York, NY, USA (2001)
23. Kawiecki, G.: Feasibility of applying distributed piezo transducers to structural damage detection. J. Intell. Mater. Syst. Struct. **9**(3), 189–197 (1998)
24. Saafi, M., Sayyah, T.: Health monitoring of concrete structures strengthened with advanced composite materials using piezoelectric transducers. Compos. B **32**(4), 333–342 (2001)
25. Wang, Q., Quek, S.T.: Flexural vibration analysis of sandwich beam coupled with piezoelectric actuator. Smart Mater. Struct. **9**, 103–109 (2000)
26. Huang, N.E., Wu, M.L.C., Long, S.R., Shen, S.S.P., Qu, W.D., Gloersen, P., Fan, K.L.: A confidence limit for the empirical mode decomposition and Hilbert spectral analysis. P. Roy. Soc.A-Math. Phy. **459**, 2317–2345 (2003)
27. Quek, S.T., Wang, Q., Zhang, L., Ang, K.K.: Sensitivity analysis of crack detection in beams by wavelet technique. Int. J. Mech. Sci. **43**, 2899–2910 (2001)
28. Herszberg, I., Bannister, M.K., Li, H.C.H., Thomson, R.S., White, C.: Structural health monitoring for advanced composite structures. Unpublished
29. Kwun, H., Bartels, K.A.: Magnetostrictive sensor technology and its applications. Ultrasonics **36**(1–5), 171–178 (1998)
30. Ghosh, D.P., Gopalakrishnan, S.: Coupled analysis of composite laminate with embedded magnetostrictive patches. Smart Mater. Struct. **14**, 1462–1473 (2005)
31. Ouyang, P.R., Tjiptoprodjo, R.C., Zhang, W.J., Yang, G.S.: Micro-motion devices technology: the state of arts review. Int. J. Adv. Manufact. Technol. **38**, 463–478 (2008)
32. Leng, J.S.: Active vibration control of smart composites featuring electro-rheological fluids. Appl. Compos. Mater. **2**(1), 59–65 (1995)
33. Phule, P., Ginder, J.: Synthesis and properties of novel magnetorheological fluids having improved stability and redispersibility. Int. J. Mod. Phys. MRS Bull, 19–2 (1998)
34. Mavroidis, C.: Development of advanced actuators using shape memory alloys and electrorheological fluids. Inc. Res Nondestr. Eval. **14**, 1–32 (2002). https://doi.org/10.1007/s00164-001-0018-6
35. Furusho, J., Zhang, G., Sakaguchi, M.: In: Proceedings of IEEE International Conferences on Robotics and Automation, pp. 3441–3448, Albuquerque, NM, 47 (1997)
36. Waram, T.: Actuator design using shape memory alloys, 2nd ed
37. Udd, E.: Fiber optic smart structures. Wiley Inc (1995)
38. Leng, J.S., Asundi, A.: Vibration measurement of smart composite structures by using the new intensity modulated optical fiber sensor. In: SFIE-The International Symposium on Industrial and Environmental Monitors and Biosensors, pp. 110–115. SPIE 3541, USA, (1998)

39. Elvin, N., Leung, C.K.Y., Sudarshanam, V.S., Ezekiel, S.: Novel fiber-optic delamination detection scheme: theoretical and experimental feasibility studies. J. Intell. Mater. Syst. Struct. **10**(4), 314–321 (2000)
40. Yan, Y.J., Cheng, L., Wua, Z.Y., Yamb, L.H.: Development in vibration-based structural damage detection technique. Mech. Syst. Signal Process. **21**, 2198–2211 (2007)
41. Wheatly, G., Kolgaard, J., Register, J., Zaidi, M.: Comparative vacuum monitoring as an alternate means of compliance. Insite Non-Destruct. Test. Condition Monit. **47**(3), 153–156 (2005)
42. Price, D.C., Batten, A., Edwards, G.C., Farmer, A.J.D., Gerasimov, V., Hedley, M., Hoschke, N, Johnson, M.E., Lewis, C.J., Murdoch, A., Prokopenko, M., Scott, D.A., Valencia, P., Wang, P.: Detection, evaluation and diagnosis of impact damage in a complex multi-agent structural health management system. In: 2nd Australasian Workshop on Structural Health Monitoring, Monash University, Melbourne, Victoria, Australia, 16–1 (2004)
43. Wang, X., Foliente, G., Su, Z., Ye, L.: Information fusion in distributed sensor network for structural damage detection. In: ACCM-4, Sydney, NSW, Australia (2004)
44. Markou, M., Singh, S.: Novelty detection: a review—Part 1: statistical approaches. Sig. Process. **83**, 2481–2497 (2003)
45. Schulz, M.J., Ghoshal, A., Sundaresan, M.J., P., Pai, F., Chung, J.H.: Theory of damage detection using constrained vibration deflection shapes. SHM, vol. 2, issues 1, pp. 0075–0099. Sage Publications (2003)
46. Ihn, J.-B., Chang, F.-K: Detection and monitoring of hidden fatigue crack growth using a built-in piezoelectric sensor/actuator network: I. Diagnostics. Smart Mater. Struct. **13**, 609–620 (2004)

Influence of Soil-Structure Interaction on the Structural Performance of D-30 Transmission Line Tower

Anitha Varghese and Job Thomas

1 Introduction

A tower is a freely standing self-supporting structure fixed to the base or foundation. Transmission line tower is one among them [1]. Transmission line tower is also called electricity pylon and is a tall, steel latticed structure used for supporting the extra-high-voltage (EHV) electric transmission lines. These lines carry currents. Therefore, these lines should be aligned at high altitudes away from the nearest objects or ground level. Transmission line towers contribute major cost of the power grid system [2].

The main components of the transmission line towers are diagonal bracings, horizontal struts, and leg members. Microwave transmission towers, radio transmission towers (both short, medium wave wireless), television transmission towers, satellite reception towers, air traffic control, flood light stand, oil drilling masts, and overhead tanks are examples for tower construction. Since tower structure is repetitive in nature, any saving in weight will build up the saving of material cumulatively. The Transmission line tower costs about 35–45% of the total cost of the transmission line, and hence, the development of an optimum design can therefore result in substantial cost reduction [3].

The transmission towers are designed considering the loads due to earthquake, cyclones, and temperature. The iterative complex computations involved in the design are carried out using supercomputers [3]. Structural optimization for eco-

A. Varghese (✉)
Department of Civil Engineering, Rajagiri School of Engineering and Technology,
Cochin 682039, Kerala, India
e-mail: anitajohn32@gmail.com

J. Thomas
Department of Civil Engineering, School of Engineering, Cochin University
of Science and Technology, Cochin 680 022, Kerala, India
e-mail: job_thomas@cusat.ac.in

Fig. 1 110 kV, D-30,
double-circuited, tension
tower
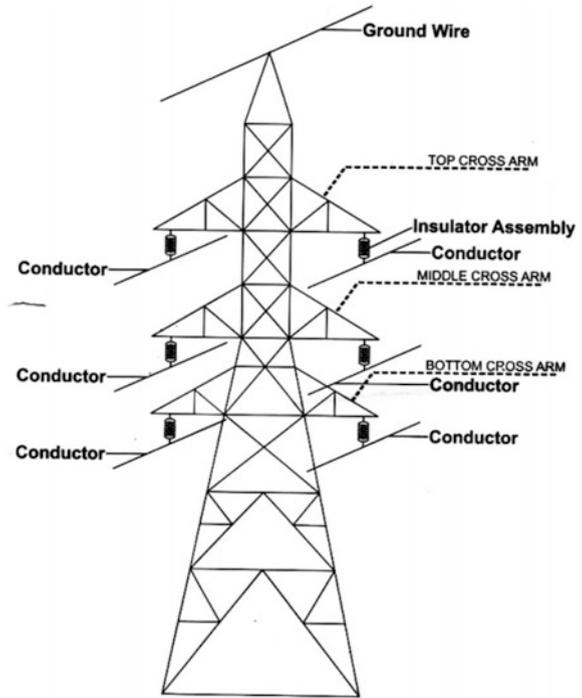
nomic design of transmission tower members involves more computational effort
and is time-consuming.

The height of the tower varies from 15 to 500 m. The most commonly used
heights are 20–45 m for power transmission, 15–50 m for flood lights, 50–200 m
for radio transmission, and 400 m for television towers. In this study, a 110 kV,
double-circuited, line deviation 30 degrees denoted by D-30 tension tower is
analyzed. The geometric details of the tower are given in Fig. 1.

The commercial finite element software, NISA, is used for modeling and anal-
ysis. The corner vertical members of the towers are called legs or column members,
and they are the main load bearing elements. The leg members are interconnected
by bracings with or without horizontals, which carry a nominal force. The legs and
bracing members will be under compression in certain load combination, and
therefore, the slenderness ratio of the members plays an important role.

2 Background

Rao [3] described a method for the development of optimized tower designs for
extra-high-voltage transmission lines. A derivative-free method of nonlinear opti-
mization is incorporated in the program, specially developed for the configuration,

Table 1 Types of towers

S. No.	Type	Purpose
1	Tangent towers with suspension strings (0°–2°)	To be used on straight run and up to 2° line deviation
2	Small angle towers with tension strings (2°–15°)	To be used for line deviation from 2° to 15°.
3	Medium angle towers with tension strings (15°–30°)	To be used for line deviations from 15° to 30° and dead ends
4	Large angle and dead-end towers with tension strings (30°–60°) and dead end	To be used for line deviations from 30° to 60° and dead ends

analysis, and design of transmission line towers. It is demonstrated that the proposed method of design helps in substantial saving in tower weight. Albermani et al. [4] found out that diaphragm bracing in transmission towers is economical to withstand lateral forces. Tort et al. [5] proposed integrating the simulated annealing (SA) optimization algorithm for weight reduction design of transmission towers. Ramalingam and Jayachandran [6] developed a model to account for bolt slip in leg splices of the transmission line tower. Yang and Hong [7] analyzed tower-line system considering the turbulent winds and the tower–wire interaction. Rao et al. [8] studied the effect of providing non-triangulated hip bracing pattern and isolated hip bracings on the failure of transmission line towers. Selvaraj et al. [9] used FRP pultruded profiles for the composite cross-arm for power transmission lines. Shu et al. [10] reported that ground surface deformations are more significant on the truss members closed to the supports.

The dynamic impedance of the foundation structure is determined. The different types of towers used for the supporting electric transmission lines are given in Table 1.

2.1 The Bracing System and Types of Bracing

Bracings are the interconnecting elements of the main skeleton. Depending on the nature of the stress, there are three categories of elements in the bracing of towers. The first category is tension bracing elements in which the force is tensile in nature in all load cases. The diagonal members connect the leg members which are tensile bracing elements. The horizontal members connecting the leg members are compression bracing elements. The bracing members of a tower with deviation in general are subjected to both tension and compression depending on the load case. These tension compression bracing elements are to be designed for both maximum tension and compression force in the element. The geometry of the common
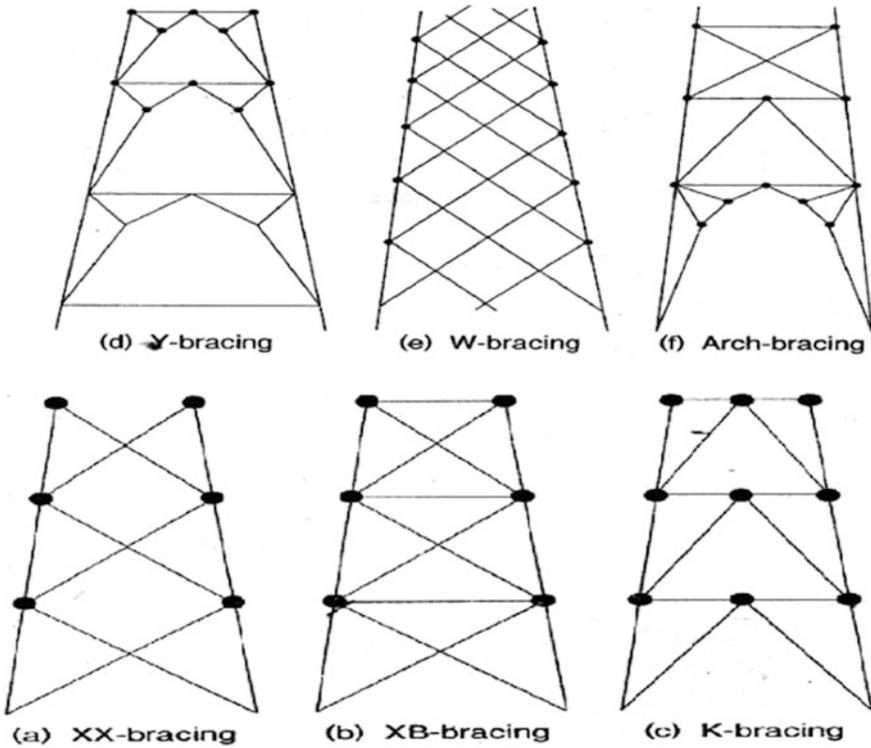
Fig. 2 Different types of bracings

bracing systems is given in Fig. 2. Depending upon the height and base dimensions, one of these bracing systems is selected.

2.2 Foundation

The tower foundation costs approximately 10–30% of the cost of the tower which is about 5–10% of the cost of transmission line project. Depending upon the type of foundation and the type of soil, the loading will vary on the tower. The failures of tower foundations are the prime cause for the collapse of the towers. The foundations of transmission line towers vary from spread footing of shallow type to deep foundations such as well or pile system depending on the uplift on foundation and the geological conditions of the soil.

2.3 Details of Tower

In this study, a D-30 electric transmission line tower is analyzed. Three cases were analyzed, namely with fixed end condition at foundation level, with pile and fixed end condition at the bottom of the pile, and the pile with soil around and fixed at bottom. Various load combinations are analyzed.

3 Finite Element Analysis of the Transmission Line Tower

Finite element method is an efficient and powerful tool for numerically solving mathematical problems. In this method, the entire continuum is divided into small elements. These elements are connected through the nodes. The commercial software Numerically Integrated element for System Analysis (NISA) is used for the analysis of the tower. The Display IV is used for the finite element modeling of geometry. A comprehensive library is available in NISA. Each element in the library is identified by two variables, NKTP and NORDR. NKTP specifies the element type, and NORDR specifies the element shape.

3.1 Modeling

The description of the model primarily consists of element data, nodal data, and material data. Element data includes element type and selection. Nodal data is expressed by nodal coordinates. Material data includes specifications of material properties.

3.1.1 Modeling of Transmission Line Tower

The members of transmission tower are modeled as 3D beam element. This element consists of node prismatic, where NKTP = 12, NORDR = 1. The stretching, bending, and torsion effects can be simulated using this element. The deformation is characterized by three translations (Ux, Uy, Uz) and three rotations (ROTX, ROTY, ROTZ). The reference properties of 3D beam element are given in Table 2

3.1.2 Modeling of Pile

The pile is also modeled using the 3D beam element. Each node is having six degrees of freedom.

Table 2 Element reference details of 3D beam element

S. No.	Item	Specification
1	Element type	NKTP = 12, 3D beam element
2	Analysis type	Static, dynamic, buckling
3	Material properties	4 properties (Ex, Nuxx, DENS, ALPX)
4	Dynamic capabilities	Constant of lumped mass, eigenvalue, transient dynamic, shock spectrum analysis

Table 3 Element reference of 3D general spring element

S. No.	Item	Description
1	Element type	NKTP = 38, 3D general spring element
2	Analysis type	Static, dynamic, buckling, etc.
3	Degree of freedom	Three per node UX, UY, UZ
4	NORDR	Line: two nodes (NORDR = 1)

3.1.3 Modeling of Soil

Soil around the pile is modeled using 3D general spring element with NKTP = 38 and NORDR = 1. This element is a two-node 3-D general spring element with six independent spring rates and three degree of freedom, namely UX, UY, UZ per node. The reference property of 3D general spring element is given in Table 3.

4 Loads

All the loads parallel and normal to the transmission line and also in the vertical direction are accounted for in the analysis of the tower. The loads acting on a transmission line tower are taken from IS: 802 [11]. Transverse, longitudinal, vertical, and torsional loads were accounted for in this study.

4.1 Transverse or Horizontal or Lateral Loads

The horizontal loads on the tower are due to wind load on conductors, wind load on ground wire, wind load [12] on insulator string, wind load on tower and horizontal component of tensions in conductors and earth wire. In the case of D-30 tower, the projected length of the wire on either side is not equal, and hence, twisting force

will be developed due to the wind effect. The direction of the transverse force is 90° to the longitudinal axis of the conductor.

4.2 Longitudinal Loads

Longitudinal forces are due to unbalanced pull due to broken conductor, unbalanced pull due to broken ground wire, and load due to temperature variation. The direction of longitudinal force is along the axis of the conductor.

4.3 Vertical Loads

The vertical loads are due to weight of tower structure, weight of power conductor, weight of ground wire, weight of lineman with tools, and weight of insulator strings and fittings. The vertical loads are acting downward in global Y direction.

4.4 Torsional Loads

The torsional loads are due to breakage of the conductors, breakage of the ground wire. The breakage of the conductors causes zero tension on one side. The tensile force will be maximum due to the unbroken condition in the tower. This causes pulling of the tower to one side and results in torsional load.

4.5 Broken Wire Condition

As per the IS:802 [11]: for double, triple, and quadruple circuit towers of small and medium angle of deviation, any two phases broken on the same side and same span or any one phase and one ground wire broken on the same side and same span whichever combination shall be taken. The design force shall be obtained for the worst case. The transverse load due to wind on conductors and ground wires is calculated. Under broken wire condition, 50% of the normal span and 10% of the broken span shall be assumed as wind span.

Fig. 3 Transmission tower
with load
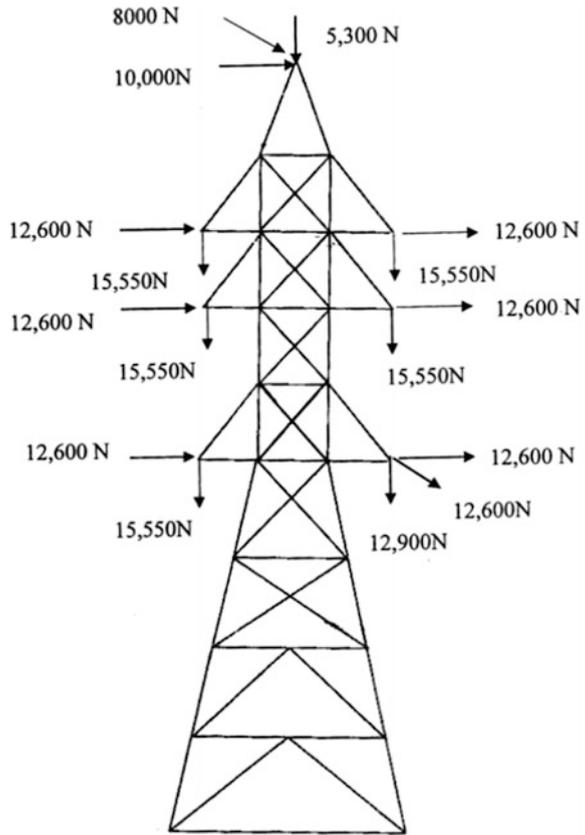
4.6 Load Combinations

The load combinations corresponding to reliability, security, and safety condition
are accounted for in the analysis. The load combinations corresponding reliability,
security, and safety conditions are to be used. Among these combinations, safety
condition is more critical, and hence, it is considered in this analysis [13, 14]. The
load values corresponding to safety condition are given in Fig. 3.

5 Methodology

Power transmission tower structure is modeled as a 3D truss. The manual method of
design suffers from the disadvantage that minimization of weight and examination
of alternative designs involves good deal of effort. In this study, the geometry of the
members of the tower was assumed initially and analysis was carried out.

The member property was selected such that all the members pass the strength criteria of design. The critical values of member forces and deformation are noted and reported.

5.1 Finite Element Analysis Procedure

The nodes are created initially. The elements are generated connecting the nodes. The boundary conditions are applied. The structural loads are applied and solved for unknown displacements. The member forces are then calculated.

5.2 Soil-Structure Interaction

In most of the civil engineering structures, the bottom-most elements of the structure will be in contact with ground. These elements transmit loads from the structure to soil. The deformation of these elements depends on the restraint offered by the surrounding soil. In this study, three aspects were analyzed. In the first case, the effect of omitting pile foundation in the model is examined by considering the bottom as fixed at the level of pile cap and is given in Fig. 4a. In the second case,

(a) Tower with Fixed bottom   (b) Tower and Pile   (c) Tower, pile and Soil
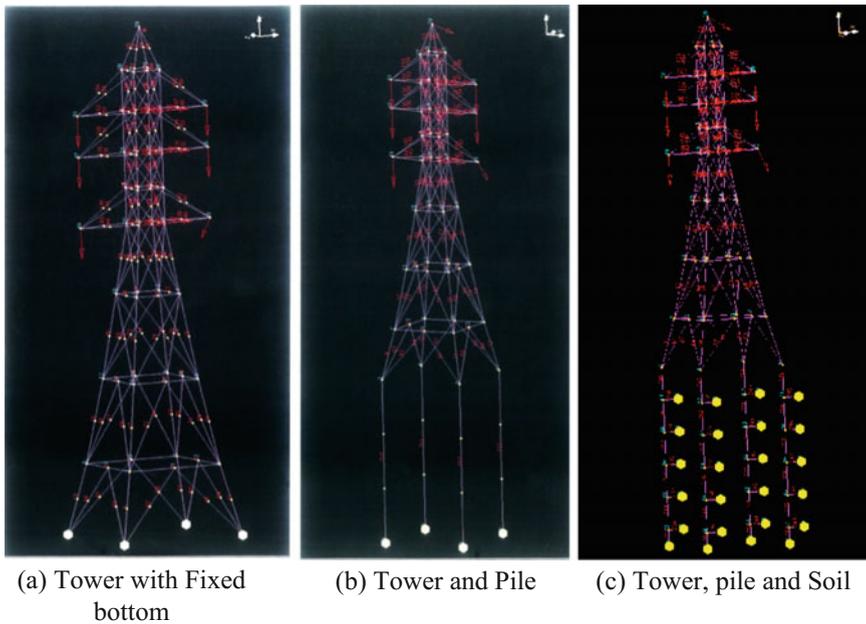
Fig. 4 Analysis cases of the study. **a** Tower with fixed bottom, **b** tower and pile, **c** tower, pile, and soil

pile was modeled below pile cap and assumed to rest on hard rock at this bottom and is given in Fig. 4b. The effect of soil media is omitted. In the third case, the pile along with soil media was modeled to study the effect of soil-structure interaction in overall behavior and is given in Fig. 4c.

The pile of diameter 0.4 m and length 10 m was modeled. The soil stiffness for this soil was calculated using the Vesic equation, and the magnitude was found to be 844 kN/m^3. Hence, the spring constant used was 67.55 kN/mm.

6   Results and Discussion

The results of the analysis are given in Table 4. The maximum deflection was found to be for tower plus pile case. This is due to the fact that the effective length of the tower is maximum in this case. The force in the structure is directly proportional to the deformation of the structure.

The tower + pile + soil is the most realistic model, in which the influence of the soil and the effect of pile are being accounted for. Thus, if the tower alone is considered, the deflection will be underestimated. Similarly, if the tower + pile is considered, the deflection will be overestimated. The underestimated deflection corresponding to tower alone case was found to be about 91% when compared to tower + pile + soil case.

The deflection of the tower + pile case was found to be 144% higher than the tower + pile + soil case. Similarly, the maximum compressive force was found to be 76% for tower alone case when compared to the tower + pile + soil case. The maximum compressive strength for tower + pile was found to be 125% of that of tower + pile + soil.

Maximum tensile load of tower alone case was found to be 69% of that of tower + pile + soil case. Similarly, the maximum tensile load of tower + pile was found to be 136% of that of tower + pile + soil case. Hence, it can be concluded that tower alone case is considered for the design. The force will be underestimated, and hence, the safety of the structure is critical. Similarly, if the tower + pile case is modeled, the member forces are overestimated, and hence, it will lead to uneconomical design.

Table 4   Analysis results

Parameter description	Tower	Tower + pile	Tower + pile + soil
Maximum deflection (mm)	96.6	151.5	105.2
Maximum Compressive load (kN)	107.9	177.2	141.8
Maximum tensile load (kN)	71.6	139.3	102.5

7   Conclusion

The compressive and tensile forces in the members of tower are considerably reduced when soil-structure interaction is modeled. This leads to the fact that soil has an important role in minimizing the design member forces in the structure.

   The safe and economical design can be made when soil-structure interaction is considered for the analysis. The analysis with fixed support at pile cap level underestimates the deflection and member loads. Similarly, the deflection and member forces are overestimated in the analysis of tower and pile system. Hence, it is proposed to carry out the analysis of transmission line tower accounting for the soil-structure interaction. In future, the influence of nonlinearity in the soil behavior and the steel members can be studied.

References

 1. Dayaratnam, P.: Design of Steel Structures. S. Chand Publications, India (2008)
 2. Natarajan, K., Santhakumar, A.R.: Reliability based optimized of Transmission line tower. Comput. Struct. **55**(3), 387–403 (1995)
 3. Rao, G.V.: Optimum designs for Transmission line towers. Comput. Struct. **57**(1), 81–92 (1995)
 4. Albermani, F., Mahendran, M., Kitipornchai, S.: Upgrading of transmission towers using a diaphragm brace system. Eng. Struct. **26**(6), 735–744 (2004)
 5. Tort, C., Şahin, S., Hasançebi, O.: Optimum design of steel lattice transmission line towers using simulated annealing and PLS-TOWER. Comput. Struct. **179**(1), 75–94 (2017)
 6. Ramalingam, R., Jayachandran, S.A.: Computational framework for mimicking prototype failure testing of transmission line towers. Eng. Struct. **123**, 181–191 (2016)
 7. Yang, S.C., Hong, H.P.: Nonlinear inelastic responses of transmission tower-line system under downburst wind. Eng. Struct. **123**, 490–500 (2016)
 8. Rao, N.P., Knight, G.M.S., Mohan, S.J., Lakshmanan, N.: Studies on failure of transmission line towers in testing. Eng. Struct. **35**, 55–70 (2012)
 9. Selvaraj, M., Kulkarni, S., Babu, R.R.: Analysis and experimental testing of a built-up composite cross arm in a transmission line tower for mechanical performance. Compos. Struct. **96**, 1–7 (2013)
10. Shu, Q., Yuan, G., Huang, Z., Ye, S.: The behaviour of the power transmission tower subjected to horizontal support's movements. Eng. Struct. **123**, 166–180 (2016)
11. IS 802 Part1/Sec1: Use of Structural Steel in Overhead Transmission line Towers—Code of Practice. Bureau of Indian Standards, New Delhi (1995)
12. IS:875 Part 3: Code of Practice for Design Loads (other than earthquake) for Buildings and Structures—Part 3 Wind loads. Bureau of Indian Standards, New Delhi (1987)
13. IS:5613 PartII/section 1: Code of Practice for Design, Installation and Maintenance of Overhead Power lines. Part II Lines above 11 kv and up to and including 220 kV, section 1, Design. Indian Standards Institution, New Delhi (1976)
14. IS:5613 Part II/Sec 2: Code of Practice for Design, Installation and Maintenance of Overhead Power lines, Part II Lines above 11 kV and up to and including 220 kV, section 2, Installation and Maintenance (1976)

Estimation of Heat Loss Factor with the Tilt Angle in a Solar Thermal Flat-Plate Collector

Anjan Karmakar, Agnimitra Biswas, Jibin T. Philip and Basil Kuriachen

1 Introduction

In today's world, there is a need to generate energy from renewable sources of energy and the most common among them is solar energy. It is freely available and abundant in almost every part of the world. Solar energy has the greatest potential of all the sources of renewable energy. Human life and all other forms of life on our planet are completely dependent on the daily flow of solar energy. For ages, man has been trying to harness the sun as an important source of energy. The best utilization of the solar energy will be when the path of the sun can be tracked. With a view to collect energy from the sun, it is necessary to predict the sun position relative to the collection device. Flat-plate collectors are the simplest and the most economical device developed for collection of solar energy. In contrast to other concentrating-type collectors, the flat-plate collectors possess advantages like non-requirement of complex systems to track apparent periodic movement of the sun, ease in construction and design, capability in harnessing of both direct and diffused radiations [1]. The absorber plate of the flat-plate collector transmits solar energy to liquid flowing in the tubes. The flow can take place due to thermosyphon effect or by forced convection. However, certain energy absorbed by the plate is lost to atmosphere due to higher temperature of the plate. The collector efficiency is dependent on the temperature of the plate which in turn is dependent on the nature of flow of fluid inside the tube, solar insolation, ambient temperature, top loss coefficient, the emissivity of the plate and glass cover, slope, etc. [2]. The convection heat loss from receiver in solar thermal power system can significantly

A. Karmakar · J. T. Philip (✉) · B. Kuriachen
National Institute of Technology, Aizawl 796012, Mizoram, India
e-mail: philip.jibin07@gmail.com

A. Biswas
National Institute of Technology, Silchar 788010, Assam, India

reduce the efficiency and consequently the cost-effectiveness of the system. It is important to assess this heat loss and subsequently improve the thermal performance of the receiver [3]. Moreover, solar collector is inherently exposed to continuously variable weather conditions, capacitance effects may be significant [4] and need to be tilted at the correct angle to maximize the performance of the system [5]. In this paper, an attempt has been taken to measure the extraterrestrial radiation and relate it with solar irradiation at particular location.

2 Experimental Setup

The line diagram of the solar thermal flat-plate collector arrangement used for this particular experiment is shown in Fig. 1. The latitude of the experimental setup was 24.8333 °N, 92.7789 °E, and the entire experiment was conducted during the month of June–July, 2016. The arrangement consists of a tank to store the water. The water from the tank is pumped to the geyser so that the constant heat input of water can be given to the collector. The flow rate is measured using the rotameter, and one feedback channel is also provided to the tank. The water through the tank is pumped to the constant head tank for storing the water to transfer to the collector to rise its temperature at the output. The overflow channel ensures that during overflow of water it is coming back to the tank to avoid the water to come out of the head tank. The water from the head tank passes to the flat-plate collector, and the flow rate was maintained at 2.5 m³/s through the input of the collector. The water then flows through the collector where it absorbs the incident radiation and gets heated up, and a rise in temperature was noted by the thermocouples connected at the input and the output of the flow tubes. This difference in temperature was used
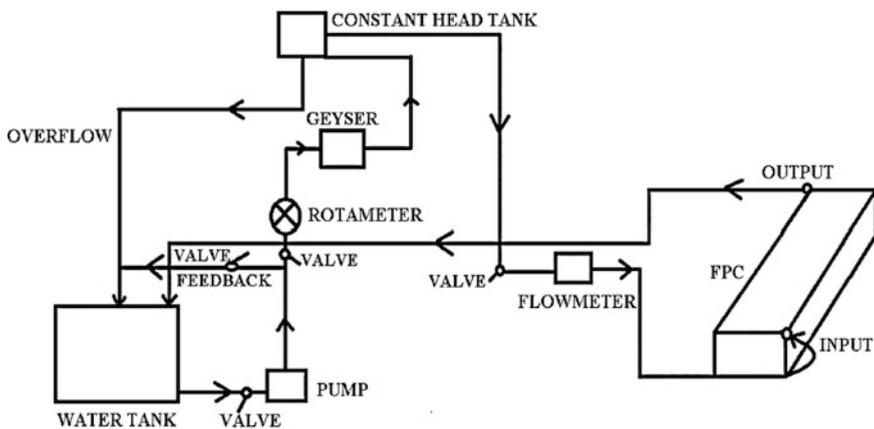
Fig. 1 Line diagram of solar thermal flat-plate collector arrangement

to find out the efficiency of the collector which finds a wide range of application in the household application because of the temperature rise to a maximum range of 55–65 °C.

2.1 Collector Efficiency

The instantaneous efficiency of the solar thermal flat-plate collector is given by,

$$\eta_i = \frac{m' C_p (T_o - T_i)}{A_c G_T} \tag{1}$$

where

m' Mass flow rate of fluid (kg/s)
C_p Fluid specific heat (J/kg °C)
T_i Input temperature (°C)
T_o Output temperature (°C)
A_c Collector area (m^2)
G_T Solar radiation (W/m^2)

Expressing the instantaneous efficiency in terms of the heat removal factor and overall heat loss coefficient, we get

$$\eta_i = F_R(\tau\alpha) - \frac{F_R U_L (T_i - T_a)}{G_T} \tag{2}$$

where

F_R Solar collector heat removal factor, dimensionless
U_L Solar collector overall heat loss coefficient, (W/m^2 °C)
$(\tau\alpha)$ A transmittance-absorptance product that is weighted according to the proportions of beam, diffuse, and ground-reflected radiation on the collector

3 Methodology

3.1 Thermal Performance Test

The thermal performance test was conducted for which the instruments used were pyranometer, ambient temperature sensor, wind speed sensor, data logger, thermal performance test setup, rotameter, pump, water jets, etc. The steady-state conditions are listed in Table 1. The experimental procedure which has been followed is as detailed below.

Table 1 Steady-state conditions

S. No.	Parameter	Deviation from the mean value over the test period
1	Total solar irradiance	± 50 W/m^2
2	Surrounding air temperature	± 1 °C
3	Fluid mass flow rate	$\pm 1\%$
4	Collector fluid inlet temperature	± 0.1 °C
5	Temperature difference between collector inlet and outlet	± 0.1 °C

- Mount the collector at angle of 30° from horizontal surface on corresponding test bed.
- Switch on the pump.
- Fill the constant head tank.
- Close the pump after filling the tank, as can be determined from the water through overflow pipe.
- After achieving set temperature, set water flow at approximately 0.02 kg/s per m^2 of aperture area of collector.
- After achieving steady-state conditions, start test for 30 min. before solar noon and 30 min after solar noon.
- After one-hour test period, close the water flow through flow meter.
- Calculate the value of efficiency by using data recorded during the test in the data logger.
- Repeat the test steps 2–9 for at least four inlet temperatures spaced evenly over the operating temperature of collector.

4 Results and Discussion

After performing the thermal performance test at three different tilt angles 30°, 32°, and 34°, the graph was plotted between the term η (%) and $(T_i - T_a)/G_T$ as shown in Figs. 2, 3, and 4. Now, from Eq. 2 it can be seen that if the *X*-axis represents the efficiency (η (%)) and the *Y*-axis represents the term $(T_i - T_a)/G_T$, then the slope of the graph on *X-Y* plot represents the product of heat removal factor (F_R) and the overall heat loss coefficient (U_L) which together give the heat loss from the entire surface of the collector due to convection and radiation. It can be noted that the product of F_R and U_L value for the tilt angle at 30°, 32°, and 34° are 4.747, 4.886, and 4.952, respectively. Hence, there is an increase in the heat loss from the collector as the tilt angle increases. This result helps in better utilization of the solar thermal flat-plate collector with proper understanding of this variation (Table 2).
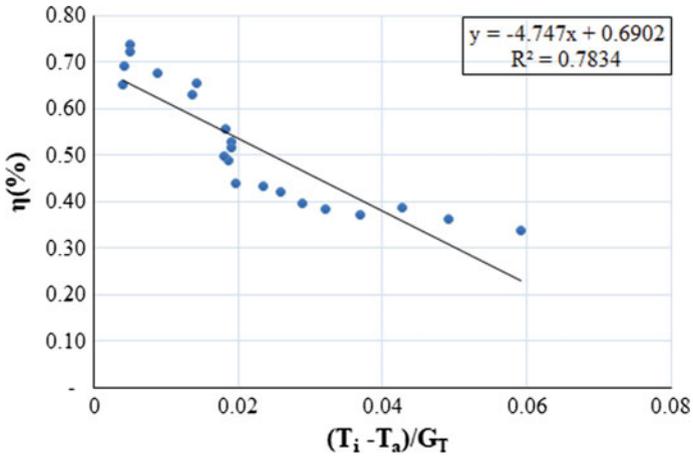
Fig. 2 η (%) versus $(T_i - T_a)/G_T$ graph for 30° tilt angle
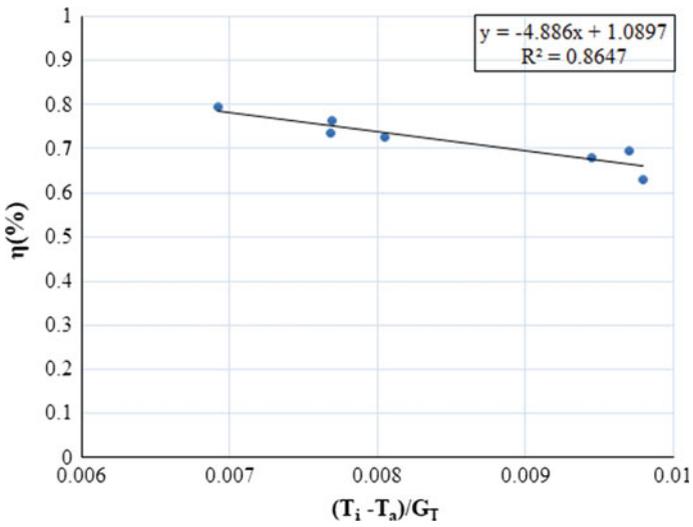
Fig. 3 η (%) versus $(T_i - T_a)/G_T$ graph for 32° tilt angle
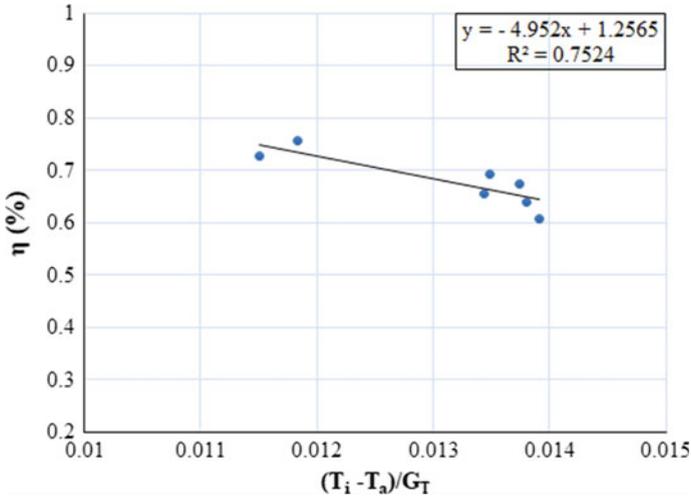
Fig. 4 η (%) versus $(T_i - T_a)/G_T$ graph for 34° tilt angle

Table 2 Product of F_R and U_L for the considered tilt angles

S. No.	Tilt angle	Product of F_R and U_L
1	30°	4.747
2	32°	4.886
3	34°	4.952

5 Conclusions

The below-detailed inferences were obtained from the present research initiative.

- As the F_R and U_L play a major role in improving the efficiency of solar thermal flat-plate collector, placing the collector at an appropriate tilt angle becomes necessary for maximum efficiency.
- The F_R and U_L values were found to be increasing with the increase in tilt angle.
- Among the various tilt angles considered for experimentation, better results were obtained at a tilt angle of 30°.
- The variation in heat removal from the collector with the tilt angle can provide further scope of research in this field and help in improving the efficiency by finding out an optimum tilt angle.

References

1. Liu, B.Y., Jordan, R.C.: The long-term average performance of flat-plate solar-energy collectors: with design data for the US, its outlying possessions and Canada. Sol. Energy **7**(2), 53–74 (1963)
2. Sekhar, Y.R., Sharma, K.V., Rao, M.B.: Evaluation of heat loss coefficients in solar flat plate collectors. ARPN J. Eng. Appl. Sci. **4**(5), 15–19 (2009)
3. Wu, S.Y., Xiao, L., Cao, Y., Li, Y.R.: Convection heat loss from cavity receiver in parabolic dish solar thermal power system: a review. Sol. Energy **84**(8), 1342–1355 (2010)
4. Klein, S.A., Duffie, J.A., Beckman, W.A.: Transient considerations of flat-plate solar collectors. J. Eng. Power **96**(2), 109–113 (1974)
5. Shariah, A., Al-Akhras, M.A., Al-Omari, I.A.: Optimizing the tilt angle of solar collectors. Renew. Energy **26**(4), 587–598 (2002)

Techno-Economic Analysis of a Grid-Connected Hybrid Solar–Wind Energy System

Monika Agrawal, Bharat Kumar Saxena and K. V. S. Rao

1 Introduction

With the growth of world's population (at a rate of 1.12% per year in 2017 [1]), the electricity demand rate is increasing. Alternative power sources that are environment-friendly are to be developed for supplying this ever-increasing energy demand [2]. In the last one decade, power generation from renewable energy resources increased by manyfolds. This was due to significant drop in the cost of solar PV modules and wind energy conversion system. It also made the renewable energy competitive with the fossil fuel-based energy in terms of energy generation cost. Reliability of multi-sources hybrid renewable energy system is better than the single source renewable energy system. Many researchers have reported various hybrid renewable energy technology options and studied various methods for designing of hybrid renewable energy system. It includes the use of battery, diesel generator, etc., for backup power generation. But for economic power generation, grid-connected hybrid system is more interesting than stand-alone hybrid system as need of battery storage and polluting diesel generator is not required [3–6].

Solar and wind resources are abundantly available in western Rajasthan region of India. In India, the total installed electric power capacity till the end of December 2017 is 333,549.98 MW [7]. Out of this, 62,847.06 MW capacity is from renewable energy sources. Till December 31, 2017, out of the total renewable installed

M. Agrawal (✉) · B. K. Saxena · K. V. S. Rao
Department of Renewable Energy, Rajasthan Technical University, Kota, India
e-mail: moneagr@gmail.com

B. K. Saxena
e-mail: bkumarsin@gmail.com

K. V. S. Rao
e-mail: kvsrao12@gmail.com

capacity, solar and wind power plants contributed 17,052.37 and 32,848.46 MW, respectively.

In this study, techno-economic analysis of grid-connected solar–wind hybrid energy system is presented to satisfy 50 MW constant load. The hybrid system components sizing, optimization, simulation and sensitivity analysis are done by using HOMER Pro 3.10.3 software. Figure 1 shows the circuit diagram of grid-connected solar–wind hybrid energy system. The lifetime of this hybrid system is assumed to be 20 years. The scaled annual average load is 1,200 MWh/day.

2 Data Used for System Simulation

2.1 Solar Radiation and Wind Speed Data

Soda site located at 26° 38′ 54.3″N latitude and 70° 51′ 12.2″E longitude in Rajasthan, India, is selected for the analysis. The altitude of site is 318 m above mean sea level. Figure 2 indicates the monthly solar radiation and wind speed at a height of 50 m from surface level at Soda site. The solar radiation data is obtained through National Renewable Energy Laboratory (NREL) database. The scaled annual average solar radiation at Soda is 5.79 kWh/m^2/day. The wind speed data is taken from HOMER through NASA surface meteorology and solar energy database. The annual average wind speed is 4.89 m/s. Thus, Soda site has very good potential for both solar and wind energy-based electricity generation.

2.2 System Components

The components of a hybrid grid-connected solar–wind energy system are as follows:
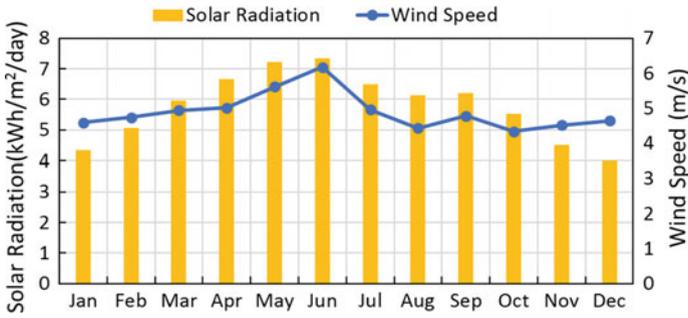
Fig. 2 Monthly variation of solar radiation and wind speed at Soda site, Jaisalmer, in India

PV Module The PV module of Canadian Solar Max Power (model CS6X-325P) having rated power capacity of 325 W is selected for this analysis. The module efficiency and derating factor are 16.94 and 88%, respectively. The capital and replacement cost of PV modules are considered as Rs. 49.50 million/MW [8] and Rs. 25 million/MW, respectively. Operation and maintenance cost is taken as 5% of the capital cost, and it comes to be Rs. 2475.10/kW per year. The degradation factor of PV module is not considered. The lifetime of PV module is considered as 25 years.

Wind Turbine Wind turbine of Vestas V82 model having rated power capacity of 1.65 MW is considered for this analysis. The wind turbine diameter and hub height are 82 and 70 m, respectively. The lifetime of wind turbine is expected to be 20 years. The capital cost, as well as replacement cost of wind turbine, is considered as Rs. 619.807 lakh/MW [9]. The operation and maintenance cost of wind turbine is taken as 5% of the capital cost and is Rs. 30.99 lakh/MW.

Converter For this system, generic-type system converter has been selected. The lifetime of converter is 15 years. This is dual mode-type converter that works into inverter mode as well as rectifier mode. The converter efficiency in inverter mode is 95%. The capital and replacement cost of system converter is taken as Rs. 35 lakh/ MW. The operating and maintenance cost is considered as 1% of the capital cost and is Rs. 3,500/kWh per year.

Grid In grid-connected hybrid renewable energy systems, grid is not the main power supply source but it acts as a function of storage system. Gird is the secondary source of energy and supplies energy to load only when solar and wind energy systems are not able to satisfy the load demand fully. For analysis of levelized cost of electricity variation, the power purchase price from the grid to system is varied as Rs. 6/kWh and Rs. 7/kWh for the purpose of sensitivity analysis. Thus, it is taken as variable with two values. Supply power price of Rs. 5/kWh is considered for the power generated by hybrid system and supplied to grid, and it is assumed as constant.

Table 1 Sizing of different combinations of hybrid solar–wind energy system

Cases	Energy sharing		Solar PV module		Wind turbine quantity
	Solar (%)	Wind (%)	Module quantity	Module power (kW)	
I	0	100	–	–	183
II	30	70	216,118	70,238.48	128
III	50	50	360,197	117,064.14	91
IV	70	30	504,276	163,889.80	54
V	100	0	720,394	234,128.28	–

2.3 System Sizing

In this study, different combinations of grid-connected hybrid SPV and wind energy systems are considered depending on the load sharing between SPV and wind such as 100, 70, 50 and 30%. To calculate the number of wind turbines and number of SPV modules, the load demand supplied by wind or solar is divided by electricity generated through single unit [10]. Table 1 shows the different cases of grid-connected solar–wind hybrid energy system based on the percentage sharing of load. The energy production of SPV module and wind turbine is 608 kWh/year per module and 2,390,625 kWh/year per turbine, respectively, for the selected site Soda.

3 Methodology

3.1 Net Present Cost (NPC)

Net present cost of the system is sum of the present value of all the system components capital cost, replacement cost, operation and maintenance cost, and cost of buying power from the grid that system acquires over its lifetime, minus the present value of all revenues such as price for power supplied by the hybrid energy system to the grid and salvage value that are received over system lifetime.

3.2 Levelized Cost of Electricity (LCOE)

In an integrated energy system, the unit cost of electricity is the main parameter for comparing energy productions from different energy sources. LCOE is the ratio of total system discounted annualized cost to total energy served by the system (E_{serve}), which includes energy served to the load and energy supplied to the grid. LCOE is calculated by using (1) [11–13].

$$\text{LCOE} = \frac{\text{CRF}(i, N) \times C_{\text{NPC,tot}}}{E_{\text{serve}}} \tag{1}$$

where CRF is the capital recovery factor and N is the project lifetime. $C_{\text{NPC,tot}}$ is the net present cost of the hybrid system. CRF is calculated by using (2), where i is the real discount rate, and it is calculated by using (3).

$$\text{CRF}(i, N) = \frac{i(1 + i)^N}{(1 + i)^N - 1} \tag{2}$$

$$i = \frac{i' - f}{1 + f} \tag{3}$$

where i' is the nominal discount rate and f is the expected inflation rate.

3.3 Renewable Fraction (RF)

Renewable fraction is the ratio of energy delivered by renewable resources to total energy served by both renewable and non-renewable energy sources. The renewable fraction is calculated by using (4) [14].

$$\text{RF} = 1 - \frac{E_{\text{non}}}{E_{\text{load}} + E_{\text{sell}}} \tag{4}$$

where E_{non} is energy supplied from the grid, E_{load} is the electrical energy served to load and E_{sell} is the excess energy supplied to the grid.

4 Sensitivity Analysis

The various sensitivity variables are considered for techno-economic analysis of proposed hybrid system, and they are as follows:

4.1 Wind Turbine Losses

In this analysis, electrical losses of 1%, environmental losses of 1% and wake effect losses of 5% are assumed. The wind turbine availability losses are considered as either 5 or 10%. The turbine overall loss factor (LF) is calculated by using (5).

$$\text{LF} = 1 - \prod_{i=1}^{n}\left(1 - \frac{L_i}{100}\right) \tag{5}$$

where L_i is each loss percentage, i.e. L_1 (availability losses) ... L_4 (electrical losses).

The LF comes out to be 0% for no turbine losses, 11.55% for availability loss of 5 and 16.20% for availability loss of 10%, respectively.

4.2 Grid Power Price

This is the price at which power is purchased from the grid. Two cases of the grid power price, i.e. Rs. 6/kWh and Rs. 7/kWh, are studied in this paper.

4.3 Real Discount Rate

The real discount rate is also called interest rate. By varying inflation rate and nominal discount rate, variations in LCOE are analyzed. In this paper, only two cases of inflation rates of 5 or 6% are considered. Five cases of nominal discount rates are taken in consideration, i.e. 8, 10, 12, 14 and 16%. Table 2 shows the different real discount rates for different inflation and nominal discount rates.

Table 2 Real discount rates

Inflation rate (f) (%)	Nominal discount rate (i') (%)	Real discount rate (i) (%)
5	8	2.86
	10	4.76
	12	6.67
	14	8.57
	16	10.48
6	8	1.89
	10	3.77
	12	5.66
	14	7.55
	16	9.43

5 Results and Discussion

5.1 Electrical Analysis

Figure 3 shows the total annual energy production and renewable fraction for different cases of hybrid energy system with varying turbine loss factor. From Fig. 3, it can be seen that for the cases where turbine losses are not neglected, the renewable fraction for case III of grid-connected hybrid solar–wind energy system is maximum amongst other cases of hybrid system taken in consideration in this study. The RF comes out to be in between 66 and 67% for case III. In case of turbine losses considered zero, the RF of case III is 68.91% and this is not maximum. If turbine loss factor is 11.55%, the values of RF are 61.97, 66.64, 67.00, 65.86 and 62.34% for the cases I–V of hybrid system, respectively. For 16.20% of turbine loss factor, value of RF for the cases I–V of hybrid energy systems is 62.34, 60.33, 65.54, 66.17 and 65.31%, respectively.

Figure 4 shows the monthly average electric power production from the case III of grid-connected solar–wind hybrid energy system. It is observed that solar and wind power productions are maximum in the month of March and June, respectively. Figure 5 indicates the hourly power production of solar and wind energy systems and power supplied from/to grid on one particular day (01 September) for case III of hybrid system. The electrical analysis for other cases of hybrid system is also done in same way.
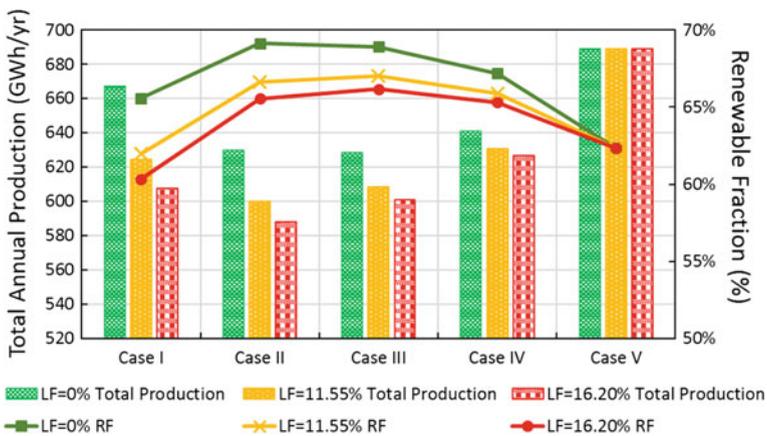
Fig. 3 Annual energy production and renewable fraction (RF)
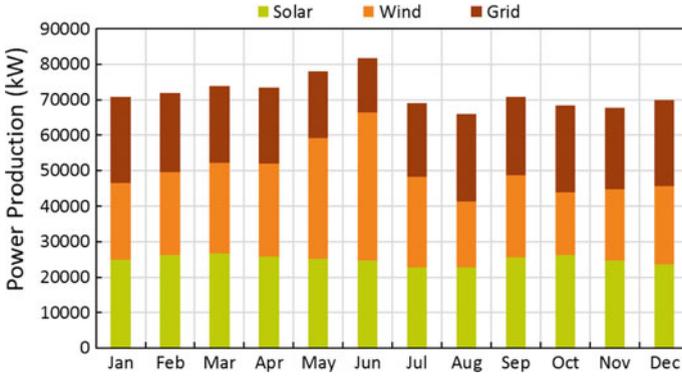
Fig. 4 Monthly average power production for the case III of grid-connected solar–wind hybrid energy system
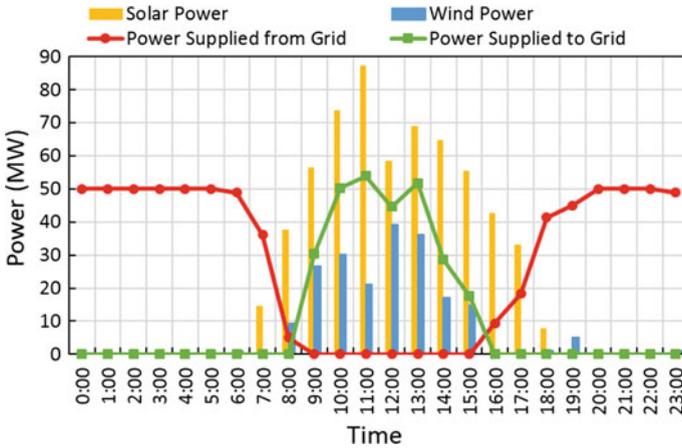
Fig. 5 Hourly power production and consumption on one day (01 September) for case III

5.2 Economic Analysis

HOMER software provides optimization results such as system capital cost, operating cost, net present cost and levelized cost of electricity (LCOE). NPC is the important economic parameter as HOMER optimized the system combinations on the basis of lowest NPC value. The NPC of the hybrid energy systems at power purchase price of Rs. 6/kWh and power sale price to grid of Rs. 5/kWh is shown in Fig. 6 by taking the cases of turbine losses into consideration. The values of NPC at power purchase price of Rs. 6/kWh are Rs. 36,324.69 million, Rs. 32,651.92 million, Rs. 30,573.58 million, Rs. 28,703.25 million and
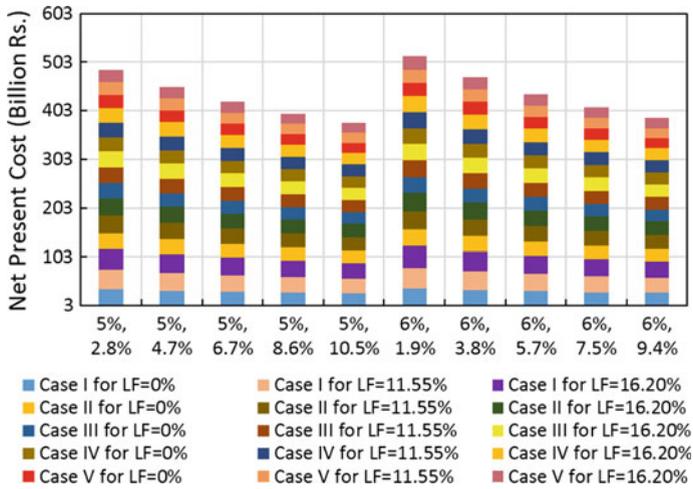
Fig. 6 Net present cost variation for different cases of hybrid system with turbine loss factor, inflation rate and nominal discount rate
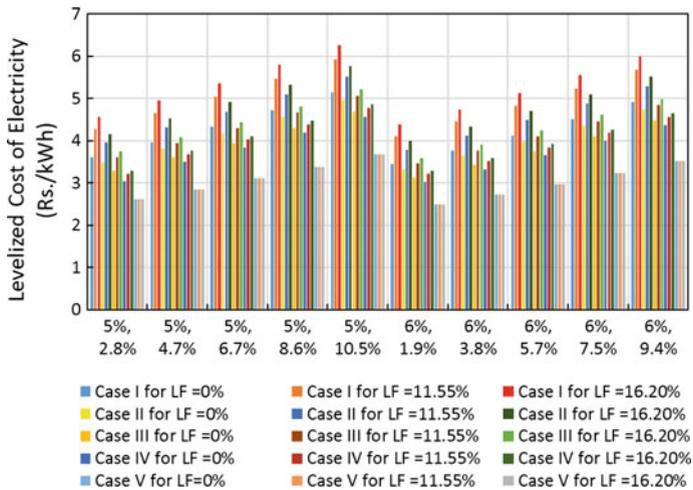
Fig. 7 Levelized cost of electricity variation with respect to inflation and discount rate

Rs. 26,285.34 million, for cases I–V of hybrid energy systems, respectively, since turbine losses are neglected and real discount rate is 2.8%.

Figure 7 shows the LCOE variation for different cases of grid-connected solar–wind hybrid energy system with respect to varying inflation rate and real discount rate at power price of Rs. 6/kWh and turbine losses are taken into consideration. It is observed that the LCOE is maximum for the case I and minimum for

Table 3 Annual energy generation and consumption and LCOE with varying turbine loss factor and grid power price

Case	Turbine loss factor (%)	Generation and consumption (GWh/year)				RF (%)	LCOE (Rs. /kWh)	
		Solar PV	Wind turbine	Grid buy	Grid sell		Power price Rs. 6/kWh	Power price Rs. 7/kWh
I	0	–	437.48	229.73	229.21	65.57	4.92	5.26
	11.55		386.97	237.47	186.44	61.97	5.67	6.05
	16.20		366.60	241.02	169.62	60.33	6.00	6.40
II	0	131.32	305.99	192.34	185.09	69.13	4.74	5.05
	11.55		270.67	197.93	155.36	66.64	5.29	5.62
	16.20		256.42	200.45	143.63	65.54	5.52	5.87
III	0	218.87	217.55	191.95	179.42	68.91	4.47	4.78
	11.55		192.43	197.20	159.56	67.00	4.84	5.17
	16.20		182.30	199.52	151.75	66.17	4.99	5.33
IV	0	306.42	129.09	205.35	187.54	67.17	4.36	4.69
	11.55		114.19	210.08	177.38	65.86	4.56	4.90
	16.20		108.18	212.12	173.40	65.31	4.64	4.99
V	0	437.75	–	251.25	229.11	62.34	3.51	3.89
	11.55							
	16.20							

case V. The LCOE at the real discount rate of 9.4% is Rs. 4.92/kWh, Rs. 4.74/kWh, Rs. 4.47/kWh, Rs. 4.36/kWh and Rs. 3.51/kWh, for the hybrid system cases I–V, respectively. If power price of Rs. 7/kWh from grid and power sell price of Rs. 5/kWh to grid is considered, then LCOE at real discount rate of 9.4% is Rs. 5.26/kWh, Rs. 5.05/kWh, Rs. 4.78/kWh, Rs. 4.69/kWh and Rs. 3.89/kWh for hybrid system cases I–V, respectively.

Table 3 shows the annual energy generation and consumption and LCOE (at 6% inflation rate and 16% nominal discount rate) for different cases of solar–wind hybrid energy system with varying turbine loss factor and grid power price.

6   Conclusions

In this paper, Soda site located at Jaisalmer, Rajasthan in India, is selected for applying a grid-connected solar PV–wind hybrid energy system. This site is having good potential for both solar and wind resources. HOMER software is used for modelling, optimization and simulation purposes. For supplying 50 MW constant load, different combinations of sharing of solar PV and wind energy systems of a hybrid system are compared.

When turbine loss factor is zero, the renewable fraction (RF) is maximum (69%) for the case II of grid-tied hybrid system and RF is minimum (62%) for case V. As turbine loss factor increases, RF decreases and LCOE increases.

For turbine loss factor of 0, 11.55 and 16.2%, and for typical case of real discount rate of 9.4%, grid power purchase price of Rs. 6/kWh and grid sale price of Rs. 5/kWh, the case III of hybrid system generates annual energy of 436,421,606, 411,303,701 and 401,175,862 kWh, respectively, and LCOE comes out to be Rs. 4.47/kWh, Rs. 4.84/kWh and Rs. 4.99/kWh, respectively. The LCOE decreases with increasing inflation rate and increases with increasing nominal discount rate.

The hybrid system, in which solar PV share is 100% and wind system share is 0% (of the total load), is found to be more feasible and economic than other combinations of SPV–wind hybrid system as the solar electricity production is more and initial capital cost is less. For this, LCOE is Rs. 3.51/kWh for the real discount rate of 9.4% and grid purchase price of Rs. 6/kWh and grid sale price of Rs. 5/kWh.

References

1. Current World Population. http://www.worldometers.info/world-population/
2. Das, B.K., Hoquea, N., Mandala, S., Pal, T.K., Raihana, MdA: A techno-economic feasibility of a stand-alone hybrid power generation for remote area application in Bangladesh. Energy **134**, 775–788 (2017). https://doi.org/10.1016/j.energy.2017.06.024
3. Usman, M., Khan, M.T., Rana, A.S., Ali, S.: Techno-economic analysis of hybrid solar-diesel-grid connected power generation system. Electr. Syst. Inf. Technol. 1–10 (2017). https://doi.org/10.1016/j.jesit.2017.06.002
4. Nacer, T., Hamidat, A., Nadjemi, O., Bey, M.: Feasibility study of grid connected photovoltaic system in family farms for electricity generation in rural area. Renew. Energy **96**, 305–318 (2016). https://doi.org/10.1016/j.renene.2016.04.093
5. Halabi, L.M., Mekhilef, S., Olatomiwa, L., Hazelton, J.: Performance analysis of hybrid PV/diesel/battery system using HOMER: a case study Sabah Malaysia. Energy Convers. Manage. **144**, 322–339 (2017). https://doi.org/10.1016/j.enconman.2017.04.070
6. Mahesh, A., Sandhu, K.S.: Hybrid wind/photovoltaic energy system developments: critical review and findings. Renew. Sustain. Energy Rev. **52**, 1135–1147 (2015). https://doi.org/10.1016/j.rser.2015.08.008
7. All India Installed Capacity (in MW) of Power Stations. http://www.cea.nic.in/reports/monthly/installedcapacity/2017/installed_capacity-12.pdf
8. Determination of Benchmark Capital Cost Norm for Solar PV power projects for FY 2016–17. http://www.cercind.gov.in/2016/orders/SO17.pdf. Last accessed 2018/01/12
9. Determination of Levellised Generic Tariff for FY 2016–17. http://cercind.gov.in/2016/orders/sm_3.pdf. Last accessed 2018/01/12
10. Masri, H., Amoura, F.: Feasibility study of a grid connected hybrid wind/PV system. Int. J. Appl. Power Eng. **2**(2), 89–98 (2013). https://doi.org/10.1109/EEEIC.2015.7165520
11. Boussetta, M., Bachtiri, R.E., Khanfara, M., Hammoumi, K.E.: Assessing the potential of hybrid PV–Wind systems to cover public facilities loads under different Moroccan climate conditions. Sustain. Energy Technol. Assess. **22**, 74–82 (2017). https://doi.org/10.1016/j.seta.2017.07.005
12. Khulna, T., Roy, N.K.: Grid connected hybrid power system design using HOMER. Int. J. Renew. Energy Res. 19–22 (2016). https://doi.org/10.1109/icaee.2015.7506786

13. Sinha, S., Chandel, S.S.: Prospects of solar photovoltaic–micro-wind based hybrid power systems in western Himalayan state of Himachal Pradesh in India. Energy Convers. Manag. **105**, 1340–1351 (2015). https://doi.org/10.1016/j.enconman.2015.08.078
14. HOMER energy. https://www.homerenergy.com/. Last accessed 2018/01/12

Optimizing an On-Grid Hybrid Power System in Educational Institution in Tamil Nadu, India

J. Vishnupriyan and P. S. Manoharan

1   Introduction

The current economic situation of the country has aggravated the situation despite the so-called introduction of social services scheme by the federal government. Even though authorities have sought alternative and sustainable energy sources for urban and rural areas in order to minimize rural–urban migration and encourage the development of educational institution and small-scale industries, by minimizing current security and unemployment problems in the country [1], both government and independent power providers (IPP) are finding it difficult to provide sustainable electricity to these communities. The strategy to promote a full menu of rural electrification options–grid and off-grid from thermal and renewable energy technologies, etc., and encourage states, local communities, and businesses to develop and contribute financially to rural electrification, seems unrealistic considering the country's centralized energy system which will require gridline extensions to provide this electricity. Some studies discussed the photovoltaic system performance of different locations [2]. On this premise, therefore, this study seeks to appraise the sustainability of various renewable sources of energy as the alternative for conventional fossil fuel so as to ensure continuous provision of electricity in the rural communities in Tamil Nadu State since the federal government strategy is elusive. This would be based on the environmental, social, and economic consequences of each energy source for sustainable development.

J. Vishnupriyan (✉) · P. S. Manoharan
Department of Electrical and Electronics Engineering, Thiagarajar College
of Engineering, Madurai, Tamil Nadu, India
e-mail: vishnupriyanj@gmail.com

P. S. Manoharan
e-mail: psmeee@tce.edu

1.1 Literature Review

Several software tools are constantly used to suggest an investigation of possible hybrid power generation systems for responding to the demand of particular areas [3, 4]. Among the tools, HOMER, which was introduced by the National Renewable Energy Laboratory, is used to propose the optimal configurations of renewable power generation systems. In developing countries, the techno-economic simulations are performed for proposing a stand-alone power generation system to provide energy in relatively small villages or locations [5]. Bhattarai and Thompson [6] proposed the off-grid electrical system in Brochet for Manitoba, Canada. The systems achieved a cost of energy (COE) of $0.512/kWh. Eunil and Sang [7] conducted several configurations for on-grid and stand-alone electrification in Kyung Hee University's Global Campus, South Korea. Lau et al. [8] proposed grid-connected photovoltaic systems for residential sector located in Malaysia. The system simulated by HOMER achieved COE of $0.1/kWh. A sustainable development through streetlighting system for Fugar City in Nigeria has been discussed by Kumar. Similarly, the impact on clean development mechanism is discussed [9]. Vishnupriyan and Manoharan [10] conducted several simulations on different climatic remote villages in the Indian state of Tamil Nadu. With the simulated hybrid combination of hydro, biomass, wind, diesel generator and battery system, the results achieved the COE of $0.14/kWh with a renewable fraction of 0.99.

2 Schematic Layout of the Work

A schematic flow diagram represents the contribution of the present work (see Fig. 1). The electrified technical institution in southern India is selected based on the resource availability. Then a detailed assessment of load profile, site layout, and the available resources in the selected institution is obtained. These collected real-time data fed into the Hybrid Optimization for Electric Renewable (HOMER) simulation software for techno-economic feasibility analysis. The HOMER software performs the simulations based on the user satisfaction of the given load demand. The selection of suitable configuration is based on the simulation results from techno-economic feasibility. This work considers different renewable energy sources like solar and wind including backup facility.
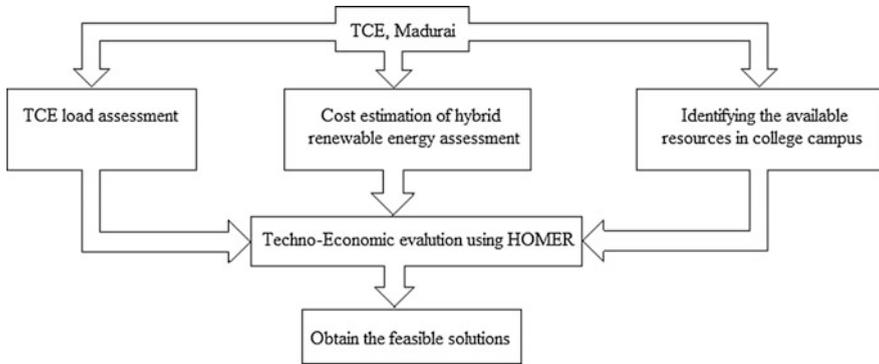
Fig. 1 Schematic layout of the work

3   Status of Study Location

3.1   Location and Population

Thiagarajar College of Engineering (TCE) is a government aided autonomous institution located in Madurai, the Indian state of Tamil Nadu, with coordinates 9.88° (North) latitude and 78.08° (East) longitude (see Fig. 2), and an area of 56 acres. The institution has about 150 classrooms, 70 laboratories, and 900 rooms for both boys and girls hostel. The average weather is 32 °C and 70% humidity.

Fig. 2 Map showing the geographic location of TCE campus
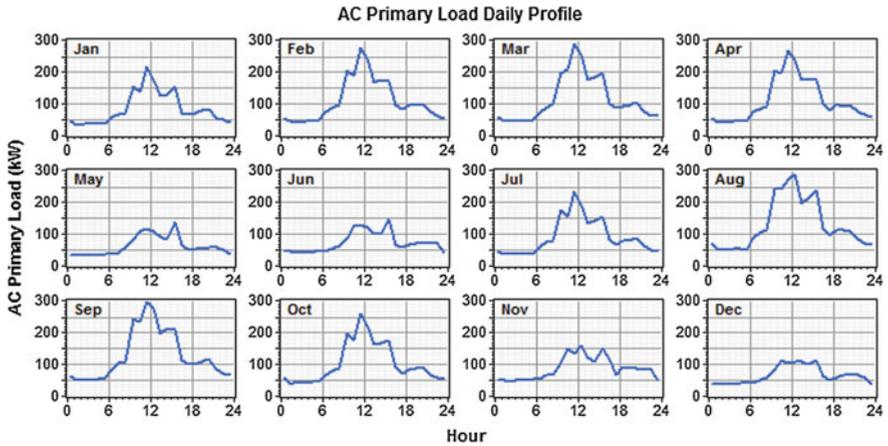
Fig. 3 Month wise hourly daily load profile of TCE, Madurai

3.2 Load Assessment

The current energy demand of TCE is supplied mainly by the Tamil Nadu Electricity Board (TNEB). Based on data collected from the TNEB, the scaled annual average energy demand for the Institution is calculated to be 2.3 MWh/day while the peak energy demand is calculated to be 512 kW (see Fig. 3). The range of load factor of this instruction is computed as 0.45–0.55.

3.3 Solar Resource

The 2016 data for daily solar radiation and solar clearness is obtained from RET screen international's climate database through various ground monitoring stations around the world from National Aeronautics and Space Administration (NASA) global satellite database [8]. The average annual solar clearness index is computed as 0.518, while the average daily radiation was calculated as 5.1 kW/m^2/day. The monthly average solar radiation and clearness index details are described (see Fig. 4).
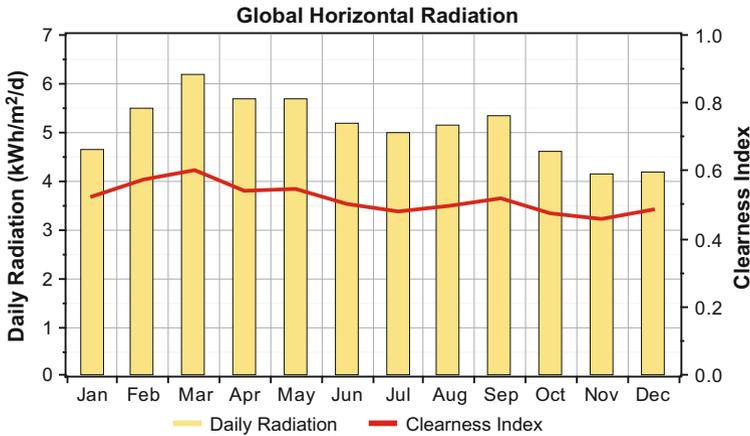
Fig. 4 Average monthly solar radiation and clearness index for Madurai
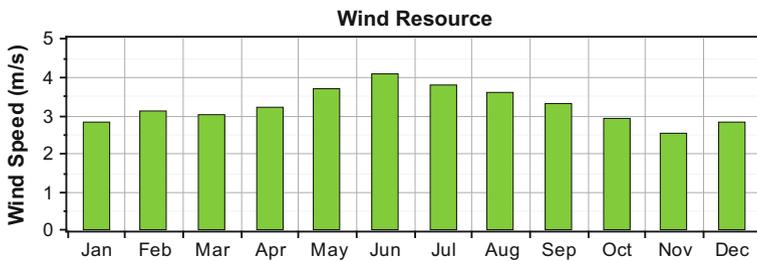
Fig. 5 Monthly average wind speed for Madurai

3.4 Wind Resource

The 2016 data for wind speed collected by the National Renewable Energy Laboratory was used. The wind speed (m/s) in the study location is graphically represented (see Fig. 5). The annual average wind speed is calculated to be at 3.234 m/s.

4 System Modeling

4.1 Photovoltaic Modeling

The photovoltaic (PV) power output is uncertain because it is affected by the environmental factors. The solar irradiation data is collected from NASA surface

meteorology and solar energy through nearby ground monitoring stations [8]. The mathematical model for power output generated from the PV is given in Eq. (1). In this equation, A represents the area of a panel (m^2), P_f represents the packing factor, I_r represents the irradiance, PV module efficiencies represented by η_m.

$$E_{PV} = A * \eta_m * P_f * I_r \qquad (1)$$

4.2 Wind Turbine Modeling

The wind turbine (WT) power output extensively depends on the wind speed of the considered study location. The power generation capacity of the WT has been computed based on the wind speed data obtained from wind monitoring station [11]. In this work, whisper 500 WT model is considered based on the literature [7]. The electrical power output of WT is calculated by Eq. (2). The wind power equation is described by cut-in speed (V_{ci}), cut-out speed (V_{co}), and rated speed (V_r).

$$P_w(t) = \begin{cases} 0 & v(t) \le v_{ci} \ (or) \ v(t) \ge v_{co} \\ P_r\left(\frac{v^3(t)-v_{ci}^3}{v_r^3-v_{ci}^3}\right) & v_{co} < v(t) < v_r \\ P_r & v_r < v(t) < v_{co} \end{cases} \qquad (2)$$

5 Evaluation Criteria

The sustainable performance evaluation of hybrid system considers the three important factors like technical, economic, and environmental are considered. The evaluation is based on the parameters net present cost (NPC), levelized cost of energy (LCOE), renewable fraction (RF), and CO_2 emission which are considered. The selection of optimum configuration is based on the least value of techno-economic considerations.

5.1 Levelized Cost of Energy (LCOE)

The LCOE is the ratio of the total annualized cost (C_{ac}) and annual load served; this can be calculated by Eq. (3). The annual load consists of permanent load (E_{PLAC}) and direct current load (E_{DC_load}).

$$\text{LCOE} = \frac{C_{ac}}{E_{\text{PLAC}} + E_{\text{DC\_load}}} \tag{3}$$

5.2 Net Present Cost (NPC)

The definition of NPC is summarizing the inflows and outflows of cash in project time. Equations (4)–(6) are used to calculate the total NPC of the suggested system. The capital recovery factor is a ratio used to calculate the series of equal annual cash flows. The Eq. (6) is used to calculate the capital recovery factor.

$$C_{\text{NPC}} = \frac{C_{\text{ann,total}}}{CRF(r, Y_{\text{PL}})} \tag{4}$$

$$C_{\text{ann, total}} = \sum_{l=0}^{N} \left(C_{\text{cap}} + C_{\text{om}} + C_{\text{replace}} + C_{\text{fuel}} - R_{\text{salvage}} \right) \tag{5}$$

$$CRF(r, Y_{\text{PL}}) = \frac{r(r+1)^{N_{\text{year}}}}{r(r+1)^{N_{\text{year}}} - 1} \tag{6}$$

$C_{\text{ann\_total}}$	Annual cost	C_{replace}	Replacement cost	r	Interest rate
C_{cap}	Capital cost	C_{fuel}	Fuel cost	N	Number of year
C_{om}	O&M cost	R_{salvage}	Total savings		

5.3 Renewable Fraction (RF)

Renewable fraction has representativeness for environmental assessment. It is the ratio of energy supplied by renewable energy sources ($P_{\text{Ren\_Gen}}$) to the total power generation in particular location (P_{Total}). The RF value can be calculated by using Eq. (7).

$$\text{RF} = \left(1 - \frac{\sum P_{\text{DG}}}{\sum P_{\text{Renew\_Gen}}} \right) \tag{7}$$
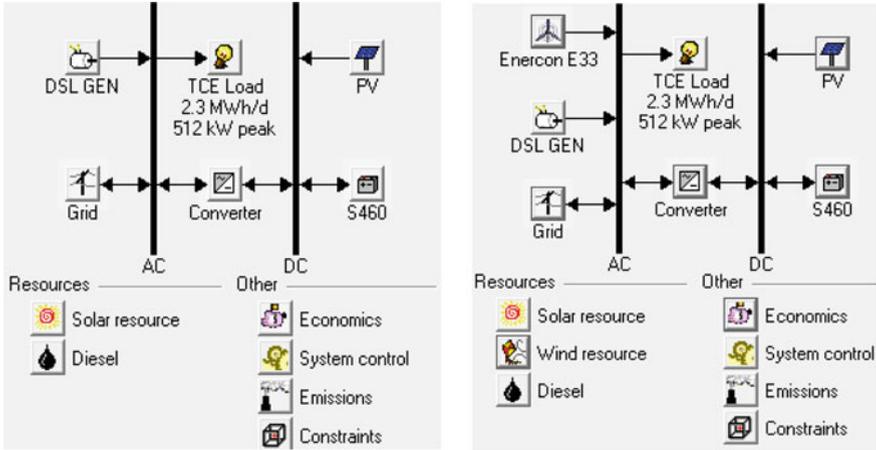
Fig. 6 HOMER simulation model of hybrid configurations

6 Simulation

The HOMER simulation diagram for the proposed hybrid system is depicted in Fig. 6. The optimum solution of such hybrid configuration is utilized to satisfy entire electrical demands of entire institutional building demand. The economic data input includes investment, replacement, operations, and maintenance (O&M) cost of system. These components details are considered based on the literature [7]. In this case study, annual interest rate of 6% and project lifetime of 25 years is considered.

7 Results and Discussions

This study considered PV array, small wind turbine models, converters, and the grid in the HOMER software for developing optimum hybrid renewable power generation systems for TCE campus. Table 1 presents the optimum configuration of the simulation results. It has been found that net metering offers best results.

The environmental details of the proposed system are given in Table 2. The negative value represents the reduction in harmful emission against existing configuration.

The potential systems with the reduction in annualized costs details are given in Table 3. It describes the electricity component production, load, and quantity from the HOMER simulation.

The monthly average electricity production is represented (see Fig. 7). Based on the simulation results, it is recommended that all components, i.e., PV array,

Table 1 Optimal renewable power generation system

Components	Existing	Proposed configurations			
	Grid only	Grid-connected system with PV		Grid-connected system with PV-Wind	
		Plain rate	Net meter	Plain rate	Net meter
PV (kW)	–	350	700	100	–
WT (kW)	–	–	–	10	10
Converter (kW)	–	280	500	100	–
Initial cost ($)	–	342,067	683,333	648,000	550,000
Operating cost ($/y)	79,995	47,054	9,227	3,724	−7,231
Total NPC ($)	1,022,607	943,569	801,287	695,608	457,561
COE ($/kWh)	0.095	0.088	0.074	0.065	0.043
RF	0.00	0.48	0.72	0.77	0.71

Table 2 Details of emission reduction

Pollutant	Existing	Emissions (kg/year)			
	Grid with DG	Grid-connected system with PV		Grid-connected system with PV-Wind	
		Plain rate	Net meter	Plain rate	Net meter
Carbon dioxide	532,179	271,665	14,234	−177,648	−104,043
Sulfur dioxide	2,307	1,178	61.7	−770	−451
Nitrogen oxide	1,128	576	30.2	−377	−221

Table 3 Annual electrical component production, load, and quantity

Component		Fraction in percentage			
		Grid-connected system with PV		Grid-connected system with PV-Wind	
		Plain rate	Net meter	Plain rate	Net meter
Production	PV array	48	72	9	0
	Wind turbine	0	0	68	71
	Grid purchase	52	28	23	29
	Total	100	100	100	100
Load	AC load	94	71	57	59
	Grid sales	6	29	43	41
	Total	100	100	100	100
Quantity	Excess electricity	0.07	0.53	2.47	2.46
	Unmet load	0	0	0	0
	Capacity shortage	0	0	0	0
	Renewable fraction	0.48	0.72	0.77	0.71

Monthly Average Electric Production
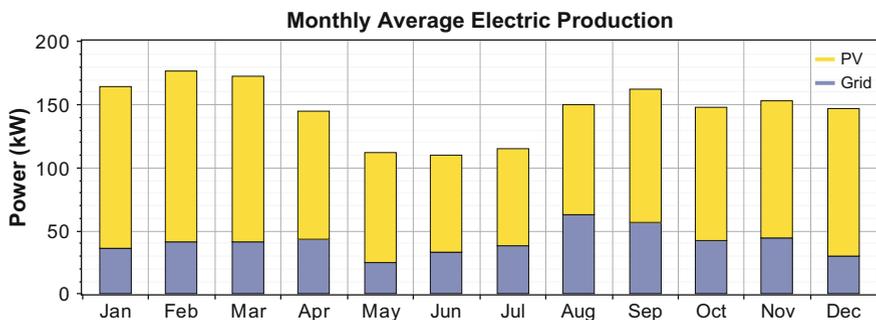
Fig. 7 Monthly average electricity production

converters, and the grid, be used in the systems. By being connected to the grid system and selling the surplus electricity, the potential system can give rise to large amounts of savings.

8   Conclusion

This article has presented the assessment of the technical–economic impact of the net metering mechanism for the particular conditions of an institutional building in Tamil Nadu. The application of this mechanism would result in a high economic incentive for integrating photovoltaic systems users with reduced environmental pollutions. The main conclusions of the simulation are as follows:

- Incorporation of more renewable sources reveals that increasing values of the renewable fraction for sustainable development.
- Net metering offers more reliable for an educational institution, in terms of techno-economic point of view.

References

1. Garba, A., Kishk, M.: Renewable energy technology means of providing sustainable electricity in Nigerian rural areas-A review In: Proceedings 30th Annual ARCOM Conference, Portsmouth, UK, Association of Researchers in Construction Management, pp. 143–151 (2014)
2. Kumar, N.M., Reddy, P.R.K., Praveen, K.: Optimal energy performance and comparison of open rack and roof mount mono c-Si photovoltaic Systems. Energy Proc. **117**, 136–144 (2017)
3. Sinha, S., Chandel, S.S.: Review of soft ware tools for hybrid renewable energy systems. Renew. Sustain. Energy Rev. **32**, 192–205 (2014)

4. Kumar, N.M., Kumar, M.R., Rejoice, P.R., Mathew, M.: Performance analysis of 100 kWp grid connected Si-poly photovoltaic system using PVsyst simulation tool. Energy Proc. **117**, 180–189 (2017)
5. Vishnupriyan, J., Manoharan, P.S.: Multi-criteria decision analysis for renewable energy integration: A southern India focus. Renew. Energy **121**, 474–488 (2018)
6. Bhattarai, P.R., Thompson, S.: Optimizing an off-grid electrical system in Brochet, Manitoba, Canada. Renew. Sustain. Energy Rev. **53**, 709–719 (2016)
7. Eunil, P., Sang, J.K.: Solutions for optimizing renewable power generation systems at Kyung-Hee University's Global Campus, South Korea. Renew. Sustain. Energy Rev. **58**, 439–449 (2016)
8. Lau, K.Y., Muhamad, N.A., Arief, Y.Z., Tan, C.W., Yatim, A.H.M.: Grid-connected photovoltaic systems for Malaysian residential sector: effects of component costs, feed-in tariffs, and carbon taxes. Energy **102**, 65–82 (2016)
9. Kumar, N.M.: Impact of clean development mechanism on eco-friendly energy recovery technology. Proc. Technol. **21**, 54–58 (2015)
10. Vishnupriyan, J., Manoharan, P.S.: Demand side management approach to rural electrification of different climate zones in Indian state of Tamil Nadu. Energy **138**, 799–815 (2017)
11. Kumar, N.M., Singh, A.K., Reddy, K.V.K.: Fossil fuel to solar power: a sustainable technical design for street lighting in Fugar City, Nigeria. Proc. Comput. Sci. **93**, 956–966 (2016)

Experimental Investigation on Fluidized Bed Gasifier Using Saw Dust as Biomass

Albin Joy, Amaljith, P. V. Afzal, T. Krishnadath, N. Nirmal, Sam Biju, Melbin Benny and C. Muraleedharan

1 Introduction

Energy in different forms is always an integral part of human activities. From ancient time onwards, man has tried different kinds of energy sources from burning of firewood to fossil fuels and nuclear energy. Out of these, fossil fuels were the ones which were extensively mined, refined, and burnt in most of the energy applications. This led to the emission of greenhouse gases like carbon dioxide at an extensive level which pushed the earth to a severe condition, namely global warming; such a situation marked the need for a pollution-free fuel [1]. Hydrogen as an energy carrier is considered in this context. Even though there are difficulties in storage, hydrogen is the sole fuel which on burning emits only water as the by-product. It also has a high calorific value which is almost three times that of fossil fuels [2]. Hydrogen is already being used as a fuel in applications like fuel cells, but if it is to be utilized in applications like engines, it has to be produced on a large scale and there have to be mechanisms for effective storage and transportation.

In this work, experimental investigation on fluidized bed gasifier for production of hydrogen is considered. Gasification is a thermochemical conversion process where solid feedstock is converted into useful and convenient gaseous fuels or chemical feedstock that can be burned to release energy or used for the production of value-added chemicals [3]. In this process, the biomass is heated in a limited supply of air which leads to different endothermic as well as exothermic reactions generating producer gas which is a mixture of hydrogen, methane, carbon monoxide, and carbon dioxide. The different mediums that can be used for gasification include air, steam, oxygen, and combinations of these. Gasification proceeds through a series of steps including drying (where moisture in the feedstock is

A. Joy · Amaljith · P. V. Afzal · T. Krishnadath · N. Nirmal
S. Biju · M. Benny (✉) · C. Muraleedharan
National Institute of Technology Calicut, Kozhikode 673601, Kerala, India
e-mail: melbinclt@gmail.com

Table 1 Major chemical reactions involved in gasification [3]

Char gasification	
$C + H_2O \rightarrow CO + H_2$	H = +131 kJ/mol
Boudouard reaction	
$C + CO_2 \rightarrow 2CO$	H = +172 kJ/mol
Methanation reaction	
$C + 2H_2 \rightarrow CH_4$	H = −74.8 kJ/mol
Water–gas shift reaction	
$CO + H_2O \rightarrow CO_2 + H_2$	H = −41.2 kJ/mol

removed), pyrolysis (thermal cracking), and gasification reactions as shown in Table 1. The exothermic reactions and the partial combustion occurring inside the gasifier provide a portion of the energy required to sustain the reaction.

Another significance of gasification of biomass is its waste to energy conversion. Biomass as the waste of different processes is available in plenty in our country and is mostly being dumped or being used in low-value applications. Biomass has the great potential to produce hydrogen. Also, carbon emitted from biomass during gasification will not contribute much to global warming because it was absorbed from the atmosphere itself by plants in the recent past [4]. So gasification can be considered as a carbon-neutral process to produce hydrogen [5]. If the carbon dioxide in the product gases can be absorbed using a sorbent, it can function as a carbon-negative process also.

In this work for experimentation, sawdust is used as the feedstock. It is one of the biomasses which is available in plenty and is of comparatively high hydrogen content. The main objective of this work is the comparison of hydrogen yield in air gasification (air as the gasifying medium) to that of air–steam gasification (mixture of air and steam as gasifying medium).

2 Materials and Methods

2.1 Materials

Sawdust is the by-product or waste product obtained from forestry-based industries. It was collected from the sawmills in the locality and was subjected to a drying process under the sun and was sieved to remove particles of size more than 1 mm. Then, the biomass was oven dried for one hour at 100 °C to remove the excess moisture content. Moisture content causes energy loss and difficulties in feeding the biomass to the gasifier through screw feeder.

Prior to the experimentation, the biomass characterization tests were done. The results of proximate analysis [6] of sawdust are given in Table 2 and ultimate analysis, on Table 3.

Table 2 Proximate analysis results

Moisture content (% mass)	11.7
Volatile matter (% mass)	72
Fixed carbon (% mass)	14.7
Ash content (% mass)	1.6

Table 3 Ultimate analysis results

Carbon (% mass)	44.58
Hydrogen (% mass)	6.2
Oxygen (% mass)	48.81
Nitrogen (% mass)	0.41

2.2 Methods

The air gasification as well as air–steam gasification was conducted in a bubbling fluidized bed gasifier. Experimental set-up consists of: (i) bubbling fluidized bed of biomass, (ii) gas cleaning unit, (iii) producer gas analyser, (iv) monitoring units for temperature, air flow, pressure, etc., different locations in the test set-up, (v) control devices. A schematic diagram of the experimental set-up is shown in Fig. 1. The bubbling fluidized bed gasifier consists of a properly insulated reactor column (2.3 m height). The innermost cylindrical core of 150 mm diameter is made of refractory material capable of withstanding temperature up to 1500 °C. Biomass is
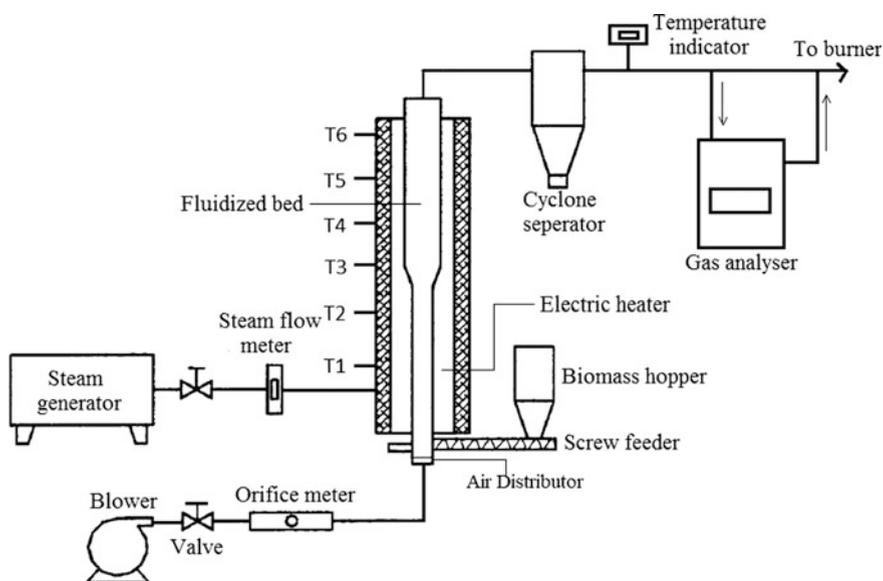
Fig. 1 Experimental set-up

fed into the gasifier bed through a screw feeder. An electric heater is provided in the reactor chamber to maintain the gasification temperature. The reactor bed consists of a bed of sand (granular river sand of size 1 mm) supported by a distributor plate and fluidized by an air blower [7]. Steam generator is provided to generate steam for air–steam gasification. The biomass undergoes incomplete combustion on the bed, and the product gas evolved moves up through a vertical chamber which is highly insulated. Thermostats are connected at different levels across the chamber to measure temperatures at specific regions. The evolved gas passes through a cyclone separator where dust particles and other particulate materials get separated. Dust free gas is analysed in the gas analyser to determine the gas composition. In case of air–steam gasification, steam is provided along with air into the vertical chamber. The flow of steam is controlled using a flow meter, thereby keeping a proper steam to biomass ratio (SBR). Superheated steam is provided to avoid any kind of moisture content that can badly effect the gasification process.

3   Results and Discussion

Based on a series of experimentation on the gasification of sawdust in a fluidized bed gasifier, the effect of operating conditions like temperature, equivalence ratio (ER), and steam to biomass ratio (SBR) on the hydrogen yield was evaluated.

3.1   *Effect of Temperature*

The hydrogen yield both in air gasification as well as air–steam gasification was found to increase as the temperature of the fluidized bed increases. These variations are plotted in Figs. 2 and 3. In air gasification and air–steam gasification, the increased yield of hydrogen with respect to temperature can be explained based on the increase in the rate of endothermic gasification reactions [8]. As temperature increases, the rate of char gasification reaction and Boudouard reaction increases [9] causing the increase in concentration of H_2 and CO. It is observed that as the temperature increases from 680 to 760 °C hydrogen yield increases from 6.4 to 8.4%. In air–steam gasification, the increase in hydrogen yield is attributed to the enhanced water–gas shift reaction in the presence of more steam in the reaction system. It is found that hydrogen yield increases from 7.35 to 8.64% as temperature increases from 640 to 700 °C in the case of air–steam gasification.

Fig. 2 Variation of product gases in air gasification with temperature at ER = 0.3
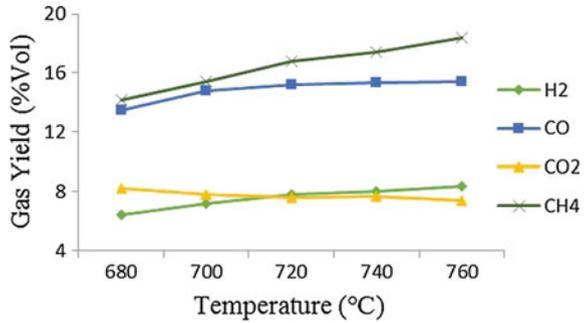
Fig. 3 Variation of product gases in air–steam gasification with temperature at ER = 0.32 and SBR = 0.66
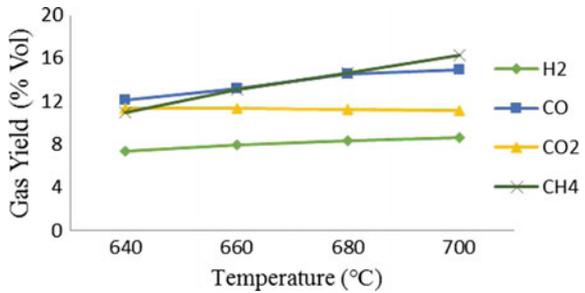
3.2 Effect of Equivalence Ratio

Equivalence ratio (ER) is one of the most important operation parameters involved in gasification. It is defined as the actual air to biomass weight ratio divided by stoichiometric air to biomass weight ratio needed for complete combustion. When the value of ER is high, it signifies high degree of combustion rather than gasification. So an optimum value of ER should be kept to have favourable biomass gasification. Studies show that too low value of ER is not favourable as it lowers reaction temperature. Too high value of ER will lead to the oxidation of H_2 and CO reducing the energy content of the producer gas. The optimum value of ER is found to exist between 0.2 and 0.4 which differs according to various operating parameters. Figure 4 shows the yield of different producer gas compositions at different ER when $T = 700$ °C. From the figure, it is clear that the hydrogen yield decreases with increase in ER from 0.3 to 0.4. As ER increases, H_2 and CO are oxidized to water and CO_2. It can be concluded that ER plays a major role in the process of gasification.

Fig. 4 Air gasification at different equivalence ratio plotted for a particular temperature of 700 °C
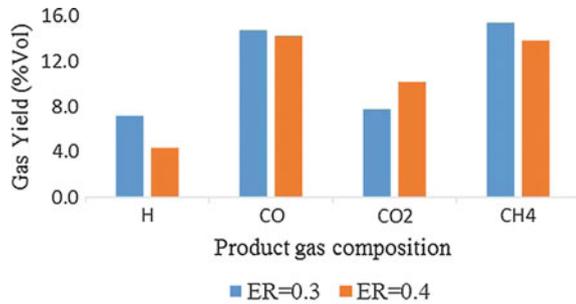
Fig. 5 Air gasification at ER = 0.3 and air–steam gasification at ER = 0.32 and SBR = 0.66 plotted for a particular temperature of 700 °C
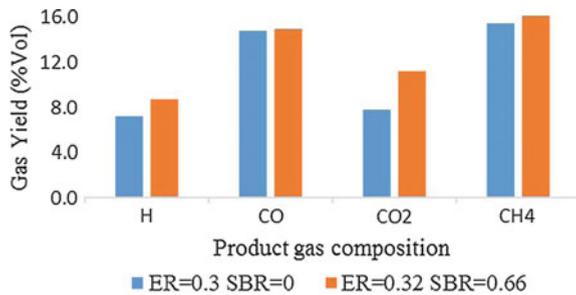
3.3 Effect of Steam to Biomass Ratio (SBR)

Air–steam gasification combines the features of air gasification and steam gasification. This will increase the hydrogen yield compared to air gasification with additional external energy input. However, the additional energy input is small compared to steam gasification. Figure 5 compares the product gas composition with respect to air gasification and air–steam gasification at different ER and SBR at $T = 700$ °C. It is perceived that even at an operating condition with higher ER (ER = 0.32), the hydrogen yield is found to be higher compared to that at an operating condition with lower ER (ER = 0.3). This is attributed to the introduction of steam in the reaction system (air–steam gasification), thereby enhancing the water–gas shift reaction yielding more hydrogen.

4 Conclusion

Experimental investigations were conducted to evaluate air and air–steam gasification in a bubbling fluidized bed gasifier with sawdust as the biomass. In the investigation, it was observed that the hydrogen yield is mainly influenced by the gasification agent and operating parameters. It was detected that at an operating

temperature of 700 °C the hydrogen yield was found to be 7.15% at an ER = 0.3 and 8.64% at ER = 0.32. The higher hydrogen yield even at a lower ER is attributed to the use of air–steam as the gasification agent. Amount of steam in the gasification system is expressed by the factor SBR. Though hydrogen yield increased with increase in SBR, beyond a certain limit, it has a negative effect. During the experiment, it was perceived that hydrogen yield increases with increase in temperature but decreases with increase in ER. In the experimental investigation with air–steam gasification, maximum hydrogen yield was 8.64% at operating conditions of T = 700 °C, ER = 0.32, and SBR = 0.66. For air gasification at operating conditions of T = 760 °C and ER = 0.3, maximum hydrogen yield was found to be 8.4%. However, the yield can be further increased by proper selection of the gasification agent and operating conditions.

References

1. Balat, H., Kırtay, E.: Hydrogen from biomass–present scenario and future prospects. Int. J. Hydrog. Energy **35**(14), 7416–7426 (2010)
2. Lv, P.M., Xiong, Z.H., Chang, J., Wu, C.Z., Chen, Y., Zhu, J.X.: An experimental study on biomass air–steam gasification in a fluidized bed. Bioresour. Technol. **95**(1), 95–101 (2004)
3. Basu, P.: Combustion and Gasification in Fluidized Beds. CRC Press, Boca Raton (2006)
4. McKendry, P.: Energy production from biomass (part 2): conversion technologies. Bioresour. Technol. **83**(1), 47–54 (2002)
5. Sara, H.R., Enrico, B., Mauro, V., Vincenzo, N.: Techno-economic analysis of hydrogen production using biomass gasification—a small scale power plant study. Energy Proc. **101**, 806–813 (2016)
6. Siedlecki, M., De Jong, W., Verkooijen, A.H.: Fluidized bed gasification as a mature and reliable technology for the production of bio-syngas and applied in the production of liquid transportation fuels—a review. Energies **4**(3), 389–434 (2011)
7. Warnecke, R.: Gasification of biomass: comparison of fixed bed and fluidized bed gasifier. Biomass Bioenerg. **18**(6), 489–497 (2000)
8. Moneti, M., Di Carlo, A., Bocci, E., Foscolo, P.U., Villarini, M., Carlini, M.: Influence of the main gasifier parameters on a real system for hydrogen production from biomass. Int. J. Hydrog. Energy **41**(28), 11965–11973 (2016)
9. Sadhwani, N., Adhikari, S., Eden, M.R.: Biomass gasification using carbon dioxide: effect of temperature, CO_2/C ratio, and the study of reactions influencing the process. Ind. Eng. Chem. Res. **55**(10), 2883–2891 (2016)

Sustainable Energy Generation from Agricultural Crop Residues

Joel George, P. Arun and C. Muraleedharan

1 Introduction

Human beings need energy for sustenance and well-being. Demand for energy in the world has been steadily increasing with the rise in global population and the rise of living standards. Present world energy scenario reveals that there is an over-dependence on fossil fuels. World primary energy consumption according to 'BP Statistical Review of World Energy' (June 2017) during the year 2016 is 13,276.3 metric tons of oil equivalent (MTOE) [1]. Growing energy demand coupled with restricted fossil fuel options and environmental apprehension has compelled developed and developing countries to explore the renewable and sustainable energy options. Energy generation from biomass is considered in the context of renewable and sustainable energy technologies. Biomass is a naturally available renewable carbon resource. Biomass can be converted into energy enriched producer gas, a mixture of gaseous products consisting of hydrogen, carbon monoxide, methane, and carbon dioxide through gasification. Gasification is a thermochemical conversion process, which occurs at sub-stoichiometric oxidizing conditions at high temperature (above 700 °C) in a reactor. Producer gas generated through biomass gasification has been identified as a versatile energy carrier which can be used as a feedstock for generating hydrogen or for combined heat and power (CHP) applications. Decentralized biomass power generation through biomass gasification has abundant scope especially in developing countries with agricultural-based economies.

Considering India, an agriculturally dominant nation, biomass-based energy generation has become one of the major focus areas of renewable energy programmes. Abundant biomass resources including various agricultural and forestry

J. George (✉) · P. Arun · C. Muraleedharan
Mechanical Engineering Department, National Institute
of Technology Calicut, Kozhikode, India
e-mail: joelpull@gmail.com

residues are locally available. It is estimated that annually 686 metric tons (MT) gross crop residue is generated in India [2]. The common agricultural residues for power generation in India includes sugarcane bagasse, rice husk, straw, cotton stalk, coconut shells, soya husk, coffee waste, jute wastes, groundnut shells. In the present work, a comparative study is carried out among three locally available crop residues—groundnut shell (GS), coffee husk (CH), and sugarcane bagasse (SB) to assess the gasification potential. These crop residues are considered as they are abundantly available in Indian geographical and agricultural context. Considering groundnut shell, a substantial amount of shell residue is produced in the de-hulling process. India is the second largest producer of groundnut having an annual production around 1.5–2 MT [3]. Coffee husk is obtained during the de-hulling process of coffee cherries to obtain coffee beans [4]. India, the seventh largest producer of coffee, accounts for about 4–5% of the world's output. The coffee production in India during the year 2015–16 was 348,000 MT [5]. India is the second largest producer of sugarcane. Sugarcane production in 2014–15 was around 356 MT. Bagasse is the milling by-product which remains after extracting sugar from the stalk.

Feasibility of these biomasses for gasification is judged based on biomass characterization followed by experimental investigation. Biomass characterization takes into consideration the proximate and ultimate analysis of biomass and the assessment of its thermochemical behavior in a thermogravimetric analyzer (TGA). The gasification potential of the biomasses is further assessed by carrying out an experimental investigation in a gasifier to assess the hydrogen yield obtained during an air gasification process. A bubbling fluidized bed (BFB) gasifier is considered as it is a cost-effective method for continuous biomass gasification. Further, air gasification is considered because it is simple and the process is autothermal. Experimental investigations on air gasification with different biomasses and the effect of operating conditions have already been reported [6–8] earlier. Pio et al. [9] have recently carried out detailed experiments with a pilot-scale bubbling fluidized bed gasifier. They proposed operating conditions with bed temperature in the range 700–850 °C and equivalence ratio in the range 0.17–0.36.

2 Materials and Methods

Selected agricultural crop residues—groundnut shell, coffee husk, and sugarcane bagasse—powdered to a particle size of 300–500 μm are used as the feedstocks. The samples collected are air dried for 2–3 days and then oven dried to reduce the moisture content to make it suitable for fluidized bed gasification. The physico-chemical behavior of the samples is analyzed through characterization tests. Hydrogen yield from each biomass sample is assessed in experimental investigation.

2.1 Biomass Characterization

Ultimate analysis is carried out to determine the elemental composition (C, H, O, N, and S) of biomass in percentage weight. The analysis was carried out using an ultimate analyzer (make: Elementar Vario EL III) at Sophisticated Analytical Instruments Facility (SAIF), STIC, Kochi. The proximate analysis determines the percentage by weight of moisture content, volatile matter, fixed carbon, and ash content in the biomass. Proximate analysis is carried out using laboratory facilities at National Institute of Technology Calicut. Thermogravimetric analysis is an analytical technique based on the measurement of the rate of change in the weight of a material as a function of temperature in a controlled atmosphere [10]. Analysis is carried out in a thermal analyzer by raising the temperature of the material gradually in a specified atmosphere at the desired rate in an electronic microbalance and plotting weight against temperature. In the investigation procedure using the thermal analyzer, nitrogen atmosphere was maintained and the temperature was raised from ambient conditions to 1000 °C at a heating rate of 10 °C/min.

2.2 Experimental Investigation

Experimental investigation is carried out in a bubbling fluidized bed gasifier setup (Fig. 1) which consists of a suitably insulated reactor column having an internal diameter of 150 mm and 2.3 m height. The top portion of the reactor column is enlarged in order to settle the unburnt biomass. The biomass is heated to gasification temperature in the fluidized bed in the heating chamber. The fluidized bed consists of a bed of inert granular particles such as river sand supported by a distributor plate. The granular bed is fluidized with air as the gasifying agent supplied by a suitable blower. The biomass is fed directly into or on the top of sand bed by a screw feeder operated by a DC motor. Controlled heating arrangement (with heater of rating 3 kW) is provided at the bottom of the reactor column to bring the biomass to the gasification temperature. A gas suction blower with speed control brings the producer gas generated out of the reactor and blows it over the cyclone separator. The generated gas is further conditioned by passing it through water scrubber, moisture remover, and oil bath. The conditioned gas is analyzed using a gas analyzer to determine the producer gas composition. Details of the operating conditions for different crop residues in experimental investigation are presented in Table 1.

1 Feeder motor
2 Hopper
3 Air inlet blower
4 Gasification chamber
5 Gas suction blower
6 Cyclone separator
7 Ash collector
8 Water scrubber
9 Moisture remover
10 Oil bath
11 Gas analyser
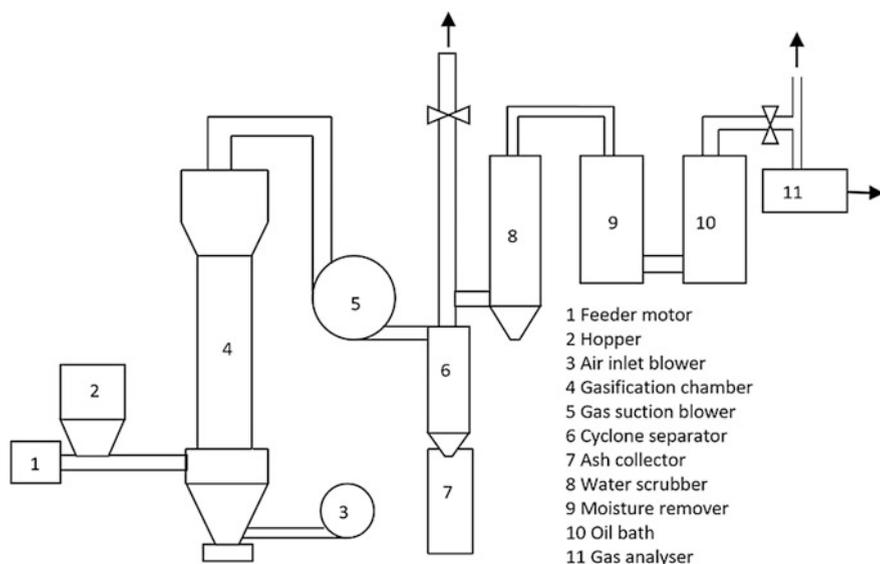
Fig. 1 Experimental setup of the bubbling fluidized bed gasifier

Table 1 Details of operating conditions for different biomasses

Biomass	Operating condition	Feed rate (kg/h)
Groundnut shell	Case 1: T = 680–800 °C, ER = 0.26 Case 2: T = 740 °C, ER = 0.24–0.32	Air supply rate = 21.3 Biomass feed rate = 16.9 Air supply rate = 21.3 Biomass feed rate = 18.3–13.7
Coffee husk	Case 1: T = 680–800 °C, ER = 0.26 Case 2: T = 740 °C, ER = 0.24–0.32	Air supply rate = 21.3 Biomass feed rate = 17.4 Air supply rate = 21.3 Biomass feed rate = 18.9–14.2
Sugarcane bagasse	Case 1: T = 680–800 °C, ER = 0.26 Case 2: T = 740 °C, ER = 0.24–0.32	Air supply rate = 21.3 Biomass feed rate = 16.9 Air supply rate = 21.3 Biomass feed rate = 18.3–13.7

3   Results and Discussion

In the present study, different agricultural crop residues are appraised as feedstocks for gasification based on the biomass characterization and experimental investigation. Physical and chemical properties are assessed through biomass characterization. The effect of operating parameters like temperature and equivalence ratio on gas yield is further studied to determine the feasibility of biomasses for gasification. The efficiency of gasification process for each biomass is also measured.

3.1 Assessment of Gasification Based on Biomass Characterization

Thermogravimetric analysis (TGA) is performed to understand the thermochemical conversion occurring during the gasification process. TGA plot (Fig. 2) provides the detailed information about the weight loss against different temperatures. Three specific zones—drying zone, devolatilization zone, and steady decomposition zone—are identified in the plot. In the drying zone (up to 250 °C), light volatiles like water is removed. A weight reduction of 8–10% is noted in this zone. A significant drop in weight of the sample (about 50%) is observed in the devolatilization zone extending from 250 to 500 °C due to the liberation of volatile hydrocarbons. A rapid thermal decomposition of hemicellulose, cellulose, and some part of lignin occurs in this zone. A steady decomposition of remaining lignin is observed above 500 °C. Comparative study of the plots reveal that sugar cane bagasse has higher volatile matter (VM) content, lower fixed carbon (FC) and ash (AH). This can be observed from the results of biomass characterization studies shown in Table 2. Table 2 also points out that the elemental percentage of hydrogen is about 6% for the biomass species considered. Based on the thermogravimetric analysis and biomass characterization studies, it can be concluded that the biomass specimens considered are feasible for gasification and the lignocellulosic biomass is capable of undergoing thermochemical conversion generating a gaseous mixture in the bubbling fluidized bed gasifier during the gasification process.

Fig. 2 Thermogravimetric analysis of biomass specimens
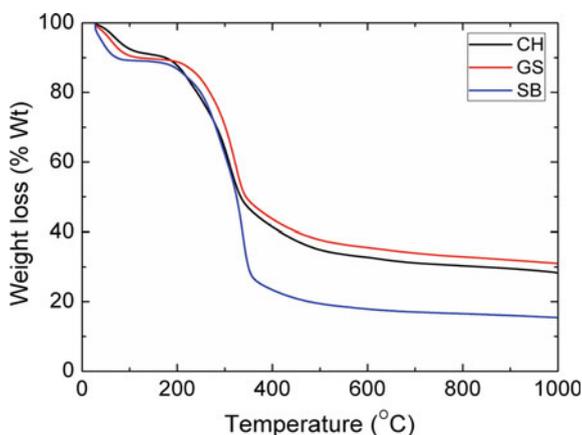
Table 2 Biomass characterization

Proximate analysis (%wt)						Ultimate analysis (%wt)				
Biomass	Biomass	FC	MC	VM	AC	C	H	O	N	S
CH	CH	17.3	10.4	64.4	7.9	41.82	6.07	50.3	0.77	0.14
GS	GS	15	14.7	66.1	4.2	42.73	6.12	50.6	1.09	0
SB	SB	10.5	14.6	73.1	1.8	43	6.03	50.08	1.66	0.12

3.2 Assessment of Gasification Based on Biomass Characterization

The assessment of gasification is carried out based on hydrogen concentration in the producer gas. The effect of operating parameters, temperature (T), and equivalence ratio (ER) on producer gas composition is illustrated in Figs. 3 and 4, respectively. Temperature (T) denotes the temperature measured at the reactor bed. Equivalence ratio (ER) is the ratio of air supplied for gasification to the stoichiometric air requirement of the biomass. It is observed that as the reactor temperature increases from 680 to 800 °C at a constant ER = 0.26, H_2 and CO concentrations increase. On the other hand, CO_2 and CH_4 concentrations decrease. The increase of H_2 and CO and decrease of CO_2 and CH_4 may be attributed to the occurring of more intense endothermic gasification reactions at high temperatures. When ER is increased from 0.24 to 0.28 at T = 740 °C, a decrease in H_2 and CO yield is observed. On the other hand, CO_2 concentration increases. At higher values of ER, oxidation reactions are promoted in the presence of more air available in the reaction system. H_2 and CO are oxidized to H_2O and CO_2 at higher values of ER, thereby reducing the H_2 and CO yields.

Fig. 3 Effect of temperature on producer gas composition
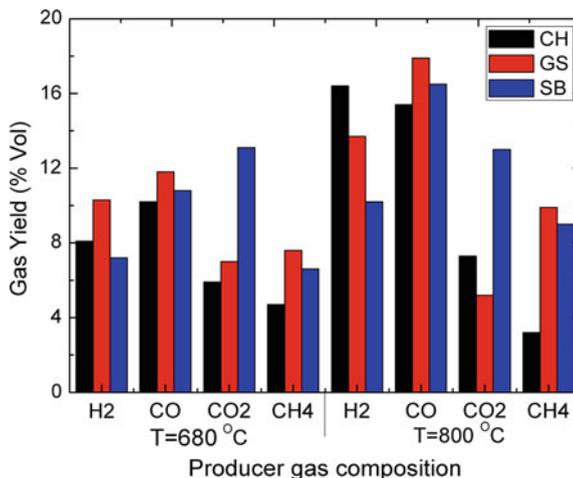
Fig. 4 Effect of equivalence ratio (ER) on producer gas composition
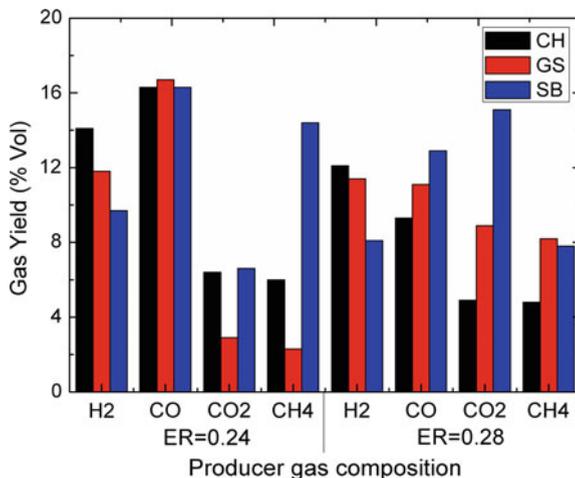
Fig. 5 Effect of temperature on hydrogen yield for different biomasses
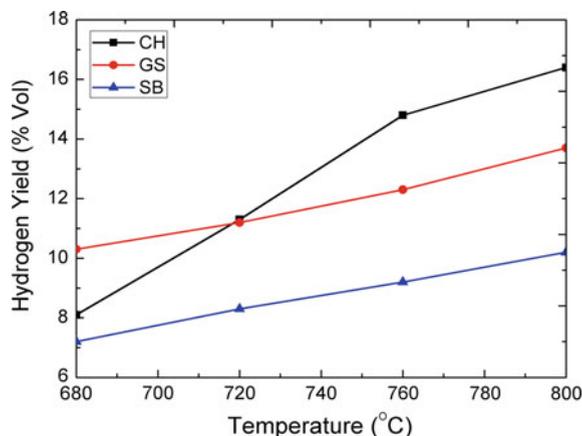
The effect of temperature and equivalence ratio on hydrogen yield for the selected agricultural crop residues in the specified operating ranges is presented in Figs. 5 and 6, respectively. It is observed that a high T and lower value of ER are preferential for higher hydrogen yield. However, in bubbling fluidized bed gasifiers, too high temperatures (above 850 °C) and too low ER values (less than 0.2) are not generally appreciated. Higher temperature may lead to bed agglomeration, and lower ER may affect the partial combustion reactions that sustain the autothermal gasification process. Apart from the operating conditions, the yield is also influenced by the physicochemical properties of crop residues. It is perceived that coffee husk (16.4%) generates more hydrogen by volume than groundnut shell (13.7%) and sugar cane bagasse (10.2%) at specified operating conditions of $T = 800$ °C and ER = 0.24.

Fig. 6 Effect of equivalence ratio (ER) on producer gas composition
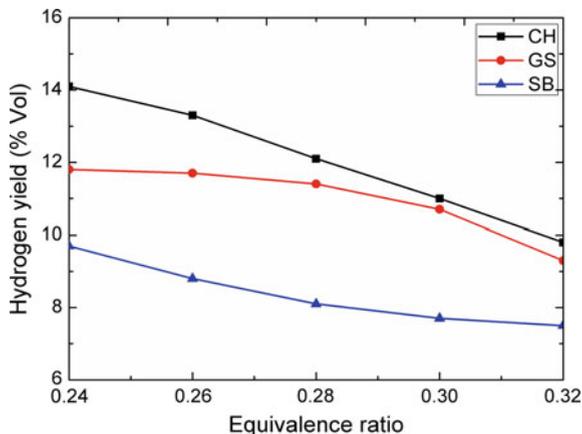
The efficacy of gasification process is appraised in terms of heating value of dry gas, dry gas yield, carbon conversion efficiency (CCE), and cold gas efficiency. The lower heating value of the dry producer gas (LHV$_{PG}$) is calculated from the volumetric percentage of H_2, CO, and CH_4 in the product gas according to Eq. (1) [11].

$$\text{LHV}_{PG}\left(\frac{\text{MJ}}{\text{Nm}^3}\right) = \text{PGY} * X * \left(\frac{4.2}{1000}\right) \tag{1}$$

where

$$X = 25.7 * H_2\% + 30 * CO\% + 85.4 * CH_4\% \tag{2}$$

Dry producer gas yield (PGY) is calculated based on the molar volume of nitrogen present in the producer gas composition. CCE is defined as the fraction of carbon in biomass feed that could be converted into product gas composition. It is calculated on the basis of volumetric percentage of CO, CO_2, and CH_4 in the producer gas and the mass percentage of carbon (C) in the biomass as shown in Eq. (3) [12].

$$\text{CCE}(\%) = \frac{\text{PGY} * (CO\% + CO_2\% + CH_4\%) * 12}{22.4 * C\%} * 100 \tag{3}$$

Cold gas efficiency (CGE) is an indication of the chemical energy of the producer gas in comparison to the biomass. It is defined as the percentage of heating value of biomass (LHV$_{BM}$) converted into the heating value of the producer gas (LHV$_{PG}$). It is calculated according to Eq. (4) [12]. *PGY* is the producer gas yield in Nm^3/kg corresponding to M_{BM} kg of biomass supplied.

Fig. 7 Effect of temperature on PGY and LHV
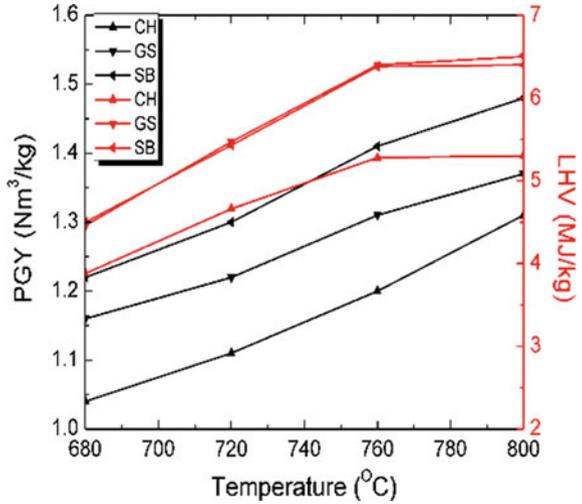
Fig. 8 Effect of temperature on CGE and CCE
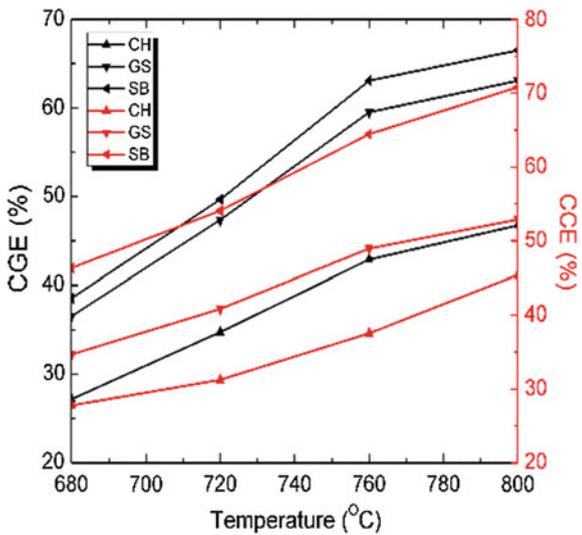
$$CGE(\%) = \frac{PGY * LHV_{PG}}{M_{BM} * LHV_{BM}} * 100 \qquad (4)$$

It is observed (from Figs. 7 and 8) that *PGY, LHV, CCE, and CGE* of all biomasses increase with increase in temperature. *CGE* and *CCE* of gasification process are comparatively higher for groundnut shell and sugarcane bagasse. This will ensure the efficiency of air gasification process. Though hydrogen yield from coffee husk is higher, *PGY and LHV* are slightly lower as compared to groundnut

shell and sugarcane bagasse. Based on the analysis, higher operating temperatures (750–800 °C) are preferred for enhanced PGYs during air gasification of biomass.

4 Conclusion

Feasibility of sustainable energy generation from agricultural crop residues through gasification is judged based on biomass characterization followed by experimental investigation. The proximate analysis identified appreciable quantity of volatile matter (64–73% by weight) in the crop residues considered. Ash content of the tested residues is less than 8%. The ultimate analysis revealed that the elemental hydrogen percentage is around 6%. High volatile content, low ash content, and high hydrogen content make the selected crop residues ideal for gasification. The thermogravimetric analysis of the residues revealed that the thermochemical behavior of lignocellulosic stuff is capable of undergoing gasification. The fluidized bed air gasification of the biomass investigated the effect of operating parameters on the selected crop residues. It was observed that hydrogen yield increased with temperature and decreased with increase in equivalence ratio. At specified operating conditions, T = 800 °C and ER = 0.24, the hydrogen yields obtained from the selected biomasses were 16. 4% for coffee husk, 13.7% for groundnut shell, and 10.2% for sugarcane. Further efficiency of gasification process for specified biomasses is also analyzed. The feasibility of agricultural crop residues for biomass gasification may be justified based on the results of the characterization test and the experimental investigations which are found to be satisfactory. The identification of the scope of crop residues for energy generation through gasification will boost up the decentralized power generation in rural sector.

References

1. BP.: BP statistical review of world energy. Br. Pet. **2017**, 8–11. URL: http://www.bp.com/content/dam/bp/en/corporate/pdf/energyeconomics/statistical-review-2017/bp-statistical-review-of-world-energy-2017full-report.pdf (2017)
2. Hiloidhari, M., Das, D., Baruah, D.C.: Bioenergy potential from crop residue biomass in India. Renew. Sustain. Energy Rev. **32**, 504–512 (2014)
3. Bharthare, P., Shrivastava, P., Singh, P., Ttiwari, A.: Peanut shell as renewable energy source and their utility in production of ethanol. Int. J. Adv. Res. **2**, 1–12 (2014)
4. Saenger, M., Hartge, E.U., Werther, J., Ogada, T., Siagi, Z.: Combustion of coffee husks. Renew. Energy **23**(1), 103–121 (2001)

5. Coffee Production in India, Coffee Industry, Cultivation, Statistics (n.d.). http://www.teacoffeespiceofindia.com/coffee/coffee-statistics. Accessed Oct 16, 2016
6. Caballero, M.A., Corella, J., Aznar, M.P., Gil, J.: Biomass gasification with air in fluidized bed. Hot gas cleanup with selected commercial and full-size nickel-based catalysts. Ind. Eng. Chem. Res. **39**(5), 1143–1154 (2000)
7. Skoulou, V., Koufodimos, G., Samaras, Z., Zabaniotou, A.: Low temperature gasification of olive kernels in a 5-kW fluidized bed reactor for H_2-rich producer gas. Int. J. Hydrog. Energy **33**(22), 6515–6524 (2008)
8. Esfahani, R.M., Wan Ab Karim Ghani, W.A., Mohd Salleh, M.A., Ali, S.: Hydrogen-rich gas production from palm kernel shell by applying air gasification in fluidized bed reactor. Energy Fuels **26**(2), 1185–1191 (2012)
9. Pio, D.T., Tarelho, L.C.A., Matos, M.A.A.: Characteristics of the gas produced during biomass direct gasification in an autothermal pilot-scale bubbling fluidized bed reactor. Energy **120**, 915–928 (2017)
10. Shinde, V.B., Singarvelu, M.: Thermo gravimetric analysis of biomass stalks for briquetting. J. Environ. Res. Dev. **9**(1), 151 (2014)
11. Loha, C., Chattopadhyay, H., Chatterjee, P.K.: Energy generation from fluidized bed gasification of rice husk. J. Renew. Sustain. Energy **5**(4), 043111 (1–10) (2013)
12. Lahijani, P., Zainal, Z.A.: Gasification of palm empty fruit bunch in a bubbling fluidized bed: a performance and agglomeration study. Bioresour. Technol. **102**, 2068–2076 (2011)

Numerical Analysis and Power Prediction of a Savonius Hydrokinetic Turbine

Bony John, Rony N Thomas and James Varghese

1 Introduction

The hydrokinetic turbines are used for harnessing energy from flowing water. The power generated using this turbine can be used to electrify remote area where grid extension is not feasible. The various advantages of hydrokinetic technology are no dams required, no harm to nearby land, no change in direction of river flow, reduced destruction of flora and fauna, and most importantly, it is green energy technology [1]. The Savonius turbine is a type of vertical axis hydrokinetic turbine. These are drag-type devices; i.e., they use drag force as main driving force. In this turbine, drag force on concave surface should be more than on the convex surface, which makes the turbine rotate. The Savonius turbines are simple in design and construction [2]. The main problem hindering the employment of hydrokinetic technology is the lack of research in the techno-economic feasibility and environmental benefits. In this paper, the design of Savonius hydrokinetic turbine is discussed.

Savonius wind turbines are subjected to lot of investigations. Kamoji et al. [3] proposed modified Savonius rotor blades with no shaft to improve the performance of the turbine. Roy and Ducoin [4] proposed a novel two-bladed Savonius turbine. Numerical study had been carried out to investigate the forces acting on the new configuration. The results showed improvement up to 20% in terms of efficiency by the proposed rotor, compared to conventional semicircular blades rotor. Khan et al. [5] and Elbatran et al. [6] conducted several numerical investigations to flow in open water channels to enhance the flow using nozzles.

B. John · J. Varghese
Cochin University of Science and Technology, Kochi, Kerala, India
e-mail: bonyjohn@gmail.com

R. N. Thomas (✉)
Department of Mechanical Engineering, SJCET, Palai, Kerala, India
e-mail: ronythomas143@gmail.com

The objective of the present study is to analyze a 2D model of Savonius hydrokinetic turbine rotor and simulate the rotation of turbine using CFD software ANSYS-Fluent. Plot the characteristic curve of turbine in terms of the dimensionless parameters, coefficient of power, and tip-speed ratio (λ). Validate the result with published data, and forecast the power curve of the turbine.

2 Methodology

The performance of a Savonius-type hydrokinetic turbine rotor was analyzed. Modeling of operation of a Savonius hydrokinetic turbine was performed using a two-dimensional geometry. Golecha et al. [7] conducted the experiments on modified Savonius rotor for river flow applications with zero overlap ratio, aspect ratio (H/D) = 0.7, blade arc angle (Ψ) = 124 °C, and blade shape factor (p/q) = 0.2. They determined the tip-speed ratio corresponding to maximum coefficient of power by plotting the characteristic curve. The geometrical parameters for rotor configuration were optimized by Kamoji et al. [3]. The diameter and height of the rotor are 245 and 170 mm, respectively, in the present study. The end plate diameter (D_o) is kept constant at 1.1D. Modified Savonius rotor was fabricated from aluminum pipe [8]. Reynolds number was set to 1.32×10^5, based on rotor diameter and undisturbed flow velocity.

Rotor considered was placed in a turbulent water flow, operating at constant angular velocity. This physical problem is reproduced by modeling the rotor rotation in a domain of flowing water under normal atmospheric conditions. The conservation equations applied to the turbulent water flow around the rotor are resolved numerically to obtain the pressure and velocity fields in the calculation domain and also the drag forces acting on the rotor blades.

The moment and power coefficients are obtained by integrating drag forces resulting from the pressure difference and viscosity of the water on the blades of device. Calculation domain was discretized into finite quadrilateral cells, and solution of numerical equations were carried out using computational fluid dynamics (CFD). The calculation domain was selected in such a way that the boundaries would not affect the performance of hydrokinetic turbine, as observed by Akwa et al. [9].

3 Meshing and Solver Settings

Sliding mesh arrangement is provided at the interface between rotating circular region and outer region representing flow channel. The diameter of circular region is set to 1.1 rotor diameters and is located 6 diameters from inlet as well as from two side walls of the calculation domain. Water flow velocity is prescribed at the inlet of the calculation domain. Pressure outlet boundary condition is applied at the outlet
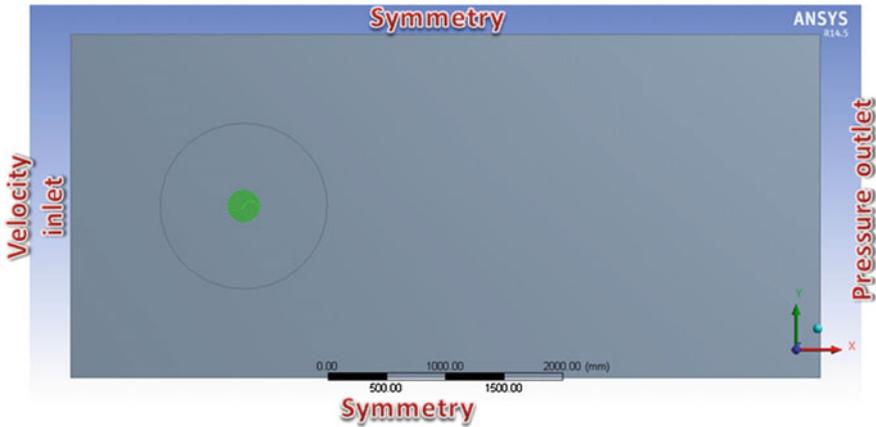
Fig. 1 Modeling of Savonius turbine

of domain. Symmetry condition is applied to the sides of the calculation domain, and no-slip condition is applied on the surface of the rotor blade. Details of the modeling and boundary conditions are shown in Fig. 1.

Uniform distribution of pressure and velocity in the flow is considered as initial condition. The rotation of the hydrokinetic turbine is set to each simulation by specifying the rotation rate of the region of sliding mesh. Finite Volume Method was used to solve the RANS equations of the turbulent water flow over the Savonius rotor, which allows the calculation of the performance coefficients of the rotor. Mass balance equation is one among these conservation equations. Equation (1) with indicial representation shows the mass balance, where $\bar{u}_i$ is the average velocity of water flow and $\acute{u}_i$ is the velocity fluctuation due to the turbulence effects, and x represents the flow direction. Meshing details of outer region and the rotating circular region is shown in Fig. 2. Inflation layers are applied along
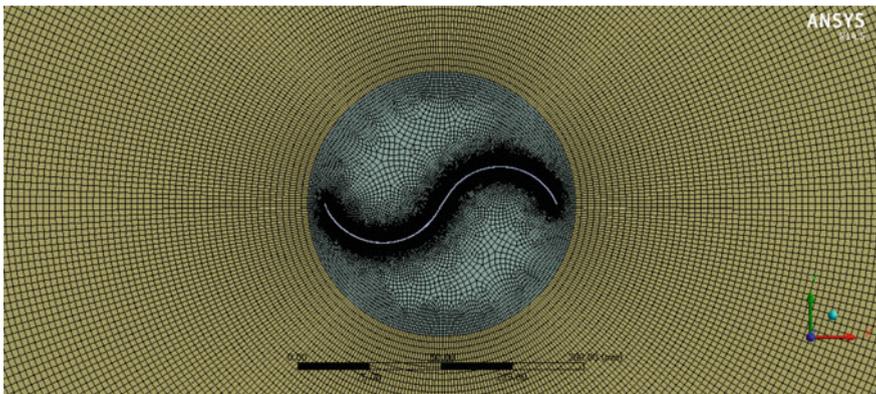
Fig. 2 Rotating circular region with Savonius blade
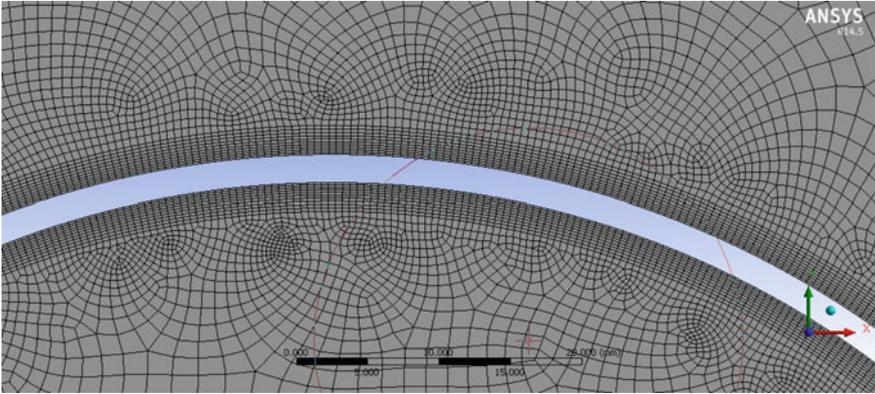
Fig. 3 Inflation meshing in the vicinity of blade surface

the blades to correctly capture the boundary layer influence on rotor performance as shown in Fig. 3.

$$\frac{\partial}{\partial x_i}(\bar{u}_i + \acute{u}_i) = 0 \tag{1}$$

The momentum equation must be solved along with the mass balance equation. Equation (2) represents the momentum equation, where t is the time, $\bar{p}$ is average pressure, ρ is the density, and μ is the dynamic viscosity of liquid water [9].

$$\frac{\partial \bar{u}_i}{\partial t} + \bar{u}_j \frac{\partial \bar{u}_i}{\partial x_j} = -\frac{1}{\rho}\frac{\partial p}{\partial x_i} + \frac{\mu}{\rho}\frac{\partial^2 \bar{u}_i}{x_i \partial x_j} = 0 \tag{2}$$

To take into account the unsteady effects, it was necessary to use the Fluent solver in a transient version. The solver was set as pressure based on absolute velocity formulation. The boundary conditions to activate the Sliding Mesh Model (SMM) were set for the rotating inner zone. The rotational speed was gradually increased from the lower value to the upper value to make the simulation process smooth and correctly develop the flow field. The boundary conditions at inlet and outlet were assigned similar to the data provided by Golecha et al. [7]. Flow velocity at inlet is kept constant so that the calculated torque is function of rotational speed only, and thus, it was simple to obtain a C_p versus λ characteristic curve.

The unsteady Reynolds-averaged Navier–Stokes equations (RANSE) were solved using the COUPLED algorithm for pressure–velocity coupling. A second-order upwind spatial discretization algorithm was used for all the mass, momentum, and turbulence equations, and a least squares cell-based algorithm was used for gradients. A second-order implicit formulation was used for transient algorithm [11]. It is well known that these second-order algorithms lead to best results because they considerably reduce false numerical diffusion and interpolation errors. At the beginning,

every simulation was performed with smaller under-relaxation factors to facilitate solution convergence. Under-relaxation factors were gradually increased to the default values, and final solutions were obtained. (RNG) k-ε turbulence model was used to capture the boundary layer effect near blade wall.

4   Equations for Data Analysis

Numerical simulation results were compared with experimental results of Golecha et al. [7] in terms of performance parameters. The average moment coefficient (C_m) per unit length of the blade is calculated by Fluent. From moment coefficient, torque per unit length (T) and power coefficient (C_p) are calculated. Power coefficient and moment coefficient of turbines were determined to analyze the turbine performance and efficiency, as presented in Eqs. (3) and (4):

$$C_p = \frac{\text{Output Power}}{\text{Input Power}} = \frac{T \times \omega}{\frac{1}{2} \rho A U^3} \tag{3}$$

$$C_m = \frac{T}{\frac{1}{2} \rho A \left(\frac{D}{2}\right) U^2} \tag{4}$$

ω is the angular velocity of the turbine; the term $0.5 \rho A U^3$ is the input power which is the maximum hydrokinetic power that can be extracted from the flowing stream; ρ is the density of water = 1000 kg/m³; (A) is the sectional area of the turbine ($H * D$); U indicates the flow stream velocity; D represents the diameter of Savonius rotor. It is important to determine the effects of tip-speed ratio (λ) on the power and moment coefficients of turbine at different cases. Therefore, λ is the ratio of the peripheral velocity of the turbine rotor to the flow stream velocity (U). In order to get different values of TSR, the angular velocity (ω) was varied to get different values of λ, whose λ was calculated by using the equation below:

$$\lambda = \frac{\omega D}{2U} \tag{5}$$

5   Results and Experimental Validation

The unstructured mesh is created using ANSYS meshing and generated 10 layers of inflation around the blade so that y^+ value is less than 1 with growth rate 1.2. Also, the grid is refined five times to conduct the grid independency test. It is found that after third grid refinement, there is no significant changes in the values obtained. Therefore, we have selected the grid 3 for further studies. Details of grid independence study is given in Table 1.

Table 1 Grid independence study

Refinement	Number of elements	C_m	C_p
GRID 1	32,341	0.223	0.154
GRID 2	56,792	0.221	0.153
GRID 3	96,907	0.215	0.149
GRID 4	156,327	0.215	0.149
GRID 5	172,367	0.215	0.149
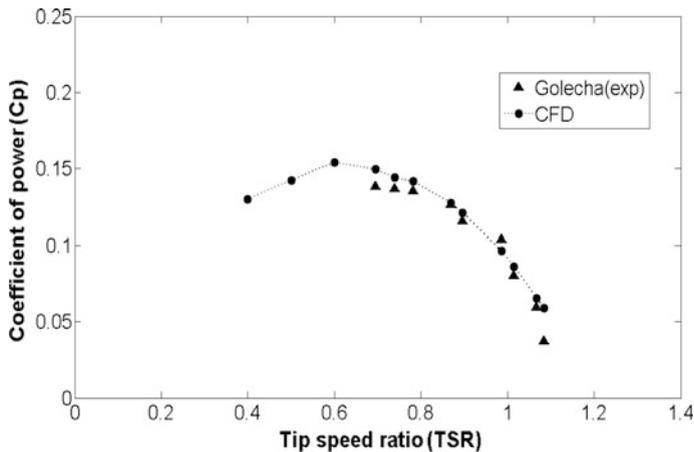
Fig. 4 Variation of power coefficient (C_p) against tip-speed ratio (λ)

Numerical simulation results were validated with experimental results of Golecha et al. [8] in terms of performance parameters.

The experimental details and data were used to simulate and validate the CFD model. A number of simulations were carried out at a Reynolds number of 1.32×10^5, since experiments were conducted by Golecha et al. [7] at this Reynolds number.

They [7] reported that uncertainties for the experimental results in different parameters, λ, moment coefficient, and power coefficient at the maximum coefficient of power were around 2.5, 4.5, and 4.8%, respectively. The comparison between experimental values of coefficient of power with the numerical results is shown in Fig. 4. The difference and error between experimental and numerical data are shown in Table 2. The average error was around 5.96%, while the maximum error was nearly 10.2%.

The error range was within the permissible limit when compared with other similar works in the literature [4–6, 10]. Hence, a good agreement was found existing between numerical and experimental results with an acceptable error. Output power, moment coefficient, and power coefficient of turbine were used to

Table 2 Difference between experimental and numerical values of moment coefficient and power coefficients at various tip-speed ratios

Tip-speed ratio (λ)	Moment coefficient (C_m)		Power coefficient (C_p)		Error (%)
	Experimental [1]	Numerical CFD	Experimental [1]	Numerical CFD	
0.693807	0.1988	0.215	0.138725	0.1492	8.2
0.737965	0.1853	0.195	0.137961	0.1439	5.2
0.782141	0.1732	0.181	0.135275	0.1416	4.5
0.868476	0.1454	0.147	0.125674	0.1277	1.1
0.899368	0.1293	0.135	0.115683	0.1214	4.4
0.981612	0.1055	0.0977	0.10416	0.0959	7.4
1.014681	0.079	0.085	0.080333	0.0862	7.5
1.065191	0.0557	0.0614	0.058044	0.0654	10.2
1.083868	0.0342	0.036	0.036137	0.039	5.2
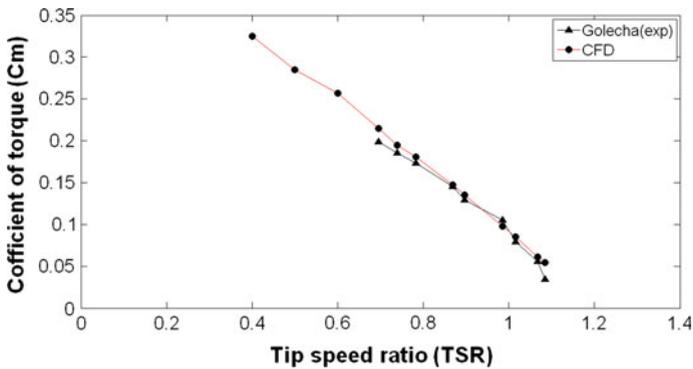
Fig. 5 Variation of moment coefficient (C_m) against tip-speed ratio (λ)

analyze the characteristics of turbine performance. The Savonius turbine was tested for different λ. The variations of moment and power coefficients at various λ for modified Savonius turbine are illustrated in Figs. 4 and 5. The maximum moment coefficient was around 0.215 at λ of 0.69, where the highest coefficient of power was about 0.15. With further increase in tip-speed ratio, both moment coefficient and power coefficient were found decreasing.

6   Power Curve Prediction

The power captured by a hydrokinetic rotor is specific to the type of rotor. Power delivered by a hydrokinetic turbine-based energy system depends on the choice of its subcomponents, viz., rotor blade profile, gear transmission system, electrical generator, and type of control mechanism employed. Therefore, proper modeling and integration of subcomponents are necessary to predict the actual power generation. The power coefficient (C_p) versus tip-speed ratio (λ) characteristic of the hydrokinetic rotor is modeled using computational fluid dynamics, and results are validated with published data.

In order to ensure maximum power coefficient, the rotor speed is varied in accordance with the water flow speed so that turbine is operating close to optimum tip-speed ratio (λ_{opt}). A variable speed operation of the hydrokinetic turbine enables its operation in the proximity of the maximum power coefficient and hence, the maximum power extraction for different flow speed is achieved. Because of superior performance of variable speed configurations over fixed speed configurations, variable speed configuration is assumed in this paper with the design tip-speed ratio being equal to the optimum tip-speed ratio (λ_{opt}). Variation of rotor torque with its rpm is shown in Fig. 6.

Mechanical power at the hydrokinetic rotor shaft (P) at any flow velocity is expressed as:

$$P = \frac{1}{2} \rho A U^3 \times C_{p,max} \tag{5}$$

For power production, the low rpm of the Savonius rotor must be scaled-up using proper gear transmission system to run a permanent magnet generator. Permanent magnet generator is widely accepted due to better reliability and lower maintenance for small-scale applications.

The output voltage of the permanent magnet generator can be rectified using uncontrolled rectifier [10]. As the flow speed varies, the frequency and magnitude
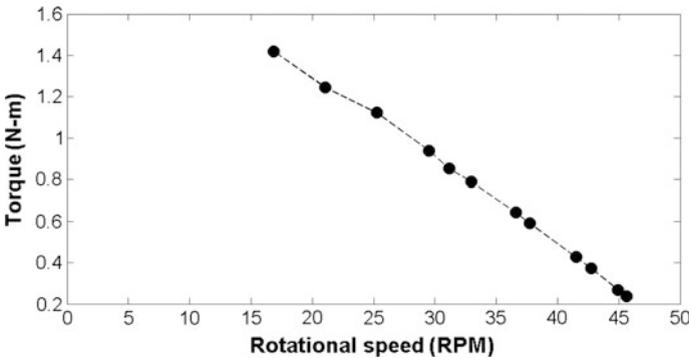
Fig. 6 Variation of torque with rpm of turbine
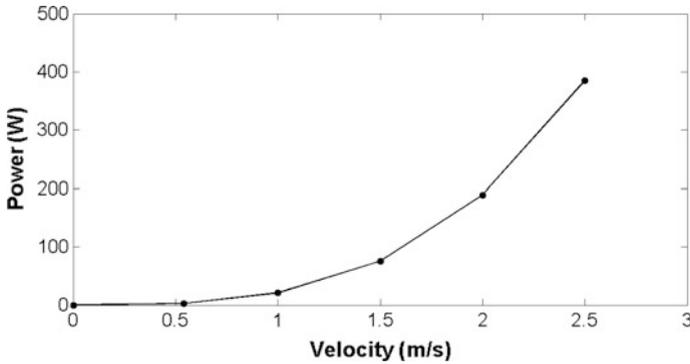
Fig. 7 Variation of power with respect to flow velocity

of the output current produced by the permanent magnet generator vary. The varying output current of generator can be converted to DC current using an uncontrolled diode rectifier. This varying DC current is made constant by passing it through a boost converter. Once steady DC is obtained, this power can be stored directly in a battery. Assuming 0.8 efficiency for gear transmission, generator, rectifier, and booster, a power curve is obtained for a Savonius rotor of sectional area 1 m^2 when working under an inlet velocity of 1 m/s and is shown in Fig. 7. A control mechanism is used to adjust the load on turbine in order to increase or decrease the angular velocity of turbine according to the inlet flow velocity. As a result, at any given flow speed U, since λ can be maintained at λ_{opt} by controlling the load on the turbine, the power output characteristics of the entire hydrokinetic machine can be obtained.

7   Conclusion

Two-dimensional model of Savonius hydrokinetic turbine rotor is developed, and the rotation of turbine in a channel of flowing water is simulated using CFD software ANSYS-Fluent. Numerical study has been conducted using a Reynolds number of 1.32×10^5 in order to achieve the objectives of the current research and comparing the simulation result with available experimental results. Output power, moment coefficient, and power coefficient of turbine were used to analyze the characteristics of turbine performance. The average error between experimental result and numerical result was around 5.96%, while the maximum error was nearly 10.2%. The Savonius turbine was tested at different λ. The maximum moment coefficient was around 0.215 at λ of 0.69, where the highest coefficient of power was about 0.15. With further increase in tip-speed ratio, both moment coefficient and power coefficient were found decreasing. Possible power production from the hydrokinetic turbine is also estimated.

References

1. Kusakana, K., Vermaak, H.J.: Hydrokinetic power generation for rural electricity supply: case of South Africa. Renew. Energy **55**, 467–473 (2013)
2. Kumar, A., Saini, P.R.: Performance parameters of Savonius type hydrokinetic turbine—a review. Renew. Sustain. Energy Rev. **46**, 289–310 (2016)
3. Kamoji, M.A., Kedare, S.B., Prabhu, S.V.: Experimental investigations on single stage modified Savonius rotor. Appl. Energy **86**, 1064–1073 (2009)
4. Roy, S., Ducoin, A.: Unsteady analysis on the instantaneous forces and moment arms acting on a novel Savonius-style wind turbine. Energy Convers. Manag. **121**, 281–296 (2016)
5. Khan, A.A., Khan, A.M., Zahid, M., Rizwan, R.: Flow acceleration by converging nozzles for power generation in existing canal system. Renew. Energy **60**, 548–552 (2013)
6. Elbatran, A.H., Yaakob, O.B., Ahmed, Y.M., Shabara, H.M.: Numerical study for the use of different nozzle shapes in microscale channels for producing clean energy. Int. J. Energy Environ. Eng. **6**,137–146 (2015)
7. Golecha, K., Eldho, T.I., Prabhu, S.V.: Influence of the deflector plate on the performance of modified Savonius water turbine, Appl. Energy **88**, 3207–3217 (2011)
8. Golecha, K., Eldho, T.I., Prabhu, S.V.: Performance study of modified Savonius water turbine with two deflector plates. Int. J. Rotat. Mach. (2012)
9. Akwa, J.V., Silva, G.A., Petry, A.P.: Discussion on the verification of the overlap ratio influence on performance coefficients of a Savonius wind rotor using computational fluid dynamics. Renew. Energy **38**, 141–149 (2012)
10. Barote, L., Marinescu, C.: PMSG wind turbine system for residential applications. In: SPEEDAM 2010 International Symposium on Power Electronics, Electrical Drives, Automation and Motion, 14–16 June, pp. 772–777 (2010)
11. Lanzafame, R., Mauro, S., Messina, M.: 2D CFD modeling of H-Darrieus wind turbines using a transition turbulence model. Energy Proc. **45**, 131–140 (2014)

Part II
Green Buildings

Green Buildings from Industrial By-Product Phosphogypsum: Transforming Mass Housing in India for Sustainable Future

Sajo Francis

1 Introduction

Glass fiber-reinforced gypsum (GFRG) wall panels are completely green and help to save the rare natural resources. The technology was adapted with suitable modifications and improvements to manufacturing GypWall from phosphogypsum [1]. Building Material Technology Promotion Council (BMTPC) of India (under the Ministry of Urban Development and Poverty Alleviation, Government of India) has certified the product, and extensive researches are conducted at FRBL and Indian Institute of Technology (IIT), Madras. BMTPC has identified GFRG technology as one of the emerging technologies for providing safe, strong, and quality housing in quick time [2].

2 Green Building

A green building is a structure designed, built, renovated, operated, or used in an ecological and resource-efficient manner using energy, water, and other resources efficiently, minimizing the overall impact on the environment.

Knowing green building material is an important step in designing a green building. Glass fiber-reinforced, load-bearing gypsum (GFRG) wall panel is an energy-efficient green building material.

S. Francis (✉)
FACT RCF Building Products Ltd, FACT CD Campus, Kochi, India
e-mail: sajofrancis@gmail.com

3   Gypsum

Gypsum consists of layers of calcium atoms and sulfate groups separated by sheets of water molecules. The effect of heating the mineral and setting the decomposition product by adding water has been known for thousands of years. Calcium sulfate dihydrate and calcium sulfate anhydrite occur in nature. The major by-product gypsums include phosphogypsum and flue-gas desulphurization (FGD) gypsum [3].

The majority of the natural gypsum in India is located in Rajasthan. Phosphogypsum is a by-product in the manufacture of phosphoric acid from rock phosphate by extraction with sulfuric acid. For every ton of phosphoric acid made, about 5 tons of phosphogypsum are generated. The amount of phosphogypsum being generated each year is directly proportional to the industrial production of P_2O_5. The stock of phosphogypsum is of environmental concern, and it is better to find ways for its consumption. It is proved that phosphogypsum can be used in the manufacture of building products, and in India, there is a huge shortage of dwelling houses [4].

Presently, the application of phosphogypsum includes (1) for soil conditioning, (2) in the cement industry as a retardant, and (3) in the production of plaster boards. The utilization of phosphogypsum depends on the degree of impurities such as fluoride and acid which depend on the type of raw material used and process adopted.

4   Properties Aiding Building Material

Gypsum is one of the first known binders of mankind. The oldest evidence of its presence is dated to 9000 BC. The construction using plaster became publically known from the eighteenth century. The rate of movement of calcium and sulfate ions in the lattice can be modified when the gypsum plaster is finely ground.

Accelerators and retarders can be added to control the workability and setting factors. The presence of anhydrite due to over dehydration may affect the setting property of the gypsum plaster. The particle size distribution of the gypsum plaster helps in lower porosity and aids smoother finish. The porosity increased with water content as it was generated due to the evaporation of water from calcium sulfate dihydrate. The property faster setting will aid gypsum as a good building material by reducing the production life cycle (Table 1).

Gypsum has a monoclinic crystal structure with a hardness of 1.6–2.2 on the Mohr scale and a natural insulator due to its low thermal conductivity. It is a good fire retarder because of its non-combustible property and stops the chances of spreading fire which ensure life safety [5]. The hydration of hemihydrates can be achieved by increased nucleation by seeding action. During hydration of hemihydrates calcium sulfate, gypsum crystallization takes place and develops strength.

Table 1 Particle size distribution of plaster from phosphogypsum

Particle size distribution			
S. No.	Size	Plaster from phosphogypsum (% by weight)	Ground plaster from phosphogypsum (% by weight)
1.	2 mm	2.18	0.654
2.	300 μ	4.05	0.581
3.	212 μ	0.69	0.153
4.	150 μ	1.35	0.571
5.	106 μ	42.93	2.320
6.	90 μ	25.94	2.880
7.	75 μ	11.44	5.571
8.	Below 63 μ	11.42	87.27

Table 2 Properties of plaster from natural and phosphogypsum

S. No.	Type of gypsum	Combined water	Water to plaster ratio	Compressive strength (N/mm^2)	Setting time—initial	Setting time—final
1.	Natural	4	70	11	12	25
2.	Natural	5.5	65	13	8	20
3.	Phosphogypsum	4.5	62	4	18	35
4.	Phosphogypsum	5.8	58	6	14	28

5 Gypsum Plaster Properties

When gypsum is heated under normal atmospheric conditions between 40 and 200 °C, it loses some of its combined water and recrystallizes to a rhombohedral-shaped crystal to form beta gypsum plaster. When gypsum is heated in water, the denser alpha plaster is formed. Beta gypsum plaster is used for manufacturing load-bearing GFRG wall panels. The plaster properties may vary depending on the source and type of gypsum (Table 2).

6 Glass Fiber-Reinforced Gypsum Wall Panel (GFRG)

The wall panels are cellular in form and produced on a flatbed table to a size of 12 m × 3 m × 124 mm. It has a good flexural strength and the lowest embodied energy rating of any load-bearing building system presently available [6]. Water repellent additives are used in the manufacture of wall panel which makes it suitable for internal or external use.

GypWall is lightweight when compared with brick or concrete. GFRG panel walling system serves as both internal and external wall and eliminates the need for bricks and reduces the consumption of cement, steel, sand, and water [7].

Building Material Technology Promotion Council of India (under the Ministry of Urban Development and Poverty Alleviation, Government of India) has certified the product, and extensive researches are conducted at FRBL and Indian Institute of Technology (IIT), Madras. Presently, this material is widely accepted and constructions are going on throughout India and abroad.

GFRG is completely green and eco-friendly which is tested to withstand earthquakes. The homeless population in India and the whole world would benefit if gypsum-based building products are used in the construction industry by bringing down the cost by 20%.

7 Reinforcement with Glass Fiber

Gypsum plaster is strong in compression but weak in tensile properties. Glass fibers are used to reinforce the gypsum plaster matrix and produce a strong composite material having improved tensile and impact properties [8].

In order to achieve strength, glass fibers are uniformly dispersed in the matrix to form a composite material with a high degree of stress distribution by fibers and give improved resistance to microcracking and crack progression.

8 The Setting Trends of Gypsum Plaster in Wall Panel Manufacture

Gypsum plaster when mixed with sufficient water it recrystallizes to form gypsum. This property of the plaster is utilized in the manufacture of plaster boards and GypWall (GFRG). The strength of GypWall (GFRG) depends on the setting properties of gypsum plaster and the material used as reinforcement. When gypsum plaster sets, it forms an interlocking mass of gypsum crystals that exhibit high strength and hardness. The setting property of gypsum plaster depends on various factors.

The recrystallization to gypsum increases with the higher solubility of the gypsum plaster. The solubility of beta plaster decreases rapidly with the increase in temperature which results in shifting the setting time.

It is seen that there is a short induction period during which disintegration occurs and small amounts of fine gypsum crystals are formed on available nucleating sites. The setting enters into an acceleration period when more and more gypsum crystals are formed. Hence, the casting of GypWall shall be completed within the induction period.

Addition of seeding nuclei reduces the induction period and aids the crystallization of gypsum. The addition depends on the ability to form gypsum nuclei and the time required to finish the casting of a wall panel. The acceleration of the setting time can be achieved by grinding or by adding some accelerators.

Certain materials will poison and inhibit the growth of gypsum crystals. The retarders may be required to extend the setting of plaster for workmanship without sacrificing the strength of GypWall [9].

The setting time will increase with the increased water content of the slurry. Water demand shall be maintained to the minimum requirement to maintain the strength if the wall panel.

9   Process Adaptations

Generally, casting wall panels is carried out using natural gypsum. In the world, itself conversion of phosphor gypsum to wall panels is not so common. The properties of phosphogypsum depend on the rock source and the process. Hence, experimental data pertaining to a particular source of phosphogypsum and its mathematical modeling is essential for understanding plaster properties.

In the case of phosphogypsum, the free water content is on the higher side. The particle size also varies, and it has a tendency of forming lumps depending on the age of the stockpile. These characteristics affect the mobility in material transfer through equipment. Hence, it is essential to clean and powder the phosphogypsum to the required size before feeding. The phosphogypsum feed bin shall be accommodated with a vibrating screen mechanism and a lump breaker system to ensure a free flow of materials. Wider conveyor belts aid mobility, and adjustable openings will help to regulate the required quantity fed (Table 3).

Table 3 Phosphogypsum plaster setting properties

S. No.	Type of gypsum	Combined water (%)	Water to plaster ratio (%)	Nucleating agent (%)	Slurry temperature (°C)	Knife set (m)	Initial Gilmore (m)	Final Gilmore (m)
1.	Phospho gypsum	5.0	58	0.07	33	22	36	44
2.	Phospho gypsum	5.6	62	0.23	35	19	32	38
3.	Phospho gypsum	5.9	62.5	0.27	35	21	35	41

Uniform calcination with proper controlling of temperature profiles inside the equipment is very important when phosphogypsum is used. The combined water range of the calcined plaster is very important for nuclei formation and to develop binding properties. E glass fibers are used to reinforce gypsum plaster matrix to improve tensile and impact properties. Glass fibers need to be uniformly dispersed in the matrix to form a homogeneous mixture which ensures a high degree of stress distribution by the fibers and give improved resistance to microcracking and crack propagation. Hence, it is necessary to ensure the properties of the glass fiber in the working environment and the effectiveness of its cutting system.

The continuous research work on the available phosphogypsum helped to fix the setting time without any loss of workability. It is very important to set the right water/plaster ratio for ensuring proper bonding of plaster and fiber.

10   Strength of Gypsum Wall Panel

Gypsum is widely used as a binding material as it quickly sets and hardens. The Egyptians were the first to use the gypsum as the building material. The set plaster strength depends on the size, amount of water used, impurities present, and the degree of interlocking and bonding of gypsum crystals. Mixing time, temperature, speed, and efficiency are very important factors in achieving maximum strength. Other requirements include good impregnation and coating of the fibers with slurry, uniform dispersion of fibers, and reasonable compaction to achieve a dense material (Table 4).

Particle size distribution affects the water demand, thereby influencing the nature of recrystallizing gypsum matrix. The factors affecting the disintegration of gypsum include the type, calcination method, impurities present, aging, and mixing.

Table 4   Mechanical properties of GypWall

S. No.	Mechanical property	Nominal value	Unit
1.	Unit weight	49	kg/m^2
2.	Compressive strength	160	kN/m
3.	Moment capacity, rib parallel to the span	2.1	kN m/m
4.	Wall panel thickness	124	mm

Table 5 Savings in GFRG construction methodology

Material	Approximate saving in % than conventional building method
Cement	50.8
Steel	35.2
River sand	76
Granite metal	27.56
Bricks	100
Water	75

11   GFRG Methodology

GFRG wall panel is energy efficient, load bearing and has high compressive and flexural strength. It has a very high level of fire resistance, thermal resistance, termite proof, and earthquake resistance. Instead of brick-by-brick construction, gypsum panel enables wall-by-wall construction leading to considerable savings in bricks, steel, cement, river sand, and construction time [10].

The modular cavities in combination with concrete form a composite material by which the strength increases many folds. The buildings designed with wall panels can resist natural disasters like earthquakes and cyclones.

The wall panels which are of size 12 m × 3 m × 124 mm weigh only 1.8 ton. Meanwhile, the standard brick wall of 23-cm-thick weighs around 19 ton. The construction methodology helps to reduce the construction time by 50% and cost by 20% (Table 5).

11.1   Affordable Housing Using Gypsum Wall Panels

In India, GFRG wall panel production has crossed 22 lakh sft which is used throughout India and abroad. GFRG construction methodology is faster than conventional methods and can adopt any type of plans and designs. Traditional building products are around for a very long time, but there are serious concerns about the impacts of these products on the environment. Hence, it is time to think above the traditional building products so that the people and the whole world are benefitted [11].

GFRG building technology is completely green and helps to save the rare natural resources and reduces carbon footprint. This concept uses load-bearing design technology, and it is gaining acceptance in India which can provide affordable houses in a reasonable time frame.

12 Conclusion

It is essential to find building materials which are green and adopt a green building methodology to protect the environment.

Green building materials and fast construction methods are the only solutions to provide affordable mass housing in India by protecting the environment. BMTPC has identified GFRG technology as one of the potential technologies for providing safe, strong, and quality housing in quick time.

References

 1. Sajo, K.F.: Gypsum—the green material of the future in housing. IIChe—Ind. Inst. Chem. Eng. Q. News Lett. (July–Sept, 2017)
 2. BMTPC—Building Material & Technology Promotion Council: Performance Appraisal Certificate, PAC NO: 1009-s/2012 dt 31.05.2012 (2012)
 3. Sajo, K.F.: Gypsum Material of the Future—For Green and Affordable Mass Housing In India. The Master Builder (July 2017)
 4. CPCB—Central Pollution Control Board (Under Ministry of Environment, Forest & Climate Change): Guidelines for Management, Handling, Utilization and Disposal of Phosphogypsum Generated from Phosphoric Acid Plants (2014)
 5. IS 3809:1979: Fire Resistant Test of Structures
 6. Building Materials & Technology Promotion Council (Ministry of Housing & Urban Poverty Alleviation, Government of India) & IIT Madras. GFRG Building, Structural Design Manual (2013)
 7. BMTPC: Prospective Construction System for Mass Housing—TECHNOLOGY PROFILE—Glass Fiber Reinforced Gypsum (GFRG) Panel Building System (2014)
 8. Ali, M.A., Grimer, F.J.: Mechanical properties of glass fiber-reinforced gypsum. J. Mater. Sci. (1969). Building Research Station, Garston, Watford, Herts, UK
 9. Lewry, A.J., Williamson, J.: The setting of gypsum plaster part 111—the effect of additives & impurities. J. Mater. Sci. (1994). Materials Department, Imperial College, London
10. FRBL—FACT-RCF Building Products Ltd: GFRG Wall Panel, Construction Manual (2011)
11. Sajo, F.: Green, affordable & rapid housing using GypWall—latest trend in building technology. Int. J. Creat. Res. Thoughts (IJCRT) (Dec 2017). FACT-RCF Building Products Ltd

Review on Applications of Smart Glass in Green Buildings

Ashwin Alias, R. Abhijith and Vineetha Thankachan

1 Introduction

Sunlight is incredible. It has been scientifically proven that when humans are exposed to natural sunlight they think clearer, feel better, and are more creative. But despite its benefits, too much heat is uncomfortable and the glare on the computer screen is often frustrating. Windows are mostly considered as a less energy-efficient building component with a high maintenance requirement. The foundations of a healthy building include factors such as ventilation, air quality, thermal comfort, noise, and lighting, and these factors serve as a basis for green certification standards to define their indoor environmental quality (IEQ) guidelines. Windows either wall us off from nature or helps in connecting humans with nature.

Glass plays a crucial role in achieving greater IEQ, and when used wisely can improve energy efficiency and ensure that building loads are not excessive due to solar gain. Glass can be used for almost every part of the building, from facades to doors and windows, from floors, walkways, and staircases to domes, canopies and skylights, from partitions and enclosures to shelves, table tops to murals, sculptures, art and decoration, etc. The main factors which play a prominent role in designing the building envelope with glass are the visual comfort, solar factor (SF)/solar heat gain coefficient (SHGC), relative heat gain (RHG), and U value.

Smart windows have the potential to set the technology to a higher standard in green buildings. Smart glass (dynamic glass) has the ability to change its properties such as the transmission of radiation in the solar spectrum in response to an electric current or

A. Alias (✉) · R. Abhijith · V. Thankachan
Department of Civil Engineering, Viswajyothi College of Engineering and Technology,
Ernakulam, Kerala, India
e-mail: ashwinalias1996@gmail.com

to the changing environmental conditions themselves. The application of such windows has the potential of reduction in the energy consumption of highly glazed buildings by reducing cooling loads, heating loads, and lighting application [1].

2 Applications of Smart Glass

The application of smart glass for building's windows can lead to a wide range of practical advantages, including saving money on air-conditioning and heating as well as eliminating the need to install and maintain motorized screens, blinds, or curtains. Another advantage of using smart glass for building's windows is that unlike blinds, smart glass can block harmful light while still maintaining a clear view of the outside world. This can enhance the level of natural daylight improving health and well-being. Therefore, it has a great effect on both productivity and attitude in the work-place.

Windows made from smart glass can adjust to exterior lighting conditions in order to create more comfortable indoor spaces and save electricity. Smart glass windows can be specially designed to help in the decrease of building's overall carbon emissions. The surface of any smart glass can be transformed from crystal clear to opaque which could create wide-open spaces or private enclosures in homes and office rooms. These transitions can be triggered by wall switches, remote controls, sensors, and timers.

Major aspects of smart glass include installation costs, electricity costs, material costs, and durability, as well as functional features such as the transition speed, possibilities for dimming, and the degree of transparency.

2.1 Assessment of Smart Glass Technologies

Active and passive smart glass technologies include electrochromic, thermochromic, suspended particle, micro-blind, and polymer dispersed liquid crystal devices [2]. Some of the prominent pros and cons of three active smart glass technologies are shown in Table 1.

The smart glass acts as climate adaptive building shells when installing in the envelope of green buildings, with the capability to save costs for heating, air-conditioning, and lighting. Dynamic glass technology utilizes multiple data sources including coordinates, weather patterns, position of the sun, window size, and placement to control the sun's energy. Table 2 shows an assessment of the various features of three popular smart glass technologies, namely smart glass, dynamic glass, and suntuitive glass [3–5].

Table 1 Pros and cons of active smart glass technologies

Factor	PDLC-active smart windows	SPD-active smart windows	Electrochromic smart windows
Key advantages	PDLC chemistry is relatively easy to produce in a film form	Can achieve a highly dark state that blocks 99.5% of the entering light No hazy appearance. The degree of opacity can be controlled by changing the applied voltage	Faster switching time compared to any other technology
Key disadvantages	It does not completely block the light in the "off" state and in the "on" state It has a hazy appearance	Not as effective as electrochromic smart windows in blocking infrared radiation	Cost of manufacturing electrochromic glass is high and is limited to applications that have flat surfaces
Common applications	Provides privacy in commercial buildings	Residential and commercial buildings	Residential and commercial buildings

Table 2 Features of various smart glass technologies available in the market

Organization	Features	Remarks
Smart glass	Solar control	Reflects up to 80% of the sun's radiant heat during the summer months, dramatically reducing the unwanted buildup of heat Retain warmth in the winter months using a modern low-e coating, argon gas, and warm-edge technology
	Anti-glare	Reduce the glare of Sun and filtering out harmful UV rays
	Warm-edge technology	Use of a spacer bar that is up to 950 times less conductive than aluminum which increasing temperature around the edges and vastly reduce condensation
View dynamic glass	Self-cleaning	Low maintenance
	Glare control	Intelligence calculates the penetration of the sun into the room and adjusts tint levels accordingly to prevent glare
	Minimize heat load	Intelligence manages the amount of solar radiation allowed through the glass based on a building's heat load specifications
	Maximize daylight	Intelligence maximizes daylight while continuously addressing heat and glare
	Personalized control	Each window, zone, or entire façade can be controlled via a smart phone or tablet

Table 2 (continued)

Organization	Features	Remarks
	Latitude and longitude	Intelligence uses precise coordinates to calculate the sun's position and anticipate its impact on the people inside
	Building orientation	Intelligence takes into account building orientation, the position of each window, and the sun's path
	Architecture	Exterior architectural features, such as overhangs and window sizes, are factored to determine how glare will impact workspaces
	Cloud cover	Light sensors and real-time weather feeds inform the system of current and upcoming weather conditions and adjust tint levels accordingly
	Preserving view	Manage building's changing needs for passive solar heat gain, solar control, and natural daylight transmittance
	Security and protection	Laminated design (using low-e glass) significantly enhances building security and reduces outside noise
	Optimizing design	Usage of all the space in building, including the precious window real estate, while maximizing occupant comfort and performance
	Installation	Installs the same as any other typical glass unit
Suntuitive dynamic glass	Smart and sustainable	– Powered by heat from direct sunlight – No manual, mechanical, or electrical intervention – Reduce greenhouse gas emissions – Can contribute toward LEED certification – Durable and maintenance-free – Energy savings

3 Developments in Smart Glass Technologies

Modern windows are being introduced into the market with various innovative technologies such as electricity generating smart windows which could help in meeting future energy needs and creating temperature-responsive buildings.

A new material which was developed at Lawrence Berkeley National Laboratory in the US could transform smart windows into solar generators. Halide perovskite solar cells exhibit a totally reversible performance over repeated phase transition cycles without any performance degradation [6]. This photovoltaic window could harness solar energy to full capacity in the future.

Photovoltaic smart window (developed at National Renewable Energy Laboratory, US) enabled by reversible photothermal complex dissociation from methylammonium lead iodide could work as a solar panel and convert sunlight into energy with 11.3% efficiency in solar power conversion [7].

Dye-sensitized solar cells (DSSC) improve the building energy efficiency by equipping buildings with electricity generating windows. DSSC production is cost-effective and consumes less power compared to silicon-based solar panels [8].

Savings of 2.4 million dollars and reduction in carbon emissions by 4000 t were reported by Empire State Building in New York after the installation of smart glass windows which required some energy to operate. Smart glass windows coated with 50–150 nm thickness vanadium dioxide do not require any such energy and respond directly to changes in temperature.

4 Conclusion

Millions of tons of glasses are manufactured using various processes every year. Most of them remain transparent and unable to change its properties. Smart glasses have the potential to change its properties which include the amount of heat that can be transmitted and conducted through the glass. This can provide heating and cooling capabilities, depending on the climate in which the smart glass is used. The use of a smart glass system provides significant cost savings with respect to heating, cooling, lighting, ventilating, and overall energy bills. Smart glass enhances indoor comfort without the use of obtrusive window shades or other sun-blocking devices. Photovoltaic smart window can help in generating electricity. Smart glass has the potential to reduce energy consumption up to about 40% in a typical commercial installation.

References

1. Baetens, R., Jelle, B.P., Gustavsen, A.: Properties, requirements and possibilities of smart windows for dynamic daylight and solar energy control in buildings: a state-of-the-art review. Sol. Energy Mater. Sol. Cells **94**(2), 87–105 (2010). https://doi.org/10.1016/j.solmat.2009.08.021
2. Wong, K.V., Chan, R.: Smart glass and its potential in energy savings. J. Energy Res. Technol. **136**(1), 012002 (2013). https://doi.org/10.1115/1.4024768
3. View Dynamic Glass. https://viewglass.com. Accessed 15 Mar 2018
4. Smart Glass. http://www.smart-glass.co.uk. Accessed 15 Mar 2018
5. Suntuitive Glass-Self tinting Glass. http://www.suntuitive.com. Accessed 15 Mar 2018
6. Lin, J., Lai, M., Dou, L., Kley, C.S., Chen, H., Peng, F., Sun, J., Lu, D., Hawks, S.A., Xie, C., Cui, F., Alivisatos, A.P., Limmer, D.T., Yang, P.: Thermochromic halide perovskite solar cells. Nat. Mater. **17**(3), 261–267 (2018). https://doi.org/10.1038/s41563-017-0006-0
7. Wheeler, L.M., Moore, D.T., Ihly, R., Stanton, N.J., Miller, E.M., Tenent, R.C., Blackburn, J.L., Neale, N.R.: Switchable photovoltaic windows enabled by reversible photothermal complex dissociation from methylammonium lead iodide. Nat. Commun. **8** (2017). https://doi.org/10.1038/s41467-017-01842-4
8. Murray, J., Ma, D., Munday, J.N.: Electrically controllable light trapping for self-powered switchable solar windows. ACS Photonics **4**(1), 1–7 (2017). https://doi.org/10.1021/acsphotonics.6b00518

Green Building Rating Systems from the Perspective of the Three Pillars of Sustainability Using Point Allocation Method

Nina Lazar and **K. Chithra**

1 Introduction

The eighteenth and nineteenth century faced a significant transition called the industrial revolution. This period witnessed a drastic increase in growth rate of population and led the way to large-scale development and massive consumption of non-renewable resources. The environmental impact of developmental activities was sounded since the early 1960s. As a result of growing concern towards the environment, the coming decades witnessed many environmental conferences [1]. In this context, the term sustainability along with the three pillars environment, society and economy gained global attention. World Green Building Council (WGBC) was established in 2002 to promote sustainable construction practices and grew fast into a worldwide network of 73 Green Building Councils [2]. Green Building Rating Systems for different occupancies have been developed by Green Building Councils across the globe to assess and recognise buildings which meet sustainability requirements, and their effectiveness has a crucial role to play. To improve the existing Green Building Rating Systems and to attain robustness, WGBC welcomes suggestions from academic and research institutions [3]. Studies on Green Building Rating Systems has been done by many researchers and analysed various aspects of Green Building Rating Systems but were limited to general level and category level. In this context, it is very much relevant to investigate the Green Building Rating Systems from the perspective of three pillars of sustainability to ensure these systems helps in achieving goals of sustainability.

N. Lazar (✉) · K. Chithra
Department of Architecture & Planning, NIT Calicut,
Kozhikode, Kerala, India
e-mail: nina_p170032ar@nitc.ac.in

K. Chithra
e-mail: chithrak@nitc.ac.in

The objective of this study is to investigate the weightage of each pillar of sustainability considered by different Green Building Rating Systems using point allocation method. A questionnaire survey was conducted, and the respondents were asked to allocate points among three pillars of sustainability based on their perspective. The results of the survey were tabulated and analysed to arrive at the weightage for each pillar of sustainability. The research outcome would be highly beneficial while developing new rating systems and also for refining the existing Green Building Rating Systems towards achieving sustainability.

2 Research Methodology

This paper begins with background study of Green Building Rating Systems followed by selection of rating systems for current research. The mandatory requirements and criteria of the selected rating systems were studied in detail and arrived at a summarised list of mandatory requirements and criteria. Based on the summarised list, questionnaire was designed. Selection of experts for the survey was done in parallel. A questionnaire survey was conducted, the results were tabulated and analysed by plotting radar charts. A statistical test was also undertaken to conclude the research. The methodology flowchart is shown (see Fig. 1).
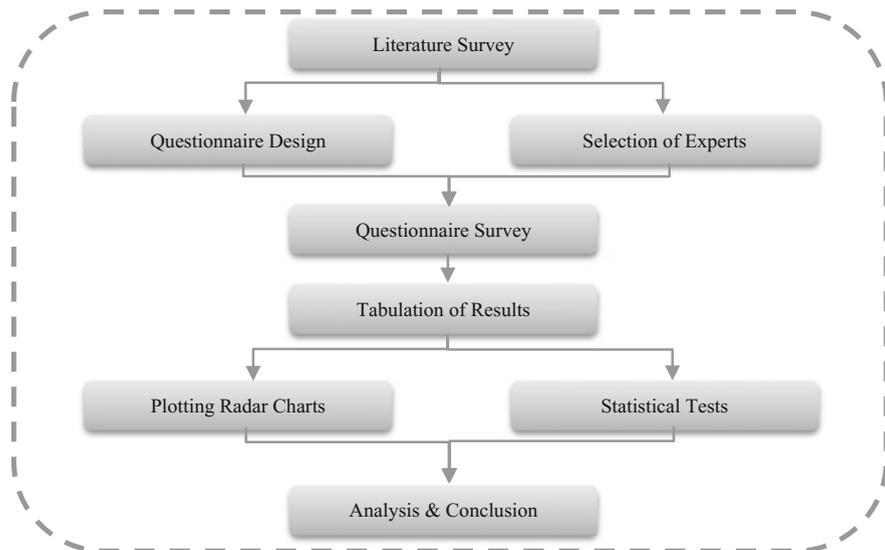
Fig. 1 Methodology flowchart

3 Literature Survey

3.1 Sustainability

Sustainability, at its base, always concerns the longevity. The basic idea of sustainability is one which survives or persists [4]. Despite the use of the word for many years with its primary meaning, during the past few decades, the word has given an entirely new meaning and purpose. The most popular definition is provided by the Brundtland Report, which defines sustainable development as "the development that meets the needs of the present without compromising the ability of future generations to meet their own needs" [5]. This definition is also in line with the sustainability concept given by World Conservation Strategy, which says that "Human beings, in their quest for economic development and enjoyment of the riches of nature, must come to terms with the reality of resource limitation and the carrying capacities of ecosystems, and must take account of the needs of future generations" [6]. Another report by IUCN, Caring for the Earth, extends and emphasises the message of World Conservation Strategy [7]. Over these years, the definition of sustainable development evolved.

Later in 2005, the World Summit identified environment, society and economy as interdependent and mutually reinforcing pillars of sustainability [8]. These three goals are represented using three concentric circles. Since there is no existence for the economy without society and no existence for a society without the environment, these three dimensions are interdependent and mutually reinforcing [9] (see Fig. 2). This concept redefines the conventional concept of interlocking circles [10] (see Fig. 3).

Fig. 2 Nested circles [21]. Nested sustainability-v2.gif by KTucker. Licensed under CC BY-SA 3.0/Desaturated
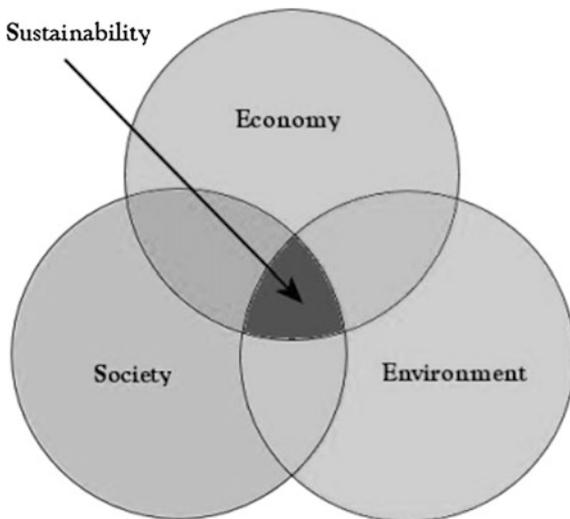
3.2 Sustainable Buildings

The concept of sustainability was extended to almost all fields and also to the built environment, and subsequently, the concept of sustainable buildings and green buildings attained importance. Thus, sustainable buildings are also grounded on the three pillars of sustainability. The definition of sustainable buildings based on three pillars given by various research groups and organisations were summarised by Kang as shown in Table 1 [11].

Table 1 Brief description of three pillars of sustainability

Pillars of sustainability	Brief description
Environment	Mitigation of climate change
	Diversity and protection of ecosystem
	Improvement of quality
	Depletion of resource
Society	Improvement of comfort
	Improvement of health
	Social inclusion and community safety
	Transparency
	Equity
Economy	Direct cost saving
	Indirect cost saving

3.3   Green Building Rating Systems

The concept of the sustainable building is an outcome of the efforts made in the building sector for the sake of sustainable development [11]. Green Building Rating systems have been developed by Green Building Councils across the globe under the purview of WGBC to recognise buildings that meet sustainable requirements.

Among the various rating systems developed across globe Building Research Establishments, Environmental Assessment Method (BREEAM) was the first and foremost Green Building Rating System. BREEAM was developed in the UK in 1990 and has been implemented in 76 countries worldwide [12]. BREEAM International New Construction 2016, Technical Manual SD233 2.0 was selected for the study [13]. BREEAM is having 50 criteria (excluding residential only criteria) classified into ten categories. BREEAM is having 14 mandatory requirements for achieving outstanding performance.

Leadership in Energy and Environmental Design (LEED) is another globally recognised rating system and has been implemented in more than 165 countries [14]. LEED Certification was developed in the USA in 1998, grew fast and is nearly the dominant building assessment system around the world [15]. LEED V4 for Building Design and Construction was selected for the study [16]. The study is limited to the new construction category. LEED is having 12 prerequisites and 43 criteria classified into eight categories.

Indian Green Building Council (IGBC) and Green Rating for Integrated Habitat Assessment (GRIHA) are the two rating systems developed in India. IGBC was formed in the year 2001 as a part of Confederation of Indian Industry (CII) with a vision to enable a sustainable built environment for all and facilitate India to be one of the global leaders in the sustainable built environment by 2025 [17]. IGBC Green New Buildings Rating System, Version 3.0 was selected for the study [18]. IGBC is having ten mandatory requirements and 42 criteria classified into seven categories.

GRIHA Council was founded by The Energy and Resources Institute (TERI) with support from Ministry of New and Renewable Energy, Government of India. TERI has developed GRIHA which was adopted as the national rating system for green buildings by the Government of India in 2007 [19]. GRIHA Version 2015 was selected for the study [20]. GRIHA is having 16 mandatory requirements and 30 criteria classified into nine categories.

IGBC and GRIHA were selected along with the most frequently studied rating systems, i.e. LEED and BREEAM [15] for the current study. The criterion for innovation and criterion for regional priority is not considered in the study since the nature of the criterion will be project specific and cannot be predicted. To have a better comparison of the selected rating systems, the categories were classified into six broader categories as shown in Table 2.

Table 2 Categories of green building rating systems

Categories	LEED	BREEAM	IGBC	GRIHA
Sustainable sites	Location and transportation Sustainable sites	Transport Land use and ecology	Site selection and planning	Site planning Construction management
Water	Water efficiency	Water	Water conservation	Water
Energy	Energy and atmosphere	Energy	Energy Efficiency	Energy
Material	Material and resources	Materials Waste	Building material and resources	Sustainable building materials Solid waste management
IEQ	Indoor environmental quality	Health and wellbeing	Indoor environmental quality	Occupant comfort and wellbeing
Others	Integrative process Innovation	Management Pollution Innovation	Sustainable architecture and design Innovation and development	Socio-economic strategies Performance monitoring and validation

4 Questionnaire Design

The questionnaire was designed in detail incorporating criteria from the four rating systems selected. Entire criteria from the chosen rating systems were listed down. If more than one criterion with same intend is occurring, the additional ones are eliminated and arrived at a summarised list of criteria. Based on the list, questionnaire survey was prepared. Against each criterion, a brief was added to understand the intent of the criterion quickly. The respondents were asked to allocate 10 points between the three pillars, i.e. environment, society and economy according to their perceived value against each criterion. Respondents were asked to assign most points to dimensions they consider most benefited by the criterion given. A brief description of each pillar based on the literature review as shown in Table 1 [11] was also noted in the questionnaire for the respondents to have a better understanding. A questionnaire survey was conducted among stakeholders from various disciplines to assess the weighing factors of three pillars of sustainability against each of the green building rating criterion.

5   Selection of Experts

The survey questionnaire was sent out to experts from different disciplines like architects, planners, engineers, project managers, academicians. The professionals mentioned above are involved in all the lifecycle stages of a project and will have a generic idea about all the aspects of a project. Academicians and researchers were also selected since much researches are going on in academic institutions regarding sustainable buildings. All the respondents were briefed about the scope of the survey, and how to respond to the questionnaire. The intent of each criterion was also explained along with brief description of three pillars of sustainability. The responses were received from each discipline as shown (See Fig. 4).

6   Analysis and Discussion

The responses received through questionnaire survey were tabulated and analysed. The analysis was done separately for mandatory requirements and criteria. Category-wise weightage towards each pillar of sustainability was calculated and plotted using radar chart.

6.1   Mandatory Requirements and Three Pillars of Sustainability

The points allocated for environment, society and economy by the respondents against each mandatory requirement was tabulated for all the selected rating
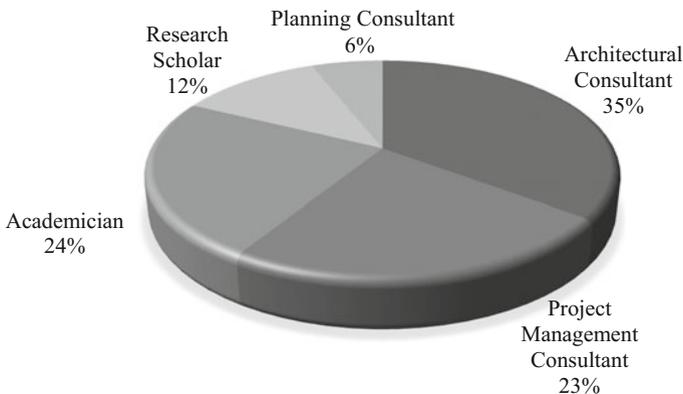
Fig. 4 Respondents category in percentage

systems. The average points for three pillars, i.e. environment, society and economy was calculated for all the categories separately and converted to a percentage for easy comparison. Based on the percentage weightage calculated, radar chart was plotted for all the selected rating systems (see Figs. 5, 6, 7 and 8). LEED rating system does not have a mandatory requirement under the categories integrative process, innovation, and location and transportation. BREEAM rating system does not have a mandatory requirement under the categories land use and ecology, transport and pollution. IGBC rating system does not have a mandatory requirement under the categories sustainable architecture and design, and innovation and development. GRIHA rating system does not have mandatory requirements under the category sustainable building materials and solid waste management.

Mandatory requirements of the selected rating systems have given importance to all the three pillars of sustainability. From the radar charts, it is evident that all the categories have given more weightage to environment except the category indoor air quality. The category indoor air quality has more weightage towards society. Categories water and energy have given more weightage to economy than society. The weightage given by each category for the three pillars of sustainability in the decreasing order for the mandatory requirements is shown in Table 3. It is also understood from the radar charts that IGBC and LEED rating system follows same structure in case of mandatory requirements.

More weightage is given to environment followed by society and economy in the descending order considering the overall weightage shown in Table 4. To test whether there is any significant difference between the weightage considered by rating systems towards each pillar Kruskal Wallis test was conducted. The test was
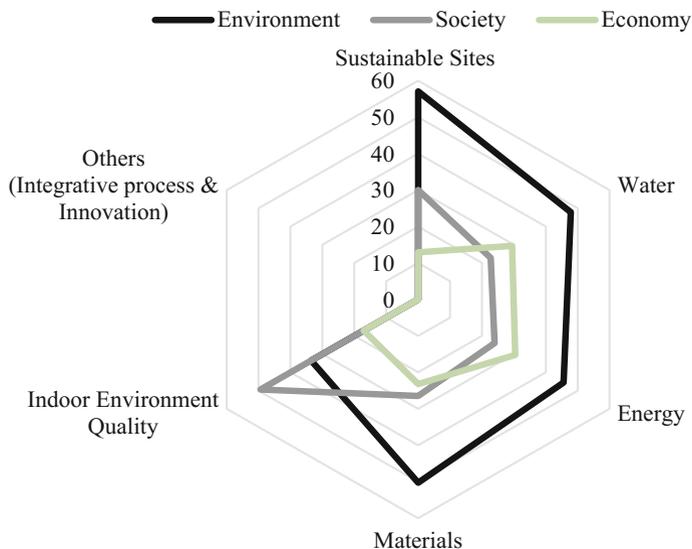
Fig. 5 Radar chart for LEED mandatory requirements
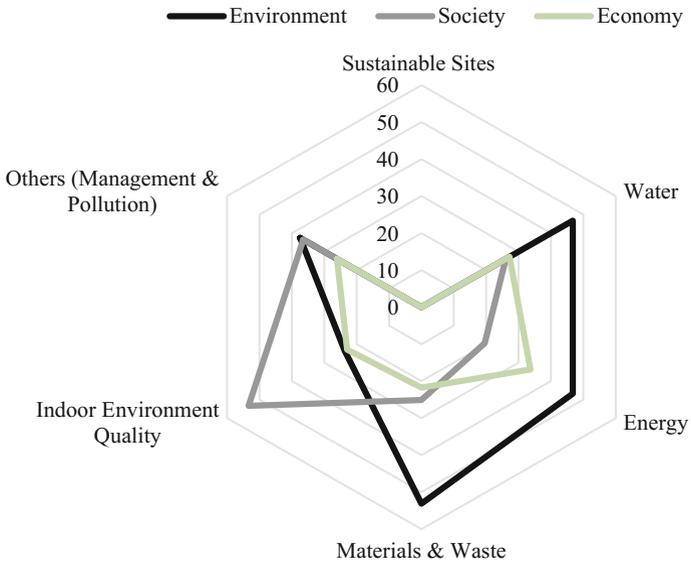
Fig. 6 Radar chart for BREEAM mandatory requirements
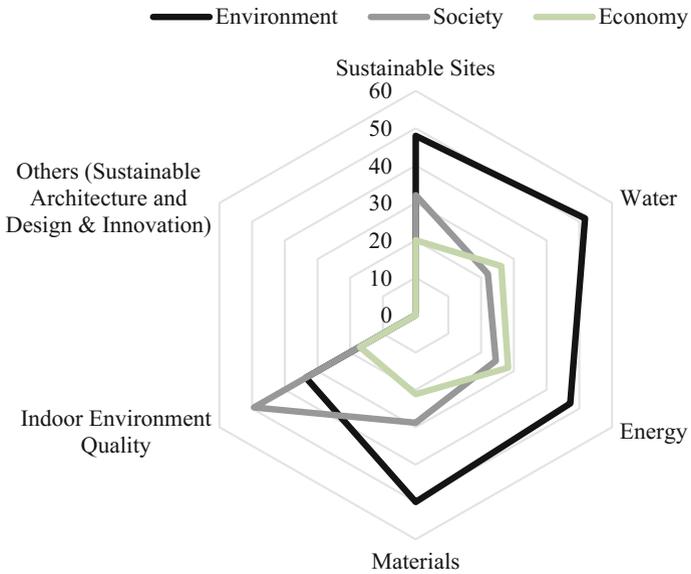
Fig. 7 Radar chart for IGBC mandatory requirements
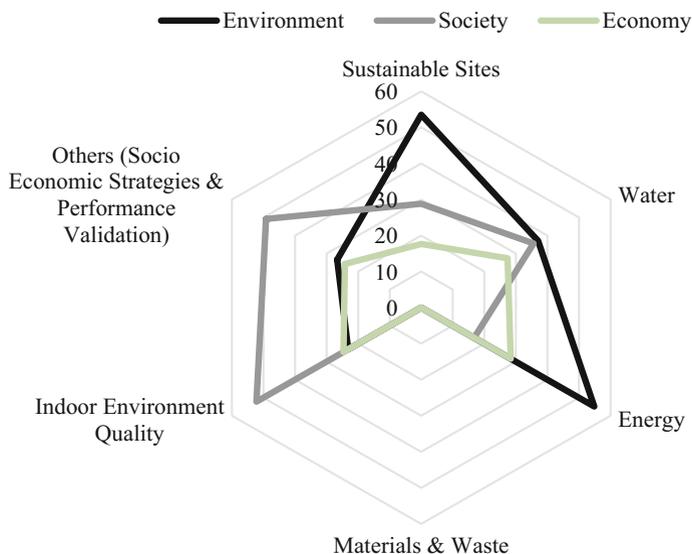
Fig. 8 Radar chart for GRIHA—mandatory requirements

Table 3 Decreasing order of weightage—mandatory requirement

Mandatory requirement		
Categories	Weightage	Remarks
Sustainable sites	Environment > Society > Economy	All systems follow the same pattern
Water	Environment > Economy > Society	The only exception is GRIHA
Energy	Environment > Economy > Society	All systems follow the same pattern
Material	Environment > Society > Economy	All systems follow the same pattern
IEQ	Society > Environment > Economy	The only exception is GRIHA

Table 4 Overall weightage for three pillars of sustainability

Mandatory requirement			
	Weightage in % for environment	Weightage in % for society	Weightage in % for economy
LEED	45.88	28.82	25.29
BREEAM	39.54	34.96	25.50
IGBC	45.82	30.94	23.24
GRIHA	39.38	36.13	24.49

conducted separately for all the three pillars. The K value obtained for environment is 19.05, for society is 21.13 and for economy is 13.18. Considering a significant level of 5% the critical chi-square value is 7.815. All the K values obtained are greater than critical chi-square value; it implies that selected rating systems do not follow same structure in case of mandatory requirements.

6.2 Criteria and Three Pillars of Sustainability

The points allocated for environment, society and economy by the respondents against each criterion was tabulated for all the selected rating systems. Corresponding to each criterion, scores are specified by each rating system. The average point given by the respondents is multiplied by the scores against each criterion and arrived at a total score for three pillars. This score is converted to a percentage for easy comparison. Based on the percentage weightage calculated, radar chart was plotted for all the selected rating systems (see Figs. 9, 10, 11 and 12). As an exception from all other selected rating systems, BREEAM has specified weightage for each category, apart from the score for each criterion. The specified weightage is different for different occupancies. Weightage for non-residential fully fitted occupancy is considered for calculations in this study. Therefore, the residence only criteria are omitted while doing the calculation.
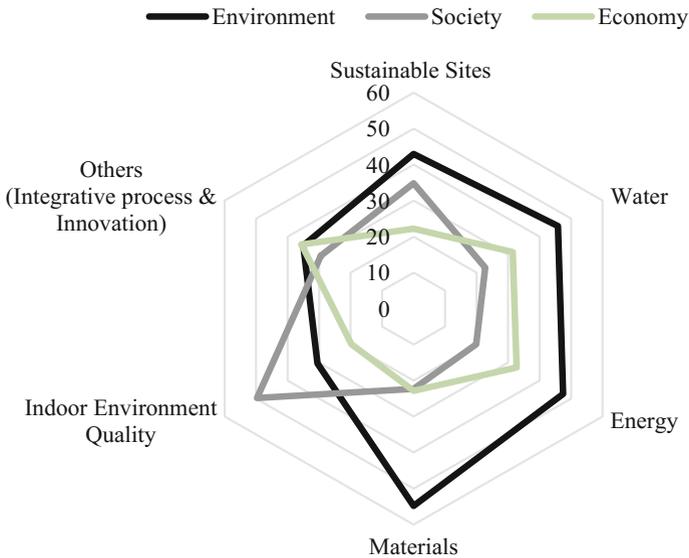
Fig. 9 Radar chart for LEED criteria
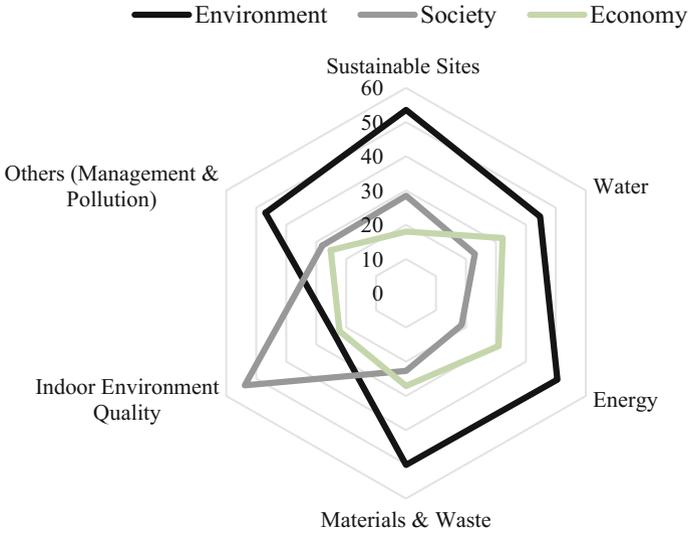
Fig. 10 Radar chart for BREEAM criteria
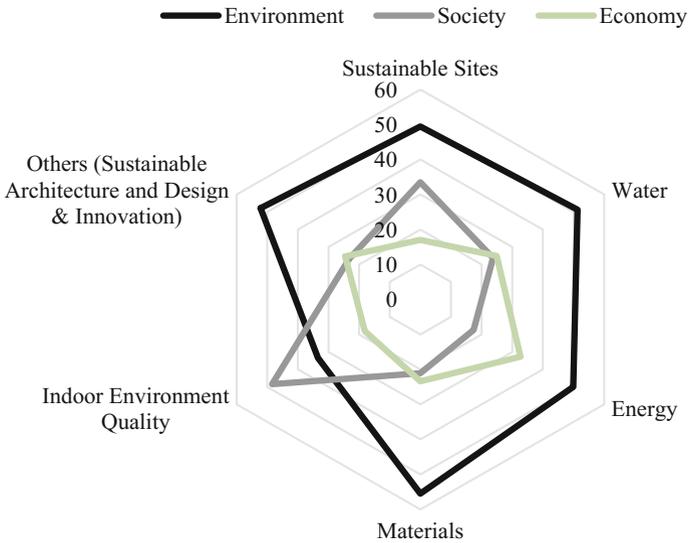
Fig. 11 Radar chart for IGBC criteria

Criteria for the selected rating systems have given importance to all the three pillars of sustainability. As in the case of mandatory requirements, it is evident from the radar chart that all the categories have given more weightage to environment except the category indoor air quality. The category indoor air quality has given
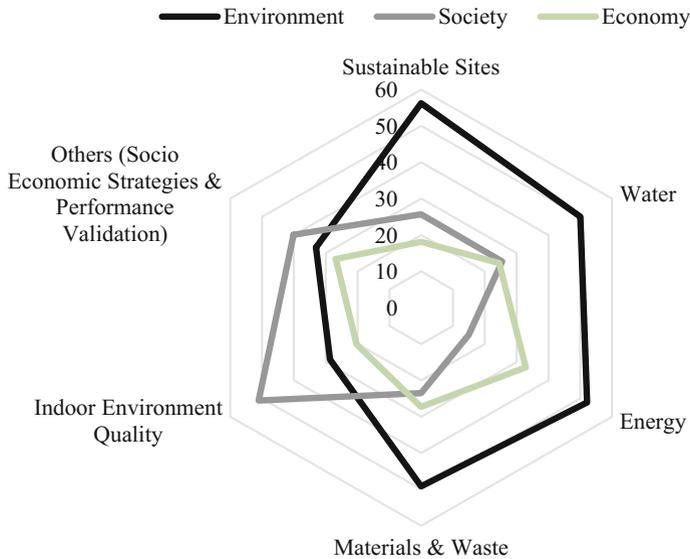
Fig. 12 Radar chart for GRIHA criteria

Table 5 Decreasing order of weightage—criteria

Criteria		
Categories	Weightage	Remarks
Sustainable sites	Environment > Society > Economy	All systems follow the same pattern
Water	Environment > Economy > Society	The only Exception is GRIHA
Energy	Environment > Economy > Society	All systems follow the same pattern
Material	Environment > Economy > Society	All systems follow the same pattern
IEQ	Society > Environment > Economy	All systems follow the same pattern

more weightage towards society. Categories water, energy and materials have given more weightage to economy than society. The weightage given by each category for the three pillars of sustainability in the decreasing order for the criteria is shown in Table 5. It is also understood from the radar charts that IGBC and LEED rating system follow the same structure in case of criteria. GRIHA rating system also follows a similar pattern; however, differ in case of other categories like socio-economic strategies and performance monitoring and validation.

More weightage is given to environment followed by society and economy in the descending order considering the overall weightage as shown in Table 6. To test whether there is any significant difference between the weightage considered by rating systems towards each pillar, Kruskal Wallis test was conducted. The test was performed separately for all the three pillars. The K value obtained for the

Table 6 Overall weightage for three pillars of sustainability

Criteria			
	Weightage in % for environment	Weightage in % for society	Weightage in % for economic
LEED	43.99	30.02	25.99
BREEAM	44.68	29.70	25.62
IGBC	49.18	25.92	24.90
GRIHA	46.40	28.13	25.47

environment is 5.06, for society is 4.89 and for economy is 0.08. Considering a significant level of 5%, the critical chi-square value is 7.815. All the K values obtained are less than critical chi-square value; it implies that selected rating systems follow same structure in case of criteria from the perspective of three pillars of sustainability.

7 Conclusion

The study investigates the weighing factors considered for three pillars of sustainability by comparatively analysing various Green Building Rating Systems. It is found that all the rating systems included in the study are having a same structural framework from the perspective of three pillars of sustainability for the criteria. All the rating systems have the weightage in the order environment > society > economy. More weightage is given to environment, followed by society and economy. The outcome of this research shows that Green Building Rating Systems has given importance to environmental, social and economic factors of sustainability. However, in the building sector, the rate of increase in green space built up is meagre, despite the growing need for it. The low value is due to the challenges of balancing the three pillars of sustainability. Since sustainable buildings are significantly costlier, these systems are not widely implemented, and thus the protection of environment remains unresolved. Hence, the pillars society and economy require more attention in this context. To achieve the right motive of sustainability, i.e. to reduce the negative impact on the environment, the sustainable systems and methodologies suggested shall be within affordable limits. The study was limited to four Green Building Rating Systems. However, the result obtained from this study is significant to conclude that more emphasis to be given to society and economy while moving towards sustainability.

References

1. Kulkarni, V., Ramachandra, T.V.: Environmental Management. Commonwealth of Learning, Canada and Indian Institute of Science, Bangalore, TERI Press, New Delhi (2009)
2. Home World Green Building Council. http://www.worldgbc.org/. Last accessed 26 July 2017
3. WorldGBC Rating Tool Task Group.: Quality Assurance Guide for Green Building Rating. Version 1.1. (2015)
4. Costanza, R., Patten, B.C.: Defining and predicting sustainability. Ecol. Econ. **15**(3), 193–196 (1995)
5. WCED.: Our Common Future: Report of the World Commission on Environment and Development (1987)
6. IUCN, UNEP, WWF: World Conservation Strategy. Living Resource Conservation for Sustainable Development. Gland, Switzerland (1980)
7. IUCN, UNEP, WWF: Caring for the Earth. A Strategy for Sustainable Living. Gland, Switzerland (1991)
8. United Nations: Resolution adopted by the General Assembly. 2005 World Summit Outcome (2005)
9. Cato, M.S.: Green Economics. An Introduction to Theory Policy and Practice. Sterling, London (2009)
10. Adams, W.M.: The future of sustainability re-thinking environment and development in the twenty-first century. Report of the IUCN Renowned Thinkers Meeting (2006)
11. Kang, H.J.: Development of a systematic model for an assessment tool for sustainable buildings based on a structural framework. Energy Build. **104**, 287–301 (2015)
12. BREEAM. http://www.breeam.com/. Last accessed 22 Oct 2017
13. BRE Global Limited: BREEAM International New Construction 2016. Technical Manual SD233 2.0. United Kingdom (2017)
14. LEED. https://new.usgbc.org/leed. Last accessed 22 Oct 2017
15. Li, Y., Chen, X., Wang, X., Xu, Y., Chen, P.-H.: A review of studies on green building assessment methods by comparative analysis. Energy Build. **146**, 152–159 (2017)
16. USGBC: LEED v 4 for Building Design and Construction (2016)
17. Indian Green Building Council. https://igbc.in/igbc/. Last accessed: 22 Oct 2017
18. IGBC: IGBC Green New Buildings Rating System Version 3.0 (2016)
19. Green Buildings Rating System India: GRIHA Home. http://grihaindia.org/. Last accessed: 22 Oct 2017
20. GRIHA Council., The Energy and Resources Institute: GRIHA V-2015 (2016)
21. KTucker: Nested Sustainability-v2.gif [digital image]. Retrieved from Wikimedia Commons website: https://commons.wikimedia.org/wiki/File:Nested_sustainability-v2.svg (2011)
22. Sustainability Hub. https://sites.google.com/site/cornellsustainabilityhub/aboutus/Sustainability%20Venn%20Diagram.jpg. Balance of Sustainability [digital image]. Retrieved from Wikimedia Commons website: https://commons.wikimedia.org/wiki/File:Sustainability_venn_diagram.jpg

Energy Savings in a Building
at Different Climatic Zones of India
by Using Insulating Materials

Yogita Sharma, Bharat Kumar Saxena and K. V. S. Rao

1 Introduction

In India, the total installed capacity of power plants as on September 30, 2017, was 331,152.75 MW. In 2016–17, energy requirement was 1,142,929 million units but the available energy was 1,135,334 million units, thus indicating an energy shortage of 7,595 million units [1]. With the help of green building constructions and by conserving energy, shortage of energy can be compensated. Four infrastructure sectors, namely industrial, transportation, agriculture, and buildings (commercial and residential) contribute largely to electricity consumption [2]. Buildings take second place in energy consumption, and it is increasing further as the large population is migrating toward urban areas and industrial buildings are going to be constructed at a rapid pace.

Buildings need electric energy during construction and after construction, which ultimately results in increase in carbon dioxide (CO_2) emissions. Average earth surface temperature is currently at 14 °C, which is expected to rise by about 1.1–6.4 °C by the end of the century [3].

In buildings, a major part of thermal comfort is given by providing thermal insulation which is either natural or recycled thermal insulation. For natural thermal insulation, bagasse, corn cob, rice, sunflower, straw bale, date palm, cotton, and pineapple leaves are being used. While in recycled thermal insulation, glass foam, textile fibers, and plastics are being used [4]. For electricity consumption in

Y. Sharma (✉) · B. K. Saxena · K. V. S. Rao
Department of Renewable Energy, Rajasthan Technical University, Kota, India
e-mail: sharmayogita@outlook.com

B. K. Saxena
e-mail: bkumarsin@gmail.com

K. V. S. Rao
e-mail: kvsrao12@gmail.com

commercial buildings, lighting consumes 59% and air-conditioning consumes 31%. While in residential buildings, lighting consumes 31% and air-conditioning consumes only 8% of the electricity [5].

The main goal of this paper is to provide an overview of the insulation materials with single- and double-glazed window glasses for the building sector. The building is insulated with expanded polystyrene or extruded polystyrene insulation. All simulations are done in five different climatic zones of India. Thus, expanded polystyrene and extruded polystyrene insulations are compared with the help of seven types of glasses.

2 Thermal Insulation

The purpose of thermal insulation is to prevent heat transfer between two systems—one inner environment and another outer environment. Insulation provides environmental and economic benefits. In this paper, 25-mm insulation on wall and 50-mm insulation on the roof are provided [6, 7]. A direct beam of sunlight during the day causes the roof to gain a significant amount of radiative heat from the sun. Roofs can represent up to 32% of the horizontal surface of built-up areas and contribute greatly to heat gain of buildings. In the market, different types of insulations are available such as glass wool, expanded polystyrene (EPS), extruded polystyrene (XPS), hemp, wood fibers, sheep wool, recycled rubber. In this paper only, EPS and XPS are considered.

2.1 Expanded Polystyrene (EPS)

Expanded polystyrene (EPS) foam is manufactured by "expanding" a polystyrene polymer. To make EPS sheets, small foam beads are put in a mold and are then exposed to steam. Exposure to steam allows beads to expand which in closed space sticks with another bead and form a fixed shape sheet of 25, 50, and 75 mm thickness. This method allows beads to stick together, but it leaves voids in between them from which moisture can pass through and resulting in decreased insulating performance [8].

2.2 Extrude Polystyrene (XPS)

XPS too uses polystyrene, but the extrusion process differs from expansion process. Extrusion allows for closed cell rigid formation of polystyrene. It is manufactured by melting plastic into a molten material, which is extruded through a thin die where it cools down into an insulation board with no voids in between, which protects it from moisture and increases its survival life and increases its insulating
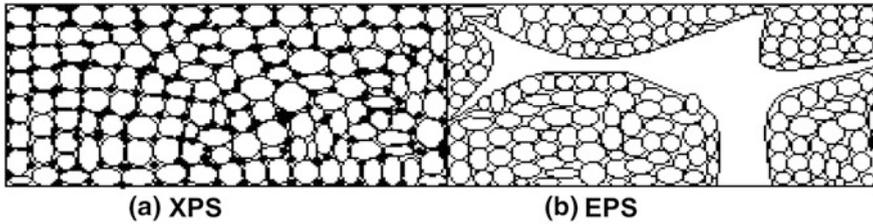
Fig. 1 Microscopic analysis of **a** XPS and **b** EPS

properties. XPS is produced by a continuous extrusion process, which results in a closed cell cross section which gives it a high compressive and tensile strength than EPS [8].

Figure 1a, b shows the microscopic images of XPS and EPS. XPS has high density compared to EPS, which is clearly evident from Fig. 1 where bead-to-bead distance in EPS is more than XPS, allowing water to penetrate in EPS insulation easily [9]. Though XPS is expensive compared to EPS, it is advised to use XPS because it is denser than EPS. Also, it has more compressive and tensile strength under heavy loads like that of slabs and walls, so XPS is also recommended due to its durability, resistance to environmental factors, and longer life span. Table 1 presents the comparison between EPS and XPS insulation.

3   Methodology

Figure 2 shows the proposed building model, simulated by eQUEST version 3.63 software for analyzing the building energy consumption [13]. Simulations are done for different cities with seven types of glasses and EPS insulation in walls and roof and again seven types of glasses with XPS insulation in walls and roof [14]. The thermal conductivity of insulation for materials EPS and XPS is taken as 0.035 W/m K and 0.028 W/m K, respectively [15, 16].

Thermal conductance (U-value) is calculated by using (1); for exterior wall assembly without insulation, it is 4.245 W/m^2 K; for exterior wall assembly with EPS insulation, it is 1.033 W/m^2 K; with XPS insulation, it is 0.8723 W/m^2 K; for exposed roof assembly without insulation, it is 2.86 W/m^2 K; for exposed roof assembly with EPS insulation, it is 0.5626 W/m^2 K; and with XPS insulation, it is 0.4685 W/m^2 K, respectively. Table 2 shows the selected glass and their properties for building energy consumption analysis.

$$U = \frac{1}{RA} \qquad (1)$$

where R is resistance and A is the unit area.

Table 1 Comparison between EPS and XPS insulation [10–12]

EPS	XPS
EPS is manufactured by expansion process	XPS is manufactured by extrusion process
EPS is environmentally friendly	XPS manufacturing involves greenhouse gas emission
EPS is not suitable for moist environment	XPS is suitable for the moist environment
EPS is less durable.	XPS is more durable
Its thermal conductivity varies from 0.030 to 0.038	Its thermal conductivity varies from 0.029 to 0.039
EPS is cheaper than XPS	XPS is expensive than EPS
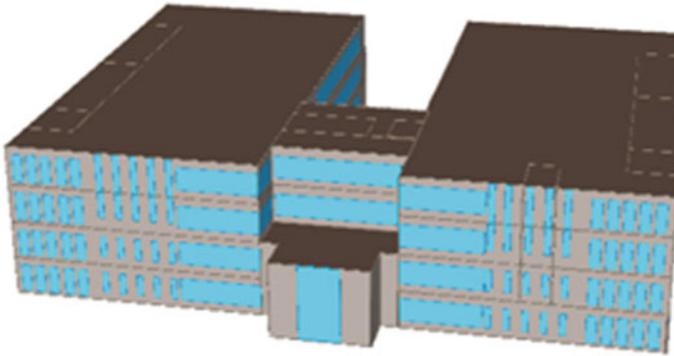
Fig. 2 3D simulation model of the proposed building

Table 2 Window glazing glass properties [17]

Color shade	Glazing type	Transmittance (%)	U-Value (W/m^2 K)	Shading coefficient
Sparkling ice (Glass 1)	Single	65	5.6	0.75
Clear cosmos (Glass 2)	Single	28	3.8	0.33
Neutral (Glass 3)	Single	50	5.0	0.58
Sparkling ice (Glass 4)	Double	59	2.8	0.64
Moonshine (Glass 5)	Double	46	1.9	0.41
SKN (Glass 6)	Double	59	1.5	0.37

Table 3 Building design specifications

Total area	10,266 m^2
Conditioned area	8,337.76 m^2
Occupancy (number)	2,145
Variable refrigerant flow units	183
Floors in building	4

3.1 Building Description

Table 3 shows the building design parameters like buildings area, occupancy, building floors, and HVAC systems.

4 Total Electricity Consumption of the Building Without Insulation, with EPS and XPS Insulation

Tables 4, 5, and 6 show the total yearly electricity consumption with respect to seven glasses, without insulation, with EPS insulation, and with XPS insulation, respectively, in five cities, namely Bengaluru, Barmer, Jaipur, Thiruvananthapuram, and Srinagar. As is evident from Tables 4, 5, and 6, total electricity consumption raises with increment in relative humidity and solar radiation.

In Srinagar, relative humidity is high but solar radiation is low, thus making consumption of electricity less as compared to other cities. In Barmer, relative humidity is less and solar radiation is high, and thus, the electricity consumption is high compared to other cities. Since Bengaluru is in the moderate climatic zone, where relative humidity is low but solar radiation is high, so electricity consumption is somewhere in between Srinagar and Jaipur. In Thiruvananthapuram, both relative

Table 4 Total annual electricity consumption of building without insulation in selected cities

Electricity consumption in MWh					
Glasses	Bengaluru	Barmer	Jaipur	Thiruvananthapuram	Srinagar
Relative humidity (%)	20–55%	25–40%	20–95%	70–90%	70–80%
Solar radiation (MJ/m^2 day)	19.70	22.3	19.42	19.45	15.40
Clear glass (MWh)	1,491.0	1,671.3	1,613.5	1,664.3	1,406.7
Glass 1 (MWh)	1,477.3	1,652.7	1,595.6	1,645.1	1,400.7
Glass 2 (MWh)	1,456.8	1,621.9	1,566.8	1,613.9	1,390.2
Glass 3 (MWh)	1,468.7	1,640.2	1,583.9	1,632.5	1,396.5
Glass 4 (MWh)	1,477.4	1,647.8	1,591.0	1,639.8	1,395.2
Glass 5 (MWh)	1,466.6	1,630.3	1,575.2	1,622.5	1,388.5
Glass 6 (MWh)	1,465.5	1,627.7	1,572.8	1,619.9	1,387.0

Table 5 Total annual electricity consumption of building with EPS insulation in selected cities

Electricity consumption in MWh					
Glasses	Bengaluru	Barmer	Jaipur	Thiruvananthapuram	Srinagar
Relative humidity	20–55%	25–40%	20–95%	70–90%	70–80%
Solar radiation (MJ/m^2 day)	19.70	22.3	19.42	19.45	15.40
Clear glass (MWh)	1,476.4	1,628.3	1,577.7	1,629.3	1,358.4
Glass 1 (MWh)	1,460.0	1,603.7	1,554.9	1,605.9	1,349.2
Glass 2 (MWh)	1,435.6	1,564.4	1,518.5	1,567.8	1,334.5
Glass 3 (MWh)	1,449.9	1,587.8	1,540.0	1,590.5	1,343.4
Glass 4 (MWh)	1,459.9	1,596.8	1,549.5	1,598.8	1,344.2
Glass 5 (MWh)	1,447.0	1,574.6	1,529.5	1,577.6	1,335.1
Glass 6 (MWh)	1,445.7	1,571.3	1,526.6	1,574.3	1,333.6

Table 6 Total annual electricity consumption of building with XPS insulation in cities

Electricity consumption in MWh					
Glasses	Bengaluru	Barmer	Jaipur	Thiruvananthapuram	Srinagar
Relative humidity	20–55%	25–40%	20–95%	70–90%	70–80%
Solar radiation (MJ/m^2 day)	19.70	22.3	19.42	19.45	15.40
Clear glass (MWh)	1,475.8	1,625.9	1,576.0	1,627.7	1,355.5
Glass 1 (MWh)	1,459.2	1,601.1	1,553.0	1,604.0	1,345.7
Glass 2 (MWh)	1,434.6	1,561.2	1,516.1	1,565.5	1,330.7
Glass 3 (MWh)	1,449.0	1,584.9	1,537.9	1,588.3	1,339.5
Glass 4 (MWh)	1,459.1	1,594.0	1,547.5	1,596.8	1,341.0
Glass 5 (MWh)	1,446.1	1,571.7	1,527.2	1,575.4	1,331.8
Glass 6 (MWh)	1,444.8	1,568.1	1,524.4	1,572.1	1,330.4

humidity and solar radiation are high, so the electricity consumption is high. Total electricity consumption is maximum without insulation. By EPS insulation, total electricity consumption is reduced. Minimum electricity consumption is obtained with XPS insulation.

5 Results

In all cities, clear glass without insulation gives a picture of what would happen if no insulation or single-/double-glazing glasses were used in the building. The building uses maximum electricity in that case. Table 7 shows the annual electricity

consumption for cooling and heating without insulation (WI), with EPS, and with XPS insulations in selected cities.

5.1 Bengaluru (12° 58'N, 77° 35'E)

From the Table 7, clear glass without insulation in Bengaluru gives maximum electricity consumption of 308.3 MWh. Best three results that are obtained are for clear cosmos, SKN (double glazing), and moonshine (double glazing) glass that give electricity consumption of 251.9, 262.3, and 263.6 MWh with XPS insulation, respectively. Figure 3 shows that using EPS and XPS insulation, electricity consumption is reduced as compared to without insulation.

5.2 Barmer (25° 45'N, 71° 23'E)

From Table 7, clear glass without insulation in Barmer gives maximum electricity consumption of 486.6 MWh. Best three results obtained are clear cosmos, SKN (double glazing), and moonshine (double glazing) glass that give electricity consumption of 377.6, 384, and 387.5 MWh with XPS insulation, respectively.

Table 7 Annual electricity consumption for cooling and heating in selected cities

WI	EPS	XPS	WI	EPS	XPS	WI	EPS	XPS
Bengaluru (MWh)			*Barmer* (MWh)			*Jaipur* (MWh)		
308.3	293.8	293.3	486.6	444.0	441.5	427.4	393.5	391.8
294.5	277.4	276.6	467.8	419.8	417.0	409.4	370.9	369.0
274.1	252.9	251.9	436.9	380.8	377.6	380.2	334.8	332.4
286.0	267.2	266.4	455.3	404.0	401.0	397.5	366.2	354.0
294.7	277.4	276.7	462.9	412.6	409.7	405.0	365.1	363.1
283.9	264.5	263.6	445.4	390.5	387.5	388.9	345.1	342.9
282.8	263.2	262.3	442.7	387.2	384.0	386.6	342.2	339.9
Thiruvananthapuram (MWh)			*Srinagar (cooling)* (MWh)			*Srinagar (heating)* (MWh)		
480.7	446.0	444.3	153.6	146.3	146.4	70.4	29.6	26.7
461.7	422.5	420.5	143.2	133.1	132.9	74.9	33.6	30.3
430.5	384.4	382.0	128.3	114.7	114.3	79.2	37.3	33.9
449.1	407.0	404.9	136.9	125.3	125.0	76.9	35.6	32.1
456.2	415.5	413.5	144.5	135.4	135.4	68.0	26.4	23.3
439.0	394.3	392.1	136.9	126.1	126.0	68.9	26.7	23.5
436.3	391.0	388.7	136.5	125.7	125.7	67.8	25.5	22.4

Fig. 3 Annual electricity consumption for cooling with EPS, XPS, and without insulation (WI) for Bengaluru city
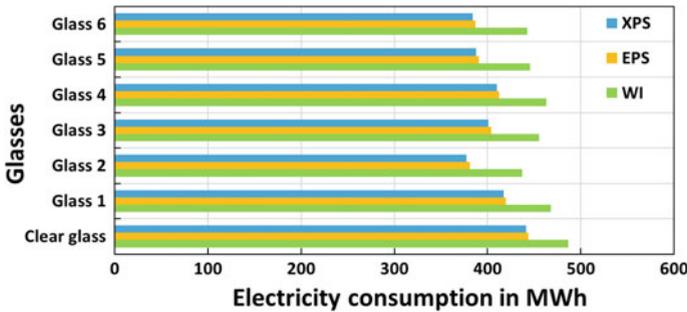
Fig. 4 Annual electricity consumption for cooling with EPS, XPS, and without insulation (WI) for Barmer city

Figure 4 shows that using EPS and XPS insulation, electricity consumption is reduced as compared to without insulation.

5.3 Jaipur (26° 49′N, 75° 48′E)

From Table 7, clear glass without insulation in Jaipur gives maximum electricity consumption 427.4 MWh. Best results are obtained with clear cosmos, SKN (double glazing), and moonshine (double glazing) glass that give electricity consumption of 332.4, 339.9, and 342.9 MWh with XPS insulation, respectively. Figure 5 shows that using EPS and XPS insulation, electricity consumption is reduced as compared to without insulation.
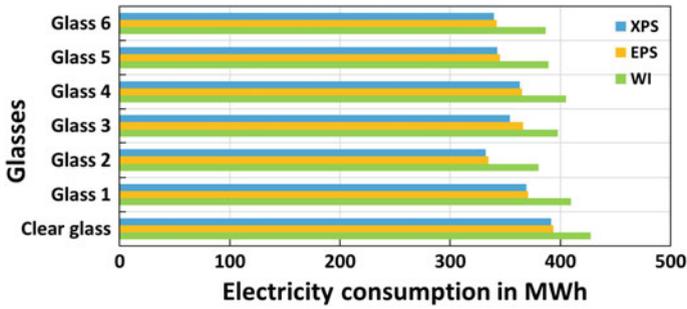
Fig. 5 Annual electricity consumption for cooling with EPS, XPS, and without insulation (WI) for Jaipur city
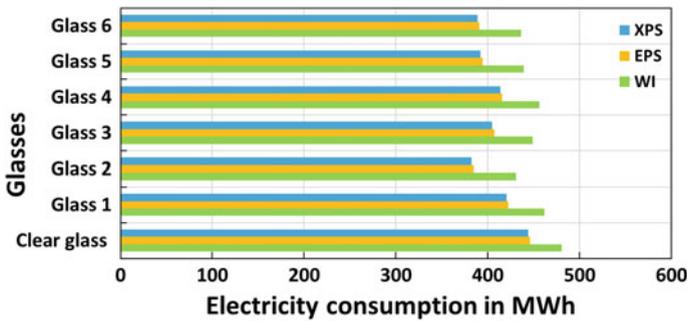
Fig. 6 Annual electricity consumption for cooling with EPS, XPS, and without insulation (WI) for Thiruvananthapuram city

5.4 Thiruvananthapuram (8° 29′N, 76° 59′E)

From Table 7, clear glass without insulation in Thiruvananthapuram gives maximum electricity consumption of 480.7 MWh. Best results that are obtained are clear cosmos, SKN (double glazing), and moonshine (double glazing) glass that give electricity consumption of 382, 388.7, and 392.1 MWh, respectively. Figure 6 shows that using EPS and XPS insulation, electricity consumption is reduced as compared to without insulation.

5.5 Srinagar (34° 05′N, 74° 50′E)

From Table 7, clear glass gives maximum electricity consumption of 153.6 MWh. Best results are obtained with clear cosmos, SKN (double glazing), and moonshine (double glazing) glass that give electricity consumption of 114.3, 125.7, and 126 MWh, respectively.
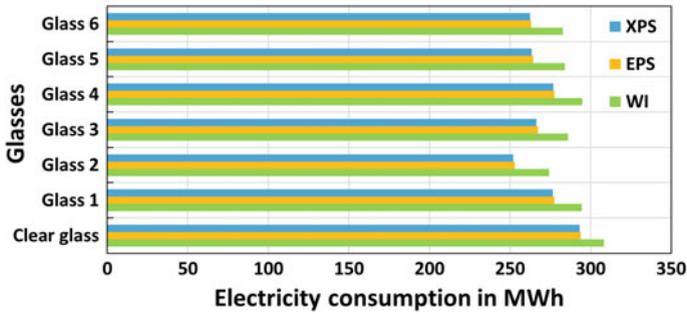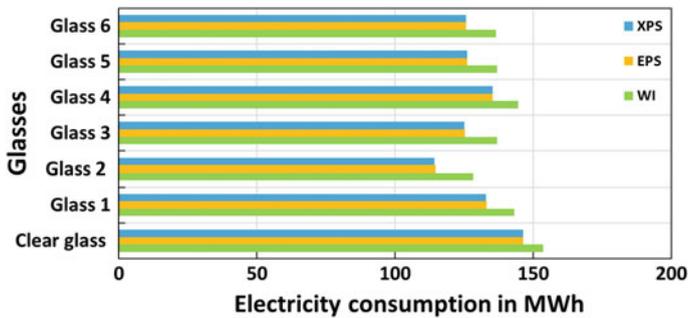
Fig. 7 Annual electricity consumption for cooling with EPS, XPS, and without insulation (WI) for Srinagar city
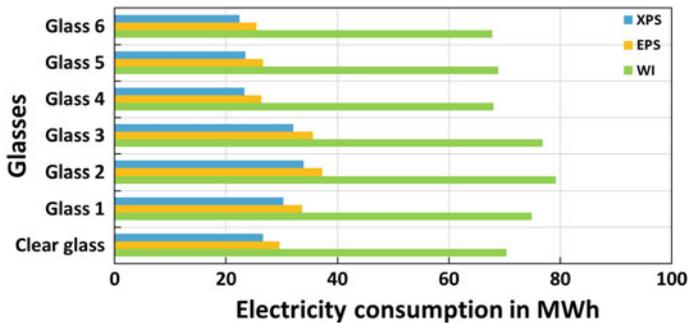
Fig. 8 Annual electricity consumption for heating with EPS, XPS, and without insulation (WI) for Srinagar city

Table 7 shows that for electricity consumption for heating demand, clear cosmos glass without insulation gives maximum electricity consumption of 79.2 MWh. Best results are obtained with SKN (double glazing) and sparkling ice (double glazing) glass that give electricity consumption of 22.4 and 23.3 MWh with XPS insulation, respectively. Figures 7 and 8 show that using EPS and XPS insulation, electricity consumption is reduced compared to without insulation. Table 8 shows the energy saving percentage comparison between five cities. Energy saving percentage is calculated with respect to maximum energy consumption in clear glass without insulation. In all cities using XPS insulation, energy saving is increased with respect to EPS insulation.

Table 8 Annual electricity savings in percentage using EPS and XPS with respect to without insulation

EPS (%)	XPS (%)	EPS (%)	XPS (%)	EPS (%)	XPS (%)
Bengaluru		*Barmer*		*Jaipur*	
04.70	04.86	08.75	09.26	07.93	08.33
10.02	10.28	13.72	14.30	13.22	13.66
17.96	18.29	21.74	22.40	21.66	22.22
13.33	13.59	16.97	17.59	14.32	17.17
10.02	10.24	15.20	15.80	14.57	15.04
14.62	14.49	19.74	20.36	19.25	19.77
14.92	14.92	20.42	21.08	19.93	20.47
Thiruvananthapuram		*Srinagar (cooling)*		*Srinagar (heating)*	
07.21	07.57	04.75	04.68	62.62	66.28
12.10	12.52	13.34	13.47	57.57	61.74
20.03	20.53	25.32	25.58	52.90	57.19
15.33	15.76	18.42	18.61	55.05	59.46
13.56	13.97	11.84	11.84	66.66	70.58
17.97	18.43	17.90	17.96	66.28	70.32
18.66	19.13	18.16	18.16	67.80	71.71

6 Conclusions

This paper shows the thermal performance of seven different types of window glasses for without insulation and two types of insulation (EPS and XPS) in walls and roof of the proposed building. Simulations are done for five different cities (Bengaluru; Barmer; Jaipur; Thiruvananthapuram; and Srinagar). In all five cities, clear cosmos glass among the seven types of glasses provided maximum energy saving for cooling demand. It varies from 17.96 to 25.58%. After clear cosmos, SKN gives large energy savings varying from 14.92 to 21.08%. After SKN, moonshine glass gives maximum energy savings for cooling demand. It varies from 14.62 to 20.36%, whereas clear glass gives minimum energy saving for cooling demand varying from 4.70 to 9.26%. Single-glazed sparkling ice glass gives energy savings varying from 10.02 to 14.30%, whereas double-glazed sparkling ice glass gives energy savings in the range from 10.02 to 15.80%.

In Srinagar for heating demand, SKN glass gives maximum energy saving. It varies from 67.80 to 71.71%. After SKN, double-glazed sparkling ice gives energy savings varying from 66.66 to 70.58%. Moonshine glass gives energy savings varying from 66.28 to 70.32%, whereas clear cosmos glass gives minimum energy saving. It varies from 52.90 to 57.19%. After clear cosmos glass, neutral glass gives minimum energy savings. It varies from 55.05 to 59.46%. After a neutral glass, single-glazed sparkling ice gives minimum energy savings. It varies from 57.57 to 61.74%. At all the locations, XPS is the better insulating material as compared to EPS insulating material in energy savings.

References

1. Statistics of electricity by the ministry of power, Govt. of India. http://powermin.nic.in/en/content/power-sector-glance-all-india
2. Mishra, S., Usmani, J.A., Varshney, S.: Energy saving analysis in building walls through thermal insulation system. Int. J. Eng. Res. Appl. **2**(5), 128–135 (2012)
3. Aditya, L., Mahlia, T.M.I., Rismanchi, B., Ng, H.M., Hasan, M.H., Metselaar, H.S.C., Muraza, O., Aditiya, H.B.: A review on insulation materials for energy conservation in buildings. Renew. Sustain. Energy Rev. **73**, 1352–1365 (2017). https://doi.org/10.1016/j.rser.2017.02.034
4. Asdrubali, F., Alessandro, F.D., Schiavoni, S.: A review of unconventional sustainable building insulation materials. Sustain. Mater. Technol. **4**, 1–17 (2015). https://doi.org/10.1016/j.susmat.2015.05.002
5. Center for Science and Environment. http://www.cseindia.org/userfiles/Energy-and-%20buildings.pdf
6. EPS vs XPS Apples-to-Apples Comparison of Rigid Foam Insulation. https://www.achfoam.com/ACH/media/ACH/docs/Foam-Control/EPS-vs-XPS.pdf, 2018/01/12
7. Schiavoni, S., Alessandro, F.D., Bianchi, F., Asdrubali, F.: Insulation materials for the building sector: a review and comparative analysis. Renew. Sustain. Energy Rev. **62**, 988–1011 (2016). https://doi.org/10.1016/j.rser.2016.05.045
8. EPS, XPS insulation magnifying image. https://www.constructionspecifier.com/selecting-polystyrene-foam-where-moisture-exposure-occurs/
9. Cai, S., Zhang, B., Cremaschi, L.: Review of moisture behavior and thermal performance of polystyrene insulation in building applications. Build. Environ. **123**, 50–65 (2017). https://doi.org/10.1016/j.buildenv.2017.06.034
10. A comparison of expanded polystyrene (eps) and extruded polystyrene insulation (XPS). https://www.dyplastproducts.com/files/103/Technical-Bulletins/52/A-comparison-of-Expanded-Polystyrene-(EPS)-and-Extruded-Polystyrene-Insulation-(XPS).pdf, 2018/01/12
11. XPS thermal insulation for buildings. http://www.insuboard.com/download/insuboard_brochure.pdf, 2018/01/12
12. Zerroug, A., Dzelzitis, E.: Analysis of results of energy consumption simulation with eQUEST and energy plus. In: International Conference Civil Engineering '15, pp. 102–107 (2015). http://llufb.llu.lv/conference/Civil_engineering/2015/Latvia_CivilEngineering2015Vol5–102-107.pdf
13. Pan, D., Chan, M., Deng, S., Lin, Z.: The effects of external wall insulation thickness on annual cooling and heating energy uses under different climates. Appl. Energy **97**, 313–318 (2012). https://doi.org/10.1016/j.apenergy.2011.12.009
14. The thermal conductivity of EPS insulation. http://www.leedsbeckett.ac.uk/teaching/vsite/low_carbon_housing/resources/thermal-conductivity-of-building-materials.pdf
15. The thermal conductivity of XPS insulation. http://www.insuboard.com/download/insuboard_brochure.pdf
16. Climate and buildings MNRE report. http://mnre.gov.in/solar-energy/ch2.pdf
17. Ran, J., Tang, M., Jiang, L., Zheng, X.: Effect of building roof insulation measures on indoor cooling and energy saving in rural areas in Chongqing. Proc. Eng. **180**, 669–675 (2017). https://doi.org/10.1016/j.proeng.2017.04.226

Comparative Study on the Effect of False Ceiling Materials on the Room Temperature

Maria Michael, Vishnu Sankar, Akshaya Paul, Anu Joy, V. J. Fainusa and C. Irine Raju

1 Introduction

The roof of buildings is directly exposed to solar radiation and absorbs heat during the daytime which leads to heat gain inside the building. The building sector currently accounts for about 30–40% of total energy use worldwide [1]. The substantial part of the global energy is used to remove the heat gain from solar radiation and maintain room temperature within the comfort range of 20–27 °C [2]. The use of HVAC has increased with the rapid increase in living standards. This has led to an increase in energy consumption and in large to global warming and is producing a strain on the electricity generation capacity. Non-renewable resources which are generally used for the generation of electricity are depleting at an unprecedented rate. As a result, a sustainable solution for providing comfortable indoor temperature is the need of the hour (Table 1).

To reduce the electrical consumption in a building, one of the solutions is to reduce the cooling load which is comparatively higher than all other electrical loads. A change in building materials can help to reduce the indoor temperature. Introducing a false ceiling is a preferred option. A false ceiling is a secondary ceiling, which is usually below the main ceiling [3]. The amount of radiation received on the roof at a particular instant is constant but the heat transferred from the atmosphere to the room through the false ceiling might vary depending on its material. The materials used as thermal barriers help to reduce energy consumption.

M. Michael (✉) · A. Paul · A. Joy · V. J. Fainusa · C. I. Raju
Rajagiri School of Engineering and Technology, Civil Engineering,
Ernakulam, India
e-mail: mariamichael1989@gmail.com

V. Sankar (✉)
Rajagiri School of Engineering and Technology, Mechanical Engineering,
Ernakulam, India
e-mail: vishnusankar9369@gmail.com

Table 1 Details of the rooms under study

S. No.	Rooms	False ceiling	Dimension of rooms
1	Room 1	Nil	2.7×4.7
2	Room 2 and 5	Wooden	2.7×4.7
3	Room 3	PVC	5×4.7
4	Room 4	PVC	3.6×4.7

In order to address these issues, a study of rooms with the same roofing and ventilation conditions, with and without false ceilings, was carried out. The inside and outside temperatures were noted, and a graph was plotted to find the room with the least temperature. The heat flux inside the room was calculated for each of the existing false ceiling materials and was compared with different alternatives to identify the best option locally available. The cost estimation of the alternatives was also done to address the financial aspect of the problem.

2 Literature Review

To achieve thermal comfort, many researchers have studied the energy consumed by HVAC systems. The studies have been conducted on roofing as well as on false ceiling materials. Hashem et al. [4] evaluated thermal effectiveness of reflective outdoor surface of a concrete roof and found that heat gain can be reduced when the solar reflectivity of the roof was increased. Kalu et al. [5] experimentally found that the inside room temperature for the thatched roof was very much lower than that of the corrugated roofs. Odeku [6] studied the thermal efficiency for low-cost housing using translucent water-based acrylic paint and suggested that it would be efficient for roofing. Sakhare et al. [7] elaborated the application of reflecting-cum-insulating (R-I) materials over the flat concrete roof surface and for the reduction of heat gain inside a building. Al-Homoud [8] emphasized the position of insulation material in the building can affect heat flow and compared various building materials and their performance characteristics. Al-Sanea [9] evaluated and compared the thermal performance of roof elements subjected to periodic changes in solar radiation, ambient temperature and nonlinear radiation exchange by a numerical model.

George et al. [10] compared different materials commonly used as ceiling material based on thermal insulation efficiency. A study was done to investigate the causes of cracks in the plaster of Paris boards and it provided a solution to replace these by textile-reinforced false ceiling. A comparative study based on thermal properties like thermal conductivity, thermal resistivity, thermal diffusivity, thermal absorptivity and specific heat capacity of asbestos and polyvinylchloride (PVC) ceiling sheets was also carried out in 2012.

The reviewed literature gives a clear idea about the high energy consumption required for HVAC and the role roofing and ceiling material play in the variation of room temperature. Even though the roof plays an important role in preventing heat gain in the building, care must be taken to select the false ceiling material also.

Conventional materials must be substituted with more sustainable materials while not compromising on thermal comfort in the building, thus reducing the electric load.

3 Case Study

3.1 Description

A residential building in Kavalangadu, Kothamangalam, Kerala (Latitude: 10.05° N, Longitude: 76.69° E and altitude: 12 m), was considered for the study. The area corresponds to the "Am-Tropical monsoon climate" according to the Koppen–Geiger climate classification. The building is a single-storied house with a room height of 3 m, and each room consists of a different false ceiling. The ventilation of the rooms is the same with door opening on the eastern side and window opening on both eastern and western side. The vertical walls are made of burnt clay bricks and are plastered. The roofing material given is Mangalore tiles. The truss work for the entire house is of wood while the battens are made of steel. With the help of thermo-hygrometer, the daily room temperature was measured. The temperature was recorded at all four corners of each room, and the average value was calculated. The weekly average temperature was computed and a graph was plotted.

3.2 Results and Discussions

Since the roofing and ventilation conditions were constant, it was inferred that the difference in room temperature in the rooms was due to the difference in the ceiling conditions. The room with wooden false ceiling was found to have the least temperature. The room with no false ceiling had the highest temperature, and the one with PVC false ceiling had a temperature between that of the other two. Thus, it was inferred that the use of false ceilings helps in reducing the room temperature. Since wood is costly, easily susceptible to decay and not readily available, other alternatives were suggested (Figs. 1 and 2).
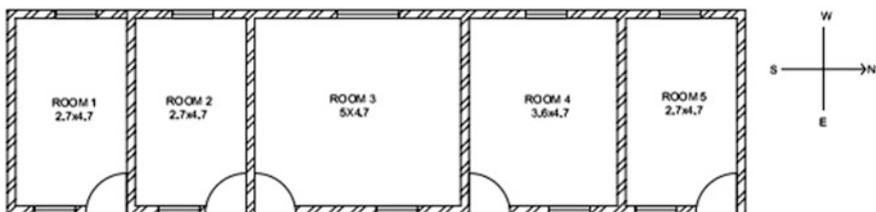

Fig. 1 Plan of the building with dimensions in metres

4 Study on Alternatives

4.1 Heat Flux Calculation

A theoretical study was done on locally available false ceiling materials with low values of thermal conductivity. Heat flux, which is the heat transfer per unit area, was calculated to study its effect on the amount of heat transferred through the roof–false ceiling combinations. Each false ceiling material was taken considering the different thicknesses available in the market and for the existing combinations in the building. Four cross sections considered for the calculation were (i) cross section having Mangalore tile, steel batten, wooden truss work, air gap and false ceiling (Sect. 1, Fig. 3); (ii) cross section having Mangalore tile, wooden truss work, air gap and false ceiling (Sect. 2, Fig. 3); (iii) cross section having Mangalore tile, steel batten, air gap and false ceiling; and (iv) cross section having Mangalore tile, air gap and false ceiling. First cross section was considered for the calculations. A constant area was assumed in all the materials in the cross section. The thickness of various components of the roof–false ceiling combination of the rooms is described in Table 2. The heat flux calculated was $\frac{0.895}{A}$, $\frac{0.908}{A}$, $\frac{2.480}{A}$ and $\frac{2.587}{A}$, respectively, for each section excluding the false ceilings, where A is surface area considered in m^2.

Since the inclined roof truss results in a triangular cross section of the air gap, an equivalent rectangular section of the same cross-sectional area was assumed for calculating the thickness of air gap. It was assumed that the heat transfer was steady and no internal heat transfer occurs. Also, the heat flow was assumed to be one-dimensional and no contact resistance is present. Heat flux was calculated using the following equations. In this method, each component was considered as resistance to the flow of heat. Resistance values were calculated using Eqs. 1 and 2, and the net resistance was calculated as the summation of all the resistances.

$$R_{\text{conv}} = \frac{1}{h \times A} \tag{1}$$
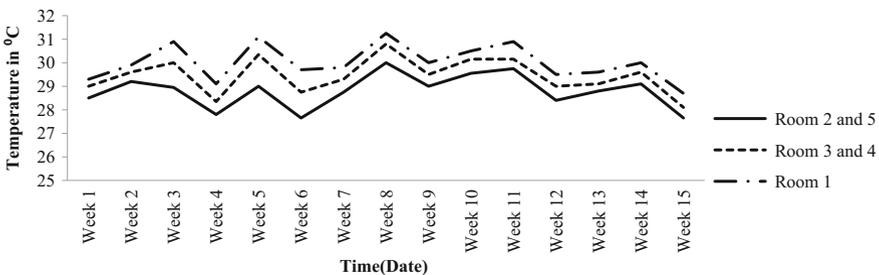
Fig. 2 Room temperature readings in different rooms

Fig. 3 Cross section of the roof showing Sects. 1 and 2
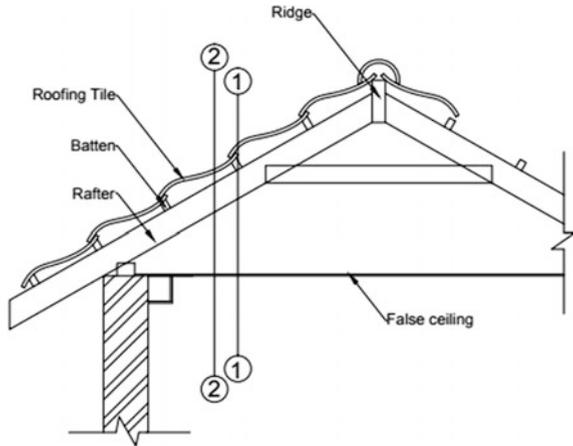
Table 2 Thickness of various components

Component parts	Thickness [mm]
Mangalore tile	15
Wooden truss work	114.3
Steel battens	25.4
Air gap	1500
Wooden false ceiling	10
PVC false ceiling	8

where

R_{conv} convective resistance of air K/W;
h convective heat coefficient in W/m² K;
A surface area considered in m².

$$R_{conv\ out} = \frac{1}{5.4 \times A} = \frac{0.1851}{A}$$

$$R_{conv\ air\ gap} = \frac{1}{5.5 \times A} = \frac{0.182}{A}$$

$$R_{conv\ in} = \frac{1}{6 \times A} = \frac{0.167}{A}$$

$$R = \frac{L}{k \times A} \tag{2}$$

where

R resistance of various components in K/W;
L thickness of each component in m;

k thermal conductivity of each component material in W/mK;
A surface area considered in m^2.

$$R_{\text{mangalore tile}} = \frac{0.015}{\left(\frac{1}{1.3}\right) \times A} = \frac{0.0195}{A}$$

$$R_{\text{steel batten}} = \frac{0.0254}{15.1 \times A} = \frac{1.682 \times 10^{-3}}{A}$$

$$R_{\text{wood truss}} = \frac{0.1143}{0.16 \times A} = \frac{0.714}{A}$$

$$R_{\text{glass wool}} = \frac{0.05}{0.0372 \times A} = \frac{1.344}{A}$$

$$\sum R = \frac{0.1851}{A} + \frac{0.182}{A} + \frac{0.167}{A} + \frac{0.0195}{A} + \frac{0.001682}{A} + \frac{0.714}{A} + \frac{1.344}{A} = \frac{2.613}{A}$$
(equivalent resistance with glass wool as insulator)

The outside temperature near the building and temperature of the air gap was measured using a thermo-hygrometer, and the average value was chosen as 33 and 32 °C, respectively. The required average inside room temperature was assumed as per ASHRAE standards as 23.5 °C. Heat transferred was then calculated according to Eq. 3.

$$Q = \frac{T_{\text{out}} - T_{\text{in}}}{\sum R} \tag{3}$$

where

Q	heat transferred in W;
T_{out}	outside temperature in °C;
T_{in}	required room temperature in °C;
$\sum R$	net resistance K/W.
$Q = \frac{33-23.5}{\frac{2.613}{A}}$	(heat transferred for glass wool false ceiling of 50 mm thickness)
$q = \frac{Q}{A} = 3.636\,\text{W/m}^2$	(heat flux for glass wool false ceiling of 50 mm thickness).

From this, the heat flux was calculated for different combinations in detail in Tables 3.

The lower value of heat flux implies less heat transfer per unit area. From the above calculations, glass wool with thickness 50 mm was found to be good material for false ceiling as it had heat flux value less than that of a wooden false ceiling material.

Table 3 Heat flux for different combinations

Material	Thermal conductivity [W/mK]	Thickness [mm]	Heat flux [W/m^2]
Fibreglass	0.040	2	7.202
		3	7.068
		4	6.939
		5	6.814
		6	6.695
		8	6.579
Glass wool	0.0372	25	4.894
		50	3.636
Calcium silicate	0.055	6	6.894
		8	6.714
Gypsum board	0.2908	12.50	7.241
Fibre cement board	0.172	4.50	7.336
		6	7.285
		8	7.219
PVC	0.190	8	7.246
Wood	0.160	10	7.132

4.2 Cost Estimation

Cost is an important factor which necessitates the call for an alternative. A comparative study was conducted based on the local market rates of the existing false ceiling materials in the study and suggested the alternative materials. Most of the false ceiling materials were available in different thickness, and the required thickness is chosen according to the need of the building. The market rates available from the survey are listed in detail in Table 4. Although these sustainable materials are available in the market, they are not widely used due to their lesser popularity. The materials were priced per square feet. Higher thickness is not usually preferred due to their increased weight which requires a stronger framework which in turn increases the cost of construction.

From Table 4, it is clear that gypsum and PVC ceilings, although being used commonly, have higher values of thermal conductivity compared to other materials. Considering the cost alone, glass wool can be recommended as a better material. Taking into account the heat flux through different materials considered and the cost, glass wool was found to be the better alternative.

Table 4 Details of local market rates of existing false ceiling materials in the study and the suggested alternatives

Material	Thermal conductivity [W/m K]	Thickness [mm]	Price/sq. ft [Rs]
Fibreglass	0.040	2	85.00
		3	125.00
		4	170.00
		5	210.00
		6	250.00
		8	350.00
Glass wool	0.0372	25	7.50
		50	14.00
Fibre cement board	0.172	4.5	26.00
		6	33.70
		8	44.00
Calcium silicate ceiling	0.055	6 (grid)	30.50
		8 (plain)	30.00
Gypsum board	0.2908	12.5	16.50
PVC ceiling	0.190	8	75
Wood	0.160	10	800

5 Conclusion

Increase in use of HVAC systems to attain comfortable conditions is leading to major environmental hazards. The effect of false ceiling materials on room temperature was studied with the help of a case study. It was found that wooden false ceiling provided more comfortable living conditions. However, use of wood is neither economical nor environment-friendly; hence, other false ceiling materials were studied to identify an alternative. Heat flux was calculated for different roof–false ceiling combinations. It was found theoretically that the use of glass wool as a false ceiling material reduces the heat transferred to the rooms. Based on the cost analysis, glass wool was found to be cheap. Although the installation charges are high for the glass wool false ceiling, the material cost is less compared to other materials; thus, it is suggested as an alternative to the existing false ceiling materials.

References

1. Waqas, A., Ud, Din Z.: Phase change material (PCM) storage for free cooling of buildings—a review. Elsevier **18**, 607–625 (2013)
2. ASHRAE Handbook of Fundamentals. American Society of Heating, Refrigerating and Air-Conditioning Engineers, Inc., Atlanta (1993)

3. Mehra, L.C., Thakkar, A.I., Patel, H.S.: Study on causes of cracking of Plaster of Paris boards & an effective solution through Textile reinforcement for sustainable false ceilings. Int. J. Sci. Res. Dev. **1**(3), 729–733 (2013)
4. Alqalaf, H.J., Alawadhi, E.M.: Thermal Analysis of a Concrete Roof with an Outdoor Reflective Surface. Am. Soc. Civil Eng. **142**(3) (2016), pp. 05015001-1–05015001-7
5. Kalu, P.N., Agboand, P.E., Nwofe, P.A.: Thermal comfort analysis of different roofing materials. Asian, J. Appl. Sci. **3**(5), 609–612 (2015)
6. Odeku, K.O., Overen, K.O., Meyer, E.L.: Thermal efficiency for low cost houses using translucent water-based acrylic paint. Mediterr. J. Soc. Sci. **5**(20), 2961–2966 (2014)
7. Sakhare, V.V., Raut, S.P., Ralegaonkar, R.V.: Performance Assessment of Sustainable Composite Roofing Assemblies Using Experimentation, vol. 118, pp. 268–275. Elsevier (2015)
8. Al-Homoud, M.S.: Performance Characteristics and Practical Applications of Common Building Thermal Insulation Materials, vol. 40, pp. 353–366. Elsevier (2005)
9. Al-Sanea, S.A.: Thermal performance of building roof elements. Elsevier Science **37**, 665–675 (2002)
10. George, N.J., et al.: Comparison of thermal insulation efficiency of some select materials used as ceiling in building design. Arch Appl. Sci. Res. **2**(3), 253–259 (2010)

Green Rating Credits for Waste Utilization in Construction

Nassif Nazeer Thaickavil and Job Thomas

1 Introduction

Construction industry plays a vital role in meeting the needs of the society and enhancing its quality of life. The construction industry is the second largest economic activity in India [1], and it generates around 10–12 million tonnes of waste annually [2]. About 50% of the world's air pollution and water pollution, 48% of all solid wastes, 42% of its greenhouse gases, and 50% of all chlorofluorocarbons released to the environment are contributed by construction activities [3]. This calls for the adoption of sustainable construction building practices which can minimize the environmental impact of construction and its allied activities.

The activities of construction, demolition, and reconstruction constitute a cyclic process, and each one generates large quantities of waste. Construction waste is the unwanted material produced directly or incidentally by the construction activities. Demolition waste includes wastes from renovation/remodeling works and from complete or partial removal/demolition of existing structures by man-made processes or natural disasters. Demolition projects often produce 20–30 times as much waste material per square meter as compared to construction projects. The volume of construction and demolition (C&D) waste produced in a region depends on many factors, which include population growth, city or regional planning, economy, technology advancement, investment in construction industry, and landfill fees [4]. The Ministry of Environment, Forest, and Climate Change has notified the Construction and Demolition Waste Management Rules, 2016, for the management of C&D waste in the country. Local bodies have been made responsible for the utilization of 10–20% material from construction and demolition waste in municipal

N. N. Thaickavil · J. Thomas (✉)
Department of Civil Engineering, Cochin University of Science
and Technology, Cochin 682022, Kerala, India
e-mail: job_thomas@cusat.ac.in

and government contracts. It also calls for setting up facilities for processing and recycling C&D wastes.

Industrial waste includes the by-product material rendered useless during a manufacturing process. Large quantities of these industrial wastes currently end up in landfills, and this poses a serious threat to the environment. Several industrial by-product wastes such as fly ash, copper slag, blast furnace slag, silica fume, quarry dust can be utilized for various construction activities depending on their properties. Materials with pozzolanic activity can be used as supplementary cementing materials in cement or concrete. Some of these by-products may be used for replacing fine aggregate in the manufacture of concrete. Fly ash-based aggregates are used in many western countries for the manufacture of concrete. Currently, researches are being carried out at the Cochin University of Science and Technology to examine the suitability of making concrete using artificial coarse aggregates manufactured from industrial by-products.

Kerala has witnessed rapid development in the recent years, and the work on many large-scale infrastructure projects is expected to start soon. This can lead to the generation of huge quantities of C&D wastes which need to be managed carefully. The tendency in the field of construction is to consider construction and demolition (C&D) waste as inert waste which is to be deposited in landfills or in uncontrolled dumps. Landfills have limited space and therefore can only receive a limited amount of waste. When one landfill reaches its maximum capacity, it needs to be replaced by another one which is again expensive to operate and maintain. In many countries, construction and demolition waste materials are used for filling/leveling of low-lying areas. Abandoned mines and quarries are also notified as special landfills for disposal of inert waste which includes construction and demolition wastes. The scarcity of landfills and high population density are issues in waste management which are particularly relevant to Kerala. An alternative strategy is to adopt the use of these waste materials in construction. Recycled concrete aggregates are a typical example of recycled materials used in construction. The latest Indian standard IS: 383 [5] allows partial replacement of aggregates in concrete with recycled aggregates. In the Indian scenario, materials alone account for about 40–60% of the total construction project costs and therefore utilization of C&D wastes and industrial by-products are a viable solution [1].

2 Green Building Concept

Green building is also known as green construction or sustainable building. It refers to a structure built using process that is environmentally responsible and resource-efficient throughout a building's life cycle. The environmentally responsible activities are instituted from identification of site to design, construction, operation, maintenance, renovation, and demolition. This requires close cooperation and expertise of the design team, the architects, the engineers, and the client at all project stages. The green building practice expands and complements the classical

building design in terms of economy, utility, durability, and comfort. Green building design propagates following aspects of construction and maintenance of built environment [3].

- Low energy consumption without sacrificing the comfort levels
- Reduce destruction of natural areas
- Minimum air and water pollution
- Low water consumption
- Limit waste generation
- Maximum recycling and reuse
- Low pollution loads
- High user productivity
- Enhance image and marketability.

3 Rating Systems

Rating systems or tools are technical instruments for assessing the environmental impact of buildings and aim to evaluate the environmental impact of buildings and construction projects [6]. A green building rating system can be defined as an evaluation tool that measures the environmental performance of a building through its life cycle [3]. These systems are established and reviewed by various statutory bodies and organizations tasked with the responsibility of enforcing green construction norms in their respective territories. Buildings are evaluated based on different criteria, and the credits are assigned if performance benchmarks are met. The seven key credit criteria generally adopted by various rating tools are site, energy, water, indoor environment quality, materials, waste and pollution and management. The most widely considered key credit criteria are 'energy' followed by 'indoor environment quality' and 'water' [7]. Table 1 gives the list of some rating systems adopted by different countries of the world.

4 Indian Rating Systems

The primary green rating systems in India are Green Rating for Integrated Habitat Assessment (GRIHA) and Indian Green Building Council (IGBC) rating system. The Bureau of Energy Efficiency (BEE) rating is another system for rating green buildings which is based on the 'energy' criterion. Central Public Works Department (CPWD) suggests a method to compare various materials based on their sustainability. Table 2 compares the credits allotted by Indian green rating systems for the management and utilization of C&D waste and industrial by-product materials in building construction.

Table 1 Green rating systems

Sl. No.	Rating system	Country of origin
1.	GRIHA	India
2.	CPWD	India
3.	IGBC	India
4.	BREEAM	UK
5.	LEED	US
6.	CASBEE	Japan
7.	Green Star	Australia
8.	BEAM Plus	Hong Kong
9.	Al-Safat	UAE
10.	AQUA	Brazil
11.	BERDE	Philippines
12.	DGNB	Germany
13.	ECOPROFILE	Norway
14.	EEWH	Taiwan
15.	G-SEED	Korea
16.	GPRS	Egypt
17.	Green Building Index	Malaysia
18.	Green Globe	Canada
19.	Green Mark	Singapore
20.	Green Ship	Indonesia
21.	GREEN^{SL}	Sri Lanka
22.	Green Star NZ	New Zealand
23.	Green Star SA	South Africa
24.	GREEN ZOOM	Russia
25.	HQE	France
26.	LiderA	Portugal
27.	LOTUS	Vietnam
28.	Minergie	Switzerland
29.	NOSTROY	Russia
30.	PEARL	UAE
31.	PromisE	Finland
32.	Protocollo ITACA	Italy
33.	QSAS	Qatar
34.	SBTool CZ	Czech Republic
35.	TARSHEED	Egypt
36.	Three Star	China
37.	TQB	Austria
38.	TREES	Thailand
39.	Valideo	Belgium
40.	VERDE	Spain

Table 2 Credits in Indian rating systems [3, 8]

Rating system	Criterion	Score
GRIHA [3]	Utilization of fly ash for RCC structures	6 points
	• Portland cement replacement with fly ash for structural concrete (min. 15% by weight)	• 1 point
	• Portland cement replacement with fly ash for structural concrete (min. 30% by weight)	• 2 points
	• For walls (min. 40% by volume)	• 2 points
	• Portland cement replacement for plaster/masonry (min. 30%)	• 2 points
	Resource recovery and safe disposal of construction wastes	1 point
IGBC [8]	Reuse of salvaged materials	2 points
	• $\geq 2.5\%$ of cost	• 1 point
	• $\geq 5\%$ of cost	• 2 points
	Percentage of materials with recycled content	2 points
	• $\geq 10\%$ of cost	• 1 point
	• $\geq 20\%$ of cost	• 2 points
	Handling of waste materials during construction (75% of waste diverted from landfills, for reuse or recycling)	1 point
	Exemplary performance	4 points
	• 95% of waste diverted from landfills for reuse or recycling	• 1 point
	• Reuse of salvaged materials $\geq 7.5\%$ of total building material by cost	• 1 point
	• Use of materials with recycled content $\geq 30\%$ of total building material by cost	• 1 point
	• Building reuse structural >75% and or non-structural (interiors) >50%	• 1 point

4.1 GRIHA

Green Rating for Integrated Habitat Assessment (GRIHA) rating system was developed by The Energy Research Institute (TERI), New Delhi, and Ministry of New and Renewable Energy, Government of India. The criteria for assessment considered in GRIHA are sustainable site planning, water management, energy optimization, sustainable building materials, waste management, health and well-being, building operation and maintenance and innovation. Each criterion has a set of pre-assigned points and GRIHA awards different levels of certification based on the percentage of points earned. Buildings scoring 50–60% points will get one star with an extra star for every additional 10% points scored. A building scoring 91–100% points will receive the maximum rating of five stars.

GRIHA specifically mentions the use of fly ash which is an industrial by-product and assigns a maximum score of six points for the same. Fly ash is a fine particulate mineral residue produced as a by-product of the firing process in coal burning thermoelectric power stations. The power sector in India depends mainly on coal-based thermal power stations, and a huge amount of fly ash is produced as a result. This is estimated to be around 110 million tonnes annually, and only half of it is actually utilized [9, 10]. The use of fly ash in construction is hence a solution to minimize the environmental impact of dumping fly ash in landfills. GRIHA encourages replacement for cement in structural concrete with up to 30% fly ash and minimum of 30% for plastering/masonry. One point is allotted for the safe disposal of construction wastes after recovery of resources [3].

4.2 IGBC Rating System

The Indian Green Building Council was established by the Confederation of Indian Industries in the year 2001. IGBC administers green building certifications based on the LEED rating system. The IGBC rating system for new buildings considers the seven criteria of sustainable architecture and planning, site selection and planning, water conservation, energy efficiency, building materials and resources, environmental quality, and innovation and development. The IGBC rating system offers five certification levels. Buildings obtaining 40–49 credits are given the level 'Certified,' and 50–59 credits are certified as 'Silver.' 'Gold' level is assigned for score of 60–74, platinum for 75–89, and super platinum for 90–100 credits. A maximum of two points each is allotted for reuse of salvaged materials and use of recycled materials. Additionally, one point each can be earned for exemplary use of salvaged or recycled materials. The IGBC rating system also assigns one point for segregation of at least 75% construction and demolition wastes at site and an additional point for segregation of 95% of the waste [8].

Table 3 CPWD sustainability index [11]

Sl. No.	Proposed parameter	Score
1.	Recycled content	10
2.	Embodied energy	10
3.	Rapidly renewable	5
4.	Locally available materials	10
5.	Functional life period	10
6.	Capital cost	10
7.	Maintenance cost	10
8.	Construction waste management	5
9.	Fly ash content	10
10.	Reduced waste	5
11.	Reduced time of construction	5
12.	Toxicity/Indoor air quality/Safety	10

4.3 CPWD Sustainability Index

The Central Public Works Department (CPWD) issued the 'Guidelines for Sustainable Habitat' in 2014 to encourage the implementation of sustainable technologies construction practices. This accounts for architectural design and layout, evaluation of sustainability index of materials, selection of electrical equipment and mechanical services, and reuse and recycling of construction and demolition waste. GRIHA and IGBC rating systems do not provide information to prioritize the different materials based on sustainability. The CPWD sustainability index helps to evaluate and compare the sustainability of different materials even though it is not a full-fledged green building rating tool. Emphasis has been given to the classification of materials based on their sustainability by computing the sustainability index. Table 3 gives the different parameters considered in the evaluation of the sustainability index. The parameters proposed to evaluate the sustainability of materials have been selected by incorporating the different criteria considered by the GRIHA and the IGBC (LEED) rating systems. Hence, CPWD sustainability index can be used to select sustainable materials before assessing green buildings using GRIHA or IGBC rating tools [11].

5 Foreign Rating Systems

Out of the different rating systems given in Table 1, the most prominent foreign rating tools are BREEAM, LEED, CASBEE, Green Star, and Beam Plus [12–14]. Table 4 discusses the different aspects of management and utilization of C&D waste and industrial by-products included in the above codes.

Table 4 Credits in foreign rating systems

Rating system	Criterion	Score
BREEAM [15]	Construction waste management • Waste reduction • Diversion from landfills	3 credits • 2 credits • 1 credit
	Recycled or secondary aggregates (25%)	1 credit
	Exemplary performance	
	• Construction waste management	• 1 credit
	• Recycled aggregate (>50%)	• 1 credit
LEED [16]	Construction and demolition waste management (recycling or salvaging)	2 points
	• 50% diverted from landfill	• 1 point
	• 75% diverted from landfill	• 2 points
	Recycled material based on cost of total value of materials • 10% of building materials • 20% of building materials	2 points • 1 point • 2 points
	Materials reuse	2 points
	• 5%	• 1 point
	• 10%	• 2 points
	Building reuse • 55% of existing floors, walls, and roof • 75% of existing floors, walls, and roof • 95% of existing floors, walls, and roof Reuse (50% of non-structural elements)	3 points • 1 point • 2 points • 3 points 1 point
CASBEE [17]	Reuse efficiency of materials used in structure	3 points
	• Electric furnace steel in major structural elements (other than reinforcement bars)	• 1 point
	• Portland blast furnace cement concrete of major structural elements	• 1 point
	• Recycled aggregate used in concrete of major structural elements	• 1 point
	Reuse efficiency of non-structural materials	3 points
	Reusability of components and materials	3 points
	• The structure and finishing materials can be separated easily	• 1 point
	• Interior finishes and equipment are not entangled and each can easily be removed separately for demolition, refurbishment, and remodeling	• 1 point
	• Reusable unit materials are used	• 1 point

Table 4 (continued)

Rating system	Criterion	Score
BEAM Plus [18]	Construction waste recycling • at least 30% • at least 60%	2 credits • 1 credit • 2 credits
	Demolition waste recycling • at least 30% • at least 60%	2 credits • 1 credit • 2 credits
	Recycled materials • site exterior surfacing work, structures, and features—at least 10% • facade and structural components—at least 10% • interior non-structural components—at least 10%	3 credits • 1 credit • 1 credit • 1 credit
	Reuse of existing sub-structure or shell • 30% or more	3 credits • 1 credit
	• 60% or more	• 2 credits
	• 90% or more	• 1 credit (bonus)
Green Star [19]	Reduction of construction and demolition waste	1 point
	Life cycle impact—building reuse • Façade reuse ✓ 50% retained ✓ 80% retained • Structure reuse ✓ 30% retained ✓ 60% retained	4 points 2 points • 1 point • 2 points 2 points • 1 point • 2 points
	Life cycle impact—concrete	3 points
	• Portland cement reduction	2 points
	✓ 30% by mass	• 1 point
	✓ 40% by mass	• 2 points
	• Water reduction (50% captured or reclaimed water for mixing)	0.5 point
	• Aggregates reduction (Portland cement limited to 5 kg/m^3) ✓ Coarse aggregate is crushed slag aggregate or another alternative materials—at least 40% (OR) ✓ Fine aggregate is manufactured sand or other alternative materials—at least 25% by mass	0.5 point
	Reused products or recycled content products • 3% products • 6% products • 9% products	3 points • 1 point • 2 points • 3 points

5.1 BREEAM

Building Research Establishment Environmental Assessment Method (BREEAM) was the first green rating system launched in the UK by Building Research Establishment (BRE) in 1990 and has greatly influenced the development of later rating systems [14]. BREEAM also offers international certification guidelines and has issued over 560,000 certificates in 76 countries. BREEAM considers the criteria of energy, health and well-being, innovation, land use, materials, management, pollution, transport, waste, and water. Each of the above categories is sub-divided into sub-categories, and credits are awarded to each on the achievement of the stated targets. BREEAM encourages proper management of construction waste and encourages the use of recycled and sustainably sourced aggregates. Separate points are allotted for reduction of construction wastes and diversion of wastes from landfills. A maximum of three credits can be secured under the sub-criterion of construction waste management with the option for an additional credit for exemplary performance. BREEAM also promotes the use of recycled concrete aggregates from C&D waste and secondary aggregates from industrial by-products. An additional credit can be earned under exemplary criterion for use of more than 50% recycled or secondary aggregate in concrete subject to a maximum transported distance of 30 km [15].

5.2 LEED

Leadership in Energy and Environmental Design (LEED) is the green building assessment tool developed by the US Green Building Council. It was launched in 1998 and is the most widely used green rating system with certifications in over 165 countries and territories. The criteria considered in LEED are location and transportation, sustainable sites, water efficiency, energy and atmosphere, materials and resources, indoor environmental quality, innovation, and regional parity. LEED assigns points for management of construction and demolition waste, material reuse, and use of recycled materials. One point is assigned for implementing the recycling or salvaging of 50% of C&D waste, and an additional point can be earned if 75% is recycled or salvaged. A point can be obtained if recycled materials used cost more than 10% of the total building material cost, and an additional point is obtained if the cost of recycled materials is 20%. Similarly, two points can be earned if the material reuse is 20%, and only a single point is obtained for 10% reuse of materials. A maximum of three points can be scored for reuse of existing floors, walls, and roofs of buildings, and a single point can be obtained for reuse of more than 50% of non-structural elements [16].

5.3 CASBEE

Comprehensive Assessment System for Built Environment Efficiency (CASBEE) is the green building rating system developed in Japan in 2001. The criteria for assessment are classified into environmental quality and performance of the building (Q) and reduction of building environmental loadings (LR). Q consists of the criteria indoor environment, quality of service, and outdoor environment on site, while LR consists of the criteria energy, resources and materials and off-site environment. CASBEE allots three points each for the reuse efficiency of structural and non-structural materials. The reuse efficiency of structural members is determined based on the quantity of electric furnace steel, Portland blast furnace cement concrete, and recycled aggregates used in the construction. Points are also allotted for the ease of separation of reusable materials [17].

5.4 BEAM Plus

Building Environmental Assessment Method (BEAM) plus is the green building assessment system developed by the Hong Kong Green Building Council Limited. Site aspects, material aspects, energy use, water use, indoor environmental quality and innovations and additions are the criteria used for assessing the green buildings. BEAM plus considers construction wastes and demolition wastes under separate heads and assigns points to each separately. Two credits can be earned for recycling 60% of construction wastes, and another two credits for recycling 60% demolition waste. If only 30% is recycled, then one credit each is allotted. BEAM Plus also promotes the use of recycled materials in exterior site works, for structural components and for non-structural components. Reuse of existing building structure is also encouraged. In addition to two credits for building reuse, a bonus credit is awarded if 90% of a building is reused [18].

5.5 Green Star

Green Star is rating tool launched by the Green Building Council of Australia in 2003. Countries such as New Zealand and South Africa have adopted their own versions of the Green Star rating system. Green Star accounts for the criteria of management, indoor environment quality, energy, transport, water, materials, land use and ecology, emissions, and innovation. Green Star assesses the life cycle impact of concrete and assigns 1 point for reduction of cement, 0.5 point for reduction of water, and 0.5 point for reduction in aggregate. It also analyzes the life cycle impact of building reuse with separate set of points for structure reuse and facade reuse. Up to three points can be scored by the use of reused or recycled products [19].

6 Conclusion

The philosophy of '3R' consisting of Reduce, Reuse and Recycle has to be implemented as '4R' with Recovery as the fourth 'R'. This helps in enhancing the value of construction and demolition waste and industrial by-products. GRIHA [3] emphasizes utilizing fly ash as a replacement for Portland cement. This is a significant step to manage the large quantities of fly ash generated from thermal power plants in the country. However, the use of other supplementary cementitious materials such as silica fume, GGBS, Ultrafine GGBS which are also industrial by-products needs to be promoted by the Indian rating systems. This can be implemented after reviewing the research data available in the published literature. Credits may also be assigned for the use of sustainably sourced alternatives for fine aggregates and coarse aggregates in concrete. This includes materials such as copper slag, blast furnace slag, cold bonded aggregates, recycled concrete aggregates which are obtained from industrial by-products and C&D wastes. CASBEE encourages the use of recycled aggregates in concrete, while BREEAM assigns credits for both recycled and secondary aggregates. Green Star specifically mentions the use of alternate coarse aggregate and fine aggregates in concrete. Construction and demolition wastes can be categorized separately with separate points for management of each type of waste as followed by BEAM Plus. The literature encouraging the utilization of C&D wastes and industrial by-products in construction has to be circulated among potential builders and contractors to create awareness among the public. Incentives or tax rebates can also be awarded to further encourage the use of these materials in construction activities. Green building practices minimize the environmental impact of buildings not only during its construction but also during its entire life cycle. Management and utilization of C&D waste and industrial by-products in construction can promote green building practices in our country thereby ensuring a sustainable and green future.

References

1. Jain, M.: Economic aspects of construction waste materials in terms of cost savings—a case of Indian construction industry. Int. J. Sci. Res. Publ. **2**(10), 1–7 (2012)
2. Ponnada, M.R., Kameswari, P.: Construction and demolition waste management—a review. Int. J. Adv. Sci. Tech. **84**, 19–46 (2015)
3. Introduction to National Rating System—GRIHA Volume I. Ministry of New and Renewable Energy, Government of India and The Energy and Resources Institute, New Delhi (2010)
4. Couto, A., Couto J.P.: Guidelines to improve construction and demolition waste management in Portugal. In: Pomffyova, M. (ed.) Process Management, pp. 285–308, Intech, Croatia (2010)

5. IS: 383 (2016): Coarse and Fine Aggregate for Concrete-Specification. Bureau of Indian standards, New Delhi, India (2016)
6. Bernardi, E., Carlucci, S., Cornaro, C., Bohne, R.A.: An analysis of the most adopted rating systems for assessing the environmental impact of buildings. Sustainability **9**(7), 1226 (2017)
7. Illankoon, I.M.C.S., Tam, V.W.Y., Le, K.N., Shen, L.: Key credit criteria among international green building rating tools. J. Clean. Prod. **164**, 209–220 (2017)
8. IGBC Green New Buildings Rating System. Indian Green Building Council, Hyderabad (2015)
9. Jain, A.K.: Fly ash utilization in Indian cement industry: current status and future prospects. In: Roving Seminars on Concrete Sustainability through Innovative Materials and Techniques, Indian Concrete Institute, Bengaluru (2011)
10. Patel, T.A., Patel, J.M., Patel, C.B.: A review on cold-bonded fly ash lightweight aggregates: less costly light weight promising material. Ind. J. Appl. Res. **5**(1), 11–13 (2015)
11. CPWD Guidelines for Sustainable Habitat. Central Public Works Department, New Delhi (2014)
12. Nguyen, B.K., Altan, H.: Comparative review of five sustainable rating systems. Procedia Eng. **21**, 376–386 (2011)
13. Say, C., Wood, A.: Sustainability rating systems around the world. CTBUH J. **2**, 18–29 (2008)
14. Doan, D.T., Ghaffarianhoseini, A., Naismith, N., Zhang, T., Amirhosein, G., Tookey, J.: A critical comparison of green rating systems. Build. Environ. **123**, 243–260 (2017)
15. BREEAM International New Construction 2016. Building Research Establishment, Watford, Great Britain (2016)
16. LEED 2009 for New Constructions and Major Renovations. U.S. Green Building Council (USGBC), Washington, DC (2009)
17. CASBEE for Buildings (New Construction). Japan Sustainable Building Consortium, Tokyo (2014)
18. BEAM Plus for New Buildings Version 1.2. Beam Society Limited, Hong Kong (2012)
19. Green Star Design & As Built v1.1. Green Building Council of Australia, Sydney (2015)

Building Systems Retrofitted with Building Automation System (BAS): Parametric Design Using TRIZ Methodology and Life Cycle Assessment

Jananee Rangaswamy, Tarun Kumar⬤, Kriti Bhalla and Vishal Mishra

1 Introduction

The three basic requirements for the sustenance of human life on Earth are namely food, clothing and shelter, which in the present-day scenario may be directly or indirectly dependent on electricity as shown in Fig. 1.

This extensive dependency of human race on electrical energy for survival can be considered to be more critical in terms of the population growth. As proposed by Malthusian Theory [1], when the exponentially growing population curve (a exponentially increasing logarithmic curve) is plotted against the linearly fitted supply curve of the limited natural resources (a non-increasing curve), a point of intersection emerges; which was also discussed in the '*Limits to Growth* (1972)'. This point at which these two curves meet is called the point of crisis. This can be summarized as below:

$$Point \ of \ Crisis = Point \ of \ Inter \sec tion \ of \ Population$$
$$growth \ curve \ and \ Supply \ of \ resources.$$

In the present scenario, the world economy is fast moving towards such a point of crisis. It is estimated that, after the point of crisis, with the increase in population, the demand for resources would also increase which, unfortunately, cannot be met in terms of supply, resulting in a greater share of the world population being deprived of the resources that are required to attain basic standards of living.

J. Rangaswamy · K. Bhalla
Ramaiah Institute of Technology, Bangalore, India

T. Kumar (✉)
CPDM, Indian Institute of Science, Bangalore, India
e-mail: tarunkumar@iisc.ac.in

V. Mishra
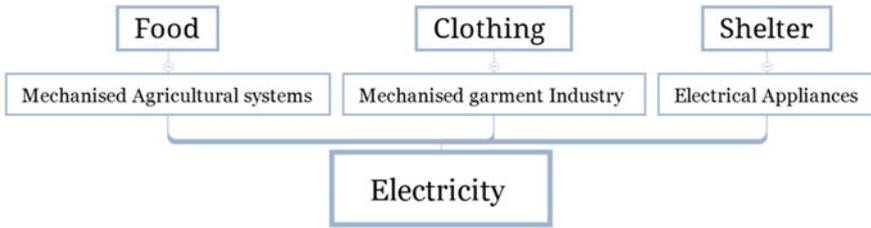Vijaya Vittala Institute of Technology, Bangalore, India

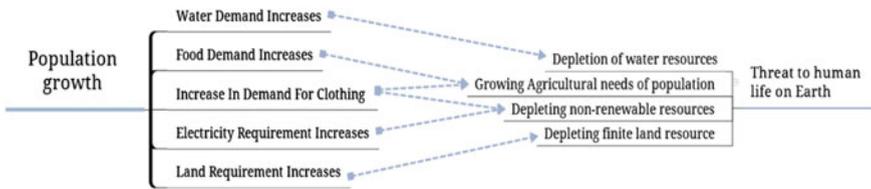**Fig. 1** Dependency of the three basic needs of mankind on electricity

Fig. 2 Impact of population growth

From Fig. 2, it can be inferred that growing human population add stress to land, water and other natural resources [2, 3]. In other words, it can be said that the population growth (P_g) is directly proportional to the stress on the limited natural resources (R_s) of planet Earth as shown in Eq. (1).

$$P_g \propto R_s \tag{1}$$

Unfortunately, population growth is not the only reason for the increasing stress on natural resources. Wastage of energy is also one of the major contributing factors resulting in increasing pressure on natural resources. The major ways in which electrical energy is wasted are as tabulated in Fig. 3. To reduce the pressure on these resources and to make them available for our future generations, there is an immediate need for smart solutions for the sustenance of human life on the planet, which can be achieved by judicious use of available resources and adopting smart ways to reduce resource wastage. Several solutions have been proposed in the past for reducing energy wastage; some of these may be realized (such as those proposed in [4]) with the advancement in technology. One such smart solution to reduce energy wastage is Building Automation Systems (BAS) also otherwise known as Building Energy Management System (BEMS) [5]. The concept of BAS has been used in association with smart grids, Internet of things (IoT) [2, 6, 7], smart technology and intelligent buildings [2, 8]; which have been known for quite some time now. This technology can be used in commercial, industrial and residential sectors accordingly, to suit varying needs of the users. Intelligent buildings use BAS which is a centralized system for automating the building components using an interlinked system of hardware, software and network devices to control the built environment
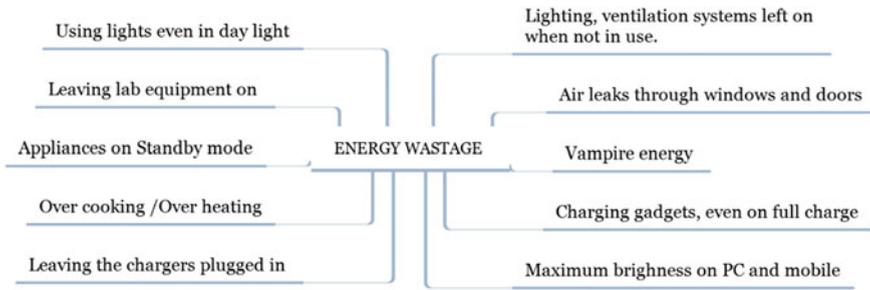
Fig. 3 Ways energy is wasted [Adapted from 4, 5]

ENERGY WASTAGE

Using lights even in day light

Leaving lab equipment on

Appliances on Standby mode

Over cooking /Over heating

Leaving the chargers plugged in

Lighting, ventilation systems left on when not in use.

Air leaks through windows and doors

Vampire energy

Charging gadgets, even on full charge

Maximum brighness on PC and mobile

Building automation system

Hardware

Smart devices

Sensor

Inbound

Stand-alone

Smart plugs

Control system

Actuator

Switch with switch board

Relay board

Computing systems

Computing

Arduino UNO/MEGA

Raspberry Pie

ZigBee

Computer

Mobile Application

Electrical appliances

HVAC System

Lighting devices

Other devices

Metering devices

Display systems

Electronic equipment

Communication system

Storage and management system

Hard disk drive

In-home display/ LCD Touch screen

Operating media/Network

Network accessing device

Router

Wired

Wireless/ Bluetooth

Software Protocol

Device Net

SOAP
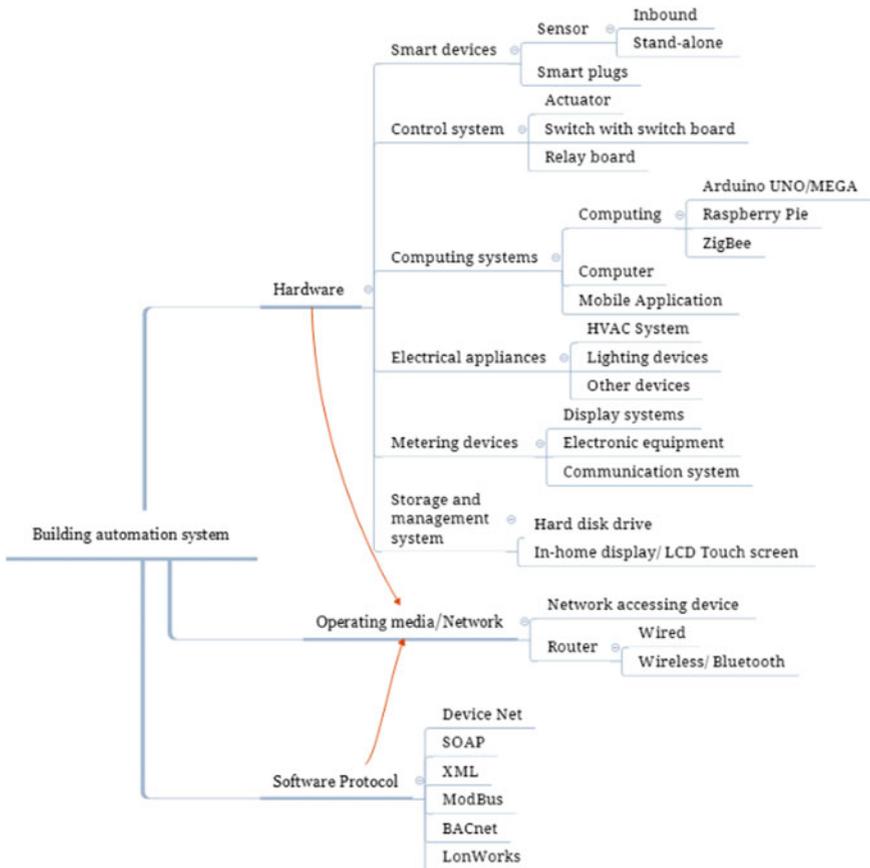
XML

ModBus

BACnet

LonWorks

Fig. 4 Components of a typical BAS module

internally [9]. This type of automation system when decentralized and applied to automate appliances in a house is termed as Smart Home Automation (SHA) [10]. According to Frances K. Aldrich in the book **"Inside the Smart Home"** a smart home has been defined as "*a residence equipped with computing and information technology which anticipates and responds to the needs of the occupants, working to promote their comfort, convenience, security and entertainment through the management of technology within the home and connections to the world beyond*" [11]. BAS can be used to control lighting systems, ventilation systems, fire alarms and security systems inside or outside the structure. These systems use sensors in combination with display systems and, which are connected to the appliance to be monitored (see Fig. 4). SHA systems give users the flexibility to monitor their energy consumptions as different types of sensors perform monitoring functions in conjugation with each other in a self-regulatory circular feedback loop. These systems mainly use sensors to reduce energy consumption at an individual level and increase the energy efficiency of the appliances and the structure [12]. The intervention of cyber-physical systems and Internet of things (IoT) in the SHA environment play a vital role in making the system easy to access and provide comfort to the user with the touch of a button. An SHA is operated using a computing device which may be a computer/computing chip or a handheld device. Hence, it can be said that the BAS and SHA systems have a vast range of advantages.

2 Methodology

Figure 5 shows that residential building sector consumes the maximum amount of energy when compared to the other sectors. As shown in Fig. 6, it can be inferred that a room is the basic unit of a residential building; and various type of buildings combine to form the basic blocks of Urban Agglomerations (Villages, Towns and Cities). Hence, a retrofit room automation (RRA) module has been physically set up in a room measuring 3.5 m × 4.0 m comprising an LED (Light emitting Diode) tube light, a three-bladed fan, a study lamp and a music system. The room also opens out to a balcony that runs throughout the length and has a width of 0.8 m. The RRA module mainly comprises of temperature sensors, PIR (Passive InfraRed) sensors, LDR (Light dependent Resistor) sensors, breadboard and relay switchboard with four switches all connected to an Arduino Mega micro-controller [13] with the help of jumper wires. A schematic circuit diagram of the system has been shown in Fig. 7, while a conceptual flowchart depicting the usage of the system has been shown in Fig. 8. The Arduino board was programmed, and the temperature sensor is used to monitor and maintain the temperature and humidity of the room; the PIR sensor is automated and detects any sort of motion in the room based on which the lighting devices may be turned on or off. This system is operated using a solar cell and will also harvest daylight by adjusting the intensity of light indoors. The electrical appliances in the room are connected through Bluetooth to an android application and are designed to have a network range of 9–10 m line of sight for any generic module

Fig. 5 Distribution of electrical energy consumption across various sectors
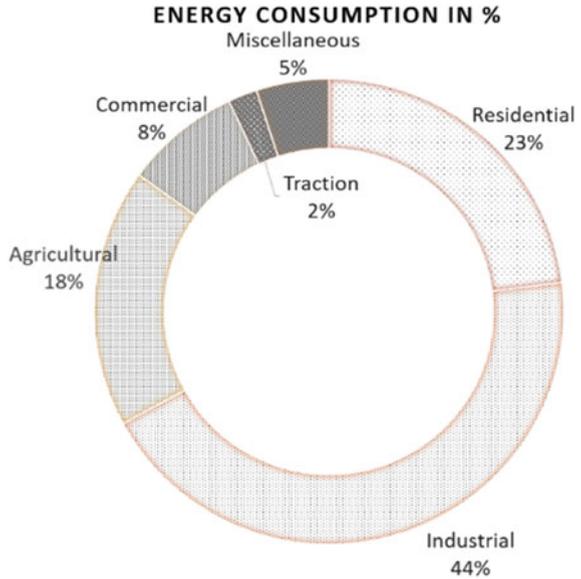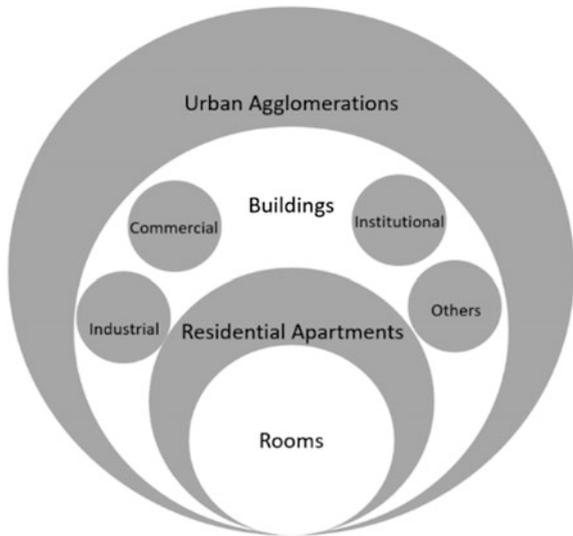

Fig. 6 Categorisation of built spaces at different scales (from rooms to Urban Agglomerations)

[14]. A 3D model of the room was made using Revit 2017—a 3D modelling software and later rendered in Key-shot 5. The plan of the room is as shown in Fig. 9, and rendered views of the room have been shown in Fig. 10a, b.
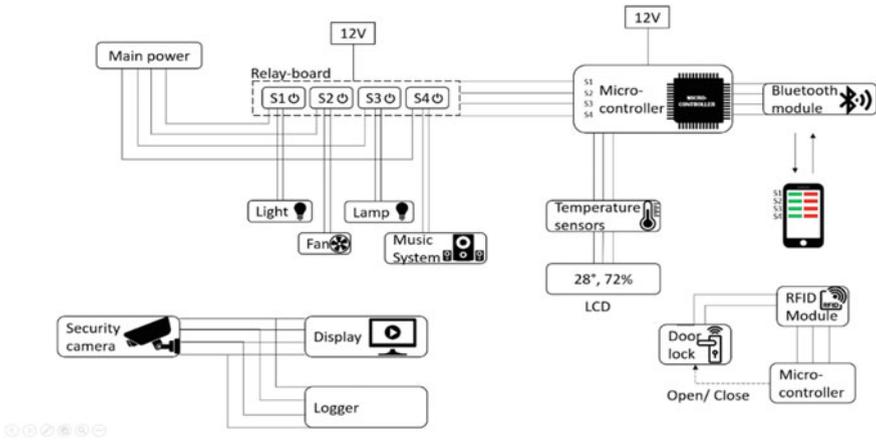
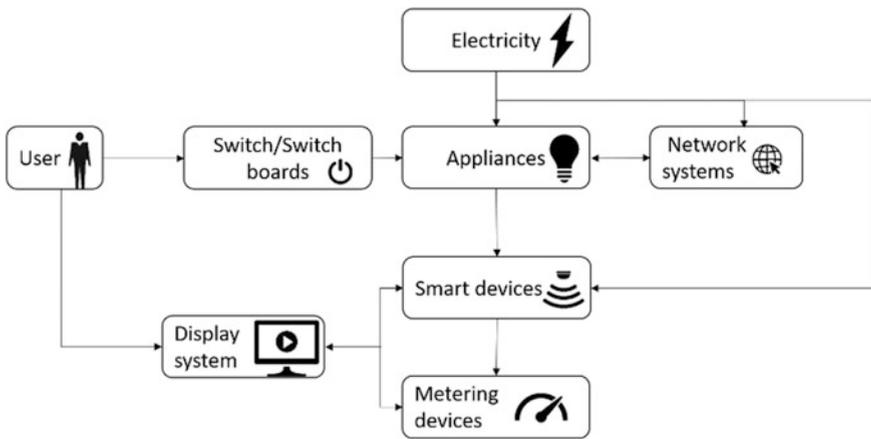**Fig. 7** Schematic circuit diagram of the RRA Module
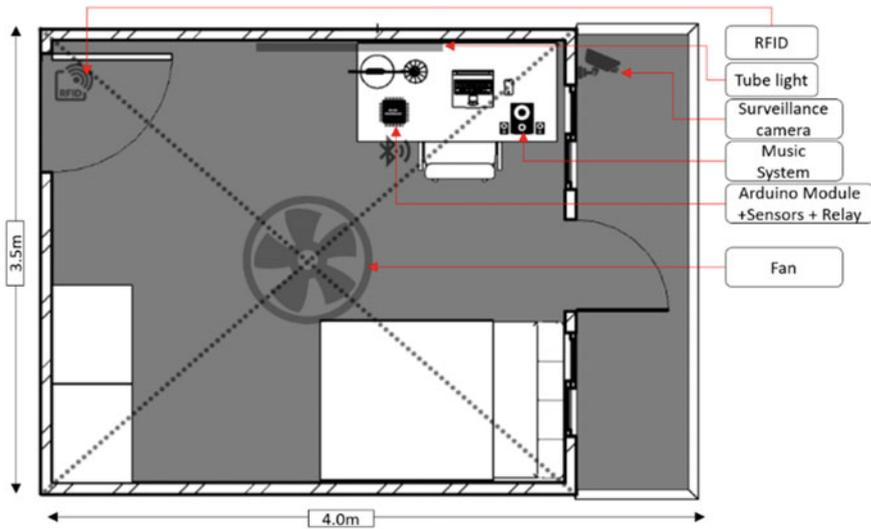

Fig. 8 Conceptual system plan of the RRA Module

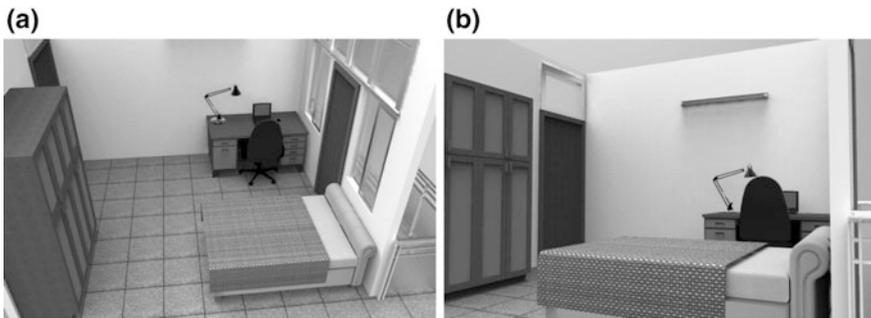**Fig. 9** Module plan of the room retrofitted with BAS

Fig. 10 **a**, **b** Rendered views of the room being retrofitted with BAS

2.1 Scope and Limitation of Study

The life cycle of the room automation model was simulated and analysed for energy used by the system during its operational phase in accordance with ISO 14040 and ISO 14044 guidelines. This simulation was carried out on SimaPro 8.4—an LCA software. The data from primary sources obtained by first-hand observation on the subject along with data from Ecoinvent 3.0 database was used for the simulating the LCA model.

The system boundary of the model comprises of the manufacturing of the individual components, their assembly, use phase, transport and their disposal phases of their life cycle. On simulating both the models, the energy efficiency of the RRA

module was compared to that of non-automated room. The models were then tested for various factors such as abiotic depletion (fossil fuels), global warming potential and human toxicity potential. Additionally, the normalized values of other factors such as eutrophication potential, acidification potential, terrestrial toxicity, photo-chemical toxicity were compared. The CML method has been used to compare both the systems on SimaPro software. These results were computed considering a cut-off value of 1% of the total environmental impacts. A security door lock for the main door and balcony was also designed using an RFID (Radio-Frequency Identification) module connected to the Arduino MEGA board. Later, a CCTV (Closed-circuit Television) surveillance module was also set up for testing added security benefits. The LCA-based approach of the study has been considered to help us understand the merits and demerits of the current RRA module. This LCA study is based on the comparative analysis of RRA module to the non-automated module on the grounds
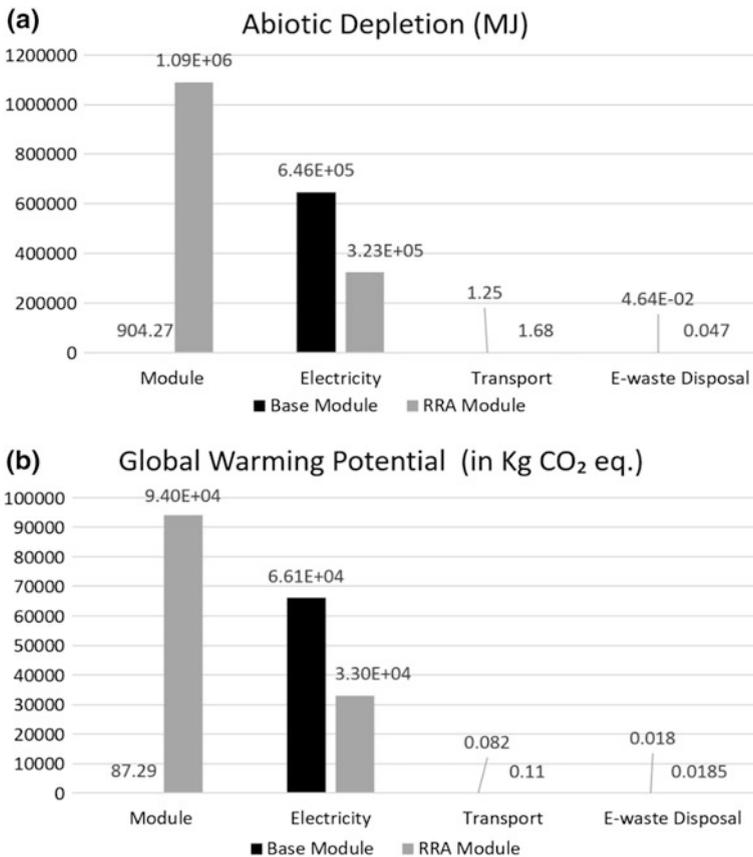

Fig. 11 **a** Abiotic depletion of base module versus RRA module. **b** Global warming potential of base module versus RRA module

of environmental factors. A TRIZ (Theory of inventive Problem Solving)-based matrix was also formulated that can be used to synthesize various parametric design solutions for setting up an RRA module.

3 Results

On performing the LCA on SimaPro, the various factors assessed have been graphically represented in Figs. 11a, b and 12. The overall life cycle energy consumption as abiotic depletion of fossil fuels for the RRA module was found to be 14.1E5 MJ which is nearly two times that obtained for a non-automated system which was found to be 6.47E5 MJ. Furthermore, it is noted that the manufacturing phase (as shown under Module section in Fig. 11a, b) scores the highest in case of RRA.

The resulting GHG emissions were analysed from global warming potential as 12.71E4 kg CO_2 eq. and 6.62E4 kg CO_2 eq. for RRA and base model, respectively.

Similarly, it was found that the environmental impact values of RRA module exceeded those of the base module for other factors such as toxicity (human, terrestrial, marine and fresh) as well (see Fig. 12). The TRIZ matrix formulated for achieving various parametric RRA designs has been depicted in Fig. 13; which needs to be comprehensively analysed.

In all the above-mentioned graphs (Figs. 11a, b and 12), it must be noted that the RRA module consumes higher energy when compared to the base module, and also, the toxicity produced during the use phase is higher in case of RRA module.
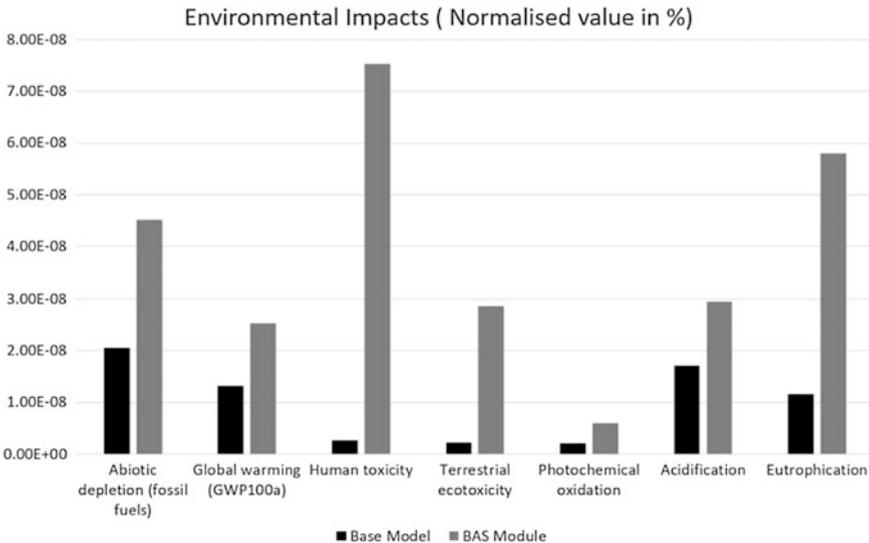

Fig. 12 Environmental impacts of base model versus BAS Module (Normalization values in %)

Subsystems/ Materials	Alternative Funtions							
Metering systems	Digital	Analog						
Computing device	Arduino	Atmel	Raspberry pie	Smart plugs	ARM	PSCoC		
Appliances	Lights	Ventilation systems	Water heating systems	Entertainment systems	Sound systems	Simulation controlled Furniture	Cleaning systems	
Network system	Bluetooth system	Wi-Fi	ZigBee	LAN	Optical fibre	X10	Power line Communications (PLC)	Li-Fi
Display/ Monitoring systems	Independent LCD screen	Smartphone Apps	Tablets	Laptops	Desktops	Server system	Smart Watch	Alexa
Software protocols	Device Net	SOAP	XML	BACnet	Lon Works	Modbus		
Security systems	Door lock with RFID	Door lock with biometric	Face recognition	Voice Recognition	Surveillance camera	Laser based	Fire alarm	Smoke alarm
Sensors	Temperature	Motion	Touch	Sound	Air quality	Air flow	Water	Proximity

Fig. 13 TRIZ matrix for parametric design concept synthesis

4 Conclusions

It can be concluded that according to the present study, the environmental impacts as obtained from LCA of RRA module are greater than that of the non-automated module, mainly due to the high energy of manufacturing for the smart module. At present, it has been found that the embodied energy in BAS cannot be paid back in a span of 10 years (assumed lifespan) by the installation and use of RRA modules. Therefore, it can be stated that the RRA module at present is not the most sustainable solution, but in future, amends can be made to make it sustainable. Nonetheless, it continues to remain one of the most promising options for sustainable and smart buildings in the near future.

A recommended solution to reduce the energy payback time would be to encourage local manufacturing of smart modules. Moreover, it would not only reduce the market price but also lessen the embodied energy and environmental costs. Using an alternate clean source of energy for manufacturing would make the system more sustainable and energy efficient. The best part about automated modules is that they can be programmed and re-programmed at any given point of time to suit the users' need. The BAS systems, along with energy efficiency, offer greater convenience to the users at the touch of a button. The mode of operation for BAS system is a typical example of universal design, providing greater accessibility for the differently-abled people by using a handheld device wirelessly connected to the module by means of smart networks (e.g. Bluetooth, WiFi Network etc.) to operate the required devices. The parametric design matrix gives us various feasible design solutions which needs to be explored comprehensively. It has been found that the room automation module can be up-scaled to BAS system (for the entire building), which could be further modified to suit different building typologies and different

user profiles. Finally, the BAS system could be enhanced and replicated at a city level therefore giving us a clearer picture of an easily achievable smart and sustainable city.

References

1. Malthus Model Double M'M for the win [Internet]. [cited 2017 Sep 23]. Available from: https://ibgeography-lancaster.wikispaces.com/1.5+Malthus+Model+Double+M%27M+for+the+win
2. Kumar, T., Mani, M.: An energy-neutrality based evaluation into the effectiveness of occupancy sensors in buildings: an integrated life-cycle study. In: Vol. II, PLEA Conference Proceedings: Design to Thrive. Edinburgh: PLEA 2017 Proceedings—Design to Thrive, pp. 2579–2586 (2017)
3. Alawadhi, S., Aldama-Nalda, A., Chourabi, H., Gil-Garcia, J., Leung, S., Mellouli, S., Nam, T., Pardo, T., Scholl, H., Walker S.: Building understanding of smart city initiatives. Electron. Gov. 40–53 (2012)
4. Streubel. R., Yang, B.: Identification of Electrical Appliances via Analysis of Power Consumption. [cited 2017 Dec 10]
5. Iváncsy, T., Tamus, Z.Á.: Analysis of the Energy Consumption of Building Automation Systems, pp. 871–881. Springer, Singapore [cited 2017 Dec 10] (2017)
6. Boll, D., De Vos, J., Botman, F., De Streel, G., Bernard, S., Flandre, D., et al.: Green SoCs for a sustainable Internet-of-Things. In: 2013 IEEE Faibl Tens Faibl Consomm FTFC 2013 (2013)
7. Is IoT Security a Ticking Bomb? [Internet]. [cited 2017 Dec 10]
8. Drăgoicea, M., Bucur, L., Pătrașcu, M.: A Service Oriented Simulation Architecture for Intelligent Building Management, pp. 14–28. Springer, Berlin, Heidelberg [cited 2017 Dec 10] (2013)
9. KMC Controls: Understanding Building Automation and Control Systems [Internet]. KMC Controls W. [cited 2017 Jan 1] (2012)
10. Louis, J.-N., Calo, A., Leiviskä, K., Pongrácz, E.: Environmental impacts and benefits of smart home automation: life cycle assessment of home energy management system. IFAC-PapersOnLine [Internet]. **48**(1), 880–885 (2015)
11. Aldrich, F.K.: In: Harper, R. (ed.) Inside the Smart Home [Internet], p. 17. Springer-Verlag, London (2003)
12. Arghira, N., Hawarah, L., Ploix, S., Jacomino, M.: Prediction of appliances energy use in smart homes. Energy [Internet] **48**(1), 128–134 (2012)
13. Arduino: Arduino Mega [Internet] (2017). Available from: https://www.arduino.cc/
14. Intorobotics: The Guide to Bluetooth Modules for Arduino [Internet]. intorobotics, robot parts (2016)

Part III
Ecological Livable Environment Construction

Analysis of the Master Planning Process in India for Its Failure in Factoring in Environmental Consideration

P. P. Anil Kumar and Ashikha Raoof

1 Introduction

Urban planning as practiced today was introduced in India by the British during their reign in the country. During the colonial period, cities like Calcutta and New Delhi, where most of the British were settled, developed as dual cities and clear distinction was seen between the brown and white parts of these cities in terms of layout, density, architecture and transportation facilities provided [1]. However, planning during this period fundamentally focused on aesthetics and was limited in terms of both functionality and area. In the early decades of post-independence with development planning primarily focusing on balanced regional development, industrial growth and housing provision, urban planning was relegated to the background [2]. During this period, in the quest for achieving rapid socio-economic development, the role of cities and urban planning was overlooked [3]. Over the years, with increasing awareness on the impacts of urbanization at the global level, today urban issues and concerns dominate governmental action [2]. In India, urban development, planning and policies are state subjects and the role of the central government is mostly limited to issuing directives, providing advisory services, setting up model legislation and providing financial assistance [2, 4]. The first major initiative to mainstream the urban planning process occurred in 1962 with the establishment of Town and Country Planning Organization (TCPO) [5]. Model regional and town planning development law of 1985 made master planning mandatory, and it provided a general framework combining the provisions of previous acts to aid the master planning process. With the introduction of 73rd and 74th amendment to the Indian constitution, the local self-governing bodies were formed as a third tier of governance with focus on economic development and social justice [2, 6, 7]. The responsibility of urban planning was entrusted to the

P. P. A. Kumar · A. Raoof (✉)
NIT, Calicut, India
e-mail: ashikha92@gmail.com

urban local bodies through the 74th amendment, and the UDPFI guidelines of 1996 were formulated to provide guidelines and aid the local bodies in the planning process [8]. Due to rapid urbanization, dynamic nature of issues arising in cities and development of modern concepts such as sustainable development and smart cities and revision of the UDPFI guidelines of 1996 became a necessity. The URDPFI guidelines of 2014 were formulated to incorporate these emerging aspects [9]. This paper attempts to study the master planning process as suggested by the URDPFI guidelines with respect to its effectiveness in integrating various aspects of environment.

2   Background Study

In the eighteenth century, due to the advent of industrialization, a shift in occupation pattern was observed first in the Great Britain and then it spread to other countries [10]. People moved from agriculture to various industrial sectors. Industrialization to achieve economic development has resulted in global environmental degradation [10].

The world is becoming increasingly urbanized, and the urban population has touched 50% of the total population [11]. This has an impact on the surrounding sensitive ecosystems such as wetlands, forests, mountain ecosystems and requires increasing amounts of resources, which could result in over-exploitation [11]. The global concern for environmental aspects of development started gaining momentum in the early 1960s due to the identification of tangible impacts such as climate change, global warming, pollution and ozone depletion. In 1972, the United Nations established the United Nations Environment Programme which aimed to provide leadership and encourage partnership in caring for the environment by inspiring, informing and enabling nations and peoples to improve their quality of life without compromising that of future generations [12]. In the same year, the Stockholm Conference was conducted and this was the first step towards international cooperation for achieving sustainable development. This conference helped the 113 participating nations to arrive at common outlook and common principles to guide the preservation and enhancement of human environment [13]. The concept of environmental assessment and environment management was introduced at the conference as part of the action plan [13]. The Stockholm Conference succeeded in bringing environmental impacts of development into the limelight. The Stockholm Conference was followed by other events such as World Population Conference of 1974, Brundtland Commission report in 1987, Agenda 21 in 1992, Kyoto Protocol of 1997 and the latest being the second edition of United Nations Environment Assembly in 2016 [14].

In India even though the evolution of environmental law commenced in 1853 with the Shore Nuisance (Bombay and Kolaba) Act of 1853, the integration of environment with development aspects began in 1972 after the Stockholm Conference [15]. The timeline (Fig. 1) shows the various initiatives taken by the
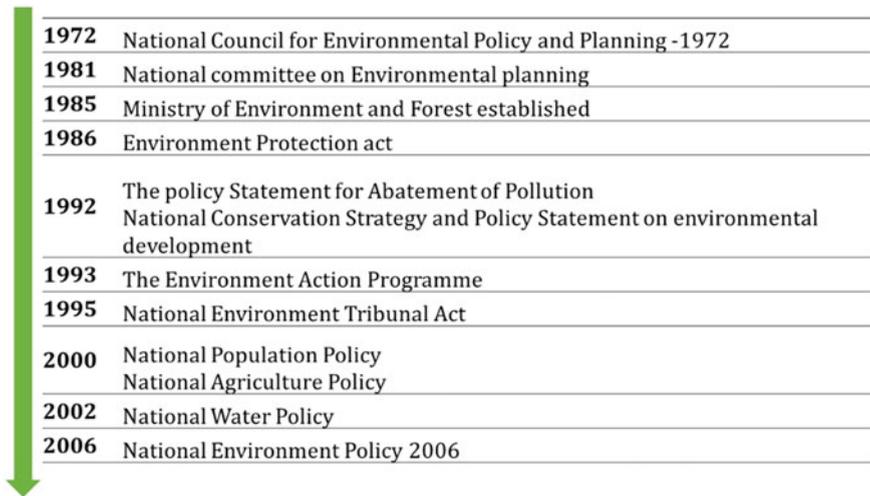
1972	National Council for Environmental Policy and Planning -1972
1981	National committee on Environmental planning
1985	Ministry of Environment and Forest established
1986	Environment Protection act
1992	The policy Statement for Abatement of Pollution National Conservation Strategy and Policy Statement on environmental development
1993	The Environment Action Programme
1995	National Environment Tribunal Act
2000	National Population Policy National Agriculture Policy
2002	National Water Policy
2006	National Environment Policy 2006

Fig. 1 Timeline showing major initiatives and acts relevant to planning

government to incorporate environmental aspects with development. Despite the efforts taken to achieve environmental integration with development, it was observed up until the formulation of National Environmental Policy in 2006, the various measures taken failed to integrate different aspects of environment under a single umbrella.

In the recent years, despite having master plans many Indian cities have experienced various environmental issues. The flood experienced by Chennai in 2015 can be seen as an example. Even though the city of Chennai developed according to various master plans, these plans were not successful in integrating environmental aspects such as natural drainage and watershed management with the land use. This resulted in the development of land uses which was not compatible with the natural environment of the city, and as a result, the natural drainage system of the city was tampered. The rainfall received by Chennai was 400 mm, and various studies showed that the original natural drainage and watersheds of the city were equipped to handle the discharge [16, 17]. According to the World Economic Forum Report [18] on environmental performance index (EPI), India was ranked 125 among the 132 countries studied in 2012 and it has further gone down to 140 out of the 179 in 2016 [19]. The index compared various indicators selected based on the MDGs and SDGs. The report stated that India was rated poor consistently on all the indicators related to environment and did moderately well in the social sector [19]. This shows that even though environmental acts, laws and policies were formulated, India was not able to successfully implement them. Lack of environmental monitoring systems, environmental governance, coordination between different agencies involved and the rigid master planning approach in place contributed to the failure of environmental policies which in turn resulted in the lower ranking [20, 21]. Hence,

it can be said that integrating environment with development is the need of the hour in India.

3 Methodology

The planning process as suggested by the URDPFI guidelines was mapped. Different stages of planning were studied in detail to understand the complexity of the planning process, and a social network analysis was carried out to identify the gaps in the existing frameworks. Various procedures involved in the implementation stages and the environmental factors considered for sanctioning proposals were studied. From the literature studies, it was observed that environmental clearance from pollution control boards was obtained through the submission of Environment Impact Assessment Report and the environmental management plan. The procedure for obtaining environmental clearance was studied, and the gaps between master planning process, preparation of detailed proposals and the procedure for obtaining environmental clearance were identified and studied. The missing links in the network, overlaps and duplication in the process, hierarchy in the system and loopholes in decision-making systems were identified.

The stakeholders involved in the planning process were identified through extensive literature study. The identified stakeholders were classified based on their role in the process and the stages of planning in which they are actively involved. The stakeholders involved in the planning process employed were identified from the URDPFI guidelines. The lists were compared to identify the stakeholders that were omitted from the planning process. Further study was carried out to understand whether the inclusion of these stakeholders in the process would help in minimizing the gaps identified in the planning process. Power centrality analysis, hierarchical clustering analysis and eccentricity analysis were carried out to study the interrelationship between various stakeholders. The role of these stakeholders was further defined properly in order to avoid duplication of work and achieve better efficiency in the planning process.

4 Analysis, Results and Discussions

The planning process as suggested by URDPFI guidelines along the implementation and environmental clearance procedure with various stakeholders involved in the process is shown in Fig. 2. It can be seen that the initial master planning is carried out by the town planner's office with limited input from other agencies which are actively involved in the implementation stage. Similarly, during implementation, the role of the town planning office is limited to formulating broad sectoral proposals and the implementation agency takes over the detailed proposal
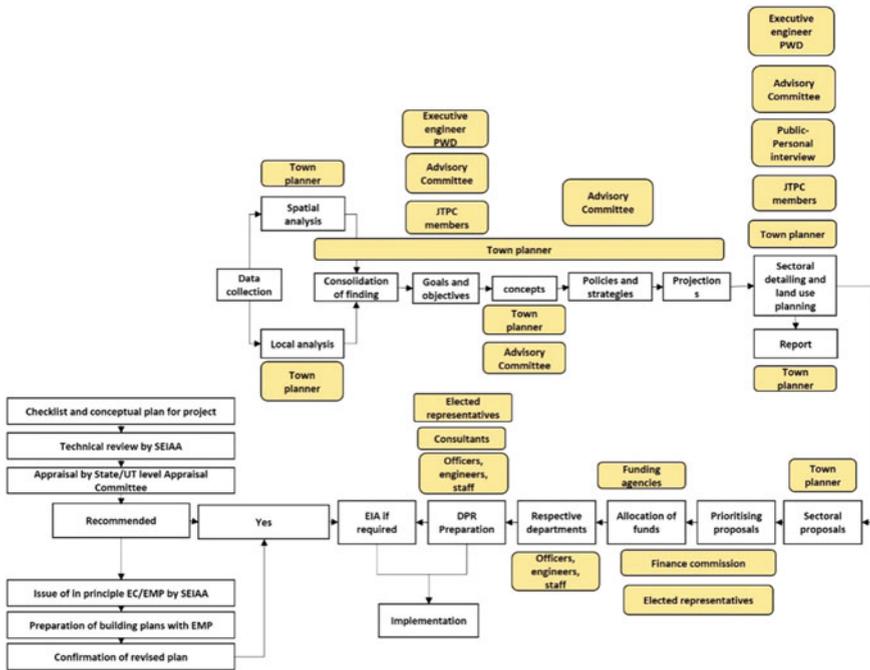
Fig. 2 Planning process employed

formulation. It can also be seen that after the environmental clearance is approved, there is no provision for regular monitoring and evaluation to ensure that the measures submitted in the environment management plan are implemented.

From the analysis, it was also found that during the initial stages of planning, especially during data collection and analysis, due importance was not given to various environmental aspects of development. The method suggested by URDPFI guidelines focuses primarily on the social–economical and infrastructural data, and the analysis suggested aims at identifying the needs, potentials and gaps in social–economical and infrastructural development. The process lacks clarity on efficiently incorporating public participation and the extent of public participation required in each stage.

It was also found that the present system is not equipped with environmental monitoring and governance systems which could help in achieving high levels of environmental integration.

The major stakeholders in planning were identified based on the literature study, and the interrelationship between these stakeholders were mapped using social network.

From the hierarchical cluster analysis of stakeholders, it was found that the town planner's office occupies the highest position (Fig. 3) in the current process whereas in an ideal process the local self-governing bodies occupy the highest level
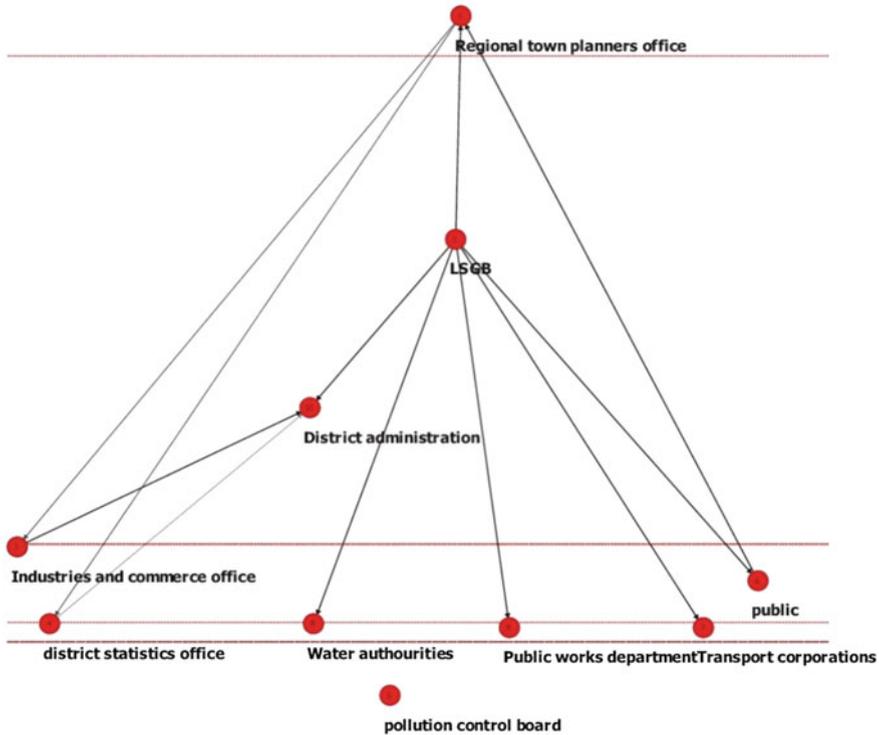
Fig. 3 Hierarchical clustering of stakeholders—existing

(Fig. 4). Power centrality analysis was carried out in order to identify the hierarchy in decision-making. LSGBs have the highest decision-making power followed by the district administration.

Eccentricity analysis was carried out to study the interrelationship between stakeholder, and it was found that the strongest correlation existed between LSGB and the town planner's office. From the analysis, it was also found that environmental institutions had the highest eccentricity which shows that they are disconnected from the planning process. Hence, there is a need to modify the planning process in order to achieve high levels of environmental compliance.

Based on the analysis results, the slight modifications are suggested to the existing planning process (Fig. 5). Environmental carrying capacity analysis, land capability analysis and strategic environmental assessment of plan proposals can be incorporated into the existing planning process in order to achieve better environmental integration. The strategic environmental assessment of plan proposals can help in improving public participation since they help measure the perceived adverse effects of the proposals. The environmental carrying capacity assessment will help in assessing the environmental sensitivity of the region, and the land
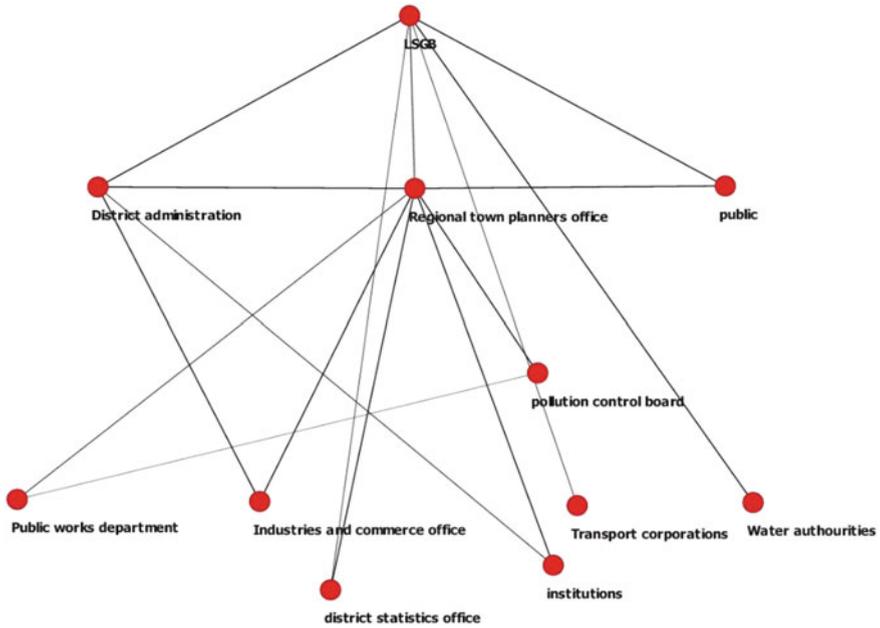
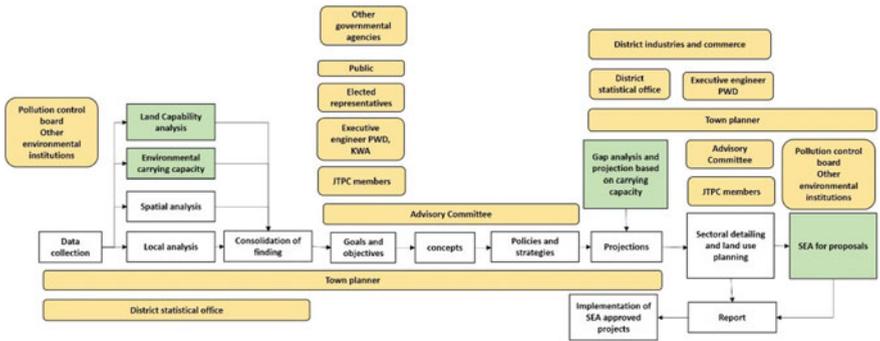**Fig. 4** Hierarchical clustering of stakeholders—ideal

Fig. 5 Modified planning process

capability assessment can assist in identifying the best-suited land use and pro-
posals for the region. These assessments also help in integrating various environ-
mental institutions with the planning process.

5 Conclusion

From the study, it can be concluded that the process employed in the preparation of master plan has to be reviewed and modified in order to achieve environmental compliance. Environmental carrying capacity assessment and land capability analysis can be incorporated into the existing situation studies and analysis stages as they can help in assessing the environmental sensitivity of the area and thereby aid in identifying the most suited land use. Strategic environmental assessment of plan proposals can be carried out on the initial draft proposals to capture and contain the adverse effects of these proposals on the environment. Modifying the existing framework to incorporate these assessments would make the planning process more comprehensive. However, the successful integration of environmental considerations with the planning process can only be ensured with proper stakeholder participation. Pollution control boards, environmentalists and environmental economists should be made part of the planning process. They can help in carrying out the environmental assessments during various stages of planning. This in turn would lead to the formulation of appropriate proposals that can cater to the social, economic and infrastructural needs of the society without compromising on the environmental needs of the region. Another major aspect overlooked by the current planning process is the monitoring and evaluation systems. Proper environmental monitoring and governing system have to be incorporated into the existing institution set-up in order to achieve sustainable development.

References

1. Chattopadhyay, S.: Blurring boundaries: The limits of "White Town" in colonial Calcutta. J. Soc. Architectural Historians **59**(2), 154–179 (2000)
2. Batra, L.: A Review of Urbanisation and Urban Policy in Post-independent India. Centre for the Study of Law and Governance, Jawaharlal Nehru University, New Delhi (2009)
3. Prakash, G.: "The Urban Turn," in Sarai Reader 02: The Cities of Everyday Life, pp. 2–7. The New Media Initiative, New Delhi, Sarai (2002)
4. Shaw, A.: Urban policy in post-Independent India: an appraisal. Economic and political weekly, pp. 224–228, 27 January 1996
5. Ministry of Urban Development: Town and Country Planning Organisation. Available: http://tcpomud.gov.in/index.html. Accessed 15 November 2017
6. Planning Commission, Government of India: Mid Term Appraisal Report—Eleventh five year plan. Oxford University Press, New Delhi (2011)
7. Local Self Government Department, Government of Kerala: Environment and Social Assessment Report, Government of Kerala, Thiruvananthapuram (2011)
8. Ministry of Urban Affairs and Employment: Urban Development Plan Formulation and Implementation Guidelines. Government of India, New Delhi (1996)
9. MacDonald, M.: Urban and Regional Development Plans Formulation & Implementation Guidelines, 2014, Ministry of Urban Development, Government of India, New Delhi (2014)
10. Singh, A.: Industrial growth and environmental degradation. Int. Edu. Res. J. **1**(5), 5–7 (2015)
11. Dodman, D., Dalal-Clayton, B., McGranah, G.: Intergrating the environment in urban planning and management, UNEP (2013)

12. United Nations Environment Program, "About UN Environment," United Nations Environment, 5 June 1972. Available: http://www.unep.org/about/who-we-are/overview. Accessed 17 November 2016
13. United Nations: Report on the United Nations Conference on Human Environment, United Nations, Stockholm (1972)
14. United Nations Environment Programme: Four Decades of Environmental Leadership, United Nations Environment, 5 June 1972. Available: http://www.unep.org/exhibit/. Accessed 11 January 2017
15. Indian Institute of Ecology and Environment: Indian Institute of Ecology and Environment, 2014. Available: http://www.ecology.edu/environmental-legislation.html. Accessed 16 November 2017
16. Mujumdar, P.P.P., Narasimhan, D.B., Bhallamudi, P.S.M., Mondal, D.A., Ghosh, D.S.: Chennai Flood 2015—A Rapid Assessment Report. Indian Institute of Science, Bangalore (2016)
17. Kumar, A., Harshawardhan, C.K., Pal, K.: Flood management—a case study of chennai city floods 2015. In: International Conference on Emerging Trends in Engineering, Technology, Science and Management, NOIDA (2017)
18. World Economic Forum, Yale Center for Environmental Law and Policy: Environmental Performance Index and Pilot Trend Environmental Performance Index, World Economic Forum (2012)
19. World Economic Forum, Yale Center for Environment, Law and Policy: Global Metrics for the Environment, World Economic Forum (2016)
20. Kumar, V., Pandit, D.: Indian urban development planning approach: quench for new paradigm. Int. J. Eng. Sci. Innovative Technol 2(2), 497–501 (2013)
21. Greenstone, M., Hanna, R.: Environmental regulations, air and water pollution, and infant mortality in India. National Bureau of Economic Research, Cambridge (2011)

A Novel Approach of IoT-Based Smart Greenhouse Farming System

S. Sofana Reka, Bharathi Kannamma Chezian
and Sanjana Sangamitra Chandra

1 Introduction

India is primarily an agrarian society. With its roots being agriculture, it is easily one of the major contributors in the GDP. But surprisingly, Indian farmers are still unaware of the benefits of modern farming techniques. But with the increasing instability in the climatic conditions and the shortage of water resources, implementation of such techniques is ever so needed. The latest technology that has promising solutions is Internet of Things (IoT). IoT has made its way into many fields such as health care, infrastructure, transportation, and home automation. But its growth in the field of agriculture is relatively slow. The need to have smart farming solutions is evident to feed the large growing population of India. We need to develop fast and efficient methods of farming. Also, there is a decrease in number of people for farming, increasing the necessity of a one-man farming solution.

So, in this regard, the smart greenhouse farming system is proposed to ease the workload on the farmers. Greenhouses are widely used to produce food in USA, UK, and the Netherlands, but in India, greenhouse technology is still at a nascent stage. By employing greenhouses, food production can be increased by utilizing even the arid and non-fertile lands, thus increasing the yield. Having better control over the processes and maintaining a favorable atmosphere for the crops leads to high quality yield by reducing the wastages.

Many systems were proposed for automating certain processes of the greenhouse and to provide remote monitoring of the parameters. GSM-based systems that provide notifications through SMS [1] and Zigbee-based WSN [2] were explored.

S. S. Reka · B. K. Chezian (✉) · S. S. Chandra
VIT University, Chennai, India
e-mail: cbharathikannammak318@gmail.com

S. S. Reka
e-mail: sofanareka.s@vit.ac.in

227

Certain other systems used android application to provide remote monitoring [3]. Some previous studies were also based on Bluetooth technology [4].

In this paper, a relatively new technology, LoRa, is studied and implemented in a farming scenario.

2 Literature Review

Though the concept of greenhouse farming is not adopted on a large scale in India, several countries have benefitted immensely from its usage. Such modern farms can sprawl for hundreds of acres. But the system can also be implemented for small-scale farms. Between efforts to eat more food grown locally, a younger generation of farmers and cheaper component-farming is getting an infusion of data and technology. As the concept of the 'Internet of Things' becomes increasingly prevalent, many systems are being devised to allow all manner of data to be gathered and analyzed, and devices controlled via wireless data networks. Connected devices such as smart thermostats and lighting systems are making their way into homes, but another big opportunity for the Internet of Things could be outdoors, in agriculture. Greenhouse though concept up to speed internationally, the Indian farming economy is only actively enrolling itself in the recent times. Initial automation efforts in the farming sector include the automatic drip irrigation systems, which were developed to water the crops automatically based on the soil moisture level. But such systems automated only one process, and other processes were still monitored and controlled manually. Important parameters to be monitored and controlled in a greenhouse include soil moisture, temperature and humidity and lighting, and it is vital that all the factors are considered. Some of the previous systems developed include an android application to monitor the greenhouse but did not include mechanisms to control it [5, 6]. One of them was based on global system for mobile communication (GSM) in which notifications are sent via SMS. The drawback to this system was that human presence is required to control the parameters. Other systems using AT8051 microcontroller core were proposed which led to some automation and automatic control, but it was complicated to interface the microcontroller to a wireless network for cloud integration. Bluetooth-based systems had a short range and could not be used for long-distance communication. Another option explored in this context was the Zigbee-based wireless sensor network(WSN). This has been widely adopted for farm monitoring and irrigation systems. WSN employing Zigbee protocol stack was efficient and led to complete automation of the process but was often too expensive. Though the WSN-based model boasts diverse nature and scalability, it poses limitations in terms of large area deployment and cost, for farming solutions. A system designed using WSN has a shorter range of coverage. A Zigbee coordinator can support only a few hundred nodes. This paper proposes a possible solution to overcome the above-discussed downfalls of the existing systems in agriculture. This system comprises of sensors and actuators which would be programmed by using an Mbed

board which can aid the overall process of agriculture by automating it and helps keep the farmer updated by sending live feeds via the Internet. The technology of LoRaWAN is used here, as it provides features such as low power and wide range which are desired for this application. The LoRa technology is to provide ranges between 5 and 10 km, and its average battery life is about 5–11 years. This is highly desirable in farming considering the vast area of implementation of the system. LoRaWAN allows around thousand nodes to be attributed to one gateway [7]. The battery life and its low power consumption also make the system implementation more economical.

3 Proposed Methodology

The prototype model system would consist of sensors and actuators which would be interfaced using STM Nucleo Mbed Board. Three sensors, namely the soil moisture sensor, light sensor, and the temperature sensor, are to be used to measure the greenhouse parameters. The corresponding actuators would trigger the irrigation system, lighting system, and the ventilation system, respectively. The ventilation system consists of fans and roof vents to provide circulation of air inside the greenhouse. These sensors measure the physical quantities, and they would be sent to the processor for processing, and depending upon the predetermined threshold, the actuators would be controlled through a power driver circuit. Additionally, the sensor values will be uploaded into the Tata server cloud in HEX format and as a JSON string. But to enable easy comprehension of data, this would be converted to decimal values. This makes it easier for the farmer to the monitor the greenhouse remotely. This data would be made available in the Microsoft Azure Cloud through a backend python script that will act as a bridge between the Tata server and the Azure Cloud. The data is thus stored in tables in the cloud. For visualization and analytics purpose, the user interface will be created using Microsoft Power BI which retrieves the data from the table storage in the Azure Cloud with aid of the dedicated account name and the key generated. The GUI created would enable the farmer to view the real-time data of the parameters in the greenhouse.

4 Hardware Setup

The hardware prototype proposed in this paper is a representative setup, consisting of a single LoRa end node. The system is based on LoRa, which is a disruptive wireless long-range technology delivering dramatic performance improvement for the M2M, IOT, and mobile and consumer markets. It boasts of low power consumption and a battery life that extends between 10 and 20 years. But the feature that makes it suitable for its use in the agriculture domain is its long range which averages around 15 km. It employs the spread spectrum technique [8], and it trades
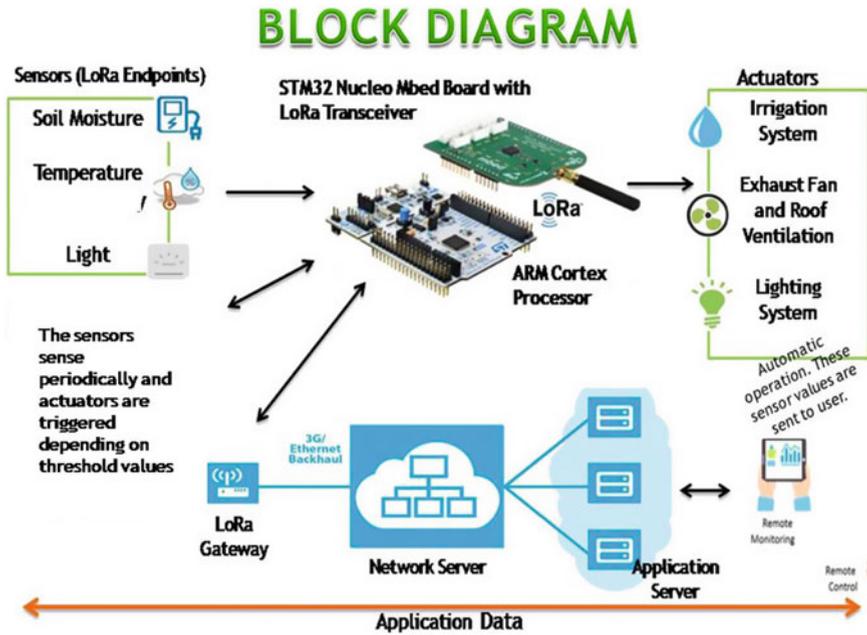
Fig. 1 Block diagram

of data rate for data sensitivity. The LoRa module used is the Semtech LoRa module, which is a module widely used in the Indian subcontinent and suggested by the Tata data communications server, the only LoRa service provider in the region. It provides two output frequencies: LF output at 433 MHz and HF output at 868 MHz. The microcontroller board chosen is the STM Nucleo L152RE, as it is compatible with the Semtech LoRa module. It is a low-power board and takes in a maximum of 300 mA. A prototype model is assembled to explain the working of the greenhouse system. Commercial greenhouses come in various structural shapes, and in this project, a working representative prototype is constructed with the gable roof structure. It is one of the most basic structures and offers the growers the most space in relationship to the perimeter than any other greenhouse style. The base of the prototype is made of foam cardboard, and the transparent sides are made of acrylic glass (for large scale and commercial deployment, appropriate industrial and commercial grade equipment and tools are to be used). The block diagram of the overall system is given in Fig. 1.

The actuators consist of two DC motors to open the vents, 2 fans, and RGB LED strip lights. The fans are placed diagonally on the two opposite sides of the greenhouse prototype which enables proper cross ventilation along with the opening of the roof vents. A submersible water pump which runs on AC current is used for the irrigation system. The photosensor reads value between 0 and 1. If

value ≥ 0.75, then the lights are triggered automatically. When sufficient natural light is available, then the artificial lights are switched off.

The ventilation system is triggered when the threshold temperature of 28 °C is reached. In the event of trigger, the roof motors are to run in the clockwise configuration for a period of 4.5 s and then stop, after the fans are switched on. When the temperature goes below this threshold with the use of the ventilation system, the fans are switched off and the motors are to run on the counterclockwise direction for the same amount of time, to close the vents. The soil moisture sensor is used to detect the moisture of soil, to judge if there is dampness around the sensor. The values yielded by it range within 0–1000. The threshold value selected is 300 when the soil moisture is suitable for the crop. When the value reaches below this threshold, the pump is turned on for a minute, considering the size of the prototype. The relay boards used offer optical isolation using the DPC 817C, between the actuators and the Nucleo, which secures the Nucleo in the event of power surges or short-circuiting. The LoRa board is mounted on top of the Nucleo, and the high output frequency is chosen.

5 Software Setup

The Nucleo board, which is of the category MBED, is programmed using the online MBED compiler. In main program, the three sensor actuator functions are configured for a periodic call for the entire duration of the program. This is done using the ticker function, a timer concept in MBED, wherein a function is attached to a ticker object, with a specific period, on whose intervals the function would be called. For the communication setup, the NwkSKey (network session key), AppKey (application key), and AppSKey (application session key), which are unique ID's for an end node, are pre-fed in the program along the Tata server credentials and the Device Extended Unique Identifier (DEVEUI). The program is fed with these data, establishing connection with the LoRa gateway. The gateway processes the LoRa packets and converts them to IP packets for transmission over the Internet.

```
light_flip.attach(&light,60);
temperature.attach(&temperature,32);
soil_moist.attach(&soil,247);
```

The sensor data type is primarily of the type float, but LoRa being a low data rate technology does not support it. Hence, the data up for transmission is converted to 16-bit data which is further split into 28-bit data, for transmission. The payload supported by the Tata server for data is around 6 bytes. The data conversion is shown below.

```
tempValue1=ldr.read_u16();
tempValue2=soilMoisture.read_u16();
tempValue3=LM35.read_u16();
AppData[0]=((tempValue1&0xFF00)>>8)&0xFF;
AppData[1]=(tempValue1&0 × 00FF);
AppData[2]=((tempValue2&0xFF00)>>8)&0xFF;
AppData[3]=(tempValue2&0x00FF);
AppData[4]=((tempValue3&0xFF00)>>8)&0xFF;
AppData[5]=(tempValue3&0x00FF);
```

The data stored in the Tata server is retrieved and sent to the Microsoft Azure Cloud table storage with the help of JSON string which is processed and sent using the backend python script run on the virtual machine. The script uses the JSON string retrieval URL, for the Tata server and the cloud storage credentials for directing the data. It also processes the base-64-type data frame from the JSON and converts it into decimal values. The Azure Cloud receives the data and stores it in the table, on a SQL query-based program which identifies the data and sorts it based on the table ID, which is added to it in the python script. The GUI was created using the Microsoft Power BI Desktop application, and it retrieves the data from the table
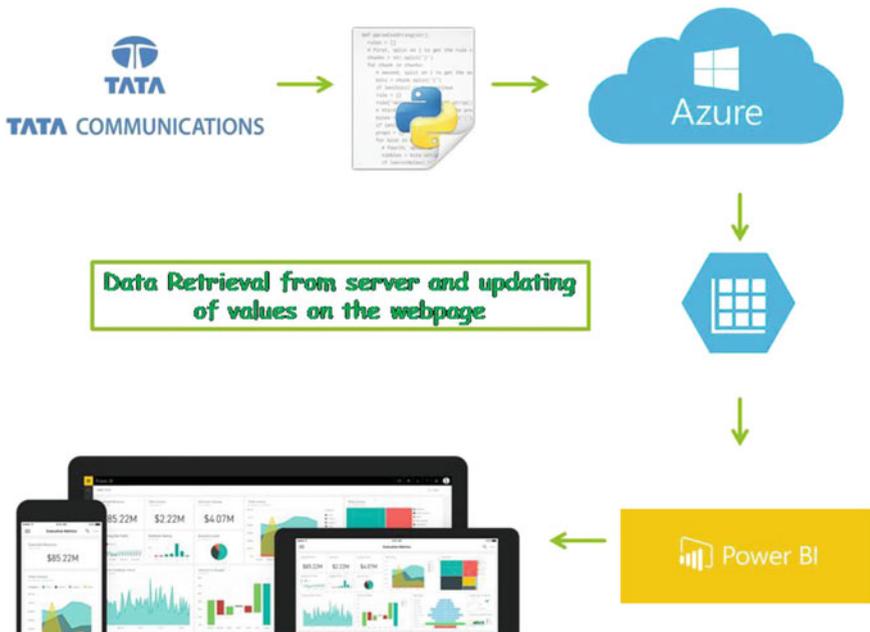

Fig. 2 Data retrieval flow

storage with the help of the pre-fed table credentials generated on the Azure platform. The GUI was published as a Webpage, which generated a URL for the page. The Webpage is updated with the data on scheduled timing set using the Power BI application.

The sequential progress of data retrieval and its direction to the GUI are explained using Fig. 2.

6 Results and Discussion

The system comprising of the sensor, actuator, and the LoRa components was all successfully developed individually, and the prototype put together is shown through Figs. (3 and 4). Though each individual component worked in accordance with its role as a stand-alone in the system, there were inconsistencies observed in the system with the integration of them. Sensor performance deviated from their respective standards by far when coupled with the power system to trigger their respective actuators. Though the performance of the LoRa transmission was intact in the system, due to the unusual behavior of the sensors on integration, led to erroneous readings on the server and hence on the GUI-based Webpage. The issue was circled on the connection of actuators to the system and was overcome using opto-isolators. The GUI (Fig. 5) was successfully connected to the server, using the
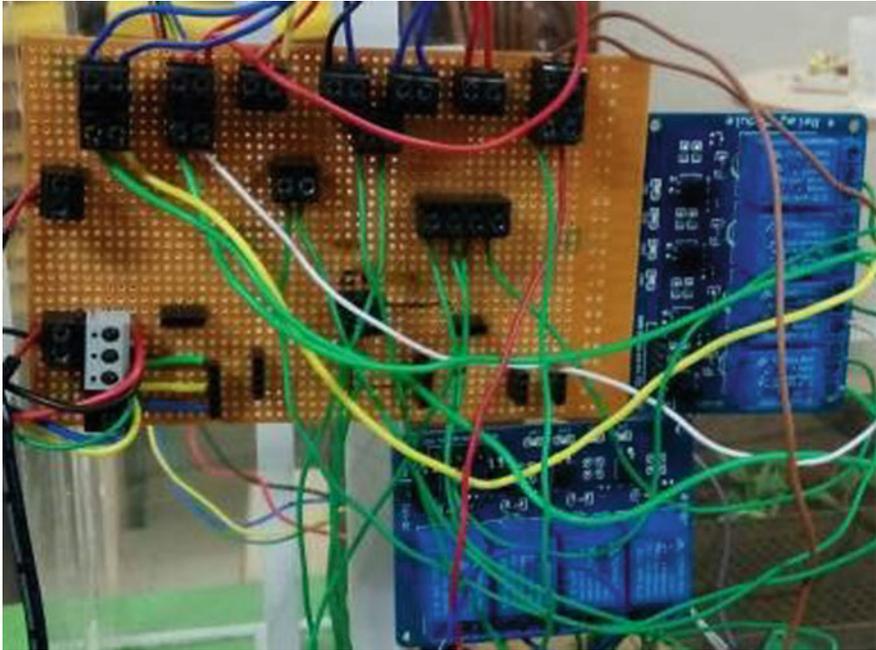

Fig. 3 Side view of the prototype

Fig. 4 Power circuit

Fig. 5 GUI Webpage

backend python code. The Webpage created updated the values based on the schedule and on the request of refresh. But there was a significant time lag observed for the refreshment of values on request which was 5–10 min.

7   Conclusion

The text has investigated on the use of LoRa technology in the field of farming. The major advantage of using LoRa is its capability to handle hundreds of nodes and its robustness to interference and noise. The LoRaWAN protocol is designed precisely for low power consumption, and this extends the battery life of the nodes to up to 20 years. As with any system and model, this system too has certain limitations and the future scope of the paper could be to overcome these limitations and provide for a better solution. Other modules such as the automatic pesticide monitoring and the theft alert could be enabled to provide for better automation. Image data can be transmitted by having better data rate and bandwidth which would further enhance the concept of remote monitoring.

References

1. Huang, H., Bian, H., Zhu, S., Jin, J.: A greenhouse remote monitoring system based on GSM. In: 2011 International Conference on Information Management, Innovation Management and Industrial Engineering (ICIII), vol. 2, pp. 357–360. IEEE (2011, November)
2. Li, R.A., Sha, X., Lin, K.: Smart greenhouse: a real-time mobile intelligent monitoring system based on WSN. In: Wireless Communications and Mobile Computing Conference (IWCMC), 2014 International, pp. 1152–1156. IEEE (2014, August)
3. Xiaofeng, L., Linlin, Q., Linjian, L., Gang, W.: Design and implementation of modern greenhouse remote monitoring system based on the Android system. In: Control Conference (CCC), 2015 34th Chinese, pp. 5742–5746. IEEE (2015, July)
4. Gang, L.L.L.: Design of greenhouse environment monitoring and controlling system based on bluetooth technology. Trans. Chin. Soc. Agric. Mach. 10, 97–100 (2006)
5. Luo, H., Yang, P., Li, Y., Xu, F.: An intelligent controlling system for greenhouse environment based on the architecture of the internet of things. Sens. Lett. 10(1–2), 514–522 (2012)
6. Xu, Z. et al.: A remote monitoring system for greenhouse based on the internet of things. In: MATEC Web of Conferences, vol. 77. EDP Sciences (2016)
7. Georgiou, O., Raza, U.: Low power wide area network analysis: can lora scale? IEEE (2016)
8. Wixted, A.J., Kinnaird, P., Larijaini, H., Tait, A., Ahmadinia, A., Strachen, N.: Evaluation of LoRa and LoRaWAN technologies for Wireless Sensor Networks. IEEE (2016, May)

Part IV
Sustainable Traffic Solutions

Comparison of Six-Phase and Three-Phase Induction Motors for Electric Vehicle Propulsion as an Improvement Toward Sustainable Transportation

Jeffin Francis, N. Aby Biju, Anupama Johnson, Jeswant Mathew, R. Sreepriya and Vishnu Sankar

1 Introduction

The enormous rise in air pollution and the depletion of nonrenewable resources has motivated the design of many electrical transportation systems, and electric vehicle is one among them. Several studies are being conducted for introducing and promoting sustainable vehicles in transportation sector, and one such technology is electric vehicle technology. Electric vehicle is one of the most preferred modes for sustainable transportation in this century, as it offers zero emission at vehicle level. The policies to use alternate energy resources rather than fossil fuels have been gaining importance in developed countries, as a mission to reduce fossil fuel dependency and effort to reduce the cost of energy production. Means of sustainable transportation include electric, hybrid, and fuel cell vehicles. The only way to increase efficiency, reduce energy consumption, and extend range is by replacing the existing three-phase by six-phase induction motor as it lowers losses and energy consumption when used in electric vehicles [1]. Another method to attain sustainable transportation is by converting the existing fossil fuel-powered vehicles into an electric vehicle. The advantages of replacing a six-phase induction motor over three-phase induction motor are:

- Extended range.
- Less energy consumption.

J. Francis · N. Aby Biju · A. Johnson · J. Mathew · V. Sankar (✉)
Mechanical Engineering, Rajagiri School of Engineering and Technology, Kochi, India
e-mail: vishnus@rajagiritech.edu.in

R. Sreepriya (✉)
Electrical and Electronics Engineering, Rajagiri School of Engineering and Technology, Kochi, India
e-mail: sreepriyar@rajagiritech.edu.in

239

- Reduces copper losses (I^2R).
- Extended battery life.

It can generate higher torque than the existing three-phase induction motor. These characteristics make the six-phase more preferable than three-phase induction motor. The batteries of electric vehicle can be charged from solar charging stations, and the dependency on fossil fuel-based energy can also be reduced.

2 Design

The six-phase induction motor is modeled in MATLAB/Simulink environment, and the torque–speed characteristics and current per phase are inferred comparing with the existing three-phase induction motor in the electric vehicles. In this paper, a dynamic model of asymmetrical six-phase, cage-type induction motor is developed to study the performance of the motor during traction in detail [2]. The study gives a detailed idea about the motor and indicates toward the smooth and promising performance of the motor.

2.1 Design Goals

- Extend the range of existing electric cars.
- Reducing the losses in the electric cars.
- More starting torque for the modeled six-phase induction motor than three-phase induction motor of same power.
- Calculate and compare the current per phase for six-phase induction motor with three-phase induction motor.
- Reduce dependency on fossil fuel-powered transport.

3 Mathematical Model of the Motor

A simplified and equivalent diagram of a six-phase induction motor is shown in Fig. 1. To develop this model, some assumptions are made and they are as follows:

(a) The air gap is uniform, and the windings are distributed in a sinusoidal manner around the air gap.
(b) There is no core loss and magnetic saturation in the core.
(c) There is no friction and windage loss in the system [3].
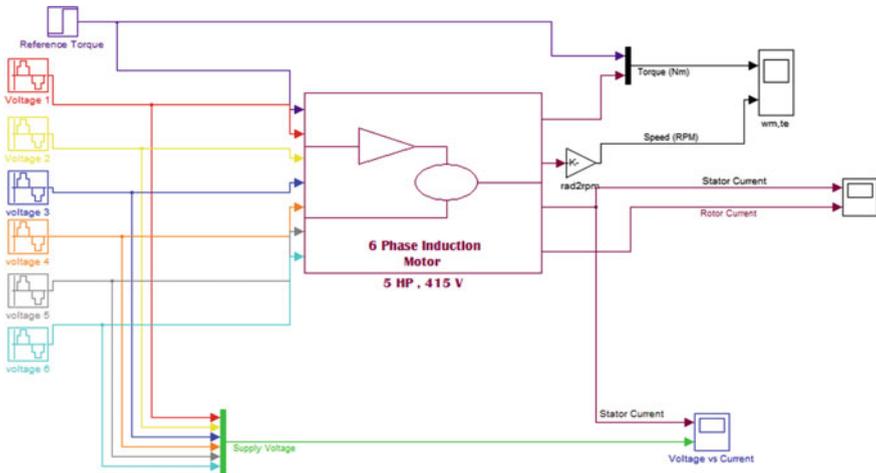
The mathematical model is shown in Fig. 1.

Fig. 1 Model of six-phase induction motor in MATLAB/Simulink environment

4 Simulation of the Motor

Six-phase stationary axis voltages are transformed into *d-q* synchronous axis voltages, and *d-q* axis currents are transformed into stationary axis voltage [4]. The input voltage is 415 V which is same as that of three-phase induction motor used in the existing electric vehicles.

The voltage equations of the motor are mentioned below:

$$Vqs1 = rsiqs1 \, + \, \rho\lambda qs1 \, + \, \omega\,\lambda ds1 \tag{1}$$

$$Vds1 = rsids1 + \rho\lambda ds1 - \omega\lambda qs1 \tag{2}$$

$$Vqs2 = rsiqs2 + \rho\lambda qs2 + \omega\,\lambda ds2 \tag{3}$$

$$Vds2 = rsids2 + \rho\lambda ds2 - \omega\lambda qs2 \tag{4}$$

$$Vqr' = rr'iqr' + \rho\lambda qr' + (\omega - \omega r)\lambda dr' \tag{5}$$

$$Vdr' = rr'idr' + \rho\lambda dr' - (\omega - \omega r)\lambda qr' \tag{6}$$

The flux linkage equations are as follows:

$$\lambda qs1 = Llsiqs1 + Llm(iqs1 + iqs2) + Lm\,(iqs1 + iqs2 + iqr') \tag{7}$$

$$\lambda ds1 = Llsids1 + Llm(ids1 + ids2) + Lm(ids1 + ids2 + idr') \tag{8}$$

Table 1 Six-phase motor parameters

Motor parameters	Lds (H)	Ldq (H)	Lm (H)	R stator (Ω)	R rotor (Ω)	Voltage (V)	Jr (kg m^2)	Poles	Rated power (kW)
	0.0132	0.011	1	1.8	2.1	415	0.02	4	3.7

$$\lambda qs2 = Llsiqs2 + Llm(iqs1 + iqs2) + Lm(iqs1 + iqs2 + iqr') \tag{9}$$

$$\lambda ds2 = Llsids2 + Llm(ids1 + ids2) + Lm(ids1 + ids2 + idr') \tag{10}$$

$$\lambda qr' = Llr'iqr' + Lm(iqs1 + iqs2 + iqr') \tag{11}$$

$$\lambda dr' = Llr'idr' + Lm(ids1 + ids2 + idr') \tag{12}$$

The electromagnetic torque can be calculated from the equation below:

$$Te = (P/2)(Lm/Lr')[\lambda dr'(iqs1 + iqs2) - \lambda qr'(ids1 + ids2)]$$

$$INPUT\ POWER = V \times I$$

where *V* and *I* are the rated voltage and rated current, respectively. After theoretically calculating the desired motor specifications, a motor whose specifications approximately fall in the range was selected. The motor which was simulated, and load test was conducted on, was 415 V, 3.7 kW, six-phase induction motor. For the comparative study, load test was conducted on a three-phase squirrel cage induction motor of 415 V and 3.7 kW. The torque–speed characteristic and current per phase were determined through the load test (Table 1).

5 Comparison of Torque and Current Per Phase of Six-Phase and Three-Phase Induction Motors

The simulation of six-phase induction motor gave the following result:

- In the steady state, no load is applied on the motor in the first 0.75 s and then a load of 35 Nm is applied.
- The motor is able to reach a steady electromagnetic torque of 35 Nm under 0.4 s.
- This result helps conclude that the motor is suitable for electric vehicle propulsion.

The torque obtained in three-phase induction motor (see Fig. 2) upon conducting a load test at 800 rpm was 26 Nm, while the simulation result for a six-phase induction motor running at same speed (800 rpm) (see Fig. 3a) gave a torque of

Fig. 2 Testing equipment to conduct load test on three-phase 5 HP induction motor

35 Nm (see Fig. 3b). The current per phase for six-phase induction motor was lesser than the conventional three-phase induction motor used in electric vehicles at various load conditions. These results clearly suggest that the three-phase induction motor can be replaced by a six-phase induction motor [5] which has reduced losses due to lesser current per phase (see Fig. 4a, b). It is evident from the result that replacing the three-phase induction motor with a six-phase induction motor improves the range, by reducing losses, in existing electric vehicles.

6 Conclusion

The use of electric vehicles in the modern world is a way of decreasing our dependency on fossil fuel and fossil fuel-powered means of transportation. The major limitations of using electric vehicles are the limited range, distance that can be travelled between successive charging of batteries, and their high cost. The conventional three-phase induction motor uses more current per phase which leads
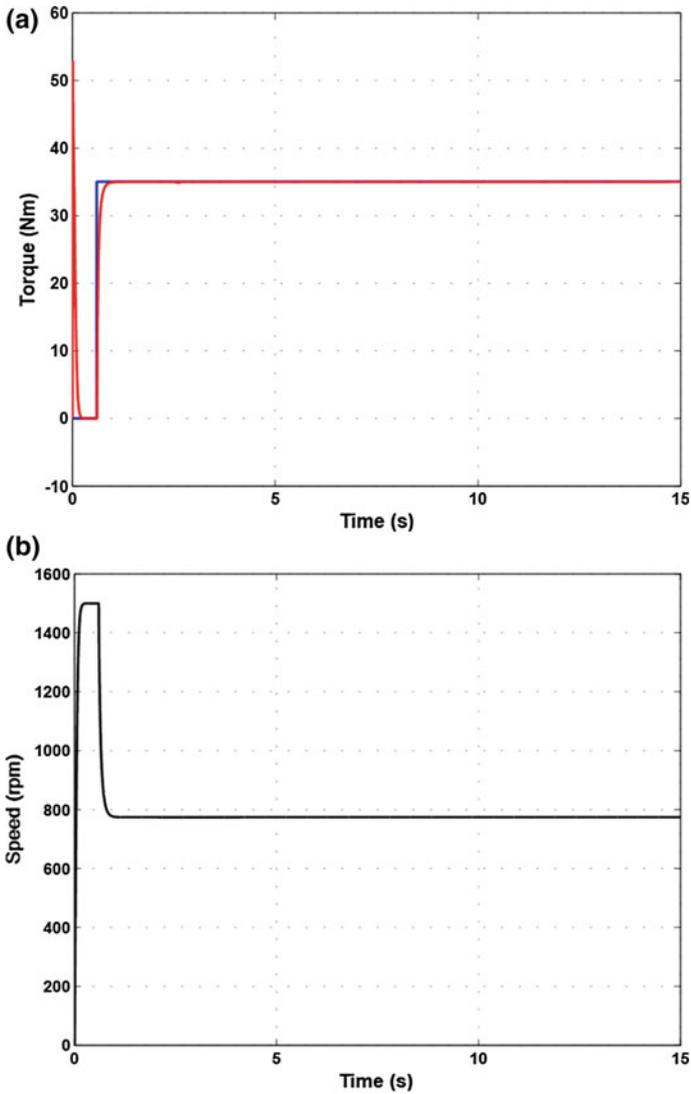
Fig. 3 **a** Torque in the first 15 s of starting a six-phase induction motor. **b** Speed in the first 15 s of starting a six-phase induction motor

to more copper losses, and this decreases the range of the electric vehicle. The simulation of six-phase induction motor shows that it requires lesser current per phase, and hence, the range of the car increases along with the capability to meet the higher starting torque requirements. The six-phase induction motor offers improved efficiency over the three-phase induction motor [6, 7]. The transient torque conditions at the starting of the motor are improved by increasing the number of phase
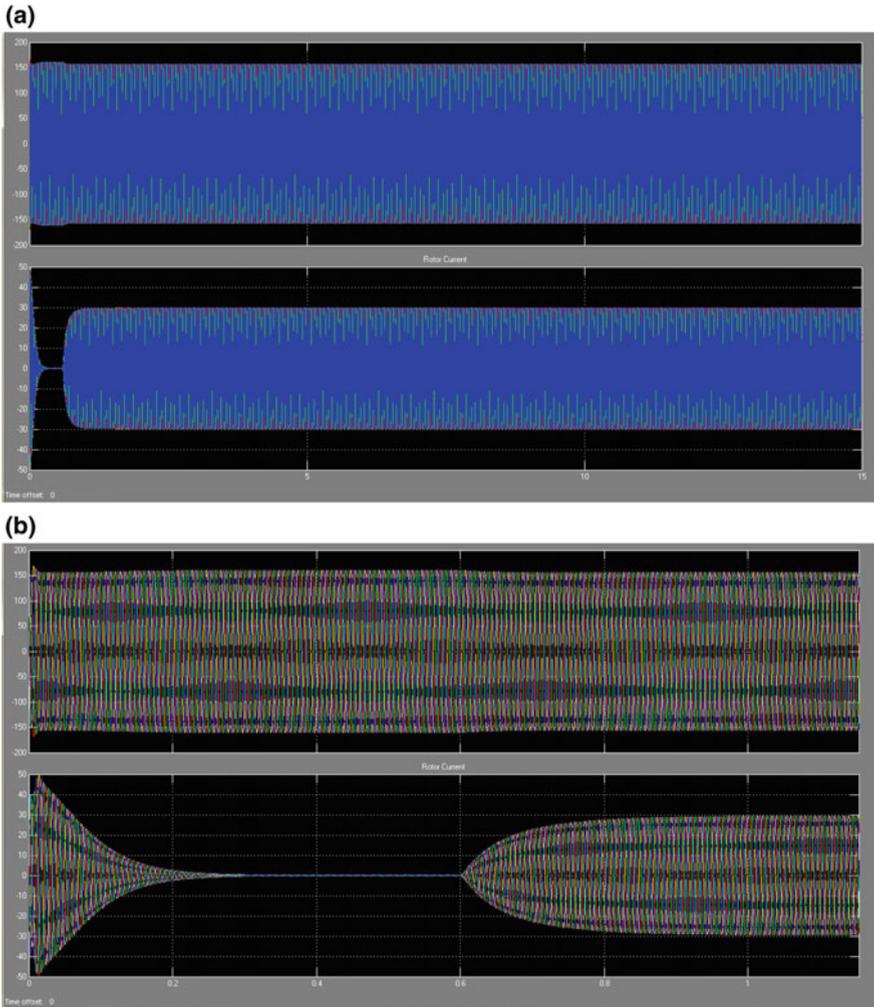
Fig. 4 a Stator and rotor currents of the six-phase induction motor. **b** Stator and rotor currents of the six-phase induction motor

of the induction motor. The replacement of three-phase induction motor drive by a six-phase induction motor drive is not very costly [8–10] or tedious, and hence, the existing electric vehicles can be easily upgraded to six-phase induction motor drive. This decreases the energy consumption of the existing electric vehicles and the ones which will be built later on. An electric vehicle powered with six-phase induction motor drive is clearly an improvement to the existing transportation system which uses three-phase induction motor drives and internal combustion engines.

7   Appendix

Vqs1, Vqs2	q axis stator voltages
Vds1, Vds2	d axis stator voltages
Vqr′, Vdr′	d-q axis rotor voltages
Va, Vb, Vc, Vx, Vy, Vz	Six-phase input voltages
ia, ib, ic, ix, iy, iz	Six-phase input currents
Lls	Stator leakage inductance
Llm	Stator mutual leakage inductance
Lm	Air gap inductance
Llr′	Rotor leakage inductance
Lr′	Rotor self-inductance
λqs1, λqs2	q axis stator flux linkages
λds1, λds2	d axis stator flux linkages
λqr′, λdr′	d-q axis rotor flux linkages
iqs1, iqs2	q axis stator currents
ids1, ids2	d axis stator currents
iqr′, idr′	d-q axis rotor currents
ω, ωr	Speed of reference frame and rotor speed, respectively
Te	Electromagnetic torque
TL	Load torque
P	Number of poles
ρ	d/dt

References

1. Venter, P., Jimoh, A.A., Munda, J.L.: Realization of a "3 & 6 Phase" induction machine. In: 20th International Conference on Electrical Machines (ICEM), pp. 447–453, IEEE, New York (2012). https://doi.org/10.1109/icelmach.2012.6349907
2. Buksnaitis, J.: Investigation and comparison of three-phase and six-phase cage motor energy parameters. Elektron. Elektrotech. **21**(3), 16–20 (2014). https://doi.org/10.5755/j01.eee.21.3.5876
3. Mandal, S.: Performance analysis of six-phase induction motor. Int. J. Eng. Res. Technol. (IJERT) **4**(2), 589–593 (2015)
4. Krause, P.C., Thomas, C.H.: Simulation of symmetrical induction machinery. IEEE Trans. Power Appar. Syst. **84**, 1038–1053 (1965). https://doi.org/10.1109/tpas.1965.4766135
5. Prakash, R., Akhtar, M.J., Behera, R.K., Parida, S.K.: Design of a three phase squirrel cage induction motor for electric propulsion system. In: Third International Conference on Advances in Control and Optimization of Dynamical Systems 2014. International Federation of Automatic Control (IFAC), vol. 47, No. 1, pp. 801–806. Elsevier, Amsterdam (2014)
6. Miranda, R.S., Jacobina, C.B., Lima, A.M.N.: Modeling and analysis of six-phase induction machine under fault condition. In: Power Electronics Conference, pp. 824–829. IEEE, New York (2009). https://doi.org/10.1109/cobep.2009.5347696

7. Singh, G.K.: High horse power ratings in AC drive by means of phase-redundancy technique some experimental investigations. In: IEEE Region 10 International Conference on Global Connectivity in Energy, Computer, Communication and Control, vol. 2, pp. 580–583. IEEE, New York (1998). https://doi.org/10.1109/tencon.1998.798286
8. Nanoty, A.S., Chudasama, A.R.: Control of designed developed six phase induction motor. Int. J. Electromagn. Appl. **2**(5), 77–84 (2012). https://doi.org/10.5923/j.ijea.20120205.01
9. Apsley, J.M., Williamson, S.: Analysis of multi-phase induction machines with winding faults. In: International Conference on Electric Machines and Drives, pp. 249–255. IEEE, New York (2005). https://doi.org/10.1109/iemdc.2005.195731
10. Rinkeviciene, R., Savickiene, Z., Uznys, D., Pitrenas, A., Šlepikas, A.: Scalar control of six-phase induction motor. In: Open Conference of Electrical, Electronic and Information Sciences (eStream). IEEE, New York (2017). https://doi.org/10.1109/estream.2017.7950304

Design and Fabrication of Wheeled Inverted Pendulum Human Transporter

Ashwath Nambiar, K. R. Athul Krishna, M. K. Nirmal, Bijil John, Vishnu Sankar and P. N. Jithin

1 Introduction

The enormous rise in air pollution and the depletion of non-renewable resources has motivated the design of many electrical transportation systems, and wheeled inverted pendulum human transporter (WIPHT) is one among them. WIPHT is a two-wheeled, electrically powered human transportation system which works on the principle of an inverted pendulum. A simple pendulum is a much popular system which is inherently stable, whereas the inverted pendulum is a statically unstable system in which the suspended mass in the case of a simple pendulum rests above the pivot point. An inverted pendulum can be further explained with a classical example of balancing an umbrella upright at the end of one's finger.

The mass of an inverted pendulum system can be balanced either by applying torque at the pivot point or by moving the pivot point horizontally according to the instantaneous tilt of the mass from the equilibrium position. The second technique is equipped with this project, and the movement is done with the help of wheels. The designing of such a system requires a closed-loop feedback system in which the instantaneous tilt of the mass from the equilibrium position is fed back to the controller. The controller finds out the required speed of the wheels such that the system gets dynamically balanced. The speed of the motor is varied through voltage control technique using PWM signals, which is the best way to control DC motors [1]. In this project, the tilt is being measured using an inertial measurement unit (IMU), i.e., MPU 6050 which is being connected to the microcontroller Arduino

A. Nambiar · K. R. Athul Krishna · M. K. Nirmal · B. John · V. Sankar (✉)
P. N. Jithin (✉)
Mechanical Engineering, Rajagiri School of Engineering and Technology,
Kochi, India
e-mail: vishnus@rajagiritech.edu.in

P. N. Jithin
e-mail: jithinpnarayanan@gmail.com

Uno R3 through an I2C interface. Locomotion of the vehicle is achieved by exploiting the feature of balancing of the system. Further, it can be explained as purposefully disturbing the system from its equilibrium position such that it moves until the disturbance is withdrawn.

Segway HT, self-balancing electric hover boards, and electric unicycle are some examples of control systems which work under inverted pendulum principle. Segway HT works similar to WIPHT, and the area in which WIPHT differs from Segway HT is in the turning method used. In WIPHT, the IMU measures the change in roll angle and gives the corresponding relative drive to the motors, whereas in Segway HT the relative drive is initiated through the handle mounted on the platform. The change in roll angle in WIPHT is created by the user from the posture he/she makes while turning.

2 Mechanical Design

The mechanical design of WIPHT is crucial when analyzed from the view of comfort as well as balancing. The chassis of WIPHT is constructed from rectangular cast iron bars (thickness 4–5 mm) and also L section (thickness 4–5 mm). The reason for using L section is to successfully attach the platform material firmly through welding. The different sections were machined to the required dimension and welded in accordance with the design made. Metal sheet has been welded over the chassis on which foot will be placed, and this platform lies between the two wheels. The width of the platform is slightly more than the average length of a human foot (approximately 30 cm). Due to affordability, durability, flexibility, lightweight, and resistance to corrosion, aluminum was chosen as platform material. A handle is being attached to the frame to support the rider. Space is allocated so that an extension from the chassis can be fastened in the future to avoid strenuous standing posture. Bottom of the platform houses the battery which is mounted on the frame using clamps which are also made by welding L section and bars. The drive motors are mounted on either side at diagonally opposite corners of the platform as in Fig. 1. The motors are oriented in such a fashion so that the weight of one motor is balanced out by the weight of the other since they are equidistant from the wheel axis.

The power is transmitted from the motor to the wheels through a chain. From the literature survey made, it was clear that for balancing this vehicle higher torque will be required at the wheel end [1]. This is the reason for an increased number of teeth in the sprocket at wheel end compared to that at the motor end. The required direction (left/right) of the user is accomplished through the posture he/she makes. That is, if he/she tilts toward right the pressure due to right foot is greater than left, which results in tilting of the whole frame toward the right. This inclination is measured by the IMU as its roll angle which actuates the relative rotation of wheels, thus resulting in the turning of the vehicle from its current direction.
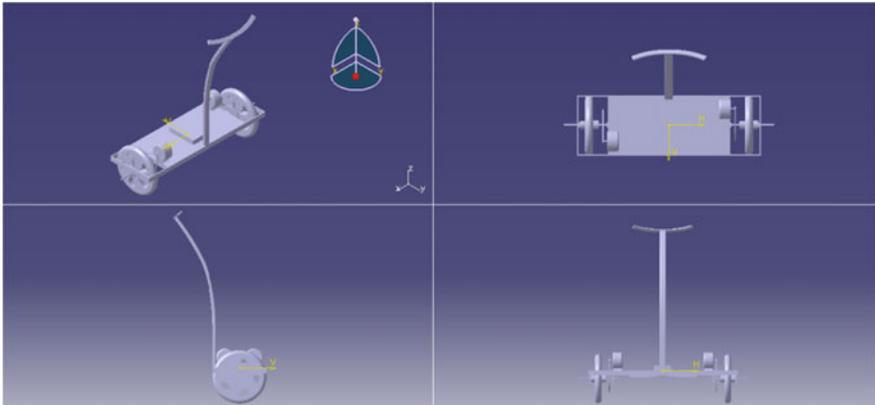
Fig. 1 CAD model of WIPHT done using CATIA V5

For better static stability, the platform should be placed below the wheel axis [2]. But the two 12 V, 18 Ah lead–acid batteries used reduce the clearance; this negligible clearance may lead to crashing while tilting the platform. The lead–acid battery being the heaviest part in the WIPHT is placed beneath the platform. The battery acts as a counterweight to the inverted pendulum system when it is attached below the wheel axis. A counterweight when added improves the static stability of the vehicle [3]. Therefore, to increase the clearance and to bring down crash, the platform is set at a height of about 55 mm from the wheel axis as in Fig. 2 and also the width of which is restricted almost equal to the wheel diameter.

Fig. 2 Distance between wheel axis and platform

Design Goals

- Utilization of renewable energy sources.
- Forced tilting of the WIPHT should move it forward or backward depending upon the tilt.
- More compact design.
- Less expensive.
- More comfortable and cozy design.
- Can overcome slight bumps and steepness on road.

3 Electronic Design

For the system to work properly the electrical and mechanical design should go hand in hand.

3.1 Components

3.1.1 Drive Motors

Drive motors for WIPHT were the prime consideration taken into account. Due to the use of renewable energy source (battery), DC motors were the obvious choice. Specifications for the DC motor were confirmed by analyzing different characteristics of our WIPHT model like the weight and size of the model, weight carrying capacity, speed consideration, and the terrain on which it operates. Free body diagram of the WIPHT model with two drive wheels on an inclined plane was analyzed to obtain the torque (τ) and angular velocity (ω) requirements.

$$OUTPUT = \tau \times \omega$$

The input power of the motor is calculated as,

$$INPUT = V \times I \times \eta$$

where V and I are the rated voltage and rated current, respectively, and η is the efficiency of a DC motor which varies around 75–85%. After theoretically calculating the desired motor specification, a motor whose specification approximately comes in that range was selected. The motor selected was 24 V, 250 W brushed DC motor.

3.1.2   Motor Driver

WIPHT is a sophisticated system which requires deterministic speed control and dynamic response to changing system demands (like the direction of rotation of motor), and this requires a motor controller. Selection of motor controller depends on the following aspects:

- Motors nominal voltage: DC motor controllers tend to offer a voltage range. Motors nominal voltage should lie within this range.
- Continuous current the controller needs to supply: Motor controller needs to provide current equal to or above the rated current.
- Control method: Various control methods include analog voltage, I2C, PWM, R/C [1]. Depending upon the control method, the right motor controller was chosen.
- Single/dual motor controller: A dual DC motor controller can control the speed and direction of two DC motors independently.

By considering the above facts and taking the factor of safety into consideration, an appropriate motor driver was selected. The specification of the motor driver is as follows: sabertooth 25A dual motor driver.

3.1.3   IMU Sensor

WIPHT system requires a sensor to quantitatively measure the pitch angle when it is being tilted [4]. Gyroscope and accelerometer sensors that are integrated into the IMU sensor are utilized as the tilt sensor to observe the pitch angle of this vehicle [5]. The IMU sensor used is MPU6050. This device combines a three-axis gyroscope and a three-axis accelerometer together with an onboard Digital Motion Processor.

3.1.4   Microcontroller

A microprocessor is used to quantitatively measure the necessary actuating force required for the corresponding tilt of the vehicle for the self-balancing condition. The input unit to the processor is the IMU sensor. The inputs from the IMU sensor are processed, and the output in PWM format is fed to the motor driver which is the output unit.

Arduino UNO R3 effectively connects these inputs and output modules to it and helps communication between them.

3.1.5 Power Supply

The maximum operating voltage of the system is 24 V. The market availability of 24 V battery of adequate capacity is scarce and expensive. Hence, two lead–acid batteries of 12 V were connected in series to obtain the operating voltage (24 V). To acquire adequate operating time for the system, batteries of higher capacity are to be used. The lead–acid battery of 12 V, 18 Ah facilitates this function.

3.1.6 PID Control

Since the system consists of a closed-loop feedback mechanism, it requires a PID control which continuously calculates an error value which is the difference between the desired set point and measured quantity [6]. Then, it applies the correction based on proportional, integral, and derivative terms.

4 Fabrication

The manufacture of the WIPHT began with the creation of a miniaturized version of it (refer Fig. 3). The experience from that helped in the manufacture of real-sized version. The prototype consisted of the same components except for the motor, motor driver, and battery. The motor used in the prototype was 12 V brushed DC motor of 500 rpm, L293d as the motor driver, and the battery was replaced by 12 V DC adapter.

From the prototype, the following details were understood:

1. WIPHT should be mechanically stable.
2. How PID tuning is done.
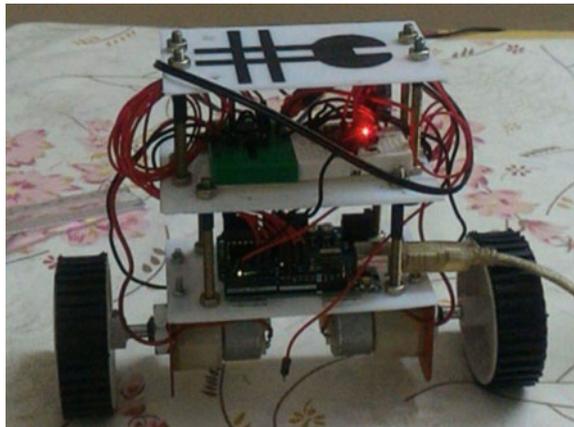

Fig. 3 A prototype of WIPHT model

Fig. 4 Old electric scooters from scrap

3. For balancing, torque at wheel end should be high.
4. Optimum orientation and placement of IMU.

Then, by simple calculations, the required specification of motor, motor driver, and battery was obtained. Taking into consideration the combination of calculated specification and availability in the market, components were selected [7]. The selected motor is 24 V, 250 W brushed DC motor, motor driver is sabertooth 25 A dual motor driver, and for an increased running time two 12 V, 18 Ah batteries were selected. After further investigation, it was understood that the same motor was used in electric scooters [8]. Old working condition motor and wheel assembly of two electric scooters were retained from scrap (refer Fig. 4).

As the final prefabrication step of WIPHT, hand-sketched design of each element was prepared and later CATIA design model was made (refer Fig. 1). After making required changes from the CATIA model, mechanical fabrication of the system was done. An immense amount of time was required for tuning the PID values of the system, and it was done using trial and error method. Certain attachment was added to the WIPHT for the easiness in tuning the system. The supporting wheels like that of training wheels used by beginner bicyclers were the attachments added to the front and back of WIPHT (refer Fig. 5). The supporting wheels were then removed after proper tuning of the system. Finally, a handle was mounted on the system and tests were done to find out the maximum speed and load the system could bear (refer Fig. 6).

5 Tuning Methodology

As mentioned earlier, WIPHT equips a closed-loop feedback system in which the instantaneous inclination of the IMU with the horizontal is measured and is fed back to the controller. The reference value to which the IMU should always

Fig. 5 Supporting wheels
added easiness in proper
tuning

Fig. 6 WIPHT model testing

maintain the inclination of the model is stored in the microcontroller, which was
done while calibration. The error between the instantaneous tilt and the reference
value is calculated each time the program iterates. So the PID controller has the
duty of taking the error in the system and reducing it to zero. Obtaining the required
values for the tuning parameters for a dynamically unstable system through trial and
error is a hazardous task. Because the vehicle is having higher torque on either
wheel, this may result in a situation where the vehicle might become out of control.

So to decrease the amount of risk and to assist the process of tuning, two wheels were attached in front and also behind the platform as in Fig. 6. After proper tuning of the system, these supporting wheels were removed.

5.1 PID Tuning

Tuning is a process in which certain parameters of a device are adjusted to obtain the required result. Here, the parameters are the proportional gain (K_p), integral gain (K_i), and derivative gain (K_d) values; thus, it is called PID tuning.

Proportional Term (K_p): K_p is proportional to the current value of the error; i.e., the proportional term directly scales the error, so with a small K_p the controller will make small attempts to minimize the error, and with a large K_p the controller will make a larger attempt. If the K_p is very small, then the controller might never minimize the error and not be able to respond to changes affecting the system, and if K_p is very large, then the system may become unstable which results in weird oscillations [9].

Integral Term (K_i): K_i accounts for the past values of the error and integrates them over time to produce the K_i term; i.e., the integral term lets the controller take up all the errors that are accumulating over time and creates the next K_i value depending on the previous errors. A larger K_i value results in a higher growth of the accumulated error.

Derivative Term (K_d): K_d estimates the future trend of the error based on the current rate of change of error; i.e., it controls the error by analyzing the rate of change of error. This helps to dampen the system, thus improving stability. The change in the system will be rapidly evident with a smaller change in K_i.

5.2 Methodology

There are many ways in which the K_p, K_i, and K_d values of the system can be tuned. Manual tuning of these values was done in order to attain stability of the system. The methodology with which the tuning was done is as follows:

Initially, the K_p, K_i, and K_d values are set to zero. Then, the K_p value is increased from zero to a point where the system starts to oscillate from its mean position. And as the K_p value was increased, it was seen that response of the system increases gradually. Keeping the K_p value a constant, the K_i value is then increased to a point such that a small inclination toward one direction tends to accelerate the vehicle in that direction. When the K_p and K_i values are properly obtained, then the K_d value is increased. The K_d value is increased such that rapid acceleration is reduced considerably. Proper K_d value results in lesser overshoots and oscillations [10]. After obtaining the rough K_p, K_i, and K_d values, a fine tuning is done. The above steps are repeated a number of times to obtain the best combination of gain values.

6   Conclusion

WIPHT is a sustainable transportation system which finds application in many areas. Further use of solar cells for charging the power source can make it mainly dependent on renewable energy sources. Due to cost restraints, brushed DC motors and lead–acid batteries were used. Otherwise, hub motors would be an excellent choice because it is easy to control a BLDC motor, it gives precise output, and finally, it does not require sprocket and chain to couple the motor with wheels. In the case of battery, lead–acid battery can be replaced by Li-ion battery. Li-ion occupies less space and higher Ah, which gives higher run time.

References

1. Vasudevan, H., et al.: Design for control of wheeled inverted pendulum platforms. Am. Soc. Mech. Eng. **7**, 041005-1–041005-12 (2015)
2. Maddukuri, S.V.P.K., Srikanth, B.: Design and fabrication of I-cycle. Int. J. Electron. Electr. Eng. **3**(5), 359–364 (2015)
3. Strakoš, P., Tůma, J.: Mathematical Modelling and Controller Design of Inverted Pendulum. Institute of Electrical and Electronics Engineers, pp. 388–393 (2017)
4. Walther, A., et al.: Bias contribution in MEMS gyroscope. J. Microelectromech. Syst. **22**(2) (2013)
5. Saukoski, M., Aaltonen, L., Halonen, K.: Zero-rate output and quadrature compensation in vibratory MEMS gyroscopes. IEEE Sens. J. **7**(12), 1639–1652 (2007)
6. Mahvan, A., Akbarzadeh, A.:Gyro stabilized two-wheeled inverted pendulum robot. In: Proceedings of the 3rd RSI International Conference on Robotics and Mechatronics, pp. 669–674 (2015)
7. Ab Ghani, S., et al.: Self-balancing unicycle controlled by Arduino. ARPN J. Eng. Appl. Sci. **11**(7), 4239–4244 (2016)
8. UmashankarNagarajan*et al*, "The Ballbot-An omnidirectional balancing mobile robot", The international journal of robotics research, (2014)
9. Deegan, P., et al.: Designing a self-stabilizing robot for dynamic mobile manipulations. In: Science and Systems-Workshop on Manipulation for Human Environment, Philadelphia, PA, USA (2006)
10. Ha, Y., Yuta, S.: Indoor navigation of an inverse pendulum type autonomous mobile robot with adaptive stabilization control system. In: International Symposium on Experimental Robotics, Stanford, CA, (1997)

Regulating Travel Demand for Sustainable Transport: Road Pricing Versus Incentive Schemes

Uday Sankar Kandolath

1 Introduction

The addition of roads or highways to existing transport infrastructure has failed to stem the increase in traffic congestion over time. This is because increasing the supply of available transport infrastructure at zero usage cost to the motorists induces demand that did not previously exist. The induced demand will create traffic that did not exist prior to the construction of transport infrastructure [1]. One method to reduce the demand for travel and thereby tackle traffic congestion is road pricing, i.e., levying a charge or toll on the motorist for the use of roads.

The rationale behind road pricing has been examined in detail by researchers and arises from the recognition that a motorist despite paying gas taxes, vehicle operating fees, and parking fees do not pay for using the road or highway [1]. Any motorist that uses a facility imposes a marginal cost of pollution and congestion on others which is not borne by the motorist. In road pricing, this marginal cost is internalized and levied from the motorist as a congestion charge.

An alternative to road pricing which penalize motorists is incentive schemes which reward motorists for exhibiting desirable travel behavior like traveling off-peak, using public transport, embracing non-motorized travel, and using less congested routes. This paper is organized as follows: Sect. 1 examines road pricing schemes and their effects, Sect. 2 looks at incentive schemes that have been used for tackling traffic congestion, and Sect. 3 identifies suggests possible directions of research.

U. S. Kandolath (✉)
Rajagiri School of Engineering & Technology, Rajagiri Valley, Kakkanad, Kochi 682039, Kerala, India
e-mail: uday.kandolath@gmail.com

2   Road Pricing

Cordon pricing is a road pricing scheme where motorists are required to pay a congestion charge for crossing a cordon. Singapore introduced the area licensing scheme [2, 3] in 1975 which required all vehicles entering the CBD also called the 'restricted zone' during peak hours to possess an area license. In 1989, charges were levied on cars only during times of congestion, which was then extended in 1994 to the entire duration from 7:30 A.M. to 6:30 P.M. This was called the whole-area licensing scheme and required cars to pay a toll of $3 during peak hours and $2 during off-peak hours. The area licensing scheme was replaced by the Electronic Road Pricing Scheme in 1998 which charges motorists based on the average speed on arterial roads and expressways. The success of the Singapore Road Pricing scheme [2, 3] led to the London Congestion Charge [4] which is a congestion charge paid by motorists entering or exiting a cordon around the CBD of London. The charge is £11.50 and is levied between 7:00 A.M and 6:00 P.M., Monday to Friday. Similar congestion charging schemes include the Stockholm Congestion Tax [5], Milan Area C [4], Durham City Congestion Charge [5], Gothenburg Congestion Charge [6], and similar schemes in Valletta, Malta [4], and Tehran [7].

Efforts to implement the congestion charge in Edinburgh, New York, Manchester, failed due to public opposition and lack of political will [8]. Despite a pilot scheme that showed desirable results between 1993 and 1995, the proposal to introduce congestion charging in Hong Kong also failed to muster public support. The toll ring roads around Trondheim, Norway, stopped levying charges from December 30, 2015 [9].

Despite the stiff public opposition to cordon pricing, the benefits are evident in places where cordon pricing has been implemented. The benefits of cordon pricing are (a) revenue generation, (b) congestion mitigation, (c) improvements in air quality, (d) modal shift to public transport, and (e) better land use management [10]. The benefits of various congestion charging schemes are listed in Tables 1 and 2.

Table 1 Effect on traffic congestion and safety of various congestion charging schemes [10]

	London	Singapore	Stockholm	Milan	Gothenburg	Rome
Traffic volume (%)	−21	−44	−20	−34	−10	−20
Travel times	−30% delays	n.a.	−33% delays	−17% decrease in congestion	−10% to −20%	+4% increase in speeds
Public transit ridership	+18%	n.a.	+5%	n.a.	+6%	+5%

Table 2 Environmental effects of various congestion charging schemes [10]

	London	Stockholm	Milan (%)	Gothenburg	Rome
CO_2	−16.4%	−13%	−22	−2.5%	−21%
NO_X	−13.4%	−8%	−10	Uncertain	n.a.
PM2.5	n.a.	n.a.	−40	Uncertain	n.a.
PM10	−15.5%	−13%	−19	Uncertain	−11%

Apart from cordon pricing, another approach to road pricing is variable pricing which is a toll levied on different parts of transport infrastructure like bridges, lanes, or tunnels. Variable pricing considers the value of travel time of the motorist and is usually implemented in three forms: (i) time of day pricing were the toll varies according to the time of day. This implies toll would be high during peak hours or heavily congested times of the day and less during times of low congestion, (ii) dynamic pricing in which the toll varies in real-time with the level of congestion and HOT lanes which are HOV lanes used by cars with multiple occupants for a charge [9, 11]. The observed benefits of variable pricing are travel time savings, reliable travel times, improved air quality, and increase in safety [12].

Germany has introduced a distance-based charge (LKW-Maut) for trucks in Germany, and mileage-based fees were introduced in a pilot program in Oregon, USA, where participants were given the option of paying a mileage-based charge in place of the gas tax [13].

3 Incentive Schemes

An incentive in the form of one-month free bus tickets was given to motorists in Osaka, Japan. It was found that there was a decrease in car use, increase in use of buses, and hence, the frequency of buses also had to be increased [14]. Free rail tickets were distributed in Melbourne [15] and Beijing [16] offered discounted transit fares to encourage off-peak commuting. The employees in Infosys, Bangalore, were offered incentives to travel off-peak as part of the Infosys-Stanford Traffic (INSTANT) [17] project for a six-month period between October 2008 to April 2009. Credits were awarded to the participant employees who arrived and swiped their ID cards at the office before the peak period. The credits enabled them to participate in a weekly lottery to win rewards. During the six-month period, it was observed that number of non-peak arrivals doubled among the participants [17].

A similar program called Incentives for Singapore's Commuters (INSINC) [18] was implemented in Singapore to encourage commuters using the public transit system during peak hours to off-peak hours and was run between January 2012 and December 2013. The participants traveling off-peak were awarded credits which could be exchanged for fixed monetary rewards or rewards earned from a lottery

system. The INSINC scheme in addition also had a social element as part of which participants were awarded bonus points when their social network friends sign-up. Another attractive feature of INSINC was a magic box offer or additional rewards which participants who achieved desirable commuting behavior receives. The INSINC scheme has evolved into the 'New Travel Smart Rewards Program' implemented by the Singapore Land Transport Authority [18]. The 'Spitsmijden' trials in the Netherlands were carried out on four different locations with the objective of reducing peak-hour traffic. Motorists who participated in the trials were offered financial incentives between 3 and 7 Euros per day. It was observed that the motorists reacted to the incentive in four different ways: (i) shift in departure times, (ii) use of alternative less congested routes, (iii) use of alternative modes, and (iv) a small proportion opted to avoid the trip altogether [19, 20]. The effects of the Spitsmijden trials are captured in Table 3.

Analysis of the results from the Spitsmijden trials shows the following four problems with 'peak-hour incentives,' namely (i) shifting congestion to shoulder periods, (ii) use of alternatives routes depends on the level of congestion associated with such routes, (iii) response varies depending on the amount of incentive and number of participants, i.e., high number of participant and average monetary rewards are more effective than low number of participants and high monetary rewards, (iv) lack of horizontal equity, (v) ineffective in mitigating effect of induced demand, (vi) high setup costs, and (vi) lack of effective enforcement or monitoring mechanism [19, 20]. Apart from the Spitsmijden trials, the following trials were also conducted in the Netherlands.

Stanford University implemented an incentive scheme called Congestion and Parking Relief Incentive (CAPRI) [21] from April 2, 2012 to September 30, 2014 to reduce peak-hour travel within the campus. Participants in the incentive scheme were encouraged to commute off-peak or walk/cycle within the campus. Participants who adhered to these conditions were awarded points each day and were given the option of trading in their points every week for (a) deterministic cash amount or (b) random cash awards by playing a chutes and ladders game much like a lottery. It was observed that commuters who won rewards in a week were more likely to shift to off-peak travel in subsequent weeks. It was also observed that friends winning rewards also encouraged some commuters to shift off-peak [21].

Table 3 Results of Spitsmijden experiments [19, 20]

Location	Incentive	Changes in behavior of motorists			
		Departure time (%)	Route change (%)	Modal shift (%)	No trip (%)
Zoetermeer	€3	35	–	10	1
Gouda	€7	4	–	14	3
Hollandse Brug	€4–6	16	9	7	6
Moerdjik Brug	€4	15	28	5	6

While incentives schemes can bring about desirable changes in travel behavior like off-peak travel, use of public transit, and adopting walking/cycling, they are unable to sustain the 'good' behavior after the termination of the incentive [20]. Hence, more research needs to be carried out to determine how the change in behavior can be sustained when incentives are withdrawn.

4 Conclusion

While road pricing can mitigate the effects of traffic congestion, public opposition, and lack of political will impede its implementation in many places. Incentive schemes can be an acceptable alternative but suffer from the following problem: The desirable travel behavior is not sustained when the incentive is withdrawn. Moreover, while the environmental benefits of road pricing are well documented, the benefits are not sustained. The environmental benefits of incentive schemes are yet to be quantified and studies. In such a scenario, the effect of combined road pricing-incentive schemes needs to be studied. While road pricing can be used to dis-incentivize driving through heavily congested or polluted areas, incentives can be used to encourage use of public transport or electric vehicles.

A third area of research needs to be the impact of taxi on-demand services like Uber, Lyft, Ola. Such taxi services use dynamic pricing, where the price of the ride depends on the demand. The effect of such taxi services on traffic congestion needs to be studied. While the proliferation of such services may reduce private car ownership, it remains to be seen whether there will be an increase in trips due to the low cost and discounts provided. The effect of providing such incentives and whether they can make a significant difference to travel behavior needs to be further investigated.

There is also lack of awareness about the long-term environmental benefits of road pricing. While there are benefits [10] environmental pollution and low air quality even in places with road pricing schemes, raises a pertinent question as to their long-term benefit.

References

1. Litman, T.: Generated Traffic and Induced Travel. Implications for Transport Planning, Victoria Transport Policy Institute, Victoria, http://www.vtpi.org/gentraf.pdf (2012)
2. Li, M.Z.F.: Estimating congestion toll by using traffic count data—Singapore's area licensing scheme. Transp. Res. Part E **35**(1), 1–10 (1999)
3. Phang, S., Toh, R.S.: Road congestion pricing in Singapore: 1975–2003. Transp. J. **43**(2), 16–25 (2004). (Research Collection School of Economics)
4. Leape, J.: The London congestion charge. J. Econ. Perspect. **20**(4), 157–176 (2006)
5. Börjesson, M., Eliasson, J., Hugosson, M.B., Brundell-Freij, K.: The Stockholm congestion charges—5 years on. Effects, acceptability and lessons learnt. Transp. Policy **20**, 1–12 (2012)

6. Andersson, D., Nässén, J.: The Gothenburg congestion charge scheme: a pre–post analysis of commuting behavior and travel satisfaction. J. Transp. Geogr. (2016)
7. Behruz, H., Safaie, A., Chavoshy, A.P.: Tehran traffic congestion charging management: a success story. In: Urban Transport XVIII: Urban Transport and the Environment in the 21st Century, No. 18, p. 445 (2012)
8. Schaller, B.: New York City's congestion pricing experience and implications for road pricing acceptance in the United States. Transp. Policy **17**, 266–273 (2010)
9. Variable Pricing, https://mobility.tamu.edu/mip/strategies-pdfs/…summary/variable-pricing-4-pg.pdf, last accessed 18 Nov 2017
10. Van Amelsfort, D., Swedish, V.: Introduction to Congestion Charging: A Guide for Practitioners in Developing Cities, Asian Development Bank and Deutsche Gesellschaft für Internationale Zusammenarbeit (GIZ) GmbH, Beijing (2015)
11. https://ops.fhwa.dot.gov/publications/congestionpricing/sec2.htm, last accessed on Oct 30, 2017
12. Value Pricing Pilot Program: Lessons Learned. Federal Highway Administration. https://ops.fhwa.dot.gov/publications/fhwahop08023/vppp_lessonslearned.pdf
13. McMullen, B.S., Zhang, L., Nakahara, K.: Distributional impacts of changing from a gasoline tax to a vehicle-mile tax for light vehicles: a case study of Oregon. Transp. Policy **17**(6), 359–366 (2010)
14. Fuji, S., Kitamura, R.: What does a one-month free bus ticket do to habitual drivers. Transportation **30**, 81–95 (2003)
15. Currie, G.: Quick and effective solution to rail overcrowding: free early bird ticket experience in Melbourne, Australia. Transp. Res. Record J. Transp. Res. Board **2146**, 35–42 (2010)
16. Zhang, Z., Fujii, H., Managi, S.: How does commuting behavior change due to incentives? An empirical study of the Beijing Subway System. Transp. Res. Part F **24**, 17–26 (2014)
17. Merugu, D., Prabhakar, B., Rama, N.: An incentive mechanism for decongesting the roads: a pilot program in Bangalore. In: NetEcon, ACM Workshop on the Economics of Networked Systems (July 2009)
18. Pluntke, C., Prabhakar, B.: INSINC: a platform for managing peak demand in public transit. JOURNEYS, Land Transport Authority Academy of Singapore (Sept 2013)
19. Bliemer, M.C.J., Dicke-Ogenia, M., Ettema, D.: Rewarding for avoiding the peak period: a synthesis of four studies in the Netherlands, p. 20 (2010)
20. Donovan, S.: Introducing Spitsmijden: experiments with peak avoidance incentives in the Netherlands. Victoria Transport Policy Institute at www.vtpi.org/spitsmijden.pdf (2011)
21. Zhu, C., Yue, J.S., Mandayam, C.V., Merugu, D., Abadi, H.K., Prabhakar, B.: Reducing road congestion through incentives: a case study. Presented at the Transportation Research Board 94th Annual Meeting (2015)

Part V
Environmental Geotechnics

Dynamic Study and Analysis of Gravity Dam Considering Foundation Interaction Effect and Sloshing Effect

Margaret Abraham, Nissy Susan Mani, Anu Mathew, Deepthi I Gopinath and Arun Balan

1 Introduction

The response of the dam gets significantly affected when the foundation soil is considered as a deformable elastic medium, due to the coupling of the stiffness of the soil and the stiffness of the structure, which in turn changes the elastic property of the system and modifies the characteristic response of the system. This process in which the reaction of the soil influences the motion of the structure and vice versa the motion of the structure influences the response of the soil is referred as soil–structure interaction (SSI). When the dam is resting on flexible foundation, due to the linking effect of the soil structure system, the movement of the dam and that of the free field motion will be different. Therefore, the dynamic analysis of the dam in this case depends on the structure, the surrounding reservoir condition and the foundation properties. The motion of free liquid surface occurs, at the time of a seismic excitation, which is termed as sloshing. Energetic sloshing can be a determined problem in the storage of water in dams. It can exert considerable thrust on the walls, which can lead to an explosion.

The amplitude of the slosh, in general, depends on the nature, amplitude and frequency of the earthquake motion, height of water in the reservoir, liquid properties and geometry of the dam. The best seismic design of triangular cross-section of dam with SSI effect is when the strain occurring in the dam section is lower [4]. On developing a 2D finite element model for different geometrical shapes of

M. Abraham (✉) · N. S. Mani
Civil Engineering, Vimal Jyothi College of Engineering, Kannur, India
e-mail: margaretabraham226@gmail.com

N. S. Mani · A. Mathew · D. I. Gopinath · A. Balan
Civil Engineering, Mangalam College of Engineering, Kottayam, India

A. Mathew · D. I. Gopinath · A. Balan
Civil Engineering, Rajagiri School of Engineering and Technology, Kochi, India

concrete gravity dam, considering dam–reservoir–foundation interaction effect by using ANSYS modal analysis it was concluded that dam–soil–water interaction is key factor for safety design of dam [2]. A study on the effect of flexibility foundation and reservoir by dynamic short-term analysis considering the seismic ground motion response of high concrete gravity dam–reservoir water–foundation system was done by Agarwal and Singh [1]. The boundaries of the unbounded medium were discretized by boundary element method to tackle SSI problems. A time-domain transient analysis of a concrete gravity dam and its foundation in a coupled manner using FEM technique and the effect of soil–structure interaction (SSI) has been incorporated using a simplified direct method by Burman et al. [3]. Volume of fluid (VOF) method is adopted inorder to simulate the sloshing effect in a water tank due to sway excitation which forms the basis for dam break problem.

2 Dynamic Analysis

2.1 Modal Analysis

A modal analysis is used to determine the vibration characteristics of a structure while it is being designed. Hence, the goal of a modal analysis is to determine the natural frequencies and mode shapes.

$$MU^{..} + CU^{.} + KU = F(t)$$

Modal Analysis with a Fixed Base
The Koyna dam which is situated in Maharashtra, India, is selected for the analysis with the geometric details as shown in Fig. 1 [5]. An earthquake of 6.5 magnitude strike near the site of Koyna dam in 1967, and no major damage was caused to the

Fig. 1 Geometrical details of the Koyna dam
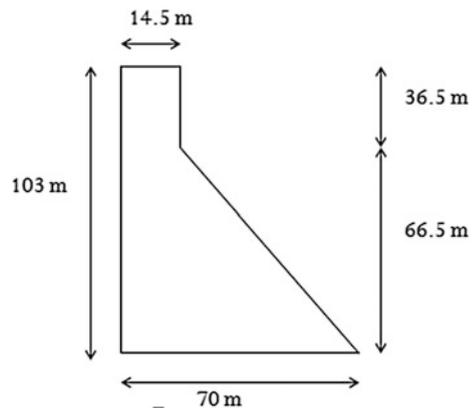
Table 1 Material properties of Koyna dam

Properties of concrete	Values
Density (kg/m^3)	2400
Modulus of elasticity (MPa)	32,000
Poisson's ratio	0.2

Fig. 2 Finite element meshed model of dam
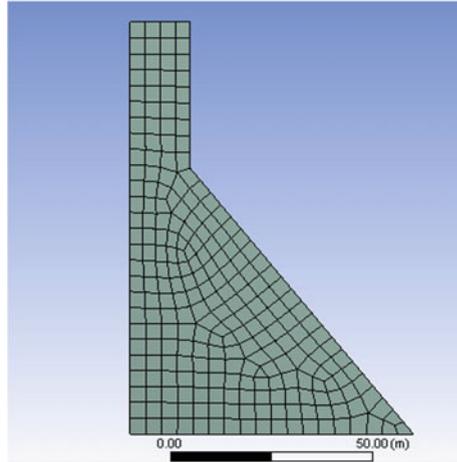
dam except some cracks were observed. Hence, Koyna dam was selected as the typical dam for the dynamic analysis. The physical properties of the dam are presented in Table 1. The finite element mesh model of the dam is shown in Fig. 2. Discretization of dam is done using PLANE 42 finite elements. The dam is assumed to have bottom fixity.

The results of modal analysis done on Koyna dam are found to be in good agreement with the work done by Chopra and Chakrabarty [5]. Figure 2 shows the comparison between the time periods. Figure 3 represents the first two mode shapes of Koyna dam (Table 2).

Next, a modal analysis considering SSI is done where foundation is also taken into account. The structural details and the material properties of the structure and the foundation are given in Fig. 4 and Table 3, respectively. The discretization of dam and the foundation by PLANE 42 finite element are shown in Fig. 5.

The modal analysis of the Koyna dam was done considering the foundation–structure interaction and Table 4 shows the results that were obtained when compared to that with the fixed base problem.

Due to the coupling of the flexible foundation to the dam body, the modal response of the dam gets varied. The time periods of the dam when having a flexible foundation were found to be higher than that of the dam with the fixed base. This is because of a reduction in the stiffness and an increase in the mass of the vibrating system which decreases the natural frequency.
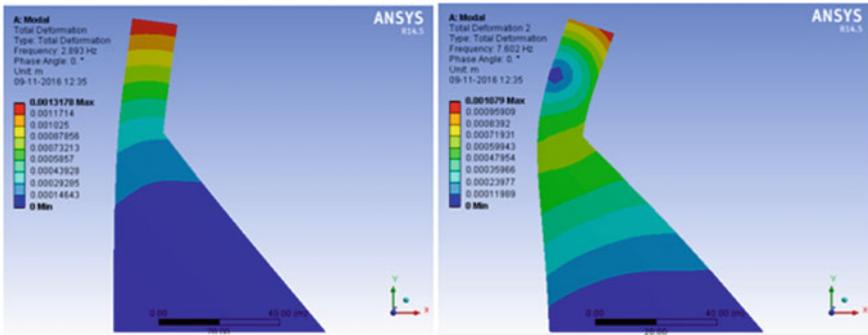
Fig. 3 Mode shapes of Koyna dam

Table 2 Time periods of Koyna dam with fixed base

Mode no.	Software result for time period (s)	Work done by Berrabah (2012), (s)
1	0.352	0.351
2	0.139	0.133

Fig. 4 Geometric details of Koyna dam foundation
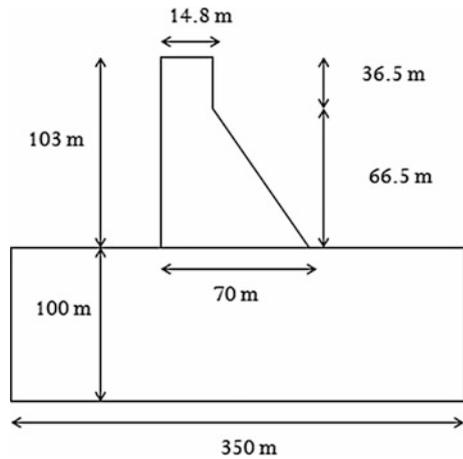
3 Transient Analysis

A transient dynamic analysis technique which yields the displacement, strain, and stress and force time history response of a structure to any combination of transient or harmonic loads is adopted here.

3.1 Transient Analysis of Dam with Fixed Base

The seismic response of the structure has been investigated when subjected to earthquake. The horizontal ground acceleration time history graph of the earthquake is shown in Fig. 6. It has a PGA of 0.47 g at 3.13 s, which is applied along the X direction. The foundation material is assumed to be of hard rock, thus having a high fixity condition. PLANE 42 finite elements are used for modelling the dam body.

The transient analysis of the Koyna dam considering the foundation as fixed base was conducted by applying Koyna earthquake motion as the input acceleration, and the results were obtained. Figures 7 and 8 show the time histories of the crest displacements and the major principal stress obtained. The graph was plotted, and they were compared with the work done by Burman et al. [3], and they were found to be in good agreement.

Table 3 Material properties of the dam and foundation

Properties of dam	Properties of foundation
Density—2400 kg/m^3	Density—2600 kg/m^3
Modulus of elasticity—32,000 MPa	Modulus of elasticity—17,500 MPa
Poisson's ratio—0.2	Poisson's ratio—0.18
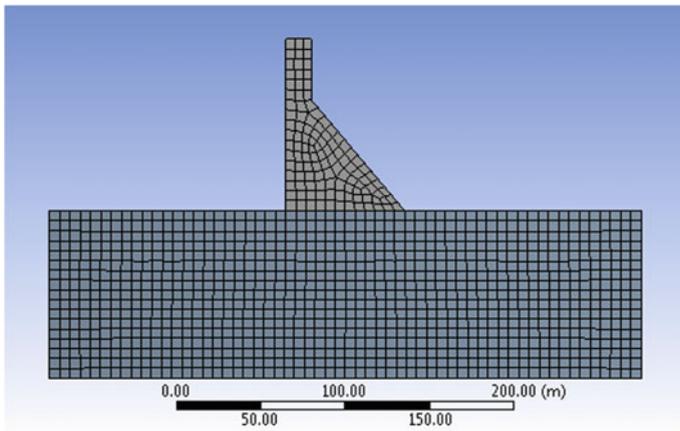
Fig. 5 Meshed model of Koyna dam considering SSI

Table 4 Time periods obtained for dam with and without SSI

Mode no.	Time period obtained for dam with fixed base, (s)	Time period obtained for dam with flexible foundation
1	0.352	0.412
2	0.139	0.201
3	0.134	0.174
4	0.127	0.137
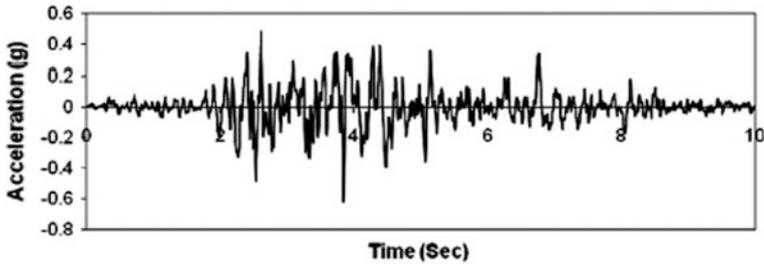
Fig. 6 Koyna longitudinal earthquake motion
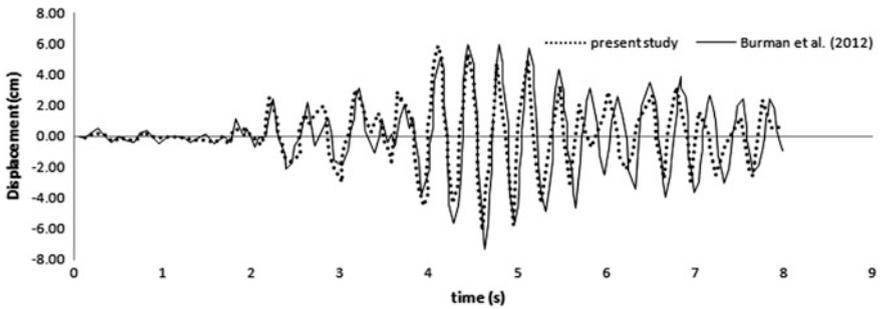
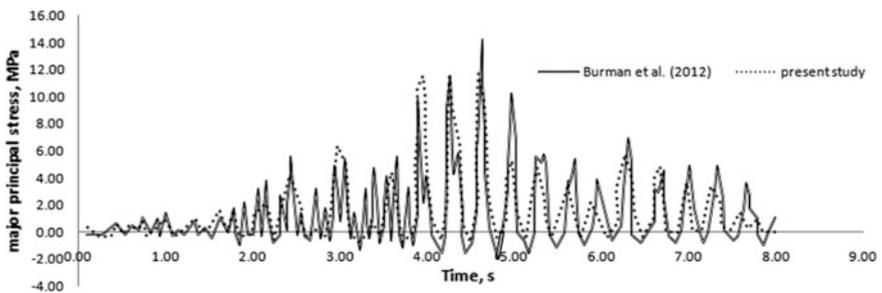**Fig. 7** Time history of crest displacement of Koyna dam with fixed base

Fig. 8 Time history of major principal stress at the neck of Koyna dam with fixed base

3.2 Transient Analysis of Dam: Considering SSI

In this study, the Koyna dam was analysed when subjected to Koyna earthquake motion by considering the foundation interaction effect. The geometrical details and the material properties of the dam body and the foundation are as same as discussed in Fig. 4 and Table 3. The time histories of the maximum crest displacements and the major principal stress at the neck of the dam were plotted and are compared to the results obtained for the dam with fixed base. Figures 9 and 10 show the time history of crest displacement and the major principal stress at the neck of the dam, respectively.

The maximum crest displacement for the fixed base problem was found to be 6.03 cm, but for the same dam with SSI, it was 8.08 cm. The maximum stress for
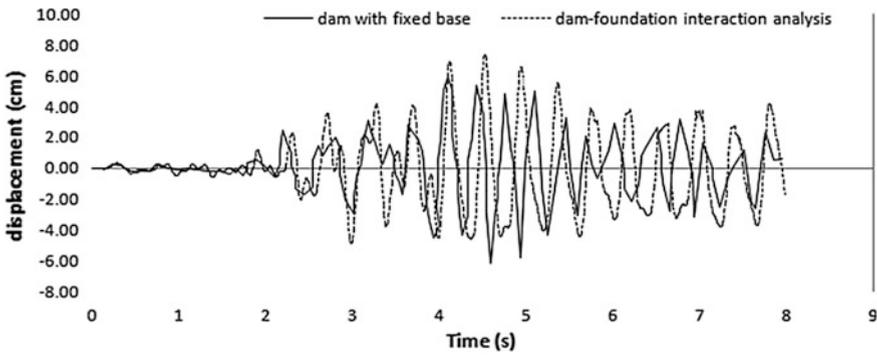
Fig. 9 Time history of crest displacement of Koyna dam considering SSI
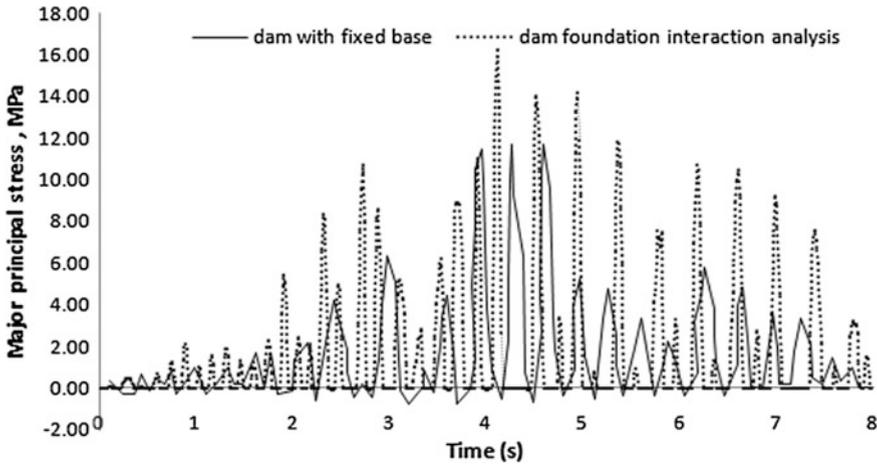
Fig. 10 Time history of principle stress of Koyna dam considering SSI

the dam with SSI was found to be 16.09 N/mm^2 while that for the dam with fixed base was 12.6 N/mm^2. Thus, it is evident that the displacements and the stresses have increased when the flexibility of the foundation is incorporated in the analysis. Hence, it is advisable to carry out the interaction analysis for massive structures like dams under flexible base. It is observed that the neck portion of the dam is the most severely stressed zone; hence, the cracks are expected to occur around the neck region of the dam. Thus, there are chances of localized failure at these regions due to seismic action which may affect the overall stability of the dam in due course.

4 Sloshing of Dam

Sloshing is defined as the standing waveforms at the free liquid surface when subjected to seismic excitations or oscillations. Dam is an example of a fluid–structure foundation–structure interaction problem. The water provides an impulsive mass that reduces the structures natural frequencies and increases damping, especially for the higher natural frequencies, which counteracts the movement caused by earthquakes. The effect of pressure waves also causes dynamic variation in the pressure distribution on the dam face. When the dam is subjected to earthquake, due to the ground excitation the reservoir water oscillates and exerts a time-varying pressure on the surface of the dam. When this effect of the fluid is incorporated to the foundation flexibility, the structural responses will be obviously different from that of the static case of water. In the present study, the sloshing behaviour of the Koyna dam is evaluated using the software FLUENT. For the purpose of validation, the sloshing behaviour of a 2D water tank is studied. This method is utilized for studying the effect of fluid sloshing on water during seismic excitation.

4.1 Sloshing of Water Tank

A partially filled 2D water tank as shown in Fig. 11a is considered for the study. The tank was given a horizontal sway excitation as,

$$x = A \sin \omega t$$

where

$$\omega = \frac{2\Pi}{T}$$

$A = 0.025$ m and $\omega = 5.54$ rad/s.
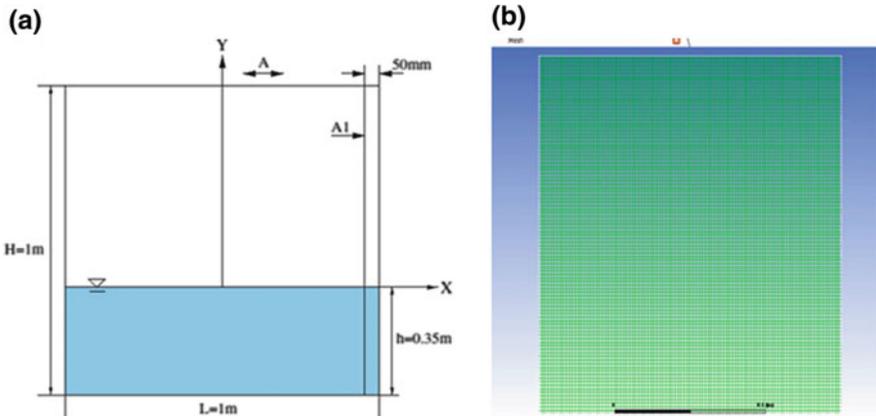$A = 0.025$ m and $\omega = 5.54$ rad/s.

Fig. 11 **a** Details of water tank and **b** meshed model of water tank in FLUENT
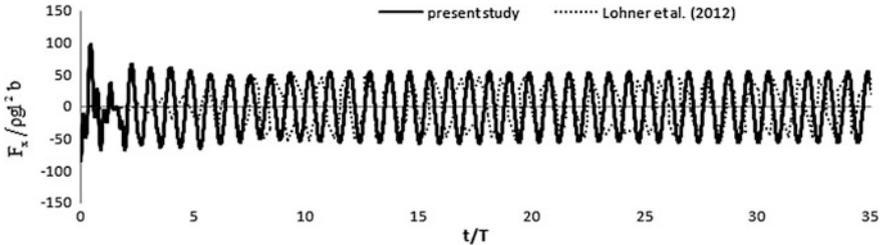

Fig. 12 Time history of lateral force on tank without FSI

The tank is modelled as a two-phase system consisting of air and water using the software FLUENT. The meshed model of the tank in FLUENT is shown in Fig. 11b. The analysis of the tank when subjected to sway excitation was conducted, and the time history of lateral force was plotted against and t/T. These are then compared to the results obtained shown in Figs. 12, 13a–c shows the volume fraction of the tank at different time.

Another study was conducted in order to find the effect of FSI on the structural response. The tank was analysed for the same sinusoidal motion by considering the fluid–structure interaction effect. The tank was given a thickness of 50 mm. The material used for tank was structural steel. The tank was analysed, and the time history of lateral pressure was plotted and was compared with results obtained for the tank without FSI. Figure 14 shows the meshed model of the tank with FSI, and Fig. 15 shows the time history of lateral force.

From Fig. 15, it is clear that the lateral pressure is increased while the tank is analysed considering the FSI. Also, for both the cases, up to about the time, $t = 10T$, the graph is unstable, which is due to the solution instability at the time of
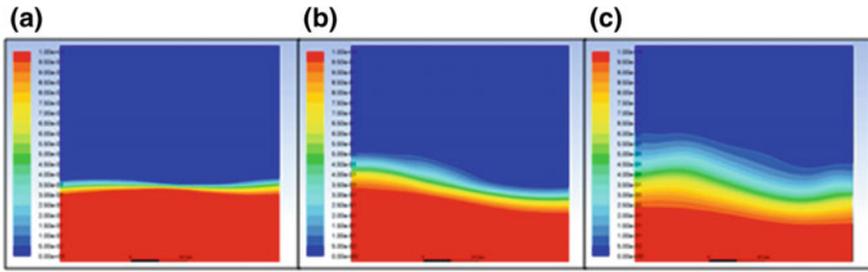
Fig. 13 Volume fraction of tank at **a** 0.3 s, **b** 1.2 s, **c** 1.9 s
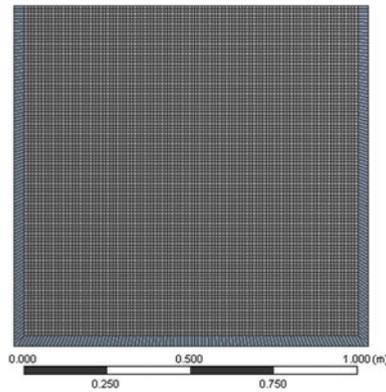

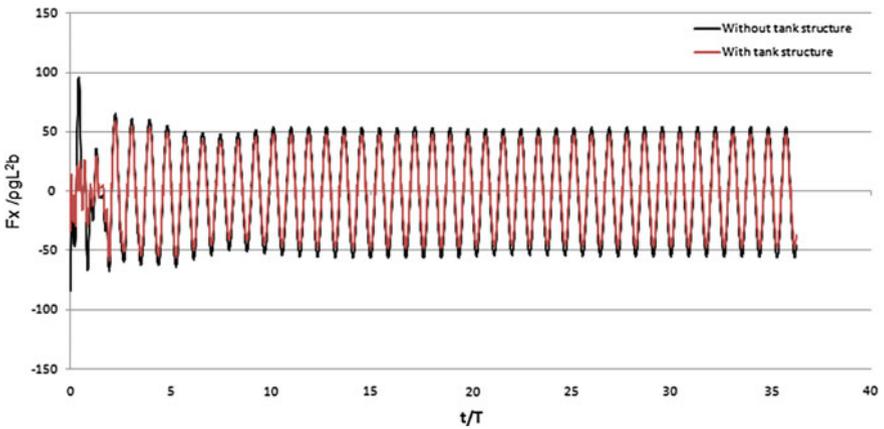
Fig. 14 Meshed model of tank with FSI

Fig. 15 Time history of lateral force on tank with FSI
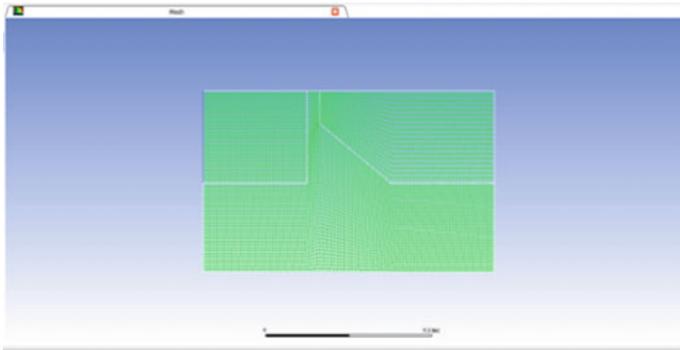
$$x = 0.025 \sin 5.52t$$

Fig. 16 Meshed finite element model of the Koyna dam in FLUENT

initialization (Fig. 16). After $t = 10T$, the graph follows a same pattern of the sinusoidal function and it stabilizes. But the pressure after the initialization is found to be greater for the tank with FSI, and the results are found to be more accurate in this case. The lateral pressure at 20.295 s was 549.44 kN, when the tank was analysed for FSI, but it was 540.44 kN, when FSI was not considered. Thus, there is variation in the response of the structure when FSI is considered. Therefore, while rigorous analysis such as the dynamic analysis of dam is performed, the effect of FSI should also be considered to get accurate results. The Koyna dam was analysed by considering fluid–foundation–structure interaction. The dam is subjected to the sinusoidal sway excitation,

$$x = 0.025 \sin 5.52t.$$

The time history of the lateral force is plotted as shown in Fig. 17. The maximum lateral force was found to be 98.1 kN. The graph follows the same pattern which is obtained for the sloshing of the tank. Here, up to $t = 2T$, there is huge instability in the graph, which is due to the solution instability due to initialization. The graph then follows a sinusoidal pattern as the input load given. After $t = 2T$, the value increases randomly and then decreases and then reaches to a stable pattern. This sudden increase and decrease in the values of the graph are due to the inertial effect of the dam structure due to seismic movement. The pressure then shows a stable sinusoidal pattern after $t = 12T$. The pressure then exerted by the fluid on the dam face follows a sinusoidal pattern with a maximum value of 98.1 kN. Figure 18a–c shows the volume fraction of water in the dam at 0.3, 1.2 and 1.9 s.

The hydrostatic pressure exerted by the fluid on the dam wall is mapped to dam structure by using workbench coupling. That is, the CFD results were coupled to workbench. The pressure obtained is mapped as hydraulic force; thus, it creates stress and deformation in the dam structure. The maximum deflection of the dam
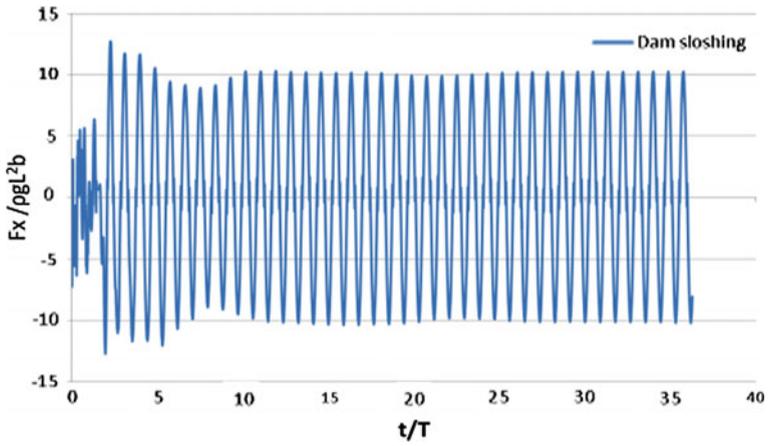
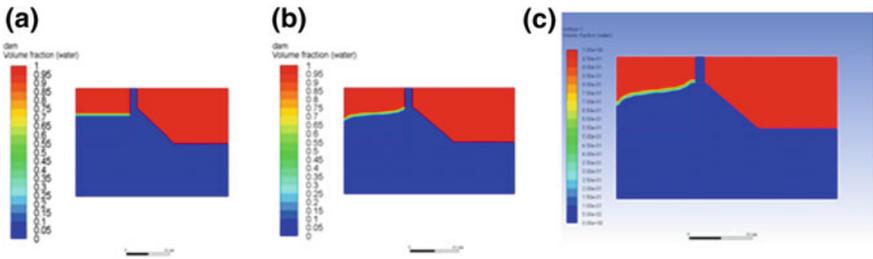**Fig. 17** Time history of lateral force exerted by fluid on dam face

Fig. 18 Volume fraction of dam at **a** 0.3 s, **b** 1.2 s, **c** 1.9 s
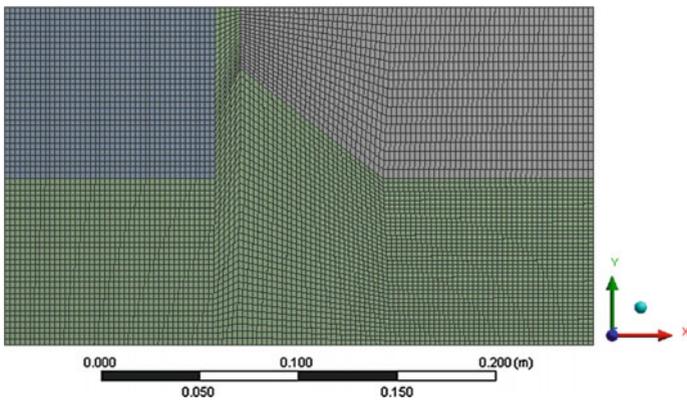

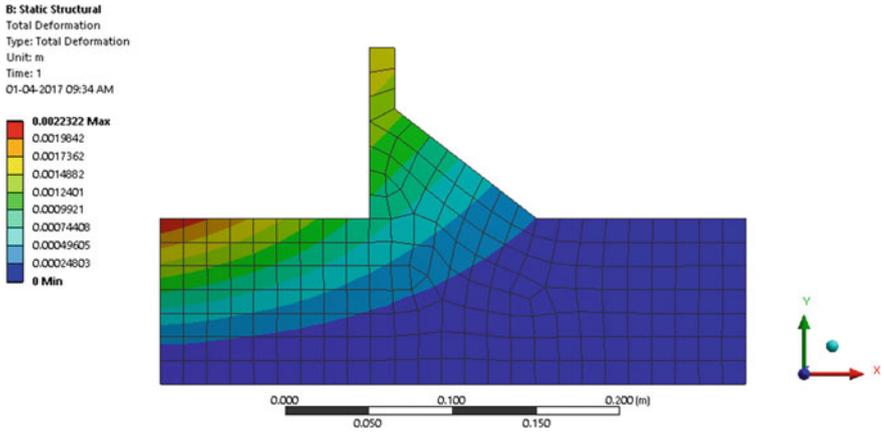**Fig. 19** Meshed model of the dam foundation reservoir system in workbench

Fig. 20 Maximum deflection of the dam
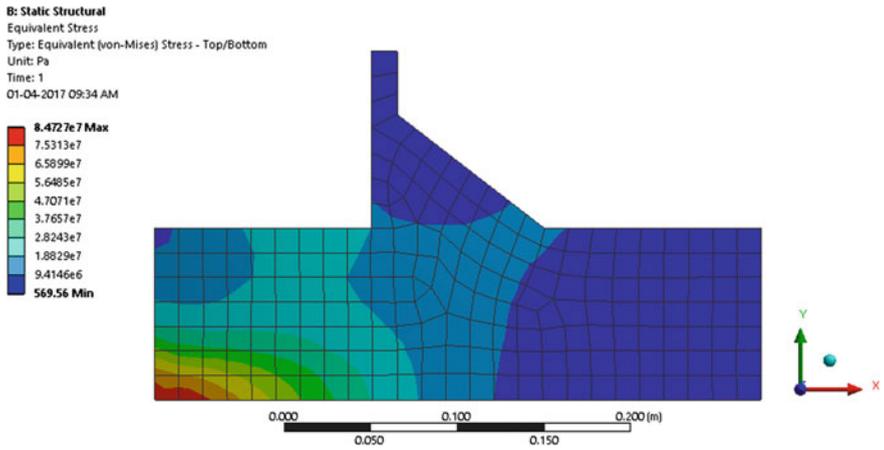

Fig. 21 Equivalent stress of the dam

when the sinusoidal hydrostatic pressure was applied was found to be 2.23 mm, and the maximum equivalent stress was 84.72 N/mm^2. Figure 19 shows the meshed model of the dam–foundation–reservoir system when mapped to the workbench by structural coupling. Figures 20 and 21 show the deflection and the stresses obtained after the analysis.

5 Conclusion

The time period of the dam with foundation was found to be higher than that of the dam with fixed base, which is due to the reduction in the stiffness and an increase in the mass of the vibrating system which decreases the natural frequency. The displacements and the stresses have increased when the flexibility of the foundation is incorporated in the analysis. Hence, it is advisable to carry out the interaction analysis for massive structures since there is a limitation of plane strain model. It is observed that the neck portion of the dam is the most severely stressed zone; hence, the cracks are expected to occur around the neck region of the dam. As the structural response is remarkably affected by the characteristics of the reservoir water and the surrounding foundation, the dam is modelled as a fluid–foundation–structure interaction problem. The methodology for the study of sloshing of the dam is validated by executing the problem in tank. Based on this study, on the tank with and without fluid–structure interaction effect the following conclusions were obtained. It was observed that there is a large increase in the hydrostatic pressure of the tank with FSI. The accurate results were obtained while fluid–structure interaction is considered. The same methodology was adopted for finding the sloshing effect of dam, and the deflection and the stresses were calculated.

References

1. Agarwal, P., Singh, B.: Seismic response of high concrete gravity dam including dam-reservoir-foundation interaction effect. J. South Asia Disaster Stud. **2**, 41–57 (2009)
2. Bakenaz, A.Z.: Hydrodynamic analysis of concrete gravity dams subjected to ground motion. In: 9th Symposium of ICOLD European Club, vol. 11, pp. 10–12 (2013)
3. Burman, A., Nayak, P., Agrawal, P., Maity, D.: Coupled gravity dam–foundation analysis using a simplified direct method of soil–structure interaction. Soil Dyn. Earthq. Eng. **34**, 62–68 (2012)
4. Bycroft, G.N., Mork, P.N.: Seismic response of dam with soil structure interaction. J. Eng. Mech. **9**, 113–295 (2006)
5. Chopra, A.K., Chakrabarty, P.: Earthquake analysis of concrete gravity dams including dam-fluid-foundation rock interaction. Earthq. Eng. Struct. Dyn. **9**, 363–383 (1981)

Development of Gutenberg–Richter Recurrence Relationship Using Earthquake Data

Shivamanth Angadi, Apurva Hiravennavar, Mayank K. Desai, Chandresh H. Solanki and Goudappa R. Dodagoudar

1 Introduction

The earthquake catalogue is a fundamental aspect of the seismic hazard study, but it also represents an important instrument to study the seismicity of a region. The catalogue should be composite, homogeneous and well-defined obtained from a merger of all the available databases in a consistent framework. The seismicity of each seismogenic zone is then quantified by the standard Gutenberg–Richter recurrence relation [3] defined by an Eq. 1:

$$\log(\lambda m) = a - bm \tag{1}$$

where λm is the mean annual rate of exceedance of magnitude m, 'a' and 'b' are the constants specific to the source zone, and these can be estimated by a least square regression analysis of the past seismicity data.

S. Angadi (✉) · M. K. Desai · C. H. Solanki
Applied Mechanics Department, S V National Institute of Technology, Surat 395007, Gujarat, India
e-mail: shiva05cv@gmail.com

M. K. Desai
e-mail: dmayank@gmail.com

C. H. Solanki
e-mail: chndresh1968@yahoo.co.in

A. Hiravennavar
Civil Engineering Department, BMIET, Surat 395007, India
e-mail: apurva7812@gmail.com

G. R. Dodagoudar
Department of Civil Engineering, IIT Madras, Chennai 360006, India
e-mail: goudar@iitm.ac.in

An important problem in defining a recurrence relation is ensuring completeness. Fitting the GR relation to incomplete data at the lower end will flatten the slope of the line which leads to an inflated estimate of the occurrence of large earthquakes [4, 5]. Because of the long recurrence time, the historical record may be too short to ensure completeness in the large earthquake range. It is imperative that any data used to establish occurrence rates of earthquakes should be complete for the time period under consideration for each magnitude range. The recurrence plot is obtained by plotting the logarithmic value of the cumulative annual rate of earthquakes greater than given magnitude versus the magnitude. The annual rate of occurrence of different magnitude classes is obtained by dividing the number of earthquakes by the completeness period of the particular, magnitude class. The seismicity parameters, λm_0 and β, are estimated using the completeness period evaluated by both Stepp's and CUVI methods. The completeness interval for any given magnitude or intensity should be equal to or longer than the intervals for smaller earthquakes, because larger shocks affect larger areas and are more likely to be reported and documented in the earlier years. Availability of earthquake data in the Gujarat region is very less (only 384 records for 197 years and magnitude ≥ 3.0 are observed). Completeness analyses have been performed by visual cumulative (CUVI) method formulated and Stepp's method [1, 2]. In the present study, different magnitude classes are adopted to estimate the period of completeness of the catalogue.

2 Preparation of Earthquake Catalogue

Past available earthquake events in India are not properly arranged, and it is necessary to do the proper manner for the estimate seismic hazard analysis. Earthquake data were collected between the intervals of 1819–2015, and data was collected from various sources like International Seismological Centre [6] Institute of Seismological Research (ISR), Gandhinagar [7], Gujarat, United States Geological Survey (USGS) [8], India Meteorological Department (IMD) [9] earthquake report. Proper care was taken to avoid the repetition of events in the catalogue and also converted the data values into moment magnitude (M_w) scale. In this present study, to do declustering and completeness analysis of magnitude two main methods have been used. The first method is visual cumulative interpretation (CUVI) method, and it is also known as graphical technique and second is Stepp's method.

3 Declustering of Earthquake Catalogue

An initial earthquake catalogue contains sub-catalogues from various recognized international and local seismological reporting agencies and historical documents of past earthquake. An earthquake of consequence is never an isolated event.

Declustering is the process of removal of dependent earthquake events (foreshocks and aftershocks) from an earthquake catalogue. Earthquake events are random and memory less, and therefore foreshocks and aftershocks to be removed from the earthquake catalogue. A larger shock is likely to be preceded and followed by a few smaller shocks called foreshocks and aftershocks, respectively. The aftershocks gradually decrease in frequency and magnitude. The foreshocks and aftershocks are expected to occur in the same epicentre area, and are, generally, associated with the same fault system of the main shock.

3.1 Histogram of Data Collection

About more than 400 earthquake events were collected, after declustering process with the minimum magnitude of 3.0 and maximum ≥ 7. The data set events between magnitude 3–4 M, 4–5 M, 5–6 M, 6–7 M and greater than 7, and the number of each earthquakes represented in histogram of each decade is as shown in Fig. 1.

4 Different Methods of Completeness Process

4.1 Visual Cumulative Interception Method

The visual cumulative method is a simple graphical procedure based on the observation that if earthquakes of a given magnitude are assumed to follow a
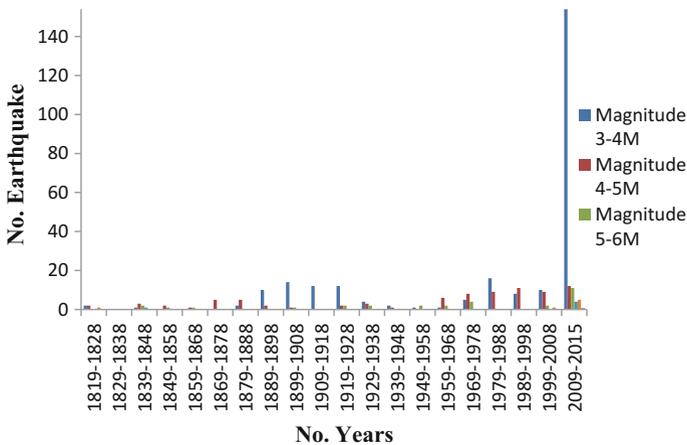

Fig. 1 Histogram of earthquakes in Gujarat, WI region

stationary occurrence process, in a complete earthquake catalogue, the average rate of occurrence of seismic events must be a constant. The procedure involves developing plots of the cumulative number of events versus the time from the beginning of the catalogue for different earthquake magnitude classes. The period of completeness for a given class is considered to begin from the earliest time when the slope of the fitting curve can be approximated by a straight line.

In visual cumulative (CUVI) method, the cumulative number of earthquakes is plotted against the year of earthquake occurrence for four magnitude bins (classes) ($3 \leq M_w < 4$, $4 \leq M_w < 5$, $5 \leq M_w < 6$, $6 \leq M_w < 7$ and $7 \leq M_w$). For a given magnitude class, the period of completeness is considered to begin at the earliest time when the slope of the fitting curve can be well approximated by a straight line [10]. The whole catalogue can be considered complete over the entire period of the catalogue for the largest magnitude class ($M_w \geq 7$). Figure 2 illustrates the results of the completeness analysis performed for the four magnitude classes.

4.2 Stepp's Method

To minimize the effect of incompleteness, introduced an empirical and statistically simple method based on the stability of the magnitude recurrence rate. This is an analytical method for finding the regional recurrence based on incomplete catalogue and developed [1, 2] as reported in [11]. This method assumes the earthquake occurrence as a Poisson distribution, and its standard deviation is expressed as

$$\chi = \frac{1}{R'} \sum_{i=1}^{R'} x_i \qquad (2)$$

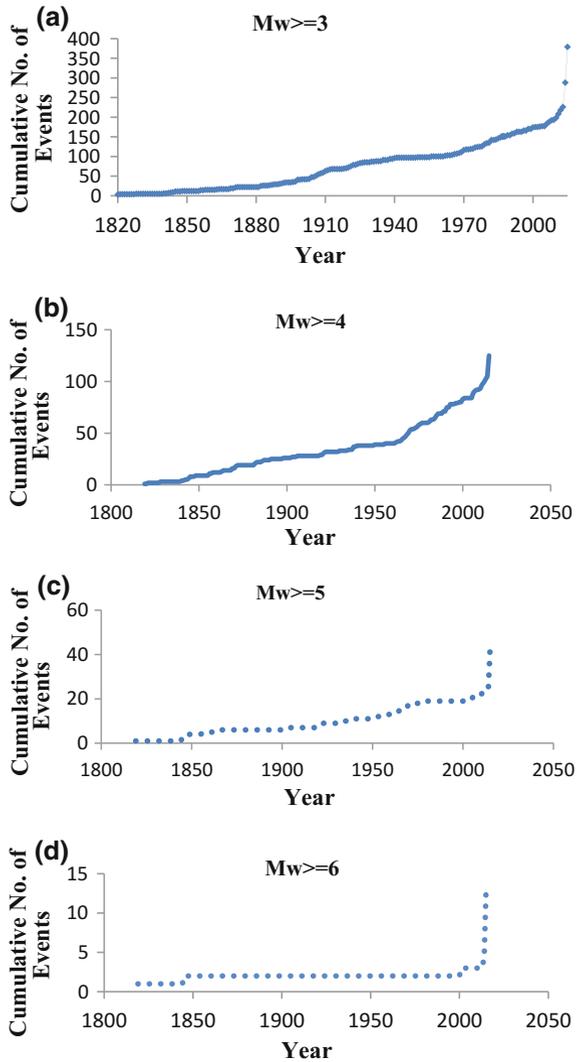and its variance is

$$\sigma_\chi^2 = \frac{\chi}{T} \qquad (3)$$

where

R' is the number of intervals,

χ is the average rate of occurrence in the period T.

Here the occurrence of earthquake is assumed to follow a Poisson distribution [1].

Fig. 2 CUVI method for catalogue completeness

5 Developed Frequency–Magnitude Recurrence Relationship

A core element in the assessment of seismic hazard in the conventional method is the estimation of the recurrence intervals of earthquakes of different magnitudes. Table 1 shows completeness year and period with the different range of magnitude. Stepp's and cumulative annual rates of occurrence of earthquakes are also tabulated

Table 1 Comparing of Gutenberg–Richter recurrence using Stepp's and CUVI methods

Magnitude range	Stepp's method		CUVI method	
	Completeness period (years)	$\log(\lambda m)$	Completeness period (years)	$\log(\lambda m)$
$3 \leq M_\mathrm{w} < 4$	60	0.5119	46	0.623
$4 \leq M_\mathrm{w} < 5$	40	0.0414	54	0.008
$5 \leq M_\mathrm{w} < 6$	130	−0.6990	82	−0.516
$6 \leq M_\mathrm{w} < 7$	150	−1.5740	172	−1.537

for different magnitude classes which are $3 \leq M_\mathrm{w} < 4$, $4 \leq M_\mathrm{w} < 5$, $5 \leq M_\mathrm{w} < 6$ and $6 \leq M_\mathrm{w} < 7$. The derived Eqs. 4 and 5 are perfectly matched and graphically fitted in Fig. 3 with each other from collected earthquake catalogue for the study region.

$$\text{CUVI,} \quad y = -0.570x + 2.564 \tag{4}$$

$$\text{STEPP's,} \quad y = -0.553x + 2.411 \tag{5}$$

The differences in the frequency–magnitude recurrence relationship are at source zones can be appreciated better, with *a* and *b* parameters from Eqs. 4 and 5.

The completeness period of Stepp's and cumulative annual rates of occurrence of earthquakes of the different magnitude classes are $3 \leq M_\mathrm{w} < 4$, $4 \leq M_\mathrm{w} < 5$, $5 \leq M_\mathrm{w} < 6$ and $6 \leq M_\mathrm{w} < 7$, respectively. Table 1 gives the comparison of completeness analysis as per Gutenberg–Richter recurrence using Stepp's and CUVI methods for the given range of earthquake catalogue.
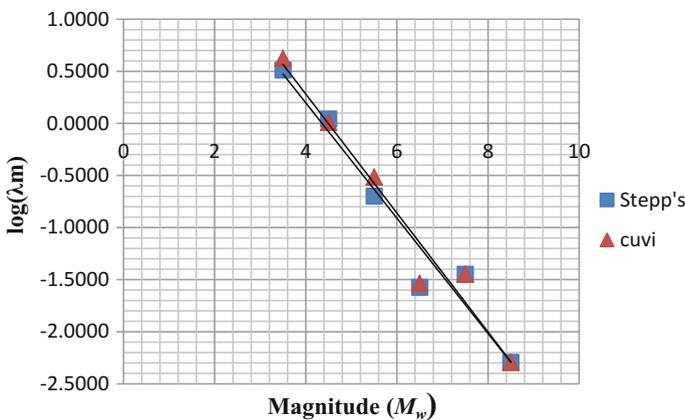

Fig. 3 GR recurrence relationships for Western India region using both Stepp's and CUVI method

Table 2 Comparison of *a* and *b* values with previous studies

Authors	Geographical area	Seismicity parameters		Data analysed for a period (years)
		a	*b*	
Ram and Rathore [12]	Entire PI	5.3	0.81	70
Jaiswal and Sinha [13]	Entire PI	4.21	0.92	160 (1842–2002)
Vipin et al. (2009)	South India	4.58	0.891	186 (1820–2006)
Lai et al. (2009)	250 km around Kanchipuram		1.26	501 (1507 –2008)
Raghu Kanth [14]	300 km around Chennai		1.06	417 (1591–2008)
Menon et al. [15]	Southern PI	5.05	1.13	501 (1507–2008)
Present Study (2016)	Western India	2.5	0.57	400 (1819–2016)

6 Conclusion

Catalogue completeness has been checked with visual cumulative method (CUVI) with magnitude–frequency diagrams. There is underreporting of the lower magnitude earthquake in the earlier periods of the 197 years earthquake catalogue compared to recent ones. The completeness analysis shows that the catalogue is complete for whole period for larger magnitude ≥ 7 Mb. Earthquakes having magnitude range 6–7, 5–6, 4–5 and 3–4 Mb may be considered to be completely recorded since 1819–2016. The seismicity parameters obtained from the present study for the Gujarat region, Western India, are compared with the previous studies (Table 2). Here the values have been compared with those that have been obtained for eastern India, Central India, Gujarat and entire Peninsular India. The Gutenberg–Richter (GR) parameters '*a*' and '*b*' obtained for Gujarat, Western India, are 2.5 and 0.57, respectively, and these results are compared with various researcher studied in India.

References

1. Stepp, J.C.: Analysis of completeness of the earthquake sample in the Puget sound area and its effect on statistical estimates of earthquake hazard. In: Proceedings of the International Conference on Microzonation, Seattle, USA, vol. 2, 897–909 (1972)
2. Stepp, J.C.: Analysis of completeness of the earthquake sample in the Puget sound area. In: S. T. Harding, (Ed.), Contributions to Seismic Zoning, NOAA Technical Report ERL 267-ESL 30 (1974)
3. Gutenberg, B., Richter, C.F.: Seismicity of the Earth and Related Phenomena. Princeton University Press, Princeton, New Jersey (1954)
4. Angadi, S., Desai, M.K., Huded, P.M., Chatra, A., Dodagouder, G.R.: Review on Variation of Seismic Hazard Parameters at Different Places of India, Indian Geotechnical Conference (IGC2016). IITM, Madras (2016)
5. Cornell, C.A.: Engineering seismic risk analysis. Bull. Seismol. Soc. Am. **58**, 1583–1606 (1968)

6. International Seismological Centre, U.K. http://www.isc.ac.uk/
7. ISR—Institute of Seismological Research (ISR), Gandhinagar, Gujarat. https://isr.gujarat.gov.in/
8. United States Geological Survey (USGS), National Earthquake Information Centre. https://www.usgs.gov/
9. India Meteorological Department, New Delhi, India. http://www.imd.gov.in/
10. Lai, C.G., Menon, A., Ornthammarath, T., Corigliano, M., Lizarraga, H.S., Dodagoudar, G.R.: Probabilistic seismic hazard assessment and stochastic site response analysis at the archaeological site of kancheepuram in Southern India. Research Report No. EUCENTRE-2009/01, University of Pavia, Pavia, Italy (2009)
11. Kijko, A., Sellevoll, M.A.: Estimation of earthquake hazard parameters from incomplete data files. Part I. Utilization of extreme and complete catalogs with different threshold magnitudes. Bull. Seismol. Soc. Am. **79**(3), 645–654. https://doi.org/10.1007/BF02602678 (1989)
12. Ram, A., Rathore, H.S.: On frequency magnitude and energy of significant Indian earthquakes. Pure Appl. Geophys. **79**, 64–70 (1970)
13. Jaiswal, K., Sinha, R.: Probabilistic seismic-hazard estimation for Peninsular India. Bull. Seismol. Soc. Am. **97**, 318–330 (2007)
14. Raghu Kanth, S.T.G.: Estimation of seismic hazard parameters for India. Seismol. Res. Lett. **81**(2), 207–217 (2010)
15. Menon, A., Ornthammarath, T., Corigliano, M., Lai, C.G.: Probabilistic seismic hazard macrozonation of Tamil Nadu in Southern India. Bull. Seismol. Soc. Am. **100**, 1320–1341 (2010)
16. Vipin, K.S., Anbazhagan, P., Sitharam, T.G.: Estimation of peak ground acceleration and spectral acceleration for south india with local site effects: probabilistic approach. Nat. Hazards Earth Syst. Sci. **9**, 865–878 (2009)
17. Shukla, J., Choudhury, D.: Seismic hazard and site-specific ground motion for typical ports of Gujarat. Nat. Hazards 60(2), 541-565 (2011). (ISSN: 0921-030X, Impact Factor: 1.529/2011) Springer, Netherlands
18. Rao, B.R., Rao, P.S.: Historical seismicity of peninsular india. Bulletin Seismol. Soc. Am. 74, 2519-2533 (1984)

Part VI
Recycling, Sanitation and Life Cycle Analysis

Elimination of Toxic Heavy Metals from Aqueous Systems Using Potential Biosorbents: A Review

S. Rangabhashiyam, R. Jayabalan, M. Asok Rajkumar and P. Balasubramanian

1 Introduction

The growing concern of environmental pollutions and their associated toxicity effects is major problem faced by the today's world. The emerging pollutants impose serious health issue and environmental damages. The contamination of water bodies due to the higher presence of inorganic pollutants in the form of heavy metal is one of the important challenges for the researchers [1, 2]. Heavy metals ions mostly have a density of greater than 5 g/cm^3 and atomic weights in the range of 63.5–200.6 [3]. Heavy metal ions reported as the precedence pollutants than the other water pollutants since heavy metal ions are highly mobile in the water ecosystems and not biodegradable, resultant in continual occurrence in the environment [4]. The generalized categories of the Heavy metals [5] are mentioned in Fig. 1.

The reasons for the heavy metals pollution in water streams are due to heavy metals in earth's crust that undergoes solubilization in groundwater, which occurs through natural phenomena and soil pH. Besides natural process, the anthropogenic

S. Rangabhashiyam (✉) · P. Balasubramanian (✉)
Department of Biotechnology & Medical Engineering, NIT Rourkela, Odisha, India
e-mail: rambhashiyam@gmail.com

P. Balasubramanian
e-mail: biobala@nitrkl.ac.in

R. Jayabalan
Department of Life Science, NIT Rourkela, Odisha, India

M. Asok Rajkumar
Dean—R&D, Gnanamani College of Technology, Namakkal, Tamil Nadu, India
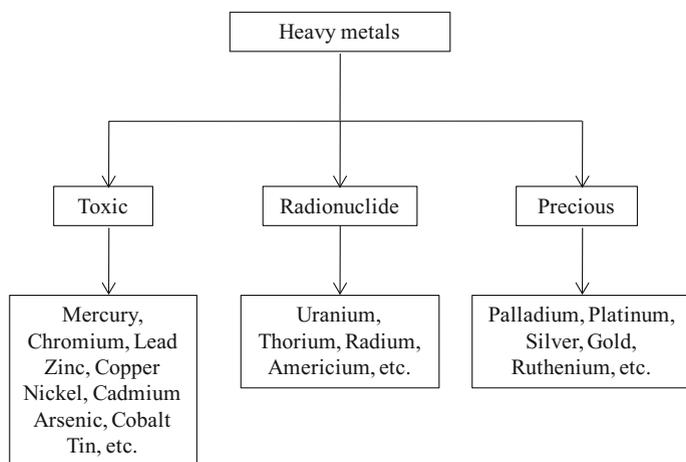
Fig. 1 Outline classification of heavy metals

activities resultants such as sewage, leachate sourced from mine tailings and landfill, liquid wastes clearance deep well, industrial lagoons wastes seepage, spills, leaks from industry and untreated or partially treated industrial effluents [6, 7]. The discharge of untreated industrial effluent acts as the most important cause for the pollution of water bodies. The wastewater is generated due the various industrial operations at different stages. The industrial sectors associated with the activities of fabrication, mining, paper and pulp, electroplating, textile, metal finishing, painting and printing, fertilizer production and batteries contribute in the metal augmented effluent streams [8, 9].

Disaster tragedy because of the toxic heavy metals pollution in water bodies is reported with Minamata disease, a neurological syndrome caused due to severe methyl mercury poisoning in Japan and Itai-Itai disease due to cadmium pollution in the river of Jintsu in Japan [10, 11]. The potential hazardous health effects due to the different toxic heavy metals in human systems [12] are presented in Fig. 2. Every toxic heavy metal exposure is linked with the property of harmful effects even at its low concentration. Therefore, various regulatory bodies prescribed the maximum allowable limit for the toxic heavy metal discharge from treated effluent into the environment. Table 1 represents the maximum permissible levels for some of the toxic heavy metals according to the World Health Organization (WHO), US Environmental Protection Agency (USEPA) and European Environment Agency (EEA) [13–15].
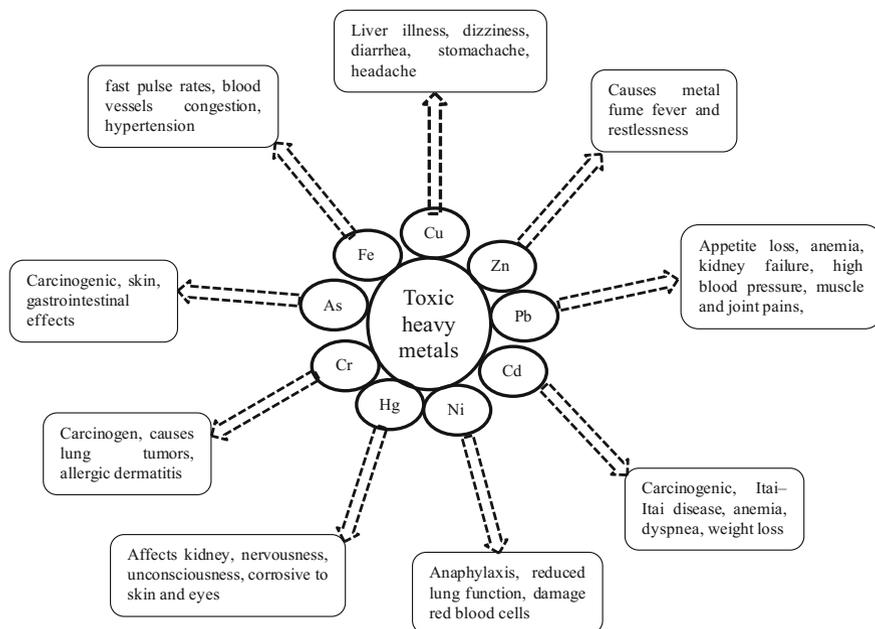
Fig. 2 Potential health effects due to toxic heavy metals

Table 1 Maximum permissible limit of some toxic heavy metals in drinking water

Toxic heavy metal	Maximum permissible limit (mg/L)		
	WHO	USEPA	EEA
Arsenic	0.01	0.01	0.01
Cadmium	0.005	0.005	0.005
Copper	1.0	1.3	–
Chromium	0.05	0.1	0.05
Lead	0.005	0.015	0.1
Mercury	0.001	0.002	0.001
Nickel	–	0.04	–
Zinc	5.0	5.0	–

2 Conventional Treatment Technologies and Biosorption

Considering the toxicity effects of heavy metals in the industrial effluents, in the recent years, there received lots of attention by researchers for the heavy metal sequestrations. The commonly used conventional methods for the removal of heavy metal ions are extraction, ion-exchange, filtration, flocculation, photocatalysis, precipitation, electrochemical treatments, etc. [16–18]. Each method is unique with their own merits and demerits (Table 2). Mostly, the conventional methods are

Table 2 Comparison of treatment technologies for the removal of heavy metals from aqueous streams

Technology	Advantages	Disadvantages
Coagulation and flocculation	Sludge production with good settling and dewatering characteristics	High cost investments for chemicals usage and higher sludge volume generation
Chemical precipitation	Simple process and requires only low capital cost investment	High maintenance costs for disposal of sludge, unsuccessful for removal of effluent with lower concentration of heavy metals
Membrane filtration	Requires less chemicals, operates at low pressure, occupies smaller space and high selective process	High cost investment needed for operation as well as for maintenance, causes membrane fouling and complex process
Flotation	Higher removal efficiency, low detention periods and more selective towards the metal removal	Requires high maintenance and operation cost
Photocatalysis	The process suitable for the simultaneous removal of metal, organic pollutant and associated with the formation of less by-products only	Limited applications and requires longer duration time
Ion-exchange	Highly selective for metal removal, large treatment capacity, more removal efficiency and fast kinetics	Higher cost of synthetic resins and limited pH tolerance
Electrochemical treatment	Free from the chemical requirements, metal selective and more efficient for metal removal	Need high initial cost investment and requires high electrical supply
Adsorption using activated carbon	Higher removal capacity, fast kinetics, higher removal efficiency and simple operation	Higher cost of activated carbon

costly, require chemicals, ineffective at low concentrations, waste sludge generation, etc. Recently, more consideration paid on working with non-conventional methods for the treatment of heavy metals.

3 Biosorption Technology

The process of biosorption is performed using biomass, which is inactive or even dead. The sources of biosorbents are from the dead biomass of bacteria, algae, fungi or in the form of waste biomass from industrial operations, the lignocellulosic biomass residues, etc. The biosorption technology has gained significant credibility in the recent years. The use of dead biomass offers the advantages of its usage even at the higher toxic metal concentrations can be subjected to adverse process conditions, free from the growth media requirements and possibilities of biomass
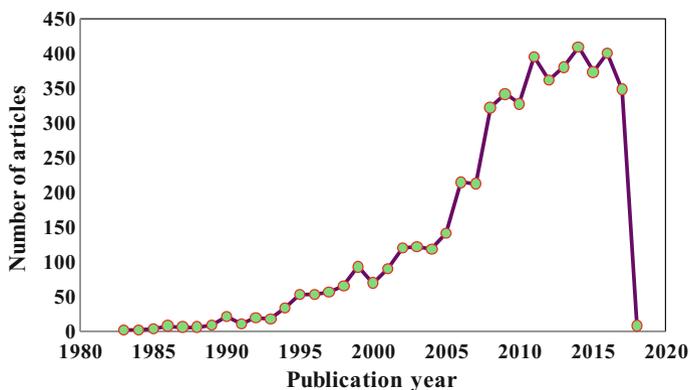
Fig. 3 Number of publications in the research area of metal biosorption

regenerations [19, 20]. The process of the heavy metal removal by the biosorbent from the aqueous solutions will be influenced by different physical and chemical factors, which will control the biosorption capacity and removal efficiency. In this regard, assessments of the biosorption parameters on the metal removal process are very essential. The batch operation of the biosorption process for the sequestration of heavy metals needs to consider the significant parameters such as initial pH, initial metal ions concentration, biosorbent dosage, size of the biosorbent, agitation speed, temperature and presence of coexisting ions (binary, ternary or multi-component system) [21]. In the present review, the biosorbents prepared from the dead microbial and lignocellulosic source are considered for the discussion. The articles published details extracted from the Scopus search using the key words metal biosorption which are illustrated in Fig. 3. Most of the articles reported on the toxic heavy metal removal using the microbial and lignocellulosic biomass residues.

4 Isotherm and Kinetic Models of Biosorption

The model expressions of the biosorption isotherm are used to understand the interactive behaviour between biosorbent and metal at constant temperature and equilibrium solute concentration. The isotherm models are significant to analyse the biosorption mechanism. The isotherm models optimize the biosorbent use through the estimation of biosorbent amount required to uptake determined concentration of metal from the aqueous solution. Moreover, it is useful in the prediction of distribution of biosorption sites and metal ions biosorbed on the biomass surface. Different equilibrium biosorption isotherm models have been employed for the biosorption investigation of heavy metals. Based on the parameters in the isotherm

Table 3 Nonlinear forms of the biosorption isotherm models

Biosorption isotherm models	Equations
Langmuir	$q_e = \frac{Q_0 K_L C_e}{1 + K_L C_e}$
Freundlich	$q_e = K_f C_e^{\frac{1}{n}}$
Temkin	$q_e = \frac{RT}{B} \ln(A_T C_e)$
Jovanovic	$q_e = q_{mj}\left(1 - e^{(K_j C_e)}\right)$
Fowler–Guggenheim	$K_{FG} C_e = \frac{\theta_{FG}}{1 - \theta_{FG}} \exp\left(\frac{2\theta_{FG} W}{RT}\right)$
Kiselev	$k_{1_K} C_e = \frac{\theta_K}{(1 - \theta_K)(1 + k_n \theta_K)}$
Halsey	$q_e = \exp\left(\frac{\ln K_H - \ln C_e}{n_H}\right)$
Harkin–Jura	$q_e = \left(\frac{A_H}{B_2 - \log C_e}\right)^{1/2}$
Redlich–Peterson	$q_e = \frac{K_{RP} C_e}{1 + a_{RP} C_e^g}$
Khan	$q_e = \frac{q_s b_K C_e}{(1 + b_K C_e)^{n_K}}$
Koble–Corrigan	$q_e = \frac{A_{KC} C_e^n}{1 + B_{KC} C_e^n}$
Sips	$q_e = \frac{q_{ms} K_S C_e^{m_s}}{1 + K_s C_e^{m_s}}$

Table 4 Kinetic models for the metal biosorption studies

Biosorption kinetic models	Equations
Pseudo-first-order	$\log(q_e - q_t) = \log q_e - \frac{k_1}{2.303} t$
Pseudo-second-order	$\frac{t}{q_t} = \frac{1}{k_2 q_e^2} + \frac{t}{q_e}$
Elovich	$q_t = \frac{1}{\beta} \ln(\alpha\beta) + \frac{1}{\beta} \ln t$
Ritchie's	$\frac{1}{q_t} = \frac{1}{k_R q_e t} + \frac{1}{q_e}$
Intra-particle diffusion	$q_t = k_{id} \sqrt{t} + I$

expression, the models are classified into two, three, four and five, respectively [22]. The nonlinear equations of biosorption isotherm models are represented in Table 3.

The biosorption kinetic models are significant in determining the rate-controlling steps of the metal removal process such as metal transport and physicochemical interactions. The investigation of the biosorption kinetic models is significant for heavy metal removal studies, since it provides vital information's on the dynamics of the biosorption process, reaction pathways and associated mechanisms. The findings of heavy metal biosorption rate are important to calculate the biosorbent residence time in the aqueous solution and important in the design of suitable biosorption process conditions. In a biosorption process, the transfer of heavy metal ions is characterized by either boundary layer diffusion or intra-particle diffusion, otherwise both. The different kinetic models [23, 24] used in the biosorption study are presented in Table 4.

5 Dead Microbial Biomass for Heavy Metal Biosorption

The biosorbents from the non-living microbial source tend to interact with the heavy metals by binding and concentrate them even at a very low concentration of the metal solution. The microbial dead biomass from algae, fungi and bacteria is widely used for the removal of heavy metals from the aqueous solutions as well as from the industrial effluent containing toxic heavy metals. The biosorption capacity of the different dead microbial towards the removal of toxic heavy metals from the aqueous solutions is summarized in Table 5.

Table 5 Biosorbents for the removal of heavy metals from aqueous solutions

Biosorbent	Heavy metal	Biosorption capacity (mg/g)	References
Microalgae			
Fucusspiralis	Cd(II)	64	[63]
Desmodesmuspleiomorphus	Cd(II)	47.1	[64]
Spirulinaplatensis	Zn(II)	30.96	[65]
Isochrysisgalbana	Cr(III)	335.27	[66]
Chlorella vulgaris	Cr(VI)	161.41	[67]
Scenedesmusobliquus	Zn(II)	330	[68]
Chlorella vulgaris	Pb(II)	169	[69]
Bacteria			
Bacillus megaterium	Cr(VI)	30.7	[70]
Bacillus firmus	Cu(II)	381	[71]
Paenibacilluspolymyxa	Cu(II)	112	[72]
Bacillus circulans	Cd(II)	26.5	[73]
Pseudomonas fluorescens	Hg(II)	72.3	[74]
Alcaligenes sp.	Pb(II)	66.7	[75]
Pseudomonas aeruginosa	Pb(II)	110	[76]
Fungi			
Rhodotorulaglutinis	Pb(II)	75.5	[77]
Aspergillusfoetidus	Cr(VI)	2.0	[78]
Polyporousversicolor	Pb(II)	57.5	[79]
Aspergillusflavus	Cu(II)	20.75	[80]
Rhizopusoryzae	Co(II)	13.56	[81]
Candida utilis	Zn(II)	181.7	[82]
Rhizopusoligosporus	Ni(II)	116	[83]
Plant biomass residue			
Grape stalk	Ni(II)	18.1	[84]
Posidoniaoceanica	Cu(II)	76.92	[85]
Ananascomosus peel	Cd(II)	18.21	[86]
Anna Witek-Krowiak	Cu(II)	30.22	[87]
Cocoa pod husk	Zn(II)	14.07	[88]
Tobacco dust	Pb(II)	39.6	[89]
Hydrillaverticillata	Cr(VI)	29.43	[90]

5.1 Algae

The biomass of *Microcystisnovacekii* is tested for the removal of Pb(II) ions from aqueous solutions. The equilibrium data of the biosorption experiments are better described by the Langmuir model compared to the Freundlich isotherm. The analysis of the Potentiometric titrations indicated the presence of negative surface charge with two acidic groups. The FT-IR characterization of the lead loaded biosorbent suggested the functional groups, amide and carboxyl involved in the lead biosorption [25]. The methylated biomass of *Spirulinaplatensis* is utilized for the removal for Cr(VI) and compared with the native biomass. The pretreated biomass presented higher performance with more than 80% removal efficiency. The methylation of *Spirulinaplatensis* biomass favored methyl esters formation, decreased the carboxylate functional group and favored the adsorption of chromate ions [26]. The biosorption investigation of *Spirulinaplatensis* and *Chlorella vulgaris* towards the removal of Ni(II), Zn(II) and Pb(II) was reported. The biosorption process is significantly influenced by the parameter of initial metal ions concentration. The biomass of *C. vulgaris* showed better biosorption towards the heavy metals than the *Spirulinaplatensis*. The pseudo-second-order kinetic model best fitted the experimental data. The analysis of FT-IR results showed carboxylate functional groups contributed in coordination/ionic exchange of bivalent ions, hydroxyl, amino and amide group involvement. The values of pH_{zpc} for the biosorbent *Spirulinaplatensis* and *C. vulgaris* are calculated as 4.0 and 3.4 [27]. Metal biosorption in binary and ternary systems was examined for the metal ions Ni (II), Zn(II) and Pb(II) using *Spirulinaplatensis* and *C. vulgaris*. The results of the separation factor represent that both the biosorbents have affinity towards the metal in the order of Pb(II) > Zn(II) > Ni(II). *C. vulgaris* behaved as better biosorbent because of higher equilibrium sorption capacities (q_{eq}) and removal efficiencies (Y_R). The biosorption capacity of the biosorbents showed decreased effect in the binary and ternary systems compared to the single-metal biosorption system [28].

   To mechanistic removal of Cr(VI) from aqueous solution studied using *C. vulgaris*, the biosorption of Cr(VI) is mainly due to the amino and carboxyl functional groups; moreover, the removal performance increased with the increases of biomass protein content. The Cr(VI) reduced because of the presence of secondary alcohol groups on the biomass and Cr(III) binding with biomass by means of ion-exchange mechanism [29]. The biosorption capacity of *Scenedesmusobliquus* and *Desmodesmuspleiomorphus* towards the removal of Zn(II) and Cd(II) in single and binary systems was examined. The two microalgae are isolated from a heavy metal contaminated site in Northern Portugal. The simultaneous biosorptive uptake of Zn (II) and Cd(II) by *Scenedesmusobliquus* and *Desmodesmuspleiomorphus* was found lesser than the single-metal biosorption system. The native biosorbents are efficient for simultaneous removal of mixtures of Zn(II) and Cd(II) up to the initial concentration of 300 mg/L [30]. The biomass of *Chlorella sorokiniana* is immobilized using alginate and tested for the removal of Cu(II), Ni(II) and Cd(II) ions from drinking water. The maximum removal efficiency attained for the removal of Cu(II),

Ni(II) and Cd(II) was 97.10, 50.94 and 64.61%, respectively. The characterization of the metal-loaded biosorbent performed through EDS analysis confirmed the bonding of metal ions to the biosorbent. Apart from the single biosorption system, study performed on binary and multi-metal systems of Cu(II), Ni(II) and Cd(II). The removal of both Cd(II) and Ni(II) showed decreased affect in the presence of Cu(II) ions [31]. The strain of microalgae, *Micractiniumreisseri* KGE33, is immobilized using silica by means of sol–gel reaction. The de-oiled biomass residue from *M. reisseri K*GE33 is used as the source of biomass. Based on the use of algal dosage, the biosorbents are denoted as IMS 14, 70, and 100, respectively. The biosorbents were assessed for the removal of Cu(II) from the aqueous solutions. The value of the point of zero charge value for IMS100 is determined as 4.5. At the initial solution pH of 5.0, the biosorbent IMS 100 showed higher Cu(II) removal efficiency of 87.1%. The thermodynamic analysis revealed spontaneous and exothermic nature of biosorption process [32]. The application of biosorbent prepared using the dry biomass of *Scenedesmusquadricauda* is used towards the removal of Cd(II) and Pb (II) from simulated and real effluents. The metal removal from synthetic solutions attained equilibrium within 60 min. The regeneration of Cd(II), Pb(II)-loaded biosorbent is analysed using HNO_3. The biosorption efficiency of 65 and 69% is achieved for Cd(II) and Pb(II) removal from industrial effluent wastewater [33].

5.2 Bacteria

The bacterial strains of *Bacillus cereus* and *Bacillus pumilus* are assessed for the biosorption of Pb(II) in the batch system. The experimental data are best fitted with pseudo-second-order kinetics and Langmuir isotherm model. The maximum biosorption capacity of the biosorbents towards Pb(II) removal from aqueous solution occurred at the initial solution pH of 6.0 [34]. Biosorption of Cr(VI) is reported using four bacterial strains. The experimental conditions of initial Cr(VI) concentration range (350–450 mg/L) and 2.0 pH showed higher removal efficiency. The tested biosorbents, *Burkholderiacepacia* AL96Co, *Corynebacteriumkutscheri* FL108Hg, *Pseudomonas aeruginosa* CA207Ni and *Rhodococcus* sp. AL03Ni showed as suitable biosorbents for removal of Cr(VI) containing industrial wastewater [35]. The biosorbents from *Staphylococcus xylosus* and *Pseudomonas* sp. are used for the removal of Cd(II) and Cr(VI). The biosorption mechanisms are controlled by the factors of biosorbent surface functional groups and surface charge distribution on the biomass. The higher removal efficiency of greater than 88% denoted *Staphylococcus xylosus* and *Pseudomonas* sp. as potential biosorbents [36]. The Cd(II) removal using the biosorbent is prepared from *Exiguobacterium* sp. isolated near the mines of Okdong (Korea). The biosorption efficiency of greater than 95% Cd(II) removal was observed. The dead biomass for Cd(II) removal performance was similar to that of the living biomass [37]. The bacteria biomass of

Comamonastestosteroni, *Enterobacterludwigii* and *Zoogloearamigerais* is studied for the removal of Cu(II), Pb(II) using fixed and suspended biomass [38].

Biosorbent prepared from the chromium-resistant bacteria *B. cereus* is isolated from the samples collected from sewage treatment plant. The removal process of Cr (VI) is found highly pH dependent, and the optimum pH is determined as 2.0. The rate-controlling step for the Cr(VI) biosorption is found due to the external mass transfer. The bioremediation of Cr(VI) involves biosorption mechanism in addition to the bio-oxidation and bio-reduction [39]. The northeast regions of China containing wastewater are associated with the problem of lead contamination. The lead-tolerant *Pseudomonas* sp. I3 is isolated from Mohe wetland and examined for the lead removal potentials. The lead biosorption by the biosorbent is confirmed through TEM-EDS analyses. The characterization results of FT-IR showed the participation of different functional groups in the Pb(II) biosorption [40]. A mutation done by ultraviolet irradiation on *Bacillus subtilis* is employed for the biosorption of heavy metals in single and multi-component systems. Fast removal of the metal ions occurred at the initial period of the biosorption process, and kinetics of the process is better described by the pseudo-first-order kinetic model. The biosorption of Hg(II), Cd(II) and Pb(II) in the binary and ternary metal system showed decreased biosorption due to the presence of other metal ions, but the biosorption sites are distinct for every metal considered. The experiments represented higher biosorption capacity in the single-metal systems [41]. The biosorption properties of polysaccharide producing *Ochrobactrumanthropi* are isolated from activated sludge examined towards the removal of cadmium, copper and chromium from aqueous solution. The maximum removal is observed at the initial solution pH values of 2.0 (Cr(VI)), 8.0 (Cd(II)) and 3.0 (Cu(II)), respectively. The biosorption parameter, initial metal concentration influenced on the uptake of metal by the biomass. The fit of equilibrium data to the biosorption isotherm models is better explained by both Langmuir and Freundlich models [42].

5.3 Fungi

The biomass of filamentous fungus, *Cephalosporiumaphidicola* IMI 68689, is tested for the removal of Pb(II) from aqueous solution. The results of the initial solution pH showed the significant influence in the uptake capacity for Pb(II) removal using *Cephalosporiumaphidicola*. The reuse examinations performed up to the cycles of five biosorption–desorption and found only 5% loss of efficiency [43]. Fungi isolates such as *Aspergillus* and *Rhizopus* are evaluated for the biosorption of Cr and Cd(II) ions. The maximum removal of Cr and Cd(II) ions is observed at the initial metal concentration of 6 mM [44]. Biosorption potential of *Trichoderma* sp. BSCR02 is evaluated for the removal of chromium from aqueous solutions. The optimal biosorbent dosage of 1.4 mg/mL was used for the biosorption of 200 mg/L initial chromium concentration and 5.0 initial solution pH. The biosorbent is reused up to five cycles without any significant decrease in removal efficiency of

biosorbent [45]. Biosorbents prepared by growing fungal isolates *Aspergillusniger* and *Aspergillusterreus* on luffa sponge, and the biosorbents are used for the removal of Pb(II) from aqueous solutions. The FT-IR analysis of the biosorbents indicated the presence of –OH, –NH, and –CH$_3$ functional groups and their involvement in the Pb(II) removal process. The SEM characterization of the biosorbents showed the homogeneous occurrence of fungal biomass on the structure of luffa sponge, which provides more contact sites for interaction with the metal ions. The Pb(II) interacted biosorbent presented muddy deposits of Pb(II) ions, confirmed the biosorption of metal ions. The biosorbents from the *Aspergillusniger* and *Aspergillusterreus* showed removal efficiency of about 51% of Pb(II) from 250 mM lead solution [46]. Batch biosorption experiments are conducted using the biosorbent from jelly fungus *Auriculariapolytricha* and are studied for the removal of Cd(II), Cu(II) and Pb(II) from aqueous solutions. The higher desorption efficiency is attained using the eluting agents of 0.05 mol/L HNO$_3$ and regenerated biosorbent reused up to six cycles of biosorption studies. The biosorption equilibrium data better fitted with the isotherm of Freundlich and Dubinin–Radushkevich, revealed the biosorbent surface as heterogeneous and favored the chemisorption mechanism of the metal removal process. The functional groups in the biosorbent such as hydroxyl, amino, carboxyl, and phosphoryl are mainly contributed in the metal biosorption process. The removals of metal ions are associated with the predominant mechanisms of synergistic ion exchange and surface complexation [47].

The fungus *Rhizopus* sp. is immobilized onto the various textile materials and tested for the removal of Cu(II) ions. The immobilized biosorbents presented better removal efficiency by reducing the Cu(II) ions concentration from 20 to 3.1–5.6 mg/L within the contact time of 150 min. The biosorption system has the merit of usage as real product, since the biomass attached with the textile media is separable, feasible to roll up, foldable, etc., and moreover offers the replacement of exhausted biosorbents after sufficient contact time [48]. The potential of two strains *Yarrowialipolytica* NCIM 3589 and *Yarrowialipolytica* NCIM 3590 is evaluated for the removal of Ni(II) from aqueous solution. The optimal conditions established for the maximum Ni(II) biosorption are initial solution pH 7.5, initial Ni(II) concentration 1000 mg/L and temperature 35 °C, respectively. The better fit of the Dubinin-Radushkevich isotherm model indicated that the biosorption of Ni(II) was due to the ion-exchange mechanism. The FT-IR analysis results showed that functional groups such as hydroxyl, carboxyl, amino and carbonyl are involved in the Ni(II) biosorption. The biosorption of Ni(II) onto the biosorbents is confirmed through the analysis of SEM–EDS characterization [49]. Biosorbent prepared from the *Penicilliumjanthinellum* isolates from mine location in Balya (Turkey) and employed for the removal of Pb(II) and Ni(II) from aqueous solutions. The biosorption factors include initial solution pH, initial Pb(II), Ni(II) concentration, biosorbent dosage and contact time. In order to understand the interaction between the parameters, optimization is conducted using Box–Behnken design. The higher removal efficiency of 76 and 47% for both Pb(II) and Ni(II) was attained at the optimal conditions of pH 4.5 (for both metals), initial metal concentrations of

123 mg/L (Pb(II)), 33 mg/L (Ni(II)), contact times of 65 min ((Pb(II)), 89 min (Ni (II)) and biosorbent dosage of 0.2 g/L((Pb(II)), 1.6 g/L (Ni(II)), respectively [50]. The optimization technique of central composite face-centred design is subjected for the Pb(II) biosorption using biosorbent prepared from *Aspergillusterreus*. The parameters of agitation speed, initial solution pH, biosorbent dosage and temperature were considered for the optimization investigations. The results of the optimization study showed that the removal efficiency of Pb(II) is affected by individual parameter of initial solution pH, biosorbent dosage, and interactive parameters between initial solution pH and biosorbent dosage, initial solution pH and agitation speed, initial solution pH and temperature. The response surface of the optimization study is adequately described by the hierarchical quadratic model [51].

6 Lignocellulosic Biomass Residue for Heavy Metal Biosorption

The agro biomass residues such as almond shell, coconut shell, ground nut shell, *Tamarindusindica* seed and walnut shell are evaluated for the biosorption of Cr(VI) from aqueous solutions. In comparison of all the five biosorbents, the biosorbent prepared using the seed of *Tamarindusindica* showed higher performance towards the removal of Cr(VI). The biosorption of Cr(VI) using *Tamarindusindica* seed is decreased at the higher initial solution pH and is better at the higher temperature considered in the study. The biosorption of Cr(VI) is associated with the chemisorption mechanism [52]. The biomass of olive stones from the processing of olive oil industry is studied for the biosorption of Fe(II) from the industrial effluent. The characterisation of the biosorbent is done using mercuric porosimetry. The uptake capacity of the biosorbent was higher at the lower sorption capacity was higher at the lower biosorbent particle size. The removal efficiency of biosorbent attained 70% at the biosorbent dosage of 125 g/L [53]. The adsorptive removal of Pb(II) and Cd(II) is carried out using banana peel biomass. Compared to Pb(II) removal, the biosorbent presented more removal capacity towards Cd(II). The results of the Langmuir isotherm model revealed that 1.0 g of biosorbent is able to biosorb 5.71 mg of Cd(II) and 2.18 mg of Pb(II) in a separate batch biosorption system [54]. The waste biomass of *Citrus reticulata* is generated after juice extraction subjected for the different physical and chemical pretreatment. The prepared adsorbents potential is evaluated for the removal of Cr(III) and Cr(VI) removal from aqueous solution. The uptake capacity of the adsorbents depends on the structural changes of the biomass due to pretreatment and chromium oxidation state in the biosorption system. The maximum biosorption capacity of Cr(III) by H_2S modified biomass was 57.31 mg/g and Cr(VI) biosorption capacity of 51.68 mg/g by PEI + glutaraldehyde pretreated biomass [55].

Cadmium biosorption is carried out by using leaves and stem biomass portions of *Portulacaoleracea* without any pre-treatment. The maximum removal efficiency

of 72% is attained. Higher removal of Cd(II) is noticed up to 45 min and then gradually attained towards equilibrium around 100 min. The equilibrium biosorption data are better fitted with the isotherm models of both the Langmuir and Freundlich model equations [56]. The potential of *Barbulalambarenensis* biomass is evaluated for the biosorption of Pb(II) from aqueous solution. The optimum biosorption condition is established as 5.0 pH, contact time 60 min and temperature of 298 K. The FT-IR characterization results identified the presence of functional groups hydroxyl, carboxyl, carbonyl and amides involved in the Pb(II) biosorption [57]. The Cr(VI) removal is tested in a batch adsorption system using native and acids modified *Swieteniamahagoni* shells. The initial solution pH of the biosorption is mainly influenced on the Cr(VI) percentage removal. The thermodynamic analysis of the experiments represented spontaneous and endothermic nature of the Cr(VI) removal process. The coexisting ions has nil effect on the Cr(VI) adsorption process [58]. The biosorption of Pb(II) from synthetic and real effluent is reported using raw and immobilized biomass of *Mangiferaindica*. The native biomass of *Mangiferaindica* showed better Pb(II) removal efficiency compared to the compared to immobilized *Mangiferaindica* biomass [59]. The biomass of *Sterculiaguttata* shell in native and $ZnCl_2$ activated employed for Cr(VI) adsorption from aqueous solution. The $ZnCl_2$ modified biomass presented higher surface area. The values of the Langmuir separation factor indicated the favorability of Cr(VI) adsorption by both native and modified adsorbents. The regeneration of biosorbent and its effective reuse is favored using the desorbing agent of 2.0 M NaOH concentration [60]. Direct burning of rice husk is associated with the problem of air pollution in Cairo and Nile Delta region (Egypt). To combat the problem experiments conducted for the use of plentifully available agro-industrial waste rice husk for biosorption of Cu(II) from water. The results showed rice husk as the potential precursor offering technical, societal, economical and ecological advantages for subjecting the rice husk towards the treatment of industrial effluents containing copper [61]. Peanut hull biomass employed as biosorbent in the native form Cu(II) removal from aqueous solution. The optimum biosorption operating conditions of the batch systems were pH 4.0, 150 rpm agitation speed, 60 min contact time, 1.0 g biosorbent dosage, 150 mg/L initial Cu(II) concentration and biosorbent particle size of particle size <0.250 mm. The experimental data are better fitted with the pseudo-second-order and intra-particle diffusion kinetic models, revealing the Cu (II) removal mechanism associated with physical and chemical adsorption process [62].

7   Biosorbent Regenerations

In order to reuse the biosorbent for good number of recycles and for the safe disposal of the exhausted biosorbent, the process of biosorbent regeneration after the biosorption process is essential. The regeneration of the biosorbent could be possible using the desorption process with the employment of suitable eluting

agents. The selection criteria of eluents for the desorption process depend on the biosorbent mechanical stability, biosorptive mechanism between the metal ions and the biomass [91]. The regeneration of the biosorbent, recycle number and desorbing agents of the metal removal process is summarized in Table 6. The biosorbent from *Lepiotahystrix* is used for the removal of Cu(II) and Pb(II) from aqueous solutions. The desorption study is performed in a batch system using 20 mL of desorbing agents of 0.1 M EDTA and 0.1 M HCl, for the contact time of 60 min. The results of the metal ions desorption showed HCl with better removal than EDTA. Moreover, the involvement of ion-exchange mechanism might affect the process of desorption for complete metal ions removal [92]. After the biosorption of Zn(II) using *Chlorella pyrenoidosa*, the metal loaded biomass is subjected for regeneration using the desorbing eluents of EDTA, HCl, and HNO_3. The desorption analysis showed that 0.1 M of HNO_3 presented better desorption process of Zn(II) from the biosorbent with the desorption efficiency of 95% [93].

Table 6 Biosorbents regeneration using desorption method

Biosorbent	Heavy metal	Number of recycles	Desorbing agents	References
Microalgae				
Synechococcus sp.	Cd(II)	5	HCl	[97]
Chlorella miniata	Cr(III)	–	NaOH, HNO_3, H_2SO_4, EDTA, Deionized H_2O	[98]
Bacteria				
Tetraselmischuii	Cd(II)	–	EDTA	[99]
Bacillus laterosporus	Ni(II), Cd(II)	3	HCl, HNO_3 and H_2SO_4	[100]
Bacillus sp.	Cu(II)	5	HNO_3	[101]
Arthrobacter sp.	Pb(II)	–	$EDTANa_2$, NH_4NO_3 and H_2O	[102]
Fungi				
Pleurotusostreatus	Cu(II), Ni(II), Zn(II) and Cr(VI)	–	HCl	[103]
Aspergillusniger	Ni(II), Zn(II), Cr(VI)	–	HCl	[104]
Mucorracemosus	Cr(VI)	–	HCl, NaOH	[105]
Plant biomass residue				
Myriophyllumspicatum	Pb(II), Cu(II), Cd(II), Ni(II), Zn(II)	3	HNO_3	[106]
Sugarcane bagasse	Co(II), Cu(II), Ni(II)	–	HNO_3	[107]
Garden grass	Cu(II)	5	H_2SO_4	[108]

The biosorption experiments of Cu(II), Cd(II), Ni(II), Pb(II) and Zn(II) removal are performed using the NaOH-treated stem biomass of *Arundodonax*. Then, the metal-loaded biosorbent is subjected to desorption using 50 mL of 0.1 M HCl. The recycles of biosorption and desorption are performed up to 3 times. The desorption efficiency of greater than 88% is attained for the elution of Cu(II), Cd(II), Ni(II), Pb (II) and Zn(II) using 0.1 M HCl [94]. The biomass of the cashew nut shell is tested for the biosorption of Cd(II), Pb(II) and Cr(III) from contaminated water. The results of biosorbent regeneration showed that higher desorption efficiency is observed for Cd(II), Pb(II), whereas lower desorption efficiency with Cr(III) removal [95]. In order to check the reuse of *Saccharomyces cerevisiae* for As(III) biosorption, the metal-loaded biosorbent is treated with eluent of 0.5 M NaOH. The desorption efficiency of more than 75% is achieved. During each cycle of biosorption and desorption process, the uptake capacity of the biosorbent is changed by 20–25% and showed that prepared biosorbent could be employed for recycles up to three to four times without significant loss compared to original biosorption capacities [96].

8   Conclusion

The biosorption plays an important role in the separation technology for heavy metal removal from aqueous systems. The present review reported the potential sources of biosorbents from the dead microbial and plant biomass residues in the application of heavy metal sequestration. The utilization of such biosorbents is recommended for heavy metal removal due to their merits of low or no cost, wide distribution, renewable source, eco-friendly and property of more affinity for heavy metal biosorption. The potential biosorbent employment in the biosorption technology is investigated as an alternate approach for the existing conventional treatment methods. The process parametric influences on the removal of heavy metals removal by different biosorbents were discussed. The explanations of the mechanisms associated with the biosorption of heavy metals are illustrated using the isotherm and kinetic models. The aspects of biosorbent regenerations using the different desorbing agents and possibilities of biosorbent recycle for successive biosorption study were also reviewed. Even though a large number of publications are available in heavy metal biosorption, the research publications are found inadequate in view of industrial scale applications.

References

1. Rangabhashiyam, S., Sujata, L., Balasubramanian, P: Biosorption characteristics of methylene blue and malachite green from simulated wastewater onto *Carica papaya* wood biosorbent. Surfaces and Interfaces. https://doi.org/10.1016/j.surfin (2017)

2. Nabil, A.F., Bnar, M.I.: The use of new chemically modified cellulose for heavy metal ion adsorption. J. Hazard. Mater. **343**, 324–331 (2018)

3. Fu, F., Wang, Q.: Removal of heavy metal ions from wastewaters: a review. J. Environ. Manage. **92**, 407–418 (2011)

4. Rangabhashiyam, S., Anu, N., Selvaraju, N.: Biosorption of heavy metals using low cost agricultural by products. Res. J. Chem. Environ. **17**, 112–123 (2013)

5. Bishop, P.L.: Pollution prevention: fundamentals and practice (2000)

6. Evanko, C.R, Dzombak, D.A: Remediation of metals-contaminated soils and groundwater. Technology Evaluation Report, TE-97-01. Ground-Water Remediation Technologies Analysis Center, Pittsburg, PA (1997)

7. Rangabhashiyam, S., Anu, N., Selvaraju, N.: Equilibrium and kinetic modeling of chromium (VI) removal from aqueous solution by a novel biosorbent. Res. J. Chem. Environ. **18**(4), 30–36 (2014)

8. Srivastava, N.K., Majumder, C.B: Novel biofiltration methods for the treatment of heavy metals from industrial wastewater. J. Hazard. Mater., 1–8 (2008)

9. Celik, A., Demirbas, A.: Removal of heavy metal ions from aqueous solutions via adsorption onto modified lignin from pulping wastes. Energy Sources **27**, 1167–1177 (2005)

10. Friberg, L., Elinder, C.G.: Encyclopedia of Occupational Health. International Labor Organization, Geneva (1985)

11. Kjellstrom, T., Shiroishi, K., Erwin, P.E.: Urinary beta./sub 2/-microglobulin excretion among people exposed to cadmium in the general environment. Environ. Res. **13**, 318–344 (1977)

12. Ahmaruzzaman, M.: Industrial wastes as low-cost potential adsorbents for the treatment of wastewater laden with heavy metals. Adv. Coll. Interface. Sci. **166**, 36–59 (2011)

13. World Health Organization (WHO). Guidelines for Drinking-Water Quality, 4th edn. 1–541 (2011)

14. Eroglu, M.S., Toprak, S., Urgan, O., Ozge, M.E., Onur, M., Arzu, D., Haldun, M., Akoglu, M., Cigdem, O., Ebru, M.A.: Parameters of water quality: interpretation and standards. Saudi Med. J. **33**, 3–8 (2012)

15. Mohod, C.V., Dhote, J.: Review of heavy metals in drinking water and their effect on human health. Int. J. Innovative Res. Sci. Eng. Technol. **2**, 2992–2996 (2013)

16. Sabolc, P., Tatjana, S.K., Jelena, R., Snezana, M., Sasa, M.L., Maja, T.S.: Utilization of fruit processing industry waste as green activated carbon for the treatment of heavy metals and chlorophenols contaminated water. J. Clean. Prod. **162**, 958–972 (2017)

17. Li, F., Liang, L., Zan, Q., Haomiao, X., Jianfang, X., Naiqiang, Y.: A novel method for the sequential removal and separation of multiple heavy metals from wastewater. J. Hazard. Mater. **342**, 617–624 (2018)

18. Nguyen, T.A.H., Ngo, H.H., Guo, W.S., Zhang, J., Liang, S., Yue, Q.Y., Li, Q., Nguyen, T. V.: Applicability of agricultural waste and by-products for adsorptive removal of heavy metals from wastewater. Biores. Technol. **148**, 574–585 (2013)

19. Gadd, G.M.: Biosorption: critical review of scientific rationale, environmental importance and significance for pollution treatment. J. Chem. Technol. Biotechnol. **84**, 13–28 (2009)

20. Kshama, A.S., Varsha, K.V.: Kinetics and equilibrium studies on biosorption of nickel from aqueous solution by dead fungal biomass of Mucorhiemalis. Chem. Eng. J. **171**, 1234–1245 (2011)

21. Rangabhashiyam, S., Selvaraju, N.: Evaluation of the biosorption potential of a novel *Caryotaurens* inflorescence waste biomass for the removal of hexavalent chromium, from aqueous solutions. J. Taiwan Inst. Chem. Eng. **47**, 59–70 (2015)

22. Rangabhashiyam, S., Anu, N., Giri, N.M.S., Selvaraju, N.: Relevance of isotherm models in biosorption of pollutants by agricultural byproducts. J. Environ. Chem. Eng. **2**, 398–414 (2014)

23. Ayushi, V., Shashi, K., Surendra, K.: Biosorption of lead ions from the aqueous solution by *Sargassumfilipendula*: equilibrium and kinetic studies. J. Environ. Chem. Eng. **4**, 4587–4599 (2016)

24. Susmita, S.G., Krishna, G.B.: Kinetics of adsorption of metal ions on inorganic materials: a review. Adv. Coll. Interface. Sci. **162**, 39–58 (2011)

25. Rita, F.L.R., Sérgia, M.S.M., Francisco, A.R.B., Clésia, C.N., Iara, C.C., Débora, C.M.: Evaluation of the potential of microalgae *Microcystisnovacekii* in the removal of Pb^{2+} from an aqueous medium. J. Hazard. Mater. **179**, 947–953 (2010)

26. Elisabetta, F., Alessandra, L., Carlo, S., Attilio, C.: Chromium (VI) removal by methylated biomass of *Spirulinaplatensis*: the effect of methylation process. Chem. Eng. J. **156**, 264–269 (2010)

27. Lívia, S.F., Mayla, S.R., Joao, C.M.C., Alessandra, L., Elisabetta, F., Patrizia, P., Attilio, C.: Adsorption of Ni^{2+}, Zn^{2+} and Pb^{2+} onto dry biomass of *Arthrospira* (*Spirulina*) platensis and *Chlorella vulgaris*. I. Single metal systems. Chem. Eng. J. **173**, 326–333 (2011)

28. Mayla, S.R., Lívia, S.F., João, C.M.C., Alessandra, L., Elisabetta, F., Attilio, C.: Metal biosorption onto dry biomass of *Arthrospira*(*Spirulina*) *platensis* and *Chlorella vulgaris*: multi-metal systems. J. Hazard. Mater. **217–218**, 246–255 (2012)

29. Qiao, H.S., Tian, T.Z., Li-Hua, C., Xin, H.X., Huan, L.C.: Hexavalent chromium detoxification by nonliving *Chlorella vulgaris* cultivated under tuned conditions. Chem. Eng. J. **228**, 993–1002 (2013)

30. Cristina, M.M., Paula, M.L.C., Xavier, F.M.: Capacity of simultaneous removal of zinc and cadmium from contaminated media, by two microalgae isolated from a polluted site. Environ. Chem. Lett. **9**, 511–517 (2011)

31. Petrovič, A., Simonič, M.: Removal of heavy metal ions from drinking water by alginate-immobilised *Chlorella sorokiniana*. Int. J. Environ. Sci. Technol. **13**, 1761–1780 (2016)

32. Hongkyun, L., Eunjung, S., Hyun, S.Y., Young, T.P., Dohyeong, K., Min, K.J., Chi, K.K., Won, S.S., Jaeyoung, C.: Biosorption of Cu(II) by immobilized microalgae using silica: kinetic, equilibrium, and thermodynamic study. Environ. Sci. Pollut. Res. **23**, 1025–1034 (2013)

33. Nourollah, M., Ehsan, M., Omidvar, F.: Biosorption of Cd and Pb ions from aqueous solutions by biomass of the green microalga *Scenedesmusquadricauda*. J. Appl. Phycol. **27**, 311–320 (2015)

34. Ferdag, C., Necip, A., Demet, Y., Asim, O.: Biosorption of lead from aqueous solutions by *Bacillus* strains possessing heavy-metal resistance. Chem. Eng. J. **73**, 422–428 (2011)

35. Ganiyu, O.O., Matthew, O.I., Oluwafemi, S.O., Olukayode, O.A.: Chromium (VI) biosorption properties of multiple resistant bacteria isolated from industrial sewerage. Environ. Monit. Assess. **185**, 6809–6818 (2013)

36. Ziagova, M., Dimitriadis, G., Aslanidou, D., Papaioannou, X., Tzannetaki, E.L., Liakopoulou, K.M.: Comparative study of Cd(II) and Cr(VI) biosorption on *Staphylococcus xylosus* and *Pseudomonas* sp. in single and binary mixtures. Biores. Technol. **98**, 2859–2865 (2007)

37. Jin, H.P., Hyo, T.C.: Characterization of cadmium biosorption by *Exiguobacterium* sp. isolated from farmland soil near Cu–Pb–Zn mine. Environ. Sci. Pollut. Res. **23**, 11814–11822 (2016)

38. Ryan, B., Majid, S., Abdolmajid, M., Hazim, A.M.Q.: Biosorption of IIPb and Cu using fixed and suspended bacteria. J. Environ. Chem. Eng. **2**, 1663–1671 (2014)

39. Paul, F.N., Zejiao, L., Jingjing, L.: The biosorption of Cr(VI) ions by dried biomass obtained from a chromium-resistant bacterium. Front. Chem. Sci. Eng. **8**, 454–464 (2014)

40. Dandan, L., Xingjian, X., Hongwen, Y., Xuerong, H.: Characterization of Pb^{2+} biosorption by psychrotrophic strain *Pseudomonas* sp. I3 isolated from permafrost soil of Mohe wetland in Northeast China. J. Environ. Manage. **196**, 8–15 (2017)

41. Ting, W., Hongwen, S.: Biosorption of heavy metals from aqueous solution by UV-mutant *Bacillus subtilis*. Environ. Sci. Pollut. Res. **20**, 7450–7463 (2013)

42. Ozdemir, G., Ozturk, T., Ceyhan, N., Isler, R., Cosar, T.: Heavy metal biosorption by biomass of *Ochrobactrumanthropi* producing exopolysaccharide in activated sludge. Biores. Technol. **90**, 71–74 (2003)

43. Tunali, S., Akar, T., Ozcan, A.S., Kiran, I., Ozcan, A.: Equilibrium and kinetics of biosorption of lead(II) from aqueous solutions by *Cephalosporiumaphidicola*. Sep. Purif. Technol. **47**, 105–112 (2006)

44. Shaheen, Z., Farrukh, A., Iqbal, A.: Tolerance and biosorption potential of filamentous fungi isolated from metal contaminated agricultural soil. Biores. Technol. **98**, 2557–2561 (2007)

45. John, R.M., Benila, S., Pasumalai, A.S.: Optimization of Chromium Biosorption by Fungal Adsorbent, *Trichoderma* sp. BSCR02 and its Desorption Studies. HAYATI. J. Biosci. **24**, 65–71 (2017)

46. Sriharsha, D.V., Lokesh, K.R., Savitha, J.: Immobilized fungi on *Luffacylindrica*: an effective biosorbent for the removal of lead. J. Taiwan Inst. Chem. Eng. **80**, 589–595 (2017)

47. Haiwei, H., Lixiang, C., Yuxuan, W., Renduo, Z., Wenfeng, W.: Biosorption behavior and mechanism of heavy metals by the fruiting body of jelly fungus (*Auriculariapolytricha*) from aqueous solutions. Appl. Microbiol. Biotechnol. **96**, 829–840 (2012)

48. Pedro, F.G., Patrik, R.L., Nils, K.P., Mohammad, J.T.: Heavy metal biosorption by *Rhizopus* Sp. Biomass Immobilized on Textiles. Water Air Soil Pollut. **225**, 1834 (2014)

49. Nikhil, R.S., Ashok, V.B., Ameeta, R.K., Smita, S.Z.: Removal of Ni (II) ions from aqueous solutions by biosorption onto two strains of *Yarrowialipolytica*. J. Environ. Manage. **102**, 115–124 (2012)

50. Aytar, P., Gedikli, S., Buruk, Y., Cabuk, A., Burnak, N.: Lead and nickel biosorption with a fungal biomass isolated from metal mine drainage: Box-Behnken experimental design. Int. J. Environ. Sci. Technol. **11**, 1631–1640 (2014)

51. Cerino, C.F.J., García, L.A.M., Garcia, R.R.B., Garza, G.M.T., Soto, R.E., Sánchez, G.M. N., Quezada, L.I.: Response surface methodology for lead biosorption on *Aspergillusterreus*. Int. J. Environ. Sci. Technol. **8**, 695–704 (2011)

52. Agarwal, G.S., Bhuptawat, H.K., Chaudhari, S.: Biosorption of aqueous chromium(VI) by tamarindusindica seeds. Biores. Technol. **97**, 949–956 (2006)

53. Leopoldo, M.N., Saloua, B.D.A., Gassan, H., Catherine, F., Salvador, R., José, A.G., Javier, O.: Adsorption of iron on crude olive stones. Ind. Crops Prod. **32**, 467–471 (2010)

54. Jamil, A., Umer, S., Waheed, Z., Muhammad, S., Amara, D., Shafique, A.: Removal of Pb (II) and Cd(II) from water by adsorption on peels of banana. Biores. Technol. **101**, 1752–1755 (2010)

55. Ammara, Z., Haq, N.B., Muhammad, A.H., Faiza, S.: Kinetic and equilibrium modeling for Cr(III) and Cr(VI) removal from aqueous solutions by *Citrus reticulata* waste biomass. Water Air Soil Pollut. **191**, 305–318 (2008)

56. Dubey, A., Mishra, A., Singhal, S.: Application of dried plant biomass as novel low-cost adsorbent for removal of cadmium from aqueous solution. Int. J. Environ. Sci. Technol. **11**, 1043–1050 (2014)

57. Olu-Owolabi, B.I., Paul, N.D., William, C.E.: Mechanism of Pb^{2+} removal from aqueous solution using a nonliving moss biomass. Chem. Eng. J. **195**, 270–275 (2012)

58. Rangabhashiyam, S., Selvaraju, N.: Efficacy of unmodified and chemically modified *Swieteniamahagoni* shells for the removal of hexavalent chromium from simulated wastewater. J. Mol. Liq. **209**, 487–497 (2015)

59. Raziya, N., Qaisar, M., Munawar, I., Jan, N.: Biosorption of Pb(II) onto immobilized and native *Mangiferaindica* waste biomass. J. Ind. Eng. Chem. **35**, 185–194 (2016)

60. Rangabhashiyam, S., Selvaraju, N.: Adsorptive remediation of hexavalent chromium from synthetic wastewater by a natural and ZnCl₂ activated *Sterculiaguttata* shell. J. Mol. Liq. **207**, 39–49 (2015)

61. AbdElhafez, S.E., Hamad, H.A., Zaatout, A.A., Malash, G.F.: Management of agricultural waste for removal of heavy metals from aqueous solution: adsorption behaviors, adsorption mechanisms, environmental protection, and techno-economic analysis. Environ. Sci. Pollut. Res. **24**, 1397–1415 (2017)

62. Rehab, M.A., Hesham, A.H., Mohamed, M.H., Gihan, F.M.: Potential of using green adsorbent of heavy metal removal from aqueous solutions: Adsorption kinetics, isotherm, thermodynamic, mechanism and economic analysis. Ecol. Eng. **91**, 317–332 (2016)

63. Cordeo, B., Lodeiro, P., Herrero, R., Sastre De Vicente, M.E.: Biosorption of cadmium by *Fucusspiralis*. Environ. Chem. **1**, 180–187 (2004)

64. Cristina, M., Monteiro, P.M.L., Castro, F., Xavier, M.: Cadmium removal by two strains of *Desmodesmuspleiomorphus* Cells. Water Air Soil Pollut. **208**, 17–27 (2010)

65. Huijuan, M., Yunfeng, X., Hong, C.: Bioremediation of surface water co-contaminated with zinc (II) and linear alkylbenzenesulfonates by *Spirulinaplatensis*. Phys. Chem. Earth, Parts A/B/C **47–48**, 152–155 (2012)

66. Kishore, K.K., Krishna, P.M., Sarada, B., VenkataR.M.: Challa: entrapment of marine microalga, *Isochrysisgalbana*, for biosorption of Cr(III) from aqueous solution: isotherms and spectroscopic characterization. Appl. Water Sci. **3**, 85–92 (2013)

67. Sibi, G.: Biosorption of chromium from electroplating and galvanizing industrial effluents under extreme conditions using *Chlorella vulgaris*. Green Energy Environ. **1**, 172–177 (2016)

68. Cristina, M.M., Paula, M.L., Castro, F., Xavier, M.: Biosorption of zinc ions from aqueous solution by the microalga *Scenedesmusobliquus*. Environ. Chem. Lett. **9**, 169–176 (2011)

69. El-Naas, M.H., AbuAl-Rub, F., Ashour, I., Al Marzouqi, M.: Effect of competitive interference on the biosorption of lead(II) by *Chlorella vulgaris*. Chem. Eng. Process. **46**, 1391–1399 (2007)

70. Srinath, T., Verma, T., Ramteke, P.W., Garg, S.K.: Chromium(VI) biosorption and bioaccumulation by chromate resistant bacteria. Chemosphere **48**, 427–435 (2002)

71. Salehizadeh, H., Shojaosadati, S.A.: Removal of metal ions from aqueous solution by polysaccharide produced from *Bacillus firmus*. Water Res. **17**, 4231–4235 (2003)

72. Acosta, M.P., Valdman, E., Leite, S.G.F., Battaglini, F., Ruzal, S.M.: Biosorption of copper by *Paenibacilluspolymyxa* cells and their Exopolysaccharide. World J. Microbiol. Biotechnol. **21**, 1157–1163 (2005)

73. InceYilmaz, E., Ensari, N.Y.: Cadmium biosorption by *Bacillus circulans* strain EB1. World J. Microbiol. Biotechnol. **21**, 777–779 (2005)

74. Sheikh, S.Z., Mun, H.C., Jung, H.S., Hyunju, P., Ju, X., Ki-Whan, C., Sung, C.Y.: Enhanced biosorption of mercury(II) and cadmium(II) by cold-induced hydrophobic exobiopolymer secreted from the psychrotroph *Pseudomonas fluorescens* BM07. Appl. Microbiol. Biotechnol. **80**, 531–544 (2008)

75. Yu, J., Sumei, Y., Chunying, T., Tao, S., Liying, D., Jinsong, L., Xin, B., Xiuhong, X., Juanjuan, Q.: Biosorption characteristic of *Alcaligenes* sp. BAPb.1 for removal of lead(II) from aqueous solution. Biotech **7**, 123 (2017)

76. Sen, S.K., Raut, S., Dora, T.K., Mohapatra, P.K.D.: Contribution of hot spring bacterial consortium in cadmium and lead bioremediation through quadratic programming model. J. Hazard. Mater. **265**, 47–60 (2014)

77. Cho, D.H., Kim, E.Y.: Characterization of Pb²⁺ biosorption from aqueous solution by *Rhodotorulaglutinis*. Bioprocess Biosyst. Eng. **25**, 271–277 (2003)

78. Prasanjit, B., Sumathi, S.: Uptake of chromium by *Aspergillusfoetidus*. J. Mater. Cycles Waste Manage. **7**, 88–92 (2005)

79. Ülkü, Y., Gülay, Ö., Filiz, B.D., Neslihan, E., Alev, E., Ayla, D.: Heavy metal biosorption by white-rot fungi. Water Sci. Technol. **38**, 323–330 (1998)

101. Waihung, L., Lau, M.N., Hong, C., Peter, H.F.Y., Shirley, N.S., Po-Keung, W.: Biosorption and desorption of copper (II) ions by *Bacillus* sp. Appl. Biochem. Biotechnol. **107**, 581–591 (2003)
102. Tianqi, W., Jun, Y., Zhimin, Y., Yue, Z., Fei, W., Huilun, C.: Isolation of lead-resistant *Arthrobacter* strain GQ-9 and its biosorption mechanism. Environ. Sci. Pollut. Res. (2017). https://doi.org/10.1007/s11356-017-0694-7
103. Amna, J., Rukhsan, B., Umer, S., Jamil, A.: Removal of heavy metals by adsorption on *Pleurotusostreatus*. Biomass Bioenerg. **35**, 1675–1682 (2011)
104. Rajender, K., Divya, B., Rajesh, S., Narsi, R.B.: Metal tolerance and sequestration of Ni(II), Zn(II) and Cr(VI) ions from simulated and electroplating wastewater in batch process: Kinetics and equilibrium study. Int. Biodeterior. Biodegradation **66**, 82–90 (2012)
105. Ting, L., Huidong, L., Zhao, L., Xiao, X., Lingli, C., Le, D.: Removal of hexavalent chromium by fungal biomass of *Mucorracemosus*: influencing factors and removal mechanism. World J. Microbiol. Biotechnol. **23**, 1685–1693 (2007)
106. Jelena, V.M., Mirjana, D.S.M.L., Mihajlović, Z.R., Lopičić, M.S.P., Tatjana, D.Š., Mirjana, Đ.R.: Compost of aquatic weed *Myriophyllumspicatum* as low-cost biosorbent for selected heavy metal ions. Water Air Soil Pollut. **225**, 1927 (2014)
107. Stela, N.C.R., Amália, L.P.X., Filipe, S.T., Megg, M.C.E., Fernanda, J.G., Laurent, F.G., Rossimiriam, P.F., Leandro, V.A.G.: Modeling mono- and multi-component adsorption of cobalt(II), copper(II), and nickel(II) metal ions from aqueous solution onto a new carboxylated sugarcane bagasse. Part I: Batch adsorption study. Ind. Crops Prod. **74**, 357–371 (2015)
108. Hossain, M.A., Ngo, H.H., Guo, W.S., Setiadi, T.: Adsorption and desorption of copper(II) ions onto garden grass. Biores. Technol. **121**, 386–395 (2012)

Inhibition Assays of Urease for Detecting Trivalent Chromium in Drinking Water

Rushikesh Fopase, Suman Nayak, Monalisha Mohanta, Paresh Kale and P. Balasubramanian

1 Introduction

Chromium is one of the most common heavy metals occurring in the soil with a wide range of industrial applications. Metallurgical industries use almost 90% of the total Cr production for making stainless steel and alloyed steel, while the remaining fraction utilizes in refractories and foundries. Leather tanning, pigment manufacturing, and plating industries use different Cr-based chemicals on a large scale [1]. Cr occurs in two primary oxidative forms in nature as trivalent (Cr^{3+}) and hexavalent (Cr^{6+}) [2]. Various hazardous effects are reported by the studies on human as well as on the ecosystem [3]. India contributes 14% of worldwide chromium production out of which the Sukinda Mines Valley in Odisha state produces 98% of total chromium. Sukinda valley is a known polluted area in the world due to the high amount of chromium leaching out in the surrounding water bodies [4].

The level of toxicity of chromium depends on the uptake and accumulation [5]. Cr^{6+} is highly water soluble and exists as chromate oxyanion (CrO_4^{-2}). The presence of excessive amount of this metal ion within the body causes hazardous effects on the individual's health. The solubility, high oxidation potential, and membrane permeability make the hexavalent chromium more toxic. Cr^{6+}, acting as the potential carcinogen, triggers the formation of reactive oxidation species and affects the DNA causing mutations [6]. Cr^{6+} is reported for detrimental effects on anti-oxidation genes resulting in increased oxidative stress in human placenta

R. Fopase · S. Nayak · P. Balasubramanian (✉)
Department of Biotechnology & Medical Engineering,
NIT Rourkela, Rourkela 769008, India
e-mail: biobala@nitrkl.ac.in

M. Mohanta · P. Kale
Department of Electrical Engineering, NIT Rourkela, Rourkela 769008, India

leading to apoptosis [7]. The effects of Cr^{6+} toxicity include respiratory tract irritation, gastrointestinal problems, dermatitis, and allergic skin reactions [8, 9]. Cr^{6+} toxicity affects the vital organs of freshwater fishes and declines the levels of proteins and glycogen in the body of fishes leading to the decrease of biodefence mechanism of fish [10].

However, Cr^{3+} cannot cross the biological membranes, and a significant amount of Cr^{3+} is bearable by mammals [11]. Cr^{3+} is relatively insoluble in water and thermodynamically stable. Cr^{3+} gets oxidized to Cr^{6+} in the presence of redox couples, for example, Mn(II)/Mn(IV) or H_2O/O_2, with redox properties [12, 13]. Transformation of Cr^{3+} into Cr^{6+} and vice versa results in the increased health hazard for humans and the environment [12]. Earlier studies reported the essentiality of Cr^{3+} as a cofactor for insulin action to regulate the blood glucose level [11]. However, recently some studies raised doubt on the requirement of Cr^{3+} as a cofactor for the action of insulin. Furthermore, Cr^{3+} showed the insignificant benefits in the patients with type 2 diabetes and impaired glucose syndrome [14]. Nevertheless, the excess amount of Cr^{3+} accumulation by these supplements may lead the formation of Cr-DNA adducts causing potential genotoxicity [15]. Thus, the controversy arises over the use of chromium as supplements.

The uncontrolled release or the excessive presence of chromium in the environment creates a non-negligible threat to the ecosystem. The threat demands to take some necessary steps for detection and elimination of chromium from the affected areas. Enzyme-based biosensors can apply for the detection of various heavy metals such as lead, arsenic, and cadmium. Urease (urea amidohydrolase; EC 3.5.1.5) is one of the well-studied enzymes for the inhibition by heavy metals due to its certain advantages. Urease has abundant sources: bacteria, algae, fungi, plants, and soil. The biological activity of soil is a direct indication of the presence of urease. Urease is sensitive toward heavy metals, for example silver, cobalt, nickel, cadmium, lead, chromium, and mercury. The metal ions interact with the cysteine residues present in its active site [17, 18]. Various urease-based biosensors are in use for the detection of heavy metals in the environment. Chromium was found to form an unstable complex with urease and thus reduces the overall enzyme activity significantly [19].

Urease is the first crystallized and known nickel-containing enzyme and can catalyze the urea into ammonia and carbon dioxide [20, 21]. The rate of catalysis may approach 10^{14} times the uncatalyzed conversion [22]. The structure and molecular weight of this enzyme vary with its source of origin such as plant, bacterial, fungal, and algal. Urease is a hexameric molecule with the active site located in the α-subunit of the molecule. The active site of the urease contains nickel and conserved amino acid sequence irrespective of the origin of the enzyme [23, 24]. Certain heavy metals found to inhibit the activity of urease by reacting with the sulfhydryl groups in the active site of urease [25].

The present work elaborates the study of jack bean urease kinetics and enzyme inhibition assays for the effect of Cr^{3+} on urease activity. The variation in the activity of the urease due to the presence of Cr^{3+} ions can apply for the detection of Cr metal present within the sample.

2 Materials and Methods

Urease-catalyzed reactions using urea as a substrate were carried out in the presence of different concentrations of Cr^{3+} for the study of the effects of Cr^{3+} ions on the enzyme activity. Comparison of inhibited enzyme activity with and without Cr gives the extent of the effect of Cr ions on the enzyme.

2.1 Materials

Commercial jack bean urease (EC 3.5.1.5) purchased from Sigma-Aldrich was used for enzyme assays. Laboratory grade urea was used as substrate obtained from Merck Chemicals. Trivalent chromium standard solution was prepared using chromium chloride obtained from Merck Chemicals. Reagents for the phenate method constituted phenol, absolute ethanol, sodium nitroprusside, trisodium citrate, and sodium hypochlorite. The reagents for phenate method include a phenate reagent (10 g of phenol to 100 mL of 95% ethanol), sodium nitroprusside solution (0.5 g in 100 mL of deionized water), and an oxidizing reagent. The oxidizing agent comprises a solution of alkaline reagent (10 g trisodium citrate and 0.5 g sodium hydroxide for 100 mL) and sodium hypochlorite in 4:1 ratio. All the chemicals were prepared using deionized water. Urease solution (0.25 mg/mL) was prepared in 0.2 M sodium phosphate buffer pH 7.0.

2.2 Determination of Enzyme Activity

Urease catalyzes the urea into ammonia and carbon dioxide as the reaction given in Eq. 1. Phenate method detects the amount of ammonia released by the action of urease.

$$(NH_2)_2CO + 2H_2O \rightarrow 2NH_4^+ + CO_3 \tag{1}$$
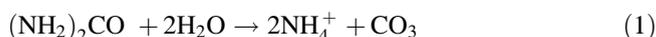
The volume of the enzyme assay was 10 mL. Urease solution (20 µL) was mixed with one mM urea solution and incubated for 15 min at 30 °C. After incubation, 0.4 mL each of phenate reagent and sodium nitroprusside, and 1 mL of an oxidizing reagent were added to the reaction mixture with gentle mixing. The

assay tubes were kept for incubation for 30 min in the dark at room temperature. Phenate reagent reacts with ammonium ions released and produces the blue-colored compound, indophenol blue. Sodium nitroprusside acts as a catalyst, while oxidizing reagent provides alkaline conditions. Amount of ammonia released determined by spectrophotometric analysis at 630 nm. The standard curve for ammonium ions was prepared using ammonium sulfate solution. Urease activity is calculated using Eq. 2.

$$\text{Urease activity} = \frac{\text{Absorbance of sample * Dilution factor}}{\text{Slope of standard curve * Time of assay * Volume of assay}} \quad (2)$$

2.3 Estimation of Enzyme Kinetics

Experiments were carried out to estimate the enzyme activity by plotting the experimental observations as suggested in Michaelis–Menten method. The hyperbolic curve is translated into a straight line to obtained the critical enzyme kinetic parameters, V_{max} (maximum velocity at the saturating substrate concentration) and K_m (the substrate concentration for which V_{max} is half of its value) as advocated by various researchers. Lineweaver–Burk plot, Eadie–Hofstee plot, and Hanes–Woolf plots were attempted in this study to find out the urease kinetics. Thus, enzyme activity was determined by varying the concentrations of urea from 0 to 4 mM at the constant enzyme concentration of 0.25 mg/L.

2.4 Inhibition Studies

The principle for the development of a biosensor to detect chromium in the potable water was based on inhibition studies of urease by Cr^{3+}. Urea of 1 mL (1 mM) was subjected to different concentrations of Cr^{3+} solutions ranging from 0.0001 to 1000 ppm. Enzyme solution (20 µL) was added to the 10 mL of the reaction mixture and incubated for 15 min at 300 C. To the mixture, 0.4 mL of phenate reagent and sodium nitroprusside were added and mixed well. Followed by the addition of 1 mL oxidizing reagent and incubation for 30 min in the dark, absorbance was measured at 630 nm using a double beam UV visible spectrophotometer. The degree of inhibition is calculated by relating the inhibited activity with the activity of pure enzyme solution as given in Eq. 3.

$$\% \text{Inhibition} = \frac{\text{Activity without inhibitor} - \text{Activity with inhibitor}}{\text{Activity without inhibitor}} \times 100 \quad (3)$$

3 Results and Discussion

3.1 Enzyme Activity

The plot of enzyme activity and substrate concentrations for the definite enzyme concentration was obtained as a hyperbolic pattern (Fig. 1). This behavior can be explained by Michaelis–Menten equation as given in Eq. 4.

$$v = \frac{V_{max} \times S}{K_m + S} \tag{4}$$

where v is the initial velocity, V_{max} is maximum velocity, and K_m is the Michaelis–Menten constant. K_m and V_{max} reveal the kinetics of the enzyme-catalyzed reaction for the definite set of experimental conditions. From Fig. 1, approximate values of K_m and V_{max} can be observed as 0.6 mM of urea and 23 mM/min, respectively. The hyperbolic curve was translated into a straight line as suggested in Lineweaver–Burk plot for precise determination of the kinetic parameters. The double reciprocal plot estimated the values of K_m and V_{max} as 0.7 mM of urea and 26.88 mM/min and represented in Fig. 2.

The Lineweaver–Burk plot gives the accurate estimation of the V_{max}. However, for K_m, the error value might increase as the reciprocal data may not necessarily give the symmetrical values. The lower concentrations of substrate influence the slope of the plot to a great extent. Researchers have suggested the different plot to avoid the drawbacks of the double reciprocal plot for calculation of V_{max} and K_m. Eadie–Hofstee plot gives the relation between the substrate concentration and velocity of the enzyme action as given in Fig. 3. The plot has given the V_{max} and K_m values as 29.94 mM/min and 0.8152 mM, respectively, which are higher than
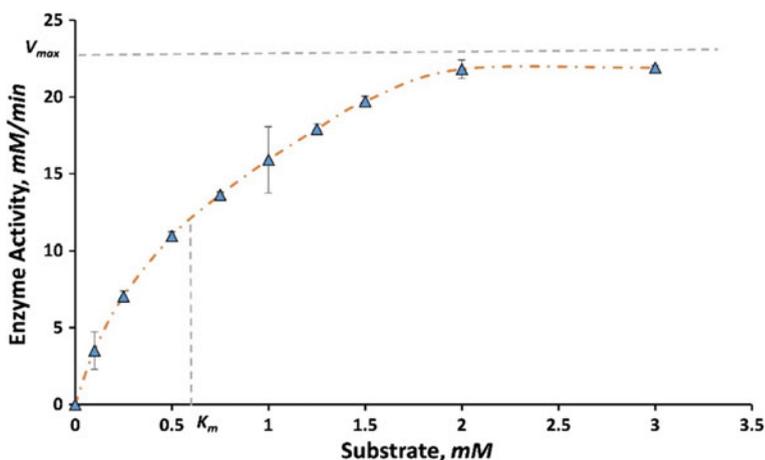
Fig. 1 Michaelis–Menten curve for urease enzyme activity
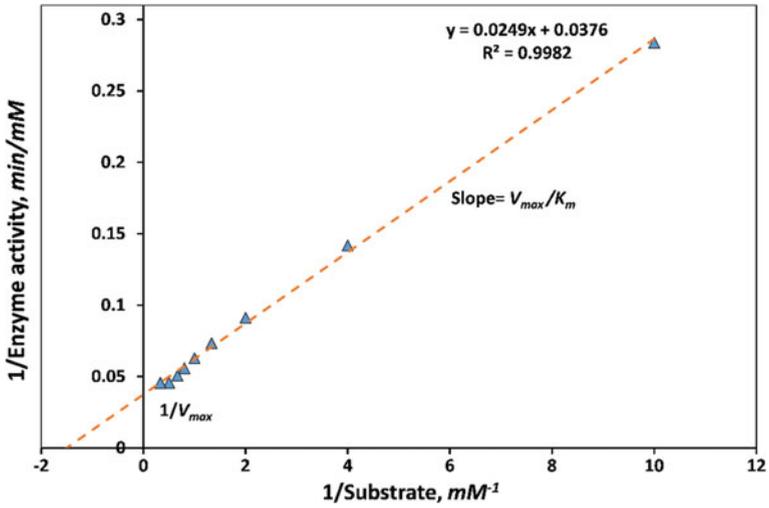
Fig. 2 Lineweaver–Burk plot for urease enzyme activity
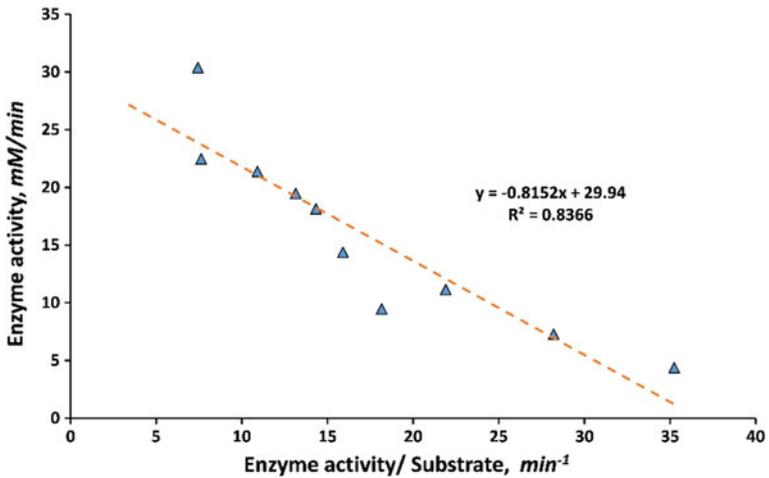
Fig. 3 Eadie–Hofstee plot for urease enzyme activity

the values obtained from Lineweaver–Burk plot. Eadie–Hofstee plot may subject to error as a parameter of enzyme activity used on both the axes. However, this approach reduced the biases based on substrate concentration while calculating the kinetic parameters.

Hanes–Woolf plot is the rearrangement of Eq. 4 for the calculation of V_{max} and K_m. The rearrangement gives the plot for the ratio of substrate concentration and velocity plotted against the substrate concentration. Hanes–Woolf plot gives the
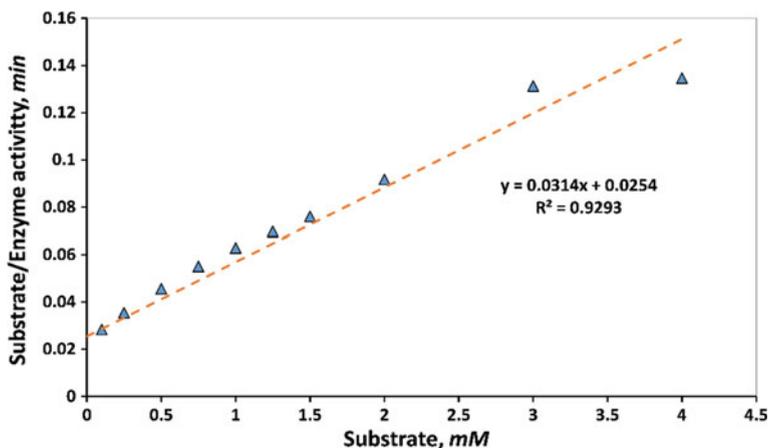
Fig. 4 Hanes–Woolf plot for urease enzyme activity

Table 1 Kinetic parameters of urease by different plots

Plot	V_{max} (mM/min)	K_m (mM)	R^2
Lineweaver–Burk plot	26.88	0.70	0.9982
Eadie–Hofstee plot	29.94	0.82	0.8366
Hanes–Woolf plot	31.85	0.81	0.9293

most accurate estimation of the enzyme activity. The calculated values of V_{max} and K_m were 31.85 mM/min and 0.81 mM of urea, and Fig. 4 represents the Hanes–Woolf plot.

Table 1 summarizes the values of V_{max} and K_m calculated from plots mentioned above. Among the three plots for determination of enzyme kinetic parameters, Lineweaver–Burk plot gives the direct relation of the rate of reaction with the inverse of the substrate concentration provided. Eadie–Hofstee plot and Hanes–Woolf plot gave similar values for both V_{max} and K_m. However, the results from Eadie–Hofstee plot might have a higher chance of error due to use of a parameter v on both of the axes. The Lineweaver–Burk plot shows the highest correlation (R^2) for the urease assay and could be preferred further.

3.2 Enzyme Inhibition Assays

Enzyme inhibition assays provide the extent of the inhibition of enzyme activity for the respective inhibitor concentration. The relation between the degree of inhibition and the inhibitor concentration gives the calibration plot to determine the inhibitor concentration.

For inhibition studies, assays were performed with the various initial concentrations of Cr^{3+} ions as they are known to react with the urease and influence the overall enzyme activity. The heavy metals ions react with the sulfhydryl groups of the active site of the urease and thereby decrease the catalytic activity. The amount of ammonia detected has given the activity of the enzyme in the presence of inhibitors.

Figure 5 shows the relationship between the inhibitor concentrations and a decrease in the enzyme activity. Urease has found sensitive for the low concentrations of Cr^{3+} and shown a decrease in the activity up to 44%. With the increased concentration of metal ion, the activity decreased further, and Cr^{3+} concentrations above 1 ppm showed the complete inhibition of the enzyme. Cr^{3+} (0.001 ppm) was the observed IC_{50} value of urease for which the activity reduces to half of its actual value.

Magomya et al. [26] studied the inhibition kinetics of soybean urease with the IC_{50} value for Cr^{3+} in between the range of 1–10 ppm [26]. Jung et al. [27] performed an inhibition assay of free as well as an immobilized urease using Cr^{3+}. The IC_{50} value of for free urease solution for Cr^{3+} was observed at 0.82 ppm, while for the immobilized enzyme the value was noted as 36.1 ppm [27]. Samborska et al. [28] studied the effect of different oxidation states of chromium on the activity of soil urease. Cr^{3+} caused a decrease in the soil urease activity to 50% for a Cr^{3+} concentration of 0.2 mg per kg of the soil solution. The soil urease was found more sensitive to the Cr^{3+} than Cr^{6+}. Cr^{6+} (0.4 mg) per kg of soil solution was the observed IC_{50} value of soil urease. Further, in the study, pure urease showed more sensitivity toward heavy metals compared to soil urease [28].

The observed decrement in the enzyme activity might be because Cr^{3+} tends to react with carboxyl and sulfhydryl groups in the active sites of the enzyme leading to changes in the enzyme structure [29]. Along with the chromium, other heavy
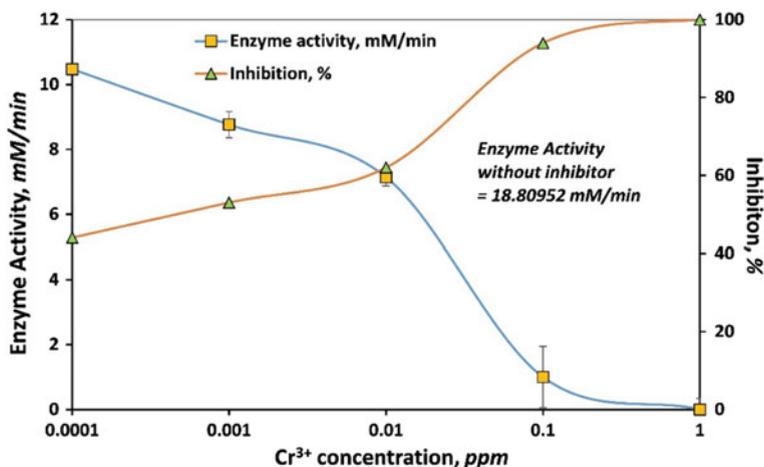

Fig. 5 Effect of Cr^{3+} on urease activity

metal ions, for example, silver, copper, mercury, nickel, cadmium, ferrous, are reported to inhibit the activity of the urease by forming insoluble metals sulfides. Non-competitive type of inhibition of urease is showed by heavy metals [30].

The sensitivity of urease to the other heavy metals is reported by various other researchers [31–33]. The order of degree of urease inhibitions while subjected to various heavy metals was as in the order as follows: Ag > Hg > Cu > Ni > Co > Cd > Fe > Zn > Pb in case of soil urease [31]. Another study suggested the inhibition order as $Cu^{2+} > As^{3+} > Cr^{3+} > Cd^{2+} > Zn^{2+} > Pb^{2+}$ in case of urease extracted from soybeans [26]. From these studies, it observed that the origin of the enzyme plays a crucial role in its activity and the tolerance for the inhibitors as chromium. The jack bean urease used for this study showed to have maximum sensitivity for the Cr^{3+} compared to the other resources.

4　Conclusion

Enzyme kinetics of the jack bean urease was studied in this work to understand the effect of trivalent chromium on urease activity. Kinetics parameters (V_{max} and K_m) are calculated using different kinetics plots (Lineweaver–Burk, Eadie–Hofstee, and Hanes–Woolf plots) relating the substrate concentration and the enzyme activity. Based on the regression analysis, Lineweaver–Burk plot was found to give reliable values (V_{max} and K_m of 26.88 mM/min and 0.7 mM, respectively) for the urease kinetic parameters. The low concentrations of Cr^{3+} affected the urease activity to considerably high level. The IC_{50} value is observed as 0.001 ppm of the metal ion. The relationship between the decreases in the enzyme activity with the inhibitor concentration can apply to determine the amount of heavy metal in the sample. The higher sensitivity of the enzyme can efficiently apply for the detection of the meager amount of chromium. Urease-based biosensor delineating the impact on enzyme function index may use for determining the chromium presence in potable water.

References

1. Dhal, B., Thatoi, H.N., Das, N.N., Pandey, B.D.: Chemical and microbial remediation of hexavalent chromium from contaminated soil and mining/metallurgical solid waste: a review. J. Hazard. Mater. **250–251**, 272–291 (2013)
2. Barnhart, J.: Occurrences, Uses, and Properties of Chromium, vol. 7, no. 26, pp. 3–7 (1997)

3. Biswas, P., Karn, A.K., Balasubramanian, P., Kale, P.G.: Biosensors and Bioelectronics Biosensor for detection of dissolved chromium in potable water : a review. Biosens. Bioelectron. **94**, 589–604 (2017)

4. Kumari, B., Tiwary, R.K., Srivastava, K.K.: Physico-chemical analysis and correlation study of water resources of the Sukinda chromite mining area, Odisha, India. Mine Water Environ. **36**(3), 356–362 (2017)

5. Peralta-Videa, J.R., Lopez, M.L., Narayan, M., Saupe, G., Gardea-Torresdey, J.: The biochemistry of environmental heavy metal uptake by plants: implications for the food chain. Int. J. Biochem. Cell Biol. **41**(8–9), 1665–1677 (2009)

6. Smith, A.H., Steinmaus, C.M.: Health effects of arsenic and chromium in drinking water: recent human findings. Annu. Rev. Public Health **30**(1), 107–122 (2009)

7. Banu, S.K., et al.: Sexually dimorphic impact of chromium accumulation on human placental oxidative stress and apoptosis. Toxicol. Sci. 1–13 (2017)

8. Baruthio, F.: Toxic effects of chromium and its compounds. Biol. Trace Elem. Res. **32**(1816), 145–153 (1992)

9. Martin, S., Griswold, W.: Human health effects of heavy metals. Environ. Sci. Technol. Briefs Citizens **15**, 1–6 (2009)

10. Aslam, S., Yousafzai, A.M.: Chromium toxicity in fish : a review article. J. Entomol. Zool. Stud. **5**(24), 1483–1488 (2017)

11. Anderson, R.A.: Chromium as an essential nutrient for humans. Regul. Toxicol. Pharmacol. **26**(26), s35–s41 (1997)

12. Lin, C.J.: The chemical transformations of chromium in natural waters—a model study. Water Air Soil Pollut. **139**(1–4), 137–158 (2002)

13. Belay, A.A.: Impacts of Chromium from Tannery Effluent and Evaluation of Alternative Treatment Options. J. Environ. Prot. (Irvine,. Calif). **1**(1), 53–58 (2010)

14. Wise, S.S., Wise, J.P.: Chromium and genomic stability. Mutat. Res. Fundam. Mol. Mech. Mutagen. **733**(1–2), 78–82 (2012)

15. Kareus, S.A., Kelley, C., Walton, H.S., Sinclair, P.R.: Release of Cr(III) from Cr(III) picolinate upon metabolic activation. J. Hazard. Mater. **84**(2–3), 163–174 (2001)

16. Byrnes, B.H., Freney, J.R.: Recent developments on the use of urease inhibitors in the tropics. Fertil. Res. **42**(1–3), 251–259 (1995)

17. Suga, T., Mamiya, G. Takishima, K.: The structure of jack bean urease. The complete amino acid sequence, limited proteolysis and reactive cysteine residues. Eur. J. Biochem. **165**, 151–165 (1988)

18. Behbehani, G.R., Barzegar, L., Mohebbian, M.: Strong inhibition of Jack bean urease by chromium (III). Biosci. Biotechnol. Res. Asia **9**(2), no. 1, 2–6 (2012)

19. Sumner, J.B.: Enzyme urease. J. Biol. Chem. **69**, 435–441 (1926)

20. Dixon, N.E., Gazzola, C., Blakeley, R.L., Zerner, B.: Jack bean urease (EC 3.5.1.5). A metalloenzyme. A simple biological role for nickel? J. Am. Chem. Soc. **97**(14), 4131–4133 (1975)

21. Pearson, M.A., Park, I.S., Schaller, R.A., Michel, L.O., Karplus, P.A., Hausinger, R.P.: Kinetic and structural characterization of urease active site variants. Biochemistry **39**(29), 8575–8584 (2000)

22. Krajewska, B.: Mono- (Ag, Hg) and di- (Cu, Hg) valent metal ions effects on the activity of jack bean urease. Probing the modes of metal binding to the enzyme. J. Enzyme Inhib. Med. Chem. **23**(4), 535–542 (2008)

23. Krajewska, B.: Ureases I. Functional, catalytic and kinetic properties: a review. J. Mol. Catal. B Enzym. **59**(1–3), 9–21 (2009)

24. Upadhyay, L.S.B.: Urease inhibitors: a review. Indian J. Biotechnol. **11**(4), 381–388 (2012)

25. Magomya, A., Barminas, J., Osemeahon, S.: Assessment of metal—induced inhibition of soybean urease as a tool for measuring heavy metals in aqueous samples, vol. 10, no. 6, pp. 61–70 (2017)

26. Jung, K., Bitton, G., Koopman, B.: Assessment of urease inhibition assays for measuring toxicity of environmental samples. Water Res. **29**(8), 1929–1933 (1995)

27. Samborska, A., Stepniewska, Z., Stepniewski, W.: Influence of different oxidation states of chromium (VI, III) on soil urease activity. Geoderma **122**(2–4), 317–322 (2004) (SPEC. IIS.)
28. Cervantes, C., et al.: Interactions of chromium with microorganisms and plants. FEMS Microbiol. Rev. **25**(3), 335–347 (2001)
29. Shaw, W.H.R.: The inhibition of urease by various metal ions. J. Am. Chem. Soc. **76**(8), 2160–2163 (1954)
30. Preininger, C., Wolfbeis, O.S.: Disposable cuvette test with integrated sensor layer for enzymatic determination of heavy metals. Biosens. Bioelectron. **11**(10), 981–990 (1996)
31. Volotovsky, V., Kim, N.: Urease-based biosensor for mercuric ions determination. Sens. Actuators B Chem. **42**(3), 233–237 (1997)
32. Krajewska, B., Brindell, M.: Thermodynamic study of competitive inhibitors' binding to urease. J. Therm. Anal. Calorim. **123**(3), 2427–2439 (2016)

Modeling Biochar Yield and Syngas Production During the Pyrolysis of Agro-Residues

G. Swagathnath, S. Rangabhashiyam, Kar Parthsarathi, S. Murugan and P. Balasubramanian

1 Introduction

Pyrolysis is a process of thermal decomposition of biomass in the oxygen-free or oxygenless environment. During the pyrolysis, biomass is converted into different products of (a) a solid product—biochar; (b) a liquid product—bio-oil; and (c) a gaseous product syngas which consists of CO, CO_2, hydrogen gas, and other hydrocarbons [1]. Various process parameters such as feedstock type, pyrolysis temperature, heating rate, and the pressure parameter for the gaseous and liquid product yield [2].

Different compositions of cellulose, hemicellulose, and lignin in the biomass affect the yield of charred product. Lignin-rich biomass yields a higher amount of charred product than the biomass which is rich in cellulose and hemicellulose [3]. The temperature and the heating rate affect the char yield inversely. Higher heating rate condition during fast pyrolysis yields lesser biochar than the biomass pyrolyzed at as lower heating rate in slow pyrolysis [4]. Thus, the yield of different pyrolysis products can be controlled by process parameters.

Biochar holds potential application in agriculture as a soil amendment for enhanced crop production [5] and simultaneously acts as an anthropogenic climate mitigation strategy [6]. The upgraded bio-oil (which is the combination of tar and pyrolysis water from the reaction) can be used as liquid fuel for the internal combustion engines. Shihadeh and Hochgreb [7] had also shown that heat release

G. Swagathnath · S. Rangabhashiyam · P. Balasubramanian (✉)
Department of Biotechnology and Medical Engineering,
NIT Rourkela, Rourkela, Odisha, India
e-mail: balap@nitrkl.ac.in

K. Parthsarathi · S. Murugan
Department of Mechanical Engineering, NIT Rourkela, Rourkela, Odisha, India

profiles of bio-oil are consistent with the slow combustion and rapid mixing as relative to the diesel engine. The volatiles are mainly composed of carbon monoxide, carbon dioxide, hydrogen gas, and hydrocarbons such as methane, ethylene which are liberated as flue gas [8]. Methane, one of the volatiles, is used as natural gas fuel.

Modeling of pyrolysis system is used to predict the product distribution based on reactions. Pyrolysis modeling helps to get the required outcome through steering the process toward the specific product. The manipulation can be done on different parameters, heating rate, pyrolysis temperature, etc.

A number of models have been developed to simulate the pyrolysis process for the prediction of products yield. But each one has its own limitation. Sharma et al. [1] have modeled the slow pyrolysis of wood and predicted the biochar yield and the flue gas composition. In this model, the authors have used the plots of experimental data of CO/CO_2, H_2/CO_2, and total hydrocarbons/CO_2 from [8, 9] to solve the set of equations with zero degrees of freedom. But in the model developed, temperature parameter has not been taken into account for the prediction of char yield.

Song [2] has taken into account of the kinetic parameters used in a gasifier reactor by considering the empirical relationships previously developed by Neves et al. [10]. One of the advantages of this model is being the temperature factor is taken into account in calculating the biochar amount and accordingly the proportion of carbon, hydrogen, and oxygen ratio in the char is obtained. Thus, the char composition varies with the temperature. Char yield is directly obtained from temperature parameter and not through the biomass composition as it has been taken an average from all the biomass composition. The biochar yield is further used to calculate the volatiles and tar yield.

An economic trade-off model as developed by Yoder et al. [11] also dealt with the prediction of biochar and bio-oil yield percentage. Biomass has been broadly classified into four main categories, namely agricultural residues, other agricultural residues, forest residues, and industrial residues. Also, in this paper, pyrolysis process has been broadly classified into fast and slow pyrolysis based on the heating rate which adds one more set of parameter that needs to be considered apart from pyrolysis temperature. The model developed by Yoder et al. [11] has been given importance on economic aspects of the pyrolysis process rather than the flue gas composition. Biomass composition has not been considered for the prediction of biochar yield is one of the disadvantages of this model.

In this research manuscript, the pyrolytic kinetics model designed by Song [2] has been further modified to predict the yield of the biochar, tar, and the flue gas composition in the pyrolytic reactor. The feedstock selection of different straw biomass has been considered. The comparison of the results was performed to understand the temperature and biomass effect on the pyrolysis products yield.

2 Model Development for Biomass Pyrolysis

The model designed by Song [2] used to predict the yields of biochar, tar, and volatile gas composition essentially derived and advanced from [10]. The mathematical model to predict the components yield based on the following assumptions: Gasification of carbon takes place in an isothermal reactor, and the biomass is well mixed; oxygen supplied is consumed entirely, and nitrogen remains inert throughout the reaction; pyrolysis of carbon takes place in the isothermal reactor condition; thus, kinetic model can be designed, and drying takes place at the start of the reaction itself (i.e., at the inlet).

In the first stage of pyrolysis, given biomass fuel (F) is pyrolyzed and converted into char (ch), volatile gas, and liquid. Liquid consists of tar and pyrolytic water (H_2O) as given in Eq. 1. The volatile gas compositions include carbon dioxide (CO_2), carbon monoxide (CO), methane (CH_4), hydrogen gas (H_2), as described in Eq. 2.

$$\text{Total liquid yield} = Y_{tar,F} + Y_{H_2O,F} + \text{Moisture content of biomass} \qquad (1)$$

$$\text{Total volatile gas yield} = Y_{H_2,F} + Y_{CO,F} + Y_{CH_4,F} + Y_{CO_2,F} \qquad (2)$$

$Y_{i,j}$ is the expression to denote yield of ith element in kilograms from jth element in kilograms. Temperature parameter input is given in Celsius, and the yield is obtained in units, kg/kg of biomass. For instance, the char yield is obtained as a kilogram of biochar obtained per kilogram of biomass.

In the second stage, i.e., during the increase in temperature, the tar again gets cracked into volatiles called secondary cracking of tar particles. During this phase, the produced targets cracked into different gaseous substance based on the composition of biomass. Moreover, the increased pressure in response to increased gaseous level in the reactor causes the recompression to tar (liquid).

To apply the pyrolysis model, the elemental composition of different biomasses should be known. These elemental compositions are given as input in the current model under discussion in order to predict the pyrolytic yields. The elemental composition of biomass is obtained from [12]. Elemental compositions of different straw biomasses are used in this model which are: Rice straw, Corn straw, Wheat straw, Barley straw and Oat straw. The elemental composition on dry ash free basis is given in Table 1. Different biochemical compositions of straw biomass are given in Table 2.

Table 1 Elemental composition of various straw biomasses [12]

Biomass	Carbon	Oxygen	Hydrogen
Rice straw	50.1	43.0	5.7
Corn straw	45.7	44.1	6.4
Wheat straw	49.4	43.6	6.1
Oat straw	48.8	44.6	6.0
Barley straw	49.4	43.6	6.2

Table 2 Biochemical composition of various straw biomasses

Biomass	Cellulose	Hemicellulose	Lignin	References
Rice straw	32–47	19–27	5–24	Binod et al. [20]
Corn straw	29.8	33.3	16.65	Shawky et al. [21]
Wheat straw	30	50	15	Sun and Cheng [22]
Oat straw	31–37	27–38	16–19	Rowell [23]
Barley straw	31–34	24–29	14–15	Rowell [23]

The char yield is only related to temperature and not of the biomass in the kinetic model designed by Song [2] as described in Eq. 3:

$$\text{Char yield} : Y_{ch,F} = 0.106 + 2.43 * \exp\left(-0.66 * T * 10^{-2}\right) \tag{3}$$

Equations (4), (5), and (6) give the composition of CHO in the biochar which is also related to the temperature as follows:

$$\text{Carbon content} : Y_{C,ch} = 0.93 - 0.92 * \exp\left(-0.42 * T * 10^{-2}\right) \tag{4}$$

$$\text{Hydrogen content} : Y_{H,ch} = \left(-0.41 * 10^{-2}\right) + \left(0.10 * \exp\left(-0.24 * T * 10^{-2}\right)\right) \tag{5}$$

$$\text{Oxygen content} : Y_{O,ch} = 0.07 + 0.85 * \exp\left(-0.48 * T * 10^{-2}\right) \tag{6}$$

The elemental composition ratio of tar to the input biomass/fuel in relation to temperature is obtained from [10] as Eqs. (7), (8), and (9) describe.

$$\text{Carbon} : Y_{C,tar} = Y_{C,F} * \left(1.05 + \left(1.9 * T * 10^{-4}\right)\right) \tag{7}$$

$$\text{Hydrogen} : Y_{H,tar} = Y_{H,F} * \left(0.93 + \left(3.8 * T * 10^{-4}\right)\right) \tag{8}$$

$$\text{Oxygen} : Y_{O,tar} = Y_{O,F} * \left(0.92 - \left(2.2 * T * 10^{-4}\right)\right) \tag{9}$$

To nullify the degrees of freedom, further three more empirical equations were introduced as Eqs. (10), (11), and (12).

$$\text{Hydrogen gas yield} : Y_{H_2,F} = 1.145 * \left(1 - \exp\left(-0.11 * T * 10^{-2}\right)\right)^{9.384} \tag{10}$$

$$\text{Carbon monoxide yield} : Y_{CO,F} = Y_{H_2,F} \left/ \left(3 * 10^{-4} + \left(\frac{0.0429}{\left(1 + \frac{T}{632}\right)^{-7.23}}\right)\right)\right. \tag{11}$$

$$\text{Methane yield} : Y_{CH_4,F} = 0.146 * Y_{CO,F} - \left(2.18 * 10^{-4}\right) \tag{12}$$

The general mass balance equations for the determination of carbon, oxygen, and hydrogen in the pyrolysis reaction are expressed as Eqs. (13), (14), and (15).

Carbon Balance

$$Y_{C,F} - Y_{C,ch} * Y_{ch,F} = Y_{C,tar} * Y_{tar,F} + Y_{C,CH_4} * Y_{CH_4,F} + Y_{C,CO} * Y_{CO,F} + Y_{C,CO_2} * Y_{CO_2,F}$$

(13)

Oxygen Balance

$$Y_{O,F} - Y_{O,ch} * Y_{ch,F} = Y_{O,tar} * Y_{tar,F} + Y_{O,CO} * Y_{CO,F} + Y_{O,CO_2} * Y_{CO_2,F} + Y_{O,H_2O} * Y_{H_2O,F}$$

(14)

Hydrogen Balance

$$Y_{H,F} - Y_{H,ch} * Y_{ch,F} = Y_{H,tar} * Y_{tar,F} + Y_{H,CH_4} * Y_{CH_4,F} + Y_{H,H_2} * Y_{H_2,F} + Y_{H,H_2O} * Y_{H_2O,F}$$

(15)

3 Results and Discussion

The present developed model is programmed and executed on 'MATLAB R2015b' platform in order to predict the yields of different pyrolysis products. The effects of temperature and biomass compositions on the yield of different pyrolysis products are analyzed. The model coded for the pyrolysis temperature range from 200 to 1000 °C, and the results are obtained as the program output, exported in the form of excel sheet.

3.1 Effect of Temperature

The developed model depicts the overall trend of the yield of char, tar, and volatile components obtained from rice straw with respect to temperature in Fig. 1. The volatiles components are , namely carbon dioxide, carbon monoxide, methane, and hydrogen gas. The char yield decreases in an exponential way and becomes steady at higher temperature due to the fixed carbon content in the biomass. The tar quantity increases at the initial pyrolysis process and then declines due to secondary cracking. Among the volatiles, the levels of hydrogen, methane, and carbon monoxide increased with increase in temperature at the later stage of pyrolysis. From Fig. 2, it is observed that at a higher yield of water is obtained at the pyrolysis
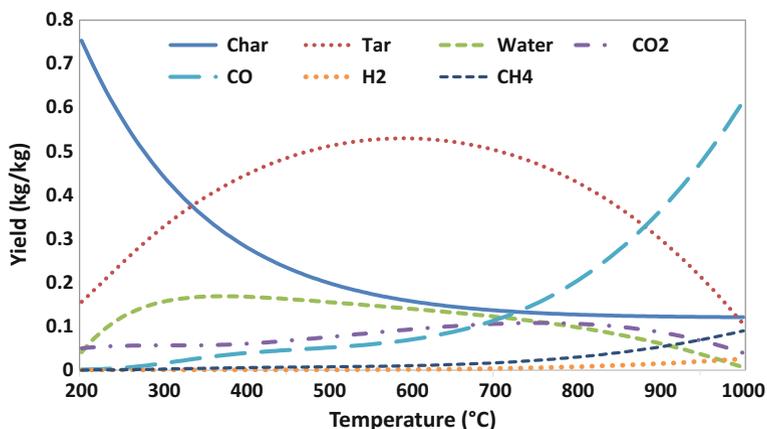
Fig. 1 Effect of pyrolysis temperature on various product yield obtained from rice straw
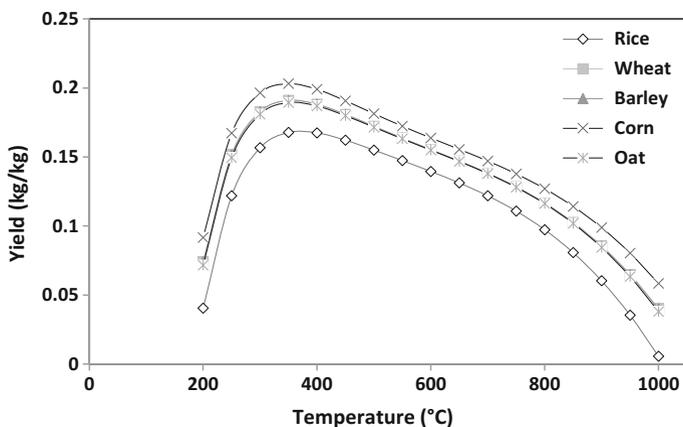
Fig. 2 Effect of pyrolysis temperature on water yield from different straw biomass

temperature around 300 °C; the results are due to the release of bound moisture in the biomass. In case of the volatile compounds, the increasing trend of carbon dioxide release was observed up to 800 °C and a further increase in temperature presented sudden drop of carbon dioxide yield (Fig. 3). Similar trends have been observed in the other four types of straws such as barley, oat, corn, and wheat. It might be due to the fact that all the studied agro-residues belonged to the category of straw that comes under the lignocellulosic biomass.

The amount of tar produced found increasing up to the temperature around 600 °C (Fig. 1). At a temperature higher than 600 °C, the yield of tar begins to decrease due to the secondary cracking of tar into gaseous species. The main

Fig. 3 Effect of temperature pyrolysis on carbon dioxide yield from different straw biomass

components of tar are benzene, toluene, styrene, phenol compounds, and a meager amount of naphthalene [13]. These compounds of tar are especially phenol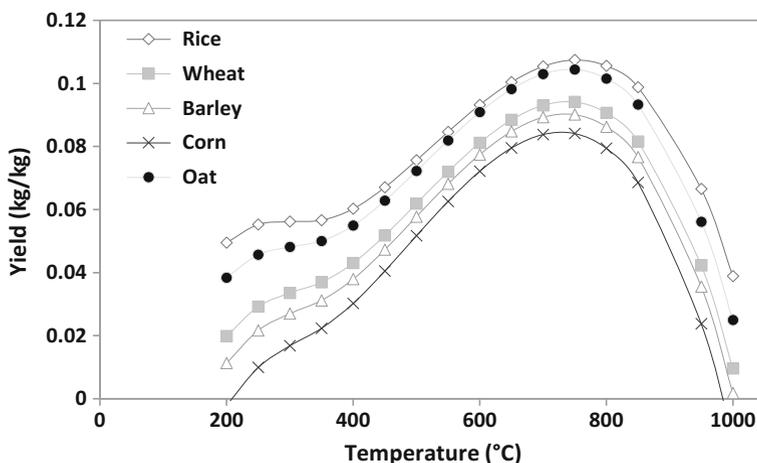s and oxygenated tar species get cracked at higher temperatures around 700 °C and produce hydrogen and carbon dioxide gases. These results in increased carbon dioxide and hydrogen gas yields in the temperature range of 700–800 °C [14].

The investigation of the pyrolysis model showed that the considered straw types of biomass produced an almost same quantity of tar. However, oat straw produced a slightly lesser quantity of tar than the other straw types. From the model used, the ratio of oxygen present in tar to the oxygen present in parent biomass was 0.8 [2]. From [12], the concentration of oxygen in the oat straw was found to be higher than the other straw types. Therefore, the presence of a higher proportion of oxygen may affect the overall tar yield of oat straw.

Figure 1 shows the yield of hydrogen and methane for the temperature effect. Both the volatiles are observed increasing in the temperature range of 800–1000 °C. Park et al. [15] showed that due to secondary thermal cracking of tar at 800 °C, there is a sudden increase in methane and carbon monoxide compounds. The carbon monoxide yield increases drastically around the temperature range of 700–800 °C as shown in Fig. 1. Im-orb et al. [16] also reported that carbon monoxide level increases from the range of temperature 500 to 700 °C.

Moisture content present in the biomass contributes to the over all liquid yield of the pyrolysis. Figure 2 indicated that the yield of water increases up to 300 °C, which may be due to the release of bound water molecules from the biomass and then decreases linearly up to 1000 °C. The water vapor produced at higher temperature reformed into hydrogen and methane in the gas phase leading to the decrease in pyrolytic water and increase in the level of hydrogen and methane [16].

Figure 3 depicts the pattern of carbon dioxide yield influenced by the temperature. Around 800 °C, the yield of carbon dioxide found highest and then followed by a decline phase up to 1000 °C. This was due to the partial oxidation of carbon to carbon monoxide at higher temperature rather than complete oxidation to form carbon dioxide.

3.2 Effect of Biomass

In the present model, the char yield is dependent directly on the pyrolytic temperature and independent of the biomass used. Thus, char yield remains almost same for all the types of straw used. However, in the pyrolytic process, the feedstock biomass utilized affects the char yield. By using Eq. (16), the calculated char yield was obtained.

$$\text{Calculated char yield} = 1 - (Y_{\text{tar,F}} + Y_{\text{H}_2\text{O,F}} + Y_{\text{H}_2\text{,F}} + Y_{\text{CO,F}} + Y_{\text{CH}_4\text{,F}} + Y_{\text{CO}_2\text{,F}})$$
(16)

It can be observed from Fig. 1, that with an increase in temperature; the char yield decreases exponentially, and at a higher temperature range, the char yield becomes almost constant. This trend of char yield found similar to the results of [17]. The result observation is because the fixed carbon content increases with increase in temperature [18].

Effect of higher pyrolysis temperature on different straw biomasses has been expressed in Fig. 4. At the higher temperature of pyrolysis, the calculated char yield of rice is higher than the calculated char yield of oats. This can be due to higher fixed carbon content in the rice straw than in comparison to the oat straw. The standard average percentage composition of CHO in the straw biomass assumed to be 49% of carbon, 5.90% of hydrogen and remaining 44% of oxygen. This standard composition is used for determining the char yield in this model. Deviation from this standard biomass composition causes the change in the biochar yield. Higher the deviation from the standard composition causes higher the variation in the biochar yields. Since all the straw biomasses have almost similar elemental (from Table 1) and biochemical composition (from Table 2), the practice of co-pyrolysis process could be promoted. This can be an energy-efficient process of using combined different straw biomasses since the straws do not need to be pyrolyzed separately due to availability restrictions. The characteristics of pyrolysis product-biochar include the particle size, density, porous structure and pH varies based on the feedstock biomass type [19].
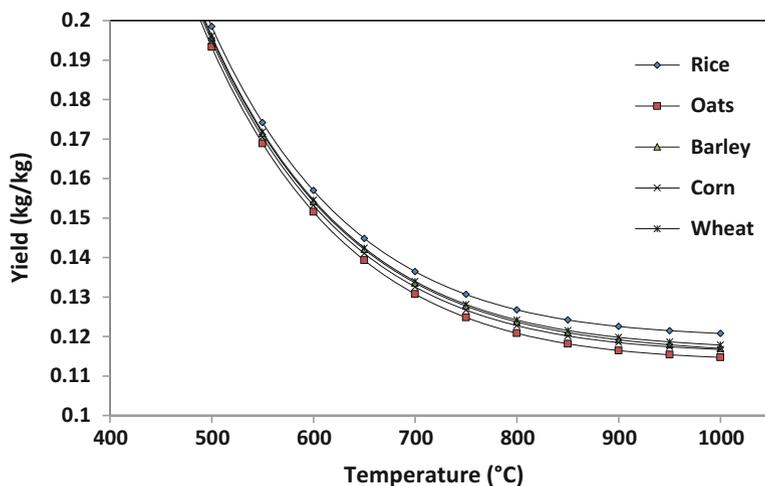
Fig. 4 Effect of various straw biomass on char yield at higher pyrolysis temperature

The hydrogen present in the straw contributes to the water yield during pyrolysis since corn straw has higher hydrogen percentage (Fig. 2). Other straws yield less amount of pyrolytic water than corn straw because of the lower hydrogen percentage. Figure 3 indicated that the rice straw produces more amount of carbon dioxide during the pyrolysis reaction due to the higher carbon percentage, whereas corn straw produces lesser amount due to the lower carbon content biomass.

4 Model Validation

The model has been validated by comparing the model predicted value with the actual experimental yield for various straw biomasses as given in Table 3. Different operating temperatures are considered, compared, and validated for each straw biomass. In the case biochar yield from barley and oat straws, model predicts the yield which slightly differs by 20% form the experimental value. In the case of tar, for wheat straw biomass, predicted value slightly differs by 21.5%, for wheat straw biomass, it is 18%, and for maize, it is 13%. Rice and barley straws tar yield prediction is almost similar to the actual experimental value. In the gaseous component yield prediction, result greatly varies for barley around 66%, and for the other straws, the difference is insignificant.

Table 3 Percentage difference in the predicted and the measured value for different pyrolytic components

Straw biomass	Operating temperature (°C)	Biochar yield		Tar yield		Gaseous component		References
		Experimental	Predicted	Experimental	Predicted	Experimental	Predicted	
Rice	510	0.2	0.18	0.51	0.51	0.27	0.31	Ji-Lu [24]
Wheat	350	0.32	0.34	0.314	0.4	0.359	0.36	Krishna et al. [25]
Oat	400	0.35	0.27	0.35	0.43	0.3	0.3	Mani et al. [26]
Barley	500	0.15	0.19	0.56	0.51	0.1	0.3	Mullen et al. [27]
Maize	400	0.34	0.27	0.381	0.44	0.28	0.29	Ravikumar et al. [28]

5 Conclusion

The model presents the simplified and generalized equations for predicting the pyrolysis yields of char, tar, and volatiles. The pyrolytic model has been designed and executed in the MATLAB R2015b software platform. The biomass elemental composition is used as input in the present model for the prediction of volatiles gas and tar composition. In this paper, the elemental compositions of straw biomasses such as rice, corn, barley, oat, and wheat were subjected to predict their conversion behaviors at various pyrolytic temperatures. The char and tar yield found almost same for the straw biomasses considered in the present investigation as all belonged to the category of lignocellulosic biomasses. The yield of carbon dioxide obtained highest at 600–700 °C. The yield of other volatiles includes carbon monoxide, hydrogen, and methane increasing around a temperature range of 700–800 °C. Further, validation of the model is also carried out for all the five types of straw biomasses, and difference of mostly around 20% is found in predicted and actual yield. The elemental compositions of different straw biomasses were witnessed equivalent in nature, and these observations encourage the employment of co-pyrolysis for an energy-efficient conversion process.

References

1. Sharma, A.K., Ravi, M.R., Kohli, S.: Modelling product composition in slow pyrolysis of wood. SESI J. **16**(1), 1–11 (2006)
2. Song, B.: Biomass pyrolysis for biochar production: kinetics, energetics and economics. Biochar 227–238 (2016)
3. Tillman, D.A.: Wood Combustion: Principle, Processes, and Economics. Elsevier, New York City, New York (2012)
4. Lehmann, J., Joseph, S.: Biochar for environmental management: science and technology (2009)
5. Steiner, T., Mosenthin, R., Zimmermann, B., Greiner, R., Roth, S.: Distribution of phytase activity, total phosphorus and phytate phosphorus in legume seeds, cereals and cereal by-products as influenced by harvest year and cultivar. Anim. Feed Sci. Technol. **133**(3), 320–334 (2007)
6. Woolf, D., Amonette, J.E., Street-Perrott, F.A., Lehmann, J., Joseph, S.: Sustainable biochar to mitigate global climate change. Nat. Commun. **1**, 56 (2010)
7. Shihadeh, A., Hochgreb, S.: Diesel engine combustion of biomass pyrolysis oils. Energy Fuels **14**(2), 260–274 (2000)
8. Boroson, M.L., Howard, J.B., Longwell, J.P., Peters, W.A.: Product yields and kinetics from the vapor phase cracking of wood pyrolysis tars. AIChE J. **35**(1), 120–128 (1989)
9. Thunman, H., Niklasson, F., Johnsson, F., Leckner, B.: Composition of volatile gases and thermochemical properties of wood for modeling of fixed or fluidized beds. Energy Fuels **15**(6), 1488–1497 (2001)
10. Neves, D., Thunman, H., Matos, A., Tarelho, L., Gómez-Barea, A.: Characterization and prediction of biomass pyrolysis products. Prog. Energy Combust. Sci. **37**(5), 611–630 (2011)
11. Yoder, J., Galinato, S., Granatstein, D., Garcia-Pérez, M.: Economic tradeoff between biochar and bio-oil production via pyrolysis. Biomass Bioenerg. **35**(5), 1851–1862 (2011)

12. Vassilev, S.V., Baxter, D., Andersen, L.K., Vassileva, C.G.: An overview of the chemical composition of biomass. Fuel **89**(5), 913–933 (2010)
13. Zhang, Y.L., Wu, W.G., Zhao, S.H., Long, Y.F., Luo, Y.H.: Experimental study on pyrolysis tar removal over rice straw char and inner pore structure evolution of char. Fuel Process. Technol. **134**, 333–344 (2015)
14. Nowakowska, M., Herbinet, O., Dufour, A., Glaude, P.A.: Detailed kinetic study of anisole pyrolysis and oxidation to understand tar formation during biomass combustion and gasification. Combust. Flame **161**(6), 1474–1488 (2014)
15. Park, J., Lee, Y., Ryu, C.: Reduction of primary tar vapor from biomass by hot char particles in fixed bed gasification. Biomass Bioenerg. **90**, 114–121 (2016)
16. Im-orb, K., Simasatitkul, L., Arpornwichanop, A.: Analysis of synthesis gas production with a flexible H_2/CO ratio from rice straw gasification. Fuel **164**, 361–373 (2016)
17. Peng, X., Ye, L.L., Wang, C.H., Zhou, H., Sun, B.: Temperature-and duration-dependent rice straw-derived biochar: Characteristics and its effects on soil properties of an Ultisol in southern China. Soil Tillage Res. **112**(2), 159–166 (2011)
18. Encinar, J.M., Gonzalez, J.F., Gonzalez, J.: Fixed-bed pyrolysis of Cynaracardunculus L. Product yields and compositions. Fuel Process. Technol. **68**(3), 209–222 (2000)
19. Zhang, Q., Yang, Z., Wu, W.: Role of crop residue management in sustainable agricultural development in the North China Plain. J. Sustain. Agric. **32**(1), 137–148 (2008)
20. Binod, P., Sindhu, R., Singhania, R.R., Vikram, S., Devi, L., Nagalakshmi, S., Kurien, N., Sukumaran, R.K., Pandey, A.: Bioethanol production from rice straw: an overview. Biores. Technol. **101**(13), 4767–4774 (2010)
21. Shawky, B.T., Mahmoud, M.G., Ghazy, E.A., Asker, M.M., Ibrahim, G.S.: Enzymatic hydrolysis of rice straw and corn stalks for monosugars production. J. Genet. Eng. Biotechnol. **9**(1), 59–63 (2011)
22. Sun, Y., Cheng, J.: Hydrolysis of lignocellulosic materials for ethanol production: a review. Biores. Technol. **83**(1), 1–11 (2002)
23. Rowell, R.M.: Opportunities for lignocellulosic materials and composites. 12–27 (1992)
24. Ji-Lu, Z.: Bio-oil from fast pyrolysis of rice husk: yields and related properties and improvement of the pyrolysis system. J. Anal. Appl. Pyrol. **80**(1), 30–35 (2007)
25. Krishna, B.B., Singh, R., Bhaskar, T.: Effect of catalyst contact on the pyrolysis of wheat straw and wheat husk. Fuel **160**, 64–70 (2015)
26. Mani, T., Murugan, P., Mahinpey, N.: Pyrolysis of oat straw and the comparison of the product yield to wheat and flax straw pyrolysis. Energy Fuels **25**(7), 2803–2807 (2011)
27. Mullen, C.A., Boateng, A.A., Hicks, K.B., Goldberg, N.M., Moreau, R.A.: Analysis and comparison of bio-oil produced by fast pyrolysis from three barley biomass/byproduct streams. Energy Fuels **24**(1), 699–706 (2009)
28. Ravikumar, C., Kumar, P.S., Subhashni, S.K., Tejaswini, P.V., Varshini, V.: Microwave assisted fast pyrolysis of corn cob, corn stover, saw dust and rice straw: Experimental investigation on bio-oil yield and high heating values. Sustainable Mater. Technol. **11**, 19–27 (2017)

Optimization of Etherification Reactions for Recycling of Tea Fungal Biomass Waste into Carboxymethylcellulose

Iragavarapu Akhil Gargey, Dash Indira, R. Jayabalan and P. Balasubramanian

1 Introduction

Cellulose ethers are industrially world's most produced ethers, and the primary source of raw material for cellulose is obtained mainly from plants. Cellulose is a polymer made of glucose monomer units. It is located in plants cell wall. Industrially, extraction of cellulose is highly tricky and expensive because it is tightly bound to hemicellulose and lignin polymer chains. Large areas of fertile lands are wasted in growing these plants to obtain cellulose. These lands are continuously reused for plantation. Microorganisms are also a significant source for production of cellulose; they take sucrose, glucose, and mannose as substrates and excrete cellulose as a waste product. Incubation periods of these microorganisms vary from 24 h to 1 week. These organisms are used industrially to produce cellulose as they overcome the difficulties faced while processing cellulose from plants. Industrially, cellulose is obtained from plants or microorganisms and converted into carboxymethylcellulose (CMC) by etherification reaction [1]. CMC is a cellulose derivative with carboxymethyl groups (–CH$_2$–COOH) bound to some of the hydroxyl groups of the glucopyranose monomers that make up the cellulose backbone. It is often used as its sodium salt, sodium carboxymethylcellulose.

CMC is the most broadly utilized cellulose ether today, with applications in the cleanser, paper material, pharmaceutical, and paint businesses. Manufacturing of CMC is less severe than that of most other cellulose ethers since all responses are worked at atmospheric pressure and economically available reagents. The etheri-

I. A. Gargey · P. Balasubramanian (✉)
Department of Biotechnology and Medical Engineering,
NIT Rourkela, Rourkela, Odisha, India
e-mail: balap@nitrkl.ac.in

D. Indira · R. Jayabalan (✉)
Department of Life Science, NIT Rourkela, Rourkela, Odisha, India
e-mail: jayabalanr@nitrkl.ac.in

fying reagent, sodium monochloroacetate, is easy to handle and exceptionally proficient. Therefore, CMC has turned into the biggest mechanical cellulose ether. Expansive amounts are delivered in unrefined business grades with no refining for use in cleansers, oil boring, and in the paper business. High-virtue evaluations are additionally utilized as sustenance added substances [2].

Kombucha tea is devoured worldwide for its invigorating and useful properties on human well-being. Reports asserting that drinking Kombucha can avert different sorts of malignancy and cardiovascular illnesses, promote liver capacities, and fortify the immune system. Kombucha tea (symbiotic association of yeast and bacteria) produces abundant mats (fungal tea biomass) rich in cellulose as a waste product [3]. This biomass waste can be used to produce cellulose ether (carboxymethylcellulose, CMC) by simple chemical conversion called Williamson's ether synthesis [4, 5].

The present paper aimed to evaluate the influencing factors on conversion of Kombucha tea waste into carboxymethylcellulose and optimizing the etherification reaction conditions to achieve the maximal yield of carboxymethylcellulose.

2 Materials and Methods

2.1 Preparation of Kombucha Tea

About 50 g of sucrose was weighed and added to the boiling water and stirred for 5 min. Then, 6 g of tea leaves/powder (green tea leaves, black tea powder, and tea waste material) was added and stirred for 5 min to make a decoction. The mixture was filtered and distributed among 15 flasks, five flasks containing one brewed tea. Each flask contained 100 ml of brewed tea. Previously inoculated culture (3 g) was added along with 10 ml of previously fermented tea liquor which reduces the pH thereby preventing the growth of contaminants. The flasks were covered with paper cloth to keep insects away. The preparation was incubated at 20 to 22 °C (the optimal incubation temperature ranges from 18 to 26 °C) in dark and away from sunlight [6].

2.2 Estimation of Various Compounds in Tea Broth as the Fermentation Proceeds Over Time

Sampling was done every third day of fermentation. Tea broth sample (5 ml) was taken from each flask after removing the mats and stored at 4 °C until analysis. HPLC was used to determine various compounds present in the broth. The concentration of biomolecules in Kombucha during fermentation was estimated using high-performance liquid chromatographic system with refractive index detector (Shimadzu, Japan). Agilent Hiplex column was used with 5-mM sulfuric acid as

mobile phase, 0.7 mL/min as flow rate, and 60 °C as column temperature. Amount of metabolites were estimated by using respective standards purchased from HiMedia, Mumbai, India, and Sigma, USA. Citric acid, sucrose, glucose, acetic acid, glycerol, and ethanol estimations were done during the 14-day period for all three tea broths.

2.3 Conversion of Tea Fungal Biomass Waste into Carboxymethylcellulose

Biomass waste (1 g) was taken in 250-ml bottle. Then, 20-ml IPA is added to the biomass powder and stirred for 5 min. The bottle was placed on a magnetic stirrer at 200 rpm, and 2 ml of 30% NaOH was added dropwise using a micropipette and stirred for an hour. The mixture was filtered, and the residue was suspended in 60-ml methanol overnight. Residue was again filtered and dried to constant weight [7]. The obtained product (as shown in Fig. 1) was subjected to Fourier transform infrared spectroscopic (FTIR) analysis for further characterization and to determine the degree of substitution.

2.4 Determination of Degree of Substitution (DS)

Etherified samples (0.2 mg) were pelletized with KBrandwere finely ground and pressed. The infrared spectra of these samples were recorded with a Perkin Elmer spectrometer between 400 and 4000 cm^{-1}. The degree of substitution of the carboxyl group in CMC can be determined by taking the ratio of the absorption spectra by following Eq. (1).

$$R\mathrm{rel} = \frac{A_{1605}}{A_{2920}} \tag{1}$$

Fig. 1 Reaction scheme of the carboxymethylation of cellulose

Table 1 Experimental range of influencing factors on etherification of tea fungal biomass waste to carboxymethyl cellulose

Factors	Name	Units	Low	High
A	NaOH reaction time	Minutes (min)	30	180
B	SMCA concentration	Grams (g)	0.2	1
C	NaOH concentration	% (w/v)	10	50
D	IPA concentration	% (v/v)	50	100
E	SMCA reaction time	Minutes (min)	30	180

The relative degree of substitution (DSrel) can be determined by following Eq. (2) [8].

$$DSrel = Rrel - 1 \tag{2}$$

The above equations were utilized to estimate the relative amount of carboxyl groups in the recycled tea waste samples.

2.5 Optimization of Reaction Parameters

Biomass waste (0.5 g) was taken in 250-ml Schott bottle. Then, 10 ml of absolute IPA was added and stirred for 5 min. One ml of 30% (w/v) NaOH was added dropwise and stirred for an hour on a hot plate magnetic stirrer. After that, 0.6 g SMCA was added and stirred for three hours on a hot plate magnetic stirrer at nearly 200 rpm and 45 °C. Mixture was filtered and suspended in 30-ml methanol overnight. Residue was again filtered and dried up to constant weight. This was repeated five times, each time varying a parameter and keeping all other parameters constant to follow a one variable at a time approach. Concentration of IPA was varied from 50 to 100% (v/v). Weight of SMCA was varied from 0.2 to 1 g. Reaction periods of both NaOH and SMCA were varied from range 30 to 180 min. Concentration of NaOH was varied over a range of 10 to 50% (w/v). The obtained products after etherification reaction from tea fungal biomass waste were subjected to FTIR analysis to determine the degree of substitutions. Table 1 outlined the range of influencing factors on experimental conditions.

3 Results and Discussion

3.1 Optimum Tea Broth for Production of Maximum Biomass

It was evident from Fig. 2 that green tea supports the maximum growth rate of tea fungus, and hence, the production of higher biomass waste compared to other two
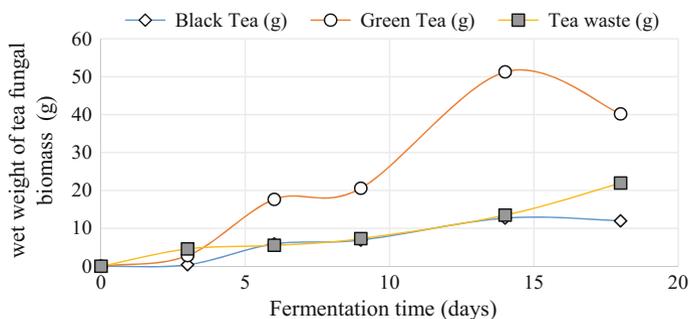
Fig. 2 Growth trend of fungal biomass on different tea substrates

tea substrates was studied. Black tea and tea waste material showed an increase in weight of fungal tea biomass up to 14 days. Tea waste material supported an increase in fungal tea biomass even after 18 days. All the tea substrates showed an increase in biomass for 14 days, and there was a slight decrease in the biomass after 14 days in green tea and black tea due to the two following reasons. Firstly, after 14 days of fermentation bacteria yeast have entered into stationary phase and the pH was decreased which led to the death of acid-sensitive cells in the biomass. Acid-sensitive microbial cells were released into the tea broth which would have decreased the weight of the fungal tea biomass. Secondly, all the collected tea fungal biomasses were blotted on a filter paper for 5 min. The rate of absorption of water from these biomasses was proportional to their wet weights. Hence, more amount of water was absorbed from biomasses which were collected on day 18. This led to the decrease in weights considerably compared to biomasses taken on day 14.

3.2 Proof of Carboxymethylation

As shown in Fig. 3, peaks at 1420 and 1320 cm^{-1} were observed in the absorbance spectra of recycled tea fungal biomass waste to carboxymethylcellulose product obtained from the etherification reaction. These peaks correspond to CH$_2$ scissoring and –OH bending vibration, respectively. Successful conversion of fungal tea biomass into CMC was indicated by the presence of peaks at 2920 and 1605 cm^{-1} which correspond to carboxymethyl group and C–H vibration, respectively. The conversion of cellulose to CMC was validated by comparing the spectra obtained from the tea biomass to that of commercially available CMC as shown in Fig. 4.
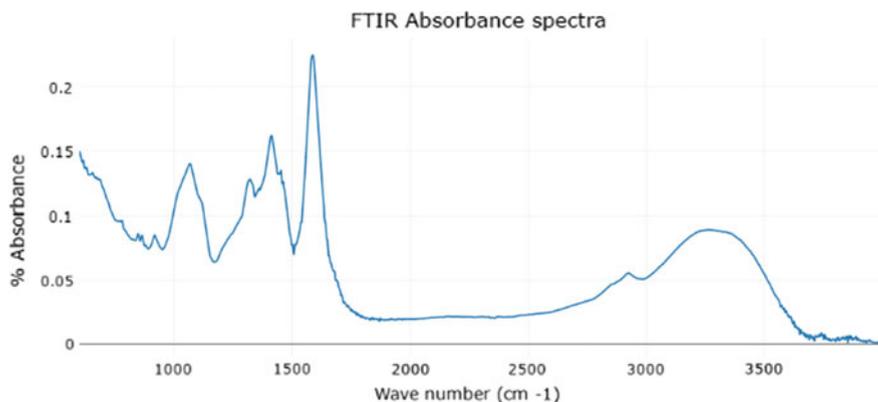
Fig. 3 FTIR spectrum of carboxymethylcellulose obtained from fungal tea biomass through etherification reaction
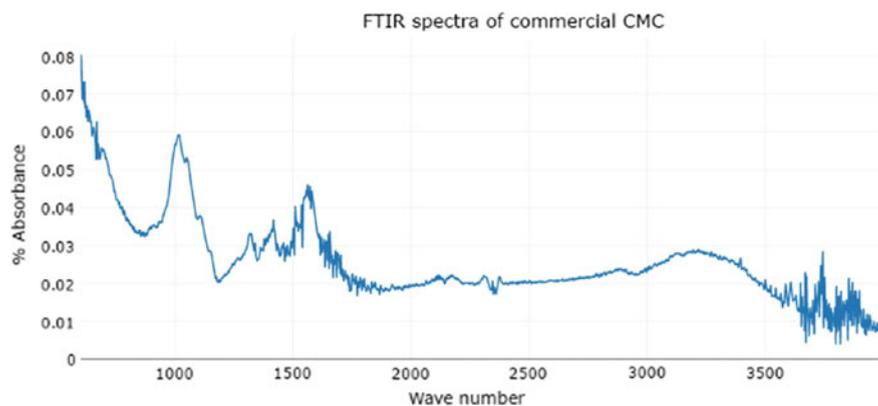
Fig. 4 FTIR spectrum of commercially available carboxymethyl cellulose

3.3 Effects of Variation of Parameters on the Degree of Substitution

3.3.1 Effect of Reaction Period of NaOH

As shown in Fig. 5, the carboxymethylation reaction was carried out in six different reaction periods ranging from 30 to 180 min. A maximum DS of 2.73 was obtained with 120 min. There was an increase of DS with reaction period up to 120 min and after that DS decreases. This increase may be because there is better reaction

Fig. 5 Effect of reaction period of NaOH on degree of substitution of CMC from fungal tea biomass

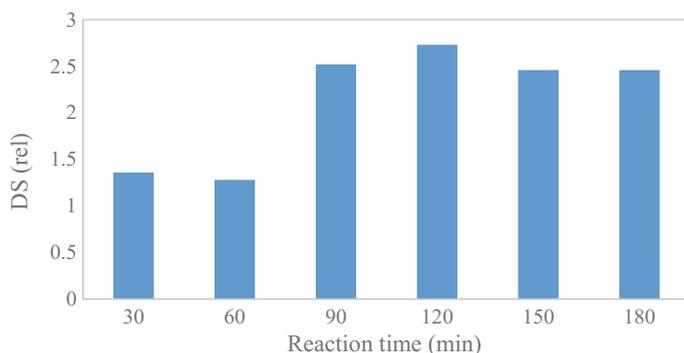environment created due to the prolonged duration of reaction [9]. This helps in diffusion and absorption of reactants to make better contact with each other. A possible explanation for the decrease after 120 min may be due to an increased degradation of the polymer.

3.3.2 Effect of Concentration of Isopropyl Alcohol

As shown in Fig. 6, the carboxymethylation reaction was carried out in three water: isopropyl alcohol concentrations. A maximum DS of 2.28 was obtained at 10:90 (v/v %). It was observed that increase in the rate of organic solvent increases the DS of the CMC produced. It was observed that isopropyl alcohol causes pronounced decrystallization of cellulose and a change of polymorphism from cellulose I to cellulose II.
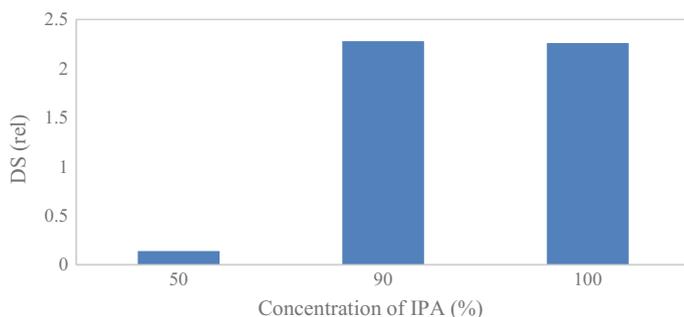

Fig. 6 Effect of various concentrations of IPA on degree of substitution of CMC from fungal tea biomass

The change of crystallinity may be due to the partition of sodium hydroxide between cellulose and reaction medium. This occurs while cellulose chains were suspended in a mixture of organic solvent, water, and sodium hydroxide. The decrease in DS after 10:90 (v/v %) may be attributed to the fact that isopropyl has a high dielectric constant and is a harmful solvent for sodium hydroxide in the presence of cellulose.

3.3.3 Effect of Concentration of SMCA

As shown in Fig. 7, the carboxymethylation reaction was carried out in five different concentrations of sodium monochloroacetate. A maximum DS of 2.9 was obtained at 1 g SMCA concentration. There was an increase in DS concentration of SMCA. The increase probably is due to higher availability of acetate ions at a higher concentration in the proximity of cellulose molecules.

3.3.4 Effect of concentration of NaOH

As shown in Fig. 8, the effect of sodium hydroxide concentration was studied by varying the concentration of the sodium hydroxide solution. It was observed that DS of CMC increased with NaOH concentration and attained a maximum DS of 3.54 at 40% (w/v) concentration. After that, the decline in DS may be due to the side reaction of sodium hydroxide and SMCA producing sodium glycolate. Predomination of this side reaction decreases SMCA concentration, and thereby, it directly affects the degree of substitution [10].
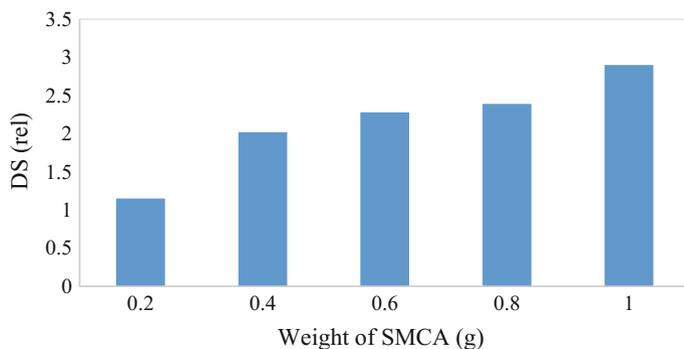
Fig. 7 Effect of various concentrations of NaOH on degree of substitution of CMC from fungal tea biomass
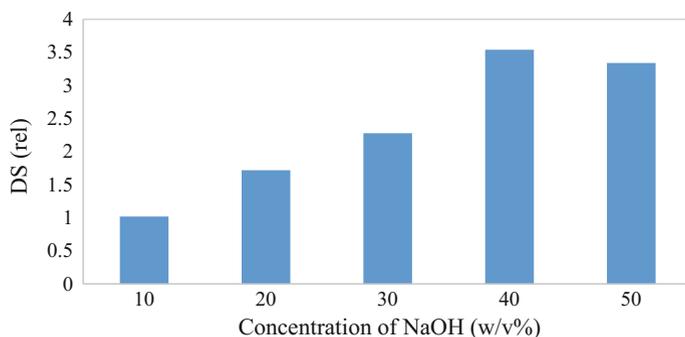
Fig. 8 Effect of various concentrations of NaOH on degree of substitution of CMC from fungal tea biomass

3.3.5 Effect of Reaction of SMCA

As shown in Fig. 9, carboxymethylation reaction was carried out in five different reaction periods. A maximum DS of 2.5 was obtained with 150 min. There was an increase in DS with reaction period up to 150 min and after that DS decreases. The increase may be due to the fact that prolonged duration of reaction allows better contact of reactants. The decline after 150 min is due to decrease in reaction efficiency. This was explained by Pusphamalar et al. [7] who carried similar studies on sago pulp waste.
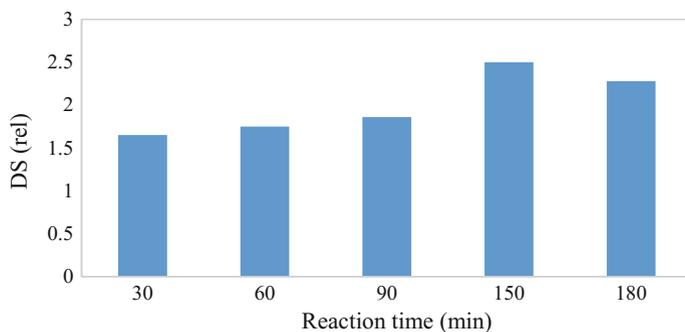

Fig. 9 Effect of various reaction periods of SMCA on degree of substitution of CMC from fungal tea biomass

4　Conclusion

The present paper evaluated the possibilities of converting tea fungal biomass waste into the useful product such as carboxymethylcellulose through etherification reactions. The influencing factors of the etherification reaction such as the concentration of SMCA, isopropyl alcohol, NaOH, and the reaction time of SMCA and NaOH were optimized using one variable at a time approach. The optimal conditions for the maximal yield of carboxymethylcellulose from cellulose obtained from tea fungal biomass waste were as follows: NaOH reaction period of 120 min; SMCA weight of 1 g; NaOH concentration of 40%; IPA concentration of 90%; SMCA reaction period of 150 min. These optimized conditions could be helpful while utilizing the tea fungal biomass waste to carboxymethylcellulose during the scale-up waste to wealth process for attaining sustainability.

References

1. Xiquan, L., Tingzhu, Q., Shaoqui, Q.: Kinetics of the carboxymethyl cellulose in the isopropyl alcohol system. Acta Polym. **41**, 220 (1990)
2. Dahlman, O., Jacobs, A., Sjoberg, J.: Molecular properties of hemicelluloses located in the surface and inner layers of hardwood and softwood pulps. Cellulose 325–334 (2003)
3. Jayabalan, R., Malabasa, R., Satishkumar, M.: Kombucha tea: metabolites. In: Fungal Metabolites (2015)
4. Tijsen, C.J., Kolk, H.J., Stamhuis, E.J., Beenackers, A.A.C.M.: An experimental study on the carboxymethylation of granular potato starch in non-aqueous media. Carbohydr. Polym. **45**, 219–226 (2001)
5. Khiari, R., Salon, M.C.B., Mhenni, M.F., Mauret, E., Belgacem, M.N.: Synthesis and characterization of cellulose carbonate using greenchemistry: Surface modification of Avicel. Carbohydr. Polym. **163**, 254–260 (2017)
6. Jayabalan, R., Radomir, M.V., Satishkumar, M., Jasmina, V.S.: A review on Kombucha tea—microbiology, composition, fermentation, beneficial effects, toxicity, and tea fungus. Compr. Rev. Food Sci. Food Saftey **13**, 538–550 (2014)
7. Pusphamalar, V., Langford, S., Ahmad, M., Lim, Y.: Optimization of reaction conditions for preparing carboxymethyl cellulose from sago waste. Carbohydr. Polym. **64**, 312–318 (2006)
8. Miyamoto, K., et al.: Preparation of carboxymethyl-gellan. Carbohydr. Polym. **30**, 161–164 (1996)
9. Bhattacharyya, D., Singhal, R.S., Kulkarni, P.R.: A comparative account of conditions for synthesis of sodium carboxymethyl starch from corn and amaranth starch. Carbohydr. Polym. **27**, 247–253 (1995)
10. Khalil, M.I., Hasem, A., Habeish, A.: Carboxymethylation of maize starch. Starch/Stärke **42**, 62–63 (1990)

Erosion Identification and Assessment of a Steel Pipeline Using EMI Technique

S. N. Khante and Nidhi Jain

1 Introduction

1.1 General

A pipeline is an integral part of our civil infrastructure. Pipes are always considered convenient and safe means of transporting liquids, gases, and even some solids. These pipelines can be prone to various damages during its service life, e.g., internal corrosion, bursting due to internal forces, cracks; leakages due to improper joints. One of the important problems that the industries dealing with gas and oil face is erosion. It is very necessary to predict and monitor erosion attack on oil and gas pipelines in service so that the materials used for pipelines can perform accurately and operate safely, and thus, it will also prevent any kind of hazards or accidents. Various conventional methods such as failure records, visual inspection, weight-loss coupon analysis are used for monitoring purpose, but these methods can consume a substantial time and can only determine erosion rates leading to damage and ultimately failure.

A large number of investigations to detect corrosion or erosion have been conducted on the problems related to the deterioration of steel pipelines. For monitoring the health of the structure, the ways generally used are visual inspection and some other kinds of remedial measures and are normally adopted when the condition of the structure becomes very serious. It is desirable to monitor the condition of the structure right from the commissioning stage in order to avert the serious deterioration levels of the structure. The electromechanical impedance technique can analyze the damage at the incipient stage itself which is very helpful for the maintenance engineers and thereby beneficial for monitoring the health of

S. N. Khante (✉) · N. Jain
Department of Applied Mechanics, Government College of Engineering, Amravati,
Maharashtra, India
e-mail: snkhante@yahoo.com

347

the structure. The EMI technique uses the piezoelectric ceramic patches (PZT) which can act as actuators as well as sensors and employ ultrasonic vibrations (typically in 30–400 kHz range) to acquire the conductance 'signature' of the structure, which governs the condition of the structure and can identify structural damages.

Many steel structures have been effectively monitored using the EMI technique. Bhalla and Naskar [1] reported detailed experimental investigation taking into consideration the practical aspects of the metal wire-based EMI technique. The technique was found to be applicable to large 2D structures using a minimum number of sensors [1]. Rankhamb and Khante [2] performed experimental work on steel pipes. The main purpose to use EMI technique was to find out the effect of temperature variation and to also detect incremental damage of pipe specimen when subjected to steady constant high temperature. This technique proved to be applicable to even high-temperature locations [2]. Bhalla [3] presented an impedance approach for identification, structural health monitoring and nondestructive evaluation (NDE) of structures using piezoimpedance transducers. Farrar and Worden [4] introduced structural health monitoring system. Ukpai [5] used the electrochemical monitoring combined with acoustic emission (AE) technique for investigating erosion and erosion–corrosion deterioration rates of gas and oil pipeline materials (X65) in a saturated CO_2 environment. Asmara et al. [6] investigated combined effects of CO_2 and HAC on artificial corrosive and erosive environment containing sand particles in 45°, 90°, and 180° elbow pipelines. Their research used theoretical calculations combined with experiments for verification [6]. Du et al. [7] presented a feasibility study on the severity monitoring and crack detection of pipelines using PZTs. To quantitatively identify the pipeline damage condition at various crack depths, a wavelet packet-based crack severity index was also built [7]. Park et al. [8] presented experimental evidence on the use of impedance-based health monitoring technique on civil structural components and utilized high-frequency structural excitations through a surface-bonded PZT to detect changes in structure due to the presence of damage. Naz (2016) used a laboratory-built test rig for eroding carbon steel plates with accelerated sand streams and came to the conclusion that normal incidence of the sand stream of larger particles and higher impact velocities cause more erosion of the carbon steel [9].

1.2 Quantification of Damage

Root-mean-square deviation (RMSD) index is used to quantify the damage. The conductance response which is benchmark signature for the PZT patches attached at the ends of metal connector is obtained. The specimen is subjected to artificial erosive damage. After damage, conductance signature is recorded. Damage index is given by

$$M = \sqrt{\frac{\sum \left(G_2 - G_1\right)^2}{\sum G_1^2}}$$

where

M RMSD%.
G_1 Baseline conductance signature.
G_2 Conductance signature obtained after erosion/damage.

2   Fabrication of Metal Connector-Based PZT

In the present investigation, metal wire-based PZT is used to identify and assess the artificial erosion of 'L'-shaped pipe specimen. For the fabrication purpose, metal wire-based connector technique was used as the PZT could not be bonded directly to the surface of the pipe due to its curved shape. The connector was in the form of an aluminum foil. The length of the foil was 200 mm, the width was 20 mm, and the thickness was 1 mm. The PZT patch was bonded at one end of the metal foil using an epoxy commercially called Araldite (Fig. 1). The manufacturing company of the PZT is Central Electronics Limited (CEL), Sahibabad. The PZT patch used was of the high-frequency range having a PZT-5H grade. The size of the patch used was 10 mm × 10 mm × 0.2 mm. A sample of a PZT patch is shown in Fig. 2a. A coaxial wire is used for obtaining signatures from LCR meter. LCR meter E4980A having a frequency range of 20 Hz–2 MHz was used for acquiring the responses (signatures in the form of conductance and susceptance) of advanced PZT patches for identifying damages of pipe specimen at any time (Fig. 2b).

Fig. 1   PZT connected to structure through aluminum foil
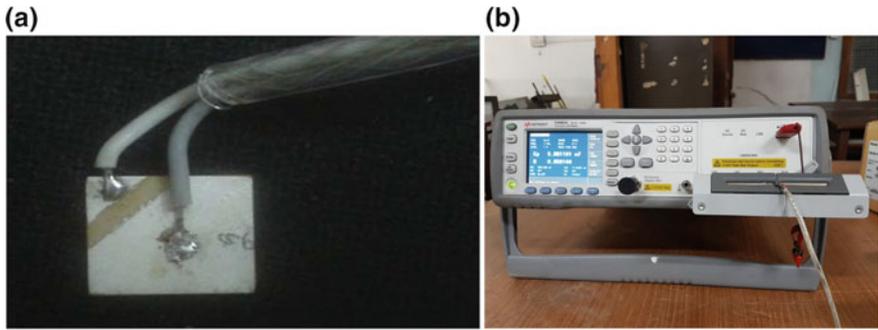
Fig. 2 **a** High-frequency PZT, **b** impedance analyzer (LCR meter)

3 Experimental Setup and Investigation

3.1 Materials and Specimen

The material consisted of a mild steel pipe of diameter of 76 mm (3 in.) and thickness of 2.4 mm. The pipe specimen consists of a short bend whose both ends are connected to the steel pipe using welding. The length of one side of the pipe which is connected to the bend is 600 mm, while the other side pipe length is kept as 300 mm, thereby making the specimen like L-shaped pipe, i.e., making an angle of 90º. Figure 3a shows a short bend which is used for joining the pipes, and Fig. 3b shows mild steel pipe which is used for the study.

Fig. 3 **a** Short bend, **b** mild steel pipe

Fig. 4 Shot-blasting gun

3.2 Setup and Procedure

The experimental setup consisted of a mild steel pipe specimen which was subjected to abrasive wear with the help of shot-blasting/grit-blasting technique. The grit was forcibly propelled against the pipe surface under 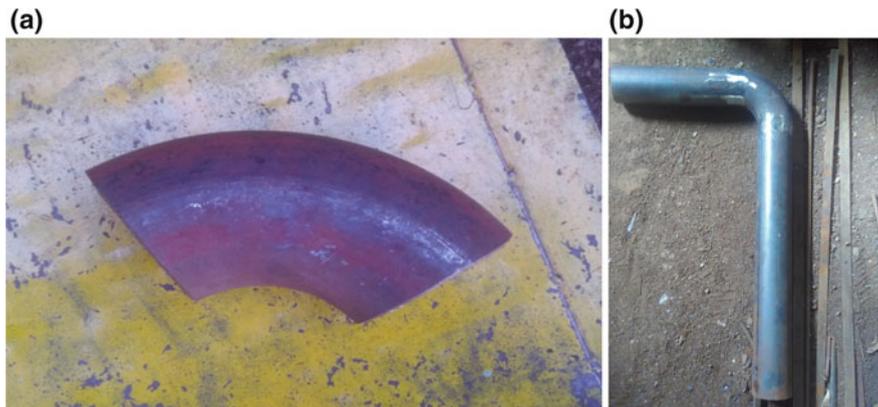high pressure. The test procedure was completed with a total number of four cycles, the blast duration of each cycle being four minutes, and the conductance signatures were obtained after each successive cycle. Figure 4 shows the nozzle of a shot-blasting gun through which the grit is propelled. Figure 5 shows the experimental arrangement which includes mild steel pipe specimen with LCR meter. Table 1 describes the operating conditions for pure erosion.

4 Results and Discussion

The wire-based PZT which is bonded to the structure is excited by means of imposing a particular frequency range. After the patch is excited, elastic waves are generated by the patch which travels through the structure and is reflected back. After each cycle of shot blasting, a certain variation was found in the structure. Figure 6a, b shows the basic and after-damage condition of the specimen from

Fig. 5 Arrangement of mild steel pipe specimen with LCR meter

Table 1 Operating conditions for pure erosion

Sr. No.	Parameter	Operating condition
1.	Nozzle diameter	18 mm
2.	Grit diameter	40 mesh (0.381 mm)
3.	Blast duration	4 min
4.	Test temperature	Room temperature ± 3 °C
5.	No. of cycles	4
6.	Angle of incidence	90°
7.	Pressure	7 bar

outside. Figure 6c, d shows the basic and after-damage condition of the specimen from inside. The portion of the red circle indicates the damaged area.

The soldered PZT patch was wired to impedance analyzer by connecting the coaxial wire with the LCR meter. The pipe specimen was subjected to the range of frequency of 100–400 kHz. For the range of frequencies, the conductance values are obtained. The graph of conductance vs frequency was plotted from the obtained data. These graphs obtained are called as signatures or conductance signatures. All the data and the graphs can be saved in Microsoft Excel. Figure 7 represents the comparison of conductance signatures obtained for healthy/baseline signature and signatures obtained for successive four cycles of erosion for four-minute duration, respectively.

By comparing the results obtained for baseline signature as well as the signatures for all the successive cycles, it can be said that the responses for every cycle are different for healthy and damaged conditions. If we compare the conductance signature for the healthy/undamaged condition of the specimen, it can be seen that after the precedence of every cycle, the lesser peak value is obtained. The decrease in peak indicates the damaged condition of the structure. The effectiveness of PZT is evident from the fact that there is a clear shift in vertical as well as the lateral direction in the recorded conductance response.
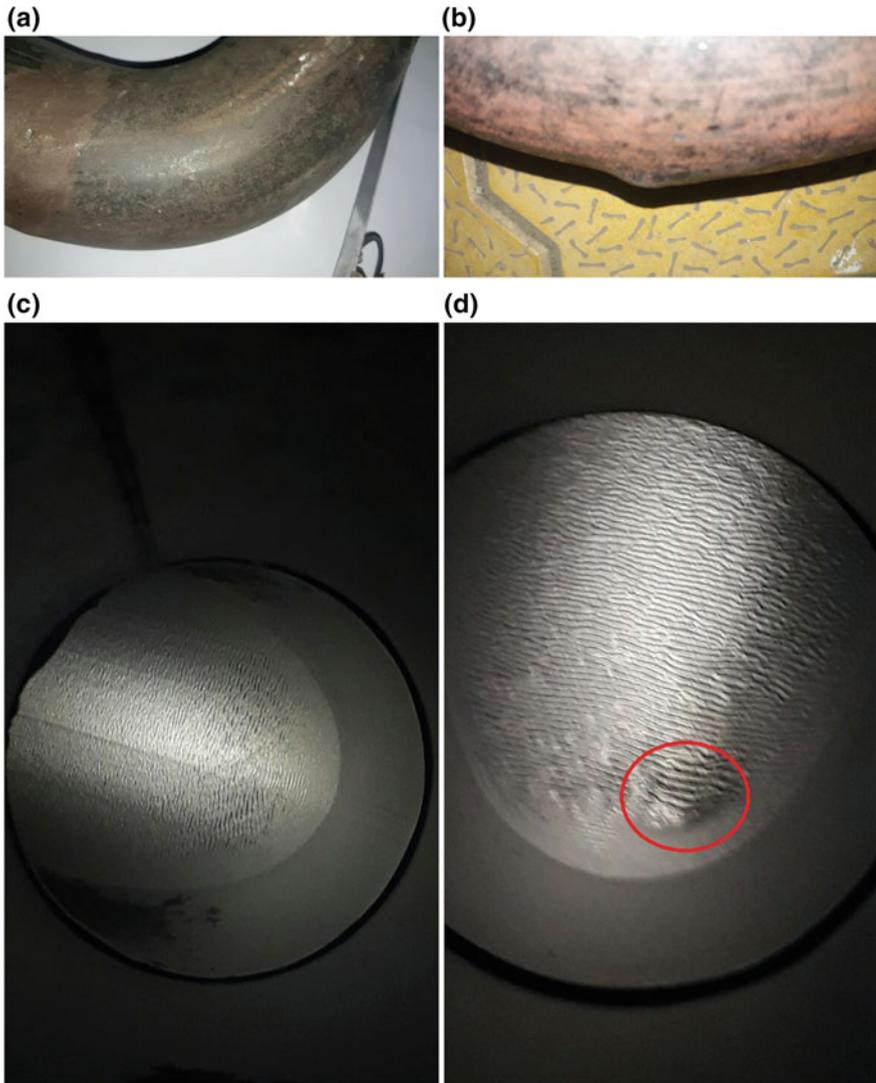
Fig. 6 **a** Undamaged pipe specimen, **b** damaged pipe specimen from outside, **c** undamaged pipe specimen, **d** damaged pipe specimen from inside

Variation was observed in conductance signature after precedence of every cycle. This is owing to the increased effect of eroding action from the shot-blasting equipment. This variation in conductance was calculated using RMSD index. Figure 8 shows the RMSD index for all the four cycles, respectively.

The RMSD indexes recorded for first, second, third, and fourth cycles were 1.66, 1.75, 1.85, and 1.86%, respectively. As the stiffness, mass, and damping of the pipe
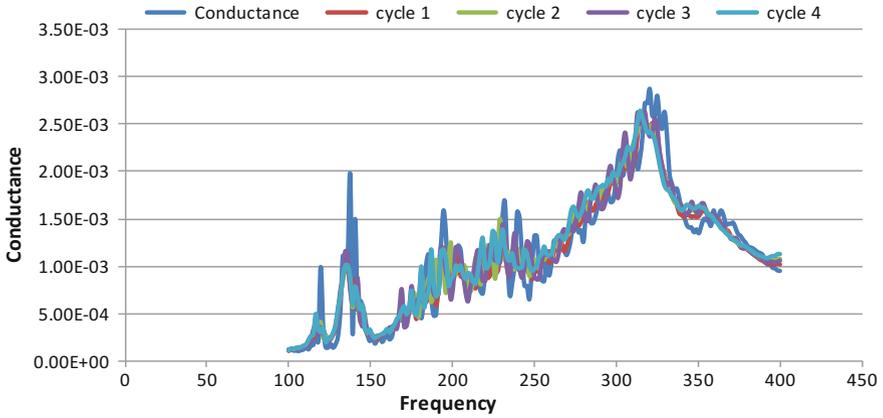
Fig. 7 Conductance signature from healthy and successive four cycles
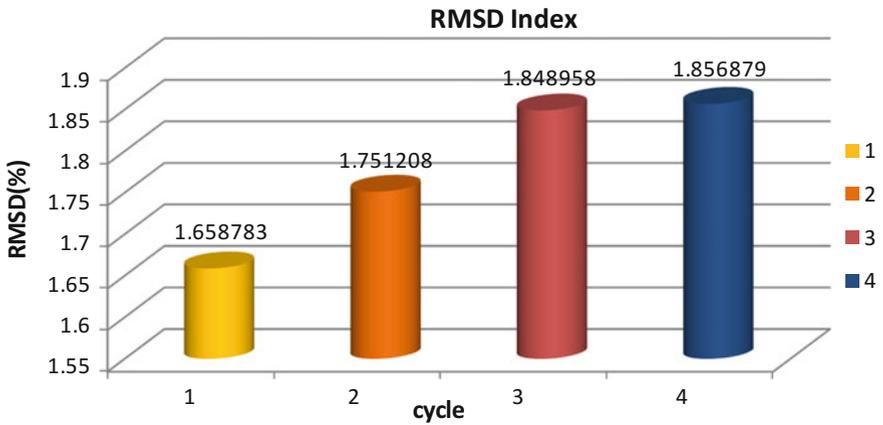
Fig. 8 RMSD index for all four cycles

bend are changing due to degradation affected by erosion, the index is found to increase from 1.66 to 1.86%. The erosion being of very small magnitude, the changes in RMSD index were also relatively less.

5   Conclusion

Pipelines are an important and integral part of oil and gas industry. The pipe failure results in immense hardship in the form of financial loss to the industry. This research intends to support the cause of health monitoring of pipes using a scientific

approach, thereby identifying the defects and flaws in pipes at incipient stages. The main conclusions of the present study are as follows:

- EMI technique is found to be a suitable technique for the identification of erosion.
- The graphs obtained identify damage by the vertical and lateral shifting of peaks for healthy and different damage conditions of the structure.
- Metal wire-based technique is an easy and effective method (for curved surfaces or for structures with complex geometries).
- Root-mean-square deviation (RMSD) index is found to be effective for damage quantification.

References

1. Bhalla, S., Naskar, S.: Metal-wire-based twin one-dimensional orthogonal array configuration of PZT patches for damage assessment of two-dimensional structures. J. Intell. Mater. Syst. Struct. (2015). https://doi.org/10.1177/1045389X15592480
2. Rankhamb, A.U., Khante, S.N.: Damage detection of curved surfaces using advanced piezo impedance transducers. Open J. Civil Eng. **2016**(6), 722–736 (2016). https://doi.org/10.4236/ojce.2016.65058
3. Bhalla, S.: A mechanical impedance approach for structural identification, health monitoring and non-destructive evaluation using piezo-impedance transducers. PhD Thesis, School of Civil and Environmental Engineering, Nanyang Technological University, Singapore (2004)
4. Farrar, C.R., Worden, K.: An introduction to structural health monitoring. Philos. Trans. Royal Soc. A **365**, 303–315 (2007). https://doi.org/10.1098/rsta.2006.1928
5. Ukpai, J.: Erosion-corrosion characterisation for pipeline materials using combined acoustic emission and electrochemical monitoring. PhD thesis, The University of Weeds (2014)
6. Asmara, Y.P., et.al.: Predicting effects of corrosion-erosion on high strength steel pipelines elbow on CO2-Acetic acid (HAC) solution. IOP conference series: materials science and engineering 114, (2016). http://dx.doi.org/10.1088/1757-899X/114/1/012128
7. Du, G., Kong, Q., Lai, T., Song, G.: Feasibility study on crack detection of pipelines using piezoceramic transducers. Int. J. Distrib. Sens. Networks, 1–7 (2013)
8. Park, G., Cudney, H.H., Inman, D.J.: Impedance-based health monitoring of civil structural components. J. Infrastruct. Syst. ASCE **6**(4), 153–160 (2000)
9. Naz, M.Y., et al.: Characterization of erosion of gas pipelines by dry sand. Inst. Sci. Technol. (2016). http://dx.doi.org/10.1080/10739149.2016.1194295

Part VII
Nanotechnology for Environmental Remediation and Protection

Emergence of Nanomodified Fibres as Soil Reinforcement—A Review

R. Aswathy and K. S. Beena

1 Introduction

Among the different methods adopted for soil stabilisation, modification of soil properties with treated fibres is less attempted. Soil reinforcements simply mean introducing a material with desirable properties to the soil, which lacks the same [1]. In the present scenario, rectifying the problems by using economical and eco-friendly means is the most befitting method. Usage of natural fibres always has an advantage over the synthetic fibres such as being economical, eco-friendly, easily available and predominantly biodegradable [1–3]. Natural fibres have crystalline cellulose as well as lignin and hemicellulose of amorphous nature, which are responsible for the strength and stiffness, respectively [4, 5].

Among the natural fibres, coir fibre contains more lignin that makes it strongest of all the natural fibres. The tensile strength of coir fibres changes with the cellulose packing and physical changes in it. The presence of hydroxyl groups in cellulose and their hydrogen bond formation brings change in its properties [2, 5]. Therefore, it is said to be highly effective as soil reinforcement [3].

The studies on reinforcing the soil began with the addition of raw fibres to the inclusion of treated fibres. There are different methods of treating the fibres such as physical, chemical, biological and nanotechnology [1, 2, 4–19]. The idea of utilising nanotechnology in fibre treatment is by impregnation of nanoparticles.

In this paper, it is intended to have a comprehensive review of the application of treated fibres in the soil. To have hands-on experience, it is proposed to modify coir fibre in the laboratory using the quick precipitation technique and analyse the

R. Aswathy · K. S. Beena (✉)
Cochin University of Science and Technology, Cochin, Kerala, India
e-mail: beenavg@gmail.com

R. Aswathy
e-mail: aswathyrajan104@gmail.com

changes using SEM analysis. Also, the mechanism of nanomodification in fibres is reviewed along with the changes in the mechanical and engineering properties of soil.

2   Soil Reinforcement with Treated Fibres

The idea of soil reinforcement has been taken ahead in such a way that currently treated fibre inclusions are studied. Intricate methods are developed in the same area for strength enhancement in the cellulosic level. Ahmad et al. [6] studied the effect of coated and uncoated empty oil palm fruit bunch fibres. The fibres were coated with acrylic butadiene styrene thermoplastic. The coated fibres were stiff and strong compared to uncoated fibres, limiting the deformations. ABS coating increased the fibre diameter and surface area, thus providing enhanced friction and adhesion in the soil–fibre matrix. Shear parameters increased for consolidated drained and consolidated undrained triaxial test for coated fibre-reinforced soil. Bateni et al. [8] investigated the effect of ABS coating on empty oil palm fruit bunch fibres, mainly focusing on the tensile strength and water absorption capacity. The tensile strength of the coated fibre showed lesser improvement compared to uncoated fibres. The ABS coating on fibres resulted in less water absorption and better protection against biodegradation.

The effect of treatment of coir fibres with sodium hydroxide and carbon tetrachloride was studied by Dutta et al. [11]. The clay reinforced with treated fibres was able to bear higher strains at failure compared to the one with untreated fibres. The peak axial stress of NaOH-treated fibre-reinforced soil increased from 81.47 to 130.03 kPa with an increase in fibre content. Whereas for CCl_4 treated fibres reinforced soil, the axial stress increased from 70.69 to 245.78 kPa. The results of XRD exhibited the presence of crystallinities on the fibre surface authorising the fibre modification.

A study on saline soil reinforced with modified polyvinyl alcohol-treated wheat straw was conducted by Li et al. [15]. The treated fibres had higher maximum tensile strength and elongation compared to untreated fibres. With the addition of lime to treated fibre-reinforced soil, the common problem of brittle failure was not observed, as in any limed soil. Rao et al. [19] studied the effect of kerosene-coated coir fibres in expansive soil. The water absorption capacity of fibres was reduced to 32% by kerosene coating. Increase in strength gain under UCS test was 2.5 times for treated fibre-reinforced soil compared to untreated fibre-reinforced soil. The split tensile strength of reinforced soil increased by 50% due to bridging effect with fiber inclusion.

The effect of antimicrobial agents on coir fibres was studied by Sumi et al. [17]. Coir yarns were treated with neem oil, tulsi oil and cashew net shell liquid. The coating by CNSL reduced the moisture absorption capacity by 34% and microbial activity by 95% and increased the tensile strength by 17%, whereas coating with neem oil was ineffective and tulsi oil gave detrimental effect. Dutta et al. [12] found

that coir fibre treated with carbon tetrachloride and sodium hydroxide improved the shear strength of the treated fibre-reinforced soil. With an increase in the confining pressure from 78.38 to 313.92 kPa, the deviator stress ratio of carbon tetrachloride and sodium hydroxide-treated coir-reinforced soil increased by about 1.5 times. The shear parameters and peak stress improvement were more with carbon tetrachloride-treated fibres, owing to its better surface cleaning effect. Considering the durability of the treated fibres, a suggestion was made for the usage of the above-treated fibres for short-term stability problems. The effect of carbon tetrachloride and sodium hydroxide-treated fibres on UCS and CBR characteristics was studied by Chinnu et al. [1]. The UCS increased by about 3.55 times for CCl_4-treated fibre-reinforced soil. CCl_4-treated fibres exhibited a better surface cleaning owing to the enhanced performance, compared to NaOH. The CBR value also showed an incremental trend for CCl_4-treated fibres with an increase from 3.81 to 5.94% corresponding to fibre increase from 0.4 to 1.2%. The water absorption capacity of treated fibres was less compared to untreated fibres.

3 Mechanism of Nanomodification

Nanotechnology is a recent approach which aims at impregnation of fibre surface with nanoparticles [4]. Two methods have been used to impregnate the surface with nanoparticle, i.e. alkali treatment and quick precipitation. Alkali treatment has been widely used and established, whereas the applicability of quick precipitation is less attempted. The treatment of fibre removes hemicellulose exposing free hydroxyl groups. Under this quick precipitation method, precipitates are formed as hydroxides, which can easily be taken up by the hydroxyl group in cellulose as shown in Fig. 1. Quick precipitation method is easy to perform and treat and does not have the disadvantage of much lignin removal as in other chemical treatments [4, 9]. This results in changing the morphology of fibre surface to a rougher one [4, 9]. The addition of these nanomodified fibres to soil improves the shear strength, tensile strength and resistance to crack propagation of the soil.
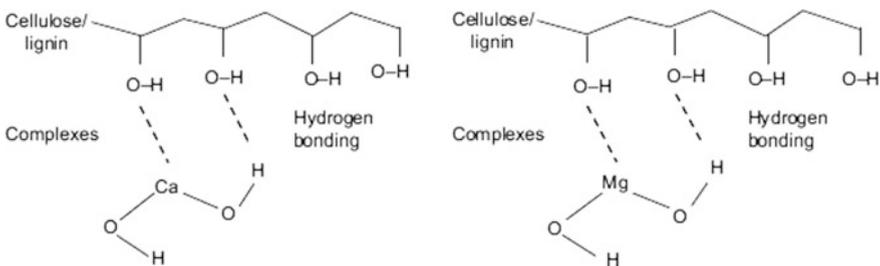

Fig. 1 Chemical structure of Ca(OH)$_2$ and Mg(OH)$_2$ modified fibres [4]

Many developments are made in the field of nanomodification of fibres for polyester composites, fabrics and recently in discrete fibres. The mechanical properties and durability of oil palm empty fruit bunch fibres were improved by impregnation with copper nanoparticles. Cationisation process and alkali solutions were used for impregnation. The improvement in fibre strength was due to better packing of cellulosic complexes and improved fibre–filler interfacial bonding. The improvement in thermal stability of fibres was also reported by Chowdhury et al. [10]. Quick precipitation method was used for impregnation of Fe_3O_4 on rice straw in a study conducted by Khandanlou et al. [14]. Unlike other fibre treatment methods, it procured less time for nanoparticle precipitation. The method was considered superior to cationisation process owing to its environment-friendly nature and cost-effectiveness. Copper nanoparticles were used by Ramli et al. [18] to produce nanoparticles on oil palm fibre-reinforced composites. The production of copper nanoparticles using reduced chemical reaction was considered as hectic and involved use of many chemicals. Apart from the SEM analysis and X-ray diffraction, biodegradability test was performed. Modified fibres were buried in soil consisting of 1:1 ratio of black soil and leaf mold for gardening, for 30, 60, 90 days. Weight loss of fibres increased with burial period. Anggraini et al. [7] studied the effect of nanomodified coir fibre in limed marine clay. The fibre was impregnated with $Al(OH)_3$ and $Fe(OH)_3$ nanoparticles. The tensile strength of modified fibres increased by 33 and 63% for ferric- and aluminium chloride-treated fibres, respectively. The peak strength increased by the addition of modified fibre. There was a reduction in loss of post-peak strength and crack propagation. Modified fibre-reinforced and limed soil withstood maximum wet/dry cycles.

The effect of nanomodified fibres was again studied by Anggraini et al. [4] but with the usage of $CaCl_2$ and $MgCl_2$ forming nanoparticles of $Ca(OH)_2$ and $Mg(OH)_2$. The tensile strength of modified fibres increased by 71 and 211% for magnesium- and calcium chloride-treated fibres, respectively. Nanoparticles helped in load sharing during stretching of fibres. Flexural load-carrying capacity of modified fibre-reinforced soil increased in the two-point bending test. An increase was observed in peak strength and shear parameters. The compaction and shear characteristics of nanomodified fibre-reinforced limed soil were studied by Sindhu et al. [16]. The maximum dry density increased, justifying the stronger interaction between soil and fibre matrix. The shear parameters increased with curing period, for modified fibre-reinforced soil. Under the model test for fibre-reinforced soil, the load-bearing capacity increased by four times. The analytical results were comparable to results from experimental studies. The fibre treatment reduced the water absorption capacity and expected to be serviceable for a longer duration in the shallow foundation. Bordoloi et al. [9] investigated the reinforcing effect of nanomodification of water hyacinth (WH) fibres by ferric hydroxide. The nanoparticle impregnation was authenticated by FE-SEM along with EDX test. The water absorption capacity of the treated fibres decreased changing the surface to hydrophobic nature and with less exposure of fibre surface to water. The tensile strength increased by 1.25 times compared to unmodified WH. The increase in tensile strength of modified fibres increased the unconfined compressive strength of

soil–fibre matrix. The CBR test (soaked and unsoaked) of modified fibre-reinforced soil showed superior bearing capacity ensuring that a reduction in pavement thickness can be provided.

4 Results of SEM Analysis of Nanomodified Coir Fibre

Here, one of the laboratory reaffirmations is done for the nanomodification of coir fibre using SEM analysis. Discrete coir fibres collected from Alappuzha are treated with $CaCl_2$ using quick precipitation method by adopting the procedure described by Anggraini et al. [7]. The reaction involved is represented in Eq. (1).

$$CaCl_2 + 2NaOH \rightarrow Ca(OH)_2 + 2NaCl \tag{1}$$
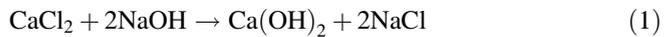
The results of SEM analysis of nanomodified coir fibres authorised the presence of nanoparticles on the surface of the fibres. The morphological changes on the surface are more effectively markable when compared with the SEM images of untreated fibres. Figure 2 shows the SEM image of unmodified coir fibre surface. It is evident that surface and pores are empty, whereas Fig. 3 shows that the surface and the pores are filled with nanoparticles of $CaCl_2$ changing the morphology to a rougher one. The rough nature of the surface is expected to increase the friction and adhesion between the soil–fibre mixture while considering the modified fibre as soil reinforcement.
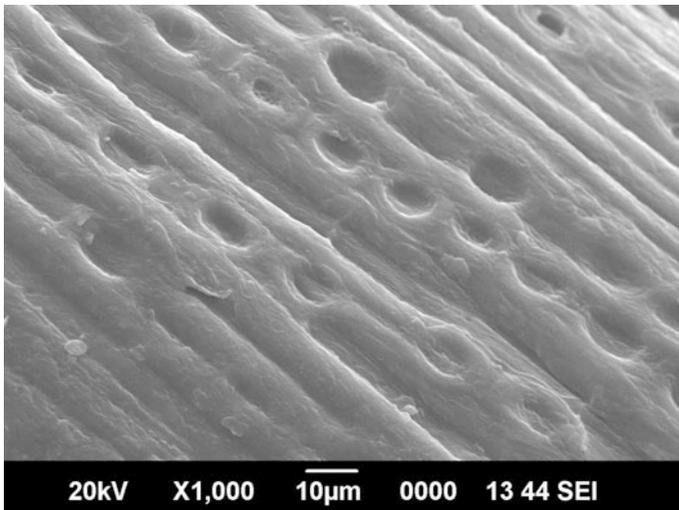

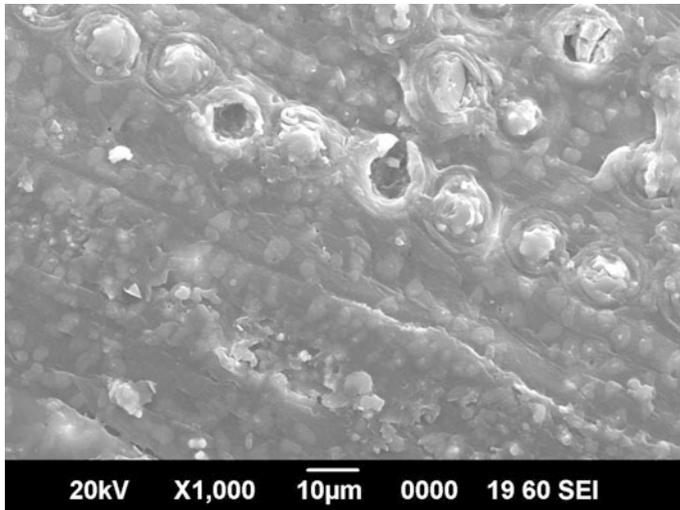**Fig. 2** SEM analysis of unmodified coir fibre

Fig. 3 SEM analysis of CaCl$_2$ modified coir fibre

5   Conclusion

Previous studies on treated fibre inclusion into soil revealed that it could result in improving the desirable properties of the soil. Nanomodification of fibres is a technique for improving the fibres with nanoimpregnations. These are expected to increase the friction and adhesion in the soil–fibre matrix when the reinforcing action is considered. Fibres modified by quick precipitation were authorised by the presence of nanoparticles from SEM analysis. The nanoparticles made the surface of the fibre to a rougher morphology. Therefore, better adhesion and friction can be expected in the fibre–soil matrix. Apparently, the tensile and shear properties of the soil can be modified by the same. A successful experimental attempt done to nanomodify the coir fibres using CaCl$_2$ is also demonstrated in this paper.

References

1. Chinnu, A.S., Sudha, A.R.: Experimental study on strength behaviour of Kuttanad soil using treated coir fibre. Int. J. Eng. Technol. **5**(9), 649–655 (2016)
2. Li, X., Tabil, L.G., Panigrahi, S.: Chemical treatments of natural fibre for use in natural fibre-reinforced composites: a review. J. Polym. Environ. **15**(1), 25–33 (2007)
3. Maliakal, T., Thiyyakandi, S.: Influence of randomly distributed coir fibres on shear strength of clay. Geotech. Geol. Eng. **31**(2), 425–433 (2013)
4. Anggraini, V., Huat, B.B.K., Asadi, A., Nahazanan, H.: Effects of coir fibres modified with Ca(OH)$_2$ and Mg(OH)$_2$ nanoparticles on mechanical properties of lime- treated marine clay. Geosynthetic Int. **23**(3), 206–218 (2016)

5. John, M.J., Anandjiwala, R.D.: Recent developments in chemical modification and characterization of natural fibre-reinforced composites. Polym. Compos. **29**(2), 187–207 (2008)
6. Ahmad, F., Bateni, F., Azmi, M.: Performance evaluation of silty sand reinforced with fibres. Geotext. Geomembr. **28**, 93–99 (2009)
7. Anggraini, V., Asadi, A., Farzadnia, N., Jahangirian, H., Huat, B.B.K.: Reinforcement benefits of nanomodified coir fibre in limed marine clay. J. Mater. Civ. Eng. **28**(6), 1–8 (2016)
8. Bateni, F., Ahmed, F., Yahya, A.S., Azmi, M.: Performance of oil palm empty fruit bunch fibres coated with acrylonitrile butadiene styrene. Constr. Build. Mater. **25**, 1824–1829 (2011)
9. Bordoloi, S., Hussain, R., Sen, S., Garg, A., Sreedeep, S.: Chemically altered natural fibre impregnated soil for improving subgrade strength of pavements. Adv. Civ. Eng. Mater. **7**(2) (2017)
10. Chowdhury, M., Beg, M., Khan, M.R., Mina, M.: Modification of oil palm empty fruit bunch fibres by nanoparticle impregnation and alkali treatment. Cellulose **20**(3), 1477–1490 (2013)
11. Dutta, R., Khatri, V.N., Venkataraman, G.: Effect of addition of treated coir fibres on the compression behavior of clay. J. Civ. Eng. **40**(2), 203–214 (2012)
12. Dutta, R., Khatri, V.N., Venkataraman, G.: Shear strength behavior of clay reinforced with treated fibre. J. Civ. Eng. **60**(2), 135–143 (2016)
13. Khalil-Abad, M.S., Yasdanshenaz, M.E., Nateghi, M.R.: Effect of cationisation on the adsorption of silver nanoparticles on cotton surfaces and its antimicrobial activity. Cellulose **16**, 1147–1157 (2009)
14. Khandanlou, R., Ahmad, M.B., Shameli, K., Kalantari, K.: Synthesis and characterization of rice straw/Fe_3O_4 nanocomposites by a quick precipitation method. Molecules **18**(6), 6597–6607 (2013)
15. Li, M., Xi Chai, S., Yuan Zhang, H., Du Pu, H., Wei, L.: Feasibility of saline soil reinforced with treated wheat straw and lime. Soils Found. **52**(2), 228–238 (2012)
16. Sindhu, A.R., Joseph, J.K.: Effect of compaction characteristics and shear strength parameter of expansive soil reinforced with nanomodified fibres and lime. Int. Res. J. Eng. Technol. **4**(4), 2450–2459 (2017)
17. Sumi, S., Unnikrishnan, N., Lea, M.: Effect of antimicrobial agents on modification of coir. Proc. Technol. **24**, 280–286 (2016)
18. Ramli, R., Khan, M.R., Chowdhary, N.K., Beg, M.D.H., Halim, R.M., Aziz, A.A., Ibrahim, Z., Zainal, N.H.: Development of Cu nanoparticle loaded oil palm fibre reinforced nanocomposite. Adv. Nanoparticles **2**, 358–365 (2013)
19. Rao, G.V.: Strength behaviour of kerosene coated coir fibre-reinforced expansive soil. Archit. Civ. Eng. **12**(2), 113–120 (2014)

Heat Transfer Enhancement in a Circular Tube Fitted with Twisted Tape Having Continuous Cut Edges Using CuO-Water Nanofluid

Veeresh Fuskele and R. M. Sarviya

Nomenclature

A	Heat transfer surface area, m^2
c_p	Specific heat of fluid, kJ/kgK
D	Inside diameter of the tube, mm
d	Depth of cut, mm
f	Friction factor
h	Heat transfer coefficient, W/m^2K
I	Current, A
k	Thermal conductivity of fluid, W/mK
L	Length of the test section, m
m	Mass flow rate of water, kg/s
Nu	Nusselt Number
P	Pressure, kPa
ΔP	Pressure drop, kPa
Pr	Prandtl Number
Q	Heat transfer rate, W
Re	Reynolds Number
t	Thickness of the test tube, mm
ΔT	Temperature difference, °C
T	Temperature, °C
$\tilde{T}$	Average temperature, °C
U	Mean axial flow velocity, m/s
V	Voltage, V
w	Width of cut, mm
W	Twisted tape width, mm
y/W	Twist ratio

V. Fuskele (✉) · R. M. Sarviya
Maulana Azad National Institute of Technology, Bhopal, MP 462003, India
e-mail: vfuskele@yahoo.com

Greek Symbols

ρ Fluid density, kg/m^3
δ Twisted tape thickness, mm
μ Dynamic viscosity, kg/m-sec
η Thermal performance factor

Subscripts

b Bulk
c Convection
i Inlet
o Outlet
p Plain
s Surface
t Turbulator
w Water

Abbreviations

PT   Plain tube
TT   Twisted tape
CCTT   Continuous cut twisted tape
R-CCTT   Continuous rectangular cut TT

1   Introduction

The heat transfer enhancement (HTE) in heat exchanging devices aims at reduction in its size/weight by improving its heat transfer capacity and thus saving energy and material cost [1, 2]. Boosting of agitation near the tube wall for thinning of boundary layer, enhancing heat exchanging areas, and improving flow conditions by altering the heat exchanging surface are the key methods for augmenting heat transfer [3]. The swirling agents are important devices for the same. Twisted tape is one of the significant agents in this category for making the thermal application apparatus more compact and less costly because of its easy installation, maintenance, and cost-effective feature [1]. This is possible due to efficient mixing of the fluid caused by the conversion of its axial flow in tube to swirl flow. The advantage of enhanced heat transfer by the use of twisted tape insert is accompanied by the penalty of pressure drop. The latest trend for improving heat transfer is use of nanofluids for refining the thermophysical properties, especially the thermal conductivity of the working fluid [1].

Literature reviewed by Dewan et al. [4] reported the use of twisted tape insert in various heat transfer augmentation applications revealing that the major cause of increase in heat transfer is the reduction of the thermal boundary layer in the vicinity of the tube wall caused by the increased turbulence there [5–7]. After this, lot of work on modified twisted tape has been reported [3] along with the use of various cut edge twisted tape. Hasanpour et al. [8] experimentally reported the effect of V-cut and U-cut twisted tape with various depth (d_r), width (W_r), and twist ratios for $5000 < Re < 15,000$. The Nusselt number ratio was reported to be maximum for V-cut, around 1.40 with $W_r = 0.3$ and $d_r = 0.45$ and the friction factor ratio varied from 1.05 to 2.2. It was found that with the decrease in W_r and increase in d_r the Nu number ratio increases and it was vice versa for the friction factor. Salman et al. [9, 10] numerically evaluated the effect of parabolic-cut, elliptical-cut, and V-cut twisted tape placed inside a constant heat fluxed tube. The investigation was carried out for different twist ratio and cut depth with in laminar flow conditions. It was found that the Nusselt number increases with the decrease in twist ratio and cut depth. Murugesan et al. [11–15] investigated the effect on heat transfer, friction factor and thermal performance factor (TPF) of a tube equipped with square-cut, trapezoidal-cut, U-cut and wing-cut twisted tape inserts with various twist ratios in turbulent flow range $2000 < Re < 12,000$. It was found that TPF for trapezoidal-cut is 1.19–1.03, for U-cut is 1.22–1.06, for square-cut TT is 1.27–1.02, and maximum for wing-cut twisted tape insert is 1.34–1.04. Similarly, Prasad et al. [16] performed experimentally analyses on the trapezoidal-cut twisted tape fitted in a U-tube heat exchanger using Al_2O_3-water nanofluid in turbulent flow conditions. Nusselt number enhancement by 34.24% and friction factor increase by 1.29 times was reported. Man et al. [5] demonstrated an experimental research on a new kind of twisted tape insert of different lengths having cut edge. The performance evaluation criteria (PEC) were reported to be in range of 0.82–1.06 with Nusselt number to be 1.15–1.9 times and friction factor 1.21–5.75 times of that for the plain tube. Rahimi et al. [6] reported through CFD analysis that use of a jagged twisted tape insert increases the Nusselt number and thermal performance by 31%. Eiamsa-ard et al. [17] studied the influences of delta-winglet twisted tape, namely straight (S-DWT) and oblique (O-DWT) delta-winglet for various depth of wing-cut ratios in a tube with uniform heat flux loading for a turbulent flow range. TPF with S-DWT was 0.88–1.21 and with O-DWT it was around 0.92–1.24. Performance of the various cut twisted tapes discussed here was found to be better than the conventional twisted tape due to the additional disturbance and higher secondary flow near the wall of the tube compared to that induced by plain.

Advanced cooling methodology includes the use of nanofluids, which play a significant role in overcoming the mounting cooling necessities generated by the increased heat-emitting appliances. This is possible due to the enhanced thermal property of the nanofluids over the traditional cooling fluids. Nanofluids as denoted as 'the fluid with suspended nanoparticles' were first familiarized by Choi [18]. The several challenges for application of nanofluids in thermotechnical systems were discussed by Saidur et al. [19]. Numerous researches have been conducted on nanofluids thermophysical properties in [20, 21]. Besides, several studies on heat

transfer enhancement by nanofluids have also been accomplished. Sidika et al. [22] studied the influence of turbulence attributes on heat transfer intensification using nanofluids considering various parameters such as type, size, and concentration of nanoparticles with varying Reynold's number. It was concluded that use of nanofluids further enhances the heat transfer along with the presence of inserts in the heat exchanging tube. This is due to the disordered fluid partying as a result of secondary flow generated by the insert, causing disruption of boundary layer near the wall. Sidika also concluded that the performance of heat exchanging device is weakened by the use of high nanoparticle concentrations. Zheng et al. [3] numerically investigated the effect of Al_2O_3/water nanofluid on thermohydraulic performance of circular tube fitted with TT having dimples and protrusions on it. It was reported that dimpled side performed better both in heat transfer and in flow resistance than protrusion side. It was also stated that the use of nanofluid further improved the heat transfer characteristics with marginal pressure drop penalty. Prasada et al. [16] similarly investigated experimentally the use of Al_2O_3/water nanofluid for better thermal performance with TT insert. Azmi et al. [23] showed the advantage of using SiO_2/water and TiO_2/water nanofluids for better performance of heat transfer tube with TT insert. Sundar et al. [24] estimated the heat transfer augmentation by the use of carbon nanotube-Fe_3O_4/water hybrid nanofluid in a tube with a TT. It was found that the hybrid nanofluid produces better performance than single-particle-based nanofluids with negligible increase in pressure drop. The effect of variation in twist length was studied by Aliabadi et al. [25] along with the Cu-water nanofluid. It was reported that the overall performance of varying length TT with mentioned nanofluid is higher than that obtained with using single techniques. He also reported the improvement in thermal performance with the growing volume percentage of nanoparticles. Experimental study of altered TT was reported by Maddah et al. [26] using Al_2O_3/water nanofluid. The experiments were performed with increasing and decreasing geometric progression twists with varying nanofluid concentration. It was reported that TT with geometric progression ratio has prominent effect on thermal and friction factor performance of double pipe heat exchanger.

The above review shows that using cut twisted tape insert for the heat transfer augmentation is a promising approach. Also, the use of nanofluid further enhances the heat transfer with marginal pressure drop penalty. In the reported work, twisted tape inserts having single cut per twist have been investigated. To further enrich the research on cut twisted tape, this work introduces the use of twisted tape insert with continuously cut edges (CTT), with constant depth ratio ($d/W = 0.025$), and width ratios ($w/W = 0.05$) as shown in Fig. 1. This work focuses on influences on the thermohydraulic performance of a horizontal circular tube fitted with a twisted tape inserts having continuous rectangular cut on the top and bottom edges (R-CTT) using CuO/water nanofluid with 0.5% volume concentration of 50-nm nanoparticle size. The measurement of Nusselt number, friction factor, and TPF was done for different twist ratio ($y = 3, 5$) of the insert and turbulent flow conditions ranging between $4000 < Re < 20{,}000$ under constant heat flux-loading condition. Comparison of the
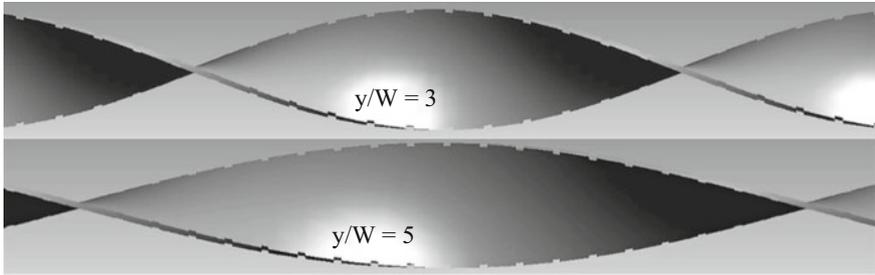
Fig. 1 Continuous rectangular cut twisted tape (R-CCTT) inserts with twist ratio 5 and 3

results obtained for the same with those for the traditional TT and the plain tube was also made.

2 Experimental Setup

The experimental setup as shown in Fig. 2 consists of a copper tube in which water flows at room temperature ($D = 20$ mm, $t = 1$ mm, and $L = 1000$ mm). The experimental setup has a developing section of 2.5 m, test section of 1 m, and then calming section of 1 m. Asbestos rope and glass wool insulation is done on the outer of the tube for minimization of the heat loss to the surroundings. Two calibrated rotameters with flow ranges of 0–20 LPM and 0–2 LPM with ±0.1 LPM
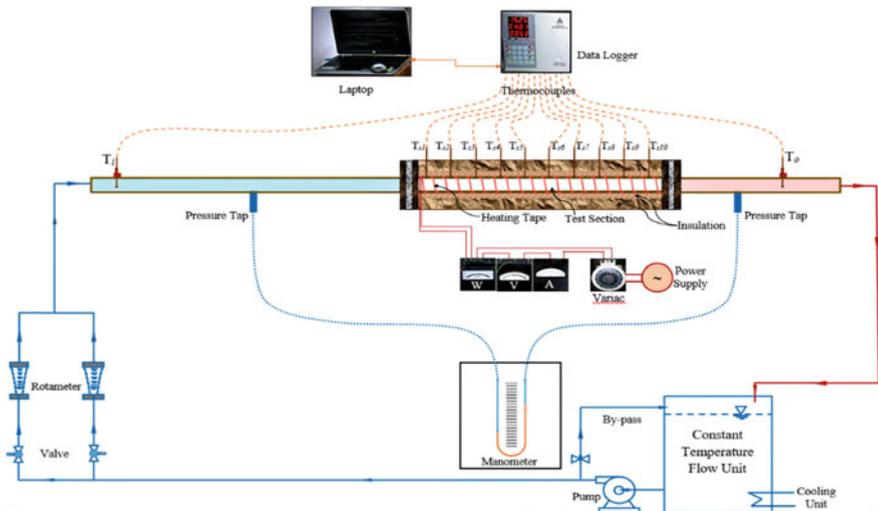

Fig. 2 Schematic diagram of experimental setup

accuracy are used for measuring the flow rates of water. K-type thermocouples with ±0.1 °C accuracy are used for measuring the wall temperature of the tube and the inlet and outlet temperature of the water.

The tube is heated using a heating tape of 1.5 KW wound over the tube to supply constant heat flux. The inlet temperature of water is kept constant at 25 °C using a constant temperature bath. The water flow rate was adjusted from 0.0206 to 0.1235 kg/sec with the Reynolds number ranging between 4000 and 20,000. As steady-state conditions were reached, all the temperatures were recorded using a data logger and pressure drop was measured using U-tube manometer.

Twisted tapes are cut from steel sheet of thickness (δ) 1 mm, length (L) 1000 mm, and tape width (W) so as to fit the inner surface of the tube. The twist ratio (y/W) is defined by ratio between one length of twist and pitch length (y) to diameter (D). Twisted tape inserts with twist ratios 3 and 5 having the rectangular cut edges both on the top and on the bottom are used to improve the fluid mixing near the walls of the test section.

3 Data Analysis

3.1 Thermophysical Properties of Nanofluid

Presynthesized CuO/water nanofluid having 50-nm-sized CuO nanoparticles in 0.5% volume fraction was purchased from Nano Research Laboratory Pvt. Ltd., Jamshedpur.

Following properties (Table 1) are taken for the nanoparticles with size 50 nm and density range specified as 6.3–6.49 g/cm^3 by the supplier, from [27].

The thermophysical properties of the nanofluid are calculated as a function of nanoparticle volume concentration along with properties of nanoparticles and base fluid. The density, specific heat, and viscosity are calculated at average bulk temperature of the nanofluid by the following equations [27]:

$$\rho_{nf} = (1 - \varnothing)\rho_w + \varnothing\rho_{np} \tag{1}$$

Table 1 Thermophysical properties of CuO nanoparticles and base fluid

Physical properties	Base fluid (Distilled water)	Nanoparticles (CuO)
Density, ρ (kg/m^3)	998.2	6350[a]
Specific heat, C_p (J/kg K)	4180	535.6
Thermal conductivity, K (W/m K)	0.6	69
Viscosity, μ (Ns/m^2)	0.001003	–

[a]as per supplier

$$C_{p,nf} = \frac{\varnothing \rho_{np} C_{p,np} + (1 - \varnothing)\rho_w C_{p,w}}{\rho_{nf}} \tag{2}$$

$$\mu_{nf} = (1 + 2.5\varnothing)\mu_{bf} \tag{3}$$

Thermal conductivity of nanofluid is calculated by the temperature-dependent model suggested by Li and Perterson [28] as follows:

$$\frac{k_{nf} - k_{bf}}{k_{bf}} = 3.761088\varnothing + 0.017924(T - 273.15) - 0.30734 \tag{4}$$

3.2 Heat Transfer and Friction Factor

The measured data are used for calculation as per the following procedures:

Heat transferred to the water in the tube, Q_w, is calculated using the following equation:

$$Q_w = mC_{p,w}(T_o - T_i) \tag{5}$$

Performing the thermal equilibrium test showed that the heat supplied by heating tape to the test section is 5–8% larger than the heat absorbed by the fluid (water).

$$Q_c = hA(\tilde{T}_s - T_b) \tag{6}$$

where A is the internal surface area of the tube wall (πDL) and T_b is the bulk mean flow temperature ($T_b = (T_o + T_i)/2$).

The average wall surface temperature (T_s) of the test tube is calculated from 10 stations of surface temperatures lined between the inlet and exit of the test tube, using the following equation:

$$\tilde{T}_s = \sum T_s / 10 \tag{7}$$

where T_s is the local wall temperature, evaluated at the wall surface of the test tube.

The average heat transfer coefficient (h) and the average Nusselt number (Nu) are then estimated as follows:

$$h = (mC_{p,w}(T_o - T_i))/A(\tilde{T}_s - T_b) \tag{8}$$

$$Nu = hD/k \tag{9}$$

In this work, the friction factor (f) is calculated as:

$$f = \frac{\Delta P}{\left(\frac{L}{D}\right)\left(\rho \frac{U^2}{2}\right)} \tag{10}$$

The heat transfer efficiency or the thermal performance factor is defined as the ratio of Nusselt number to the friction ratio at the same pressure drop which is derived from Dittus–Boelter equation and Blasius equation of turbulent flows [29]

$$\eta = \left(Nu_t/Nu_p\right)/\left(f_h/f_p\right)^{\frac{1}{3}} \tag{11}$$

All of thermophysical properties of the water are determined at the overall bulk mean water temperature.

4 Results and Discussion

4.1 Validation of Test Section With/Without Twisted Tape

In order to validate the experimental setup, tests were conducted for the plain tube and tube with twisted tape and the results were compared with those from the past correlations stated as follows:

Nusselt number correlations for plain tube:

Correlation of Dittus–Boelter [29]:

$$Nu = 0.023 Re_h^{0.8} Pr_h^{0.4} \tag{12}$$

Correlation of Gnielinski [30]:

$$Nu = \frac{(f/8)(Re - 1000)Pr}{1 + 12.7(f/8)^{1/2}(Pr^{2/3} - 1)} \tag{13}$$

Friction factor correlations for plain tube:

Correlation of Blasius [29]:

$$f = 0.318 Re^{-0.25} \tag{14}$$

Correlation of Petukhov [30]:

$$f = (0.79 \ln Re - 1.64)^{-2} \tag{15}$$

Nusselt number and friction factor correlations for conventional twisted tape are given by Manglik and Bergles [31]:

$$Nu = \left(1 + \frac{0.769}{(y/W)}\right)\left[0.023Re^{0.8}Pr^{0.4}\left(\frac{\pi}{\pi - 4\delta/D}\right)^{0.8}\left(\frac{\pi + 2 - 2\delta/D}{\pi - 4\delta/D}\right)^{0.2}\right]\varphi$$

(16)

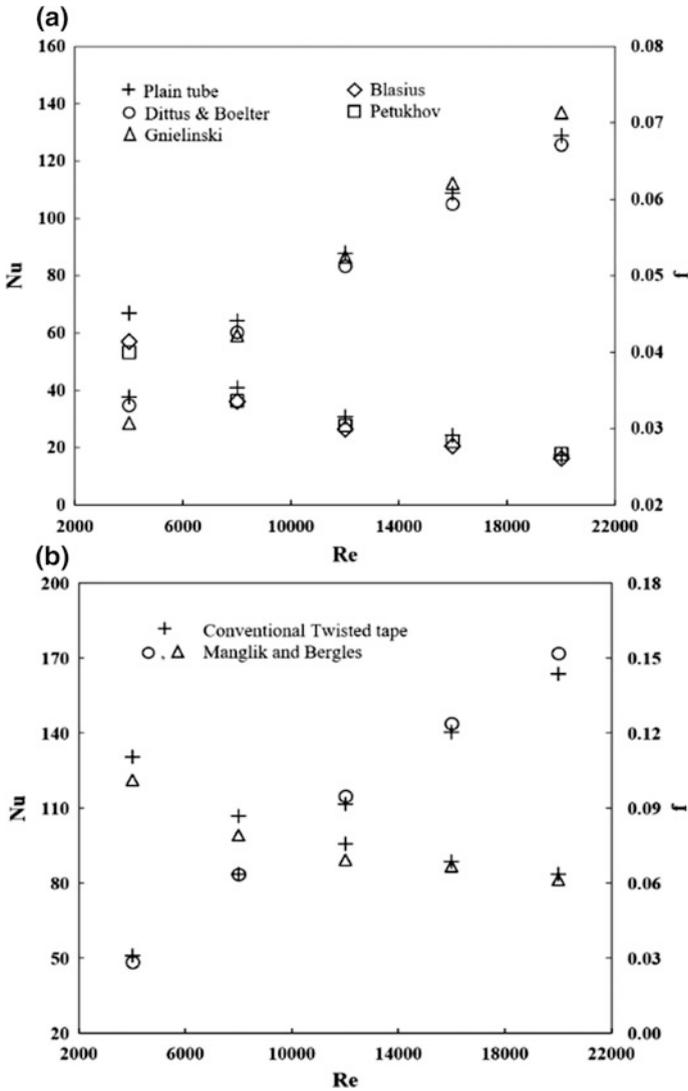where $\varphi = (\mu_b/\mu_s)^{0.18} = (T_b/T_s)^{0.45}$

Fig. 3 **a** Validation of plain tube, **b** validation of conventional twisted tape

$$f = \left(1 + 2.06\left(1 + (2(y/W)/\pi)^2\right)^{-0.74}\right)$$
$$\left[0.079Re^{-0.25}\left(\frac{\pi}{\pi - 4\delta/D}\right)^{1.75}\left(\frac{\pi + 2 - 2\delta/D}{\pi - 4\delta/D}\right)^{1.25}\right] \tag{17}$$

Validation of plain tube is shown in Fig. 3a. It is evident that the average deviations of Nusselt number are ±5.34 and ±6.70% from the Dittus–Boelter and Gnielinski correlations, respectively, and of friction factor is ±4.32 and ±4.76% from the Blasius and Petukhov equations, respectively. Figure 3b, depicts the validation of test tube fitted with conventional twisted tape with twist ratio 5. Evidently, deviations in the Nusselt number and friction factor are ±5.17 and ±8.94%, respectively, than those from the Manglik-Bergles correlations.

4.2 Effect of Twisted Tape with Continuous Square-Cut Edges on Heat Transfer

Figure 4 depicts the Nusselt number variation with Reynolds number for plain tube, TT and R-CCTT of twist ratios 3 and 5 with working fluid as water. It is evident from the figure that the Nusselt number for R-CCTT is significantly higher than the plain tube, because it causes the flow to spiral along the tube length and disturb the entire flow field that leads to higher heat transfer rate. It is also observed that the
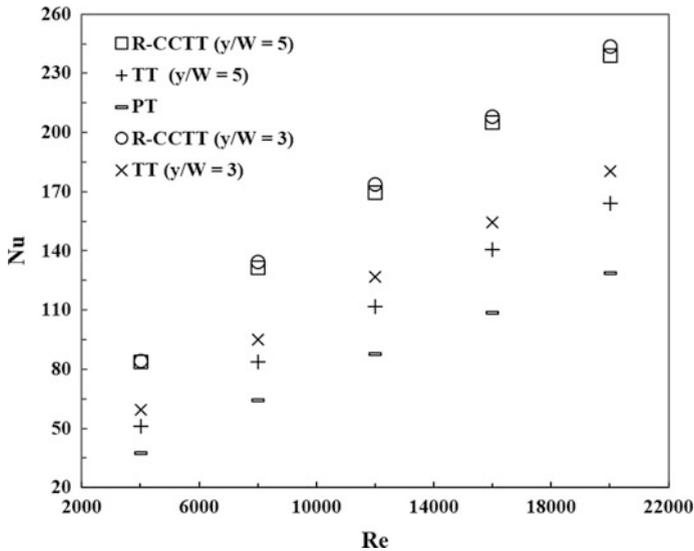

Fig. 4 Comparison of Nusselt number (*Nu*) for R-CCTT with TT and plain tube

Nusselt number for R-CCTT is higher than that for conventional TT. This is expected because the removal of viscous sublayer near tube wall is presumed [4] to take place due to the additional turbulence generated by the continuous cut edges of R-CCTT and thus leading to a superior heat transfer improvement than TT. Considering the effect of twist ratio, it was found that lower twist ratio offers higher heat transfer rate than the higher twist ratio because intensity of turbulence and flow length obtained from lower twist ratio were higher than those at higher twist ratio. Over the range investigated the Nusselt number for R-CCTT with twist ratios 5 and 3 are 2.21–1.85 and 2.23–1.89 times than that of plain tube and 1.63–1.46 and 1.42–1.35 times than that of conventional TT.

Further experimentation was done for CuO/water nanofluids at twist ratio 5 of TT and R-CCTT. Equation (9) was used for calculation of experimental Nusselt number for CuO/water nanofluid with 0.5% volume concentration and the data are represented in Fig. 5. It can be seen that use of CuO/water nanofluid further increases the Nusselt number by 40–76% when compared to that for water in case of R-CCTT, and by 31–42% in case of conventional TT and 23–35% in case of PT. Also, Nusselt number with the use of R-CCTT in case of nanofluid is 1.93–3.17 times than that of plain tube and 1.56–2.03 times than that of TT. The increased turbulence caused by the continuous cut edges of the TT is responsible for disruption of boundary layer near the tube wall which in turn results in higher value of Nusselt number in case of R-CCTT. Further augmentation in Nusselt number in case of nanofluid is due to the enhanced thermal conductivity of the base fluid due to addition the of nano-sized particles.
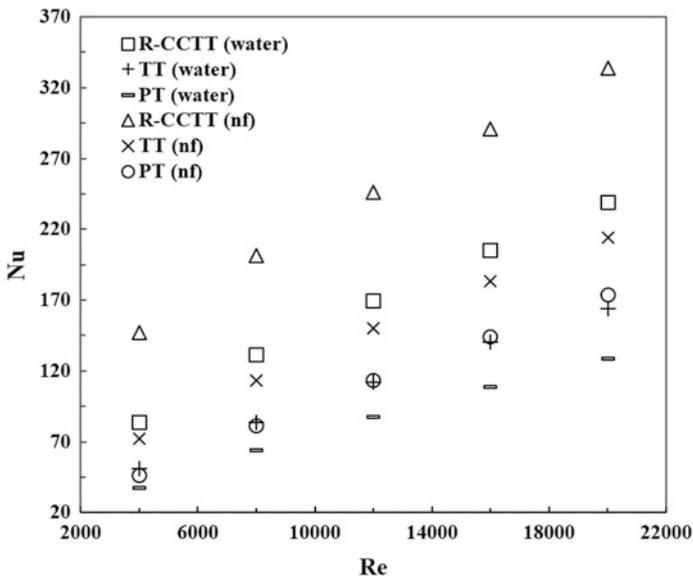

Fig. 5 Comparison of Nu with water and nanofluid for PT, TT, and R-CCTT ($y/W = 5$)

4.3 Effect of Twisted Tape with Continuous Square-Cut Edges on Friction Factor

The variation of friction factor with Reynolds number is shown in Fig. 6. It shows that with increasing Reynolds number the friction factor decreases. It is observed that the friction factor for R-CCTT is significantly higher than the plain tube but not much higher than the conventional twisted tape. The mean friction factor for the case of R-CCTT with twist ratios 5 is 2.9 times the plain tube and 1.3 times the conventional TT and with twist ratio 3 it is 3.5 times the plain tube and 1.1 times the conventional TT.

Figure 7 depicts the effect of nanofluid on friction factor in case of plain tube, TT, and R-CCTT. It can be observed that the friction factor is 1.48–2.05 times than that of water in case of R-CCTT and 1.10–1.21 times in case of TT. It is also observed that the friction factor is 4.15–6.56 times than that of plain tube and 1.64–2.16 times than TT in case of nanofluid as operating medium. The higher value of friction factor in case of R-CCTT is attributed to the enlarged agitation near the tube wall caused by the cut edges in the TT and also in case of nanofluid.
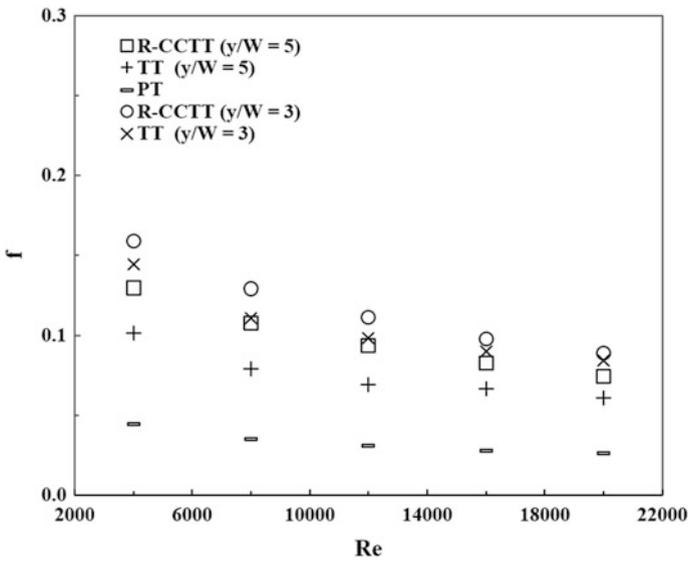

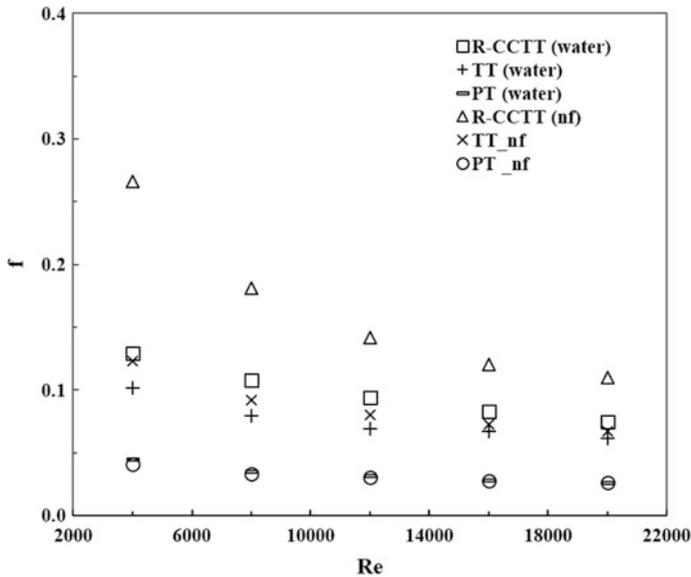**Fig. 6** Comparison of friction factor (*f*) for R-CCTT, TT, and plain tube

Fig. 7 Comparison of Nu with water and nanofluid for PT, TT, and R-CCTT ($y/W = 5$)

4.4 Performance Evaluation Analysis

The quality of enhancement concept is derived from the thermal performance ratio/ factor or heat transfer efficiency. The variation of thermal performance factor (TPF) with Reynolds number for water as working fluid is plotted in Fig. 8. The performance ratio obtained with twist ratios 5 and 3 fall in the ranges of 1.31–1.56, 1.26–1.46 for R-CCTT insert. The improvement in TPF is ruled by the impact of heat transfer enrichment due to the existence of R-CCTT.

Further, Fig. 9 shows that the use of nanofluid increases the TPF to 1.23–1.38 times for R-CCTT and 1.27–1.33 times for TT in comparison with water. Also, the TPF for R-CCTT is 1.32–1.57 times of that of TT in case of nanofluid as the operating fluid. The upgradation in TPF is governed by the improved thermal conductivity of the base fluid and thus by the augmented heat transfer rate.

The results show that performance ratio for all the cases of R-CCTT insert is greater than unity which means that the application of enhancement is fruitful from the point of total energy savings and is higher than that of the conventional twisted tapes and other cut edge twisted tape as reported in the previous investigations in the literature survey.
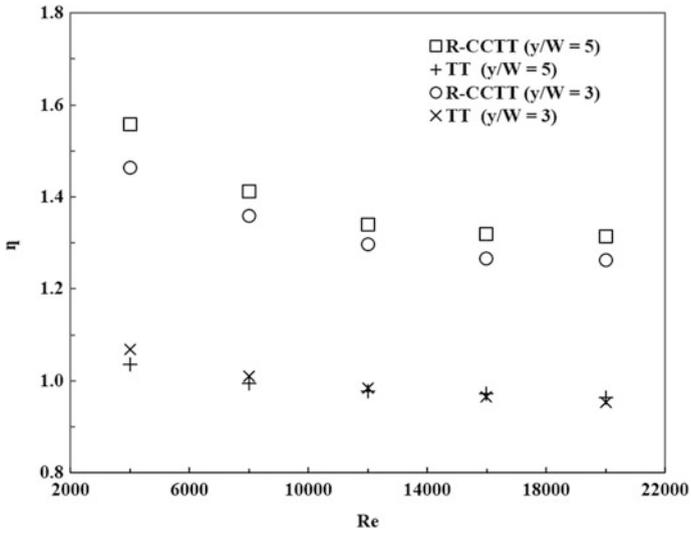
Fig. 8 Comparison of TPF for R-CCTT and TT
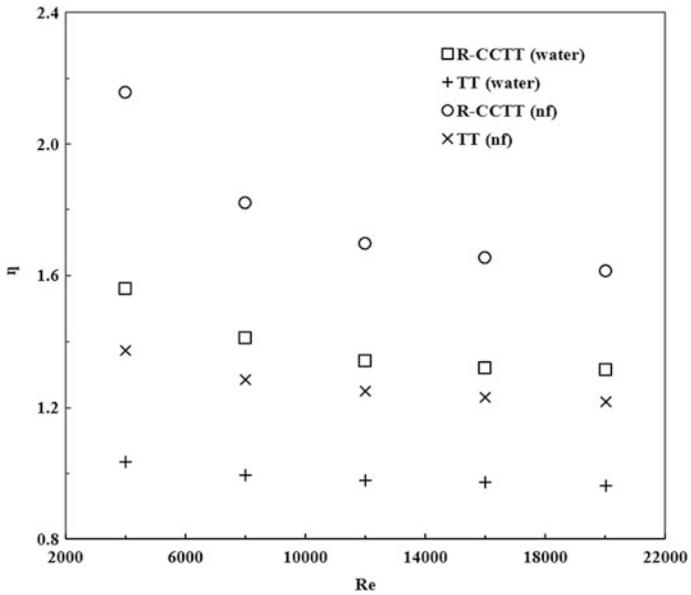

Fig. 9 Comparison of TPF with water and nanofluid for R-CCTT and TT

5   Conclusion

Experimental investigations for heat transfer and pressure drop effects in a circular tube inserted with continuous rectangular cut edges twisted tape having twist ratios 5 and 3 are performed for turbulent flow range $4000 < Re < 20{,}000$. Increase in heat transfer rate along with friction factor is observed with decreasing the twist ratio, as compared to plain tube. Twisted tape inserts with continuous rectangular cut edges for twist ratios 5 and 3 augment the heat transfer rate 2.21 and 2.23 times that of plain tube and 1.63 and 1.42 times that of conventional twisted tape in case of water and 3.17 times that of plain tube and 2.16 times that of TT in case of nanofluid as the working fluid. Moreover, the performance ratio for R-CCTT is greater than one having 1.56 as the maximum value in case of water; therefore, augmentation is beneficial from the point of energy savings. Employment of nanofluid further improves the performance factor to 2.16. From the experimental results in the present work, it is concluded that the R-CCTT proves to be a beneficial insert than the other forms of twisted tape (as shown in the previous investigations in the literature survey) as the heat transfer augmentation is very large compared to the marginal pressure drop penalty and use of nanofluid with R-CCTT further improves the performance of the heat exchanging device.

References

1. Saysroy, A., Eiamsa-ard, S.: Enhancing convective heat transfer in laminar and turbulent flow regions using multi-channel twisted tape inserts. Int. J. Therm. Sci. **121**, 55–74 (2017). https://doi.org/10.1016/j.ijthermalsci.2017.07.002
2. Lin, Z.M., Wang, L.B., Lin, M., Dang, W., Zhang, Y.H.: Numerical study of the laminar flow and heat transfer characteristics in a tube inserting a twisted tape having parallelogram winglet vortex generators. Appl. Therm. Eng. **115**, 644–658 (2017). https://doi.org/10.1016/j.applthermaleng.2016.12.142
3. Zheng, L., Xie, Y., Zhang, D.: Numerical investigation on heat transfer performance and flow characteristics in circular tubes with dimpled twisted tapes using Al_2O^3-water nanofluid. Int. J. Heat Mass Transf. **111**, 962–981 (2017). https://doi.org/10.1016/j.ijheatmasstransfer.2017.04.062
4. Dewan, A., Mahanta, P., Raju, K.S., Kumar, P.S.: Review of passive heat transfer augmentation techniques. Proc. Inst. Mechanical Eng. Part A: J. Power Energy **218**(7), 509–527 (2004)
5. Man, C., Yao, J., Wang, C.: The experimental study on the heat transfer and friction factor characteristics in tube with a new kind of twisted tape insert. Int. Commun. Heat Mass Transfer **75**, 124–129 (2016)
6. Rahimi, M., Shabanian, S.R., Alsairafi, A.A.: Experimental and CFD studies on heat transfer and friction factor characteristics of a tube equipped with modified twisted tape inserts. Chem. Eng. Process. **48**(3), 762–770 (2009)
7. Seemawute, P., Eiamsa-Ard, S.: Thermohydraulics of turbulent flow through a round tube by a peripherally-cut twisted tape with an alternate axis. Int. Commun. Heat Mass Transfer **37**(6), 652–659 (2010)

8. Hasanpour, A., Farhadi, M., Sedighi, K.: Experimental heat transfer and pressure drop study on typical, perforated, V-cut and U-cut twisted tapes in a helically corrugated heat exchanger. Int. Commun. Heat Mass Transfer **71**, 126–136 (2016)

9. Salman, S.D., Kadhum, A.A.H., Takriff, M.S., Mohamad, A.B.: Numerical investigation of heat transfer and friction factor characteristics in a circular tube fitted with V-cut twisted tape inserts. Sci. World J. 2013 (2013)

10. Salman, S.D., Kadhum, A.A.H., Takriff, M.S., Mohamad, A.B.: CFD analysis of heat transfer and friction factor characteristics in a circular tube fitted with parabolic-cut twisted tape inserts. Aust. J. Basic Appl. Sci. **7**(7), 69–76 (2013)

11. Murugesan, P., Mayilsamy, K., Suresh, S.: Turbulent heat transfer and pressure drop in tube fitted with square-cut twisted tape. Chin. J. Chem. Eng. **18**(4), 609–617 (2010)

12. Murugesan, P., Mayilsamy, K., Suresh, S., Srinivasan, P.S.S.: Heat transfer and pressure drop characteristics of turbulent flow in a tube fitted with trapezoidal-cut twisted tape insert. Int. J. Acad. Res. **1**(1), 123–128 (2009)

13. Murugesan, P., Mayilsamy, K., Suresh, S.: Heat transfer in tubes fitted with trapezoidal-cut and plain twisted tape inserts. Chem. Eng. Commun. **198**(7), 886–904 (2011)

14. Murugesan, P., Mayilsamy, K., Suresh, S.: Heat transfer and friction factor in a tube equipped with U-cut twisted tape insert. Jordan J. Mech. Ind. Eng. **5**(6), 559–565 (2011)

15. Murugesan, P., Mayilsamy, K., Suresh, S.: Heat transfer in a tube fitted with vertical and horizontal wing-cut twisted tapes. Exp. Heat Transf. **25**(1), 30–47 (2012)

16. Prasad, P.D., Gupta, A.V.S.S.K.S., Deepak, K.: Investigation of trapezoidal-cut twisted tape insert in a double pipe U-tube heat exchanger using Al2O3/water nanofluid. Proc. Mater. Sci. **10**, 50–63 (2015)

17. Eiamsa-Ard, S., Wongcharee, K., Eiamsa-Ard, P., Thianpong, C.: Heat transfer enhancement in a tube using delta-winglet twisted tape inserts. Appl. Therm. Eng. **30**(4), 310–318 (2010)

18. Choi, S.U.S.: Enhancing thermal conductivity of fluids with nanoparticles. Off. Sci. Tech. Inform. Tech. Rep. **231**(1), 99–105 (1995)

19. Saidur, R.K., Leong, Y., Mohammad, H.A.: A review on applications and challenges of nanofluids. Renew. Sustain. Energy Rev. **15**, 1646–1668 (2011)

20. Khanafer, K.K., Vafai, K.: A critical synthesis of thermophysical characteristics of nanofluids. Int. J. Heat Mass Transfer **54**, 4410–4428 (2011)

21. Fan, J., Wang, L.Q.: Review of heat conduction in nanofluids. ASME J. Heat Transfer **133**, 040801 (2011)

22. Sidika, N.A.C., Samiona, S., Musa, M.N., Muhammad, M.J., Muhammad, A.I., Yazid, M.N. A.W.M., Mamat, R.: The significant effect of turbulence characteristics on heat transfer enhancement using nanofluids: a comprehensive review. Int. Commun. Heat Mass Transf. **72**, 39–47 (2016). https://doi.org/10.1016/j.icheatmasstransfer.2016.01.002

23. Azmi, W.H., Sharma, K.V., Mamat, R., Anuar, S.: Turbulent forced convection heat transfer of nanofluids with twisted tape insert in a plain tube. Energy Proc. **52**, 296–307 (2014). https://doi.org/10.1016/j.egypro.2014.07.081

24. Sundar L.S., Sousa A.C.M., Singh M.K.: Heat transfer enhancement of low volume concentration of carbon nanotube-Fe3O4/water hybrid nanofluids in a tube with twisted tape inserts under turbulent flow. J. Therm. Sci. Eng. Appl. **7**, 021015-1-12 (2015). https://doi.org/10.1115/1.4029622

25. Aliabadi, M.K., Eskandari, M.: Influence of twist length variations on thermal–hydraulic specifications of twisted-tape inserts in presence of Cu–water nanofluid. Exp. Thermal Fluid Sci. **61**, 230–240 (2015)

26. Maddah, H., Alizadeh, M., Ghasemi, N., Alwid, S.R.W.: Experimental study of Al2O3/water nanofluid turbulent heat transfer enhancement in the horizontal double pipes fitted with modified twisted tapes. Int. J. Heat Mass Transf. **78**, 1042–1054 (2014). https://doi.org/10.1016/j.ijheatmasstransfer.2014.07.059

27. Fotukian, S.M., Esfahany, M.N.: Experimental study of turbulent convective heat transfer and pressure drop of dilute CuO/water nanofluid inside a circular tube. Int. Commun. Heat Mass Transfer **37**(2), 214–219 (2010)

28. Li, Calvin H., Peterson, G.P.: Experimental investigation of temperature and volume fraction variations on the effective thermal conductivity of nanoparticles suspensions (nanofluids). J. Appl. Phys. **99**(084314), 1–8 (2006)
29. Bergman, T.L., Incropera, F.P.: Fundamentals of heat and mass transfer. Wiley, Berlin (2011)
30. Eiamsa-Ard, S., Promvonge, P.: Performance assessment in a heat exchanger tube with alternate clockwise and counter-clockwise twisted-tape inserts. Int. J. Heat Mass Transf. **53** (7), 1364–1372 (2010)
31. Manglik, R.M., Bergles, A.E.: Heat transfer and pressure drop correlations for twisted-tape inserts in isothermal tubes: part II-transition and turbulent flows. Trans. Am. Soc. Mech. Eng. J. Heat Transfer **115**, 890 (1993)

Part VIII
Green Manufacturing and Materials

Supplementary Cement Replacement Materials for Sustainable Concrete

Job Thomas, Nassif Nazeer Thaickavil and T. N. Syamala

1 Introduction

Use of supplementary cement replacement materials in concrete helps to mitigate the adverse environmental impacts associated with the cement production process. The cement industry alone is a major contributor to global warming accounting for 8% of the world's total CO_2 emissions releasing one tonne of CO_2 for every tonne of cement produced [1, 2]. The emphasis on green construction practices calls for exploring ways to replace cement in concrete with suitable eco-friendly supplementary cementing materials. This helps to reduce the embodied carbon dioxide (eCO_2) of concrete. The partial replacement of cement with ground-granulated blast furnace slag (GGBS) has become an accepted practice worldwide. Granulated blast furnace slag is obtained as a by-product of the steel manufacturing process [3]. The molten slag from the furnace is rapidly cooled to form granules and then these granules are ground to the fineness of Portland cement. GGBS is a cementing material consisting primarily of silicates and aluminates of calcium and other bases. The processing of GGBS saves substantial amounts of energy and releases lower CO_2 to the atmosphere when compared to the production of Ordinary Portland Cement (OPC).

Ultrafine GGBS is a relatively new engineered material obtained from GGBS and is a potential eco-friendly alternative to replace cement in concrete. Ultrafine GGBS is manufactured by the process of controlled granulation of slag with high glass content having high reactivity. The production process is very much similar to GGBS and the only difference is in the size of particles. Silica fume is another highly reactive pozzolanic material and is a by-product of the smelting process in silicon and ferrosilicon industry. It is collected from the flue gases from electric arc

J. Thomas (✉) · N. N. Thaickavil · T. N. Syamala
Department of Civil Engineering, Cochin University of Science and Technology,
Cochin 682022, Kerala, India
e-mail: job_thomas@cusat.ac.in

furnaces. It is also called as micro-silica, condensed silica fume, volatilised silica or silica dust. The use of silica fumes is known to enhance the properties of concrete and finds application in the production of high-strength concrete [4].

The objective of this study is to evaluate the potential of using ultrafine GGBS to partially replace cement in high-performance concrete. The effects of ultrafine GGBS, GGBS and silica fume on the properties of concrete are investigated and compared.

2   Literature Review

Sharmila and Dhinakaran [5] investigated the strength and durability properties of concrete containing ultrafine slag. It was reported that the strength of concrete increased up to 10% replacement of cement. On further increase in the replacement ratio, the compressive strength of concrete was found to decrease. The durability properties of capillary suction, water absorption, porosity, and chloride ion penetration were also improved when 10% of cement was replaced with ultrafine slag. Ansari et al. [6] studied the compressive strength of concrete with ultrafine GGBS and fly ash and up to 15–20% increase in the compressive strength of concrete was observed with the increase in the mineral content. Teng et al. [7] reported that the strength and durability properties of concrete improved when 30% cement was replaced with ultrafine GGBS. Karthikeyan and Dhinakaran [8] suggested that the optimum percentage of replacement of cement with ultrafine GGBS is 5%, considering the strength and durability criteria. Suthar et al. [9] carried out an experimental investigation to evaluate the compressive strength and flexural strength of high-performance concrete for M70 grade by partially replacing cement with ultrafine GGBS, fly ash and silica fume. It was reported that the results indicated that concrete showed excellent fresh and hardened properties. Tofik et al. [10] investigated the compressive strength and flexural strength and it was reported that the addition of ultrafine GGBS showed better performance compared to other slag materials and micro-silica. It was reported that the results indicated that concrete showed excellent fresh and hardened properties. Lim et al. [11] investigated the strength and durability properties of high-strength concrete with ultrafine GGBS. It was found that addition of 30% ultrafine GGBS increased the flexural strength and modulus of elasticity of the concrete mixes. It can be observed that the percentage of cement replacement suggested by different authors is different. This may be due to the variation in the quality and the properties of the slag are used for producing the ultrafine GGBS.

Samad et al. [12] studied the strength of concrete containing GGBS as supplementary cementing material for three levels of cement replacement at 30, 40 and 50%. It was reported that up to 50% replacement of cement with GGBS did not affect the strength of concrete significantly. Duan et al. [13] investigated the effects of GGBS on the pore structure, micro-hardness and morphology of the interfacial transition zone of concrete at 28 days and reported that the compressive strength and durability of concrete depends on the quality of the pore structure and

interfacial transition zone. Siddique and Kaur [14] studied the properties of concrete containing ground-granulated blast furnace slag (GGBS) for cement replacement levels of 20, 40 and 60%. It was observed that the addition of GGBS in the mix resulted in the reduction of compressive strength, splitting tensile strength and modulus of elasticity of concrete.

Khodabakshian et al. [15] studied the effect of replacing cement in concrete with silica fume at replacement levels of 2.5, 5 and 10%. The compressive strength and durability of concrete was found to improve with the addition of silica fume. Pradhan and Dutta [16] investigated the mechanical properties of concrete such as compressive strength, compacting factor, and slump of concrete by replacing cement with 0, 5, 10, 15 and 20% silica fume. It was observed that the maximum compressive strength was obtained at 20% cement replacement. Jianyong and Pei [17] studied the changes on mechanical properties by the addition of GGBS and silica fume. The test results showed that compressive and split tensile strengths of concrete improved on blending cement with 10–15% of mineral admixture.

3 Experimental Study

The properties of concrete specimens with three different pozzolanic materials were studied. The variables considered in the study are the type and percentage content of pozzolanic material and grade of concrete. Compressive strength test, test for modulus of elasticity, split tensile strength test and flexural strength test were conducted to evaluate the strength of concrete containing supplementary cementing materials. The durability characteristics of concrete were evaluated by conducting sulphate attack test, rapid chloride permeability test and acid attack test.

3.1 Material Characterisation

Cement used in the study was Ordinary Portland Cement (OPC) conforming to IS: 12269 [18]. The properties of cement were determined by laboratory tests. Manufactured sand (quarry sand) is the fine aggregate used in the study. Sieve analysis as per IS: 383 [19] indicated that fine aggregate belonged to Zone II. Crushed stone aggregates of size 12.5 and 20 mm were used as coarse aggregates. The proportioning of aggregate was determined for the target-specified gradation in IS: 383 [19]. A mixture of 12.5 and 20 mm size aggregates mixed in equal quantities was used. The properties of cement, fine aggregate and coarse aggregate are given in Table 1.

The mineral admixtures considered in the study are ultrafine GGBS, GGBS and silica fume. Specific gravities of GGBS, ultrafine GGBS and silica fume were found to be 2.8, 2.9 and 2.2, respectively. The chemical composition of mineral admixtures had been determined by laboratory testing and the details are given in Table 2.

Table 1 Properties of materials

Sl. No.	Material	Property	Magnitude
1.	Cement	Specific gravity	3.10
		Fineness	4%
		Standard consistency	27.5%
		Initial setting time	125 min
		Final setting time	230 min
		Compressive strength—7 days	39 MPa
		Compressive strength—28 days	55.6 MPa
2.	Fine aggregate	Specific gravity	2.73
		Loose bulk density	1415 kg/m^3
3.	Coarse aggregate (20 mm)	Specific gravity	2.70
		Loose bulk density	1380 kg/m^3
		Water absorption	0.70
4.	Coarse aggregate (12.5 mm)	Specific gravity	2.70
		Loose bulk density	1380 kg/m^3
		Water absorption	0.80

Table 2 Chemical composition of mineral admixtures

Sl. No.	Chemical compound	Ultrafine GGBS (%)	GGBS (%)	Silica fume (%)
1.	SiO_2	32.16	39.18	97.08
2.	Al_2O_3	18.10	10.18	0.21
3.	Fe_2O_3	1.28	2.02	–
4.	CaO	35.89	31.82	1.90
5.	MgO	7.88	8.52	0.39
6.	SO_3	0.48	–	0.18
7.	Na_2O	0.81	1.14	0.08
8.	K_2O	0.34	0.30	0.16

The scanning electron microgram (SEM) images of the mineral admixtures are provided in Fig. 1 and it can be inferred that ultrafine GGBS is finer and hence more reactive than GGBS. The average particle size of ultrafine GGBS is 5 μ whilst that of GGBS is 45 μ. The X-ray powder diffraction (XRD) images of the mineral admixtures are given in Fig. 2. It can be noticed that the XRD image for ultrafine GGBS shows low peaks which means that it is amorphous without any detectable crystalline phase. The absence of crystalline phase and smaller particle size implies that ultrafine GGBS shows a high degree of reactivity.

The sustainability of the materials is measured as a function of embodied energy and CO_2 equivalent. The energy use and CO_2 release associated with the manufacture of one tonne of each material is given in Table 3. To obtain the values of embodied energy and CO_2 equivalent, the additional energy spent on grinding and additional CO_2 released have been added to the respective values for GGBS. It can
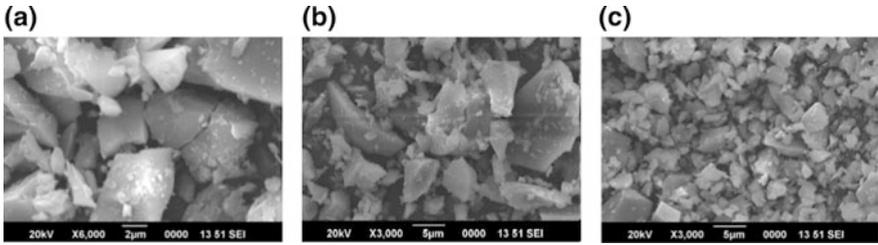
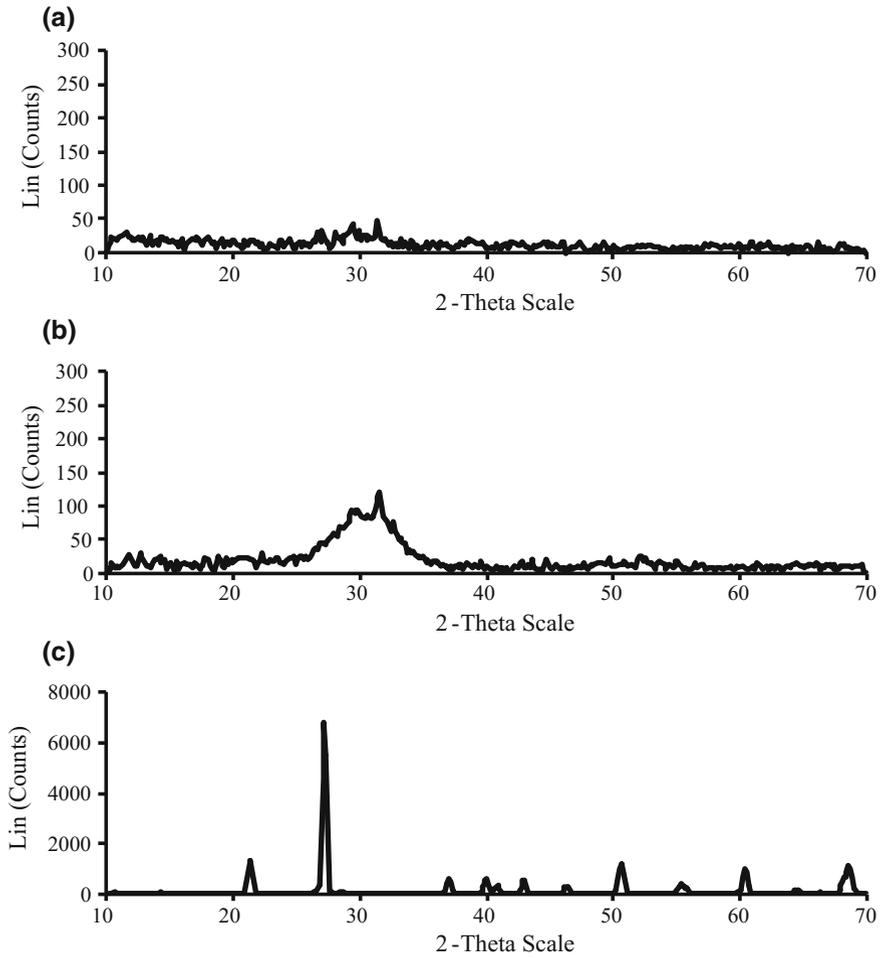**Fig. 1** SEM analysis **a** ultrafine GGBS **b** GGBS **c** silica fume

Fig. 2 XRD analysis **a** ultrafine GGBS **b** GGBS **c** silica fume

Table 3 Environmental burden

Sl. No.	Parameter	Impact (manufacture of 1 tonne)			
		OPC[a]	Ultrafine GGBS	GGBS[a]	Silica fume[c]
1.	CO_2 Equivalent in kg per tonne	950	140[b]	50	14
2.	Embodied energy in MJ per tonne	5000	2160	1300	36

[a]After Samad et al. [12], [b]After Loreti [20], [c]After Jones et al. [21]

be noticed that the use of supplementary cementing materials can contribute significantly in reducing the environmental impacts of OPC (Table 3).

3.2 Mix Proportioning

The weights of the constituent materials were determined by the absolute volume method given by IS: 10262 [22]. The grades of concrete considered in the study were M30, M60 and M80. Concrete containing GGBS is known to be particularly sensitive to carbonation [23]. Divsholi et al. [23] reported that a mix with 10% GGBS had exhibited a carbonation rate similar to that of control mix and that carbonation increases with the increase in percentage of GGBS used. Hence, the maximum percentage of cement replacement with GGBS and ultrafine GGBS has been limited to 10% in this study. Duval and Kadri [24] suggested that the workability and setting of the mix is affected when silica fume content is increased beyond 10%. Hence, the silica fume content is limited to 10% by volume of the cement in this study.

The cement in concrete is replaced with the mineral admixtures for 5 and 10% of the total cementations material and no replacement is made for the control mix. The control mixes are denoted by 30C100, 60C100 and 80C100. The first term represents the grade of concrete, second term stands for the binder and the third term gives the percentage of binder material in the mix. All mixes are designated according to this system. A poly-carboxylic ether-based super plasticizer was used for M60 and M80 concrete. The specific gravity of the chemical admixture was found out to be 1.08. The mix designations and corresponding proportions are given in Table 4. The dosage of admixture (A), weight of water, cement (C), ultrafine GGBS (FG), GGBS (G), silica fume (SF), fine aggregate (FA) and coarse aggregate (CA), water-binder ratio (W/B) and dosage of high-performance super plasticizer admixture are tabulated.

Table 4 Details of concrete mixes

Sl. No.	Mix ID	A (%)	W/B Ratio	Water (kg)	Cementing materials (kg)				FA (kg)	CA (kg)
					C	FG	G	SF		
1	30C100	–	0.50	175	350	–	–	–	778	1160
2	30FG5	–	0.50	175	332.5	16.3	–	–	778	1160
3	30FG10	–	0.50	175	315	32.7	–	–	778	1160
4	30G5	–	0.50	175	332.5	–	15.8	–	778	1160
5	30G10	–	0.50	175	315	–	31.6	–	778	1160
6	30SF5	–	0.50	175	332.5	–	–	12.4	778	1160
7	30SF10	–	0.50	175	315	–	–	24.8	778	1160
8	60C100	0.5	0.35	175	500	–	–	–	725	1080
9	60FG5	0.5	0.35	175	475	23.4	–	–	725	1080
10	60FG10	0.5	0.35	175	450	46.8	–	–	725	1080
11	60G5	0.5	0.35	175	475	–	22.6	–	725	1080
12	60G10	0.5	0.35	175	450	–	45.2	–	725	1080
13	60SF5	0.5	0.35	175	475	–	–	17.8	725	1080
14	60SF10	0.5	0.35	175	450	–	–	35.5	725	1080
15	80C100	0.5	0.23	184	800	–	–	–	606	902
16	80FG5	0.5	0.23	184	760	37.5	–	–	606	902
17	80FG10	0.5	0.23	184	720	74.9	–	–	606	902
18	80G5	0.5	0.23	184	760	–	36.13	–	606	902
19	80G10	0.5	0.23	184	720	–	72.26	–	606	902
20	80SF5	0.5	0.23	184	760	–	–	28.4	606	902
21	80SF10	0.5	0.23	184	720	–	–	56.8	606	902

3.3 Testing

All specimens were tested for workability and strength as per procedure specified in the relevant IS codes. The workability of fresh concrete was determined by the slump test for M30 concrete as per IS: 1199 [25]. For M60 and M80 concrete slump flow test was done and the flow diameter was measured as shown in Fig. 3 as per ASTM C1611 [26].

Cube and cylinder specimens were cured for 28 days by immersion and tested on a digital compression testing machine of 3000 kN capacity to determine the compressive strength and split tensile strength, respectively. The compressive strength and split tensile tests were conducted as per IS: 516 [27] and IS: 5816 [28], respectively. The modulus of elasticity and flexural strength were tested in a universal testing machine of capacity 1000 kN according to IS: 516 [27]. Figure 4 shows the cube and cylinder specimens before curing.

The durability of specimens was evaluated by conducting tests to determine the acid attack resistance, sulphate resistance and resistance to chloride penetration. Acid attack resistance and sulphate attack resistance were measured by determining

Fig. 3 Slump flow test

Fig. 4 Cube and cylinder specimens before curing

the weight loss of cube specimens of size 150 mm × 150 mm × 150 mm. Acid attack resistance was measured as per ASTM C267 [29]. The specimens were dried and weighed after initially curing in water for 28 days. To determine acid attack resistance, the specimens were immersed in 3% H_2SO_4 for 90 days and the pH of the solution was maintained constant throughout. Sulphate attack resistance was determined similarly by immersing cube specimens in sulphate water containing 5% sodium sulphate and 5% magnesium sulphate by weight of water for 90 days according to ASTM C452 [30]. The concentration of sulphate was maintained

throughout the test period. After 90 days, the specimens were taken out and the weight losses were determined after wiping off water and grit from the surface. Resistance to chloride penetration is determined by RCPT test as per ASTM C1202 [31] on disc specimens of 100 mm diameter and 50 mm thickness.

4 Results and Discussion

The results of the experimental study on the effect of replacing cement with mineral admixtures are presented in subsequent sections.

4.1 Slump of Fresh Concrete

Concrete containing ultrafine GGBS showed the highest workability across all grades of concrete as seen from Fig. 5. The workability of concrete increased with the increase in pozzolanic content for concrete containing ultrafine GGBS and GGBS, whereas it decreased with increase in silica fume content. With the increase in content of silica fume beyond 5%, the volume of fines increases considerably. The spherically shaped silica fume particles also attract the super plasticizer particles to its surface, thereby increasing the water demand, resulting in lower workability (Fig. 5).
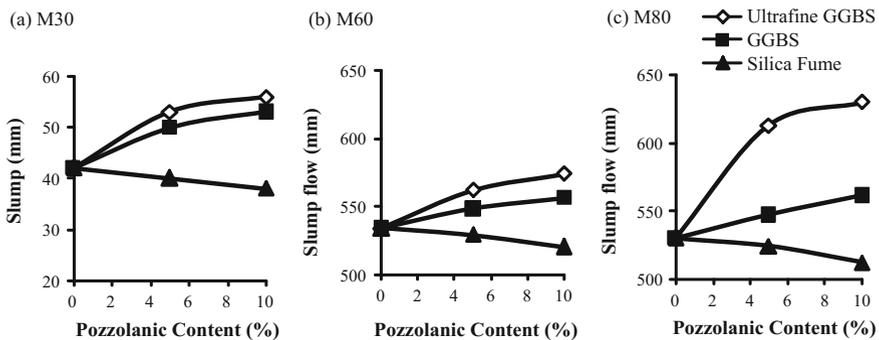

Fig. 5 Effect of addition of low energy cement replacement materials on workability

4.2 Compressive Strength of Concrete

From Figs. 6 and 7, the compressive strength of concrete was found to increase with the addition of mineral additives. The mixes containing ultrafine GGBS showed an improvement of 30–45% improvement in the compressive strength compared to the control mix. The enhancement in compressive strength of concrete mixes containing mineral admixtures may be due to the pozzolanic nature of these materials. The pozzolanic reaction between $Ca(OH)_2$ in concrete and silicates of mineral admixtures gives rise to the formation of secondary C–S–H gel. This results in the formation of a denser microstructure ultimately leading to higher strength gain. Ultrafine GGBS has got a unique chemical composition mainly of CaO and SiO_2. Due to its unique particle size distribution and the presence of CaO, ultrafine GGBS aids the formation of a denser pore structure resulting in higher compressive
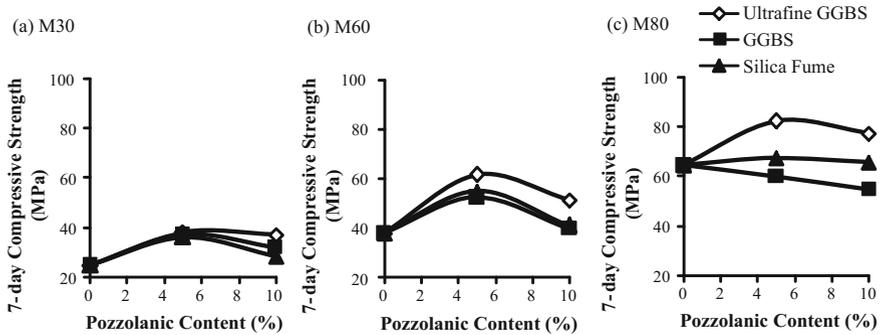

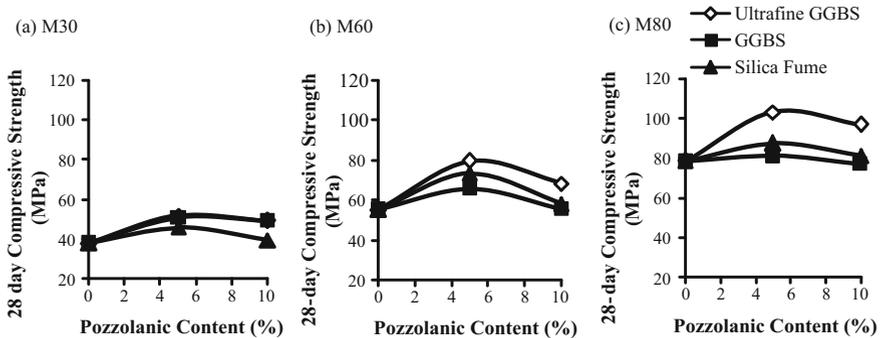**Fig. 6** Effect of addition of low energy cement replacement materials on 7-day compressive strength

Fig. 7 Effect of addition of low energy cement replacement materials on 28-day compressive strength

strength at all ages. The water demand also gets decreased because of the high glass content in ultrafine GGBS, which has water repelling property. The higher specific surface area of ultrafine GGBS improves its reactivity and results in a concrete with higher strength compared to concrete containing GGBS.

For M60 and M80 concrete, concrete containing GGBS shows the lowest compressive strength amongst the mixes containing mineral admixtures. The amorphous silica in silica fume produces secondary calcium-silicate-hydrates (C–S–H) and also alters the orientation of $Ca(OH)_2$, thereby enhancing the microstructure of concrete. Hence, concrete containing silica fume achieved higher strength for M60 and M80 grade concrete. The presence of excess water in M30 concrete reduces the strength of concrete, masking the effect of the reactive silica fume.

The strength of concrete was found to increase up to 5% replacement of cement as the fine mineral admixtures fill the gaps in the hardened mass, which would otherwise be left void. The mineral admixtures possess oxides with lesser pozzolanic reactivity and the excess replacement of cement leads to the inclusion of the unreacted inert particles inside the hardened mass which causes a decrease in the strength of concrete.

The compressive strength of concrete is not affected when up to 10% of cement is replaced with mineral admixtures and can be recommended without any changes in the original mix design.

4.3 Split Tensile Strength of Concrete

Test results indicate that the inclusion of pozzolanic materials in concrete improved the split tensile strength of concrete as shown in Fig. 8. Maximum split tensile strength was observed for concrete with ultrafine GGBS. In all the test results, 5% replacement of cement with pozzolanic material gave better results. The improvement in split tensile strength can be attributed to a stronger transition zone and
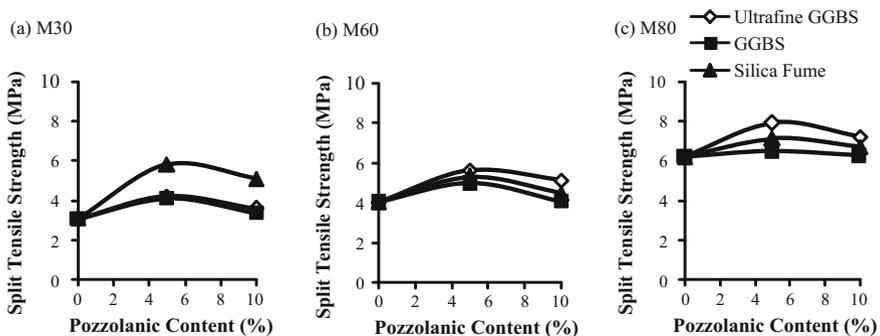

Fig. 8 Effect of addition of low energy cement replacement materials on split tensile strength
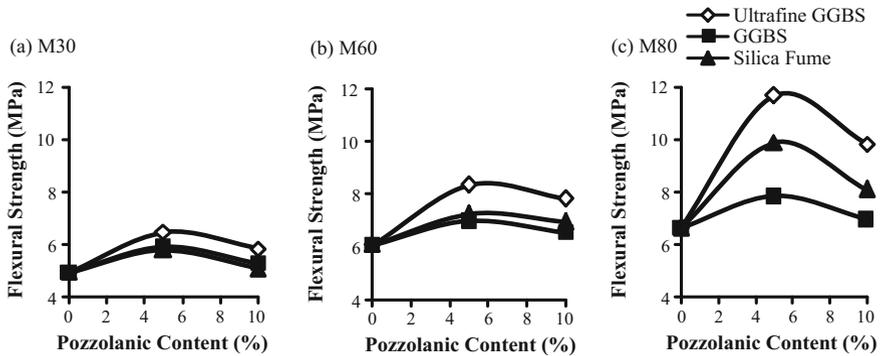
Fig. 9 Effect of addition of low energy cement replacement materials on flexural strength

denser pore structure as a result of the addition of mineral admixtures. The split tensile strength obtained at 10% replacement of cement is comparable to the strength of the control mix.

4.4 Flexural Strength of Concrete

The results of flexural strength indicate that the inclusion of pozzolanic materials in concrete improved the flexural strength of concrete and are shown in Fig. 9. Maximum flexural strength was observed for concrete with ultrafine GGBS. 5% replacement of cement with pozzolanic material gave better results for all grades and for all materials. The improvement in split tensile strength may due to the alteration of the microstructure of concrete leading to a stronger transition zone. At 10% replacement of cement, no loss of flexural strength was observed.

4.5 Modulus of Elasticity of Concrete

The variation of modulus of elasticity with different concrete mixes is similar to the variation of compressive strength. The comparison of the results is shown in Fig. 10. Maximum modulus of elasticity was observed for mix containing 5% ultrafine GGBS. The formation of a better transition zone and improvement of microstructure of concrete result in better elastic properties of concrete containing ultrafine GGBS.
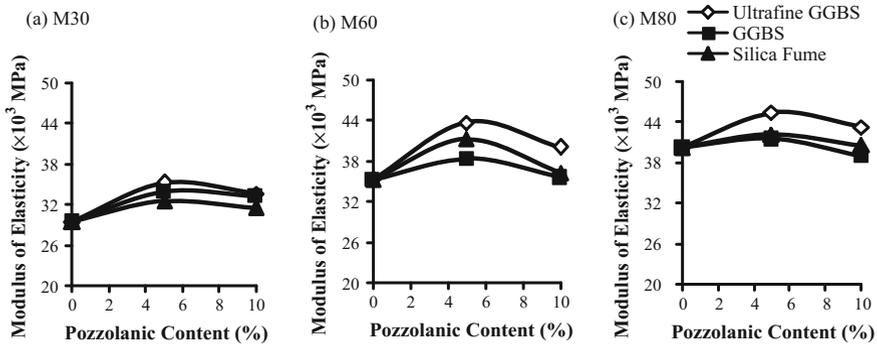
Fig. 10 Effect of addition of low energy cement replacement materials on modulus of elasticity

4.6 Sulphuric Acid Resistance of Concrete

The formation of gypsum and ettringite disrupts the concrete mass due to the expansion in volume by these reaction products. This leads to tensile stresses causing cracking and spalling of concrete. The results of the acid attack test indicate that incorporation of pozzolanic materials improves the resistance of concrete against acid attack. For all grades of concrete, concrete with pozzolanic materials showed a better performance than the control mix. Concrete with silica fume admixture shows the highest resistance to acid as shown in Fig. 11. Silica fume converts calcium hydroxide in concrete to calcium-silicate hydrate, thereby refining the pore structure and hence reducing the permeability of concrete. The attack of sulphuric acid mainly occurs on a narrow zone in the transition zone and the thickness of the interfacial transition zone gets reduced as a result of the attack [32]. Silica fume behaves like a filler material and fills in the capillary pores and in the voids in the interfacial transition zone, thereby enhancing the acid resistance of concrete. It can also be observed that the acid attack resistance offered by the
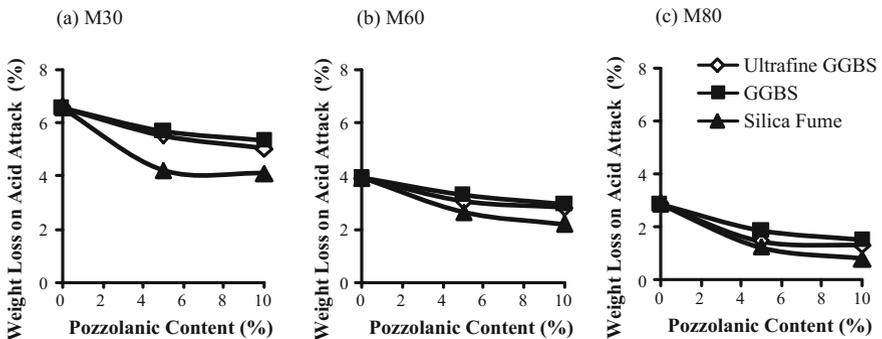

Fig. 11 Effect of addition of low energy cement replacement materials on acid attack resistance
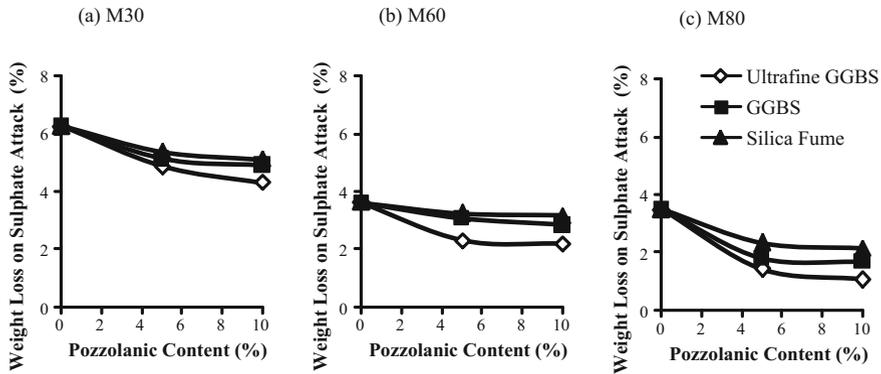
Fig. 12 Effect of addition of low energy cement replacement materials on sulphate attack resistance

addition of ultrafine GGBS is better compared to that by GGBS and this may be due to the micro-filling of the voids by ultrafine GGBS. It can be observed that better resistance to acid attack is offered when 10% of cement is replaced with pozzolanic materials.

4.7 Sulphate Attack Resistance of Concrete

Sulphate attack results in the production of ettringite, thereby causing an expansion in volume and internal stresses in concrete. This results in cracking of concrete at the microstructure level and leads to the deterioration of concrete. The sulphate attack resistance of concrete improves with the increase in pozzolanic content for all grades of concrete. As shown in Fig. 12, concrete with ultrafine GGBS shows better resistance to the attack of sulphates. The presence of CaO and absence of tricalcium aluminate in ultrafine GGBS enhances the durability of concrete. The finer particles of ultrafine GGBS ensure better filling of voids, thereby improving the imperme-ability of concrete. The interfacial zone is denser for concrete of higher grades. The available surface for attack is hence limited and the resistance offered to sulphate attack is better. At 10% replacement of cement with supplementary cementing materials, a better resistance to sulphate attack is offered.

4.8 Chloride Penetration Resistance

The chloride permeability is assessed based on the charge passing through the specimen and the results of the test are tabulated in Table 5.

Table 5 Chloride permeability as per ASTM C1202 [31]

Charge passed (C)	Degree of permeability	Mix designation
>4000	High	–
2000–4000	Moderate	30C100, 60C100
		30G5, 30G10
		30SF5, 30SF10
		80C100
1000–2000	Low	30FG5, 30FG10
		60FG5, 60FG10
		60G5, 60G10
		80G5, 80G10
		60SF5, 60SF10
		80SF5, 80SF10
100–1000	Very low	80FG5, 80FG10
<100	Negligible	–

The maximum resistance to chloride penetration is seen in M80 concrete mixes containing ultrafine GGBS at a cement replacement ratio of 10%. M30 grade concrete containing GGBS and silica fume and control mixes of M30 and M60 concrete show lower durability as per RCPT test results. The enhanced durability is due to the denser pore structure resulting from the use of ultrafine GGBS.

5 Conclusion

Ultrafine GGBS, GGBS and silica fume are easily available industrial by-products which can be used in place of cement without affecting the mechanical properties of concrete. The use of ultrafine GGBS significantly enhances the workability, strength and durability characteristics of concrete when compared to the control mix. The maximum recommendable dosage of ultrafine GGBS is found to be 10% by volume of cementing materials in the mix. Increasing the percentage of silica fumes in the mix significantly affects the workability of concrete. The durability of concrete is also enhanced when 10% of the cement in the mix was replaced with the mineral admixtures. The efficient utilisation of industrial by-products in concrete not only helps to improve its properties, but also opens up new vistas in the field of eco-friendly concrete production.

References

1. IEA/WBCSD: Energy efficiency and CO_2 emission reduction potentials and policies in the cement industry. In: Towards a Plan of Action, Workshop Proceedings, Paris, France, 2006, International Energy Agency, p. 13 (2006)
2. AP 42: Compilation of Air Pollutant Emission Factors, Volume I: Stationary Point and Area Sources. Environmental Protection Agency. Washington, DC (2005)
3. Siddique, R.: Ground granulated blast furnace slag. In: Waste Materials and By-Products in Concrete. Springer, Heidelberg (2008)
4. Ramezanianpour, A.A.: Silica fume. In: Cement Replacement Materials. Springer, Heidelberg (2014)
5. Sharmila, P., Dhinakaran, G.: Strength and durability of ultra fine slag based high strength concrete. Struct. Eng. Mech. **55**(3), 675–686 (2015)
6. Ansari, U.S., Chaudhri, I.M., Ghuge, N.P., Phatangre, R.R.: Concrete with Alccofine and fly ash: an economical and environment friendly approach. Int. J. Mod. Trends Eng. Res. **2**(3), 279–285 (2014)
7. Teng, S., Lim, T.Y.D., Divsholi, B.S.: Durability and mechanical properties of high strength concrete incorporating ultra fine Ground Granulated Blast-furnace Slag. Constr. Build. Mater. **40**, 875–881 (2013)
8. Karthikeyan, K., Dhinakaran, G.: Effect of grinding on strength and durability of GGBFS-based concrete. Jordan J. Civ. Eng. **8**(4), 442–454 (2014)
9. Suthar, S., Shah, B.K., Patel, P.J.: Study on effect of Alccofine and fly ash on the mechanical properties of high performance concrete. Int. J. Sci. Res. Dev. **1**(3), 464–467 (2013)
10. Tofik, M., Patel, Y., Upadhyay, S.P., Darji, A.R., Jamnu, M.A.: To study on high performance concrete with Alccofine and waste glass powder. Int. J. Sci. Res. Dev. **2**(4), 939–941 (2014)
11. Lim, D.T.Y., Xu, D., Divsholi, B.S., Kondeaivendhan, B., Teng, S.: Effect of ultra fine slag replacement on durability and mechanical properties of high strength concrete. In: 36th Conference on Our World in Concrete and Structures, Singapore (2011)
12. Samad, S., Shah, A., Limbachiya, M.C.: Strength development characteristics of concrete produced with blended cement using ground granulated blast furnace slag (GGBS) under various curing conditions. Sadhana **42**(7), 1203–1213 (2017)
13. Duan, P., Shui, Z., Chen, W., Shen, C.: Enhancing microstructure and durability of concrete from ground granulated blast furnace slag and metakaolin as cement replacement materials. J. Mater. Res. Technol. **2**(1), 52–59 (2013)
14. Siddique, R., Kaur, D.: Properties of concrete containing ground granulated blast furnace slag (GGBFS) at elevated temperatures. J. Adv. Res. **3**, 45–51 (2012)
15. Khodabakhshian, A., Ghalehnovi, M., de Brito, J., Shamsabadi, E.A.: Durability performance of structural concrete containing silica fume and marble industry waste powder. J. Cleaner Prod. **170**, 42–60 (2018). http://dx.doi.org/10.1016/j.jclepro.2017.09.116
16. Pradhan, D., Dutta, D.: Influence of silica fume on normal concrete. Int. J. Eng. Res. Appl. **3**(5), 79–82 (2013)
17. Jianyong, L., Pei, T.: Effect of slag and silica fume on mechanical properties of high strength concrete. Cem. Concr. Res. **27**(6), 833–837 (1997)
18. IS: 12269 (1987) Indian Standard. Ordinary Portland cement 53 grade—specification. Bureau of Indian standards. New Delhi, India (1987)
19. IS: 383 (2016) Indian Standard. Coarse and fine aggregate for concrete—specification. Bureau of Indian standards. New Delhi, India (1987)

20. Loreti, C.: Cement sector greenhouse gas emissions reduction case studies CEC-600-2009-005. California Energy Commission, Sacramento (2009)
21. Jones, R., McCarthy, M., Newlands, M.: Fly ash route to low embodied CO_2 and implications for concrete construction. In: 2011 World of Coal Ash (WOCA) Conference, Denver, USA (2011)
22. IS: 10262 (2009) Indian Standard. Concrete mix proportioning—guidelines. Bureau of Indian standards. New Delhi, India (2009)
23. Divsholi, B.S., Lim, T.Y.D., Teng, S.: Durability properties and microstructure of ground granulated blast furnace slag cement concrete. Int. J. Concr. Struct. Mater. **8**(2), 157–164 (2014)
24. Duval, R., Kadri, E.H.: Influence of silica fume on the workability and the compressive strength of high-performance concretes. Cem. Concr. Res. **28**(4), 533–547 (1998)
25. IS: 1199: Methods of sampling and analysis of concrete. Bureau of Indian Standards, New Delhi, India (1959)
26. ASTM C1611 M-14: Standard test method for slump flow of self-consolidating concrete. American Society for Testing and Materials, Pennsylvania, USA (2014)
27. IS: 516: Methods of test for strength of concrete. Bureau of Indian Standards, New Delhi, India (1959)
28. IS: 5816: Splitting tensile strength of concrete—method of test. Bureau of Indian Standards, New Delhi, India (1999)
29. ASTM C267-01: Standard test methods for chemical resistance of mortars, grouts, and monolithic surfacings and polymer concretes. American Society for Testing and Materials, Pennsylvania, USA (2012)
30. ASTM C452-15: Standard test method for potential expansion of Portland-cement mortars exposed to sulfate. American Society for Testing and Materials, Pennsylvania, USA (2015)
31. ASTM C1202-17: Standard test method for electrical indication of concrete's ability to resist chloride ion penetration. American Society for Testing and Materials, Pennsylvania, USA (2017)
32. Gutberlet, T., Hilbig, H., Beddoe, R.E.: Acid attack on hydrated cement—effect of mineral acids on the degradation process. Cem. Concr. Res. **74**, 35–43 (2015)

Partial Replacement of Aggregates with Granulated Waste Plastic in Solid Concrete Blocks—An Intensive Study

Aysha Zeneeb Majeed, Tressa Kurian, Babitha Davis, Shaun Thomas Alex, Kevin Shelly Fernandez and Amala V. Mathew

1 Introduction

Plastics are used excessively, with its disposal being one of the greatest issues faced today. Around 10,000 ton of plastic per day is generated, which constitutes 9% of the total municipal solid waste (MSW) generated in India as per the studies done by Central Pollution Control Board of India. The recycling of plastic helps in reducing the emission of certain harmful gases such as carbon dioxide (CO_2), nitrogen oxide (NO), and sulphur dioxide (SO_2). Apart from these advantages, plastic is a non-biodegradable product which takes long time to decompose [1]. With rapid urbanization, particularly in India, the need for concrete buildings is on a rise. As the generated waste plastics face a huge problem for disposal, and as landfilling method is found to be costly, the best solution is to utilize the formed plastics in various forms, which includes its usage in manufacture of construction materials. Addition of plastic improves durability, water, and chemical attack resistance of concrete and also proves to be economical.

As solid concrete blocks are major components in building construction, use of plastic wastes in building blocks as a partial replacement of coarse aggregates is a pertinent area of current research. Many studies were done during the past few decades, to understand the behavior of concrete with plastic as partial replacement of aggregates. In a study conducted on concrete blocks, by adding recycled polymer materials, reduction in compressive strength was reported. The reduction in strength was mainly attributed to the poor bonding between cement paste and plastic aggregates and also due to the lower strength of plastic aggregates [2]. Similarly, in an investigation carried out on concrete cubes with various percentages of plastics, with increase in the percentage of waste plastic, the compressive strength and flexural strength values of plastic concrete mix was found to be lower than the

A. Z. Majeed (✉) · T. Kurian · B. Davis · S. T. Alex · K. S. Fernandez · A. V. Mathew
Rajagiri School of Engineering and Technology, Kochi, India
e-mail: aysha_z@ymail.com

values for the corresponding conventional concrete mixes at all curing ages. The reason for this reduction in strength reported was due to the low adhesive strength between the surface of the plastic and cement paste, and also due to the hydrophobic behavior of waste plastic which may restrict the hydration of cement [3]. Further, various studies were done to investigate the effect of fibers on improving ductility and strength of concrete. When waste plastic was added in concrete for the manufacture of non-structural slabs as reinforcement, it was found to be effective in limiting the drying shrinkage, while there was an ample reduction in flexural as well as compressive strength [4]. On the other hand, in certain studies done on incorporating non-biodegradable waste plastic fibers in concrete used for the construction of slabs, it was reported that the load carrying capacity of concrete increased with the increase in fiber content [5].

Addition of plastic also affects the workability of the concrete mix, which varies with the shape and size of plastic aggregate. It was reported that the slump of fresh concrete decreased with addition of flaky and porous plastic aggregate due to its sharp edges and angular particle size [6], while the slump increased with addition of spherical plastic aggregates [7]. Also, when plastic was melted and coated over aggregates before its use in manufacturing concrete, there was a decrease in porosity and water absorption observed, while the soundness was found to increase [8].

In addition, studies have reported that the incorporation of plastic aggregates changes the failure behavior of concrete. The resulting concrete was found to be more ductile and could arrest cracks generated during mechanical failure. Also, the addition of plastic as aggregate decreases fresh and dry densities of the concrete as its weight reduces [9]. In a study which involved addition of 0.5% of domestic waste plastic, the compressive strength of cube in 7 days increased up to 0.68% and in 28 days increased up to 5.12% when compared to plain concrete mix [10]. Also, concrete containing plastic aggregates exhibited more ductile behavior than concrete made with conventional aggregates. This ductile behavior could be of significant advantage in reducing crack formation and propagation [1].

2   Research Significance

Comprehensive study on the use of plastic waste as aggregates in the use of cement mortar and concrete has been carried out over the decades. In particular, the performance of concrete blocks, including compressive strength, durability, porosity, etc., was reviewed and published. However, flexural behavior of concrete blocks, partially replaced with granulated plastic, is not looked into. A review in this area is in need, as the flexural behavior of building blocks is a key parameter to be considered for construction of buildings particularly in earthquake-prone areas. This experimental study focuses on how the replacement of aggregates with granulated plastic affects both compressive and flexural tensile strength of concrete blocks and thus proposes a suitable mix proportion, if used in construction industry.

3 Materials Used

3.1 Ordinary Portland Cement

OPC 53 grade was used in the current study as the main binder in the mixes. Fineness and standard consistency of cement were found to be 9 and 39%, respectively, conforming to IS specifications [11, 12]. Specific gravity of cement was found to be 3.106 g/cc conforming to IS specifications [13].

3.2 Fine Aggregates

Manufactured sand is used as fine aggregate in this study. The grain size distribution obtained by carrying out sieve analysis of sand (Table 1) conforms to Zone 2 of fine aggregates (Fig. 1) [14]. The specific gravity and bulk density of fine aggregates were found to be 2.695 and 1.73 g/cc, respectively, conforming to IS specifications [15]. Optimum volume of bulking of fine aggregates was found to be at 4% as given in Table 2 (Fig. 2).

3.3 Coarse Aggregates

Coarse aggregates of 12.5 mm size were used for the study. The specific gravity and bulk density of coarse aggregates were found to be 2.86 and 1.55 g/cc, respectively, which lie in the range conforming to IS specifications [15]. Aggregate crushing value was found to be 28.40% which is less than 35% conforming to IS specifications [16].

Table 1 Sieve analysis of fine aggregates

Sieve size (mm)	Aggregate wt retained (kg)	% wt retained	Cumulative % wt retained	Cumulative % passing
4.75	0.029	2.9	2.9	97.1
2.36	0.132	13.2	16.1	83.9
1.18	0.227	22.7	38.8	61.2
0.6	0.134	13.4	52.2	47.8
0.3	0.352	35.2	87.4	12.6
0.15	0.103	10.3	97.7	2.3
Pan	0.023	2.3	100	0

Fig. 1 Grain size distribution for fine aggregates'

Percent Finer, %

Sieve Size, mm
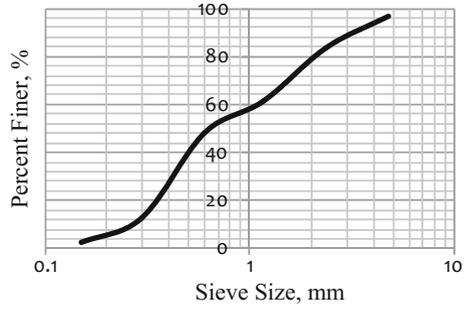
Table 2 Bulking of fine aggregates

Moisture content (%)	Volume (ml)	% Bulking
0	146	7.4
2	162	19.1
4	170	25.0
6	158	16.2
10	136	0

Fig. 2 Bulking of fine aggregates

% Bulking

Moisture Content, %
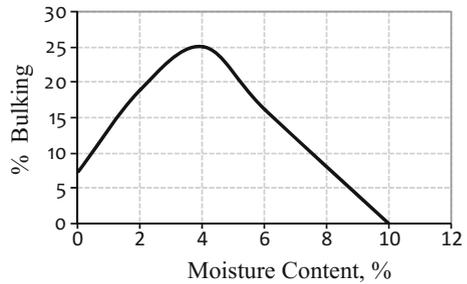
3.4 Plastic

High-density polyethylene (HDPE) plastic in the form of granules was used (Fig. 3). Bulk density of plastic was found to be 0.5 g/cc. The crushing value obtained was 5.07%.

4 Methodology

The present study focuses on understanding the behavior of standard concrete blocks used for construction of residential buildings in India. Thus, the characteristics of concrete blocks of size $300 \times 200 \times 150$ mm subjected to the action of

Fig. 3 Granulated plastic aggregates used in the study

axial compressive load and transverse load were studied. All specimens used for the test were cast from the same batch of materials. The mix ratio for the block considered in the study was 1:8:14 (cement: quarry dust: aggregate). The experimental mix was prepared by adding the above constituents and granulated plastic. The proportion of plastic replaced was varied from 5 to 20% with an increase of 5% by volume of aggregates initially. The proportioned materials were mixed in drum mixers conforming to IS 516:1959 [17]. The required quantity of water was then added into the mixer. Later, this concrete mix was poured into the mold and vibrated to achieve proper compaction. When the molds were completely filled, the mix was further compacted through direct compression along with vibration. The blocks were then tested for compression and flexure after 7 days and 28 days of curing (Fig. 4a). The average of all the observations was estimated. The optimum mix ratio with regard to compressive as well as flexural tensile strength was identified from the test results. From the results of initial tests, the optimum range was found to lie between 10 and 20% (Fig. 4b, c). Hence, the next set of specimens was casted by narrowing down the range of waste plastic percentage starting from 12 to 18%.

5 Mix Proportions

Mix proportions details of solid blocks with granulated plastic as replacement of coarse aggregate is given in Table 3.
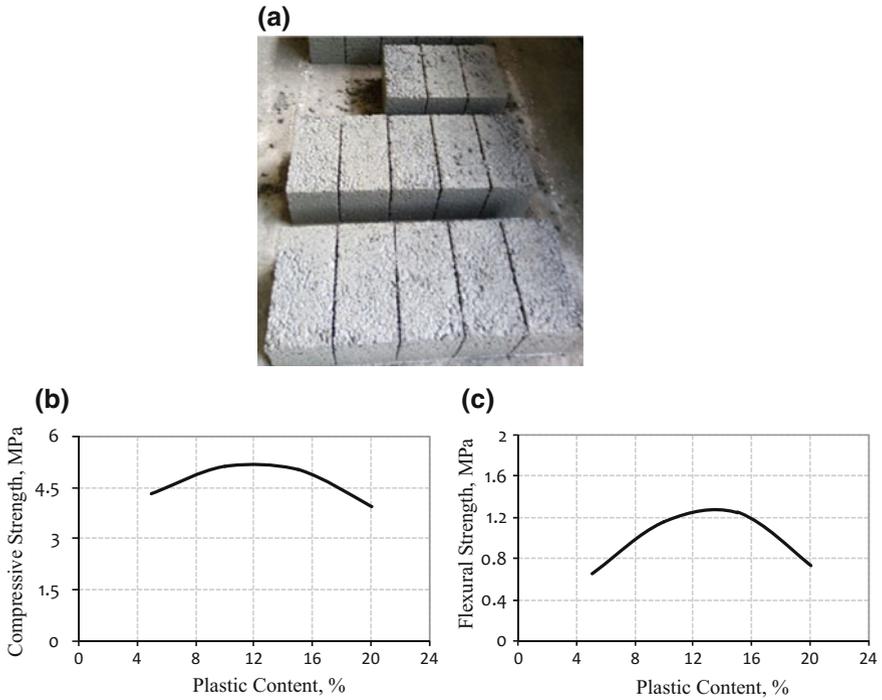
(a)

(b)

(c)

Fig. 4 **a** Solid concrete blocks mixed with granulated plastic casted in varying mixes, and variation of **b** compressive and **c** flexural strength of bricks with varying plastic content

Table 3 Mix proportions for solid blocks with granulated plastic as replacement of coarse aggregate

Mix No.	Cement (kg/m^3)	Granulated plastic (%)	Granulated plastic (kg/m^3)	Water content (kg/m^3)	w/c Ratio	Sand (kg/m^3)	Coarse aggregate (kg/m^3)
1	99.3	0	0.0	81.5	0.8	794	1389
2	99.3	12	90.5	81.5	0.8	794	1222
3	99.3	14	105.6	81.5	0.8	794	1195
4	99.3	16	120.7	81.5	0.8	794	1167
5	99.3	18	135.9	81.5	0.8	794	1139

6 Results and Discussion

6.1 Compressive Strength

The compressive strength was found to decrease with increase in replacement of aggregates with granulated waste plastic (Fig. 5). The variation in compressive
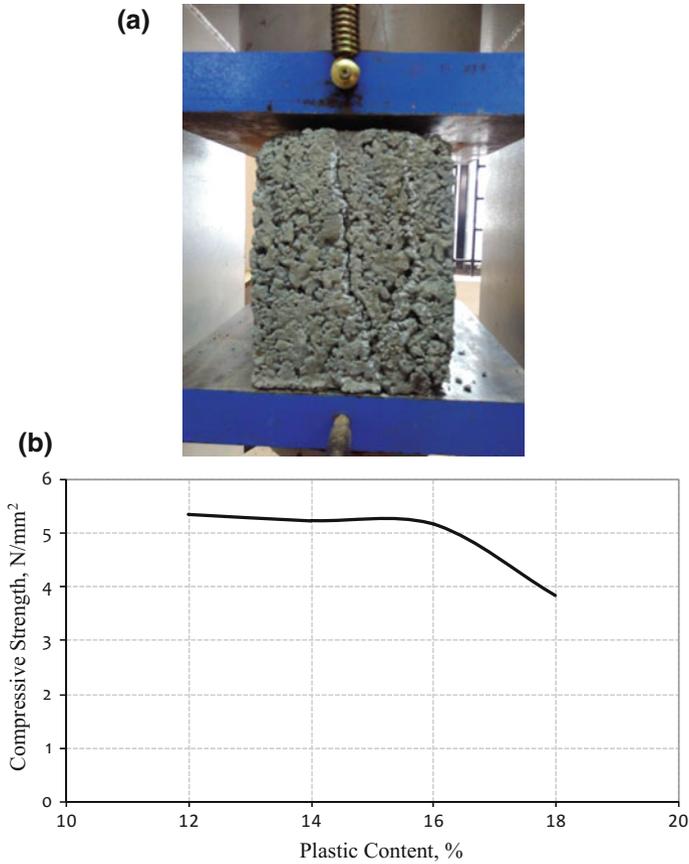
Fig. 5 **a** Typical failure pattern of concrete block specimens under axial compression, **b** variation of compressive strength with increase in plastic aggregate content

Table 4 Compressive strength of concrete blocks with varying percentage of plastic content

No.	Percentage replacement with plastic (%)	Average compressive strength (N/mm^2)
1.	0	6.96
2.	12	5.33
3.	14	5.22
4.	16	5.15
5.	18	3.85

strength of the concrete block with varying percentage of plastic aggregates is shown in Table 4. The compressive strength of proposed solid concrete block conforms to IS recommendation having minimum average compressive strength of 4 N/mm^2 for the blocks to be used as load bearing units [18].

6.2 Flexural Strength

The flexural strength was also found to decrease with increase in replacement of aggregate with granulated waste plastic (Fig. 6). This may be due to weak bonding between plastic aggregates and cement or due to the low strength of granulated plastic. The tensile strength of the concrete block partially replaced with plastic is shown in Table 5.
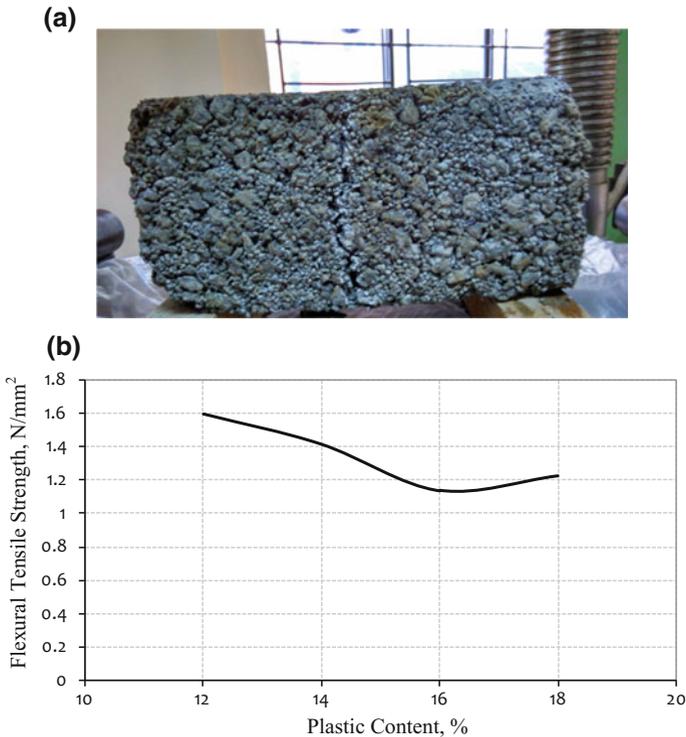
(a)

(b)

Fig. 6 **a** Typical failure pattern of concrete block specimens under flexure, **b** variation of tensile strength with increase in plastic aggregate content

Table 5 Flexural tensile strength of concrete blocks with varying percentage of plastic

No.	Percentage replacement with plastic (%)	Average flexural strength (N/mm^2)
1.	0	2.02
2.	12	1.60
3.	14	1.42
4.	16	1.14
5.	18	1.23

6.3 Water Absorption

The water absorption was found to decrease with increase in replacement of aggregates up to 12% and then found to increase with further replacement as shown in Table 6 (Fig. 7). Water absorption of blocks was observed to be much less than 10% by mass and hence conforms to IS specifications [18].

6.4 Block Density

The block density for various percentage of plastic replacement was estimated, and it was observed that the block density decreases with increase in replacement of coarse aggregate with plastic. The block density obtained for the block specimens was not less than 1800 kg/m^3 conforming to IS specifications [18] as given in Table 7.

Table 6 Water absorption of concrete blocks with varying percentage of plastic content

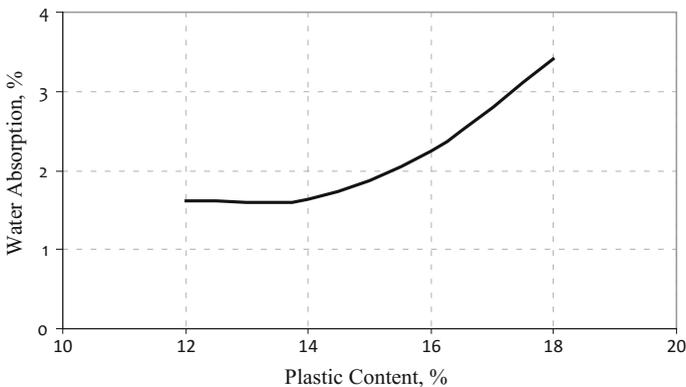| Percentage replacement with plastic (%)	Sample 1		Water absorption %
	Wet wt (kg)	Dry wt (kg)	
0	20.6	20.2	1.98
12	18.9	18.6	1.61
14	18.7	18.4	1.63
16	18.1	17.7	2.25
18	18.2	17.6	3.40

Fig. 7 Variation of water absorption of concrete blocks with varying % of plastic content

Table 7 Block density of concrete blocks with varying percentage of plastic content

Percentage of cement replaced (%)	Dry weight (kg)	Block density (kg/m³)
0	20.2	2244
12	18.6	2067
14	18.4	2044
16	17.7	1967
18	17.6	1956

7   Conclusions

The results obtained from the study done on the replacement of aggregate fraction with plastic waste indicates that plastic waste can be used to prepare lightweight concrete blocks with reasonable compressive and flexural tensile strength as compared to conventional concrete blocks. A reduction in both compressive strength and flexural strength was observed with increase in the percentage of plastic aggregates. However, concrete blocks with 12–14% of plastic aggregates shall be considered as an optimum percentage of replacement considering key parameters affecting their behavior, viz. compressive strength, flexural tensile strength, water absorption, and weight reduction. Thus, the method proves to be an alternative solution for waste plastic disposal other than the recycling methods and shall be recommended to be used as construction material, especially in earthquake-prone areas.

References

1. Siddique, R., Khatib, J., Kaur, I.: Use of recycled plastic in concrete: a review. J. Waste Manage. **28**, 1835–1852 (2008)
2. Rahman, M.M., Islam, M.A., Ahmed, M., Salam, M.A.: Recycled polymer materials as aggregates for concrete and blocks. J. Chem. Eng. IEB **ChE. 27**(1), 53–57(2012)
3. Ismail, Z.Z., Al-Hashmi, E.A.: Use of waste plastic in concrete mixture as aggregate replacement. Waste Manage. **28**, 2041–2047 (2008)
4. AL-Buhaisi, K.U.: Investigating the use of recycled plastics as shrinkage reinforcement in non-structural concrete slabs. M.Sc. thesis, The University of Gaza (2013)
5. Malagavelli, V., Rao, P.N.: Effect of non bio degradable waste in Concrete slabs. Int. J. Civ. Struct. Eng. **1**(3), 449–457 (2010). ISSN 0976-4399
6. Batayneh, M., Marie, I., Asi, I.: Use of selected waste materials in concrete mixes. Waste Manage. **27**, 1870–1876 (2007)
7. Al-Manaseer, A.A., Dalal, T.R.: Concrete containing plastic aggregates. Concr. Int. **19**, 47–52 (1997)
8. Vasudevan, R., Nigam, S.K., Velkennedy, R., Ramalinga, A., Sekar, C., Sundarakannan, B.: Utilization of waste polymers for flexible pavement and easy disposal of waste polymers. In: International Conference on Sustainable Solid Waste Management, Chennai, India, pp. 105–111

9. Saikia, N., de Brito, J.: Use of plastic waste as aggregate in cement mortar and concrete preparation: a review. Constr. Build. Mater. (34), 385–401 (2012)
10. Kandasamy, R., Murugesan, R.: Fibre reinforced concrete using domestic waste plastics as fibres. ARPN J. Eng. Appl. Sci. **6**(3), 75–82 (2011). ISSN 1819-6608
11. IS 4031-1 (1996) Methods of physical tests for hydraulic cement, Part 1: Determination of fineness by dry sieving (Second Revision), CED 2 (Cement and Concrete). Bureau of Indian Standard, New Delhi (1996)
12. IS 4031-4 (1988) Methods of physical tests for hydraulic cement, Part 4: Determination of consistency of standard cement paste, CED 2 (Cement and Concrete). Bureau of Indian Standard, New Delhi (1988)
13. IS 4031-11 (1988) Methods of physical tests for hydraulic cement, Part 11: Determination of density, CED 2 (Cement and Concrete). Bureau of Indian Standard, New Delhi (1988)
14. IS 383 (1970) Specification for coarse and fine aggregates from natural sources for concrete (Second Revision), CED 2 (Cement and Concrete). Bureau of Indian Standard, New Delhi (1970)
15. IS 2386-3 (1963) Methods of test for aggregates for concrete, Part 3: Specific gravity, density, voids, absorption and bulking, CED 2 (Cement and Concrete). Bureau of Indian Standard, New Delhi (1963)
16. IS 2386-4 (1963) Methods of test for aggregates for concrete, Part 4: Mechanical properties, CED 2 (Cement and Concrete). Bureau of Indian Standard, New Delhi (1963)
17. IS 516 (1959) Method of tests for strength of concrete (Second Revision), CED 2 (Cement and Concrete). Bureau of Indian Standard, New Delhi (1959)
18. IS 2185-1 (2005) Concrete masonry units, Part 1: Hollow and solid concrete blocks (Third Revision), [CED 53: Cement Matrix Products]. Bureau of Indian Standard, New Delhi (2005)

Compressive Strength and Water Absorption Characteristics of Fly Ash and Wood Ash Replaced Cement Mortar Bricks

L. Divakar, R. K. Chethan Gowda, Abhishek Pulgur and H. C. Maruthi

1 Introduction

Brick is the construction of the structure of each unit, which is usually joined by the means of mortar. Concrete is a common classification in India used for growth, low cost, and skilled labor. The disadvantages of cement waste are the use of cement, which is an important contributing factor to the greenhouse effect that causes global warming, and it is essential to consider this with strict regulations and limitations [1]. At the same time, energy demand in the industry and in energy has brought a great deal of coal ash, which in the future can increase globally to an unprecedented level, as Covey points out. Cement can be replaced by ash and wood ash and can be used as a rock block for strength and durability [2, 3].

According to Aakash [4], the construction of building materials, especially brick-using ashes, is considered a solution to the widespread problem of domestic fly ash. Fly ash bricks are comparatively lighter in weight and stronger than common conventional cement bricks. Digging bricks, lighter and lighter than conventional cement bricks. Fly ash is a product in a heat-generating plant, which is grappling with environmental pollution. Its use as an important material in brick production will not only create more job opportunities it can also be a solution for disposal problems. Due to the excellent quality and ecological features, the flying ash bricks were recovered [5–7].

Wood ash is a product during the burning of wood products during energy production in factories producing paper, garment, and wood products. Wood ashes

L. Divakar · R. K. Chethan Gowda (✉) · A. Pulgur · H. C. Maruthi
Department of Civil Engineering, Ramaiah University of Applied Sciences, Bengaluru, Karnataka 560056, India
e-mail: chethanrk06@gmail.com

L. Divakar
e-mail: dldivak@gmail.com

are composed of organic compounds and elements. Types of wood and methods of combustion affect chemical and physical properties. Due to its strong force, there was virtually no damage during transport, and the uniformity of the metals needed for joints and plastics was reduced by nearly 50%.

2 Experimental Procedure

2.1 Materials Used

Cement Ordinary Portland cement (OPC) 53 grade is used for the entire experimental investigation. The physical properties of the cement were tested according to IS: 12269—2013 [8]. The pertinent parameters are provided in Table 1.

Fly Ash Fly ash conforming to Class F was procured locally which is used as a replacement for OPC. Specific gravity test and fineness test were performed according to IS 1727 [9] and IS 8425 [10], respectively, and the test results are given in Table 1.

Wood Ash Wood ash is the residues that are left after burning of wood in fireplaces like homes, industries, and power plants are collected. The specific gravity and fineness were determined conforming to IS 1727 and IS 8425, respectively. The results are given in Table 1.

Fine Aggregates Locally available manufacturing sand (M-sand) was used as fine aggregates. Specific gravity and sieve analysis tests were carried out according to IS 2386 (part III) [11] and IS 383 [12], respectively. The results are given in Tables 1 and 2, respectively, and particle size distribution is plotted in Fig. 1.

2.2 Methods

The proportions of binder to manufacture sand for the mortar bricks were fixed at 1:3. The binder was prepared by proportioning various ratios of cement and fly ash, cement and wood ash. The specimens were prepared according to ASTM

Table 1 Physical properties of binder and aggregate

Materials used	Cement	Fly ash	Wood ash	Fine aggregate	Relevant code
Specific gravity	3.12	2.2	2.16	2.56	IS 1727 and IS 2386 part III
Fineness (%)	9	6	7	–	IS 8425 and IS 1727
Fineness modulus	–	–	–	3.77	IS 383

Table 2 Sieve analysis of M-sand

Sieve size	% Passing	Requirements for zone 3 as per is 383
4.75 mm	99.46	90–100
2.36 mm	98.89	85–100
1.18 mm	97.90	75–100
600 μm	70.53	60–79
300 μm	10.14	12–40
150 μm	0	0–10
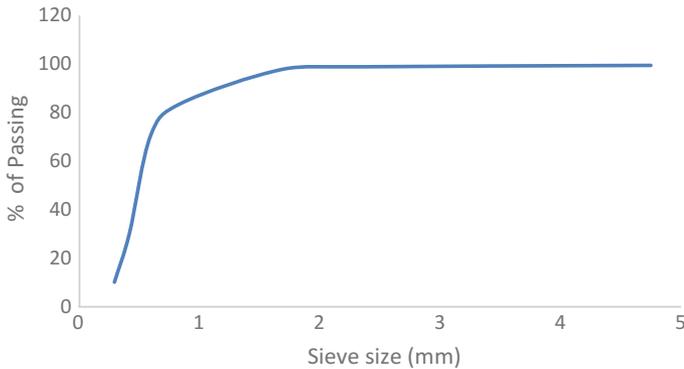
Fig. 1 Sieve analysis of M-sand

C67-2017. The mixing was done with the help of the pan mixer. The weighed quantity of cement, Class F fly ash, wood ash, and M-sand are thoroughly mixed in dry state in a pan mixer with the help of trowel, and then, water is added as per the mix requirement. Eleven mixes with different percentage of fly ash and wood ash, i.e., 0, 10, 20, 30, 40, and 50% replaced with cement, were prepared. The mix proportions of the fly ash and wood ash bricks are presented in Tables 3 and 4, respectively.

Table 3 Mix proportions of fly ash bricks

Mixture	FA0	FA10	FA20	FA30	FA40	FA50
Fine aggregate (kg/m^3)	1575	1575	1575	1575	1575	1575
Cement (kg/m^3)	525	472.5	420	367.5	315	262.5
Fly ash (kg/m^3)	0	52.5	105	157.5	210	262.5

Table 4 Mix proportions of wood ash bricks

Mixture	WA0	WA10	WA20	WA30	WA40	WA50
Fine aggregate (kg/m^3)	1575	1575	1575	1575	1575	1575
Cement (kg/m^3)	525	472.5	420	367.5	315	262.5
Wood ash (kg/m^3)	0	52.5	105	157.5	210	262.5

3 Results and Discussion

The following section discusses the compressive strength and water absorption properties of bricks with various proportions of binders.

3.1 Compressive Strength

The compressive strength of the bricks was determined in a compression testing machine as per IS 2815 Part 1. For the test, six samples of each composition were tested; the results are given in Tables 5 and 6. The variations of results are plotted in Fig. 2.

From the Fig. 2, it can be observed that the compressive strengths of fly ash replaced cement mortar bricks increase with an increase in fly ash content, whereas in wood ash replaced bricks, the compressive strength decreases as the percentage of wood ash increases, but with reference to the control cement bricks, all fly ash replaced bricks achieved reasonable compressive strength.

3.2 Water Absorption

The bricks were tested in accordance with the procedure laid down in IS 3495 Part 2 [13], after immersion in cold water for 24 h. Results are given in Tables 5 and 6 for fly ash and wood ash bricks, and the variations of results are shown in Fig. 3.

Table 5 Water absorption and compressive strength of fly ash bricks

Mix type	FA0	FA10	FA20	FA30	FA40	FA50
Compressive strength (MPa)	10.10	10.18	17.55	18.25	20.69	21.55
Water absorption (%)	6.53	4.88	5.03	6.86	9.03	11.69

Table 6 Water absorption and compressive strength of fly ash bricks

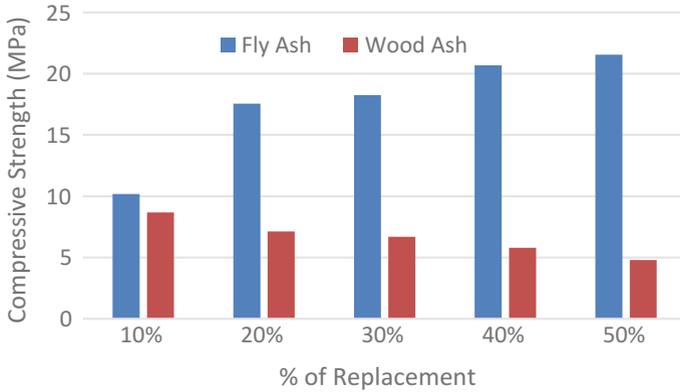| Mix type	WA0	WA10	WA20	WA30	WA40	WA50
Compressive strength (MPa)	10.10	8.68	7.13	6.69	5.79	4.79
Water absorption (%)	6.53	5.89	6.85	7.85	10.69	13.03

Fig. 2 Compressive strength of bricks

Fig. 3 Water absorption of bricks

From the figure, it can be observed that the percentage of water absorption in both fly ash and wood ash replaced cement mortar bricks increases with an increase in percentage of fly ash and wood ash content. It is also absorbed that fly ash replaced bricks have less water absorption compared to the wood ash replaced bricks.

4 Conclusions

The following conclusion can be drawn from the present investigation.

- Compressive strength of fly ash replaced cement mortar bricks goes on increasing as the percentage fly ash content varies from 10 to 50%.
- Compressive strength of wood ash replaced cement mortar bricks goes on decreasing as the percentage fly ash content varies from 10 to 50%.
- Compared to the wood ash replaced cement mortars bricks, fly ash replaced bricks showed better strength.
- Percentage of water absorption in both fly ash and wood ash replaced cement mortar bricks increases as the percentage of fly ash and wood as content varies from 10 to 50%.
- It is also absorbed that fly ash replaced cement brick has less water absorption compared to the wood ash replaced bricks.

References

1. Malhotra, V.M.: High-performance high-volume fly ash concrete. ACI **24**(7), 1–5 (2002)
2. Patil, B.B., Kumbhar, P.D.: Strength and durability properties of high performance concrete incorporating high reactivity metakaolin. Int. J. Modern Eng. Res. **2**, 1099–1104 (2012)
3. Pacheco, T., Shasavandi, A.: Using metakaolin to improve the compressive strength and the durability of fly ash based concrete. Int. Seminar 25 (2011)
4. Aakash, D.P., Devendra, B.G.: Engineering properties of clay bricks with use of fly ash. Int. J. Res. Eng. Technol. **03**(09), 75–80 (2014)
5. Apurva, K., Samruddha, R., Bagasse, M.R.: Ash as an effective replacement in fly ash bricks. Int. J. Eng. Trends Technol. **4**(10) (2013)
6. Ashish, K.P., Rinku, P.: Comparative study of compressive strength of bricks made with various materials to clay bricks. Int. J. Sci. Res. Publ. **2**(7) (2012)
7. Rajendra Prasad, H.N., Vivek Prasad, H.G.: An approach for alternative solution in brick manufacturing. Int. J. Sci. Environ. Technol. **3**(3), 1105–1114 (2014)
8. IS 12269: Ordinary Portland Cement 53 Grade Specification (2013)
9. IS 1727: Methods of Test for Pozzolanic Materials (1967)
10. IS 8425: Code of Practice for Determination of Specific Surface Area of Powers by Air Permeability Methods (1977)
11. IS 2386: Part III, Methods of Test for Aggregates for Concrete (1963)
12. IS 383: Specification for Coarse and Fine Aggregates from Natural Sources for Concrete (1970)
13. IS 3495: Part-1 and Part-2 method of testing of burnt clay bricks (1992)

Influence of Steel Fibres on Mechanical Properties of Geopolymer Concrete

Abhishek Pulgur, L. Divakar, R. K. Chethan Gowda and B. Nagesh

1 Introduction

Concrete is the most used material next to water in the world, and the primary binder for the concrete is ordinary Portland cement (OPC). Its production has lots of environmental impact due to emission of carbon dioxide during its production and the amount of fossil fuel energy required in its production which is next to steel and aluminum [1]. Cement concrete (CC) has good compressive strength, but due to micro-cracks, it has very low flexural strength approximately square root of its compressive strength on 28 days [2, 3]. According to Yazici et al. [4] flexural strength of the concrete with fibers enhanced up to 3–81% more than normal cement concrete. The choice of fibers influence properties of concrete in fresh and hardened state such as workability, compressive strength, flexural strength, modulus of elasticity, stress–strain relation. Hao and Hao [5].

The geopolymer binder emerged as the potential binder for the cement paste, with this the geopolymer concrete. The existing literature indicates that the geopolymer concrete has poor workability, and addition of fibers further reduces the workability of the mix [6]. The study deals with the development of mix with optimum fiber content having excellent workability and strength at ambient curing conditions. The paper presents an experimental study on influence of fiber content on the properties of concrete such as workability, compressive strength, flexural strength, and impact resistance of concrete to drop weight test.

A. Pulgur (✉) · L. Divakar · R. K. Chethan Gowda · B. Nagesh
Department of Civil Engineering, Ramaiah University of Applied Sciences,
Bengaluru 560056, Karnataka, India
e-mail: abhishek.pulgur@gmail.com

2 Experimental Procedure

2.1 Materials Used

In this study, ground-granulated blast-furnace slag (GGBS) and class F fly ash are used as binder. These were procured from M/S ACC plant, Bengaluru. The chemical composition determined by X-ray fluorescence and physical properties of fly ash and GGBS presented in Tables 1 and 2, respectively. Manufactured sand (M-Sand) and 20-mm-down angular granite stones which are surface saturate dry (SSD) are used as fine and coarse aggregates from the locally available source. The physical properties of the coarse and fine aggregate are given in Table 3. Steel fibers were used to prepare fiber reinforced geopolymer concrete which was end hooked type and having aspect ratio of 75. Sodium hydroxide flakes of 97% purity and sodium silicate solution are used to prepare 14M sodium silicate solution which is used as alkaline activator. The molar ratio of SiO_2 to Na_2O was 1.66 (SiO_2 = 37.37%, Na_2O = 23.21% and H_2O = 39.42%) in the sodium silicate solution used in the current study, and the ratio of sodium silicate solution to sodium hydroxide solution is maintained at 2.5.

Table 1 Chemical composition of fly ash and GGBS

Sample (%)	SiO_2	Al_2O_3	Fe_2O_3	CaO	Na_2O	K_2O	SO_3
Fly ash (type F)	56.21	28.50	8.56	1.50	0.28	1.14	0.25
GGBS	30.35	15.75	1.85	36.52	0.36	0.45	0.14

Table 2 Physical properties of binder materials

Materials	Fly ash	GGBS	Relevant standard
Specific gravity	2.3	2.62	IS4031-part 11-2005
Specific surface area (m^3/kg)	325	350	IS 4031-part 2-1999
Loss on ignition (%)	0.75	2.1	IS 1727-1967
Soundness (expansion) (mm)	1	1	IS 1727-1967 and IS 4031-1968

Table 3 Physical properties of aggregates

Materials	Coarse aggregate	Fine aggregate	Relevant standard
Specific gravity	2.6	2.43	IS2386-part 3-1963
Bulk density (kg/m^3)	1685.2	1623.91	IS2386-part 3-1963
Water absorption (%)	0.3	1.3	IS2386-part 3-1963
Fineness modulus	7.17	3.65	IS2386-part 1-1963

Table 4 Mix proportions of GPC

Mixture	SF0	SF1	SF1.5	SF2	SF2.5	SF3
Coarse aggregate (kg/m^3)	1200	1200	1200	1200	1200	1200
Fine aggregate (kg/m^3)	600	600	600	600	600	600
Fly ash (kg/m^3)	240	240	240	240	240	240
GGBS (kg/m^3)	160	160	160	160	160	160
Activator solution (kg/m^3)	200	200	200	200	200	200
Fiber content[a]	0	1	1.5	2	2.5	3

[a]Fiber content in percentage of weight of total binder considered

2.2 Methods

The mix proportion of the geopolymer concrete was done according to Patankar et al. [7], and the various concrete mix proportions considered for the current study are given in Table 4. In the current study, the parameter studied was change in percentage of steel fibers for the same proportion of fine aggregate, coarse aggregate, binder, and activator solution.

Geopolymer concrete (GPC) specimens for compressive strength, specimens for flexural strength, and split tensile strength were prepared in accordance with IS516-1959 [8] and ASTM C192/C192M-16a [9], respectively. The workability of the fresh GPC was determined as per IS1199-1959 [10] and ASTM C143/C143M-15a [11]. The specimens were cast, covered with plastic sheet, and kept in ambient temperature for 24 h and demolded. The specimens were tested for compressive strength on 7 and 28 days according to IS516-1959 and ASTM C39/C39M-17b [12], flexural strength in accordance with both IS516-1959 and ASTM C78/C78M-16 [13], and split tensile strength on 28 days conforming to IS516-1959 and ASTM C496/C496M-17 [14]. The toughness of the specimen under drop weight test was determined using $60 \times 60 \times 6$ cm unreinforced slabs on 28th day. The hammer of weight 7.7 kg was dropped freely from a height of 700 mm. The number of blows required for the appearance of the first crack and ultimate failure is noted.

3 Results and Discussion

In this section, the effects of variation of steel fibers on the workability, compressive strength, flexural strength, tensile strength, and toughness of the steel fiber reinforced geopolymer concrete are discussed.

3.1   Effect of Steel Fibers on Workability

Workability of concrete is ease of working with concrete in different stages such as handling, placing, compacting, and finishing. Workability of the concrete can be found using slump test, compaction factor, Vee-Bee test, flow test, etc., depending on the stiffness of the mix. In the current study, the workability of the concrete mix was found using slump test and Vee-Bee test.

The slump values for the geopolymer concrete mixes are given which are plotted in Fig. 1. It can be noted that with the increase in percentage of steel fibers, the slump value of the concrete mix kept on decreasing which indicates higher the fiber content harsher is the mix. The results obtained in the current study matches with earlier research as presented by Nematollahi et al. [15].

3.2   Effect of Steel Fibers on Compressive Strength

The most essential property of the concrete is its compressive strength as it is used for grading of concrete, design parameter for various structural component, etc. The compressive strength of the GPC mixes was determined on $100 \times 100 \times 100$ mm cube specimens and 150×300 mm cylinder specimens. The results of the compressive strength of GPC mixes are presented in Table 5 and plotted in Fig. 2. The compressive strength presented in Table 5 is mean value of results obtained on three identical specimens. It is observed that as the percentage of increases the compressive strength increased until certain percentage and there is a slight decrease in the compressive strength of the GPC mixes. The results obtained are following the same trend as indicated by Nematollahi et al. [15] and Qian and
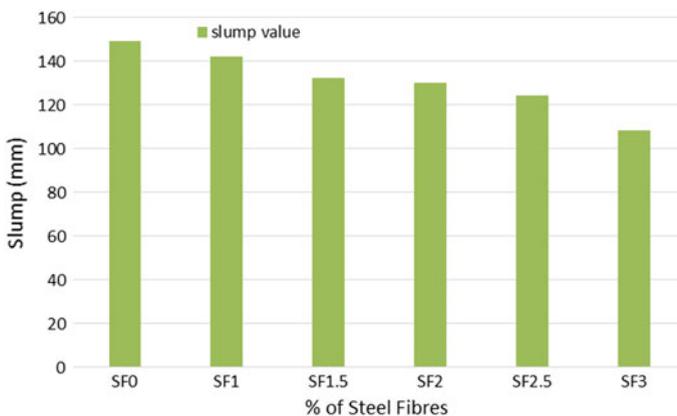
Fig. 1 Effect of fiber percentage on workability

Table 5 Strength properties of GPC

Mixture	Compressive strength (MPa)		Flexural strength (MPa)	Split tensile strength (MPa)		No. of hammer blows	
	07 days	28 days	28 days	07 days	28 days	Initial crack	Ultimate failure
SF0	30.84	38.45	5.473	2.36	2.7	4	13
SF1	33.25	40.53	6.248	2.69	2.94	–	–
SF1.5	35.74	43.57	6.647	2.93	3.15	–	–
SF2	38.54	47.24	7.214	3.03	3.47	6	23
SF2.5	36.63	45.91	7.625	2.84	3.1	5	19
SF3	34.54	46.67	8.072	2.49	2.8	–	–
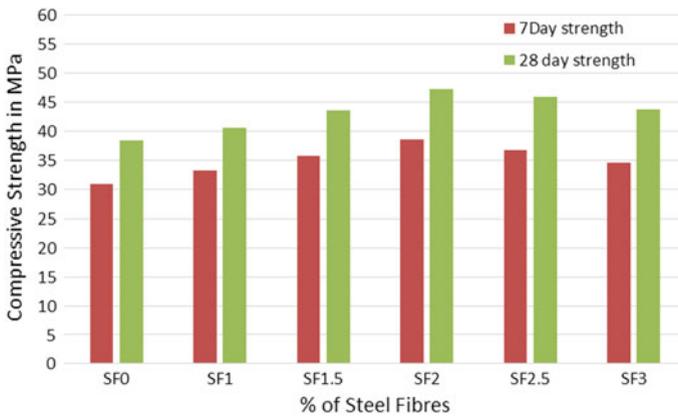
Fig. 2 Effect of fiber percentage on compressive strength

Stroeven [16]. The decrease in compressive strength after certain percentage of fibers may be due to poor bond characteristics between fibers and geopolymer paste matrix, improper distribution, or balling effect at few places in the mix.

3.3 Effect of Steel Fibers on Flexural and Split Tensile Strength

The split tensile strength was found out for standard cylinder specimens, and flexural strength was found for prisms of 100 × 100 × 500 mm on 7 and 28 days. The results of the specimens are presented in Table 5 and plotted in Fig. 3. It was found that as the percentage of steel fiber increased, the split tensile strength and
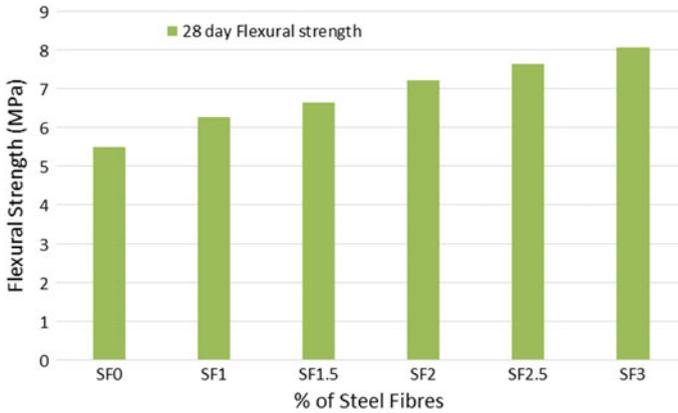
Fig. 3 Effect of fiber percentage on flexural strength
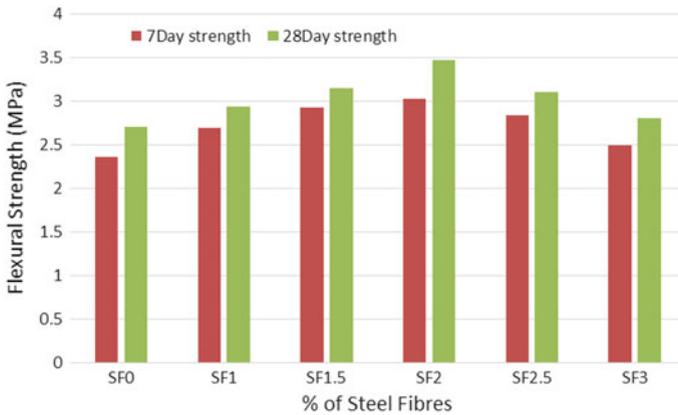
Fig. 4 Effect of fiber percentage on split tensile strength

flexural strength of the GPC mix increased. The results of split tensile strength are presented in Table 5 and plotted in Fig. 4. The increase in split tensile strength was found until 2% after which the strength decreased, which might be attributed to the compressive nature of load that is being applied on the specimen, as the same trend was observed for the specimens subjected to compressive loads. The flexural strength of the specimen increased as the percentage of the fibers increased in the mix, the increase in the flexural strength can be attributed to crack arresting properties of the fibers in the mix.

3.4 Effect of Steel Fiber on Impact Energy

Based on the compressive strength, flexural strength, and split tensile strength results, we can observe that 2 and 2.5% performed better in all aspects so these mixes were considered for drop weight test. The parameters considered for the study were number of blows required for the appearance of the first crack and number of blows for the ultimate failure. It was observed that as the fiber content increased, the number of blows required for both initial crack appearance and ultimate failure decreased for the two mixes considered. The results of the study are presented in Table 5. The SF2.5 had less impact strength as compared to the SF2 which may be due to the balling effect or improper orientation or improper distribution of the fibers. The change in impact energy follows the same trend as that of compressive and flexural strength results.

4 Conclusions

In the current study, the effects of percentage of steel fibers on workability, compressive strength, and flexural strength are studied experimentally. The following conclusions are drawn:

- The compressive strength of the specimens is 7.5–25% more than GPC specimens without fibers in the mix for 7 days and 5.5–23% more on 28th day. The mix with 2% of fiber had 25 and 23% higher strength as compared to mix without fibers.
- The addition of steel fibers increased the split tensile, and flexural strength of the GPC mixes by 14–48% and 4–28.5%, respectively, after 28 days of curing.
- The impact test of the specimens was done by drop weight test on unreinforced GPC slabs; further, research should be conducted on reinforced GPC slabs and parameters such as crack width, crack propagation, energy absorbed, and other factors. Also, a relation between number of blows and the impact energy absorbed by the specimen should be established.

References

1. Malhotra, V.M.: High-performance high-volume fly ash concrete. ACI **24**(7), 1–5 (2002)
2. Francis, A.O., Edwin, G.B., Deatherage, J.H.: Splitting tensile strength and compressive strength relationship at early ages. ACI Mater. J. **88**(2), 115–121 (1991)
3. Choi, Y., Yuan, R.L.: Experimental relationship between splitting tensile strength and compressive strength of GFRC and PFRC. Cem. Concr. Res. **35**(8), 1587–1591 (2005)
4. Yazici, S., Inan, G., Tabak, V.: Effect of aspect ratio and volume fraction of steel fiber on the mechanical properties of SFRC. Constr. Build. Mater. **21**, 1250–1253 (2007)

5. Hao, Y., Hao, H.: Dynamic compressive behavior of spiral steel fiber reinforced concrete in split Hopkinson pressure bar tests. Constr. Build. Mater. **48**, 521–532 (2013)
6. Lee, N.K., Lee, H.K.: Setting and mechanical properties of alkali-activated fly ash/slag concrete manufactured at room temperature. Constr. Build. Mater. **47**, 1201–1209 (2013)
7. Patankar, S.V., Ghugal, Y.M., Jamkar, S.S.: Mix design of fly ash based geopolymer concrete. In: Advances in Structural Engineering. Elsevier, India (2015)
8. IS 516: Methods of tests for strength of concrete. Bureau of Indian Standards, New Delhi, India (1959)
9. ASTM C192/C192M-16a: Standard practice for making and curing concrete test specimens in the laboratory. ASTM International, West Conshohocken, PA (2016)
10. IS 1199: Methods of sampling and analysis of concrete. Bureau of Indian Standards, New Delhi, India (1959)
11. ASTM C143/C143M-15a: Standard test method for slump of hydraulic-cement concrete. ASTM International, West Conshohocken, PA (2015)
12. ASTM C39/C39M-17b: Standard test method for compressive strength of cylindrical concrete specimens. ASTM International, West Conshohocken, PA (2017)
13. ASTM C78/C78M-16: Standard test method for flexural strength of concrete (using simple beam with third-point loading). ASTM International, West Conshohocken, PA (2016)
14. ASTM C496/C496M-17: Standard test method for splitting tensile strength of cylindrical concrete specimens. ASTM International, West Conshohocken, PA (2017)
15. Nematollahi, B., Sanjayan, J., Chai, J.X.H., Lu, T.M.: Properties of fresh and hardened glass fiber reinforced fly ash based geopolymer concrete. Key Eng. Mater. **594–595**, 629–633 (2014)
16. Qian, C.X., Stroeven P.: Development of hybrid polypropylene and steel fiber reinforced concrete. Cem. Concr. Res. **30**, 63–69 (2000)

Solid-State Reduction Studies on Manganese Ores

Jibin Noble and Krishna Kant Prasad

1 Introduction

Manganese is better known for its stronghold in the steel production, consuming more than 90% of the manganese produced today. It improves the physical and mechanical properties of steel. Some of its important functions are: It improves strength, hardenability, machinability, and wear resistance, and it reduces hot shortness by forming harmless manganese or iron–manganese precipitates. It also acts as strong deoxidizer and desulphurizer and mild carbide former. The range of addition of manganese in steels varies from 0.25 to 14% depending upon the requirements. In case of steels for structurals, improving wear-resistance and for some tools, manganese addition will be about 0.25–1.5% and for hadfield steels it will be about 12–14%. The addition of manganese during the production of steels is in the form of ferromanganese [1, 2].

Ferromanganese is defined as an alloy of iron with a sufficient amount of manganese as a means of introducing it into iron and steel. Two viable routes of production of ferromanganese are blast furnace and submerged arc electric furnace production.

The reduction of manganese ore takes place in stages:

$$MnO_2 \rightarrow Mn_2O_3 \rightarrow Mn_3O_4 \rightarrow MnO \rightarrow Mn\ Carbides/Metallic\ Mn$$

J. Noble (✉)
Mechanical Engineering, Rajagiri School of Engineering and Technology,
Kakkanad, Kochi, Kerala, India
e-mail: jibinnoble@yahoo.co.in

K. K. Prasad
Department of Metallurgical & Materials Engineering, National Institute of Technology
Karnataka, Surathkal, PO Srinivasnagar, Mangalore 575025, India

The reactions for the above transformations are given below. It can take place according to any combinations of the reaction [3].

$$4MnO_2 = 2Mn_2O_3 + O_2 \tag{1}$$

$$3Mn_2O_3 + C = 2Mn_3O_4 + CO \tag{2}$$

$$3Mn_2O_3 + CO = 2Mn_3O_4 + CO_2 \tag{3}$$

$$3Mn_2O_3 + Fe_3C = 2Mn_3O_4 + 3Fe + CO \tag{4}$$

and

$$Mn_3O_4 + C = 3MnO + CO \tag{5}$$

$$Mn_3O_4 + CO = 3MnO + CO_2 \tag{6}$$

$$Mn_3O_4 + Fe_3C = 3MnO + 3Fe + CO \tag{7}$$
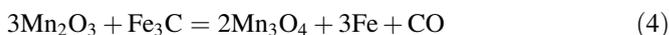
Reduction of MnO to metallic Mn

$$MnO + CO = Mn + CO_2 \tag{8}$$

$$MnO + C = Mn + CO \tag{9}$$

$$MnO + Fe_3C = Mn + 3Fe + CO \tag{10}$$

Reduction of MnO to Mn carbides

$$MnO + 4/3C = 1/3Mn_3C + CO \tag{11}$$

$$MnO + 4/3Fe_3C = 1/3Mn_3C + 4Fe + CO \tag{12}$$

$$MnO + 10/7C = 1/7Mn_7C_3 + CO \tag{13}$$

$$MnO + 10/7Fe_3C = 1/7Mn_7C_3 + 30/7Fe + CO \tag{14}$$
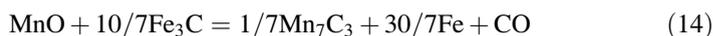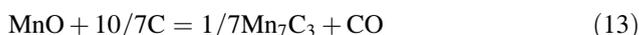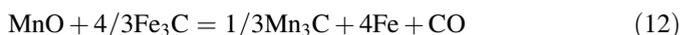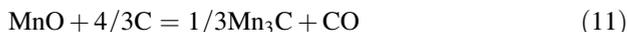
The reaction (1) usually occurs between 400 and 700 °C. Reduction of Mn_2O_3 and Mn_3O_4 by carbon or Fe_3C is more thermodynamically favorable compared to carbon monoxide at temperatures above 700 °C. Even though the expected carbides are Mn_3C and Mn_7C_3 according to Kuo and Persson [4, 5], the most likely to form are (Fe, Mn)$_3$C and (Fe, Mn)$_7$C$_3$ at temperatures ranging from 1000 to 1300 °C [3]. The reduction up to MnO requires only a slight reducing atmosphere, but reduction of it to metal solid carbon is required as the reactions are highly endothermic. According to the studies done, it was found that manganese is easier to reduce to carbides than to the metallic form as the heat of formation for the latter is high [1, 6, 7].

According to the studies of R. H. Eric et al., reduction of manganese ores was possible at lower temperatures using mixture of methane and hydrogen [8].

Cem Akil and Ahmet Geveci conducted a study to find out the optimum condition to produce manganese carbide. They conducted the experiments by varying

the temperature, duration of heating, stoichiometric carbon percentage, and CaO percentage in argon atmosphere [6]. They found that the maximum reduction obtained at 1250 °C, 4 h, 100% of stoichiometric carbon percentage, and 5% CaO addition. The manganese carbide formed at the above optimum condition is Mn_7C_3.

According to the studies of W. D. Grimsley, the products of reactions at 1000 and 1100 °C were $CaMn_2O_4$ and MnO. He found that maximum reduction occurred at 1300 °C when there was excess carbon and the product formed was (Fe, $Mn)_7C_3$ [7].

The objective of this study was to find out the optimum conditions to produce a charge material with high content of iron and manganese carbides for the ferro-manganese production so as to reduce the electrical power consumption during its production. Two possible routes have been envisaged under industrial situation: tunnel kiln and rotary kiln method. Laboratory experiments are planned to simulate the above process routes.

2 Experimental Procedure

2.1 Materials Used in Experiments

The main materials used in the experiments were manganese ore, pet coke, LECO, MgO, and bainite [9, 10]. These were obtained from different sources and prepared carefully for the experiments as explained below.

2.2 Manganese Ore

Manganese ore was obtained from Thermit Alloys (P) Limited, Shimoga, Karnataka, in the form of −30 mesh size. From the screen analysis, it is found that −80 + 150 size range is more in quantity, so ores within that range are sieved out from the lot and used for the preparation of briquettes. In case of pellets −100 mesh size ores is required, so ores in that range are also sieved out from the lot.

2.3 Chemical Analysis of Manganese Ore

Data given by Thermit Alloys (P) Limited, Shimoga, Karnataka.

$$Mn—47.30\%, \quad Fe—12.67\%, \quad SiO_2—1.61\%$$

Result of the chemical analysis done at Analytical Research & Metallurgical Laboratories Pvt. Ltd., Bangalore. The method used for analysis is inductively coupled plasma optical emission spectrometer.

$$Mn\text{——}42.02\%, \quad Fe\text{——}17.94\%, \quad SiO_2\text{——}6.53\%, \quad Al_2O_3\text{——}4.10\%$$

2.4 Mineralogy of the Ore

The ore was found to be pyrolusite.

X-ray diffraction analysis of the manganese ore was conducted at the Department of Metallurgical and Materials Engineering. Results are shown in Fig. 1.

2.5 Pet Coke

Pet coke was obtained in the form of +10 mm mesh. The fixed carbon percentage in this is 98%. The big pieces were put into a double-roll crusher to reduce the size. The output of the double-roll crusher was put into the ball mill for further grinding in to very fine powder. This very fine powder is used in the experiments as reducing agent.
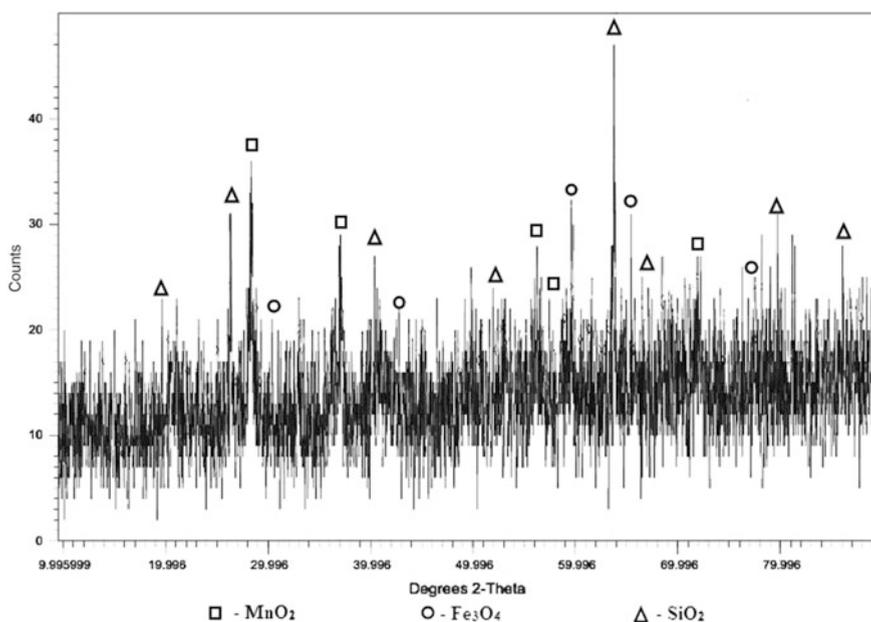
Fig. 1 XRD analysis of manganese ore

2.6 LECO

LECO was obtained in the form of +10 m mesh. The fixed carbon percentage in this is 72% and ash 14%. The big pieces were put into a double-roll crusher to reduce the size. The output of the double-roll crusher was put into the ball mill for further grinding in to very fine powder. This very fine powder is used in the experiments as reducing agent.

2.7 Magnesium Oxide Light

As per previous workers, it was necessary to add magnesium or calcium oxide in the range of 5–15% to all the agglomerates in order to prevent their collapse during reduction as substantial liquid-phase forms. It was decided to use in the present work 10% (of the weight of ore + reductant mixture) of MgO in all samples.

2.8 Experimental Setup

Experiments were performed in a tube furnace, which was designed to work at temperatures up to 1400 °C with the working tube made of 99.80% recrystallised alumina. The furnace was heated with four silicon carbide heating elements.

Paraffin oil-filled glass gas bubbler was placed in the path of nitrogen gas flow, at the exit of furnace tube. This glass bubbler is used to ensure that the gas was flowing and to establish that the furnace was gas tight.

Calibration of furnace temperatures was done at controller set temperatures of 1000, 1100, 1200, 1300, and 1350 °C by using a Pt/Pt 13% Rh thermocouple inserted into the furnace tube and taking measurements at different points in the hot zone of the furnace. According to these calibration tests, the central part (10 cm distance) of the furnace was found to be constant within ±10 °C and the crucibles were placed in this interval in all of the experiments.

2.9 Experimental Procedure

2.9.1 Briquettes

Manganese ore in the size range −80 + 150 is used for the preparation of briquettes. Briquettes are made with the help of a die-punch of internal diameter 10 mm. Load

of about 1 tonne is applied on the die-punch with the help of a 40-tonne universal testing machine to get the samples compacted. Total weight of ore and carbon (pet coke/LECO) was arranged to 2.5 g. MgO was added as flux and binder in amount of 10% of the weight of ore + reductant mixture.

2.9.2 Pellets

Manganese ore in the size range −100 is used for the preparation of Pellets. With the help of Disc Pelletiser, the green pellets are made. The pellets are then dried in an electric oven by keeping them at 150 °C for about 1 h. MgO was added as flux in amount of 10% of the weight of ore + reductant mixture. Bentonite is also added as binder in amount of 2% of the weight of ore + reductant mixture.

By changing manganese ore and active carbon (pet coke/LECO) amounts, briquettes and pellets of different compositions were made. These samples were reduced in different temperatures in order to determine the optimum conditions. Experiments were done using the combinations of the parameters given in Table 1.

Experiments were conducted by placing the samples into the predetermined hot zone inside the tube furnace. To keep the samples inside the furnace, a boat-shaped ceramic piece is used. After keeping in boat, the samples are well covered with charcoal. Nitrogen gas is passed in order to create an inert atmosphere inside the tube. The briquettes are kept in the set temperature for 45 min, whereas pellets are kept for about 1 h 15 min so that the temperature reaches till its core. Different temperatures, manganese ore, and active carbon (pet coke/LECO) percentages were tested in order to find the optimum conditions for carbothermic reduction of manganese ore.

At the end of a run, the furnace was turned off and crucibles were allowed to cool to room temperature in the furnace. Nitrogen gas is passed till the samples were cooled to room temperature. The samples were then weighed, and weight loss is determined. Using the weight loss data, % reduction values were calculated. The stability of the reduced sampled is determined with the help of Hounsfield Tensometer. Then, samples were taken for X-ray Diffraction, SEM-EDS, and chemical analysis. The optimum conditions were decided considering chemical weight loss, SEM-EDS, and X-ray diffraction analyses.

Table 1 Experimental variables

Variable	Test range
Temperature (°C)	1100–1150–1200–1250
Manganese ore: pet coke/LECO	70:30–80:20–90:10–100:0

3 Results and Discussion

3.1 Experimental Results

The experimental result of the eight experiments performed is given in Table 2.

From the EDAX and XRD analysis, it could be inferred that at lower temperatures various lower oxides of iron and manganese were formed. In case of manganese oxides, it was found that at 1150 °C most of the MnO_2 got transformed to Mn_2O_3 and this got transformed to Mn_3O_4 when temperature increased to 1200 °C and finally to MnO when the temperature increased to 1250 °C. Significant quantities of manganese carbides started to form only at temperatures 1250 °C even though some formations were seen at lower temperatures. But it was seen in the XRD analysis that up to a temperature of 1150 °C SiC was most likely to form; thereafter, different forms of iron carbides were formed.

On conducting the experiment at 1250 °C, the samples that survived the test were (a) briquettes with 20% pet coke, (b and c) pellets with 10% pet coke and LECO, and (d and e) pellets with 20% pet coke and LECO. From the XRD analysis, it was found that, in case of pet coke, 20% addition was found to be more effective in formation of carbides. When the proportion was increased to 30%, the samples completely collapsed during reduction, especially at higher temperatures.

With LECO, carbides formed at both 20 and 30%. At 30%, manganese carbides and metallic manganese formed more compared to 20%, but the samples were very weak. By considering all the results such as weight loss data, XRD analysis and EDAX, addition of 20% LECO was found to be most effective.

The reduced pellets were more stable compared to briquettes. After reduction, pellets retained their shape, whereas with briquettes cracks formed over the surface. Probably, the higher porosity of pellets is helping in the easy exit of gases formed during reduction. Also reduced pellets showed more strength compared to reduced briquettes.

The XRD results of pellets with 20% LECO at temperatures 1150, 1200, and 1250 °C are shown in Figs. 2, 3, and 4.

In some samples at a temperature of 1200 °C, iron manganese carbides formed in a rib-like structure, whereas at 1250 °C there was evidence of melting of these ribs. See Figs. 6, 7, 8, and 9. Even though the rib formation is not well understood, this gave evidence for the formation of carbides in the samples (Fig. 5).

4 Conclusions

In the present work, an attempt was made toward the optimization of conditions for producing iron and manganese carbides from manganese ore. The following conclusions were drawn:

Table 2 Percentage weight loss

| | Mn ore: pet coke/LECO (%) | Weight loss (%) | | | | | | | |
| | | 1100 °C | | 1150 °C | | 1200 °C | | 1250 °C | |
		Samples with pet coke	Samples with LECO	Samples with pet coke	Samples with LECO	Samples with pet coke	Samples with LECO	Samples with pet coke	Samples with LECO
Briquettes	100:0	26.1	26.1	26.7	26.7	26.8	26.8	–	–
	90:10	35.1	31.6	48.7	42.4	–	34.4	–	–
	80:20	32.8	30.8	38.2	–	53.2	–	45.21	–
	70:30	–	–	–	–	–	–	–	–
Pellets	100:0	25.4	25.4	25.7	25.7	26.8	26.8	–	–
	90:10	34.5	29.4	35	33.5	33.1	34.7	35.42	49.37
	80:20	33.5	46.9	44.5	45.7	40.7	46.1	43.71	45.25
	70:30	–	23.9	–	41.5	–	45.9	–	–
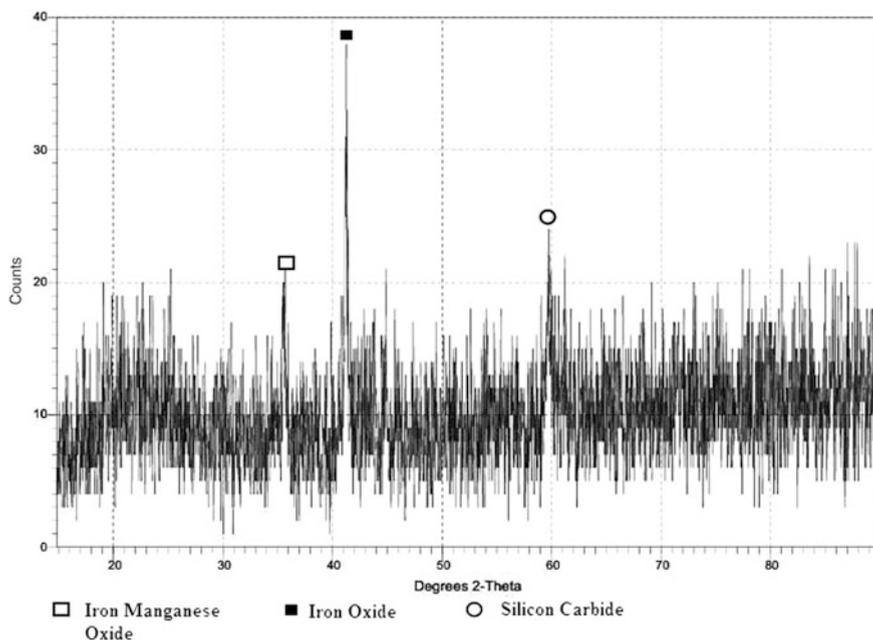
Fig. 2 XRD analysis of sample reduced at 1150 °C (20% LECO, pellet)
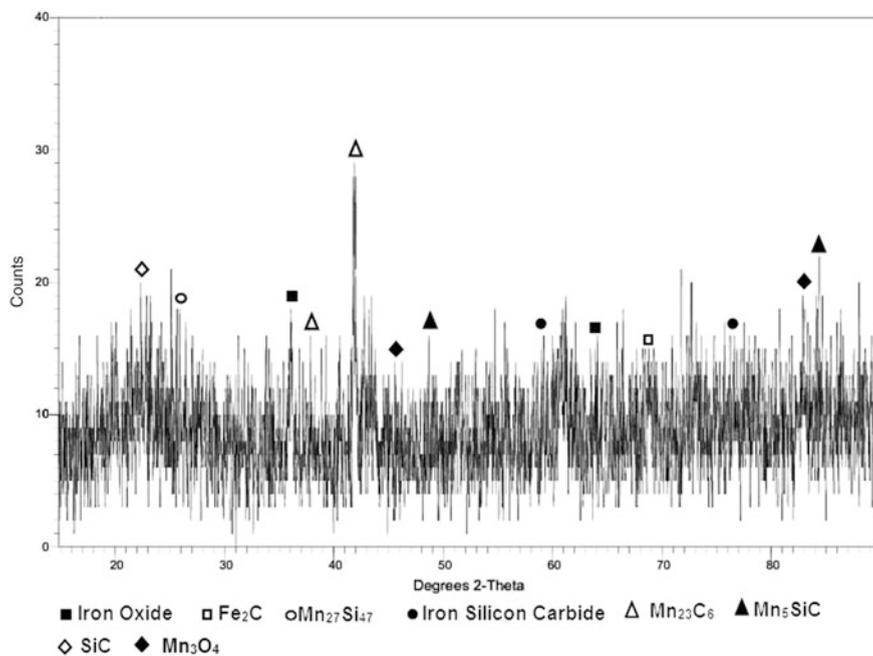
Fig. 3 XRD analysis of sample reduced at 1200 °C (20% LECO, pellet)
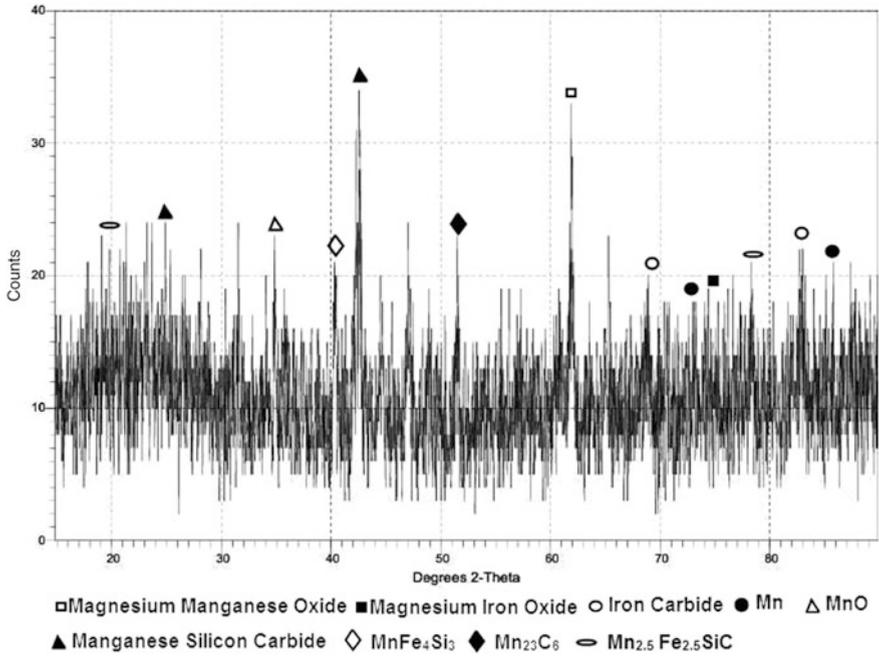
Fig. 4 XRD analysis of sample reduced at 1250 °C (20% LECO, pellet)
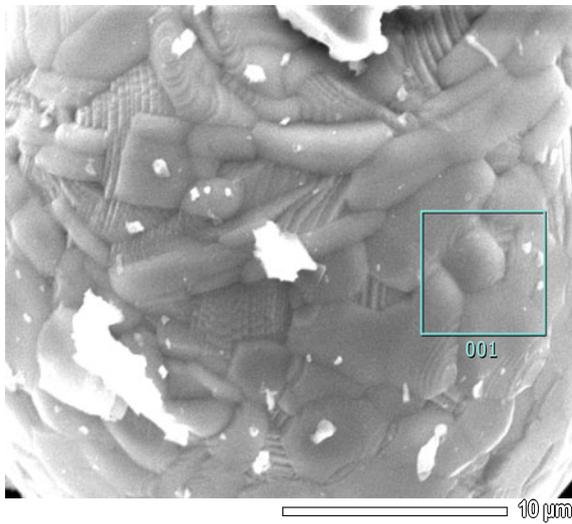
Fig. 5 Pellet with 10% pet coke reduced at 1200 °C

Fig. 6 Pellet with 20% pet coke reduced at 120
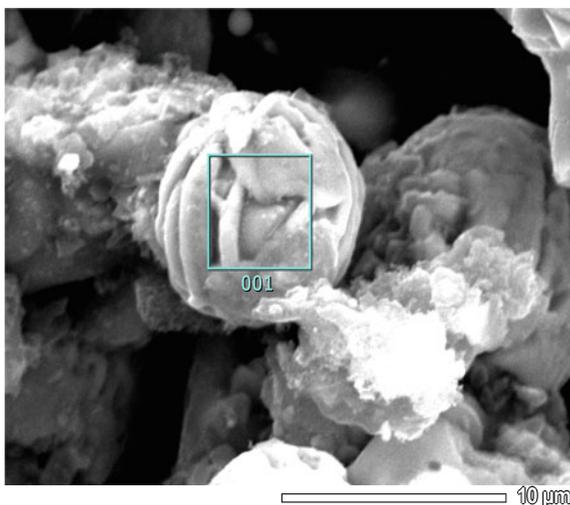
Fig. 7 Briquette with 20% pet coke reduced at 1250 °C
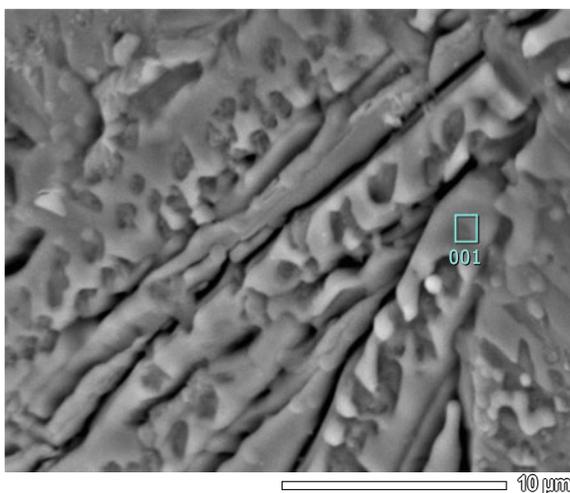
1. Significant amount of carbides (Fe–Mn–Si carbides) formed only at temperatures 1250 °C and above and only when the internal reductant (pet coke or LECO) was 20% or more. Carbide formation was accompanied by the apparent fusion of the carbide phase. In one case, rib-like formation of carbide was observed.

2. Pet coke tends to make more carbon available for reaction as compared to LECO. Indications are that only fixed carbon is made available for reduction of MnO and FeO. Assuming that higher oxides of Fe and Mn are reduced to bivalent oxides by the gases from the surrounding charcoal, the stoichiometric requirement for carbide formation of pet coke is 12% and of LECO is 16%.

Fig. 8 Pellet with 30% LECO reduced at 1200 °C
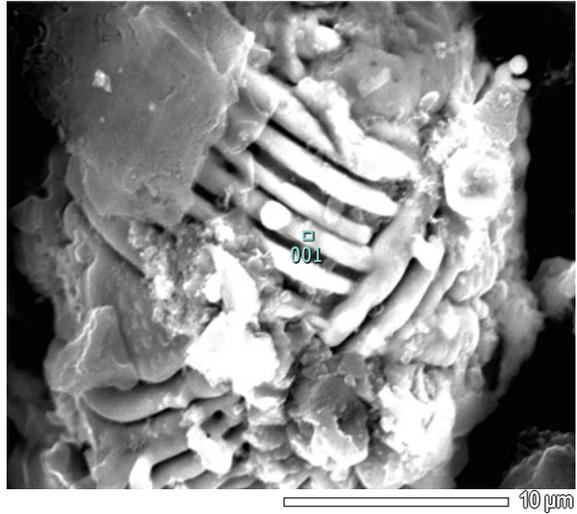
Fig. 9 Pellet with 20% LECO reduced at 1250 °C
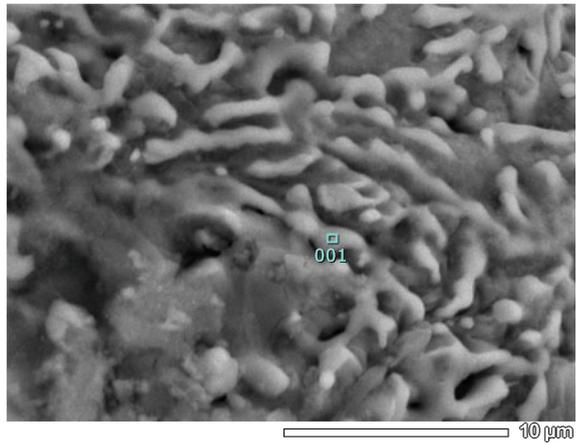
3. LECO tends to give a higher reduction rate as compared to pet coke.
4. At higher carbon contents both pellets and briquettes have lower strength.
5. Pellets are more stable than briquettes. Pellets retain shape more easily than briquettes. Probably, the higher porosity of pellets is helping in the easy exit of gases formed during reduction. In briquettes, these gases tend to leave more cracks.

References

1. Gupta, C.K., Suri, A.K.: Ferroalloys Technology in India, pp. 52–67. Milind Publications Private Limited, New Delhi (1982)
2. Hooper, R.T.: The production of ferromanganese. J. Met. 88–92 (1968)
3. Yi, L., Huang, Z., Jiang, T., Zhao, P., Zhong, R., Liang, Z. :Carbothermic Reduction of Ferruginous ManganeseOre for Mn/Fe Beneficiation: Morphology Evolution and Separation Characteristic. MDPI (2017)
4. Berg, K.L., Olsen, S.E.: Kinetics of manganese ore reduction by carbon monoxide. Metall. Mater. Trans. B **31B**, 477–490 (2000)
5. Kuo, K., Persson, L.E.: A contribution to the constitution of the ternary system Fe-Mn-C. Isothermal sections at 1050°, 910° and 690 °C. J. Iron Steel Inst. **178**, 39–44 (1954)
6. Akhil, C., Geveci, A.: Optimization of conditions to produce manganese and iron carbides from Denizli-Tavas manganese ore by solid state reduction. Turk. J. Eng. Env. Sci. **32**, 125–131 (2008)
7. Grimsley, W.D., See, J.B., King, R. P.: The mechanism and rate of reduction of Mamatwan manganese ore fines by carbon. J. S. Afr. Inst. Min. Metall. **78**, 51–62 (1977)
8. Eric, R.H., Bhalla, A., Halli, P., Taskinen, P.: Solid state reduction of iron, manganese and chromium oxide ores with methane. In: Applications of Process Engineering Principles in Materials Processing, Energy and Environmental Technologies. The Minerals, Metals & Materials Series, pp. 307–318. Springer, Cham (2017)
9. Ostrovski, O., Anacleto, N., Ganguly, S.: Reduction of manganese ores by methane containing gas. In: Proceedings of the Tenth International Ferroalloys Congress; INFACON X: Transformation through Technology, pp. 173–183 (2004)
10. Kononov, R., Ostrovski, O., Ganguly, S.: Carbothermal soild state reduction of manganese ores: 2. Non-isothermal and isothermal reduction in different gas atmospheres. ISIJ Int. **49**(8), 1107–1114 (2009)

A Study on Effect of Additives on Strength Characteristics of Marine Clay

Anu Mathew, Nikhil Sivaramakrishnan, Sobha Cyrus and M. Kavitha

1 Introduction

Marine clay is variable and complex material but because of its low cost and availability it may be altered by addition of small amounts of additives to the soil. Soil stabilization means refining the properties of soil by mechanical or chemical means to create an improved soil material having the desired engineering properties. As large areas are covered with highly plastic and expansive soil, it has become necessary to improve engineering properties of soil before construction. With increasing scarcity of river sand, soil and natural aggregates across the country, there is a need to substitute soil and sand with other materials which are sustainable and economical [1]. Lime treatment or stabilization has been conventionally used in engineering practice to improve the strength characteristics and engineering properties of cohesive soils [2, 3]. Lime generally improves the performance of soils. Lime treatment has a number of natural disadvantages, such as carbonation, sulphate attack and environment impact [4]. Bio-enzymes have been developed as a

A. Mathew (✉) · M. Kavitha
Civil Engineering, Rajagiri School of Engineering and Technology,
Kakkanad, Kochi, Kerala, India
e-mail: anumk@rajagiritech.edu.in

M. Kavitha
e-mail: kavitham@rajagiritech.edu.in

N. Sivaramakrishnan
Civil Engineering, Government Engineering College, Kannur, Kannur, Kerala, India
e-mail: nikhilsivaramakrishnan@gmail.com

S. Cyrus
Civil Engineering, School of Engineering, CUSAT, Kochi, Kerala, India
e-mail: sobharoythomas@gmail.com

new chemical for soil stabilization. Bio-enzymes are chemicals, organic and liquid concentrated substances which are used to improve the stability of soil sub-base of pavement structures. The stability or bearing capacity of soil can be increased by the use of controlled compaction or by the addition of suitable admixtures or stabilizers. The present work focuses on the effect of additives such as lime, copper slag and terrazyme on marine clay.

2 Materials Used

The soil used for the investigation is Cochin marine clay, collected from Valanjambalam, Cochin, Kerela. The boring was carried out by auger method. The sides were protected by casing pipes during boring. The representative samples were taken from a depth of 12.5 m. The soil was dark grey in colour on visual inspection. The samples were sealed in polythene bags and brought to the laboratory. The collected sample was mixed immediately to make it into a homogenous soil mass and was stored in polythene bags, so that its natural moisture content is maintained, and stored in a tank for further tests.

Representative samples of moist marine clay were spread in large trays and exposed to sunlight and dried to constant weight. The lumps formed during drying were broken by a wooden mallet. The samples were pulverized using a heavy hammer and passed through 1.18-mm sieve. The clay samples so prepared were kept in polythene bags. The property of marine clay used for the study is given in Table 1. The different additives used were lime, copper slag and terrazyme which is a bio-enzyme.

Table 1 Index properties of the soil used

Property	Air-dried clay
Moisture content (%)	6
Specific gravity	2.52
Atterberg limits	
Liquid limit (%)	86
Plastic limit (%)	33
Shrinkage limit (%)	24
Grain size distribution	
Clay (%)	13
Silt (%)	39
Sand (%)	48

3   Sample Preparation

Soil samples have been prepared by varying lime percentage as 0, 2, 4, 6 and 8% at OMC for unconfined compressive test. Samples were prepared based on the optimum lime content and was cured for 7 days and then tested. Soil samples have been prepared by varying copper slag percentage as 0, 18, 20, 22 at OMC. The optimum copper slag content mixed with optimum lime content samples was prepared and cured for 7 days and then tested. Soil samples have been prepared by varying terrazyme percentage as 0.25, 0.5, 0.75% at OMC, and optimum terrazyme content was found. Samples were prepared with optimum moisture content and cured for one to six weeks and tested.

4   Results and Discussions

4.1   Effect of Lime

UCC tests were conducted on air-dried marine clay mixed with various percentages of lime. The percentages of lime used were 2, 4, 6, 8. The stress–strain curves showing the variation of treated marine clay are shown in Fig. 1. It can be seen from the figure that when lime is added to the soil, the nature of the stress–strain curves changes from a ductile nature to a brittle one. This is evident from the figure that as the percentage of lime added increases, the unconfined compressive strength increases up to 5% of lime and then decreases. It clearly indicates that the axial stress at failure, for lime-treated marine clay is more than that of air-dried marine clay for all percentages of lime. Also for all percentages of lime, the unconfined compressive strength is greater than that of untreated marine clay. It can be seen that the soil becomes more brittle and the failure occurs at a strain lesser than that of uncured sample.

The variation of unconfined compressive strength with lime content is depicted in Fig. 2. The UCC strength increases with increase in lime content up to 5% and then decreases. The UCC strength of marine clay increases from 304 to 500 kPa showing up to 64% increase upon addition of lime. Upon curing, the unconfined compressive strength is increased from 304 to 722 kPa showing a 138% increase. It can be concluded from the figure that the optimum lime content for both cured and uncured lime-treated marine clay is 5%. Curing of lime causes 2.15 times increase in unconfined compressive strength than the uncured state.

In order to study the effect of curing on the strength of marine clay, UCC samples were prepared at lime contents of 2, 4, 6 and 8% at maximum dry density and OMC. The samples were placed inside polythene bags, and the moisture content was maintained for 7 days. The stress–strain characteristics of marine clay treated with lime after curing for 7 days are plotted and are as shown in Fig. 3.
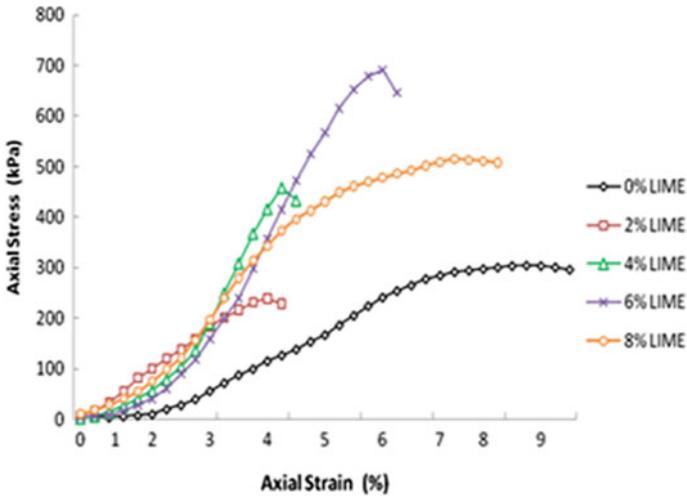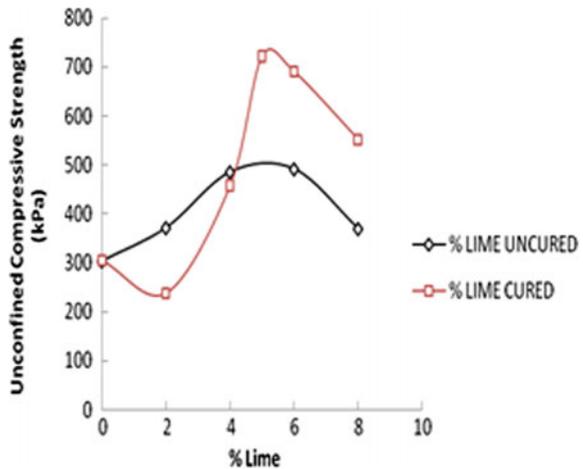
Fig. 1 Stress–strain curves of marine clay treated with different percentages of lime

Fig. 2 Curve showing optimum lime content

From Figs. 1 and 3, the change in the nature of the curve from ductile for soil alone, to a gradual brittle nature for soil treated with lime (uncured) and then to an extremely brittle failure for lime-treated and cured marine clay can be inferred.

The grain size distribution curves for soil alone, lime-treated marine clay (cured and uncured) are shown in Fig. 4. The clay, silt and sand contents of air-dried clay, lime-treated marine clay (cured and uncured) are (13, 39, 48%), (8, 40, 52%) and (13, 40, 57%), respectively. The curve shows the shift in particle passing 75-μ sieve from
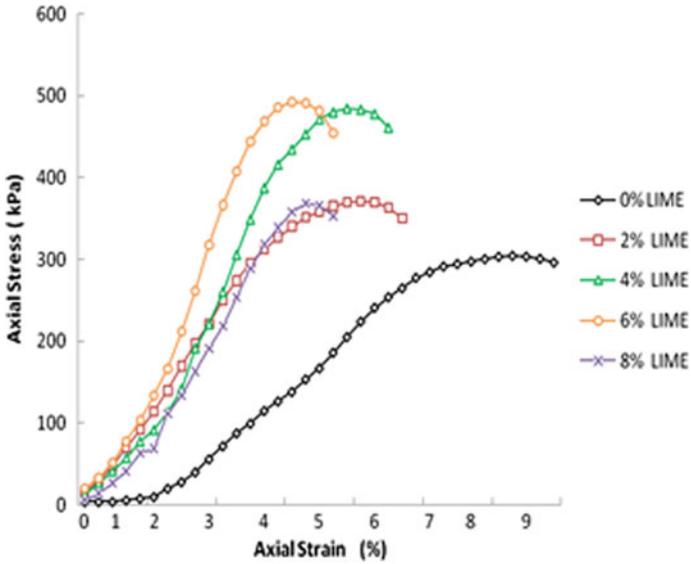
Fig. 3 UCC curves showing variation in strength of lime-treated marine clay on curing

Fig. 4 Grain size distribution curves of marine clay treated with lime
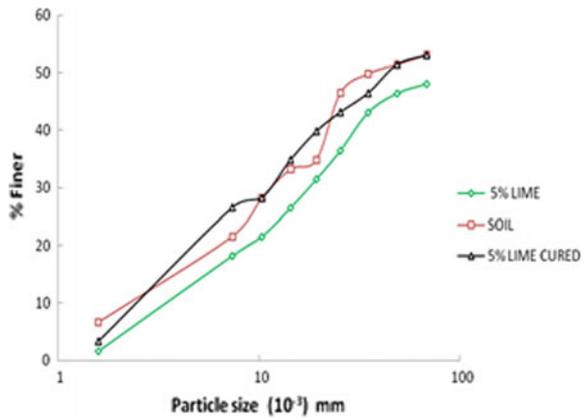
48% of air-dried marine clay to 52 and 57% (cured and uncured) for lime-treated marine clay. This clearly indicates that agglomeration has occurred when lime is added to soil, because of the increase in unconfined compressive strength.

4.2 Effect of Copper Slag

Since the addition of copper slag had an adverse effect on the strength characteristics of marine clay shown in Fig. 5a, it was decided to add the optimum lime content obtained in the above section to copper slag-amended marine clay. Hence, UCC tests were conducted on soil samples mixed with 5% lime and copper slag content varying from 18 to 25%. Figure 5b shows typical stress–strain characteristics of marine clay when treated with 5% lime and varying copper slag content.

The UCC strength increases with increase in copper slag content up to 20% and then decreases. The unconfined compressive strength is increased from 304 to 792 kPa showing a 161% increase which may be due to high internal friction of copper slag.

Figure 5b shows that optimum copper slag content is 20% when mixed with 5% lime, which can be reaffirmed from Fig. 6.

In order to understand the effect of curing UCC tests were conducted on soil samples mixed with 20% copper slag and 5% lime cured for 7 days. Figure 7 shows the effect of curing on the stress–strain characteristics of marine clay mixed with copper slag and lime. Upon curing, the unconfined compressive strength is increased from 304 to 611 kPa showing a 101% increase.

The grain size distribution curves for soil alone, copper slag and lime-treated marine clay (cured and uncured) are shown in Fig. 8. The clay, silt and sand contents of air-dried clay, marine clay mixed with copper slag and lime (cured and uncured) are (13, 39, 48%), (2, 30, 68%) and (6, 42, 52%), respectively. The curve shows the shift in particle passing 75-μ sieve from 48% of air-dried marine clay to 68 and 52% for copper slag and lime-treated marine clay (cured and uncured). This clearly indicates that agglomeration has occurred when lime is added to soil, which could be one of the reasons for the increase in unconfined compressive strength.
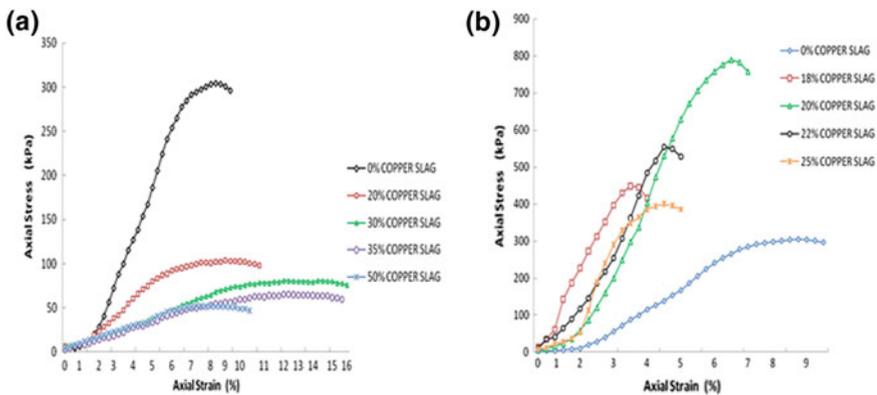

Fig. 5 a Stress–strain curves of marine clay treated with copper slag. b Stress–strain curves of marine clay treated with copper slag and 5% lime

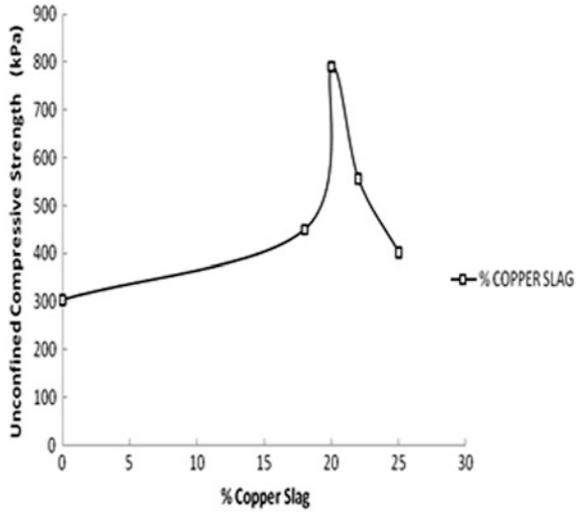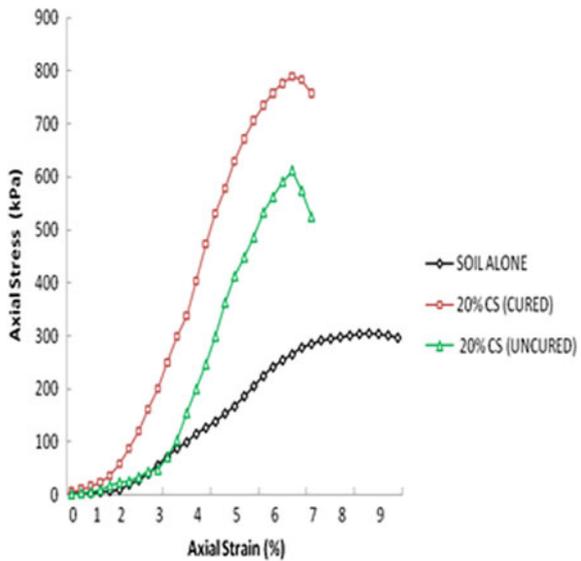**Fig. 6** Curve showing
optimum copper slag content

Fig. 7 UCC curves showing
variation in strength of lime
mixed copper slag-treated
marine clay on curing

4.3 Effect of Terrazyme

UCC tests were conducted on air-dried marine clay mixed with various percentages
of terrazyme. Terrazyme is a viscous liquid; hence, it is mixed with sufficient
amount of water (OMC). It was then added to the soil and mixed thoroughly, and
the test was conducted immediately. The percentages of terrazyme used were 0.25,
0.5, 1.0, 1.5 to the weight of soil. The stress–strain curves showing the variation of

Fig. 8 Grain size distribution curves of marine clay treated with lime and copper slag
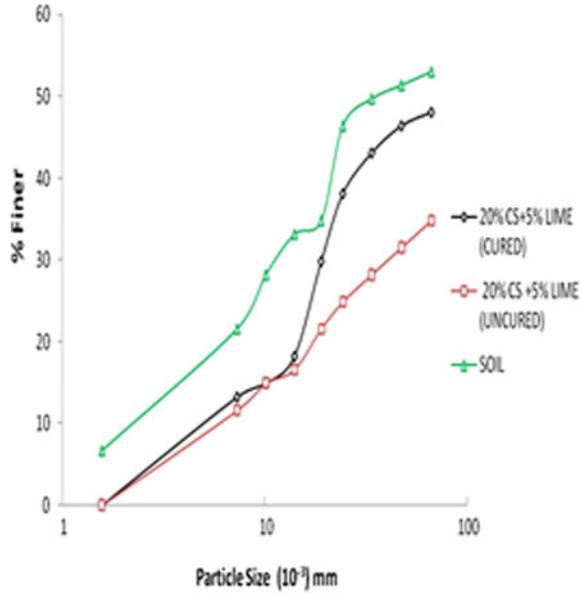
treated marine clay are shown in Fig. 9. It can be seen from the figure that when terrazyme is added to the soil, the nature of the stress–strain curves changes from a ductile nature to a brittle one. It is evident from Fig. 9 that as the percentage of terrazyme added increases, the unconfined compressive strength increases up to 0.5% and then decreases. It clearly indicates that the axial stress at failure, for terrazyme-treated marine clay is more than that of air-dried marine clay for all percentages of terrazyme. Also from Fig. 9, it can also be concluded that for all percentages of terrazyme, the unconfined compressive strength is greater than that of untreated marine clay. It can also be concluded from the figure that the optimum terrazyme content is 0.5%. It shows an increase in strength from 304 to 593 kPa accounting for a 95% increase. Figure 10 also shows that optimum terrazyme content is 0.5%.

In order to study the effect of curing on the strength of marine clay, UCC samples were prepared with 0.5% terrazyme at maximum dry density and OMC. The samples were placed inside polythene bags, and the moisture content was maintained for 7, 14, 21, 28, 35, 42 days. The stress–strain characteristics of marine clay treated with terrazyme after curing for every 7 days are plotted and are as shown in Fig. 11. With curing, it can be seen that the soil becomes more brittle and the failure occurs at a lesser strain than that of uncured sample. Upon curing, the unconfined compressive strength is increased to 673, 763, 806, 820, 904 kPa, respectively, showing an increase of 121, 141, 151, 165, 167 and 197% during this period. Figure 12 depicts the percentage increase in strength upon curing. It can be concluded that initially the UCC value of the terrazyme-treated marine clay is comparatively less but upon curing for longer period the strength increases largely.
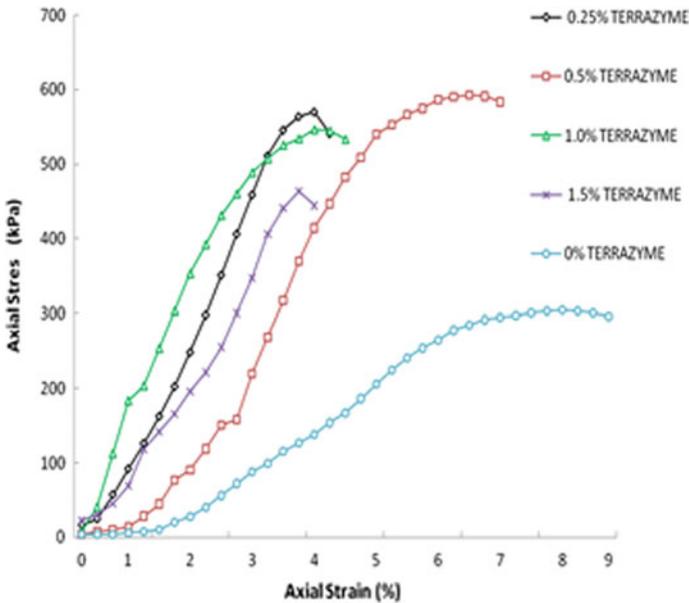
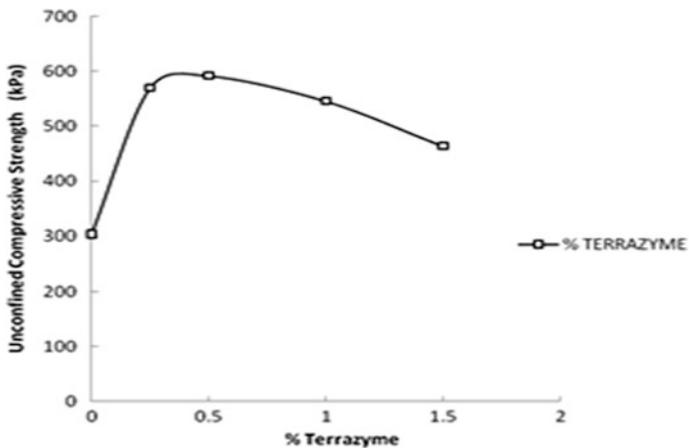**Fig. 9** Stress–strain curves of marine clay treated with terrazyme

Fig. 10 Curve showing optimum terrazyme content

The grain size distribution curves for soil alone, terrazyme-treated marine clay (cured and uncured) are shown in Fig. 13. The clay, silt and sand contents of air-dried clay, marine clay mixed with terrazyme (cured and uncured) are (13, 39, 48%), (10, 41, 49%) and (7, 23, 70%), respectively. The curve shows the shift in particle passing 75-μ sieve from 48% of air-dried marine clay to 47 and 70% for terrazyme-treated marine clay (cured and uncured).
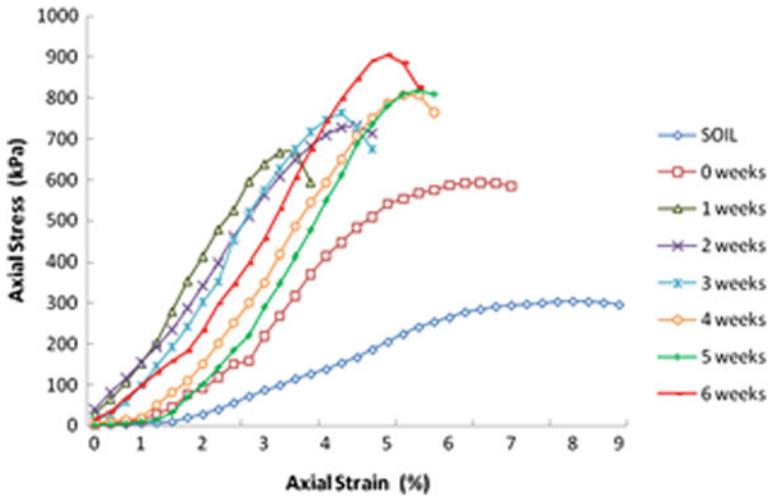
Fig. 11 UCC curves showing variation in strength of terrazyme-treated marine clay on curing

Fig. 12 Percentage increase in strength of soil with terrazyme on curing
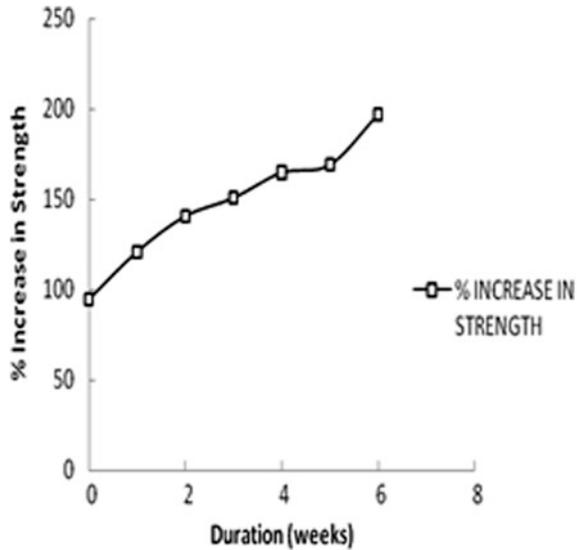
5 Conclusion

Addition of lime to marine clay increases the unconfined compressive strength value by 71% in uncured condition and to 133% in cured condition. The optimum content of lime for maximum unconfined compressive strength is found to be 5% in both cured and uncured conditions. The strength of soil decreased by 33% with the

Fig. 13 Grain size
distribution curves of marine
clay treated with terrazyme
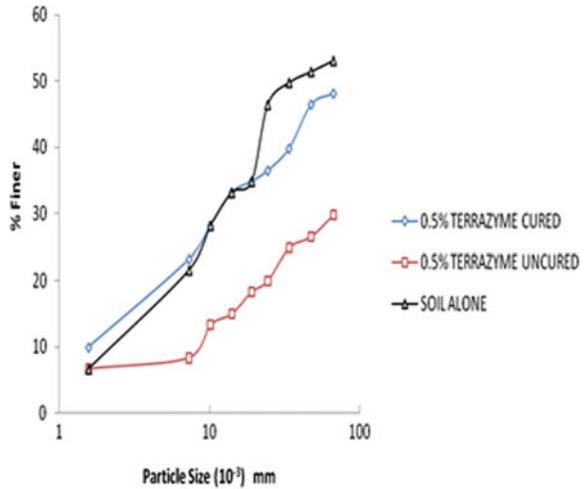
addition of copper slag alone, but with the addition of lime, strength increased by 160% when cured and 101% when uncured. The optimum percentage of copper slag was found to be 20% along with addition of 5% lime. With the addition of terrazyme, the strength increased by 95% without curing and increased by 197% when cured for six weeks. The optimum content of terrazyme was found to be 0.5 g per kilogram of soil. The results indicate that there is an optimum content for each additive and among the additives used for study terrazyme proved to be the best. Hence, terrazyme can be used as a replacement for lime which poses risks to the environment, to stabilize marine clay.

References

1. Darga Kumar, N., Lavnya, C., Sreerama Rao, A.: A review on utilization of copper slag in geotechnical applications. In: Proceedings of Indian Geotechnical Conference, Kochi, vol. 1, pp. 445–448 (2011)
2. Khattab, S.A.A., Al-Mukhtar, M., Fleureau, J.M.: Long-term characteristics of a lime treated plastic soil. J. Mater. Civ. Eng. **19**(4), 358–366 (2007)
3. Muntohar, A.S., Widianti, A., Hartono, E., Diana, W.: Engineering properties of silty soil stabilized with lime and rice husk ash and reinforced with waste plastic fiber. J. Mater. Civ. Eng. (ASCE) **25**(9), 1260–1270 (2013)
4. Jawad, I.T., Taha, M.R., Majeed, Z.H., Khan, T.A.: Soil stabilization using lime: advantages, disadvantages and proposing a potential alternative. Res. J. Appl. Sci. Eng. Technol. **8**(4), 510–520 (2014)

A Brief Study of the Particulate Matter Emissions During the EDM Process

Anand Prakash Dwivedi and Sounak Kumar Choudhury

1 Introduction

These days, the advanced machining processes are taking over the conventional machining processes for creating intricate shapes and miniature features in difficult-to-machine materials. Electric discharge machining (EDM) has attracted the attention of the researchers because of its wide industrial applications. EDM is a well-known and established advanced machining process which is used all over the world for creating complex geometries and machining very hard and electrically conducting materials by the action of an electric spark. Usually, such materials and shapes cannot be machined using the conventional machining processes.

EDM started around 1770 when a Scientist named J. Priestly studied and observed the erosive effects of sparks, ever since then the process has been in the phase of continuous development. In the year 1930, electric discharges were used for the first time to machine metals and diamonds. At that time, the process was said to be known as the "arc or spark machining" [1]. The concept of resistor–capacitor (RC) circuits was introduced for the first time by two Russian Scientists, B. R. Lazarenko and N. I. Lazarenko, in the year 1943 [2]. With this, it became easier to control the pulse time, since they also defined the capacitor charge energy during EDM. Further developments in the machine brought the concept of simple servo-systems which can control the inter-electrode gap (IEG) automatically between the two electrodes. Then around the 1980s came the concept of computer numeric control (CNC) in EDM, which automated the overall machining process of EDM. This also brought changes in the structure and increased the efficiency of the

A. P. Dwivedi (✉) · S. K. Choudhury
Department of Mechanical Engineering, Indian Institute of Technology Kanpur,
Kanpur 208016, India
e-mail: anandpd@iitk.ac.in

machining process. One of the recent advancements in this process is the intro-duction of an adaptive control monitoring system which has given round the clock functioning to this process [3]. EDM finds application in a number of industries like automotive, aeronautical, nuclear which deals with the machining of hard materials. Moreover, the accuracy level achieved using EDM is significantly better than the other non-conventional machining processes. Peak discharge current and pulse on-time are the key input parameters of this process, which can alter the machining and the wear rate [4].

All through this development stage of the EDM process, various aspects of machining of different materials have been explored and many such works are still going on. The environmental side of the EDM process still remains significantly unexplored and needs immediate and special attention, as the process results in the emission of a lot of hazardous and harmful PM and aerosols [5] during the machining, which are severely harmful both for the operator and for the environ-ment [6].

This paper is an attempt to fill in the research voids associated with the emission of such harmful materials. The authors have carried out a preliminary investigation of the PM emissions during the EDM process for the machining of AISI-D3 tool steel.

1.1 Working Principle

EDM is a non-contact-type electrothermal unconventional controlled metal removal process, in which the electrical energy is utilized to generate an electric spark, with the thermal energy of the spark the material removal takes place. The high tem-perature generated at the tool–workpiece interface causes the material to melt and evaporate from the workpiece at a controlled rate. In this way, the workpiece is machined in the desired shape [7]. The detailed schematic diagram of the EDM process is shown in Fig. 1.

1.2 Process Characteristics

The EDM process is basically a non-contact-type electrothermal process used for machining electrically conducting materials, irrespective of its hardness. The material removal rate from the workpiece and tool, during the machining process, depends on the thermal properties of both the electrodes.
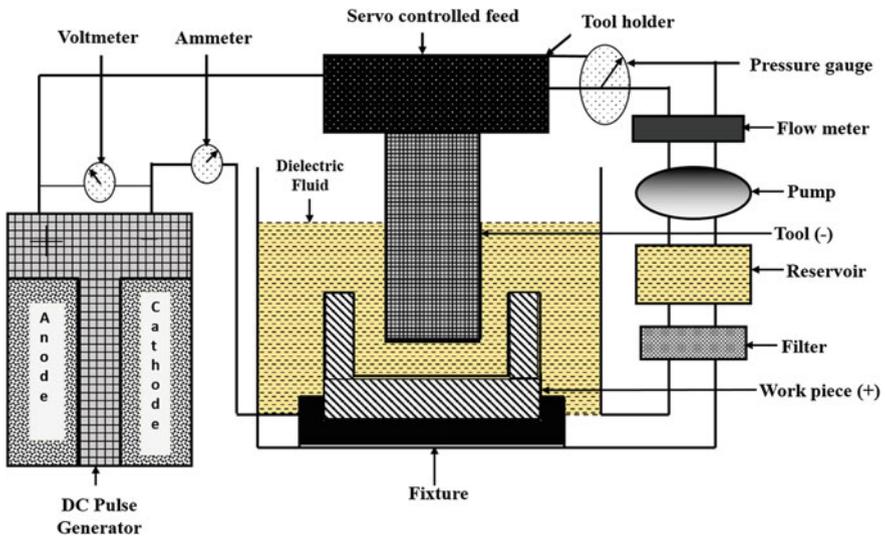
Fig. 1 A schematic diagram of the EDM process

2 Materials and Methods

2.1 Experimental Setup

The experimental setup used for the present study is shown in Fig. 2. Experiments have been performed on the ELEKTRA 5535 Z-axis Numerical Control (EZNC) electric discharge machine. The different experimental parameters used during the study of AISI-D3 steel machining are shown in Table 1. Experiments were performed on AISI-D3 steel flats of thickness 5 mm. Copper rod of 10 mm diameter has been used as the tool electrode.

2.2 Tool and Workpiece Materials

AISI-D3 tool steel has been taken as the workpiece material since it is widely used in the die, roll, and punch manufacturing industries.

Copper has been used as the tool electrode material. It is the most commonly used EDM tool material because of its high thermoelectrical conductivity, ease of machinability, economic nature, and easy availability.

Fig. 2 Experimental setup on ELEKTRA 5535 ZNC EDM machine

Table 1 Experimental parameters

Input parameters	Values
Current settings (A)	30
Voltage (V)	75
Ton (μsec)	150
Toff (μsec)	58.33
Polarity	Positive
Feed rate (mm/sec)	0.88
Dielectric	EDM (paraffin) oil

2.3 Particulate Matter (PM) Emission

The PM emissions during the EDM process have been captured and measured using the GRIMM portable aerosol spectrometer (PAS) as shown in Fig. 3. The spectrometer was connected to the EDM, and then machining was performed on the

Fig. 3 Portable aerosol spectrometer for PM measurement

AISI-D3 workpiece. The spectrometer has been operated to capture the emissions continuously for 132 min with a sample interval of 1 min each, i.e., the machine captured a total of 132 observations in 132 min of continuous operation.

The data captured shows the actual mass (in µg/m^3) of aerosol emission corresponding to the size of PM. A detailed analysis of the captured PM data is done in the results and discussion section.

3 Results and Discussion

The results obtained from the spectrometer show that the EDM process releases a high amount of PM during the machining process. These aerosol particles are of different sizes which can be as large as 20 µ or even bigger than that and the finer particles can be as small as 1 µ or even lesser. All these particles, be it the finer ones or the coarser ones are harmful to both the operator and the environment. Some researchers have thus recommended the use of water or gas-based dielectrics [8].

Figure 4 shows the graphical trend of the aerosol emissions during the observation period of the study. It can be seen from the figure that the peaks at some points are very high, i.e., the emission level (mass in µg/m^3) is almost close to 4000 µg/m^3.

In order to confirm the presence of the aerosols, the PAS filter (47 mm in diameter and made of Teflon) which is installed in the instrument was analyzed through the SEM, EDS, and ICPMS techniques. All these are discussed in the later part of this section.

Figure 4 clearly depicts the aerosol emission trend during the EDM process. It includes the emission contents ranging from 1 to 20 µm (>1, >2, 3, 4, 5, 10, 15, 20 µm). Furthermore, the following analyses have been done to analyze the emissions in detail.
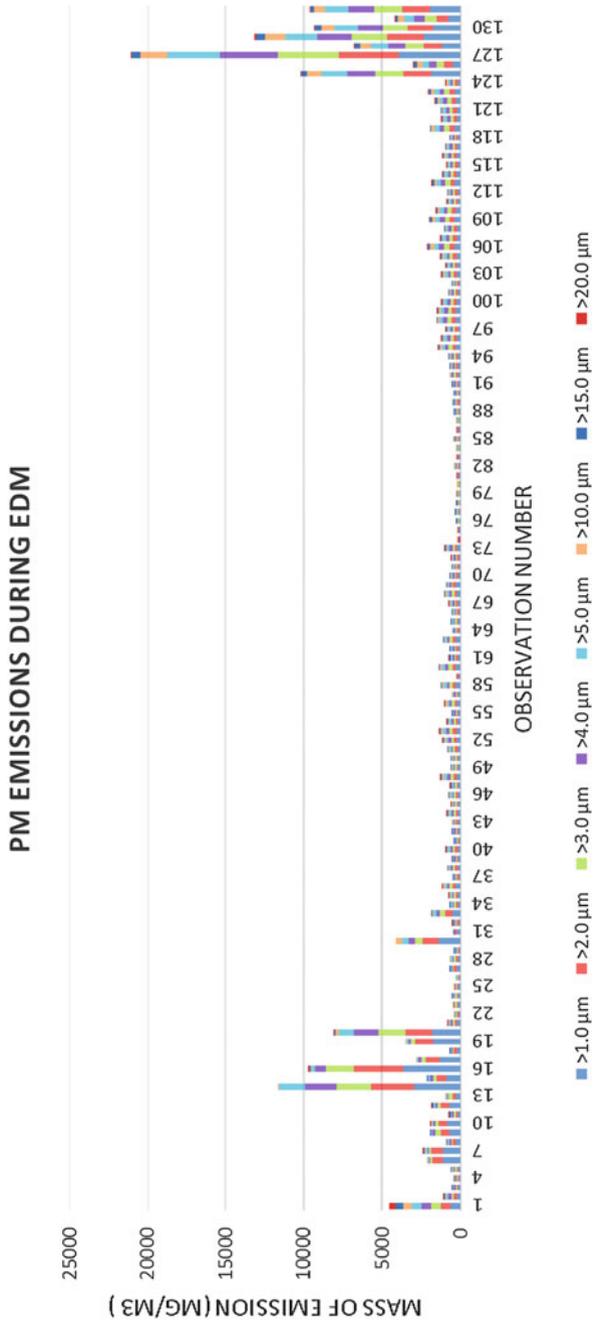
Fig. 4 PM emissions during the EDM process

3.1 Scanning Electron Microscope (SEM) Imaging

The PAS filter was further analyzed with the SEM. Figure 5a shows the deposition of matter clusters distributed all over the sample surface. Moreover, Fig. 5b shows the material deposition mapping on the filter surface. Both the images clearly show the emissive material deposition on the PAS filter. The mapping image depicts the deposition variation on the PAS filter after the EDM process.

3.2 Energy Dispersive Spectroscopy (EDS)

In order to analyze the constituents released during the EDM process, the deposited material was further examined using the EDS technique. Figure 6 shows the EDS images giving details of the aerosols captured by the portable aerosol spectrometer device. Out of the total deposition captured, Carbon (C) occupies 32.85% (by mass), Iron (Fe) 2.48% (by mass), Copper (Cu) 1.80% (by mass), Chromium (Cr) 0.21% (by mass), and Nickel (Ni) 0.17% (by mass).

3.3 Inductively Coupled Plasma Mass Spectroscopy (ICPMS)

After the EDS process, ICPMS technique is employed to get the intensity versus particle mass spectra. Figure 7 shows the intensity versus mass plots for the EDM process. The maximum intensity obtained during the process (as shown by the spectra) is slightly more than 11×10^6 counts per s. This figure also indicates the presence of different matters of varying intensities deposited on the PAS Teflon filter, during the EDM process.
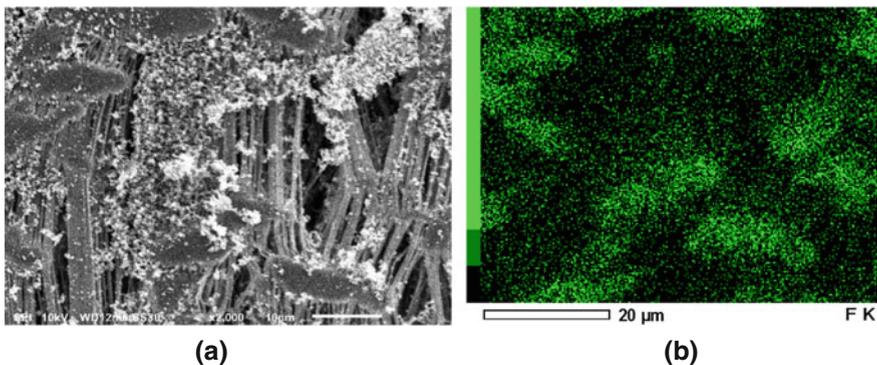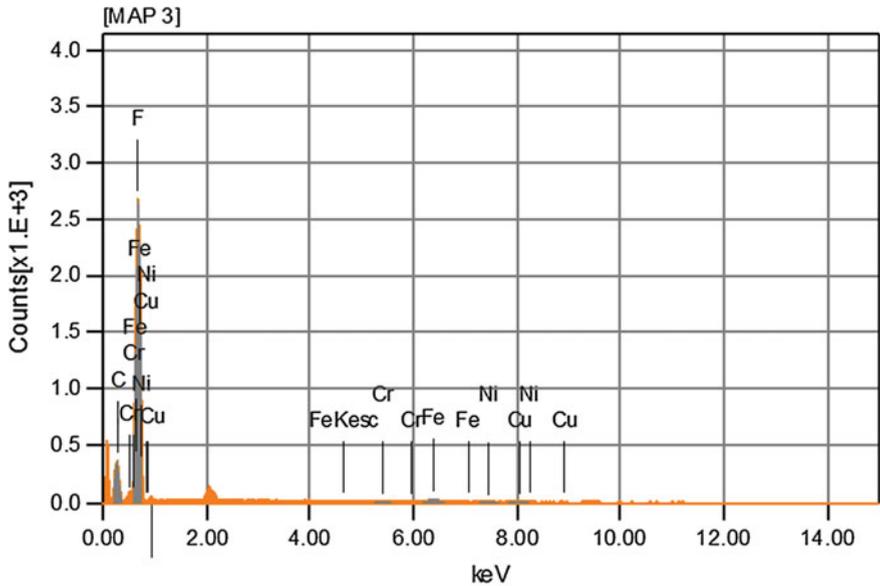

(a)   **(b)**

Fig. 5 SEM image and deposition mapping showing clusters of material deposition

Fig. 6 EDS image showing the materials deposited on the spectrometer filter after the EDM process

Chemical formula	mass%	Atom%	Sigma	Net	K ratio	Line
C•	32.85	44.81	0.09	8669	0.0008690	K
F	62.48	53.88	0.25	63266	0.0437566	K
Cr•	0.21	0.07	0.06	258	0.0000840	K
Fe•	2.48	0.73	0.08	2222	0.0009689	K
Ni•	0.17	0.05	0.08	108	0.0000660	K
Cu•	1.80	0.46	0.13	930	0.0006625	K
Total	100.00	100.00				

4   Conclusion

From the present study, it can be concluded that although EDM being one of the most important advanced machining processes used these days for creating intricate shapes and machining complex geometries in high strength conducting materials, yet the process is not completely eco-friendly. It is harmful both for the operator and the environment also. Many particulate matters of different sizes ranging up to 20 μ have been investigated during the machining process. This can prove to be hazardous for the operators for prolonged operations. The study is further being
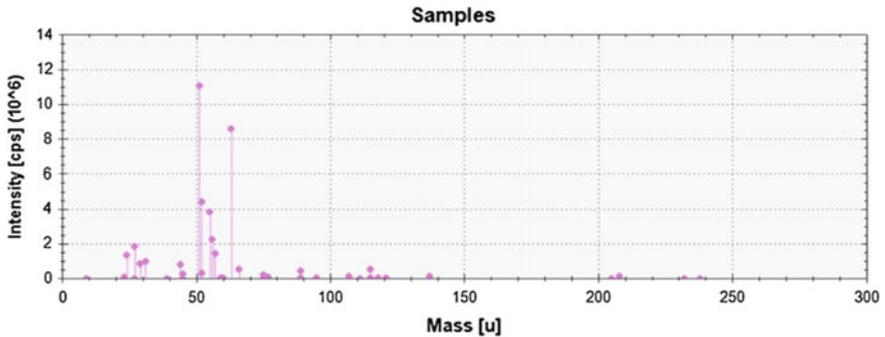
Fig. 7 ICPMS plots showing the intensity of the PM deposition on the spectrometer filter after the EDM process

carried out on the effect of different input variables and their effect on the emissions. More attention of the scientific community is required to make these advanced machining processes environment friendly and harmless for the society.

This being a preliminary study shows a promising research avenue in the direction of environmental aspects of the EDM process. This side of the EDM process should be more and more investigated, and proper solutions should be recommended for the production industry to make EDM as an eco-friendly process.

References

1. Ho, K.H., Newman, S.T.: State of the art electrical discharge machining (EDM). Int. J. Mach. Tool Manuf. **43**, 1287–1300 (2003)
2. Lazarenko, B.R.: To invert the effect of wear on electric power contacts. Dissertation of the All-Union Institute of Electro Technique in Moscow/CCCP, Russia (1943)
3. Kumar, S., Singh, R., Singh, T.P., Sethi, B.L.: Surface modification by electrical discharge machining: a review. Int. J. Mater. Process. Technol. **209**, 3675–3687 (2009)
4. Torres, A., Puertas, I., Luis, C.J.: Modeling of surface finish, electrode wear and material removal rate in electrical discharge machining of hard-to-machine alloys. Precis. Eng. **40**, 33–45 (2015)
5. Sutherland, J.W.: Environmental attributes of manufacturing processes. In: Handbook of Environmentally Conscious Manufacturing, chap. 13, pp. 293–316 (2001)
6. Cho, M.H.: Environmental Constituents of Electrical Discharge Machining. MIT, USA (2004)
7. Dwivedi, A.P., Choudhury, S.K.: Effect of tool rotation on MRR, TWR and surface integrity of AISI-D3 steel using rotary EDM process. Mater. Manuf. Process. **31**(14), 1844–1852 (2016)
8. Leao, F.N., Pashby, I.R.: A review on the use of environmentally-friendly dielectric fluids in electrical discharge machining. J. Mater. Process. Technol. **149**, 341–346 (2004)

A Preliminary Study of the Air Pollutants Discharge During the Electric Discharge Machining Process

Anand Prakash Dwivedi and Sounak Kumar Choudhury

1 Introduction

Electric Discharge Machining (EDM) process is one of the most widely used unconventional machining processes which is commonly used across the world for machining hard to cut materials and creating complex geometries in high strength and electrically conducting materials and their alloys, by the action of the electric spark. In general, such objectives are not achieved by many of the other conventional or unconventional machining processes. Because of this, even after the advent of many modern machining techniques, EDM holds its own place in the machining industries. The process has very wide applications in various industrial sectors. Henceforth, EDM remains a topic for continuous research, so that the process can be improved further to increase the productivity as well as the applications, which ultimately leads to the overall process and efficiency enhancement.

This process came into existence around 1770 when an English Scientist J. Priestly studied the erosive effects of sparks. Ever since then this process has been in the phase of continuous development and even now, there are many researchers working for the further development for the improvement of this process. It was in the year 1930 when the electric discharges were first used for the machining of metals and diamonds. Basically, during the initial days, this process was known as the "arc or spark machining" process, as it was completely based on the electrical discharges [1]. Then, later on, the concept of RC (resistor–capacitor) circuits came into the picture for the first time by two Russian Scientists, B. R. Lazarenko and N. I. Lazarenko, in the year 1943 [2]. Further developments in the EDM introduced the concept of simple servo systems for controlling the inter-electrode gap (IEG) automatically between the tool and the workpiece.

A. P. Dwivedi (✉) · S. K. Choudhury
Department of Mechanical Engineering, Indian Institute of Technology Kanpur,
Kanpur 208016, India
e-mail: anandpd@iitk.ac.in

The EDM process got overall automated around the 1980s when the concept of computer numeric control (CNC) system in EDM was introduced. This CNC system brought many changes in the structure and enhanced the efficiency of the machining process significantly. Recently, because of the introduction of an adaptive control monitoring system, this process has achieved round the clock functioning [3]. This process has got applications in a number of industries like nuclear, aeronautical, automotive which deals with the machining of hard materials.

During this development stage of the EDM process, different facets of machining of various materials have been investigated and many researchers are still working on this process. But, the environmental effect and facets of the EDM process are yet to get proper attention of the research community. During the EDM process, there is a significant level of pollutant emissions in the environment, which is very harmful and hazardous for the operator and the environment also [4]. This is a threat to the occupational safety, which needs immediate attention as this field is left still significantly unexplored [5].

This paper is in line with the above-discussed research gap. The authors here have studied specifically, the environmental side of the EDM process. A comprehensive study has been made for the air pollutants discharged during the EDM process for the machining of AISI-D3 tool steel (which is widely used in the tool, die and rolling industries). The EDM process results in the emission of carbon monoxide (CO), nitric oxide (NO), nitrogen oxide (NO_x), nitrogen dioxide (NO_2), and other fumes (as shown in Fig. 1), a detailed study and analysis of such pollutants have been made, and their emissions have been captured and calculated, which is discussed in detail in the results and discussion section of this paper.

1.1 Process Mechanism

EDM is an electrothermal unconventional controlled metal removal process, where the electrical energy is utilized to generate an electric spark and due to the thermal energy of the spark melting and vaporization of both the electrode materials occur, and in this way the material removal takes place in the EDM process. The molten material is flushed away from the machining cavity by the action of the forceful dielectric flush at the machining interface. The electric spark here plays a major role in the material removal process, and the rate of material removal depends on the intensity of the electric spark. A pulsating (on/off) electric charge carrying high-frequency current is given to through the electrode to the workpiece, which results in the removal of material at a controlled rate from both the electrodes (i.e., the tool and the workpiece). Also, the EDM process provides better accuracy level of machining, as the exact tool shape is replicated on the workpiece surface. The major contributing parameters which can alter the machining and the wear rates of the EDM process are the peak discharge current (I_p) and pulse on-time (T_{on}) [6, 7]. The detailed process mechanism of the EDM process is shown in Fig. 2. The tool and the workpiece are connected to the two terminals of the power supply, and

Fig. 1 Fumes emerging out during the EDM process
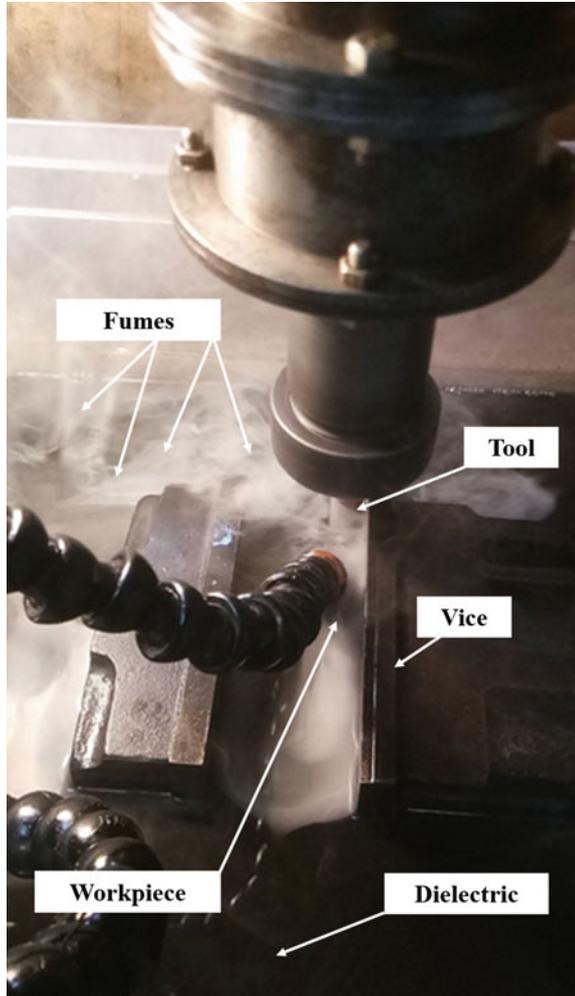
when they are brought closer to each other in the presence of a dielectric medium and at a threshold inter-electrode gap, there occurs an electric spark which removes the material from the electrode surface as discussed before.

1.2 Process Characteristics

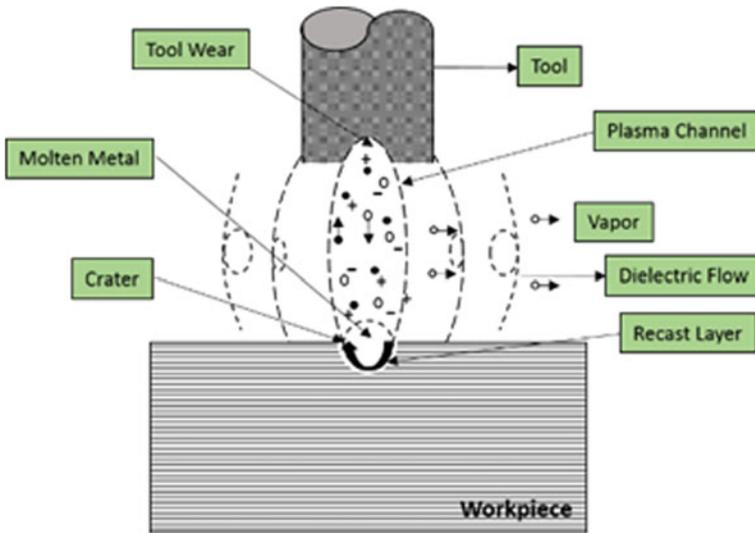(a) The EDM process can be used for machining electrically conducting materials of any hardness.

Fig. 2 EDM process mechanism

(b) The material removal (or erosion) rate (MRR) during the EDM process depends on the thermal properties of the workpiece, rather than its hardness or strength.
(c) Similarly, the tool wear (or erosion) rate (TWR) during the EDM process depends on the thermal properties of the tool material.
(d) There is no physical contact between the tool and workpiece with each other at any point of time during the EDM process.

2 Materials and Methods

2.1 Experimental Setup

ELEKTRA 5535 Z-axis Numerical Control (EZNC) Electric Discharge Machine has been used for carrying out the present study. The experimental setup used is shown in Fig. 2. For carrying out the environmental analysis of the pollutants emerging out during the EDM process, Horiba analyzers for NO, NO_2, NO_x, and CO are used (as shown in Fig. 3).

The experimental parameters used during the study of AISI-D3 tool steel machining are given in Table 1. Experiments were performed on AISI-D3 steel flats of thickness 5 mm. Copper rod of 10 mm diameter has been used as the tool electrode.
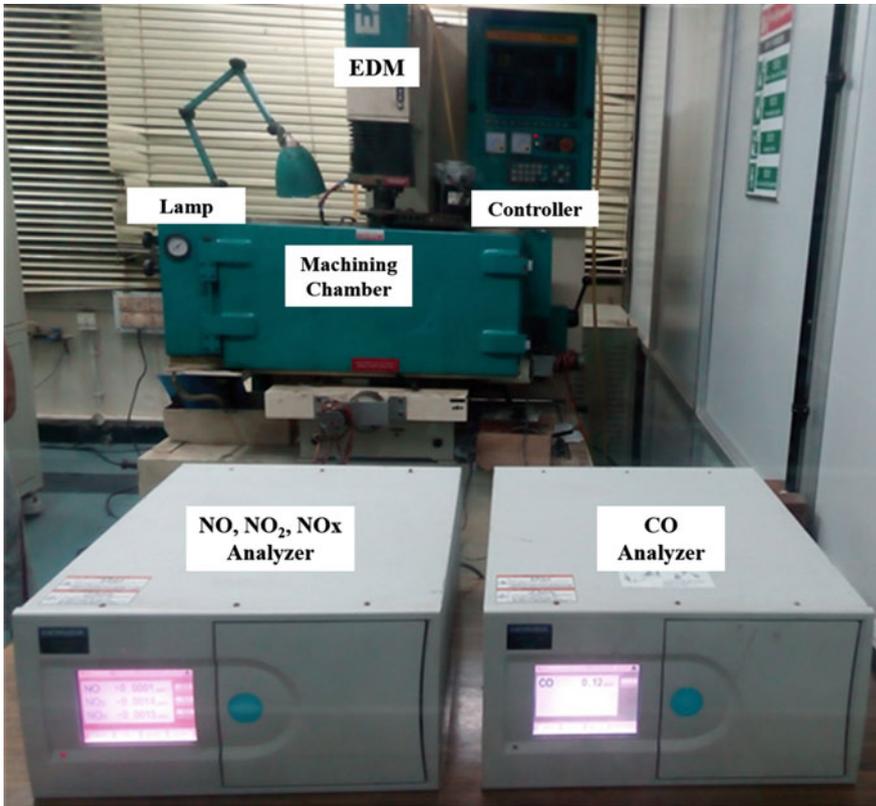
Fig. 3 ELEKTRA 5535 ZNC EDM with NO_x and CO analyzers

Table 1 Experimental parameters

Input parameters	Values
Current settings (A)	25
Voltage (V)	75
T_{on} (μs)	150
T_{off} (μs)	58.33
Polarity	Positive
Feed rate (mm/s)	0.88
Dielectric	EDM (paraffin) oil

2.2 Tool and Workpiece Materials

Copper rods of 10 mm diameter (as shown in Fig. 4) have been used as the tool electrode. Because of its high thermo-electrical conductivity, easy availability, economic nature, and ease of machinability, it is the most commonly used EDM
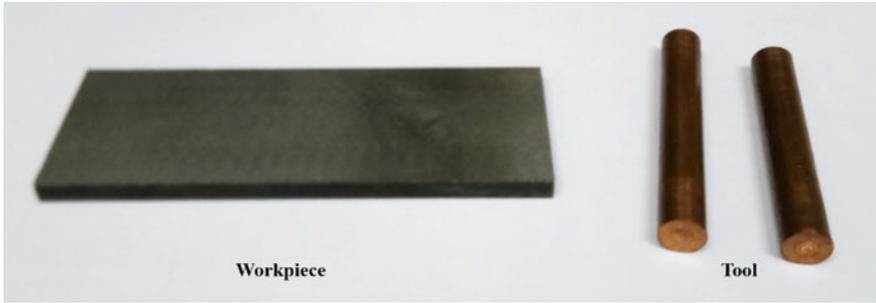
Fig. 4 Tool and workpiece images

tool material. AISI-D3 tool steel plates of 5-mm thickness have been used as the workpiece material. The major application of this type of steel is found in the tool making, die making, rolling, and punch manufacturing industries.

3   Results and Discussion

The results obtained from the NO_x and CO analyzers are shown in Figs. 5 and 6. Table 2 shows the minimum and maximum levels of emissions captured in ppm by the analyzers; it also shows the average value of emissions during the EDM machining process.
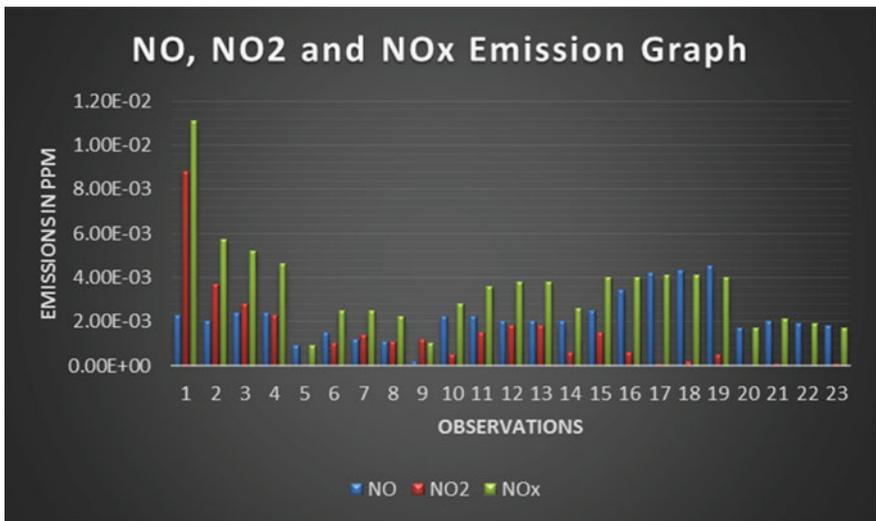

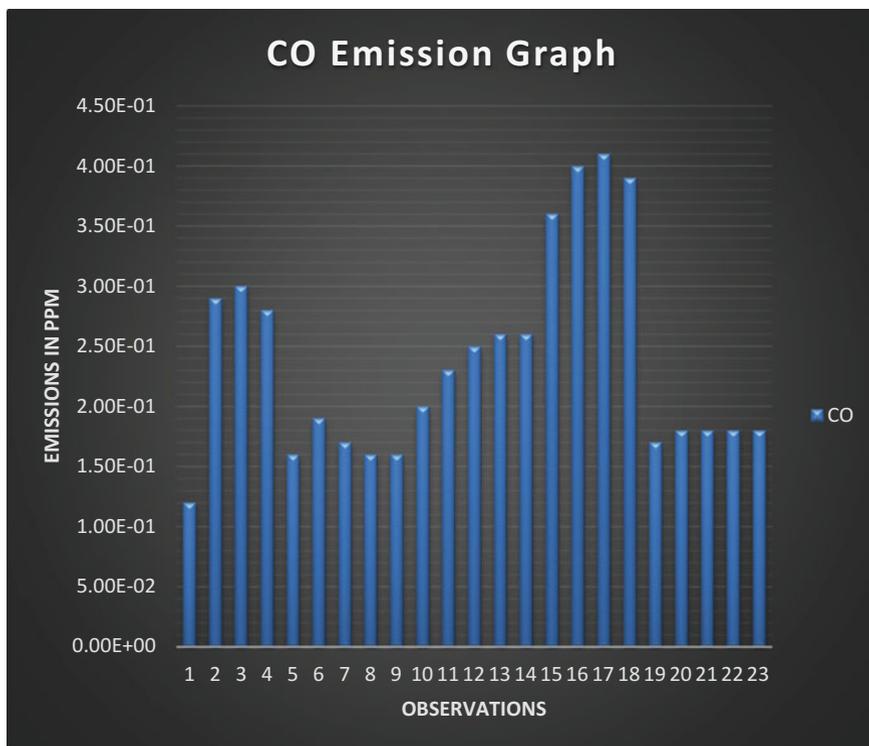**Fig. 5**   NO, NO_2, and NO_x emissions during the EDM process

Fig. 6 CO emission during the EDM process

3.1 NO, NO$_2$, and NO$_x$ Emissions

During the experimentation process, a significant amount of nitric oxide (NO), nitrogen dioxide (NO$_2$), and nitrogen oxide (NO$_x$) were evolved and captured by the Horiba NO$_x$ analyzer (as shown in Fig. 3). Table 2 clearly shows the maximum levels of these gases, which are 0.0045, 0.0088, and 0.01 ppm, respectively. During the process, the average emission was recorded to be 0.0022, 0.00137, and 0.00347 ppm, respectively, for NO, NO$_2$, and NO$_x$.

Table 2 PM emissions during the EDM process

S. No.	Pollutant	Maximum emission (ppm)	Minimum emission (ppm)	Average emission (ppm)
1.	NO	0.0045	0.0002	0.0022
2.	NO$_2$	0.0088	0.00	0.00137
3.	NO$_x$	0.01	0.0009	0.00347
4.	CO	0.41	0.17	0.238

Overall, there were 23 sets of observation made, the values of which have been plotted and shown in Fig. 5. Each set of observation contains the values of all three gases, viz., NO, NO_2, and NO_x. The graph clearly indicates that there were significant emissions which were recorded by the NO_x analyzer throughout the machining process.

3.2 CO Emission

During the EDM machining process apart from NO_x, there were some other harmful flue gases also which evolved in the environment like carbon monoxide (CO). The Horiba CO analyzer (as shown in Fig. 3) was used to capture the levels of CO emissions during the EDM process. Table 2 clearly shows the maximum levels CO emission during the process. During the machining process, the maximum level of CO emission was recorded to be 0.41 ppm, whereas the average CO emission was found to be 0.238 ppm.

Here also, there were a total of 23 sets of observation made, the values of which have been plotted and shown in Fig. 6. Compared to the NO_x, CO emissions were found to be more and they showed average and increasing trends. The CO emission graph clearly indicates that there was a significant level of emissions throughout the machining process (as shown in Fig. 6).

4 Conclusion

By the presented study, it can be concluded that though EDM being one of the foremost important unconventional machining processes used across the world for creating complex shapes and making intricate geometries in high-strength-conducting materials, yet the process is not completely eco-friendly.

It results in the emission of many harmful air pollutants like CO, NO, NO_2, and NO_x. This is not healthy for both the occupational safety and environmental perspectives. In long run, persons exposed to such working conditions will have serious health issues, as these flue gases have a very bad impact on both the operator as well as the environment. Further research work is going on in this direction to reduce these emissions and make this process eco-friendly. The authors here seek more attention from the scientific community toward this facet of machining so that to make these advanced machining processes eco-friendly and harmless for the society.

References

1. Ho, K.H., Newman, S.T.: State of the art electrical discharge machining (EDM). Int. J. Mach. Tool Manuf. **43**, 1287–1300 (2003)
2. Lazarenko, B.R.: To invert the effect of wear on electric power contacts. Dissertation of the All-Union Institute of Electro Technique in Moscow/CCCP, Russia (1943)
3. Kumar, S., Singh, R., Singh, T.P., Sethi, B.L.: Surface modification by electrical discharge machining: a review. Int. J. Mater. Process. Technol. **209**, 3675–3687 (2009)
4. Cho, M.H.: Environmental Constituents of Electrical Discharge Machining. MIT, USA (2004)
5. Sutherland, J.W.: Environmental attributes of manufacturing processes. In: Handbook of Environmentally Conscious Manufacturing, chap. 13, pp. 293–316 (2001)
6. Torres, A., Puertas, I., Luis, C.J.: Modeling of surface finish, electrode wear and material removal rate in electrical discharge machining of hard-to-machine alloys. Precis. Eng. **40**, 33–45 (2015)
7. Dwivedi, A.P., Choudhury, S.K.: Effect of tool rotation on MRR, TWR and surface integrity of AISI-D3 steel using rotary EDM process. Mater. Manuf. Process. **31**(14), 1844–1852 (2016)